SCHOLARLY PUBLICATIONS

A CURRENT AWARENESS BULLETIN
OF RESEARCH OUTPUT

@DTU

(43rd Edition)

JULY 2016

BY: CENTRAL LIBRARY

DELHI TECHNOLOGICAL UNIVERSITY
(FORMERLY *DELHI COLLEGE OF ENGINEERING)*
GOVT. OF N.C.T. OF DELHI
SHAHBAD DAULATPUR, MAIN BAWANA ROAD
DELHI 110042

PREFACE

This is the **Forty third** Issue of Current Awareness Bulletin started by Delhi Technological University, Central Library. The aim of the bulletin is to compile, preserve and disseminate information published by the faculty, students and alumni for mutual benefits. The bulletin also aims to propagate the intellectual contribution of Delhi Technological University (DTU) as a whole to the academia.

The bulletin contains information resources available in the internet in the form of articles, reports, presentations published in international journals, websites, etc. by the faculty and students of DTU. The publications of faculty and student which are not covered in this bulletin may be because of the reason that the full text either was not accessible or could not be searched by the search engine used by the library for this purpose.

The learned faculty and students are requested to provide their uncovered publications to the library either through email or in CD, etc to make the bulletin more comprehensive.

This issue contains the information published during **July 2016**. The arrangement of the contents is alphabetical. The full text of the article which is either subscribed by the university or available in the web is provided in this bulletin.

Central Library

CONTENTS

1. Active ROCOF Relay for Islanding Detection, ***7.1Pankaj Gupta***, R. S. Bhatia, Member, IEEE and D. K. Jain, Electrical Engineering, DTU

2. AN ANALYSIS OF REACTION TO GREEN PRODUCT INITIATIVES, ***6.Gaurav Dawar*** and ***3.Dr. Seema Singh***, Department of Humanities, DTU

3. Application of statistical tools and hypothesis testing of adsorption data obtained for removal of heavy metals from aqueous solutions, Achla Kaushal, ***3.S.K.Singh***, Department of Environmental Engineering, DTU

4. Atomic Structure Calculations and Study of Plasma Parameters of Al-Like Ions, Arun Goyal, Indu Khatri, Avnindra Kumar Singh, Man Mohan, ***3.Rinku Sharma*** and Narendra Singh, Applied Physics, DTU

5. Controlled deposition of functionalized silica coated zinc oxide nano-assemblies at the air/water interface for blood cancer detection, Chandra ***3.Mouli Pandey,*** Srishti Dewan, Seema Chawla, Birendra Kumar Yadav, Gajjala Sumana, ***3.Bansi Dhar Malhotra,*** Department of Biotechnology, DTU

6. Dezert- Smarandache Theory based Classification of EMG Signals, ***3.Preeti Meena*** and ***3.Malti Bansal***, Department of ECE, DTU

7. Disposition Decisions in Reverse Logistics: Graph Theory and Matrix Approach, ***3.Saurabh Agrawal***, Mechanical, Production & Industrial Engineering Department, DTU

8. ECG Peaks Detection using Principal Component Analysis, ***3.Sahil Dalal*** and ***3.Rajesh Birok,*** Department of ECE, DTU

9. ECG Signals Analysis using PCA with Neural Network and Fuzzy Logic, ***6.Sahil Dalal*** and ***3.Rajesh Birok***, Electronics & Communication Engineering, DTU

10. Energy and Exergy Analysis of Solar Triple Effect Refrigeration Cycle, Manoj Dixit, S. C. Kaushik, and ***3.Akhilesh Arora***, Mechanical Engineering, DTU

11. Friction Stir Processed Copper Studies with Carbon Nanotubes, ***3.V.Jeganathan Arulmoni1*** and ***3.R.S. Mishra***, Mechanical Engineering, DTU

12. Highly Sensitive Electrochemical Immunosensor based on Graphene-Wrapped Copper Oxide-Cysteine Hierarchical Structure for Detection of Pathogenic Bacteria, Chandra Mouli Pandey, Ida Tiwari, Vidya Nand Singh, K.N. Sood, Gajjala Sumana and ***3.Bansi Dhar Malhotra***, Department of Biotechnology, DTU

13. Influence of gate metal engineering on small-signal and noise behaviour of silicon nanowire MOSFET for low-noise amplifiers, Neha Gupta and Rishu Chaujar, Microelectronics Research Lab, Department of Engineering Physics, DTU

14. In-situ electrosynthesized nanostructured Mn3O4-polyaniline nanofibers-biointerface for endocrine disrupting chemical detection, Nawab Singha, Md. Azahar Ali b, Kali Sureshc, Ved Varun Agrawald, Prabhakar Raie, Ashutosh Sharmae, ***3.B.D. Malhotra*** and Renu Johna, Department of Biotechnology, DTU

15. Middle Node Optimization Aigorithm for Global Optimal Path Planning, ***3.Ananya Chandra, 3.Vibhu Jawa, 3.Ishan Mishra***, and ***3.M. Sameer Khan***, DTU

16. New proposal for MCML based three input logic implementation, ***3.Neeta PANDEY, 3.Kirti GUPTA*** and ***3.Bharat CHOUDHARY***, ECE DTU

17. Optimization of High-k and Gate Metal Workfunction for Improved Analog and Intermodulation Performance of Gate Stack (GS)-, GEWE-SiNW MOSFET, ***3.Neha Gupta*** and ***3.Rishu Chaujar***, Microelectronics Research Lab, Engineering Physics, DTU

18. Potential application of mono/bi-layer molybdenum disulfide (MoS2) sheet as an efficient transparent conducting electrode in silicon heterojunction solar cells, ***3.Rimjhim Chaudhary, 3.Kamlesh Patel, 3.Ravindra K. Sinha, Sanjeev Kumar***, and ***3.Pawan K. Tyagi***, Applied Physics, DTU

19. Preclinical evaluation of Di-sodium Alpha ketoglutarate against Isoniazid-Rifampicin Induced Hepatotoxicity, ***6.Lalita Mehra, 6.Priyanka Chhabra, 6.Amit Kumar, 6.Aseem Bhatnagar, 3.Yasha Hasija,*** and ***6.Gaurav Mittal***, Department of Biotechnology, DTU

20. Question Answering over Knowledge Base using Factual Memory Networks, ***3.Sarthak Jain***, Department of Computer Engineering, DTU

21. Ranking of Software Effort Estimation Selection Criteria Based On Fuzzy Set Theory, ***3.Aparna Jindal, 3.Rakesh Garg*** and ***3.Ashu Bansal***, Department of Production and Industrial Engineering, DTU

22. Sequential Optimization for PV Panel Parameter Estimation, ***3.Pallavi Bharadwaj, 3.Kunal Narayan Chaudhury*** and ***3.Vinod John***, Electrical Engineering, DTU

23. Spectroscopic investigation on thermally stable Dy3+ doped zinc phosphate glass for white light emitting diodes, ***3.Kaushal Jha, 3.M. Jayasimhadri***, Luminescent Materials Research Lab, Department of Applied Physics, DTU

24. SVM-KNN and Pixel Gradient based Segmentation Technique for Brain MRI Tumor Images Classification 6.Sahil Dalal, 3.Rajesh Birok, 6.Sanchit Kumar, Department of ECE, DTU

25. Thermoexergetic analysis of Steam Power Plant Rajat Pardal, ***3.B. B. Arora*** and ***3.Subhashish Maji,*** Mechanical Engineering, DTU

26. Tunable unidirectional scattering of ellipsoidal single nanoparticle, ***3.Reena, 3.Yogita Kalra, 3.Ajeet Kumar*** and ***3.R. K. Sinha***, Applied Physics, DTU

27. ZVS-ZCS High Voltage Gain Integrated Boost Converter For DC Microgrid, Shelas Sathyan, H. M. Suryawanshi, Bhim Singh, Chandan Chakraborty, ***3.Vishal Verma***, and M. S. Ballal, Electrical Engineering, DTU

1. Chancellor	
2. Pro Vice Chancellor	***2.1. Ex Pro Vice Chancellor***
3. Faculty	***3.1. Ex Faculty***
4. Teaching-cum-Research Fellow	
5. Alumni	
6. Research Scholar	***6.1. Ex Research Scholar***
7. PG Scholar	***7.1. Ex PG Scholar***
8. Undergraduate Student	***8.1. Ex Undergraduate Student***

This article has been accepted for publication in a future issue of this journal, but has not been fully edited. Content may change prior to final publication. Citation information: DOI 10.1109/TPWRD.2016.2540723, IEEE Transactions on Power Delivery

Active ROCOF Relay for Islanding Detection

Pankaj Gupta, R. S. Bhatia, *Member, IEEE* and D. K. Jain, *Senior Member, IEEE*

***Abstract*—Intentional frequency perturbation by recently researched active islanding detection techniques for inverter based distributed generation (DG) define new threshold settings for the frequency relays. This innovation has enabled the modern frequency relays to operate inside the non-detection zone (NDZ) of the conventional frequency relays. However, the effect of such perturbation on the performance of the rate of change of frequency (ROCOF) relays has not been researched so far. This paper evaluates the performance of ROCOF relays under such perturbations for an inverter interfaced DG and proposes an algorithm along with the new threshold settings to enable it work under the NDZ. The proposed algorithm is able to differentiate between an islanding and a non-islanding event. The operating principle of relay is based on low frequency current injection through grid side voltage source converter (VSC) control of doubly fed induction generator (DFIG) and therefore, the relay is defined as "active ROCOF relay". Simulations are done in MATLAB.**

***Index Terms*—Active distribution system (ADS), distributed generation (DG), islanding detection techniques (IDT), loss of mains (LOM), rate of change of frequency (ROCOF), voltage source converter (VSC).**

I. Introduction

Future smart grid is moving towards high penetration of distributed generation in distribution system [1]. This makes the distribution system an active distribution system (ADS). Beside several benefits, the ADS adversely affect the conventional protection schemes which were designed for passive distribution system [2-3]. Therefore, the ADS management and its protection have emerged as an active area of research [4]. Islanding protection is one of the major protection issues with ADS, as an unintentional islanding may cause safety hazards due to an active DG in the island [5]. It may damage the consumer appliances and if unsynchronized reclosing with grid happens, it may damage the DG itself. Islanding detection has been one of the interesting research topics during the last decade [6-7].There is a wide variety of islanding detection technique which can be broadly classified into remote and local techniques. A remote islanding detection technique is based on monitoring parameters at utility side and is generally communication based such as power line cable communication (PLCC) [8-9], microprocessor or supervisory control and data acquisition (SCADA) system [10-11] or transfer trip relaying [11-12]. These techniques are reliable and accurate but are complex to implement as well as expensive. On the other hand local techniques which are either passive or active are cheap and easy to implement. Passive techniques are based on measurement of a system parameter at DG site and comparing it with a preset threshold, for example under voltage (UV)/over voltage (OV) [13], under frequency (UF)/over frequency (OF) [14-15], phase criteria [16], rate of change of frequency (ROCOF) [17-21], vector surge relay (VSR) [22], rate of change of phase angle difference (ROCPAD)[23] etc. But the passive techniques have inherent non detection zone (NDZ) and fails during low or zero power imbalance condition [24]. An active technique intentionally perturbs a system's local parameter and observes the resulting reaction for confirmation of islanding for example active frequency drift [25-26], Sandia frequency shift [27-28], current injection based techniques [29-32] etc. However, these local active techniques have smaller NDZ, but they may cause power quality problems. Further, various other techniques which mixes two or more techniques were also developed and are known as hybrid techniques for example positive feedback, voltage unbalance (VU) and total harmonic distortion (THD) [33-34], average rate of voltage change and real power shift [35], intelligent islanding detection [36-37] etc. However, the research is still open to develop a perfect IDT which has negligible NDZ.

Frequency perturbation based active IDT were recently researched to detect LOM during the worst case [29-31]. This is achieved by injecting a low frequency periodic current through q-axis current controller of grid side VSC. This technique perturbs the frequency inside the NDZ, which is then identified by some specific techniques like calculating average value of frequency deviation over few cycles (AFDVavg) [30] or cross correlation schemes [31] etc. This has enabled them to detect islanding inside NDZ of frequency relays without affecting the stability of DG [30]. However, the effects such perturbations on the ROCOF relay performance has not been evaluated so far. There is a possibility that the ROCOF relay can also operate inside the NDZ with some modifications. This will be a useful innovation as the ROCOF relay is widely used in the industry for islanding detection. Various algorithms are proposed in the literature to make it more effective [17-21], yet there has been no literature on active ROCOF method or any other method which mitigates the NDZ of ROCOF relay.

P. Gupta is with the Department of Electronics and Communication Engineering, Indira Gandhi Delhi Technical University for Women, Delhi 110006, India (e-mail: joinpankaj@yahoo.co.in).

R. S. Bhatia is with the Department of Electrical Engineering, National Institute of Technology, Kurukshetra 136119, Haryana, India (e-mail: rsibhatia@yahoo.co.in).

D. K. Jain is with the Department of Electrical Engineering, Deenbandhu Chhoturam University of Science and Technology, Murthal 131039,Haryana, India (e-mail: jaindk66@gmail.com).

0885-8977 (c) 2016 IEEE. Personal use is permitted, but republication/redistribution requires IEEE permission. See http://www.ieee.org/publications_standards/publications/rights/index.html for more information.

This article has been accepted for publication in a future issue of this journal, but has not been fully edited. Content may change prior to final publication. Citation information: DOI 10.1109/TPWRD.2016.2540723, IEEE Transactions on Power Delivery

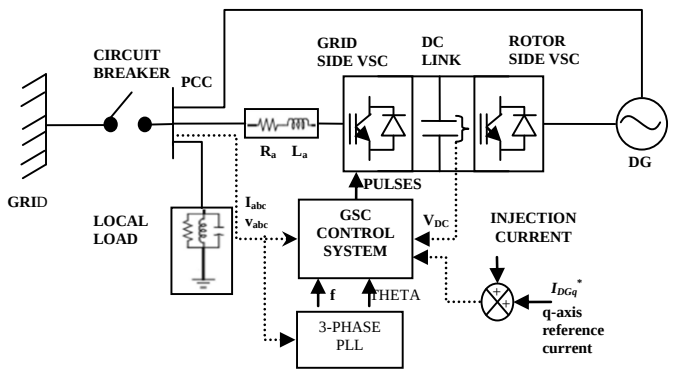


Fig.1. Circuit diagram of the test system

TABLE I
TEST SYSTEM PARAMETERS

Parameter	Value	Parameter	Value	Parameter	Value
V_{abc} (L-L)	575V	f_0	60Hz	R	0.069Ω
I_a (L-L)	6.8kA	R_a	5.95mΩ	L	182μH
S_{DG}	4.8MW	L_a	11.75μH	C	38.5mF
V_{DC}	1200V	*f*(PWM)	1620	Q_f	1
k_p	0.3	τ_i	6		

An active ROCOF relay for LOM detection of an inverter interfaced DG inside the NDZ of existing ROCOF relay is presented in the paper. The performance of existing ROCOF relay is evaluated and modifications are suggested to enable it work inside the NDZ. The active ROCOF relay structure is developed and the threshold settings are obtained for various load quality factor (Q_f). The algorithm is so designed that it eliminates the nuisance tripping during the non islanding switching events. Section II describes the test system. Section III reviews the theory of low frequency current injection based IDT. Section IV presents the theory and the structures of conventional and the proposed active ROCOF relay. Section V discusses the results and evaluates the performance of the proposed relay. Section VI concludes the paper.

II. TEST SYSTEM DESCRIPTION

The test system shown by the single line diagram in Fig.1 is taken from [30], and the test circuit parameters are tabulated in Table I. The DG is DFIG type, which is synchronized to utility with the help of a 3-phase phase locked loop (PLL) [38]. The local load is tuned to consume the rated DG capacity at a fundamental frequency (f_0) of 60Hz. Islanding under zero power imbalance situation is done by opening the circuit breaker at point of common coupling (PCC). Fig. 2 shows the grid side converter control system. The injection of low frequency periodic current is done through q-axis current control of grid side converter of DG as shown in Fig.1 and Fig.2. The control system of GSC obtains the reference values of DG's output current and voltages in d-q frame of reference which acts an as input to the pulse width modulation (PWM) for generating VSC's pulses. The test system undertaken passes the UL 1741 standard criteria for testing islanding.

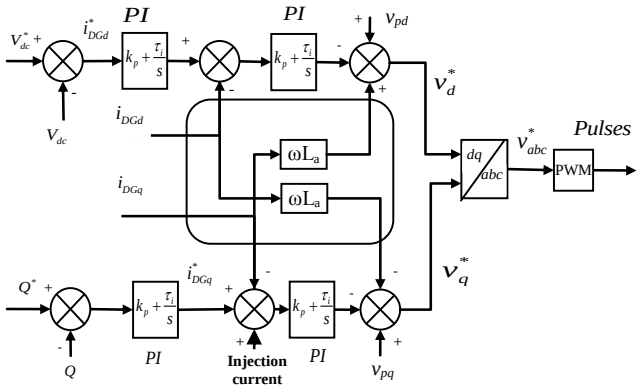


Fig.2. Grid side converter control system

III. LOW FREQUENCY CURRENT INJECTION BASED ISLANDING DETECTION TECHNIQUE

This section reviews the low frequency current injection based islanding detection technique (IDT) [29-31]. The steady state DG output current (i_{DGd}, i_{DGq}) in *dq* frame of reference [29-31], can be written as (1).

$$\begin{bmatrix} i_{DGd} \\ i_{DGq} \end{bmatrix} = \begin{bmatrix} i_{DGd}^* \\ i_{DGq}^* \end{bmatrix} \tag{1}$$

where i_{DGd}^* and i_{DGq}^* are the DG's d-q-axis reference current. The (1) in *abc* coordinate system can be expressed as (2).

$$\begin{bmatrix} i_{DGa} \\ i_{DGb} \\ i_{DGc} \end{bmatrix} = \begin{bmatrix} i_{DGd}^* \cos(\omega_0 t) - i_{DGq}^* \sin(\omega_0 t) \\ i_{DGd}^* \cos(\omega_0 t - 2\pi/3) - i_{DGq}^* \sin(\omega_0 t - 2\pi/3) \\ i_{DGd}^* \cos(\omega_0 t + 2\pi/3) - i_{DGq}^* \sin(\omega_0 t + 2\pi/3) \end{bmatrix} \tag{2}$$

The DG regulates its reactive power by keeping the q-axis reference current to zero, to maintain the unity power factor. The low frequency current injection based IDT changes the DG's q-axis reference current of test system as in (3)

$$i_{DGq}^* = I_q \cos \omega_q t \tag{3}$$

where I_q is the amplitude, which is kept very small and f_q be the reference current frequency. The further analysis can be done on per phase basis as the test system is assumed as a balanced system. Thus the DG output current for phase 'a' can be expressed as (4) and (5),

$$i_{DGa} = i_{DGd}^* \cos(\omega_0 t) - I_q \cos(\omega_q t) \sin(\omega_0 t) \tag{4}$$

or

$$i_{DGa} = i_{DGd}^* \cos(\omega_0 t) - \frac{1}{2} I_q [\sin(\omega_1 t) + \sin(\omega_2 t)] \tag{5}$$

where
$$\left.\begin{aligned} \omega_1 &= 2\pi(f_0 - f_q) \\ \omega_2 &= 2\pi(f_0 + f_q) \end{aligned}\right\} \tag{6}$$

This generates the two side band frequencies as ω_1 and ω_2. The side band components of current are forced to flow through load during LOM as the low impedance path offered by the grid is disconnected [29-30]. The DG's voltage can be computed by multiplying the individual current components to the respective impedances at the corresponding frequencies.

0885-8977 (c) 2016 IEEE. Personal use is permitted, but republication/redistribution requires IEEE permission. See http://www.ieee.org/publications_standards/publications/rights/index.html for more information.

This article has been accepted for publication in a future issue of this journal, but has not been fully edited. Content may change prior to final publication. Citation information: DOI 10.1109/TPWRD.2016.2540723, IEEE Transactions on Power Delivery

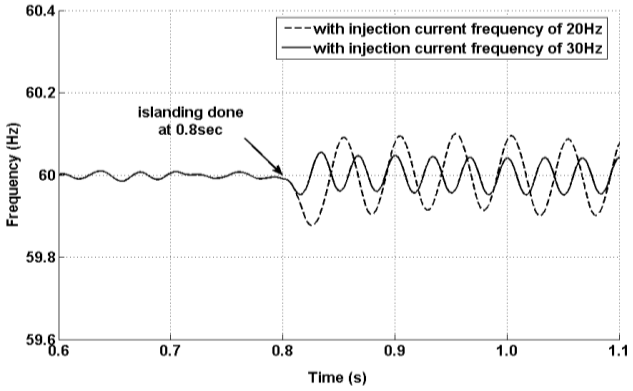


Fig.3. Frequency deviation curve for f_q=20Hz and 30 Hz during pre and post LOM

The reciprocal of equivalent impedance of parallel RLC load at any frequency other than fundamental frequency can be expressed as in (7),

$$\frac{1}{Z_{eq}(\omega)} = \frac{1}{R} + \frac{1}{j\omega L} + j\omega C \tag{7}$$

where magnitude and phase (φ) of equivalent impedance (Z_{eq}) can be expressed as in (8) and (9), respectively.

$$\left|Z_{eq}\right| = \frac{1}{\left\{\left(\frac{1}{R}\right)^2 + \left(\omega C - \frac{1}{\omega L}\right)^2\right\}^{\frac{1}{2}}} \tag{8}$$

$$\text{Phase } (\varphi) = -\tan^{-1}\left[\frac{R\left(\omega^2 LC - 1\right)}{\omega L}\right] \tag{9}$$

However, the Z_{eq} at fundamental angular frequency (ω_0) is equal to R due to resonance. Therefore, voltage of phase 'a' at DG terminal can obtained by superposition of three voltages at their corresponding frequencies, as expressed in (10)

$$v_{DGa} = v_{DG}(\omega_0) + v_{DG}(\omega_1) + v_{DG}(\omega_2) \tag{10}$$

where,

$$v_{DG}(\omega_0) = Ri^*_{DGd}\cos\omega_0 t \tag{11}$$

$$v_{DG}(\omega_1) = -\frac{I_q}{2\left\{\left(1/R\right)^2 + \left(\omega_1 C - 1/\omega_1 L\right)^2\right\}^{\frac{1}{2}}}\sin(\omega_1 t + \varphi_1) \tag{12}$$

$$v_{DG}(\omega_2) = -\frac{I_q}{2\left\{\left(1/R\right)^2 + \left(\omega_2 C - 1/\omega_2 L\right)^2\right\}^{\frac{1}{2}}}\sin(\omega_2 t + \varphi_2) \tag{13}$$

$$\varphi_1 = -\tan^{-1}\left[\frac{R\left(\omega_1^2 LC - 1\right)}{\omega_1 L}\right] \tag{14}$$

$$\varphi_2 = -\tan^{-1}\left[\frac{R\left(\omega_2^2 LC - 1\right)}{\omega_2 L}\right] \tag{15}$$

Equation (10) shows that the DG's output frequency is deviated in case of LOM. Fig.3 shows the pre and post LOM frequency deviation curve, with respect to different injection current frequencies. The obtained frequency deviation is also a periodic deviation and follows the reference current. This deviation is utilized previously by AFDVavg technique [30] and cross correlation [31] to detect LOM. The frequency measurement at PCC is done with the help of a PLL. The recommended value of amplitude of reference current is 1% of the DG capacity [29-31] and f_q is 20Hz or 30Hz.

IV. ROCOF Relay Theory and Structure

The conventional ROCOF relay operates during LOM, if only if there is some significant amount of power imbalance between generation (P_{DG}) and the load power (P_{Load}) [17-22]. Thus, a conventional ROCOF relays does not operate during the worst case i.e. when the power imbalance is zero or very low. Since conventional ROCOF relay has a large measurement window of around 500ms, it does not mal-operate during small variation in frequency resulting from non-islanding switching events. One way, it is advantageous, as it avoid trips during non-islanding switching transients, on the other way it has a drawback of NDZ due to reduced sensitivity. The proposed active ROCOF relay intentionally perturbs the frequency during low power imbalance with very small periodic deviation. The measurement window is reduced to 50ms, so that it responds to small variations in frequency. Further, the time delays and the algorithm is so proposed that it responds to LOM events only. The chances of mal-operation of relay is very small as it mal-operates only when there is a permanent frequency deviation for at least 12cycles. The detailed theory and the structure of conventional and active ROCOF relay is discussed under the subsection A and B.

A. *Conventional ROCOF Relay*

The conventional ROCOF relay considered in this paper works on the formula given by (16-18), [17-22]. The corresponding ROCOF relay structure is given in Fig.4. The frequency is determined from PCC voltage waveform and measurement is done through a phase locked loop module. The effective value of ROCOF is computed by (16) [19], having a measurement window of 500ms as recommended in DS3 grid code modification by EIRGRID. A trip signal is initiated if the measured value of ROCOF i.e. β is greater than Tc, which is 1Hz/s defined for a measurement window of 500ms. The effective value of ROCOF can be approximately calculated by formula expressed in (16) [17-22].

$$ROCOF = \frac{1}{n}\sum_{k=1}^{n}\left|\frac{df}{dt}(k)\right| \tag{16}$$

where, $n = \frac{\Delta t}{T_s}$ (17)

n = Total number of samples obtained in a given measurement window size of Δt.

k = 1, 2, 3……..nth sample and T_s = Sampling time.

$$\frac{df}{dt}(k) = \frac{f(t_k) - f(t_k - \Delta t)}{\Delta t} \tag{18}$$

0885-8977 (c) 2016 IEEE. Personal use is permitted, but republication/redistribution requires IEEE permission. See http://www.ieee.org/publications_standards/publications/rights/index.html for more information.

This article has been accepted for publication in a future issue of this journal, but has not been fully edited. Content may change prior to final publication. Citation information: DOI 10.1109/TPWRD.2016.2540723, IEEE Transactions on Power Delivery

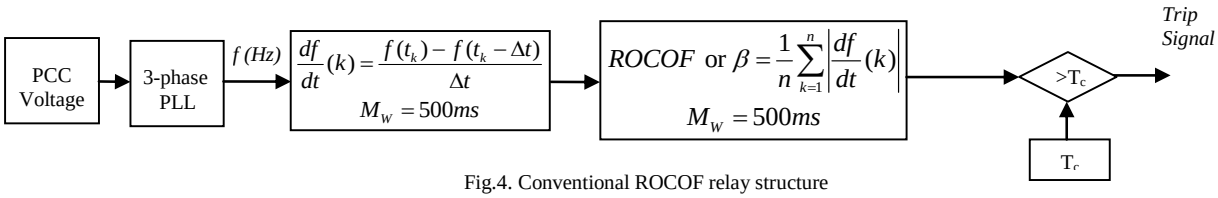


Fig.4. Conventional ROCOF relay structure

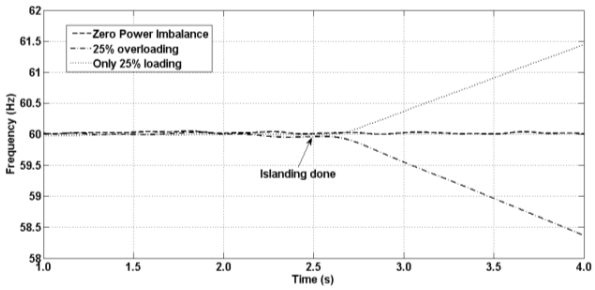


Fig.5. Frequency trend for various loading condition during pre and post LOM

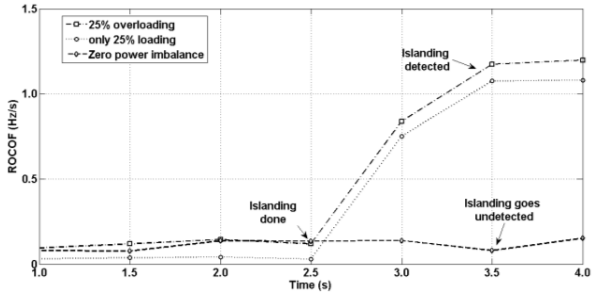


Fig.6. ROCOF trend for various loading condition during pre and post LOM

$f(t_k)$ -Measured value of frequency at the time of k^{th} sample i.e. t_k.

$f(t_k - \Delta t)$ -Measured value of frequency, Δt before the k^{th} sample time i.e. $t_k - \Delta t$.

The operation of ROCOF relays depends upon the dynamic change in the frequency during islanding due to the power imbalance between the generation and the load. The dynamic change in frequency is directly proportional power imbalance at PCC subsequent to islanding and can be approximated [17-22] as in (19),

$$\frac{df}{dt} = \frac{(P_{DG} - P_{Load})}{2 \times S_{DG} \times H_{SG}} \times f_0 \quad (19)$$

where, P_{DG} -DG output power

P_{load} - Load power

f_0 - rated fundamental frequency

S_{DG} -DG rating

H_{SG} - Inertia constant of generating plant

Thus, if P_{DG} is equal to P_{load} subsequent to islanding, the dynamic change in frequency becomes zero i.e. frequency of system does not change subsequent to islanding. Therefore, the ROCOF relay will not respond and the islanding goes undetected. The frequency relay and conventional ROCOF relay response under different loading cases is shown in Fig.5 and Fig.6 respectively. Simulation is run for 4s and islanding is done at 2.5s. It can be seen from Fig.5 and Fig.6 that the frequency relay and the conventional ROCOF relay detects islanding within 1s of formation of island for overloading and light loading cases but fails to detect islanding under zero power imbalance condition.

B. Proposed Active ROCOF Relay

The reduced sensitivity and the large inherent NDZ of conventional ROCOF relay is improved by the proposed active ROCOF relay without jeopardizing its attribute to non response during the non-islanding switching events. The proposed active ROCOF relay implements a smaller measurement window of 50ms but with special conditions such as time delays and intentional frequency perturbations.

The method utilizes the frequency deviation intentionally obtained for LOM detection under the worst case by [29-31]. This is done by injecting a small periodic current through q-axis current controller of grid side VSC. The amplitude of injection current is kept to 1% of the DG rating and a frequency lower than the fundamental frequency. As discussed in Section III, the frequency perturbation IDT perturbs the frequency inside the NDZ of frequency relays, which is very small, thus the conventional ROCOF relays are not able to detect this variation due to the large measurement window size of 500ms as shown in Fig.6. However, if the measurement size is reduced to 50ms, the relay may show a periodic deviation. But the threshold value of 1Hz/s can't be taken as relay setting as it will result in mal-operation of the relay.

The structure and algorithm of proposed active ROCOF relay is shown in Fig.7 and Fig.8, respectively. At first a continuous injection of small periodic current with a low frequency of 30Hz is done through q-axis current controller of GSC. A stiff grid provides a low impedance path to this current and it does not have any effect on PCC voltage and frequency. During LOM, the injection current is forced to flow through local load which in turn result in small but significant periodic frequency deviation. A three phase PLL measures the PCC frequency and the obtained frequency is then processed by df/dt with a measurement window of 50ms. An effective ROCOF is then calculated at every 50ms. There may be three events which may arrive, where the proposed algorithm have to make a correct decision. They are as follows:

- LOM happens with significant amount of power imbalance at point of common coupling (PCC).
- LOM happens with Zero or very small power imbalance at PCC and
- Non-islanding switching events causing frequency deviations.

The effective value of ROCOF is calculated for 50ms with an injection current frequency (f_q) of 30 Hz. So, for the first event i.e. LOM with significant amount of power imbalance, the measured ROCOF will be greater than the predefined threshold value of T_1 i.e. 10Hz/s.

0885-8977 (c) 2016 IEEE. Personal use is permitted, but republication/redistribution requires IEEE permission. See http://www.ieee.org/publications_standards/publications/rights/index.html for more information.

This article has been accepted for publication in a future issue of this journal, but has not been fully edited. Content may change prior to final publication. Citation information: DOI 10.1109/TPWRD.2016.2540723, IEEE Transactions on Power Delivery

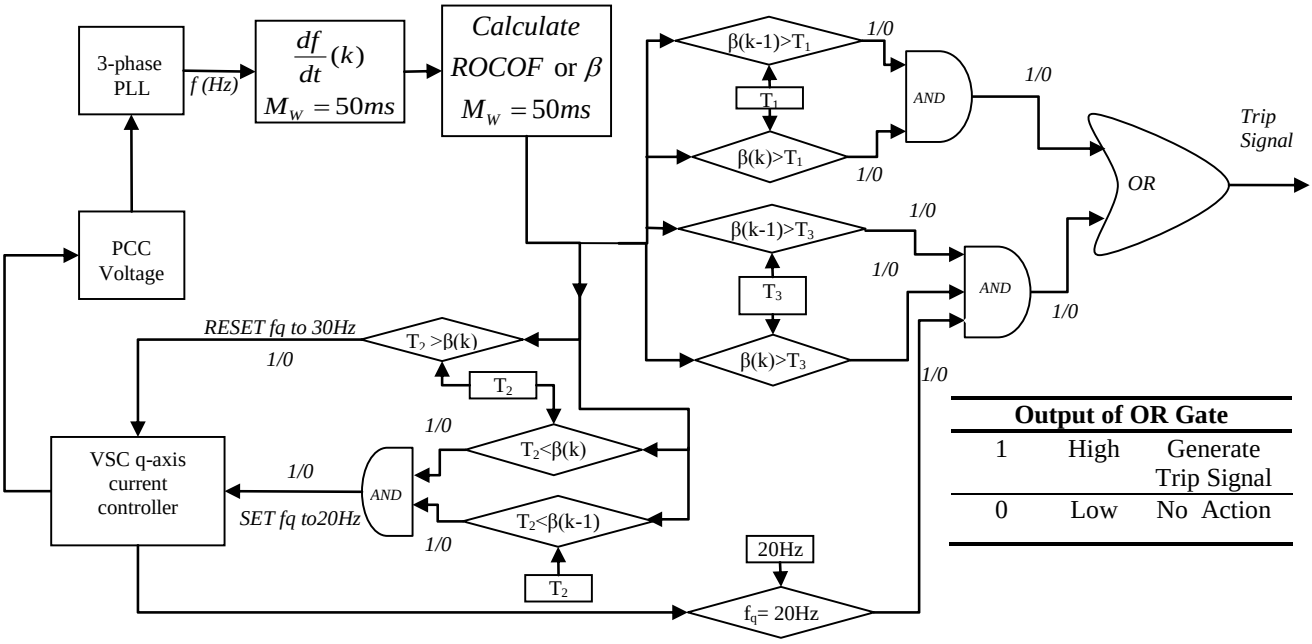


Fig.7. Active ROCOF relay structure

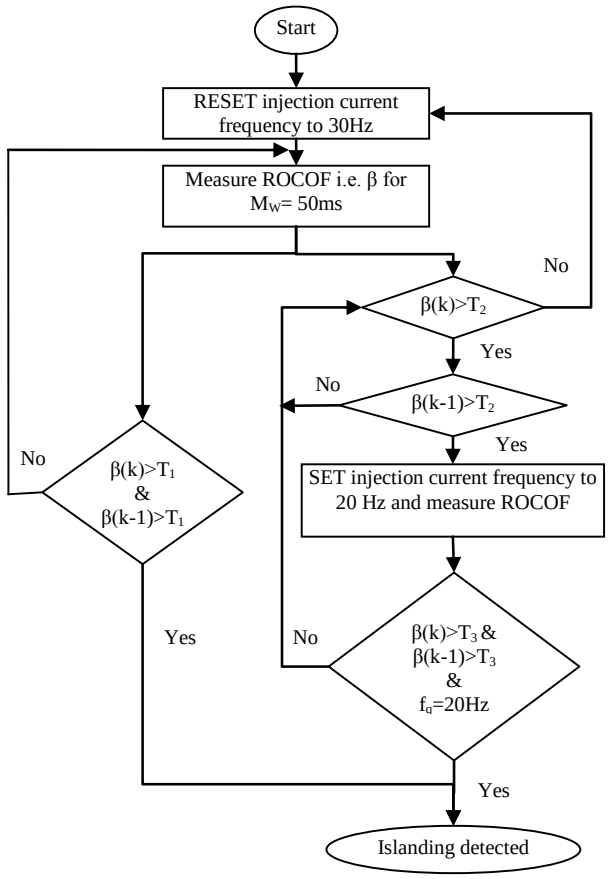


Fig.8. Flowchart of proposed algorithm

The active ROCOF will trip the DG if ROCOF is greater than T_1 for at least two consecutive times. This ensures that the change is permanent and thus, there is an intentional time delay of at least 50ms i.e. 3 cycles. The minimum time for decision making in this case is 100ms i.e. 6 cycles.

For the other two events i.e. LOM happens with small or zero power imbalances and non-islanding switching event, the measured ROCOF is compared with predefined threshold setting of T_2. If the measured value of ROCOF is greater than T_2 for the two consecutive times, then it suspects the occurrence of either of the next two events. A control signal is send to current controller of grid side converter (GSC) to SET the injection current frequency f_q to20Hz. To eliminate the possibility of false tripping under non-islanding switching events the ROCOF is again calculated but with f_q= 20Hz for next 3-cycles (50ms). If ROCOF is greater than the threshold value T_3 for the next two consecutive times and if the injection current frequency is also 20Hz, then LOM is confirmed otherwise it was a non-islanding switching event. The intentional time delay in this case is 150ms and the minimum time for decision making is 200ms i.e. 12 cycles. Thus the suggested ROCOF relay algorithm as shown in Fig. 8 and the corresponding ROCOF relay structure as shown in Fig. 7, along with the suggested time delays are successfully able to detect islanding inside the NDZ.

In case, for all the events stated above, if the measured ROCOF value falls below the predefined threshold value T_2, it RESETs the injection current frequency to 30Hz and repeats all the step as per algorithm as suggested in Fig.8.

V. Results and Discussion

The conventional ROCOF relay detects LOM successfully during the light loading and overloading conditions but LOM goes undetected during zero imbalance condition as can be seen from Fig.5 and Fig.6. The active ROCOF relay performance is evaluated by simulating the test system discussed in section II.

0885-8977 (c) 2016 IEEE. Personal use is permitted, but republication/redistribution requires IEEE permission. See http://www.ieee.org/publications_standards/publications/rights/index.html for more information.

This article has been accepted for publication in a future issue of this journal, but has not been fully edited. Content may change prior to final publication. Citation information: DOI 10.1109/TPWRD.2016.2540723, IEEE Transactions on Power Delivery

TABLE II
THRESHOLD SETTINGS

Load Values			Load Quality Factor (Q_f)	T_2 (Hz/s) (f_q=30Hz)	T_3 (Hz/s) (f_q=20Hz)
R (mΩ)	L (μH)	C (mF)			
68.88	182	385.29	1	4.00	5.50
68.88	91	77.059	2	3.70	5.00
68.88	60	115.588	3	3.45	4.60
68.88	45	154.118	4	3.00	4.20

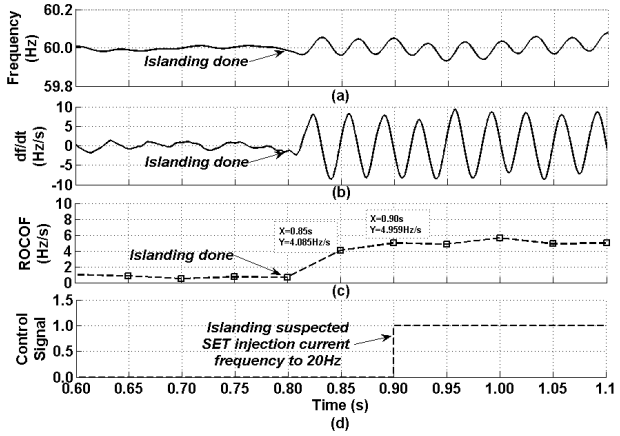


Fig.9. Active ROCOF relay performance with injection current frequency of 30Hz (a) DG frequency (b) df/dt (c) ROCOF (d) control signal.

The simulations are run for 1.1s and the events (LOM, switching of load) are scheduled at 0.8s. The detailed investigation pertaining to active ROCOF relay is discussed in the next subsections.

A. *Threshold Settings*

The threshold settings can be classified on the basis of injection current frequencies and load quality factor. It has already been reported in [30], that the DG ratings does not affects the frequency deviation, however the deviation is affected by load quality factor and injection current frequencies. The threshold settings are decided by running the simulations many time under zero power imbalance condition and taking the average of ROCOF response received just after LOM. However, threshold T_1 is the threshold value for large or significant power imbalance condition and therefore set as 10Hz/s for a measurement window of 50ms. This means that a frequency deviation of 0.5Hz over 50ms will result in 10Hz/s, which is a sure case of islanding. The threshold settings for injection current frequencies of 30Hz and 20Hz for LOM under low or zero power imbalances with respect to load quality factor (Q_f) are obtained and tabulated in Table II.

B. *Response of Active ROCOF Relay to Injection Current Frequencies*

The injection current frequency has a great impact on the response of active ROCOF relay. The threshold value goes low when injection current frequency approaches near to 60Hz which can be seen from Table II. The various threshold values with respect to injection current frequencies of 20Hz and 30Hz are given in Table II.

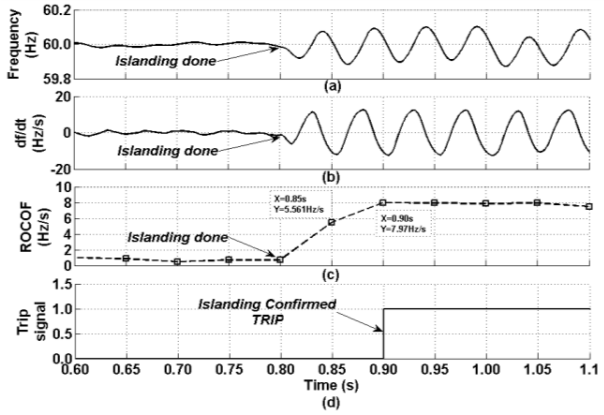


Fig.10. Active ROCOF relay performance with injection current frequency of 20Hz (a) DG frequency (b) df/dt (c) ROCOF (d) Trip signal.

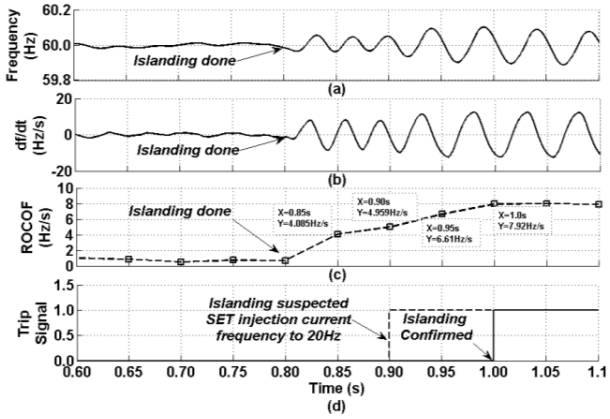


Fig.11. Active ROCOF relay performance during zero power imbalance condition (a) DG frequency (b) df/dt (c) ROCOF (d) Trip signal.

The response of active ROCOF relay to injection current frequencies of 30Hz and 20Hz is evaluated in this subsection. Figs.9 (a-d) and Figs.10 (a-d) depicts the response of an active ROCOF relay, when subjected to injection current frequencies of 30Hz and 20Hz, respectively, during the LOM under the zero power imbalance situations with a load having quality factor of 1. The load with quality factor of 1 is recommended in IEEE standard 1547.1 for testing islanding. It can be seen from Figs.9 (a-d) and Figs.10 (a-d), that the LOM is done at 0.8s and is successfully detected by active ROCOF relay at 0.9s. The ROCOF curve crosses the predefined threshold by two consecutive times in both the cases at 0.9s confirming the formation of island.

C. *Islanding Under Zero Power Imbalance Condition*

The active ROCOF relay is found to be effective in detecting LOM during zero power imbalance condition i.e. inside the NDZ of conventional ROCOF relay as depicted in Figs.11 (a-d). The LOM is simulated at 0.8s and simulation is run for 1.1s. The active ROCOF relay response reaches the predefined threshold of 4Hz/s at 0.85s as shown in Fig.11(c). After a time delay of 50ms, the measured ROCOF value is again found to be greater than 4Hz/s confirming it as a permanent change. Thus a control signal is send to current controller of GSC to SET the injection current frequency to 20Hz. This SETs the injection current frequency to 20Hz as can be seen from Fig.11 (a).

0885-8977 (c) 2016 IEEE. Personal use is permitted, but republication/redistribution requires IEEE permission. See http://www.ieee.org/publications_standards/publications/rights/index.html for more information.

This article has been accepted for publication in a future issue of this journal, but has not been fully edited. Content may change prior to final publication. Citation information: DOI 10.1109/TPWRD.2016.2540723, IEEE Transactions on Power Delivery

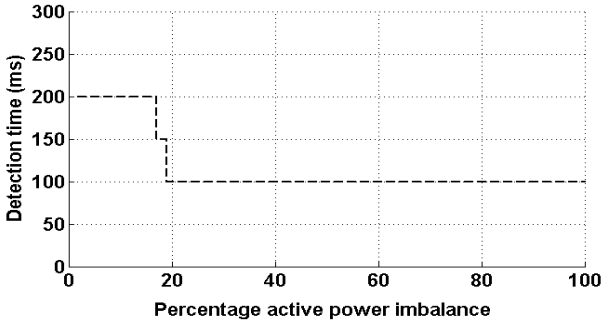


Fig.12. Active ROCOF relay's detection time vs percentage active power imbalance performance curve

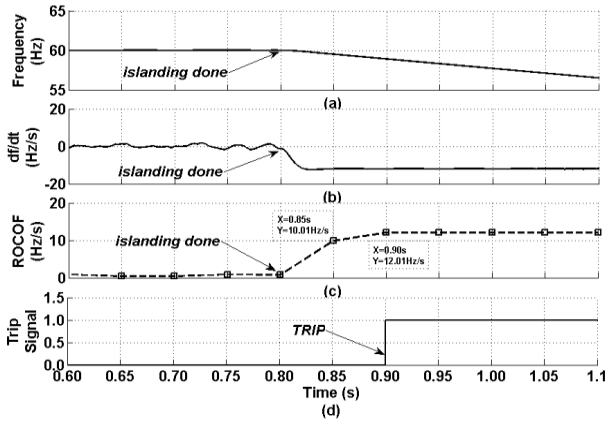


Fig.13. Active ROCOF relay performance during 19% of active power imbalance (a) DG frequency (b) df/dt (c) ROCOF (d) Trip signal.

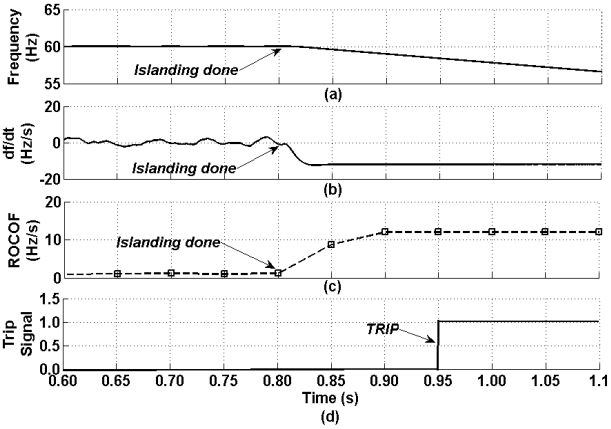


Fig.14. Active ROCOF relay performance during 18% of active power imbalance (a) DG frequency (b) df/dt (c) ROCOF (d) Trip signal.

The measured ROCOF value is now compared with T3 which is 5.5Hz/s for Q_f =1. It can be seen from Fig.11(c), that the measured ROCOF value goes above the predefined threshold value of 5.5Hz/s for the two consecutive times confirming it to be a permanent change. A trip signal is initiated at 1.0s as shown in Fig.11 (d).The active ROCOF relay is successfully able to detect islanding during zero power imbalance condition in a time period of 200ms i.e. 12cycles.

D. Performance of Active ROCOF Relay with respect to Active power Imbalance

Fig.12 depicts the performance curve between detection time and percentage active power imbalance subsequent to LOM for the proposed active ROCOF relay.

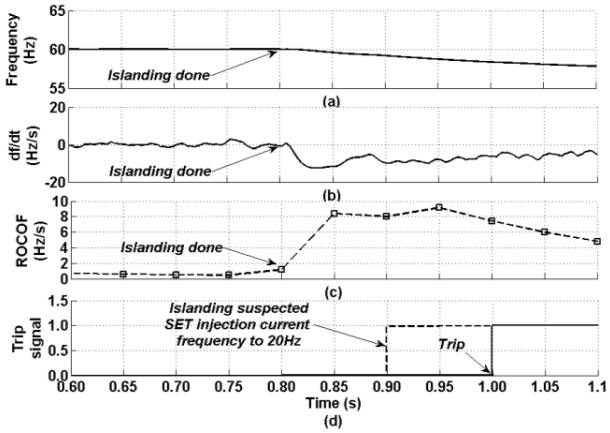


Fig.15. Active ROCOF relay performance during 16% of active power imbalance (a) DG frequency (b) df/dt (c) ROCOF (d) Trip signal.

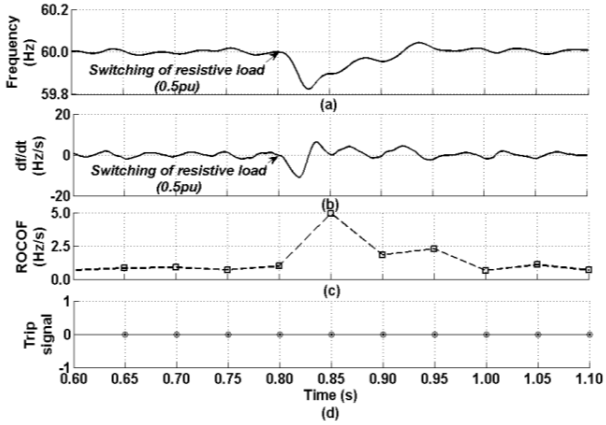


Fig.16. Active ROCOF relay performance during a resistive load switching (a) DG frequency (b) df/dt (c) ROCOF (d) Trip signal.

The LOM detection time for each value of active power imbalance case (considering an increment of 1%) have been recorded by running the test system simulation many times. The critical points were found to be as 18%, where the detection time is found to be 150ms and 16%, where the detection time is found to be 200ms. Figs.13 (a-d) and Figs.14 (a-d) shows the cases of 19% and 18% power imbalance condition. It can be seen that LOM is detected at 0.9s in Figs.13 (a-d) for 19% but for 18%, it takes a long time of 150ms i.e. the LOM is detected at 0.95s.

It can be also be observed that when active power imbalance goes below or equal to 16%, the detection time is found to be 200ms as depicted in Figs.15(a-d) and Fig.12. The LOM is detected at 1.00s for 16% active power imbalance.

E. Non-Islanding Switching Events

Figs.16 (a-d), Figs.17 (a-d) and Figs.18 (a-d), depicts the ROCOF trend for switching of an extra resistive, inductive and capacitive load of 0.5pu, respectively. The ROCOF relay does not mal-operate during switching transients as it does not satisfy the conditions stated in the algorithm.

The time delays (50ms-150ms) as suggested in the paper are sufficient to verify that the change is permanent or not and this avoids the mal-operation of relay during the momentary frequency deviations.

0885-8977 (c) 2016 IEEE. Personal use is permitted, but republication/redistribution requires IEEE permission. See http://www.ieee.org/publications_standards/publications/rights/index.html for more information.

This article has been accepted for publication in a future issue of this journal, but has not been fully edited. Content may change prior to final publication. Citation information: DOI 10.1109/TPWRD.2016.2540723, IEEE Transactions on Power Delivery

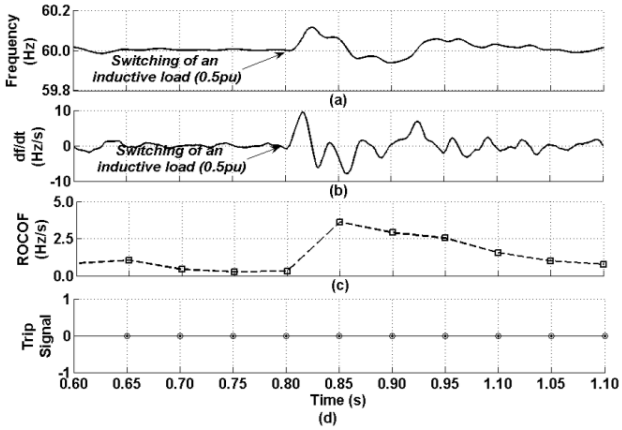


Fig.17. Active ROCOF relay performance during an inductive load switching (a) DG frequency (b) df/dt (c) ROCOF (d) Trip signal.

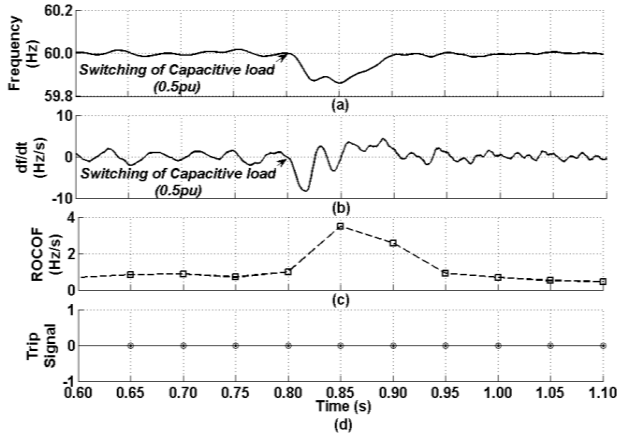


Fig.18. Active ROCOF relay performance during a capacitive load switching (a) DG frequency (b) df/dt (c) ROCOF (d) Trip signal

F. Effect on Power Quality

It has already been reported in [30], that if the injection current amplitude is kept small i.e. within 1% of DG rating then it does not have much effect on the power quality of the signal. The power factor and total harmonic distortion remain inside the permissible limits. In this paper, the injection current amplitude is kept within the 1% of the DG rating and it's frequency is chosen as 20Hz and 30Hz as recommended in [30].

VI. Conclusions

The active ROCOF relay proposed in the paper is successfully implemented to detect islanding of inverter based DG during low or zero power imbalance condition. The following are the specific observations to conclude:

- Intentional frequency perturbations can be utilized as an islanding detection parameter with suggested ROCOF threshold settings and algorithm proposed in the paper. The threshold settings for active ROCOF relay have been obtained.
- A measurement window of 50ms is sufficient to detect the small deviation in frequency, but it should always be accompanied by time delays and conditions suggested in the paper. This avoids the mal-operation of relay during switching transients.
- The active ROCOF relay may mal-operate only in a condition, when there is a continuous frequency deviation of a significant value for more than 12 cycles i.e. 200ms.
- The proposed active ROCOF relay detects islanding in a minimum detection time of 100ms for a percentage active power imbalance of more than 18%.
- For a percentage active power imbalance of less than 18% but more than 16%, the relay takes 150ms for decision making. Whereas for less the 16% it takes 200ms for decision making.
- ROCOF calculation time is not included in the detection time calculation and is assumed to be very less for a fast processor.
- Injection current is kept to a very low value, almost 1% of the rated DG capacity, in order to maintain the power factor and the power quality.
- The method detects islanding for all such loads whose quality factor is less than the quality factor of the load, chosen for threshold setting.

Various cases are successfully simulated and the test results are shown in the paper. It is encouraging to know that the ROCOF relay can be utilized to detect islanding under low power imbalance condition, with some modifications in size of measurement window and its algorithm.

VII. References

[1] M. Liserre, T. Sauter, and J. Y. Hung, "Future energy systems: Integrating renewable energy sources into the smart power grid through industrial electronics," *IEEE Industrial Electronics Magazine*, vol. 4, no. 1, pp. 18–37, 2010.

[2] "IEEE Standard conformance test procedures for equipment interconnecting distributed resources with electric power systems", *IEEE 1547.1 Standard*, 2005.

[3] S. Chowdhury, S. P. Chowdhury, and P. Crossley, "Microgrids and active distribution networks," *The Institution of Engineering and Technology*, London, U.K., vol. 1, 2009.

[4] J. M. Guerrero, M. Chandorkar, T. L. Lee, and P. C. Loh, "Advanced control architectures for intelligent microgrids—part I: decentralized and hierarchical control," *IEEE Transactions on Industrial Electronics*, vol. 60, no. 4, pp. 1263 – 1270, 2013.

[5] M. Geidl, "Protection of power systems with distributed generation: State of the art," *Power Systems Laboratory*, Swiss Federal Institute of Technology (ETH), Zurich, 2005.

[6] K. N. E. K. Ahmad, J. Selvaraj, and N. A. Rahim, "A review of the islanding detection methods in grid-connected PV inverters", *Renewable and Sustainable Energy Reviews*, vol. 21, pp- 756-766, 2013.

[7] C. Li, C. Cao, Y. Cao, Y. Kuang, L. Zeng, and B. Fang, "A review of islanding detection methods for microgrid", *Renewable and Sustainable Energy Reviews*, vol. 35, pp. 211-220, 2014.

[8] M. E. Ropp, K. Aaker, J. Haigh, and N. Sabbah , "Using power line carrier communications to prevent islanding", *Proceedings 28th IEEE Photovoltaic Specialists Conference*, pp. 1675–1678, 2000.

[9] W. Xu, G. Zhang, C. Li, W. Wang, G. Wang, and J. Kliber, "A power line signaling based technique for anti-islanding protection of distributed generators - Part I: scheme and analysis", *IEEE Transactions on Power Delivery*, vol. 22, no. 3, pp. 1758-1766, 2007.

[10] M. A. Redfern, J. Barrett, and O. Usta, "A new microprocessor based islanding protection algorithm for dispersed storage and generation units", *IEEE Transactions on Power Delivery*, vol. 10, no. 3, pp. 1249-1254, 1995.

[11] A. Etxegarai, P. Eguía, and I. Zamora, "Analysis of remote islanding detection methods for distributed resources", *International Conference on Renewable Energies and Power Quality, ICREPQ*, pp. 13-15, 2011.

[12] R. E. Bratton, "Transfer-trip relaying over a digitally multiplexed fiber optic link", *IEEE Transactions on Power Apparatus and System*, vol. 103, no. 2, pp. 403–406, 1984.

0885-8977 (c) 2016 IEEE. Personal use is permitted, but republication/redistribution requires IEEE permission. See http://www.ieee.org/publications_standards/publications/rights/index.html for more information.

This article has been accepted for publication in a future issue of this journal, but has not been fully edited. Content may change prior to final publication. Citation information: DOI 10.1109/TPWRD.2016.2540723, IEEE Transactions on Power Delivery

[13] J. C. M. Vieira, D. S. Correa, W. Freitas, and W. Xu, "Performance curves of voltage relays for islanding detection of distributed generators", *IEEE Transactions on Power Systems*, vol. 20, no. 3, pp. 1660-1662, 2005.

[14] W. Bower, and M. Ropp, "Evaluation of islanding detection methods for utility interactive inverters in photovoltaic systems", no. SAND2002-3591, *Sandia National Labs*., Albuquerque, NM (US), Livermore, CA (US), 2002.

[15] M. Yingram, and S. Premrudeepreechacharn, "Investigation over/under-voltage protection of passive islanding detection method of distributed generations in electrical distribution systems", *IEEE International Conference on Renewable Energy Research and Applications (ICRERA)*, pp. 1-5, 2012.

[16] M. E. Ropp, M. Begovic, A. Rohatgi, G. A. Kern, R. H. Bonn, and S. Gonzalez, "Determining the relative effectiveness of islanding prevention techniques using phase criteria and non-detection zones," *IEEE Transactions on Energy Conversion*, vol. 15, no. 3, pp. 290-296, 2000.

[17] J. C. M. Vieira, W. Freitas, W. Xu, and A. Morelato, "Efficient coordination of ROCOF and frequency relays for distributed generation protection by using the application region", *IEEE Transactions on Power Delivery*, vol. 21, no. 4, pp. 1878-1884, 2006.

[18] C. F. Ten, and P. A. Crossley, "Evaluation of ROCOF relay performances on networks with distributed generation", *IET 9th International Conference on Developments in Power System Protection*, pp. 523- 528, 2008.

[19] B. Liu, D. Thomas, K. Jia, and M. Woolfson, "Advanced ROCOF protection of synchronous generator*," IEEE PES Innovative Smart Grid Technologies (ISGT)*, pp. 1-6, 2011.

[20] C. M. Affonso, W. Freitas, W. Xu, and L. C. P. D. Silva, "Performance of ROCOF relays for embedded generation applications." *IEE Proceedings-Generation, Transmission and Distribution*, vol. 152, no. 1, pp. 109-114, 2005.

[21] J. C. M. Vieira, W. Freitas, Z. Huang, W. Xu and A. Morelato, "Formulas for predicting the dynamic performance of ROCOF relays for embedded generation applications", *IEE Proceedings- Generation, Transmission and Distribution*, vol. 153, no. 4, pp. 399-406, 2006.

[22] W. Freitas, W. Xu, C. M. Affonso, and Z. Huang, "Comparative analysis between ROCOF and vector surge relays for distributed generation applications," *IEEE Transactions on Power Delivery*, vol. 20, no. 2, pp. 1315-1324, 2005.

[23] A. Samui, and S. R. Samantaray, "Assessment of ROCPAD relay for islanding detection in distributed generation", *IEEE Transactions on Smart Grid*, vol. 2, no. 2, pp. 391-398, 2011.

[24] R. S. Kunte, and W. Gao, "Comparison and review of islanding detection techniques for distributed energy resources," *40th North American Power Symposium*, pp. 1-8, 2008.

[25] M. E. Ropp, M. Begovic, and A. Rohatgi, "Analysis and performance assessment of the active frequency drift method of islanding prevention", *IEEE Transactions on Energy conversion*, vol. 14, no. 3, pp. 810-816, 1999.

[26] A. Yafaoui, B. Wu, and S. Kouro, "Improved active frequency drift anti-islanding detection method for grid connected photovoltaic systems", *IEEE Transactions on Power Electronics*, vol. 27, no. 5, pp. 2367-2375, 2012.

[27] X. Wang, W. Freitas, W. Xu, and V. Dinavahi, "Impact of DG interface controls on the Sandia frequency shift anti-islanding method", *IEEE Transactions on Energy Conversion*, vol. 22, no. 3, pp. 792-794, 2007.

[28] H. H. Zeineldin, and S. Kennedy, "Sandia frequency-shift parameter selection to eliminate non-detection zones", *IEEE Transactions on Power Delivery*, vol. 24, no. 1, pp. 486-487, 2009.

[29] G. Hernandez – Gonzalez and R. Iravani, "Current injection for active islanding detection of electronically - interfaced distributed resources," *IEEE Transactions on Power Delivery*, vol. 21, no. 3, pp. 1698-1705, 2006.

[30] P. Gupta, R. S. Bhatia, and D. K. Jain, "Average absolute frequency deviation value based active islanding detection technique," *IEEE Transactions on Smart Grid*, vol. 6, no.1, pp. 26-35, 2015.

[31] H. Y. Lee, B. M. Han, and H. J. Cha, "Novel islanding detection method for distributed generation," *IEEE Energy Conversion Congress and Exposition*, pp. 3378-3384, 2009.

[32] H. Karimi, A. Yazdani, and R. Iravani, "Negative-sequence current injection for fast islanding detection of a distributed resource unit", *IEEE Transactions on Power Electronics*, vol. 23, no. 1, pp. 298-307, 2008.

[33] V. Menon, and M. H. Nehrir "A hybrid islanding detection technique using voltage unbalance and frequency set point", *IEEE Transactions on Power System*, vol. 22, no. 1, pp. 442–448, 2007.

[34] S. I. Jang, and K. H. Kim, "An islanding detection method for distributed generations using voltage unbalance and total harmonic distortion of current", *IEEE Transactions on Power Delivery*, vol. 19, no. 2, pp. 745–752, 2004.

[35] P. Mahat, Z. Chen, and B. B. Jensen, "A hybrid islanding detection technique using average rate of voltage change and real power shift", *IEEE Transactions on Power Delivery*, vol. 24, no. 2, pp. 764-771, 2009.

[36] H. Vahedi, and M. Karrari, "Adaptive fuzzy Sandia frequency-shift method for islanding protection of inverter-based distributed generation", *IEEE Transactions on Power Delivery*, vol. 28, no. 1, pp. 84- 92, 2013.

[37] W. K. A. Najy, H. H. Zeineldin, A. H. K. Alaboudy, and W. L. Woon, "A Bayesian passive islanding detection method for inverter-based distributed generation using ESPRIT", *IEEE Transactions on Power Delivery*, vol. 26, no. 4, pp. 2687-2696, 2011.

[38] C. Schauder, and H. Mehta, "Vector analysis and control of advanced static VAR compensators," *IEE Proceedings on Generation, Transmission and Distribution*, vol. 140, no. 4, pp. 299-306, 1993.

VIII. BIOGRAPHIES



Pankaj Gupta received B. E. in Electrical Engineering from BIT, Durg, India, in 2000 and the M. E. in Electrical Engineering from Delhi College of Engineering, Delhi University, Delhi, India, in 2003. He is currently working toward the Ph.D. at the National Institute of Technology, Kurukshetra, Haryana, India. He is an Assistant Professor with the Department of ECE, Indira Gandhi Delhi Technical University for Women, Delhi, India. His research interests include power system protection, renewable energy systems and islanding detection techniques.



Dr. R. S. Bhatia received B. Tech in Electrical Engineering from Guru Nanak Engineering College, Ludhiana, India in 1987. He received M. Tech and the Ph.D. in Electrical Engineering from the Regional Engineering College, Kurukshetra, Haryana, India in 1993 and 2008, respectively. He is currently a Professor with the Department of Electrical Engineering at the National Institute of Technology, Kurukshetra, Haryana, India. His research interests include power electronics, electric power quality, electrical circuits and renewable energy systems.



Dr. D. K. Jain received the B.Sc, M. Tech and Ph.D. in Electrical Engineering from Regional Engineering College, Kurukshetra, Haryana, India, in 1987, 1993 and 2001, respectively. He is currently a Professor with the Deparment of Electrical Engineering at Deenbandhu Chhoturam University of Science and Technology, Murthal, Haryana, India. His research interests include power system protection, electric power quality, electric drives, and renewable energy systems.

0885-8977 (c) 2016 IEEE. Personal use is permitted, but republication/redistribution requires IEEE permission. See http://www.ieee.org/publications_standards/publications/rights/index.html for more information.

AN ANALYSIS OF REACTION TO GREEN PRODUCT INITIATIVES

[1]Gaurav Dawar, [2]Dr. Seema Singh

[1]Research Scholar, [2]Associate Professor, Department of Humanities,

Delhi Technological University (India)

ABSTRACT

The purpose of this paper is to investigate the reaction of consumer towards green product initiatives of the companies and impact of Household Income on Consumer's Green consumption decision. The study conducted is exploratory in nature with four levels of income. The survey of 300 respondents has been conducted and responses gathered have been analyzed on the basis of descriptive statistics. It was found from the study that the consumers in the region have high awareness about recycle, organic and energy efficient product but their utility is limited due to higher pricing by companies. The study is one of the first to focus on the consumption decision of females in relation to the green products offered by the companies.

Keywords: Sustainable Development, Green Marketing, Environmental, Ecological, Green Product, Green Products.

I INTRODUCTION

Sustainability has become the mantra for companies seekingto create a competitive advantage in the global marketplace.Recent interviews with over 750 CEOs from around the worldrevealed that 93 percent feel that implementing sustainabilityprograms that mesh with their corebusinesses would becritical to the future success of those businesses (UN GlobalCompact, 2010). These programs range from developingtotally new green products, developing recycled orrefurbished products to engaging in greener processes.

Thenewly produced goods that result are made of reclaimed/recycled/refurbished components. We propose that consumersevaluate these types of products differently than new greenproducts. Third, strategies for developing green processes canbe developed from firms' everyday business activities. Thesemethods may include reducing water usage, plant/manufacturing emissions, energy consumption, solid wastes,and acid rain emissions (sulfur dioxide, nitrogen oxide, and ammonia).

The challenge of healthier communities begins with environmental concern and collective adoption of Green behaviors, because the choices consumers make with regard to the environment influence thehealth and quality of

life for both current and future generations. Ingeneral terms, environmental concern is a "concept that can refer tofeelings [consumers have] about many different green issues" (Zimmer,Stafford, and Stafford 1994, p. 64). The topic became an important one in1962 when Rachel Carson's Silent Spring was published and has recentlybecome even more critical with today's concerns about creating a sustainableand healthy environment.

Economic world is now thinking in favor of the fairer sex. Now-a-days women are not only playing role of hardcore 'housewives', they are also playing a different role of 'chief purchasing officer' & controlling 85% of buying decisions. In today's world, they are working as multi-tasker by playing a role of house maker as well as professional women with their hard work. With their new role as a professional, there has been a gradual evolution in the status of women & now they are called as marketers. As a professional India, women hold 25% of jobs in different sectors, although in 1980 it was only 10%. An Indian woman today has a greater sense of empowerment and economic freedom, which indicates that their consumption pattern has changed.

Gender has been studied as a predictor of attitudes for many years based on the notion that males and females possess distinct characteristics, and green research has suggested that females might be more environmentally concerned than males (Lee 2009; Mostafa 2007; Schwartz and Miller 1991).

II REVIEW OF LITERATURE

Pacific Gas and Electric has admitted that CompactFlorescent Light bulbs are not as long lasting as hadoriginally claimed and their green advantages in terms ofenergy and hazardous waste may not be as significant asanticipated (Smith, 2011). Nissan's electric car, the Leaf, willonly achieve its promised 100-mile range under idealconditions; any use of heater, air conditioner, or otherenergy-drawing device can significantly reduce the Leaf'srange (Ramsey, 2010).

MiglaniSurinder (1997) has investigated the buying behavior of Indian women by using a well-structured questionnaire with 500 respondents fromDelhi-NCR region. His findings were that there is change in the role of Indian women and they now fit in the role of a facilitator than purchasing on family needs and wants. She also considers the importance of corporate social responsibility while making a buying decision.

Irawan Ronnie (1998) has investigated the factors influencing green purchasing behavior of university students in Jakarta. The findings of the research were Environmental Concern, Perceived Seriousness of Environmental Problems, and Perceived Environmental Responsibility-were significantly affecting green purchasing behavior and there was no gender differences on these significant variables. The researcher concluded that there are different variable that can influence the green purchasing behavior but independently only three variable environmental concerns, perceived seriousness of environmental problem and perceived environmental responsibility had the significant influence.

Dennis Charles (2000) has researched on shoppers, particularly women, and factors influencing them. The researcher has used comparison experiment, semi-structured questionnaire and focus group to compare a traditional e-shopping website with a social e-shopping one. The findings of the research were young women prefer social e-

shopping sites. Both utilitarian and hedonic young adult female shoppers found social e-shopping enjoyable and useful. However, although many participants found the social e-shopping site more difficult to use, this was outweighed by their enjoyment of the site and its usefulness. The study demonstrated the potential value of the concept of social e-shopping for future research. The researcher concluded social e-shopping can be a valuable strategy for e-retailers wanting to gain competitive advantage and to positively increase the e-shopping behavior intentions of young women.

Fowler (2002) reported that 42 percent of people will not buy green products, fearing that the products will not work as well as conventional products. A 2007 Gfk Roper study found that 61 percent of consumers believe that green products performed less effectively than non-green (Gfk Custom Research North America, 2009). More recently, however, Manget et al., 2009 discovered that almost half of the respondents in a multi-country survey indicated that green products offer comparable or superior quality over conventional alternatives.

Collins M. Christy (2007) has investigated customer's values, beliefs on sustainable corporate performance and their buying behavior. To achieve the research objectives a well-structured questionnaire was used where in total 300 respondents from Aldi and Albert Heijn supermarkets in the city of Groningen, Netherlands. The research explored values, beliefs about the importance of SCP, and buying behaviors of supermarket customers from within a stakeholder framework. Beliefs about the importance of SCP (both social and environmental, but not economic) were found to be related to values. Also, it was found that customers' environmentally responsible buying behaviors were related to their beliefs about the importance of environmental SCP. However their socially responsible buying was not related to their beliefs about the importance of social SCP. The researcher concluded that Marketing professionals have a central role to play in moving towards a greater level of corporate transparency and sustainability.

Veisten (2007) determined that willingness to pay forecologically labeled tables ranged from 2-16 percent abovethose of unlabeled products. Laroche et al. (2001) found that13.1 percent of respondents were willing to pay a higher pricefor green products. Sammer and Wustenhagen (2006) foundthat consumers were willing to pay a 50 percent pricepremium for a washing machine labeled as energy efficient.Vlosky et al. (1999) analyzed the effects of environmentalattitudes on a consumer's willingness to pay, concluding thatconsumers with higher levels of environmental consciousnessare willing to pay more for environmentally friendly products,and D'Souza et al. (2006) found that quality is moreimportant than price to consumers.

Laroche Michel (2008) has investigated aboutconsumers' willingness to pay more for environmentally friendly products. Awell-structured questionnaire was used where in total 500 respondents were sampled. Concerns related to the environment are evident in the increasingly ecologically conscious marketplace. Using various statistical analyses, investigated the demographic, psychological and behavioral profiles of consumers who are willing to pay more for environmentally friendly products. The findings of the research were that this segment of consumers were more likely to be females, married and with at least one child living at home. They reported that today's ecological

problems are severe, that corporations do not act responsibly toward the environment and that behaving in an ecologically favorable fashion is important and not inconvenient. The researcher concluded They place a high importance on security and warm relationships with others, and they often consider ecological issues when making a purchase.

Chatterjee (2009) examined consumer reaction to green category (or line) extensions of well-known brands. Their primary findings relevant to the current project are that consumers have significantly positive reactions to green extensions if the category has high environmental impact (e.g. paper towels, detergents), and that for existing customers, line extensions are preferred over category extensions.

Essoussi and Linton (2010) investigated consumers' willingness to pay for recycled products. They found that though consumers were willing to pay a price premium, this premium narrowed as the functional risk of the product category rose. The price premium represented the additional value consumers place on recycled versus non-recycled products. Extending this line of thought presents the possibility that, for certain product categories, recycled products may be perceived less positively than new green products.

Flannery Tim (2010) has investigated the gap between the consumer attitude and purchase behavior of green products.He surveyeda total of 2000 Australian consumers completed an online survey using structured questionnaire for one of four product categories, namely: televisions, digital cameras, air conditioners and washing machines. The findings were Respondents who cared about the environment tended to be guided by self-transcendence values of equality, helpfulness, forgiveness and loving. Unexpectedly, even those respondents who were more concerned about how their purchases affected their own individual situation still had positive attitudes towards purchasing green products.

Gan Christopher (2010) has investigated Consumers' purchasing behavior towards green products in New Zealand. A survey of total 500 respondents were done using structured questionnaire. He found thatpeople engage in environmental behavior as a result of their desire to solve environmental problem, to become role models and a belief that they can help to preserve the environment. However, consumers' indications of positive attitude towards environmental issues do not necessarily lead to actual environmentally friendly purchasing behavior. Majority of consumers do not purchase products based on the environmental concern alone and there will not trade-off other product attributes for a better environment.

Bjork Peter (2013) has investigated the value of green labels- consumers perceptive.A survey of 200 respondents was done. The value-attitude-behavior model was tested in this study, and the effects of greenlabels on the consumer decision making processes were assessed. The findings of the research were that Finnish consumers have a positive attitude toward green labels and are willing to pay a higher price for productsmarked with a green label. Attitudes have a direct effect on consumer behavior, but values correlate only with the variable willingness- to-pay.

Past research has found that a company and its products areconsidered as non-separate entities (Brown and Dacin, 1997),and therefore the image of a company's practices can have asignificant impact on consumers. Research also shows that 79percent of US consumers feel that a company's environmentalpractices influence decisions about which products andservices they recommend to others (Gfk Custom ResearchNorth America, 2009). Of the consumers, 53 percent preferto purchase products and services from a company with astrong environmental reputation. D'Souza et al. (2006) statethat "consumer's perception of the firm's corporate strategiestoward environmental issues is expected to contribute to theformation of the overall perception about green products."Brown and Dacin (1997) reported that a company's corporatesocial responsibility (CSR) activities have a positive impact onproduct preference, though the impact is not direct. PositiveCSR activities have a positive impact on the evaluation of thecompany, which, in turn, has a positive impact on theproduct.

An attempt has been made to examine the different elements of buying behavior of females towardsgreen product in Delhi and NCR and are they willing to pay more for an green product.

To examine the different elements of environmental concern, we utilize different dimensions identified by Zimmer, Stafford, and Stafford (1994). This allowed us to determine whether the level of importance of certain types of environmental concern is significantly related to the willingness to spend more on an green product.

Thus we test the following hypothesis:

H1: There is a significance difference between the attitudes of respondent of different house hold income towards different environmental friendly practices.

III RESEARCH METHODOLOGY

The present study conducted is exploratory in nature and survey method has been used for data collection. The data is collected from 300 females from across Delhi and NCR from November 2014 to December 2014. The sampling of population is done on the basis of females pursuing their graduation and post-graduation, working women, professionals, entrepreneur & housewives and Convenience samplinghas been used for the study.The data collected has been tabulated and analyzed systematically with the help of Descriptive Statistics.Cron batch Alpha has been applied to test the reliability of the questionnaire.

The questionnaire has 10 questions with multiple choice options and 5 point likert scale. The result of Cron batch Alpha is .80 (Table 1) which is greater than 0.7, therefore the data is considered to be reliable.

The demographic profile of 300 females who has completed the survey is 63% of females are single; 43% of females are graduate, 39% are postgraduate and 12 % are Doctorate; 28% of females are organizational employees, 14% are students, 11% are housewives and 8% are entrepreneur and 3% are retired females.The age group of females in survey is 57% of females are of age group 20 to less than 30, 30% of females are of the age group30 to less than 40, 7% of the age group of 40 to less than 50, 5% of the age group more than 50.

The females of different income group is 27% females have total household income of 5 to less than 10 lakhs, 17% are of 15 to less than 20 lakhs and 24% are of 10 to less than 15 and 24% are of the income group of 20 lakhs and above.

In our survey we have also tried to identify the area of origin of our respondents as Delhi being a cosmopolitan city. 41% of our respondents have originated from North India, 18% are from South India, 17% are from East India, 11% from Central India.

IV DATA ANALYSIS

In our survey of green products 63% of the females are single, 43% are post graduate, 28% are organizational employees. From the survey we can conclude that 90% of the respondents in our survey are energy efficient including the respondents who sometimes act energy efficient. And also around 50% of the respondents consider them environmental friendly including the respondents who sometimes act environmental friendly. Also from the survey it is clear that only 45% female consider buying products which are labeled as green. Also the survey showed that 40% out of the sample population is affected by friends/relatives/colleagues opinion while making decision when they are shopping for green products, 29% is affected by T.V, newspaper and magazine ads and 19% are affected by point of purchase.

The data of females from Delhi & NCRshows that 45% of total females consider themselves energy efficient (chart 1), 50% considers themselves as environmental friendly (Chart 2), 45% buy the product which are labeledas environmentally safe (Chart 3). 42% of the respondent's mentions relative or friends' influence the decision to buy green product (Chart 4).

Chart 5 shows that about 60% of the women respondents have heard about organic products and 30% of them have actually used it. This shows that there is enough awareness about ecofriendly products among females as their responses have been collected from different demographics. Chat 6 no shows that 29% of the female respondents have heard about recycled product and 19% have actually used it.

Char 7 highlights the reasons of less usage of organic products. Our respondent's awareness of organic products is quite high. It is about 60% and usability rate among respondents is 30%. They highlighted various factors for less usage of these products. Survey shows that 35% of respondents feel that organic products are not used as it does not fulfill the respondents' expected performance level and 17% considers that the appearance of the organic product unattractive and 12% find organic products expensive.Chart 8 shows 23% of Respondents with medium awareness level of recyclable products feels that reason for less usage of recyclable products is product appearance not appealing and 15% feels that product is too expensive to buy.

Chat 9 shows that 70% of respondents says that it is very important for a product to be energy efficient. Whereas 47% of the respondents say it is important to be environmental friendly. While almost the same majority also consider products possessing the trait of being environment friendly is not that important.Chart 10 shows 60% of Respondents said that they consider Ozone depletion and greenhouse effect of the product on environment very

important while buying the product. Internet based advertisement and out-door ads has very less impact.In case of organic products out of the total sample 60% of the respondents have heard about the product and 32% have actually used the product. The major reason for not using the organic product is reduced performance possibility according to the survey. While In case of recyclable products out of the total sample 10% of the respondents have heard about the product and 19% have actually used the product. In case of energy efficient products out of the total sample only 1% of the respondents have heard about the product and 16% have actually used the product. On the other hand in case of wastage reduction products out of the total sample only 5% of the respondents have heard about the product and 10% have actually used the product. In case of solar power products out of the total sample only 3% of the respondents have heard about the product and 6% have actually used the product. In case of green construction material out of the total sample only 1% of the respondents have heard about the product and 4% have actually used the product. The major reason for not using the wastage reduction product, solar power product and green construction material is that it too expensive and the reason for not using the recyclable product and energy efficient products is that the product appearance is not appealing according to the survey.The level of the importance the respondents attach with the energy efficient product is very high than the other aspects in the survey and on the other hand wastage reduction product are not considered important related to environment protection.According to the survey generally 40% of the people think that green products are of same quality versus similar products but not green and 39% of the respondents think that green products are of higher quality versus similar products but not green and 10% consider the quality as inferior. If a product is available for Rs.100 then the maximum amount the respondent is ready to pay is Rs.131 for another product which is almost similar except that it is also green. This shows the willingness of people who are ready to pay more for green products.Also there is no significance difference between the attitudes of respondent of different house hold income towards different environmental friendly practices. In this case we can say that female respondents with different house hold income have similar attitude and buying behavior towards different green products and they try to convince friends, relatives and colleagues not to buy products which are harmful to the environment.

V CONCLUSION & SUGGESTIONS

Our findings do offer insight into perceptions of environmental concern and willingness to pay forgreen product. These findings suggest that educational messages should be targeted toward people to encourage purchase of such products. The findings also suggest that respondents who are particularly concerned with waste may be more likely to spend more money on an environmentally friendly product. Therefore, a reduced usage of energy via simpler packaging and recycling innovations may be supported by a group of consumers. Educating consumers on why green products cost more as well as the benefits of using green products, particularly where health benefits are concerned (i.e., reduced factory emissions, pesticide-free agriculture, reduce ozone depletion), may be helpful in closing the gap between consumers merely possessing a pro-environmental attitude and extending that attitude to

intentions to adopt pro-environmental behaviors—in the case here, spending more money on an environmentally friendly product. However, because our research only examined willingness to pay forgreen product and not behavior, this speculation needs to be examined in future research.Although a movement toward reducing the costs of these environmentally friendly products might be helpful, it may not be realistic. Another alternative is increased government subsidies for companies developing green products so that the cost to the consumer can be reduced. If the ultimate universal goal is a sustainable environment with long-term health benefits for all consumers, then collective effort among consumers and businesses is critical.In short, the research begins to understand who is willing to pay more for an environmentally friendly product and it showed that one should allow for the development of effective communications to different groups of consumers to educate them on the benefits of purchasing these products. Addressing salient needs is critical in moving from environmental concern to action, and consumers need to play an active role in maintaining their environment to protect their own community and personal health.

VI LIMITATIONS

- Sample size of the study was 300, we can increase the sample size and replicate the research for more accurate results.
- Environment concern is huge issue nowadays so many more sections and issues can be targeted and the report can be replicated to get the result.
- Time was one of the limitations.
- The questionnaire can be replicated by involving many other factors of buying behavior and attitude.
- The study is focused only on female consumer; male consumer can be also targeted to get more effective result.

REFERENCES

- Aaker, David A. and Richard P. Bagozzi. 1982. Attitudes toward Public Policy Alternatives to Reduce Air Pollution. Journal of Public Policy & Marketing, 1: 85–94.
- Abdul-Muhmin, Alhassan G. 2007. Explaining Consumers' Willingness to be Environmentally Friendly. International Journal of Consumer Studies, 31 (May): 237–247.
- Allen, Jeff, Duane Davis, and Mark Soskin. 1993. Using Coupon Incentives in Recycling Aluminum:A Market Approach to Energy Conservation Policy. Journal of Consumer Affairs, 27 (winter):300–319.
- American Public Health Association. 2007. Addressing the Urgent Threat of Global Climate Change to Public Health and the Environment.

- Anderson Jr., Thomas W. and William Cunningham. 1972. The Socially Conscious Consumer. Journal of Marketing, 36 (July): 23–31.
- Antil, John. 1984. Socially Responsible Consumers: Profile and Implications for Public Policy. Journal of Micromarketing, 4 (December): 18–39.
- Baugh, Joyce A. 1991. African-Americans and the Environment: A Review Essay. Policy Studies Journal, 19 (Spring): 182–191.
- Bone, Paula Fitzgerald, Karen Russo France, and Kathryn J. Aikin. 2009. On Break-up Cliches Guiding Health Literacy's Future. Journal of Consumer Affairs, 43 (summer): 185–198.
- Chang, N. and Fong, C. (2010), "Green product quality,green corporate image, green customer satisfaction, andgreen customer loyalty", African Journal of BusinessManagement, Vol. 4 No. 13, pp. 2836-44.
- Chatterjee, P. (2009), "Green brand extension strategy andonline communities", Journal of Systems and InformationTechnology, Vol. 11 No. 4, pp. 367-84.
- D'Souza, C., Taghian, M. and Khosla, R. (2007),"Examination of environmental beliefs and its impact onthe influence of price, quality and demographiccharacteristics with respect to green purchase intention",Journal of Targeting, Measurement and Analysis for Marketing,Vol. 15 No. 2, pp. 69-78.
- Diamantopoulos, Adamantios, Bodo B. Schlegelmilch, Rudolf R. Sinkovics, and Greg M. Bohlen. 2003. Can Socio-Demographics Still Play a Role in Profiling Green Consumers? A Review of the Evidence and an Empirical Investigation. Journal of Business Research, 56 (June): 465–480.
- Do Paco, Arminda and Mario Raposa. 2009. "Green" Segmentation: An Application to thePortuguese Consumer Market. Marketing Intelligence & Planning, 27 (3): 364–379.
- Drumwright, Minette. 1994. Socially Responsible Organizational Buying: Environmental Concern as a Noneconomic Buying Criterion. Journal of Marketing, 58 (July): 1–19.
- D'Souza, Clare, Mehdi Taghian, Peter Lamb, and Roman Peretiatko. 2007. Green Decisions:Demographics and Consumer Understanding of Environmental Labels. International Journalof Consumer Studies, 31 (July): 371–376.
- Ebi, Kristie L., David M. Mills, Joel B. Smith, and Anne Grambsch. 2006. Climate Change and Health Impacts in the United States: An Update on the Results of the U.S. National Assessment. Environmental Health Perspectives, 114 (September): 1318–1324.
- Ellen, Pam Scholder, Joshua Lyle Wiener and Cathy Cobb-Walgren. 1991. The Role of Perceived Consumer Effectiveness in Motivating Environmentally Conscious Behaviors. Journal of PublicPolicy & Marketing, 10 (Fall): 102–117.
- Fuller, R.A. Graduate Environmental Sciences. International Graduate (Accessed April 16, 2010)
- Gallup Poll. 2009. Water Pollution Americans' Top Green Concern. 117079.

- Grantham, Susan. 2007. But What Do They Really Think? Identifying Consumers' Values Relevant to Adopting Biotechnologically Produced Foods. Journal of Public Affairs, 7 (November):372–382.
- Hartman Group (2007), Hartman Report on Sustainability:Understanding the Consumer Perspective, Hartman Group,Bellevue, WA
- Hansman, Harrie and Veronique Schutjens. 1993. Dynamics in Market Segmentation: A Demographic Perspective on Age-specific Consumption. Marketing and Research Today, 21 (3):139–147.
- Harrell, Gilbert and Diane M. McConocha. 1992. Personal Factors Related to Consumer Product Disposal Tendencies. Journal of Consumer Affairs, 26 (winter): 397–417.
- Jones, Robert E. and Lewis F. Carter. 1994. Concern for the Environment Among Black Americans: An Assessment of Common Assumptions. Social Science Quarterly, 75 (September): 560–579.
- Martha Barlett, CEO of Trendsight Group, a marketing Consultancy firm "Marketing to Women" – Advertising express – ICFAI[2]
- Philips, Hugh, How customers actually shop, Journal of Market Research Society, January 1993,Vol 35 Issue 1, pp 51 – 62.
- Simintiras, Pre-purchase satisfaction and first time buying behavior, European Journal of Marketing, 1997,Vol 31 issue 11/12, pp 737 – 872.
- Shainesh, Understanding buying behavior, International Journal of Technology Management, 2004, Vol 28 issue 1, pp 118 – 127.
- Vandermerwe, S. and Oliff, M.D 1990." Customers drive corporations green", Long Range Planning", vol. 23, no. 6, pp. 10-16.
- Veisten, K. (2007), "Willingness to pay for eco-labeled woodfurniture: choice-based conjoint analysis versus open-endedcontingent valuation", Journal of Forest Economics, Vol. 13No. 1, pp. 29-48.
- Yeung, S.P 2005." Teaching approaches in geography and students‟environmental attitudes‟, The Environmentalist", vol 24, no. 1, pp 101-17.
- Zelenym L., Chua, P. and Alrich, C 2000." Elaborating on gender differences in environmentalism, Journal of Social Issues", vol. 56, no. 3, pp 443-57.

APPENDIX

Table 1 Reliability Statistics

Cronbach's Alpha	Cronbach's Alpha Based on Standardized Items	N of Items
.704	.800	10

Chart 1

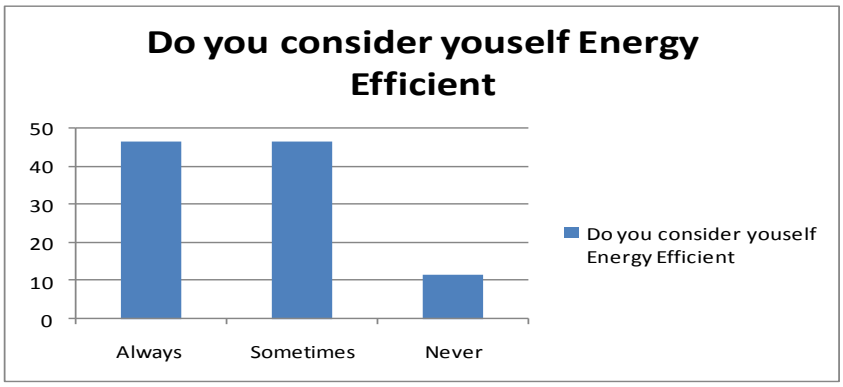


Chart 2

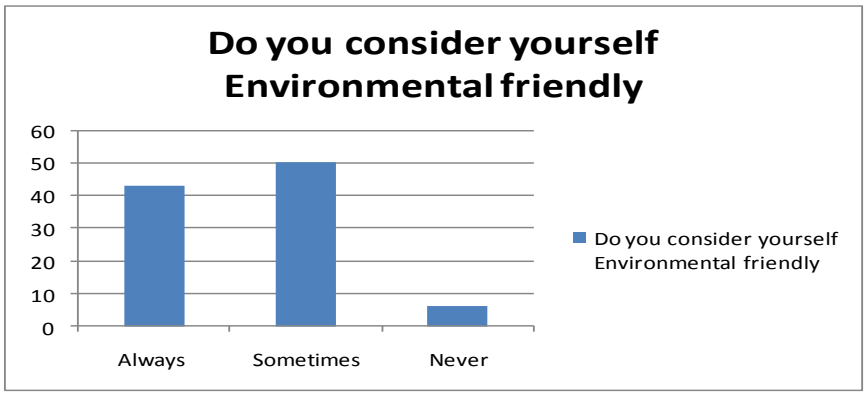


Chart 3

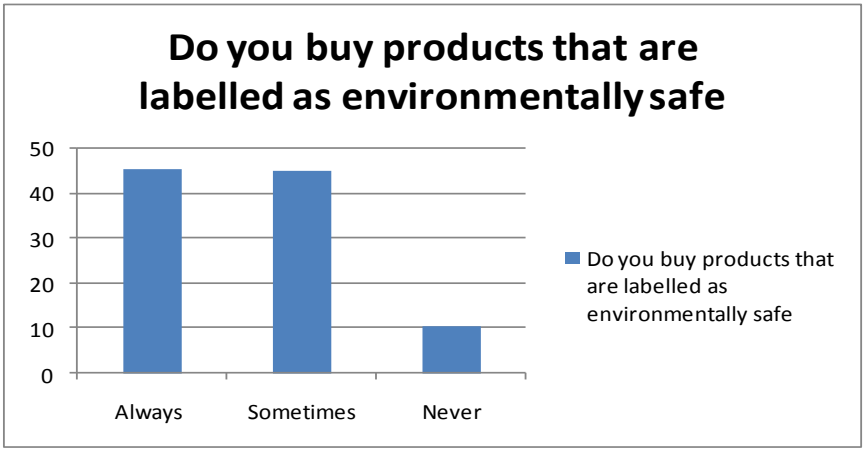


Chart 4

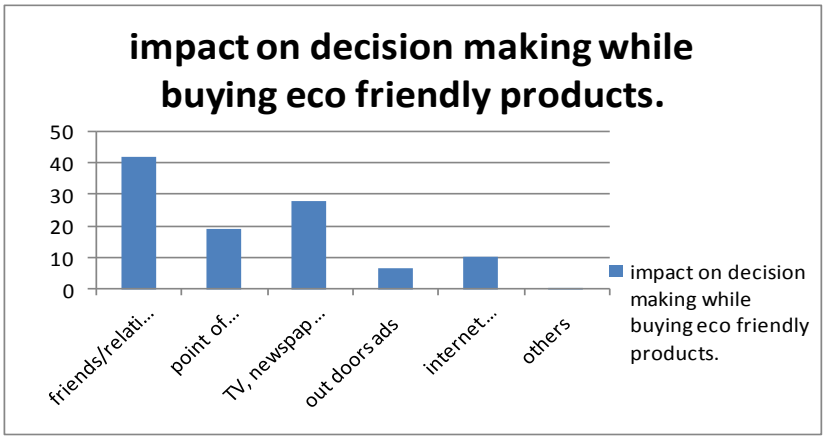


Chart 5

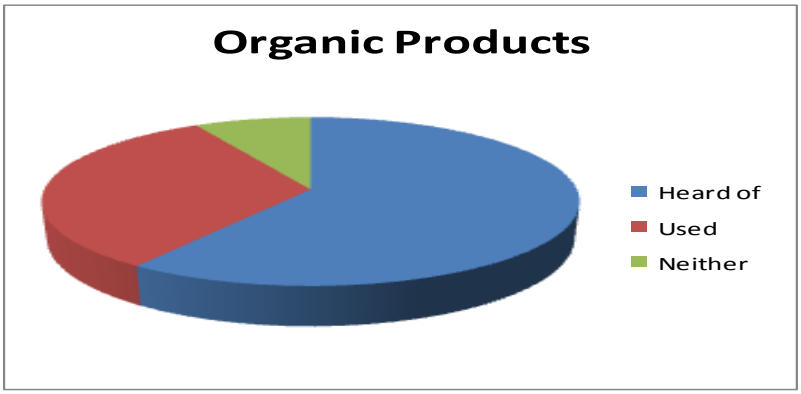


Chart 6

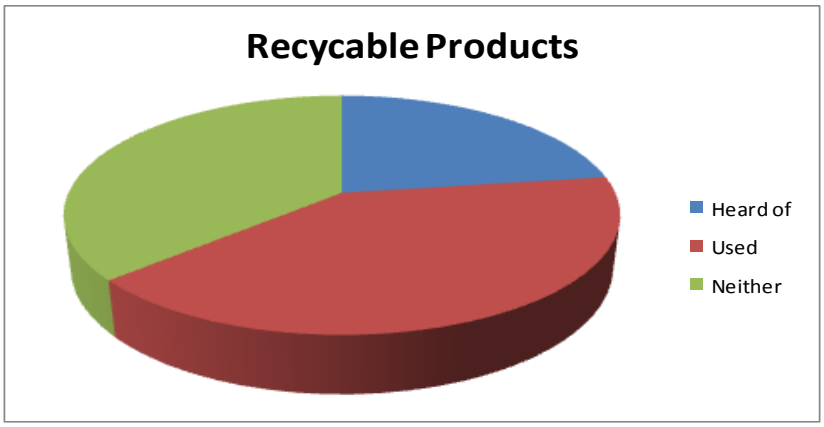


Chart 7

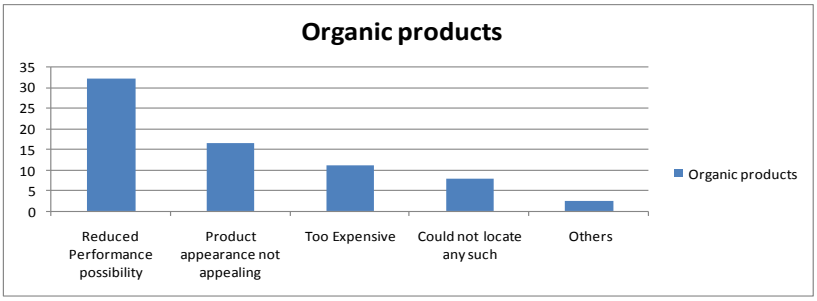


Chart 8

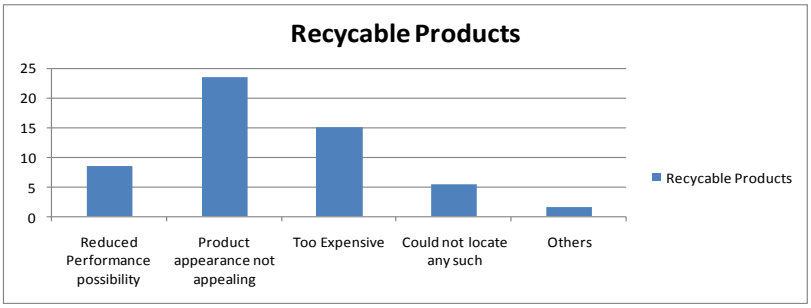


Chart 9

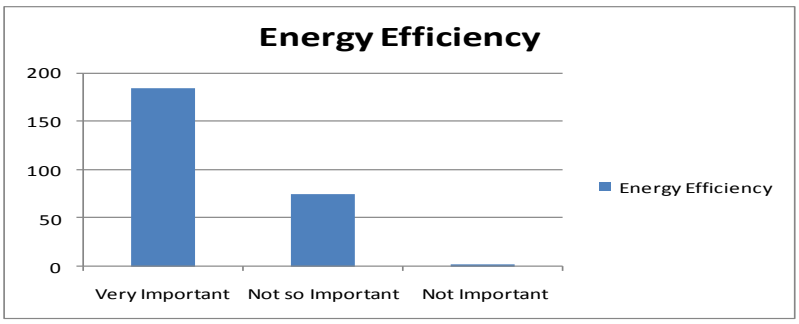
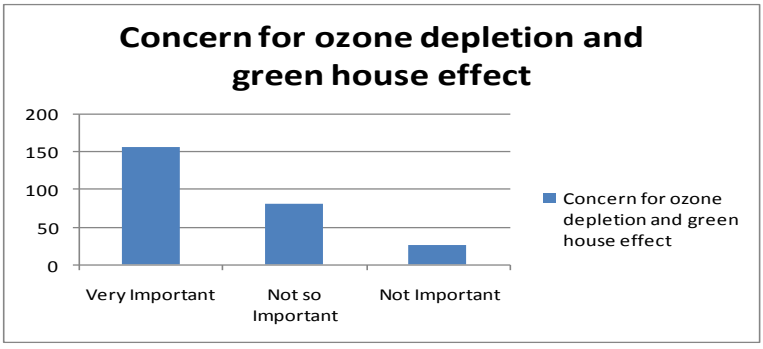

Energy Efficiency
200
150
100
50
0
Very Important
Not so Important
Not Important
Energy Efficiency

Chart 10


Concern for ozone depletion and green house effect
200
150
100
50
0
Very Important
Not so Important
Not Important
Concern for ozone depletion and green house effect

Volume 4, Issue 1 (2016) 82-84 ISSN 2347 - 3258
International Journal of Advance Research and Innovation

Application of statistical tools and hypothesis testing of adsorption data obtained for removal of heavy metals from aqueous solutions

Achla Kaushal[1,*], S.K.Singh[2]
[1]Faculty in Chemical Engineering Department, Directorate of Training and Technical Education, Delhi. India
[2]Department of Environmental Engineering, Delhi Technological University, Delhi, India.

Article Info
Article history:
Received January 2016
Received in revised form
20 February 2016
Accepted March 2016
Available online June 2016

Keywords
Adsorption, experimental data, statistical analysis, hypothesis testing,

Abstract

Hypothesis testing is useful statistical tool understood as a critical testing of the experimental data. The experiment for the removal of heavy metal ions from aqueous solution by adsorption was carried out with the deliberate object of testing hypothesis through different tests meant for the purpose using available data obtained from experiments. Decisions about the validity and significance of the data were made on the basis of hypothesis testing. It enabled us to make probability statements about the adsorption parameters. In the present study, dried mango leaf powder was used to remove Cu, Zn and Pb from heavy metal samples prepared in lab. the experimental data was tested using different statistical tools namely Student's t-tests, F-test to test the equality of variance of two normal populations, Chi-square test to test the effectiveness of the adsorption in removing heavy metal ions, ANOVA for the analysis of significance of difference between means of multiple samples at the same time, all within 5% level of significance.

1. Introduction

Adsorption is a known phenomenon in water treatment since ancient times. It is a common phenomenon in gaseous phase, but is used effectively in treatment of waste water. Literature has shown the use of charcoal prepared from wood char for reducing ores of Cu, Zn and Sn to manufacture bronze by Egyptians and Sumerians during 3750 BC. 450 BC onwards, purification of drinking water drinking came into practice using sand and charcoal filters. [1]. During several decades, concentrations of natural organic materials (NOMs), synthetic organic chemicals (SOCs) and trace heavy metals have increased in all water bodies and drinking water supplies to harmful levels. Lead, mercury, nickel, chromium, thallium, zinc, copper, cobalt, selenium, arsenic and cadmium are the heavy metals known for their toxicity and persistency, are mostly non-biodegradable, unlike organic pollutants. They find their way into water bodies through industrial, domestic and municipal discharges. Their presence in water is a serious threats to all forms of life, because they are mutagenic and carcinogenic in nature. Their presence above prescribed limits in body can cause severe damages to vital organs of the body, such as kidney, liver and brain, reproductive and nervous system [3].

Of all the methods of waste water treatment, adsorption with low cost agricultural waste is one of the trusted methods in heavy metal removal for its cost effectiveness, availability of wide range of adsorbents and reliable metal removal efficiency. A large number of adsorbents prepared from agricultural wastes have been exploited by the researchers for this purpose, such as sawdust, tea waste, palm shell, coconut shell, bamboo activated charcoal, olive cake etc.. Experimental data for the adsorption process obtained in terms of %age removal of heavy metal ions w.r.t. pH, time, temperature, adsorbent dose and metal ion concentration in the sample is analysed by fitting them into non-linear forms such as Langmuir and Freundlich isotherm models[3].

Efforts are put to describe the process qualitatively and quantitatively statistically. The hypothesis testing is based on the null hypothesis (H_o), keeping an alternative hypothesis (H_a). It is assumed that the null hypothesis is true, probabilities are assigned to different possible sample results, but this is possible only if we proceed with an alternative hypothesis. Level of significance is normally determined before testing the hypothesis. It is the maximum value of the probability of rejecting null hypothesis. Our sample results decide if the null hypothesis can be accepted or rejected. If null hypothesis is rejected, alternative hypothesis is accepted.

Various hypothesis tests known as tests of significance developed by statisticians are classified as parametric tests, the standard tests and non-parametric tests, the distribution-free tests of hypotheses.

The important parametric tests, based on the assumption that the data is distributed normally, are z-test, t-test, F-test and χ^2-test.

Z-test is used for judging the significance of significance of mean, median and mode etc by comparing the sample mean with some hypothesized value of the population mean when sample is large (n>30). For a normal and infinite population and known population variance,

$z = (\bar{X} - \mu_{Ho}) / (\sigma_p/\sqrt{n})$, H_a may be one sided or two sided.

T-test, based on distribution is the appropriate test to judge the significance of differences between the two sample means for small samples when the population variance is unknown. For a normal and infinite population, small sample size and unknown population variance,

Corresponding Author,
***E-mail address:** achla001@hotmail.com
+919811200429
All rights reserved: http://www.ijari.org

$t = (\bar{X} - \mu_{Ho})/(\sigma_s/\sqrt{n})$ for (n-1) degree of freedoms and H_a may be one sided or two sided.

$\sigma_s = \sqrt{[\{\Sigma(X_i - \bar{X})^2\}/(n-1)]}$

F-test based on the F-distribution is used to compare the variance of two samples. It is also used in analysis of variance (ANOVA) to judge the significance of means of multiple samples at the same time.

$F = \sigma_{s1}^2 / \sigma_{s2}^2$

$\sigma_{s1}^2 = \{\Sigma(X_{1i} - \bar{X}_1)^2\}/(n_1-1)$

$\sigma_{s2}^2 = \{\Sigma(X_{2i} - \bar{X}_2)^2\}/(n_2-1)$

While performing calculation, F is always taken > 1.

χ^2-test is a technique used to test the goodness of fit, independence and significance of population variance.

$\chi^2 = \sum\{(O_{ij} - E_{ij})^2/E_{ij}\}$

O_{ij}= Observed frequency of the cell in the i^{th} row and j^{th} column.

E_{ij}= Expected frequency of the cell in the i^{th} row and j^{th} column. [4]

2. Materials and Method

Analytical grade Zn metal chips were dissolved in a few drops of conc. H_2SO_4 and then diluted with distilled water to prepare the stock solution. Stock solution was further diluted to concentrations in the range 10-100ppm with the help of distilled water. Mango tree leaves collected from the University campus were washed, dried and crushed to 60 mesh size. They were thoroughly washed to remove all the colour, bone dried in a hot air oven and then stored in air tight container. It was used to determine the % removal of Zn ions from the solutions prepared as mentioned above in the range 1-10 g/L. 12 Erlenmeyer flasks were used at a time in the 'Orbital' constant temperature variable speed shaker at 22°C and 150 rpm for 100 minutes to carry out batch experiment. The concentration of heavy metal was determined by Atomic Absorption Spectrophotometer using air-acetylene flame. Percentage removal of zinc from the solution after the batch adsorption was calculated as

$\% \text{ Removal} = [(C_i - C_o)/C_i]*100$

Where C_o represents the final zinc ion concentration and C_i represents the initial zinc ion concentration in the solution.

The equilibrium adsorption capacity is calculated as

$q_e = [(C_i - C_e)V]/m$

Where V is the volume of the solution in liters and m is the mass of the adsorbent used [5].

3. Results and Discussion

Adsorption of zinc metal ions was carried out on mango leaves powder batch wise. The experiment was conducted for zinc ion metal concentration in the range 10-100 ppm, adsorbent dose 1-10 g/L for the pH between 2-8 at 20°C and at 150 rpm. After each batch experiment, the solution was filtered with Whitman filter paper no. 40 and the concentration of zinc in the filtrate was examined with the help of AAS. Data collected from samples was used for hypotheses testing 1) to judge the maximum lead ion removal from solution 2) to judge the time required to attain equilibrium 3) To test the equality of variance of two n-populations 4) To test the effectiveness of the experiment 5) to judge the significance of means of multiple sample at the same time.

3.1. **Hypothesis testing to judge the maximum removal of the zinc ions from the samples** containing 100 ppm was done with two-tailed t-test within 5% level of significance. Calculations in Table 1 showed the standard deviation was 21.74747, t-observed was -2.41959 and t-tabulated was -2.447 at 5% level of significance for 6 degrees of freedom (d.f.) for 2-tailed t-distribution.

Since $t_{observed} < t_{tabulated}$, null hypothesis was accepted.

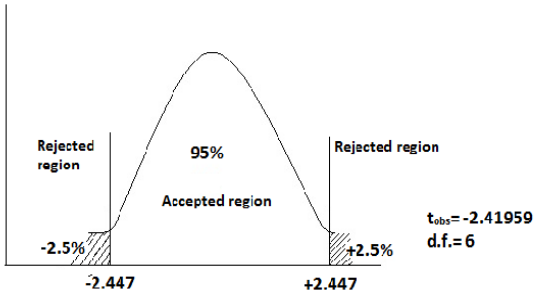


Fig. 1 t-Distribution for two–tailed test

2. Hypothesis testing to judge the time required to attain equilibrium was done with one-tailed t-test within 5% level of significance. Calculations (Table 2) showed the standard deviation was 19.467, $t_{observed}$ was -1.99227 and $t_{tabulated}$ was 2.015 at 5% level of significance for 6 degrees of freedom (d.f.) for 1-tailed t-distribution.

Since $t_{observed} < t_{tabulated}$, null hypothesis was accepted.

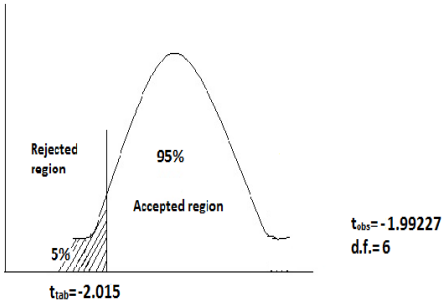


Fig 2. t- Distribution for one – tailed test

3. Hypothesis testing to test the equality of variance of two n-populations, samples collected for initial zinc ion concentrations 100ppm and 50 ppm, was done with F-test within 5% level of significance. It was assumed that the samples have been drawn randomly from two normal populations, observations are independent and there are no measurement errors.

Calculations in Table 3 showed that the variances for two samples were 520.1429 and 423.5714, $F_{calculated}$ was 1.227993 and $F_{tabulated}$ was 4.28 at 5% level of significance for 6 degrees of freedom (d.f.) for F-distribution. Since $F_{calculated} < F_{tabulated}$, null hypothesis was accepted.

4. Hypothesis testing to test the effectiveness of the experiment was done with χ^2-test within 5% level of significance. 60 experiment were conducted varying values of pH [2-8], metal ion concentration (10-100ppm) and adsorbent dose (1-20)g/L. Metal ion removal frequencies were observed for % removal between groups 0-20% [1], 20-40% [2], 40-60% [3], 60-80% [4] and 80-100% [5]. Since the frequencies in groups 1 and 5 were less than 10, they were combined with groups 2 and 4 respectively to

make the frequencies greater than 10. Expected frequencies for each group were equal and 12 each.

Calculations (Table 4) showed that $\chi^2_{calculated}$ was 3.583 and $\chi^2_{tabulated}$ was 9.488 at 5% level of significance for 4 degrees of freedom (d.f.). Since $\chi^2_{calculated} < \chi^2_{tabulated}$, null hypothesis was accepted.

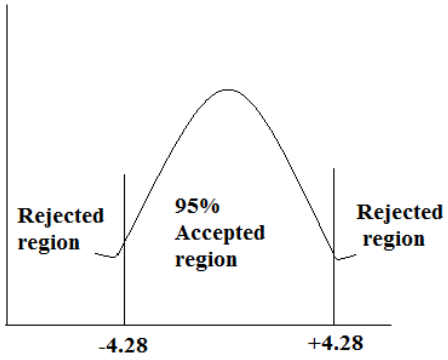


Fig. 3 F- Distribution for 100ppm and 50ppm samples

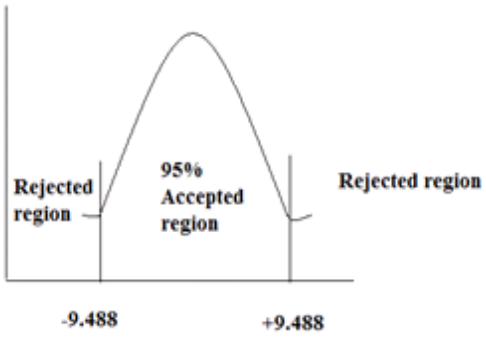


Fig. 4 Chi Square Distribution

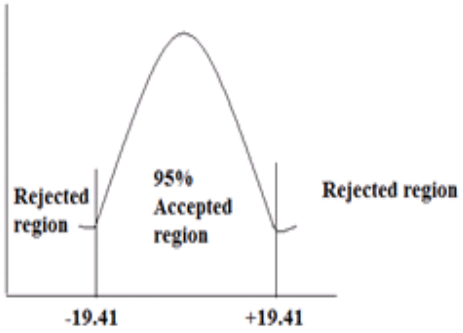


Fig. 4 ANOVA: F-Distribution

4. Analysis of variance (ANOVA) is a useful statistical tool used to test the differences in the means of multiple populations by studying the variations within each sample, since the application t-test and z-test is is limited to two samples only. We compared three populations i.e. adsorption capacities of mango tree leaves for three different heavy metal ions, Zn, Cu and Pb for varying values of adsorbent dose (table 5). F-ratio calculated was 0.018187 and tabulated was 19.41 for (2,12) degrees of freedom. Since F-ratio $_{calculated}$<F-ratio $_{tabulated}$, null hypothesis was accepted.

Conclusions

Hypotheses are the clear and concise statements, assumptions or formal questions for the available data, capable to be tested, which are meant to be accepted or rejected. A hypothesis testing validates these assumptions. In the above study, our assumptions, called the null hypothesis, framed for different situations a) to judge the maximum removal of Zn with by mango tree leaves b) to judge the equilibrium time c) to compare the variances of two different samples of zinc ion concentration d) to check the effectiveness of the experiment and e) to test the difference of means of three different samples at the same time were tested at 5% level of confidence each. All the calculated values were found to be within the accepted region of the probability chart and hence the null hypotheses were accepted.

Paired t-test to compare two related samples, statistical tests for correlation coefficients and adsorption isotherm are recommended for future studies.

References

[1.] Anderson T.W., 1958, An Introduction to Multivariate Analysis, New York: John Wiley & sons.

[2.] Bowley A.L., 1937, Elements of Statistics, 6th ed. London: P.S.King and Staples Ltd.

[3.] Cafer S, Omer S, Ahin M. M., 2012, Applications on agricultural and forest waste adsorbents for the removal of lead (II) from contaminated waters, int. J. Environ. Sci. Technol., 9: 379-394.

[4.] Chance W.A., 1975, Statistical Methods for Decision Making, Bombay: D.B>Taraporevala Sons & co. Pvt Ltd.

[5.] Dabrowski A, 2001, Adsorption—from theory to practice, Adv. Colloid Interface Sci.93, 135–224.

[6.] Ferhan C. and Ozgur A., 2011, Activated Carbon for Water and Wastewater treatment: Integration of Adsorption and Biological Treatment, First Edition, WILEY-VCH Verlag GmbH & Co. KGaA, Weinheim.

[7.] Goel P.K., 2006, Water pollution, Causes, Effects and Control, N. Delhi: New age international publishers, Revised second edition.

[8.] Kothari C.R., 2005, Research Methodology: Methods & Techniques, New Delhi: New Age International (P) Limited, Publishers.

[9.] Qaiser S, Saleemi A.R. and Ahmad M.M., 2007, Heavy metal uptake by agro based waste materials, Electronic j of Biotech, 10(3).

atoms

MDPI

Article

Atomic Structure Calculations and Study of Plasma Parameters of Al-Like Ions

Arun Goyal [1,*], Indu Khatri [1], Avnindra Kumar Singh [1,2], Man Mohan [1], Rinku Sharma [3] and Narendra Singh [4]

[1] Department of Physics and Astrophysics, University of Delhi, Delhi-110007, India; indu.khatri.du@gmail.com (I.K.); avni.physics@gmail.com (A.K.S.); drmanmohan.05@gmail.com (M.M.)
[2] Department of Physics, D.D.U. College, University of Delhi, Delhi-110015, India
[3] Department of Applied Physics, Delhi Technological University, Delhi-110042, India; rinkusharmagtbit@gmail.com
[4] Department of Physics, Shyamlal College, University of Delhi, Delhi-110032, India; nsingh76@yahoo.co.in
* Correspondence: arun.goyal.du@gmail.com

Academic Editor: James F. Babb
Received: 7 November 2015; Accepted: 30 June 2016; Published: 11 July 2016

Abstract: In the present paper, the spectroscopic properties and plasma characteristics of Al-like ions are investigated in an extensive and detailed manner by adopting the GRASP2K package based on fully relativistic Multi-Configuration Dirac–Hartree–Fock (MCDHF) wave-functions in the active space approximation. We have presented energy levels for Al-like ions for Valence-Valence (VV) and Core-Valence (CV) correlations under the scheme of active space. We have also provided radiative data for E1 transitions for Al-like ions and studied the variation of the transition wavelength and transition probability for electric dipole (E1) Extreme Ultraviolet (EUV) transitions with nuclear charge. Our calculated energy levels and transition wavelengths match well with available theoretical and experimental results. The discrepancies of the GRASP2K code results with CIV3 and RMPBT (Relativistic Many Body Perturbation Theory) results are also discussed. The variations of the line intensity ratio, electron density, plasma frequency and plasma skin depth with plasma temperature and nuclear charge are discussed graphically in detail for optically thin plasma in Local Thermodynamic Equilibrium (LTE). We believe that our obtained results may be beneficial for comparisons and in fusion and astrophysical plasma research.

Keywords: energy levels; radiative data; transition wavelengths; line intensity

1. Introduction

In recent years, medium Z-elements are the most probable candidates for plasma diagnostics and modeling, as spectral lines of higher wavelengths and the atomic spectra of their ions may be employed to compute various parameters, like plasma temperature, electron density, etc. [1–4]. The necessity of highly accurate and consistent plasma parameters required in order to quantify the plasma and for the detailed understanding of the particle confinement, H modes, fusion products, etc., arises from the fact that the accurate and precise measurements of these parameters at superfluous conditions are very cumbersome due to a limited number of experimental techniques. In the past few years, the identification and detailed study and analysis of spectral lines on the experimental side through atomic data have boosted the research progress in plasma physics for highly ionized elements. Therefore, the calculations of various atomic and plasma parameters by implementing several theoretical and experimental methods have become an extensive and active area of research owing to a specific interest in fusion and astrophysical plasma applications, laser physics and nanoplasmonic applications. Since a number of experimental discoveries and examinations on neutral to highly ionized medium to

high Z ions have been presented in the literature [5–10], in this paper, we have furnished the plasma characteristics with Multi-Configuration Dirac–Hartree–Fock (MCDHF) calculations for highly ionized Al-like ions.

In the last few years, various theoretical and experimental studies of highly ionized Al-like ions have been performed by implementing several types of technology [11–37], which has boosted the fame and prominence of Al-like ions. Safronova et al. [38,39] have presented energy levels and radiative data of Al-like ions by making use of Relativistic Many Body Perturbation Theory (RMBPT). Wavelengths and oscillator strengths of Al-like ions from $Z = 26 - 31$ have been reported by Wei et al. [40] by using the MCDHF method. Gupta et al. [41] have listed the energy levels and radiative data for Al-like Cu by performing CIV3 calculations. Sansonetti [42,43] has compiled the spectroscopic data of strontium ions from singly-ionized to H-like and rubidium ions from neutral to Rb XXXXVII. Dong et al. [44] have calculated lifetimes, excitation energies and radiative rates for Al-like iron group elements by applying the MCDHF method. Atomic binding energies of the lithium to dubnium isoelectronic sequence (including Al-like ions) have been studied by Rodrigues et al. [45] in Dirac–Fock approximation. Santana et al. [46] have performed multi-reference Møller–Plesset perturbation theory calculations to check the lowest 40 levels of Al-like iron group elements. Recently, Argamam et al. [47] have calculated the total energy, spin and charge density of all ions of elements of $Z = 1 - 29$ under the formulation of Density-Functional Theory (DFT).

Although much work on the theoretical and experimental side of Al-like ions has been published in the literature, there is a scarcity of atomic data of Al-like ions and the elaborate study of plasma parameters using accurate atomic data. In recent years, characterization of plasmas has become an interesting and significant area of research for understanding and analyzing the utilization of multi-lateral spectroscopic sources. Therefore, we have computed energy levels and radiative data for Extreme Ultraviolet (EUV) transitions from ground state and studied graphically the effect of the increase of nuclear charge on transition wavelength and transition probability for EUV transitions for Al-like ions. We have also investigated the effect of nuclear charge on the line intensity ratio, electron density, plasma frequency and skin depth at high values of plasma temperature in optically thin plasma in LTE for Al-like ions. We have also analyzed the effect of electron density and plasma temperature on the plasma parameter and coupling parameters for the diagnosis and characterization of cold, dense and strongly-coupled plasma at high temperature. The present calculations will be beneficial and helpful for the investigation and breakdown of fusion and astrophysical plasma [48–51] and in nanoplasmonic applications in various fields, such as biomedical, chemical physics, optical physics, etc., [52–59].

2. Theoretical Method

2.1. Computational Procedure

The description of the theoretical base of the MCDHF method has been explained in an elaborate form by Grant [60–63]. Therefore, we discuss only a brief synopsis here. The Dirac–Coulomb Hamiltonian is given by:

$$H_{DC} = \sum_{i=1}^{N} \left(c\alpha_i \cdot p_i + (\beta_i - 1)\, c^2 + V_i^N \right) + \sum_{i>j}^{N} \frac{1}{r_{ij}} \tag{1}$$

where α and β are 4×4 Dirac spin matrices, c is the speed of light, V^N represents the monopole part of the electron-nucleus Coulomb interaction and the last term denotes Coulomb interaction between the electrons. An Atomic State Function (ASF) interpreting fine structure levels for the N electron system is constructed by the linear combination of symmetrically fitted and appropriate Configuration State Functions (CSFs).

$$|\psi_\alpha\ (PJM)\rangle = \sum_{i=1}^{n} C_i\,(\delta)\,|\phi(\gamma_i\ (PJM))\rangle \tag{2}$$

In Equation (2), ϕ is CSF, which represents a particular state with a given parity and angular momentum (J, M). δ represents the orbital occupation numbers, population, coupling, etc. The configuration state functions γ_i are fabricated by the multiplication of one-electron Dirac orbitals. In Equation (2), C_i (δ) are the expansion mixing coefficients for each CSFs, which are attained by means of diagonalization of the Dirac–Coulomb Hamiltonian, given in Equation (1). After this, the radial part of the Dirac orbitals and expansion mixing coefficients are both optimized to self-consistency through the Relativistic Self-Consistent Field (RSCF) method. In the next step, the Breit interaction:

$$H_{Breit} = -\sum_{i>j}^{N}\left[\alpha_i.\alpha_j\frac{\cos(\omega_{ij}r_{ij}/c)}{r_{ij}} + (\alpha_i.\nabla_i)\left(\alpha_j.\nabla_j\right)\frac{\cos(\omega_{ij}r_{ij}/c)-1}{\omega_{ij}^2 r_{ij}/c^2}\right] \quad (3)$$

due to the exchange of virtual photons between two electrons and QED corrections due to vacuum polarization and self-energy effects are taken into account by performing Relativistic Configuration Interaction (RCI) calculations.

2.2. Calculation Procedure

In our MCDHF calculations, we have considered different correlations in a simple and systematic way. To categorize the correlation, atomic electrons may be split into two parts, namely valence electrons and core electrons. Valence-Valence (VV) correlation is the correlation between valence electrons, whereas the correlation between valence electrons and core electrons is defined as Core-Valence (CV) correlation. On the other hand, the correlation between core-electrons is called Core-Core (CC) correlation. In the MCDHF method, these correlations are described by the different constraints included in Equation (2), during the fabrication of CSFs. In VV correlation, CSFs are constructed by the excitation of valence electrons to higher shells, keeping core electrons fixed. In CV correlation, CSFs are generated by the single excitation from the core and one or more excitations from the valence. At last, the CC correlation can be considered by allowing doublet, triplet or more excitations from the core.

In the present paper, to construct atomic state functions, we have used the active space approach in the EOL (Define)scheme. For this purpose, we excite electrons from reference configurations to the active set. For the relativistic fine-structure terms belonging to the $3s^2 3p$ ground state, we perform Single and Double (SD) excitations from the $3s^2 3p$ set to the active space, and for terms related to $3s3p^2$ and $3s^2 3d$, we have done SD excitations from the {$3s3p^2$, $3s^2 3d$} multi-reference set to generate configuration state functions. In the above process, we produce CSFs of definite parity P and total angular momentum J. By applying limitation or boundation to the excitations, the effect of different types of correlations may be included in a proper way. Since the orbitals having the same principle quantum number acquire similar energies, therefore orbitals have been increased in a systematic way in order to handle the convergence of our computations and to enhance the active set layer by layer. To reduce processing time as a result of the large number of orbitals, we optimized the set of orbitals for even and odd parity states separately. Thus, we enhanced the size of the active set as shown below until the convergence is achieved.

$$\mathrm{AS1} = \{n = 3, l = 0-2\}$$

$$\mathrm{AS2} = \mathrm{AS1} + \{n = 4, l = 0-3\}$$

$$\mathrm{AS3} = \mathrm{AS2} + \{n = 5, l = 0-4\}$$

$$\mathrm{AS4} = \mathrm{AS3} + \{n = 6, l = 0-4\}$$

$$\mathrm{AS4} = \mathrm{AS3} + \{n = 7, l = 0-4\}$$

In the present work, in order to explain the inner properties, such as fine structure, transitions, etc., we consider VV and CV correlation effects, and during each active set only newly-added orbitals are optimized by keeping previously optimized orbitals frozen to reduce the computational time. We have also included QED and Breit interactions by performing Relativistic Configuration Interaction (RCI) calculations in order to examine and analyze the effect of higher order correlation effects. Ultimately, we enlarge the size of the multi-reference set to {$3s^2 3p$, 3s3p3d, 3s3p4s} and {$3s3p^2$, $3s^2 3d$} for odd parity states and even parity states, respectively. In the next step, we have determined energies and rates from optimized orbitals. To compute transition parameters, we have employed the biorthogonal transformation [51] of the ASFs.

3. Results and Discussion

3.1. Energy Levels and Radiative Data

The accomplishment of our computations relies on judicious selection of the multi-reference set. In Table 1, we present our fine structure energies of 12 levels belonging to the configurations $3s^2 3p$, $3s3p^2$ and $3s^2 3d$ of Cu XVII, Zn XVIII, Ge XX, Rb XXVI and Sr XXVII calculated by the MCDHF method. To assist readers with the identification of energy levels, we list the configurations in LSJ (L is orbital angular momentum, S is spin and J is total angular momentum) under the first column "Configurations" in Table 1. In the next columns of Table 1, we list energy levels for VV and CV correlations with increasing active set. Since for higher principal quantum numbers the number of CSFs increases very rapidly, so it is very cumbersome to get convergence. Therefore, in this paper, we have limited our CV calculations up to $n = 6$ in which we have an excited electron from core orbital 2p, whereas for VV calculations, it is not very difficult to achieve convergence for higher values of principal quantum number. Furthermore, due to the limitation of our computer calculation, we have done calculations only for VV and CV models. By comparing our VV and CV calculations for $n = 6$, we predict that the adding of additional CSFs by taking excitation from the core pushed down the ground state, except for $3s3p^2\ ^2S_{1/2}$, $3s3p^2\ ^2P_{1/2}$, $3s3p^2\ ^2P_{3/2}$ and $3s^2 3d\ ^2D_{3/2,5/2}$. We also predict that the position of $3s3p^2\ ^2S_{1/2}$ and $3s3p^2\ ^2P_{1/2}$ changes for Al-like Ge, Rb and Sr. From Table 1, one can see that the maximum difference of our CV calculations with NIST is 3179 cm^{-1} for the $3s3p^2\ ^2S_{1/2}$ level for Sr XXVII. In Table 1, we have also studied the discrepancy of our results calculated by using the GRASP2K code with other results calculated by other codes. Our reported energy levels for Al-like Cu for levels $3s^2 3p\ ^2P^o_{3/2}$, $3s3p^2\ ^4P_{1/2}$, $3s3p^2\ ^4P_{5/2}$, $3s3p^2\ ^2D_{3/2}$ and $3s3p^2\ ^2D_{5/2}$ are close to NIST, as compared to the results reported by Gupta et al. [41] using the CIV3 code. On the other hand, for other levels, the results by Gupta et al. [41] are close to the NIST results. The maximum discrepancy of our results with Gupta et al. [41] is 2785 cm^{-1} for $3s3p^2\ ^2P_{3/2}$. This shows that our results are also in good agreement with the results by Gupta et al. [41]. Further, energy levels experimentally observed by Sugar et al. [12] for Al-like Zn are close to NIST as compared, theoretically calculated by us using the GRASP2K code, except for $3s3p^2\ ^2D_{3/2}$, $3s3p^2\ ^2D_{5/2}$, and the maximum percentage difference with Sugar et al. [12] is 2985 cm^{-1} for $3s3p^2\ ^2P_{3/2}$. Further, results reported by Safronova et al. [38] using RMBPT for Al-like Zn are close to NIST as compared to the results by GRASP2K, except for the levels, and the maximum deviation of our results with Safronova et al. [38] is 3225 cm^{-1} for $3s3p^2\ ^2P_{3/2}$. The difference between our results and the RMBPT results is the amount of electron correlation. These are the reasons behind the discrepancies of our results calculated by GRASP2K and other codes, such as RMBPT and CIV3. Therefore, it will be very useful for readers to understand the difference between other methods and the currently-developed code GRASP2K.

Table 1. Aluminum-like isoelectronic sequence: excitation energies (in cm^{-1}) from Multi-Configuration Dirac–Hartree–Fock (MCDHF) calculations, experiments and other theoretical calculations, Diff. (in cm^{-1}) with NIST, Diff.^{ref} (in cm^{-1}) with other results. VV, Valence-Valence; CV, Core-Valence.

Cu											
Configurations	**VV**				**CV**			**NIST**	**Ref. [41]**	**Diff.**	**Diff.^{ref}**
	***n* = 4**	***n* = 5**	***n* = 6**	***n* = 7**	***n* = 4**	***n* = 5**	***n* = 6**				
$3s^2 3p\ ^2P^o_{1/2}$	0	0	0	0	0	0	0	0	0	0	0
$3s^2 3p\ ^2P^o_{3/2}$	33,012	33,103	33,117	33,121	33,215	33,021	33,233	33,239	33,231	6	2
$3s3p^2\ ^4P_{1/2}$	275,539	276,003	276,098	276,121	276,393	276,507	277,136	277,231	277,018	95	118
$3s3p^2\ ^4P_{3/2}$	290,024	290,481	290,577	290,602	290,854	291,014	291,649	291,810	291,749	161	100
$3s3p^2\ ^4P_{5/2}$	305,982	306,418	306,512	306,535	306,764	306,961	307,584	307,708	307,482	124	102
$3s3p^2\ ^2D_{3/2}$	372,211	372,306	372,353	372,358	373,159	372,845	373,184	372,236	371,135	948	2049
$3s3p^2\ ^2D_{5/2}$	377,646	377,742	377,790	377,795	378,581	378,293	378,648	377,783	376,849	865	1799
$3s3p^2\ ^2S_{1/2}$	448,218	447,924	447,922	447,904	448,298	447,345	447,383	444,759	444,858	2624	2525
$3s3p^2\ ^2P_{1/2}$	484,224	483,980	483,986	483,973	483,784	482,863	482,937	480,016	480,269	2921	2668
$3s3p^2\ ^2P_{3/2}$	495,323	495,091	495,102	495,094	494,167	493,288	493,397	490,467	490,612	2930	2785
$3s^2 3d\ ^2D_{3/2}$	578,586	577,747	577,748	577,742	577,777	576,221	576,056	574,180	575,511	1876	545
$3s^2 3d\ ^2D_{5/2}$	582,476	581,641	581,648	581,642	581,821	580,260	580,102	578,243	579,601	1859	501
Zn											
Configurations	**VV**				**CV**			**NIST**	**Ref. [12,38]**	**Diff.**	**Diff.^{ref}**
	***n* = 4**	***n* = 5**	***n* = 6**	***n* = 7**	***n* = 4**	***n* = 5**	***n* = 6**				
$3s^2 3p\ ^2P^o_{1/2}$	0	0	0	0	0	0	0	0	0	0	0
$3s^2 3p\ ^2P^o_{3/2}$	39,252	39,332	39,352	39,356	39,467	39,247	39,346	39,483	39,482 [a] 39,441 [b]	137	136 [a] 95 [b]
$3s3p^2\ ^4P_{1/2}$	293,690	294,143	294,240	294,262	294,565	294,650	295,273	295200	295,565 [b]	73	292 [b]
$3s3p^2\ ^4P_{3/2}$	311,359	311,812	311,911	311,935	312,214	312,358	312,990	312,993	313,401 [b]	3	411 [b]
$3s3p^2\ ^4P_{5/2}$	329,845	330,275	330,370	330,394	330,647	330,828	331,445	331,359	331,743 [b]	86	298 [b]
$3s3p^2\ ^2D_{3/2}$	398,396	398,483	398,534	398,539	399,352	399,004	399,347	398,390	401,063 [a] 398,202 [b]	957	1716 [a] 1145 [b]

Table 1. *Cont.*

Zn											
Configurations	**VV**				**CV**			**NIST**	**Ref. [12,38]**	**Diff.**	**Diff.^{ref}**
	***n* = 4**	***n* = 5**	***n* = 6**	***n* = 7**	***n* = 4**	***n* = 5**	***n* = 6**				
$3s3p^2\ ^2D_{5/2}$	405,589	405,684	405,737	405,743	406,541	406,229	406,592	405,760	407,005 [a] 405,567 [b]	832	413 [a] 1025 [b]
$3s3p^2\ ^2S_{1/2}$	476,279	475,983	475,990	475,974	476,211	475,232	475,293	472,601	472,583 [a] 472,400 [b]	2692	2710 [a] 2893 [b]
$3s3p^2\ ^2P_{1/2}$	517,541	517,277	517,288	517,274	517,162	516,197	516,278	513373	513,350 [a] 513,114 [b]	2905	2928 [a] 3164 [b]
$3s3p^2\ ^2P_{3/2}$	529,352	529,111	529,129	529,121	528,134	527,222	527,339	524,382	524,354 [a] 524,114 [b]	2957	2985 [a] 3225 [b]
$3s^23d\ ^2D_{3/2}$	613,765	612,920	612,925	612,918	612,900	611,308	611,167	609,252	609,219 [a] 608,425 [b]	1915	1948 [a] 2742 [b]
$3s^23d\ ^2D_{5/2}$	618,568	617,725	617,735	617,729	617,874	616,275	616,141	614,272	614,214 [a] 613,395 [b]	1869	1927 [a] 2746 [b]
Ge											
Configurations	**VV**				**CV**			**NIST**		**Diff.**	
	***n* = 4**	***n* = 5**	***n* = 6**	***n* = 7**	***n* = 4**	***n* = 5**	***n* = 6**				
$3s^23p\ ^2P^o_{1/2}$	0	0	0	0	0	0	0	0		0	
$3s^23p\ ^2P^o_{3/2}$	54,325	54,374	54,417	54,422	54,568	542,98	54,572	54,564		8	
$3s3p^2\ ^4P_{1/2}$	331,139	331,559	331,668	331,692	332,052	332,079	332,689				
$3s3p^2\ ^4P_{3/2}$	356,988	357,425	357,538	357,564	357,895	358,004	358,630				
$3s3p^2\ ^4P_{5/2}$	381,052	381,453	381,562	381,586	381,895	382,033	382,635				
$3s3p^2\ ^2D_{3/2}$	453,950	454,013	454,080	454,087	454,922	454,513	454,858	453,869		989	
$3s3p^2\ ^2D_{5/2}$	466,163	466,252	466,324	466,332	467,154	466,808	467,185	466,407		778	
$3s3p^2\ ^2P_{1/2}$	534,573	534,269	534,300	534,287	534,241	533,224	533,314	530,521		2793	
$3s3p^2\ ^2S_{1/2}$	589,387	589,081	589,111	589,098	589,143	588,103	588,190	585,257		2933	
$3s3p^2\ ^2P_{3/2}$	602,113	601,848	601,888	601,881	600,802	599,833	599,958	597,020		2938	
$3s^23d\ ^2D_{3/2}$	686,908	686,054	686,070	686,062	685,949	684,312	684,193	682,246		1947	
$3s^23d\ ^2D_{5/2}$	693,914	693,062	693,082	693,076	693,164	691,518	691,408	689,533		1875	

Table 1. *Cont.*

Rb									
Configurations	**VV**				**CV**			**NIST**	**Diff.**
	***n* = 4**	***n* = 5**	***n* = 6**	***n* = 7**	***n* = 4**	***n* = 5**	***n* = 6**		
$3s^2 3p\ ^2P^o_{1/2}$	0	0	0	0	0	0	0	0	0
$3s^2 3p\ ^2P^o_{3/2}$	110,871	110,922	110,947	110,962	111,202	110,804	110,952	111,140	188
$3s3p^2\ ^4P_{1/2}$	431,229	431,578	431,694	431,728	432,222	432,068	432,657		
$3s3p^2\ ^4P_{3/2}$	492,049	492,464	492,589	492,626	493,091	493,100	493,730		
$3s3p^2\ ^4P_{5/2}$	532,051	532,378	532,494	532,527	532,436	532,976	533,550		
$3s3p^2\ ^2D_{3/2}$	615,166	615,202	615,278	615,295	616,172	615,618	615,968	614,900	1068
$3s3p^2\ ^2D_{5/2}$	653,652	653,781	653,868	653,890	654,237	654,394	654,824	654,160	664
$3s3p^2\ ^2P_{1/2}$	697,265	696,970	697029	697,032	696,475	695,384	695,519	692,660	2859
$3s3p^2\ ^2S_{1/2}$	807,338	806,983	807,035	807,034	807,429	806,248	806,353	803,460	2893
$3s3p^2\ ^2P_{3/2}$	817,637	817,345	817,405	817,410	816,252	815,150	815,286	812,510	2776
$3s^2 3d\ ^2D_{3/2}$	892,285	891,474	891,470	891,465	891,150	889,467	889,357	887,290	2067
$3s^2 3d\ ^2D_{5/2}$	906,272	905,468	905,460	905,457	905,395	903,767	903,662	901,780	1882
Sr									
Configurations	**VV**				**CV**			**NIST**	**Diff.**
	***n* = 4**	***n* = 5**	***n* = 6**	***n* = 7**	***n* = 4**	***n* = 5**	***n* = 6**		
$3s^2 3p\ ^2P^o_{1/2}$	0	0	0	0	0	0	0	0	0
$3s^2 3p\ ^2P^o_{3/2}$	126,134	126,200	126,215	126,231	126,484	126,054	126,211	126,410	199
$3s3p^2\ ^4P_{1/2}$	452,427	452,799	452,880	452,914	453,304	453,345	453,759	453,140	619
$3s3p^2\ ^4P_{3/2}$	523,935	524,036	524,127	524,165	524,529	524,751	525,212	525,050	162
$3s3p^2\ ^4P_{5/2}$	566,888	567,248	567,319	567,352	567,184	567,905	568,303	568,030	273
$3s3p^2\ ^2D_{3/2}$	652,579	652,194	652,229	652,248	653,000	652,654	652,833	651,640	1193
$3s3p^2\ ^2D_{5/2}$	699,145	699,350	699,379	699,402	699,591	700,025	700,297	699,540	757
$3s3p^2\ ^2P_{1/2}$	733,800	733,548	733,575	733,580	732,821	731,952	731,924	728,900	3024
$3s3p^2\ ^2S_{1/2}$	859,193	858,873	858,892	858,892	859,219	858,251	858,189	855,010	3179
$3s3p^2\ ^2P_{3/2}$	867,966	867,223	867,243	867,249	865,973	865,077	865,040	862,070	2970
$3s^2 3d\ ^2D_{3/2}$	939,073	938,203	938,169	938,162	937,675	936,228	935,948	933,830	2118
$3s^2 3d\ ^2D_{5/2}$	954,081	953,288	953,279	953,273	953,083	951,677	951,397	949,440	1957

Diff = |CV (n = 6) − NIST| ; Diff = |CV (n = 6) − Ref. [12, 38]|; [a] [12]; [b] [38].

Table 2. Radiative data for Al-like ions.

Transition No.	Cu										
	Transition		λ_c (in Å)	λ (in Å)	A		gf		S		dT
	i	j			B	C	B	C	B	C	
1	$3s^23p\ ^2P^o_{1/2}$	$3s3p^2\ ^4P_{1/2}$	361.00 [d] 361.00 [g] 361.16 [h]	360.83	8.08E +07	9.33E +07	3.15E − 03	3.64E − 03	3.75E − 03	4.33E − 03	0.134
2	$3s^23p\ ^2P^o_{1/2}$	$3s3p^2\ ^4P_{3/2}$	342.80 [d] 342.80 [g] 342.70 [h]	342.88	1.73E +06	1.72E +06	1.22E − 04	1.21E − 04	1.38E − 04	1.37E − 04	0.006
3	$3s^23p\ ^2P^o_{1/2}$	$3s3p^2\ ^2D_{3/2}$	269.40 [g] 268.65 [h]	267.96	3.84E +09	3.93E +09	1.65E −01	1.69E −01	1.46E −01	1.49E −01	0.022
4	$3s^23p\ ^2P^o_{1/2}$	$3s3p^2\ ^2S_{1/2}$	224.80 [g] 224.84 [h]	223.52	2.99E +10	3.13E +10	4.48E −01	4.70E −01	3.29E −01	3.46E −01	0.047
5	$3s^23p\ ^2P^o_{1/2}$	$3s3p^2\ ^2P_{1/2}$	208.20 [g] 208.33 [h]	207.07	1.16E +10	1.16E +10	1.49E −01	1.49E −01	1.02E −01	1.02E −01	0.001
6	$3s^23p\ ^2P^o_{1/2}$	$3s3p^2\ ^2P_{3/2}$	203.80 [g] 203.88 [h]	202.68	1.09E +10	1.11E +10	2.69E −01	2.75E −01	1.79E −01	1.83E −01	0.023
7	$3s^23p\ ^2P^o_{1/2}$	$3s^23d\ ^2D_{3/2}$	173.54 [f] 173.80 [g] 174.17 [h]	173.59	4.47E +10	4.48E +10	8.07E −01	8.09E −01	4.61E −01	4.62E −01	0.002
Transition No.	**Zn**										
	Transition		**λ_c (inÅ)**	**λ (in Å)**	**A**		**gf**		**S**		**dT**
	i	**j**			**B**	**C**	**B**	**C**	**B**	**C**	
1	$3s^23p\ ^2P^o_{1/2}$	$3s3p^2\ ^4P_{1/2}$	338.50 [e]	338.67	1.15E +08	1.32E +08	3.95E −03	4.54E −03	4.40E −03	5.07E −03	0.131
2	$3s^23p\ ^2P^o_{1/2}$	$3s3p^2\ ^4P_{3/2}$	319.20 [e]	319.93	2.41E +06	2.42E +06	1.47E −04	1.48E −04	1.55E −04	1.55E −04	0.006
3	$3s^23p\ ^2P^o_{1/2}$	$3s3p^2\ ^2D_{3/2}$		250.75	4.55E +09	4.43E +09	1.71E −01	1.66E −01	1.41E −01	1.37E −01	0.023
4	$3s^23p\ ^2P^o_{1/2}$	$3s3p^2\ ^2S_{1/2}$	211.60 [a]	210.40	3.44E +10	3.61E +10	4.57E −01	4.80E −01	3.17E −01	3.32E −01	0.047
5	$3s^23p\ ^2P^o_{1/2}$	$3s3p^2\ ^2P_{1/2}$	194.79 [a]	193.69	1.07E +10	1.07E +10	1.20E −01	1.20E −01	7.67E −02	7.68E −02	0.002
6	$3s^23p\ ^2P^o_{1/2}$	$3s3p^2\ ^2P_{3/2}$	190.71 [a]	189.89	1.26E +10	1.23E +10	2.71E −01	2.65E −01	1.69E −01	1.65E −01	0.023
7	$3s^23p\ ^2P^o_{1/2}$	$3s^23d\ ^2D_{3/2}$	164.14 [a] 163.60 [f]	163.84	4.79E +10	4.78E +10	7.69E −01	7.67E −01	4.14E −01	4.13E −01	0.002

Table 2. *Cont.*

Transition No.	Ge										
	Transition		λ_c (in Å)	λ (in Å)	A		gf		S		dT
	i	j			B	C	B	C	B	C	
1	$3s^23p\ ^2P^o_{1/2}$	$3s3p^2\ ^4P_{1/2}$		300.58	2.21E +08	2.53E +08	5.98E −03	6.86E −03	5.92E −03	6.78E −03	0.127
2	$3s^23p\ ^2P^o_{1/2}$	$3s3p^2\ ^4P_{3/2}$		278.84	4.52E +06	4.54E +06	2.11E −04	2.12E −04	1.93E −04	1.94E −04	0.005
3	$3s^23p\ ^2P^o_{1/2}$	$3s3p^2\ ^2D_{3/2}$		219.85	5.85E +09	6.04E +09	1.70E −01	1.75E −01	1.23E −01	1.27E −01	0.031
4	$3s^23p\ ^2P^o_{1/2}$	$3s3p^2\ ^2S_{1/2}$		170.01	9.06E +09	9.08E +09	7.85E −02	7.87E −02	4.39E −02	4.40E −02	0.002
5	$3s^23p\ ^2P^o_{1/2}$	$3s3p^2\ ^2P_{1/2}$		187.51	4.40E +10	4.62E +10	4.64E −01	4.87E −01	2.86E −01	3.01E −01	0.047
6	$3s^23p\ ^2P^o_{1/2}$	$3s3p^2\ ^2P_{3/2}$		166.68	1.57E +10	1.62E +10	2.62E −01	2.69E −01	1.44E −01	1.48E −01	0.027
7	$3s^23p\ ^2P^o_{1/2}$	$3s^23d\ ^2D_{3/2}$		146.16	5.42E +10	5.43E +10	6.94E −01	6.96E −01	3.34E −01	3.35E −01	0.003
Transition No.	**Rb**										
	Transition		λ_c (in Å)	λ (in Å)	A		gf		S		dT
	i	j			B	C	B	C	B	C	
1	$3s^23p\ ^2P^o_{1/2}$	$3s3p^2\ ^4P_{1/2}$		231.13	8.76E +08	9.95E +08	1.40E −02	1.59E −02	1.07E −02	1.21E −02	0.120
2	$3s^23p\ ^2P^o_{1/2}$	$3s3p^2\ ^4P_{3/2}$		202.54	1.77E +07	1.80E +07	4.35E −04	4.44E −04	2.90E −04	2.96E −04	0.021
3	$3s^23p\ ^2P^o_{1/2}$	$3s3p^2\ ^2D_{3/2}$	162.63 [h]	162.35	1.14E +10	1.19E +10	1.80E −01	1.88E −01	0.96E −01	1.00E −01	0.042
4	$3s^23p\ ^2P^o_{1/2}$	$3s3p^2\ ^2S_{1/2}$	124.46 [h]	124.02	6.43E +09	6.46E +09	2.97E −02	2.98E −02	1.21E −02	1.22E −02	0.004
5	$3s^23p\ ^2P^o_{1/2}$	$3s3p^2\ ^2P_{1/2}$	144.37 [h]	143.78	7.19E +10	7.56E +10	4.45E −01	4.69E −01	2.11E −01	2.22E −01	0.049
6	$3s^23p\ ^2P^o_{1/2}$	$3s3p^2\ ^2P_{3/2}$	123.07 [h]	122.66	3.56E +10	3.66E +10	3.21E −01	3.30E −01	1.30E −01	1.33E −01	0.026
7	$3s^23p\ ^2P^o_{1/2}$	$3s^23d\ ^2D_{3/2}$	112.71 [h]	112.44	6.64E +10	6.66E +10	5.03E −01	5.05E −01	1.86E −01	1.87E −01	0.003
Transition No.	**Sr**										
	Transition		λ_c (in Å)	λ (in Å)	A		gf		S		dT
	i	j			B	C	B	C	B	C	
1	$3s^23p\ ^2P^o_{1/2}$	$3s3p^2\ ^4P_{1/2}$		220.38	1.10E +09	1.26E +09	1.61E −02	1.83E −02	1.17E −02	1.33E −02	0.118
2	$3s^23p\ ^2P^o_{1/2}$	$3s3p^2\ ^4P_{3/2}$		190.40	2.26E +07	2.32E +07	4.91E −04	5.04E −04	3.08E −04	3.16E −04	0.024
3	$3s^23p\ ^2P^o_{1/2}$	$3s3p^2\ ^2D_{3/2}$	153.47 [h]	153.18	1.29E +10	1.35E +10	1.82E −02	1.90E −01	9.18E −02	9.60E −02	0.043
4	$3s^23p\ ^2P^o_{1/2}$	$3s3p^2\ ^2S_{1/2}$	116.92 [h]	116.52	6.10E +09	6.12E +09	2.48E −02	2.49E −02	9.53E −03	9.56E −03	0.003
5	$3s^23p\ ^2P^o_{1/2}$	$3s3p^2\ ^2P_{1/2}$	137.19 [h]	136.63	7.85E +10	8.26E +10	4.39E −01	4.62E −01	1.98E −01	2.08E −01	0.049
6	$3s^23p\ ^2P^o_{1/2}$	$3s3p^2\ ^2P_{3/2}$	115.98 [h]	115.60	4.42E +10	4.53E +10	3.54E −01	3.63E −01	1.35E −01	1.38E −01	0.024
7	$3s^23p\ ^2P^o_{1/2}$	$3s^23d\ ^2D_{3/2}$	107.10 [h]	106.84	6.60E +10	6.61E +10	4.52E −01	4.52E −01	1.59E −01	1.59E −01	0.001

[a] [12]; [d] [14]; [e] [15]; [f] [40]; [g] [41]; [h] NIST.

The transition parameters, such as radiative rates (A_{ji}), oscillator strength (f_{ij}) and line strength (S_{ij}) for multipole transitions in terms of a reduced matrix element, are defined by the formula given below:

$$\langle \psi_\alpha (PJM) ||Q_k^{(\lambda)}||\psi_{\alpha'} (P'J'M')\rangle \quad (4)$$

where $Q_k^{(\lambda)}$ is the corresponding transition operator in the length or velocity gauge and ψ_α (PJM) and ψ_α (P′J′M′) are initial and final atomic state functions. In Table 2, we list the values of the transition wavelength with line strengths, oscillator strengths and radiative rates in the Babushkin and Coulomb gauge for E1 transitions from the ground state for core-valence correlation of Cu XVII, Zn XVIII, Ge XX, Rb XXVI and Sr XXVII. From Table 2 and Figure 1a, we can view that with the increase in nuclear charge, the transition wavelength of E1 EUV transitions from the ground state decreases. Similarly, from Table 2 and Figure 1b, it is revealed that transition probability increases with nuclear charge for all E1 EUV transitions from the ground state, except transition No. 4. In Table 2, we have also tabulated the values of δT, which is an accuracy indicator for electric transitions, and it is the deviation of the ratio of the length and velocity form of line strengths from unity. One can see that the maximum value of δT is not more than 0.133, and hence, this confirms that our presented result is reliable. We have also made a comparison of our computed transition wavelengths with wavelengths from experimental measurement or other theoretical calculations in Table 2, and there is no major discrepancy between our results and other results available in the literature.

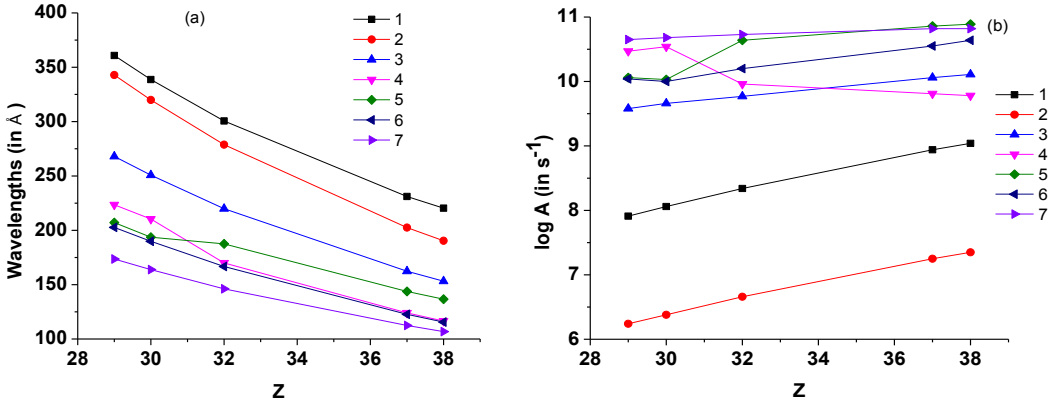


Figure 1. (Color online) Variation of (**a**) transition wavelength and (**b**) the transition probability as a function of nuclear charge (Z) for Extreme Ultraviolet (EUV) Transitions 1–7 using Table 2.

3.2. Line Intensity Ratio and Plasma Parameters

The variation in spectroscopic parameters leads to changes in plasma temperature, and the diagnosis of the elemental composition from various experimental spectroscopic techniques becomes simple and straightforward, if the plasma is optically thin and in Local Thermodynamic Equilibrium (LTE). The reason behind this is that the optically thick line produces a deformed or asymmetrical peak in the spectrum because of saturation and self-absorption in the line profile. This causes wrong and inaccurate measurement of electron density and plasma temperature [64–68]. At higher values of temperature, kinematic excitement or movement of electrons increases, thereby increasing the number of collisions between electrons and, hence, LTE can be achieved very easily at higher values of temperature. Therefore, we have studied the characteristics of plasma at high values of temperature and the effect of plasma temperature and nuclear charge on the line intensity ratio for optically thin plasma. The line intensity ratio of two spectral lines of the same atom or ion is defined by the expression:

$$R = \frac{I_1}{I_2} = \frac{\lambda_2}{\lambda_1}\frac{A_1}{A_2}\frac{g_1}{g_2}\exp\left(-\frac{E_1 - E_2}{kT}\right) \quad (5)$$

where I, g, λ and A are intensity, statistical weight, wavelength and transition probability, respectively. E, k and T are the energy of the upper level in eV, the Boltzmann constant and excitation temperature in K, respectively. The subscripts 1 and 2 denote the spectral lines of the same atom or ion. According to Equation (5), the line intensity ratio of two spectral lines is completely ruled by the exponential term. In Table 3, we have shown the line intensity ratio (R) at high temperatures for Al-like ions. Currently, several heating methods are in progress at the International Thermonuclear Experimental Reactor (ITER) to boost the plasma temperature to the required 1.5×10^8 °C or 4×10^{10} K [69]. Therefore, we have considered the maximum plasma temperature of 1010 K in this paper. Since for a lower value of $\Delta E = E_1 - E_2$, exponential terms become very small, hence the line intensity ratio is very small for two spectral lines having a difference between upper energy levels being very small. Therefore, we have computed the line intensity for the ratio for two spectral lines, 1 and 7. The indices used for denoting the spectral lines are indicated in the first column "Transition No." in Table 2.

Table 3. Plasma temperature (T in K), line intensity ratio (R in 10^3), electron density (n_e in 10^{21} cm^{-3}), plasma frequency (ω_e) in PHz and skin depth (δ) in nm for optically thin plasma for Spectral Lines 1 and 7 of Al-like ions.

Cu					
T (in K)	**R**	$\mathbf{n_e}$	$\mathbf{n_{fit}}$	ω_e	δ
2×10^6	0.927	0.115	0.115	0.96289	495.1601
4×10^6	1.033	0.162	0.162	1.14284	417.193
6×10^6	1.070	0.199	0.199	1.266644	376.4159
8×10^6	1.090	0.230	0.230	1.361733	350.131
1×10^7	1.102	0.257	0.257	1.439443	331.2287
1×10^8	1.145	0.813	0.813	2.560196	186.2298
1×10^9	1.149	2.570	2.570	4.551919	104.7437
1×10^{10}	1.150	8.128	8.129	8.095055	58.89829
Zn					
T (in K)	**R**	$\mathbf{n_e}$	$\mathbf{n_{fit}}$	ω_e	δ
2×10^6	0.686	0.135	0.135	1.043266	457.012
4×10^6	0.768	0.192	0.192	1.244167	383.2162
6×10^6	0.798	0.235	0.235	1.376455	346.3862
8×10^6	0.813	0.271	0.271	1.47813	322.5595
1×10^7	0.823	0.303	0.303	1.562965	305.0515
1×10^8	0.857	0.959	0.959	2.780592	171.4688
1×10^9	0.860	3.033	3.034	4.944976	96.41804
1×10^{10}	0.861	9.593	9.598	8.794379	54.21473
Ge					
T (in K)	**R**	$\mathbf{n_e}$	$\mathbf{n_{fit}}$	ω_e	δ
2×10^6	0.392	0.187	0.187	1.22786	388.3057
4×10^6	0.444	0.264	0.264	1.458915	326.8079
6×10^6	0.464	0.324	0.324	1.61622	295.0000
8×10^6	0.473	0.374	0.374	1.736456	274.5736
1×10^7	0.480	0.418	0.418	1.835761	259.7206
1×10^8	0.501	1.321	1.322	3.263468	146.0976
1×10^9	0.504	4.179	4.178	5.804491	82.14069
1×10^{10}	0.504	13.210	13.211	10.31999	46.20012
Rb					
T (in K)	**R**	$\mathbf{n_e}$	$\mathbf{n_{fit}}$	ω_e	δ
2×10^6	0.112	0.410	0.410	1.801505	262.2422
4×10^6	0.132	0.580	0.580	2.142681	220.4857
6×10^6	0.140	0.710	0.710	2.370679	199.2807
8×10^6	0.143	0.820	0.820	2.547713	185.4332
1×10^7	0.146	0.916	0.917	2.692721	175.4473
1×10^8	0.155	2.899	2.899	4.790355	98.62123
1×10^9	0.156	9.167	9.166	8.518384	55.46013
1×10^{10}	0.156	28.990	28.986	15.14843	31.18677

Table 3. *Cont.*

Sr					
T (in K)	**R**	$\mathbf{n_e}$	$\mathbf{n_{fit}}$	ω_e	δ
2×10^6	0.087	0.482	0.482	1.971294	241.8639
4×10^6	0.104	0.682	0.682	2.344877	203.3304
6×10^6	0.110	0.835	0.835	2.594605	183.7601
8×10^6	0.113	0.965	0.964	2.789277	170.9349
1×10^7	0.115	1.079	1.078	2.949434	161.653
1×10^8	0.123	3.411	3.411	5.244074	90.91879
1×10^9	0.124	10.789	10.786	9.326497	51.12154
1×10^{10}	0.124	34.110	34.115	16.58322	28.75105

In Figure 2a,b, we can see the behavior of the line intensity ratio with plasma temperature and nuclear charge. From Figure 2a and Table 3, we observe that the line intensity ratio increases with plasma temperature, and for a plasma temperature more than or equal to 10^9 K, the increase in the value of R is less than 0.087, which is very small, showing that the effect of higher temperatures on a line intensity ratio is almost negligible or the line intensity ratio becomes almost constant. From Figure 2b, we predict that the line intensity ratio decreases very rapidly with the nuclear charge for a plasma temperature of 10^{10} K. By comparing our calculated line intensity ratio with the measured ratio at different delay times, experimentalists can achieve the time window where the plasma is in LTE and optically thin.

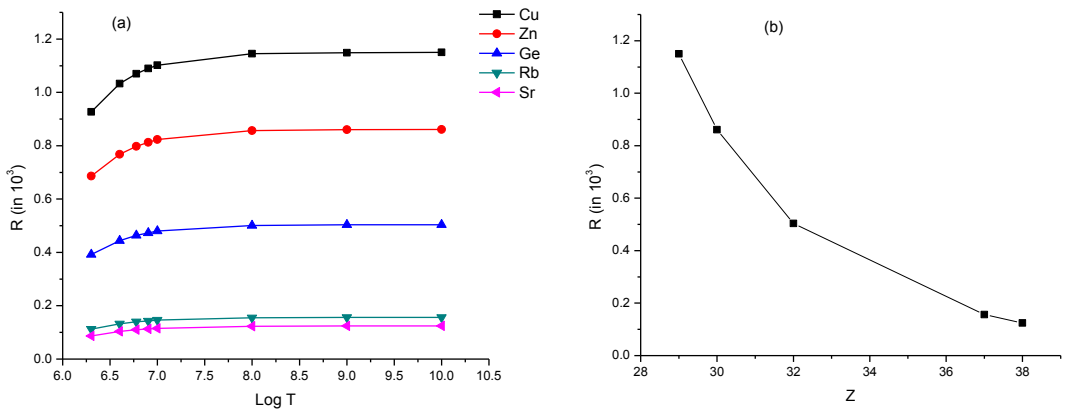


Figure 2. (Color online) Variation of the line intensity ratio with (**a**) plasma temperature and (**b**) nuclear charge at T = 10^{10} K for Al-like ions for Spectral Lines 1 and 7 using Table 2.

The total number of collisions between electrons must be large to attain LTE. For this objective, the McWhirter criterion [70] for a minimum or limiting value of electron density is defined by the inequality:

$$n_e \geqslant 1.6 \times 10^{12} T^{1/2} (\Delta E)^3 \quad (6)$$

In Equation (6), n_e is the electron density, T is the plasma temperature in K and $\Delta E = E_1 - E_2$ in eV. In Table 3, we have also tabulated the limiting values of electron density at different values of plasma temperature for Spectral Lines 1 and 7. The value of electron density is 10^{21} cm^{-3}, and matter with this solid density is very popular due to its presence in all types of stars, such as white dwarf stars [71]. The plasmas having such a solid density are inertial confinement fusion plasmas [72,73]. From Figure 3a, one can see that the value of electron density increases with plasma temperature for Al-like ions, which shows that the number of collisions in the plasma increases with the increase in plasma temperature. From Figure 3b and Table 3, we have also deduced that the electron density increases very expeditiously with nuclear charge. In the present paper, we have also presented the fitting values of electron density in Table 3, and our fitted values of electron density are in good agreement with the calculated electron density and, hence, confirm the authenticity and credibility

of our fitted parameters given in Table 4. By employing fitting parameters K and C in the straight line equation $\log_{10} n_e = K \log_{10} T + C$, one easily determines the limiting value of electron density for a particular value of plasma temperature for Al-like ions. Thus, this information may be advantageous for experimentalists for producing optically thin plasma in LTE at higher temperatures for Al-like ions.

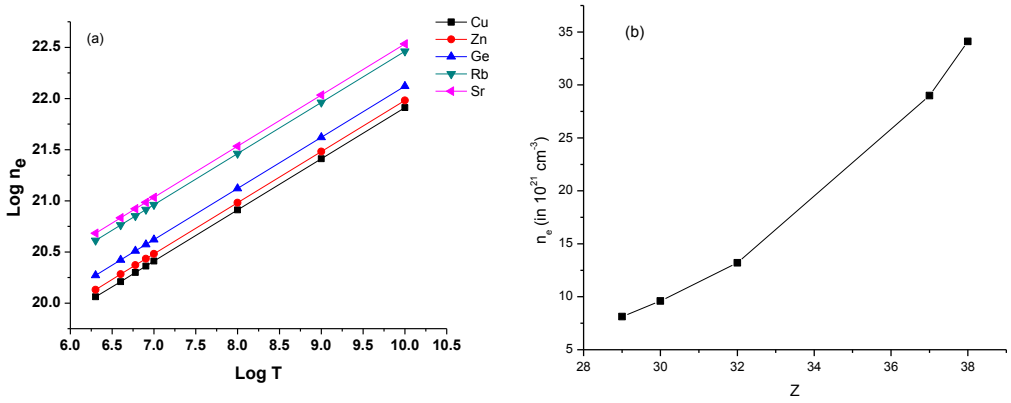


Figure 3. (Color online) Variation of electron density with (**a**) plasma temperature and (**b**) nuclear charge at T = 10^{10} K for Al-like ions for Spectral Lines 1 and 7 using Table 2.

Table 4. Plasma fitting parameters K and C for Al-like ions.

Z	K	C
29	0.500	16.909
30	0.500	16.979
32	0.499	17.121
37	0.500	17.462
38	0.500	17.532

The relation between electron density and the electron plasma frequency with which electrons oscillate or the frequency of plasma oscillation is given by the expression:

$$\omega_e = 8.979 \times 10^4 \, n_e^{1/2} \text{Hz} \tag{7}$$

According to the above equation, plasma frequency is directly proportional to the square root of electron density and, hence, depends on the one-fourth power of the plasma temperature by Equation (6). In Table 3 and Figure 4a, we can see that with increasing electron density and plasma temperature, electrons oscillate with higher frequency due to thermal agitation. As can be seen from Table 3 and Figure 4b, the electron density increases with an increase in nuclear charge, and therefore, plasma frequency also increases with nuclear charge. In this work, the highest plasma frequency is 16.58 PHz at a plasma temperature of 10^{10} K for Sr XXVII, which lies in the ultraviolet region.

The depth to which electromagnetic radiations can penetrate plasma, known as skin depth, is inversely proportional to the square root of electron density and is given by the following relation:

$$\delta = 5.31 \times 10^5 n_e^{-1/2} \text{cm} \tag{8}$$

From Equation (8), the plasma skin depth is inversely proportional to electron density and, hence, inversely proportional to the one-fourth power of the plasma temperature by Equation (6). Therefore, from Table 3 and Figure 5a, it is revealed that as plasma temperature and electron density increase, the skin depth of the plasma decreases rapidly for Al-like ions. From Table 3 and Figure 5b, we conclude that with the increment in the values of the nuclear charge of Al-like ions, i.e., with the increase in the number of protons w.r.t electrons, plasma skin depth decreases. In this paper, the minimum value of the plasma skin depth is 28.751 nm at T = 10^{10} K for Sr XXVII or we can say that at 16.58 PHz, the skin

depth is 28.751 nm. This implies that Al-like ions' plasma is highly conductive, and hence, we deduce that electron density and plasma temperature play a significant role in reducing the skin depth of the plasma and controlling the conductivity of plasma. Since skin depth is in nm, therefore the size of the plasmon will be in nm; hence Al-like ions' plasma may be beneficial in several applications, such as solar cells, spectroscopy and cancer treatment.

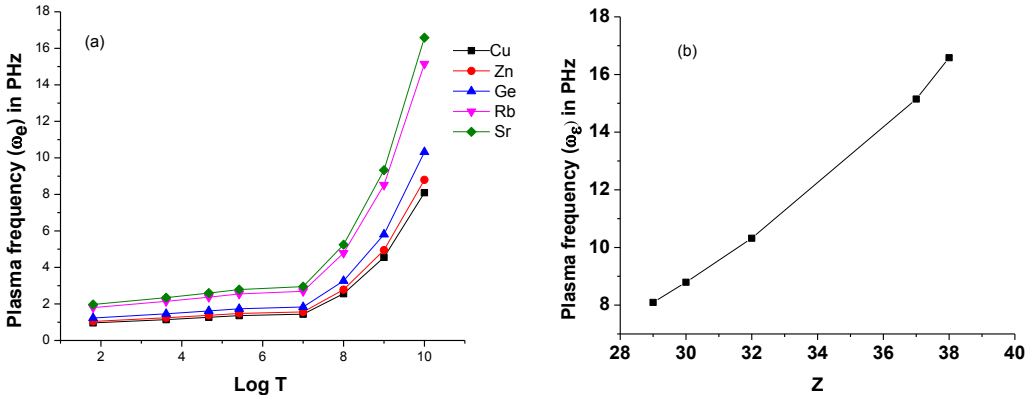


Figure 4. (Color online) Variation of plasma frequency with (**a**) plasma temperature and (**b**) nuclear charge at T = 10^{10} K for Al-like ions for Spectral Lines 1 and 7 using Table 2.

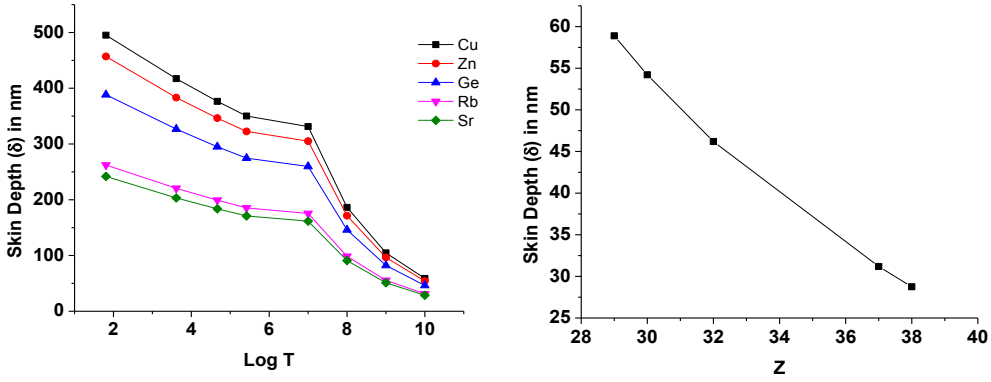


Figure 5. (Color online) Variation of skin depth with (**a**) plasma temperature and (**b**) nuclear charge at T = 10^{10} K for Al-like ions for Spectral Lines 1 and 7 using Table 2.

The plasma parameter (Λ) may be defined in terms of electron density and plasma temperature by the following expression:

$$\Lambda = 4\pi \times 7.43 \times 10^2 \times n_e^{-1/2} T^{1/2} \quad (9)$$

The Coulomb coupling parameter (Γ) and plasma parameter (Λ) for plasma are related to each other as follows

$$\Gamma \approx \Lambda^{-2/3} \quad (10)$$

The above two parameters play a vital role in differentiating between strongly-coupled plasma and weakly-coupled plasma and in the determination of plasma characteristics. From Table 3, we determine that for all values of plasma temperature and corresponding electron density, $\Lambda < 1$ and $\Gamma > 1$. Since for strongly-coupled plasma, the coupling parameter should be greater than unity, the optically thin plasma in LTE is a cold, dense and strongly-coupled plasma for Al-like ions, which also correspond to the conditions prevailing in white dwarf and neutron stars [74]. Further, the ratio of potential energy due to Coulomb interaction between neighboring particles and the kinetic energy of particles is governed by the coupling parameter. In the present work, $\Gamma > 1$; this shows that the electrons are conducted by their interactions in the plasma.

4. Conclusions

In the present work, we have discussed the spectroscopic properties and plasma characteristics of Al-like ions in the plasma atmosphere by employing the GRASP2K package based on the MCDHF method, taking into account the contribution of QED and Breit corrections. We have also reported the energy levels and radiative data for E1 transitions from the ground state belonging to the configurations $3s^23p$, $3s3p^2$ and $3s^23d$ for Al-like ions. The energy levels and transition wavelengths presented in this paper were compared to the data available in the literature, and good agreement was found. We have graphically studied the behavior of transition wavelengths and radiative rates for EUV transitions with nuclear charge. We have also investigated and diagnosed graphically the behavior of the line intensity ratio, electron density, plasma frequency and skin depth of highly ionized Al-like ions with plasma temperature and nuclear charge for optically thin plasma in LTE.

As a conclusion, we conclude that the work presented in this paper is a reliable examination of the spectroscopic properties, and plasma characteristics will be useful in the modeling and characterization of plasma. Further, the atomic data may be useful in the designation and analysis of EUV spectral lines with the exploration of new data from fusion and astrophysical plasma sources.

Acknowledgments: Arun Goyal and Indu Khatri are thankful to U.G.C. (University Grants Commission), India, for their Junior Research Fellowship. Man Mohan (M.M.) is thankful to U.G.C. for the Basic Science Research Fellowship.

Author Contributions: Indu Khatri and Arun Goyal proposed the main idea of the paper and performed the calculations. Man Mohan and Avnindra Kumar Singh provided the required computer hardware. Rinku Sharma and Narendra Singh were involved in the discussion and in writing the manuscript.

Conflicts of Interest: The authors declare no conflict of interest.

References

1. Masoudnia, L.; Bleiner, D. Optimum Pump Pulse Duration for X-Ray Ar-Plasma Lasing. *Photonics* **2015**, *2*, 164–183. [CrossRef]
2. Porquet, D.; Dubau, J.; Grosso, N. He-like Ions as Practical Astrophysical Plasma Diagnostics: From Stellar Coronae to Active Galactic Nuclei. *Space Sci. Rev.* **2010**, *157*, 103–134. [CrossRef]
3. Salik, M.; Hanif, M.; Wang, J.; Zhang, X. Plasma properties of nano-second laser ablated iron target in air. *Int. J. Phys. Sci.* **2013**, *8*, 1738–1745.
4. Esaulov, A.A.; Johnson, W.R.; Safronova, A.S.; Safronova, U.I.; Kantsyrev, V.L.; Weller, M.E.; Ouart, N.D. Plasma ionization and resistivity models for low-, mid- and higher-atomic number plasmas and their applications to radiative properties of z-pinches. *High Energy Density Phys.* **2012**, *8*, 217–223. [CrossRef]
5. Li, C.-Y.; Wang, T.-T.; Zhen, J.-F.; Chen, Y. Line-profile analysis of excitation spectroscopy in the even $4p^5$ ($^2P_{1/2}$)nl′ [K′] J (l′ = 1,3) autoionizing resonances of Kr. *Sci. China Chem.* **2013**, *56*, 1623–1632. [CrossRef]
6. Lundeen, S.R.; Fehrenbach, C.W. Polarizability of Kr6+ from high-L Kr5+ fine-structure measurements. *Phys. Rev. A* **2007**, *75*, 032523. [CrossRef]
7. Santana, J.A.; Lepson, J.K.; Träbert, E.; Beiersdorfer, P. Electron-correlation effects on the 3C to 3D line-intensity ratio in the Ne-like ions Ar^{8+} to Kr^{26+}. *Phys. Rev. A* **2015**, *91*, 012502. [CrossRef]
8. Kink, I.; Laming, J.M.; Takacs, E.; Porto, J.V.; Gillaspy, J.D.; Silver, E.; Schnopper, H.; Bandler, S.R.; Barbera, M.; Brickhouse, N.; et al. Analysis of broadband x-ray spectra of highly charged krypton from a microcalorimeter detector of an electron-beam ion trap. *Phys. Rev. E* **2001**, *63*, 046409. [CrossRef] [PubMed]
9. Kukla, K.W.; Livingston, A.E.; Vogt, C.M.V.; Berry, H.G.; Dunford, R.W.; Curtis, L.J.; Cheng, S. Extreme-ultraviolet wavelength and lifetime measurements in highly ionized krypton. *Can. J. Phys.* **2005**, *83*, 1127–1139. [CrossRef]
10. Rice, J.E.; Fournier, K.B.; Goetz, J.A.; Marmar, E.S.; Terry, J.L. X-ray observations of 2l-nl' transitions and configuration-interaction effects from Kr, Mo, Nb and Zr in near neon-like charge states from tokamak plasmas. *J. Phys. B* **2000**, *33*, 5435–5462. [CrossRef]
11. Farrag, A.; Koenig, E.L.; Sinzelle, J. Systematic trends of the relativistic energy levels and oscillator strengths for electric dipole transitions within the ground complex of aluminium-like ions. *J. Phys. B* **1981**, *14*, 3325–3344. [CrossRef]

12. Sugar, J.; Kaufman, V. Wavelengths and Energy Levels of Zn XII to Zn XX. *Phys. Scr.* **1986**, *34*, 797–804. [CrossRef]
13. Huang, K.-N. Energy-level scheme and transition probabilities of Al-like ions. *At. Data Nucl. Data Tables* **1986**, *34*, 1–77. [CrossRef]
14. Träbert, E.; Hutton, R.; Martinson, I. Intercombination lines of Mg I-, Al I- and Si I-like ions in the beam foil spectra of Ti, Fe, Ni and Cu. *Z. Phys. D* **1987**, *5*, 125–131. [CrossRef]
15. Träbert, E.; Heckmann, P.H.; Wiese, W.L. Wavelength and lifetime measurements on intercombination transitions in 12- to 14-electron ions of Zn. *Z. Phys. D* **1988**, *8*, 209–210. [CrossRef]
16. Shirai, T.; Nakagaki, T.; Nakai, Y.; Sugar, J.; Ishii, K.; Mori, K. Spectral Data and Grotrian Diagrams for Highly Ionized Copper, Cu X-Cu XXIX. *J. Phys. Chem. Ref. Data* **1991**, *20*, 1–81. [CrossRef]
17. Wyart, J.F.; Gautheir, J.C.; Geindre, J.P.; Tragin, N.; Monier, P.; Klisnick, A.; Carillon, A. Interpretation of a spectrum of laser irradiated strontium in the range 115-208 Å. *Phys. Scr.* **1987**, *36*, 227. [CrossRef]
18. TFR Group; Wyart, J.F. On the spectra of highly-ionized krypton, strontium, zirconium and rhodium excited in the plasma of the TFR tokamak. *Phys. Scr.* **1988**, *37*, 66. [CrossRef]
19. Kaufman, J.R.; Kaufman, V.; Sugar, J.; Pittman, T.L. Magnetic-dipole transitions observed in highly ionized Ga, Ge, As, and Kr. *Phys. Rev. A* **1983**, *27*, 1721–1723. [CrossRef]
20. Burrell, K.H.; Groebner, R.J.; Brooks, N.H.; Rottler, L. Magnetic dipole transitions in the n=3 level of highly ionized zinc, germanium, and selenium. *Phys. Rev. A* **1984**, *29*, 1343–1347. [CrossRef]
21. Sugar, J.; Musgrove, A. Energy Levels of Zinc, Zn I through Zn XXX. *J. Phys. Chem. Ref. Data* **1995**, *24*, 1803–1872. [CrossRef]
22. Lavin, C.; Alvarez, A.B.; Martin, I. Systematic in the relativistic oscillator strengths for fine-structure transitions in the aluminium isoelectronic sequence. *J. Quant. Spectrosc. Radiat. Transf.* **1997**, *57*, 831–845. [CrossRef]
23. Litzen, U.; Redfros, A. Fine structure splitting of the term $3s3p^2\ ^4P$ in Al-like ions. *Phys. Lett. A* **1988**, *127*, 88–91. [CrossRef]
24. Ekberg, J.O.; Redfros, A.; Brown, C.M.; Feldman, U.; Seely, J.F. Transitions and energy levels in Al-like Ge XX, Se XXII, Sr XXVI, Y XXVII and Zr XXVIII. *Phys. Scr.* **1991**, *44*, 539. [CrossRef]
25. Jupen, C.; Curtis, L.J. Isoelectronic comparison of the Al-like $3s^2\ 3p\ ^2P$–$3s3p^2\ ^4P$ transitions in the ions P III-Mo XXX. *Phys. Scr.* **1996**, *53*, 312. [CrossRef]
26. Biemont, E.; Fremat, Y.; Quinet, P. Ionization potentials of atoms and ions from lithium to tin (z= 50). *At. Data Nucl. Data Tables* **1999**, *71*, 117–146. [CrossRef]
27. Sugar, J.; Musgrove, A. Energy Levels of Copper, Cu I through Cu XXIX. *J. Phys. Chem. Ref. Data* **1990**, *19*, 527. [CrossRef]
28. Wouters, A.; Schwob, J.L.; Suckewer, S.; Seely, J.F.; Feldman, U.; Davè, J.H. Spectra in the 60345-Å wavelength region of the elements Fe, Ni, Zn, Ge, Se, and Mo injected into the Princeton Large Torus tokamak. *J. Opt. Soc. Am. B* **1988**, *5*, 1520–1527. [CrossRef]
29. Hinnov, E.; Boody, F.; Cohen, S.; Feldman, U.; Hosea, J.; Sato, K.; Schwob, J.L.; Suckewer, S.; Wouters, A. Spectrum lines of highly ionized zinc, germanium, selenium, zirconium, molybdenum, and silver injected into Princeton Large Torus and Tokamak Fusion Test Reactor tokamak discharges. *J. Opt. Soc. Am. B* **1986**, *3*, 1288–1294. [CrossRef]
30. Sugar, J.; Kaufmann, V. Predicted wavelengths and transition rates for magnetic-dipole transitions within $3s^2\ 3p^n$ ground configurations of ionized Cu to Mo. *J. Opt. Soc. Am. B* **1984**, *1*, 218–223. [CrossRef]
31. Sugar, J.; Kaufmann, V. Copper spectra in a laser-generated plasma: measurements and classifications of Cu xii to Cu xxi. *J. Opt. Soc. Am. B* **1986**, *3*, 704–710. [CrossRef]
32. Träbert, E.; Heckmann, P.H.; Hutton, R.; Martinson, I. Intercombination lines in delayed beam-foil spectra. *J. Opt. Soc. Am. B* **1988**, *5*, 2173–2182. [CrossRef]
33. Sugar, J.; Kaufman, V.; Rowan, W.L. Aluminum like spectra of copper through molybdenum. *J. Opt. Soc. Am. B* **1988**, *5*, 2183–2189. [CrossRef]
34. Kim, Y.-K.; Sugar, J.; Kaufman, V.; Ali, M.A. Quantum-electrodynamic contributions to Spin–orbit splitting in the ground state of aluminum like ions. *J. Opt. Soc. Am. B* **1988**, *5*, 2225–2229. [CrossRef]
35. Träbert, E.; Wagner, C.; Heckmann, P.H.; Brage, T. A beam-foil study of the 3s3p3d 4F levels in the Al-like ions of Ti, Fe and Ni. *Phys. Scr.* **1993**, *48*, 593. [CrossRef]

36. Gaardsted, J.U.; Brage, T.; Fischer, C.F.; Sonnek, D. Experimental and theoretical study of core-excited states of Al III. *Phys. Scr.* **1990**, *42*, 543. [CrossRef]
37. Thornbury, J.F.; Hibbert, A.; Träbert, E. The lifetimes of the $3s^2 4s\ ^2S$ states in the aluminium sequence. *Phys. Scr.* **1989**, *40*, 472. [CrossRef]
38. Safronova, U.I.; Namba, C.; Abritton, J.R.; Johnson, W.R.; Safronova, M.S. Relativistic many-body calculations of energies of n=3 states in aluminum like ions. *Phys. Rev. A* **2002**, *65*, 022507. [CrossRef]
39. Safronova, U.I.; Sataka, M.; Abritton, J.R.; Johnson, W.R.; Safronova, M.S. Relativistic many-body calculations of electric-dipole lifetimes, transition rates, and oscillator strengths for n=3 states in Al-like ions. *At. Data Nucl. Data Tables* **2003**, *84*, 1–83. [CrossRef]
40. Wei, H.L.; Zhang, H.; Ma, C.W.; Zhang, J.Y.; Cheng, X.L. The MCDF calculations of n=3–4 transitions in some Al-like ions (Fe^{13+}–Ga^{18+}). *Phys. Scr.* **2008**, *77*, 035301. [CrossRef]
41. Gupta, G.P.; Msezane, A.Z. Large-scale CIV3 calculations of fine-structure energy levels and radiative rates in Al-like copper. *Can. J. Phys.* **2009**, *87*, 895–907. [CrossRef]
42. Sansonetti, J.E. Wavelengths, Transition Probabilities, and Energy Levels for the Spectra of Strontium Ions (Sr II through Sr XXXVIII). *J. Phys. Chem. Ref. Data* **2012**, *41*, 013102. [CrossRef]
43. Sansonetti, J.E. Wavelengths, Transition Probabilities, and Energy Levels for the Spectra of Rubidium (RbI through RbXXXVII). *J. Phys. Chem. Ref. Data* **2006**, *35*, 301–402. [CrossRef]
44. Dong, C.Z.; Kato, T.; Fritzsche, S.; Koike, F. Lifetimes and branching fractions of the high angular momentum states of aluminium-like iron group elements. *Mon. Not. R. Astron. Soc.* **2006**, *369*, 1735–1740. [CrossRef]
45. Rodrigues, G.C.; Indelicato, P.; Santos, J.P.; Patte, P.; Parente, F. Systematic calculation of total atomic energies of ground state configurations. *At. Data Nucl. Data Tables* **2004**, *86*, 117–233. [CrossRef]
46. Santana, J.A.; Ishikawa, Y.; Träbert, E. Multireference Møller–Plesset perturbation theory results on levels and transition rates in Al-like ions of iron group elements. *Phys. Scr.* **2009**, *79*, 065301. [CrossRef]
47. Argamam, U.; Makov, G. Higher ionization energies of atoms in density-functional theory. *Phys. Rev. A* **2013**, *88*, 042504. [CrossRef]
48. Kumar, S.T.A.; Hartog, D.J.D.; Chapman, B.E.; Mullane, M.O.; Nornberg, M.; Craig, D.; Eilerman, S.; Fiksel, G.; Parke, E.; Reusch, J. High resolution charge-exchange spectroscopic measurements of aluminum impurity ions in a high temperature plasma. *Plasma Phys. Control. Fusion* **2012**, *54*, 012002. [CrossRef]
49. Surmick, D.M.; Parriger, C.G. Electron density determination of aluminium laser-induced plasma. *J. Phys. B* **2015**, *48*, 115701. [CrossRef]
50. Surmick, D.M.; Parriger, C.G. Time-resolved aluminium laser-induced plasma temperature measurements. *J. Phys. Conf. Ser.* **2014**, *548*, 012046. [CrossRef]
51. Vinko, S.M.; Ciricosta, O.; Preston, T.R.; Rackstraw, D.S.; Brown, C.R.D.; Burian, T.; Chalupsky, J.; Cho, B.I.; Chung, H.-K.; Englehorn, K.; et al. Investigation of femtosecond collisional ionization rates in a solid. *Nat. Commun.* **2015**, *6*, 6397. [CrossRef] [PubMed]
52. Saber, M.G.; Sagor, R.H. Design and study of nano-plasmonic couplers using aluminium arsenide and alumina. *IET Optoelectron* **2015**, *9*, 125–130. [CrossRef]
53. Martin, J.; Plain, J. Fabrication of aluminium nanostructures for plasmonics. *J. Phys. D Appl. Phys.* **2015**, *48*, 184002. [CrossRef]
54. Fang, Y.; Sun, M. Nanoplasmonic waveguides: towards applications in integrated nanophotonic circuits. *Light Sci. Appl.* **2015**, *4*, e294. [CrossRef]
55. Boriskina, S.V.; Ghasemi, H.; Chen, G. Plasmonic materials for energy: From physics to applications. *Mater. Today* **2013**, *16*, 375–386. [CrossRef]
56. Stockman, M.I. Nanoplasmonics: past, present, and glimpse into future. *Phys. Today* **2011**, *64*, 39–44. [CrossRef]
57. Shahbazyan, T.V.; Stockman, M.I. *Plasmonics: Theory and Applications*; Springe: Heidelberg, Germany, 2013.
58. Klimov, V. *Nanoplasmonics*; CRC Press: New York, NY, USA, 2014.
59. Chon, J.W.M.; Iniewski, K. *Nanoplasmonics: Advanced Device Applications*; CRC Press: New York, NY, USA, 2013.
60. Grant, I.P. *Relativistic Quantum Theory of Atoms and Molecules: Theory and Computation*; Springer: New York, NY, USA, 2007.
61. Jonsson, P.; He, X.; Fischer, C.F.; Grant, I.P. New version: Grasp2K relativistic atomic structure package. *Comput. Phys. Commun.* **2007**, *177*, 597–622. [CrossRef]

62. Parpia, F.A.; Fischer, C.F.; Grant, I.P. GRASP92: A package for large-scale relativistic atomic structure calculations. *Comput. Phys. Commun.* **1996**, *94*, 249–271. [CrossRef]
63. Olsen, J.; Godefroid, M.R.; Jonsson, P.A.; Malmquist, P.A.; Froese, F.C. Transition probability calculations for atoms using nonorthogonal orbitals. *Phys. Rev. E* **1995**, *52*, 4499–4508. [CrossRef]
64. Aragon, C.; Aguilera, J.A. Characterization of laser induced plasmas by optical emission spectroscopy: A review of experiments and methods. *Spectrochim. Acta Part B* **2008**, *63*, 893–916. [CrossRef]
65. Fantoni, R.; Caneve, L.; Colao, F.; Fornarini, L.; Lazic, V.; Spizzichino, V. *Advances in Spectroscopy for Lasers and Sensing*; Springer: New York, NY, USA, 2006; pp. 229–254.
66. Griem, H.R. *Principles of Plasma Spectroscopy*; Cambridge University Press: Cambridge, UK, 1997.
67. Hutchinson, I.H. *Principles of Plasma Diagnostics*, 2nd ed.; Cambridge University Press: New York, NY, USA, 2005.
68. Kunze, H.J. *Introduction to Plasma Spectroscopy*; Springer Series on Atomic, Optical and Plasma Physics: London, UK; New York, NY, USA, 2009.
69. ITER Homepage. Available online: https://www.iter.org/sci/plasmaheating (accessed on 1 July 2016).
70. McWhirter, R.W.P. *Plasma Diagnostic Techniques*; Huddleston, R.H., Leonard, S.L., Eds.; Academic Press: New York, NY, USA, 1965.
71. Vinko, S.M.; Ciricosta, O.; Cho, B.I.; Engelhorn, K.; Chung, H.-K.; Brown, C.R.; Chalupsky, K.; Falcone, R.W.; Graves, C.; et al. Creation and diagnosis of a solid-density plasma with an X-ray free-electron laser. *Nature* **2012**, *482*, 59–62. [CrossRef] [PubMed]
72. Lindl, J. Development of the indirect-drive approach to inertial confinement fusion and the target physics basis for ignition and gain. *Phys. Plasmas* **1995**, *2*, 3933–4024. [CrossRef]
73. Velarde, G.; Ronen, Y.; Martinez-Val, J.M. *Nuclear Fusion by Inertial Confinement: A Comprehensive Treatise*; CRC Press: New York, NY, USA, 1993.
74. Fitzpatrick, R. *Plasma Physics: An Introduction*; CRC Press: New York, NY, USA, 2014.



© 2016 by the authors; licensee MDPI, Basel, Switzerland. This article is an open access article distributed under the terms and conditions of the Creative Commons Attribution (CC-BY) license (http://creativecommons.org/licenses/by/4.0/).

Analytica Chimica Acta xxx (2016) 1–10

Contents lists available at ScienceDirect

Analytica Chimica Acta

journal homepage: www.elsevier.com/locate/aca

Controlled deposition of functionalized silica coated zinc oxide nano-assemblies at the air/water interface for blood cancer detection

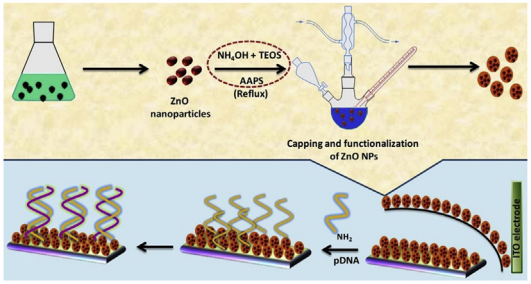
Chandra Mouli Pandey [a, b, 1], Srishti Dewan [a, c, 1], Seema Chawla [c], Birendra Kumar Yadav [d], Gajjala Sumana [a, *], Bansi Dhar Malhotra [a, b, **]

[a] Biomedical Instrumentation Section, CSIR-National Physical Laboratory, New Delhi 110012, India
[b] Nanobioelectronics Laboratory, Department of Biotechnology, Delhi Technological University, Delhi 110042, India
[c] Biomedical Engineering Department, Deenbandhu Chhotu Ram University of Science & Technology, Haryana 131039, India
[d] Rajiv Gandhi Cancer Institute and Research Centre, Rohini, Delhi 110085, India

HIGHLIGHTS

- Stable and controlled deposition of Am-Si@ZnO nano-assemblies using LB technique.
- Uniform monolayer deposition of the Am-Si@ZnO LB film within the nanometer range.
- Am-Si@ZnO LB film shows enhanced electrochemical properties.
- Fabricated nucleic acid sensor is ultrasensitive (1×10^{-16} M) for CML detection.
- Validation with clinical samples of CML positive patients shows its potential for clinical diagnosis.

GRAPHICAL ABSTRACT



ARTICLE INFO

Article history:
Received 23 May 2016
Received in revised form
18 July 2016
Accepted 20 July 2016
Available online xxx

Keywords:
Langmuir-blodgett monolayer
Zinc oxide
Chronic myelogenous leukemia
Cancer
Nucleic acid biosensor

ABSTRACT

We report results of the studies relating to controlled deposition of the amino-functionalized silica-coated zinc oxide (Am-Si@ZnO) nano-assemblies onto an indium tin oxide (ITO) coated glass substrate using Langmuir-Blodgett (LB) technique. The monolayers have been deposited by transferring the spread solution of Am-Si@ZnO stearic acid prepared in chloroform at the air-water interface, at optimized pressure (16 mN/m), concentration (10 mg/ml) and temperature (23 °C). The high-resolution transmission electron microscopic studies of the Am-Si@ZnO nanocomposite reveal that the nanoparticles have a microscopic structure comprising of hexagonal assemblies of ZnO with typical dimensions of 30 nm. The surface morphology of the LB multilayer observed by scanning electron microscopy shows uniform surface of the Am-Si@ZnO film in the nanometer range (<80 nm). These electrodes have been utilized for chronic myelogenous leukemia (CML) detection by covalently immobilizing the amino-terminated oligonucleotide probe sequence *via* glutaraldehyde as a crosslinker. The response studies of these fabricated electrodes carried out using electrochemical impedance spectroscopy show that this Am-Si@ZnO LB film based nucleic acid sensor exhibits a linear response to complementary DNA (10^{-6}

* Corresponding author. Biomedical Instrumentation Section, CSIR-National Physical Laboratory, New Delhi 110012, India.
** Corresponding author. Nanobioelectronics Laboratory, Department of Biotechnology, Delhi Technological University, Delhi 110042, India.
E-mail addresses: sumanagajjala@gmail.com (G. Sumana), bansi.malhotra@gmail.com (B.D. Malhotra).
[1] These authors contributed equally to this work.

http://dx.doi.org/10.1016/j.aca.2016.07.024
0003-2670/© 2016 Published by Elsevier B.V.

Please cite this article in press as: C.M. Pandey, et al., Controlled deposition of functionalized silica coated zinc oxide nano-assemblies at the air/water interface for blood cancer detection, Analytica Chimica Acta (2016), http://dx.doi.org/10.1016/j.aca.2016.07.024

-10^{-16} M) with a detection limit of 1×10^{-16} M. This fabricated platform is validated with clinical samples of CML positive patients and the results demonstrate its immense potential for clinical diagnosis.
© 2016 Published by Elsevier B.V.

1. Introduction

Leukemia is a progressive disease wherein the bone marrow and other blood-forming organs produce increased numbers of abnormal leukocytes, leading to anemia and other manifestations [1]. Chronic myeloid leukemia (CML) is one of the most common type of leukemia, which is induced by the active breakpoint cluster region (BCR)/Abelson (ABL) oncogene [2]. The abnormality is produced by reciprocal translocation of chromosome 9 and 22 and it usually occurs in more than 95% of the CML patients [3,4]. The molecular analysis of this translocation shows that the breakpoints on chromosome 22 occur within 5.8 kilobases (kb) of the breakpoint cluster region (BCR) gene [3]. Thus, BCR/ABL is an important biomarker for early diagnosis of the disease, and for detection of minimal residual leukemia cells in the CML patients, especially after the bone marrow transplantation [5]. The conventional techniques like chromosome analysis, fluorescence *in situ* hybridization, flow cytometry, real-time quantitative reverse transcription polymerase chain reaction can be used for the BCR/ABL fusion gene detection [6]. However, some of the major drawbacks of these techniques include poor precision, cost and long delay etc. [7].

The electrochemical DNA biosensors based on nucleic acid hybridization have recently been explored for diagnosis of blood cancer [8–10]. DNA biosensors offer a new approach for rapid, sensitive, simple and low-cost detection of specific nucleic acid sequences [9,11]. Some electrochemical DNA sensors based on quantum dots (QD) and conducting polymers have been reported for detection of BCR/ABL oncogene [12,13]. It has been found that the immobilizing matrix plays an important role towards the fabrication of a biosensor [14,15]. In this context, an important issue for QD application in biosystems is the short/long-term toxicity of QDs [16]. Quantum dots are known to damage DNA and reduce the activity due to factors such as the surface coating [17]. Lin et al. fabricated an electro-chemical DNA biosensor based on glassy carbon electrode using methylene blue (MB) as the hybridization indicator [18]. This sensor shows the detection limit of 5.9×10^{-8} M. An impedance biosensor for detection of CML, based on DNA immobilized gold nanoparticles/gold modified electrode with a detection limit of 1.0×10^{-12} mol L^{-1} was fabricated by Ensafi et al. [19]. However, validation with the clinical patient samples was not reported. In spite of these developments, there is an urgent need for the availability of a sensitive, specific and mediator free reusable biosensor that can be used for early and reliable detection of CML.

The assembly of a modified material onto an electrode surface is crucial for the construction of an electrochemical biosensor as biomolecules are known to get denatured quickly due to physiological changes [20–22]. For the fabrication of a high-performance miniaturized biosensor, an important step is the deposition of ultra-thin ordered structures because the performance of the device depends strongly on the molecular arrangement [23,24]. In this regard, the composition of a monolayer based matrix has been found largely based on the Langmuir–Blodgett (LB) technique that involves the transfer of a monolayer, assembled at the gas–liquid interface to a solid substrate [25,26]. Recently, nanostructured oxides of metals like zinc, iron, titanium, have been found to play a significant role since they provide desired orientation to the biomolecules with negligible conformational changes [27–29]. Among the various metal oxides, zinc oxide nanoparticles (ZnONPs) due to their easy fabrication, biocompatibility, environmental friendly nature, and non-toxic synthesis route can be used for biosensor application [30–32]. Zinc oxide is a wide band gap semiconductor (Eg = 3.37 eV), which makes it more attractive for fabrication of high-efficiency nano-devices because of its high exciton binding energy of 60 meV and high mechanical and thermal stabilities [33,34].

We report results of studies relating to the fabrication of a novel electrochemical DNA sensor based on amino-functionalized silica coated ZnONPs (Am-Si@ZnO NPs) using LB technique. This platform has been utilized for the detection of BCR-ABL fusion gene of CML by covalently immobilizing probe sequence specific to CML. This optimized Am-Si@ZnO nano-assembly shows excellent specificity for single-base mismatch and complementary DNA after hybridization and the specific probe has been used for the assay of a PCR clinical sample of CML patient.

2. Material and methods

2.1. Chemicals

Zinc nitrate hexahydrate ($Zn(NO_3)_2 \cdot 6H_2O$), tetraethyl orthosilicate (TEOS, 98%), n-(2-aminoethyl)-3-aminopropyltrimethoxysilane (AAPS, 80%), lithium hydroxide ($LiOH \cdot H_2O$), glutaraldehyde were purchased from Sigma–Aldrich (USA). The other reagents were of analytical grade and were used as received. CML specific probe oligonucleotide sequence, complementary, non-complementary and one-base mismatch target sequence used in this work are procured from Sigma-Aldrich, USA and are as follows.

Probe DNA (pDNA): Amine–5′–TGT CCA CAG CAT TCC GCT GACC–3′
Complementary: 5′–GGT CAG CGG AAT GCT GTG GACA–3′
One-base mismatch: 5′–GCT CAG CGG AAT GCT GTG GACA–3′
Non-complementary: 5′–TAC TCG CAA TAA CGT GAT CTCC–3′

The reagents were prepared in deionized water (Millipore, 18.0 MΩ cm), and the solutions and glassware were autoclaved prior to use. Tris-E buffer (1 M Tris-HCl and 0.5 M EDTA, pH 8.0) was used to prepare all oligonucleotide solutions and stored at −20 °C.

2.2. Synthesis of zinc oxide nanoparticles

Zinc oxide nanoparticles (ZnONPs) were synthesized by a previously reported method with slight modifications [35,36]. The alkaline solution was prepared by dissolving $Zn(NO_3)_2 \cdot 6H_2O$ and LiOH of equal concentration (0.1 M) in water and ethylene glycol (5:1) [37]. The solution was kept for 6 h without stirring, and the temperature was maintained at 100 °C. After the hydrolysis reaction, the white precipitates thus formed were collected by centrifugation and thoroughly washed with deionized water (5 times) and dried in vacuum oven (60 °C) [35].

Please cite this article in press as: C.M. Pandey, et al., Controlled deposition of functionalized silica coated zinc oxide nano-assemblies at the air/water interface for blood cancer detection, Analytica Chimica Acta (2016), http://dx.doi.org/10.1016/j.aca.2016.07.024

2.3. Synthesis of silica-coated zinc oxide nanoparticles

Surface modification of ZnONPs with silica was carried out in two steps using modified sol-gel process [38,39]. Solution (A) was prepared by adding ethanol and water (7:3) in a round bottomed flask that was continuously stirred and maintained at pH 12.0 using NH_4OH. For the preparation of solution (B), TEOS (30 wt %) was added to the prepared ZnONPs, and the solution was ultrasonicated for 15–20 min (Fig. 1(A)) [40]. For modification of the surface, TEOS was contemplated, to render the surface more hydrophobic and make them compatible with other organic media [41]. This solution was thus injected into solution (A) with continuous stirring for 12 h at room temperature. The silica coated ZnONPs (Si@ZnONPs) were centrifuged and washed with ethanol (5–6 times), and dried overnight, in a vacuum oven at 80 °C.

2.4. Functionalization of Si@ZnO nanoparticles

The amino functionalization of the Si@ZnO NPs was carried out using APTES to render them suitable for covalent immobilization of biomolecules on the surface. Functionalization of Si@ZnO (500 mg) was carried out using 0.075 mmol of AAPS by overnight refluxing in toluene [40].

2.5. Langmuir-Blodgett film preparation

Prior to deposition, ITO was hydrolyzed by immersing in the $H_2O_2/NH_4OH/H_2O$ solution (1:1:5, v/v) for about 30 min at 80 °C. The Langmuir trough was used for the preparation of Langmuir films of Am-Si@ZnO nanoparticles on hydrolyzed ITO glass (2 mm × 1 mm). Freshly prepared solution of Am-Si@ZnO NPs was diluted in chloroform (10 mg/ml) with stearic acid (1 mg/ml) in the ratio of 2:1, respectively and ultrasonicated for 30 min just before spreading (Fig. 1(B)). An optimized amount (30 μl) of the prepared material was spread at the water/air interface of the trough. After 15 min (chloroform evaporation), the particles were compressed with a barrier speed of 30 cm^2/s to record the surface area isotherm. The value of pressure at which quasi-solid behavior of monolayer appeared was found to be 16 mN/m at 23 °C. At this optimized pressure and temperature, the monolayers (2, 3 and 6) were transferred by vertical deposition, with interval of 300 s and 60 s for top and bottom dipper position, respectively.

2.6. Immobilization of probe DNA and hybridization

Glutaraldehyde was used as a cross-linker for bioconjugation of aminated pDNA to the Am-Si@ZnO/ITO electrode surface. For this purpose, the Am-Si@ZnO/ITO surface was activated by incubation in aqueous glutaraldehyde solution (0.1% v/v) for 1 h followed by washing with deionized water [42]. For coupling between the amine terminal of pDNA and the glutaraldehyde-modified Am-Si@ZnO/ITO electrode, 20 μL of pDNA was spread onto the modified electrode surface and kept in a humid chamber at room temperature (25 °C) for 4 h. The pDNA/Am-Si@ZnO/ITO bioelectrode was then rinsed with Tris–HCl (10 mM) and EDTA (1 mM) buffer solution (TE, pH 8.0) to remove any physically adsorbed pDNA on the electrode surface. This bioelectrode was further used for detection of CML by hybridizing various concentrations (10^{-6}-10^{-16}) of complementary target DNA.

2.7. Instruments

Monolayers deposition was done in an LB trough (NIMA 601A). Ultraviolet–visible (UV-Vis) absorption studies were carried out on UV-Vis spectrophotometer (Phoenix 2200DPCV). Fourier transform infrared (FTIR) measurements were employed in attenuated total reflection (ATR) mode, with germanium waveguide, on a Perkin–Elmer Spectrum BX II spectrophotometer. The FTIR signal was obtained by averaging 64 scans at the resolution of 4 cm^{-1}. Contact angle (CA) measurements were taken on a contact angle meter

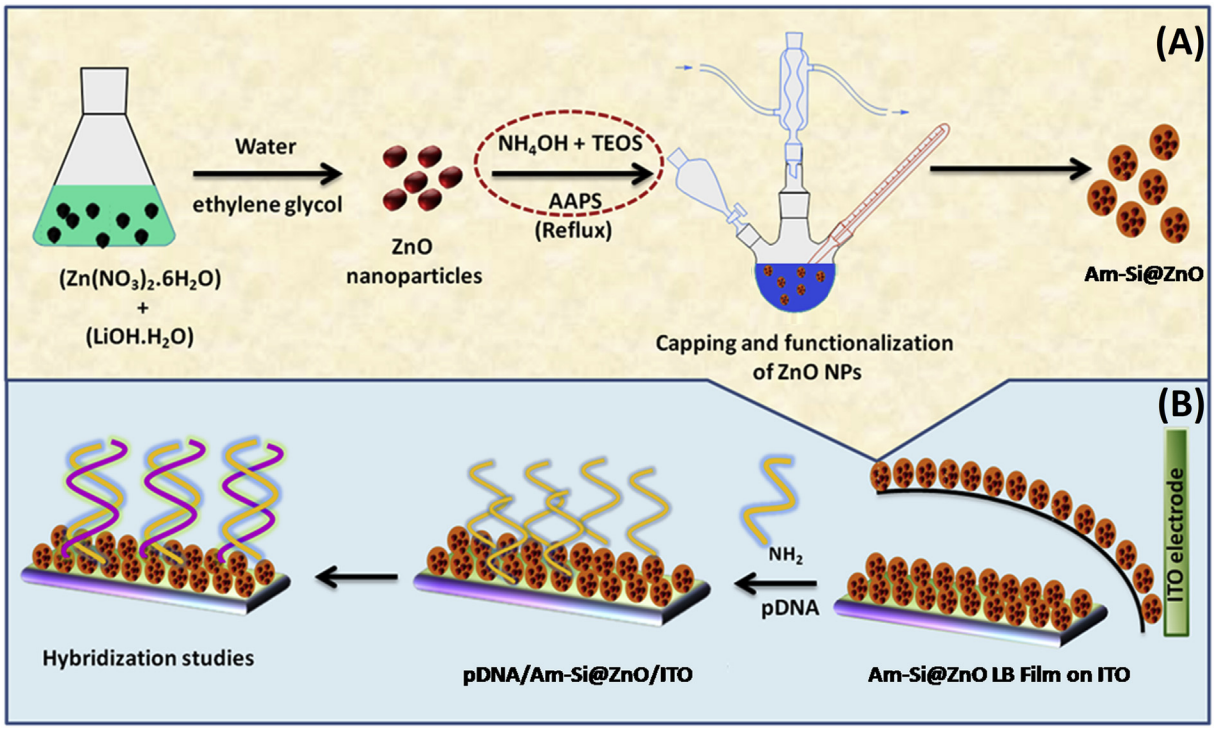


Fig. 1. Schematic illustration for the (A) synthesis of Am-Si@ZnO and (B) LB deposition Am-Si@ZnO on ITO electrode and subsequent DNA sensor fabrication.

Please cite this article in press as: C.M. Pandey, et al., Controlled deposition of functionalized silica coated zinc oxide nano-assemblies at the air/water interface for blood cancer detection, Analytica Chimica Acta (2016), http://dx.doi.org/10.1016/j.aca.2016.07.024

(Data Physics OCA15EC). The morphological characterization was carried out on a field emission transmission electron microscope (TEM; JEOL JEM-2100F) at an accelerating voltage of 200 keV and on a scanning electron microscope (SEM, LEO 440). Electrochemical characterization was conducted on an Autolab potentiostat/galvanostat (Eco Chemie, Netherlands) using a three-electrode system with ITO as the working electrode, Ag/AgCl as a reference electrode, and platinum foil as a counter electrode, in phosphate-buffer saline (PBS 100 mM, pH 7.4, and 0.9% NaCl).

3. Results and discussion

3.1. Characterization

The results of X-ray diffraction studies conducted on ZnO NPs show presence of the sharp peaks at $2\theta = 36.25°$ (101), 31.77° (100), 34.42° (002), 56.60° (110), 62.86° (103), indicating polycrystalline structure (JCPDS 36-1451), having hexagonal shape with lattice constants $a = b = 0.32$ nm and $c = 0.52$ nm (Fig. S1). No other characteristic peaks of any impurities were observed, suggesting that high-quality ZnONPs were synthesized. The crystalline size of the synthesized ZnONPs was found to be 10.25 nm using the Debye-Scherrer formula. Further, the UV–Vis absorption specta of ZnO nanoparticles shows an excitonic absorption peak at about 290 nm (Fig. S2(A)), that lies much below the band gap wavelength of 388 nm of bulk ZnO. The peak at ~290 nm in the spectra is due to the interband transition of the copper electrons from a deep level of valence band [36]. The blue shift in the peak centered at ~290 nm in absorption spectra is ascribed to the transition of electrons from the most inner shell of copper to the uppermost shell as the time passes. This behavior is typically shown by many semiconductors which arise due to internal electric fields within the crystal and inelastic scattering of the charge carriers by photons [36]. In case of the Am-Si@ZnO NPs, a peak is observed around ~375 nm (Fig. S2(B)) shows a red shift, in the peaks.

3.2. Zeta potential studies

The size distribution profile of the aqueous suspension of ZnONPs exhibits a particle size of around 15 nm determined via dynamic light scattering technique (Fig. S3(A)). On coating, the ZnONPs with silica the average particle size increased to 60 nm due to coating of the ZnONPs by silica (Fig. S3(B)). The total surface charge of the synthesized ZnONPs was determined using the Smoluchowski method, and the results are shown in Fig. S3. The ZnONPs exhibit a zeta potential value of 10 mV (Fig. S3(C)). After encapsulation with SiO_2 the zeta potential was found to be −34 mV (Fig. S3(D)). To investigate the effect of APTES functionalization on the Si@ZnO, the surface charge of the nanoparticles was measured, and an increase in the zeta potential from −34 mV to −25 mV was observed indicating presence of the positively charged $-NH_2$ groups. This is indirect evidence showing that the amino group is perhaps conjugated to the Si@ZnO NPs, due to hydrolysis between the APTES and TEOS.

3.3. Microscopic analysis of the nanocomposite ZnONPs and Si@ZnO NPs

The TEM images of the ZnONPs and Si@ZnO NPs are shown in Fig. 2. It appears that ZnONPs are polydispersed in size and that the nanoparticles are spherical or hexagonal in shape (Fig. 2(A)). The diameter of the ZnONPs is in the range of 10–15 nm which is in agreement with the apparent crystallite size determined by XRD. Fig. 2(B) shows hexagonal morphology of the ZnONPs while Fig. 2(C) shows high-resolution TEM image of a hexagonal ZnO in the same sample and the lattice image shows (002) plane of ZnO with d-spacing value as expected for perfect crystalline ZnO. The TEM image of bare silica shows the size of the particle to be as 50 nm (Fig. 2(D)). After surface modification, spherical aggregates of silica coating on hexagonal ZnONPs were observed with size of 70–80 nm (Fig. 2(E)). The HRTEM images of Si@ZnO are shown in Fig. 2(F), which clearly shows wrapping of the ZnO with SiO_2.

3.4. Surface measurements of Am-Si@ZnO Langmuir monolayer

The pressure area isotherms of Am-Si@ZnO Langmuir monolayer on air-water subphase were recorded at different temperatures with varying ratio of the material with respect to stearic acid. Stearic acid acted as a spacer between the particles, as it reduced the aggregate formation and improved the spreading behavior of monolayer on the surface [43]. At 23 °C an optimized quantity (30 μl) of prepared solution with stearic acid (in 2:1 ratio), the area-pressure curve (Fig. 3(A)) showed a sharp kick. The pressure at which material showed the quasi-solid behavior of monolayer was found to be 16 mN/m and the collapsing pressure was found to be 38 mN/m. The observed mean molecular area of the surface was determined to be 2315 $Å^2$/particle, when the surface pressure was set at 0 mN/m.

3.5. Transfer characteristics of Am-Si@ZnO Langmuir monolayers

Langmuir monolayers of Am-Si@ZnO nanoparticles were transferred on hydrolyzed ITO substrate with surface pressure of 16 mN/m at 23 °C. The hydrophobic substrate was positioned perpendicular to the air-water interface, and the monolayers were subsequently deposited by vertical dipping at a rate of 10 mm min^{-1} to obtain Y-type multilayer film (6 layers) shown in Fig. 3(B). The single monolayer of Am-Si@ZnO was transferred onto the hydrophobic substrate in each upward and downward stroke. Transfer onto the substrate as estimated from the change in surface area at the air-water interface, was nearly the same for each monolayer and the results of kinetic measurements as a function of time reveals that it took 30 min for stable monolayers formation (Fig. 3(C)).

3.6. FTIR studies

FT-IR spectra of the bare ZnONPs shows a prominent peak at ~453 cm^{-1} (Fig S4 (i)), due to the stretching vibration of Zn–O bond. While the peaks observed at 1550–1700 cm^{-1} and 3100–3600 cm^{-1} can be attributed to the hydroxyl groups [44]. The Si–O–Si asymmetric stretching vibration band of 980–1190 cm^{-1} is found only in the Am-Si@ZnO NPs spectrum (Fig S4 (ii)), compared to the bare ZnONPs. In Am-Si@ZnO NPs, N–H stretch and hydroxyl group at 3300-3400 cm^{-1} and 3250-3330 cm^{-1} respectively are observed, indicating presence of the primary amine in nanocomposite [40,45].

3.7. Morphological characterization of the electrode and bioelectrode

The morphological studies of the different layers of Am-Si@ZnO LB film on the ITO electrode were studied using SEM. The SEM image of four layers of Am-Si@ZnO nanoparticles (Fig. 4(A)) shows that particles are far apart whereas in the six layers (Fig. 4(B)) the particle distribution is denser (Fig. 4(C)). After immobilization of pDNA on the 6 layered Am-Si@ZnO/ITO electrode globular structures appeared onto the Am-Si@ZnO LB film confirming the attachment of DNA onto the Am-Si@ZnO LB film (Fig. 4(D)). Further, experiments were carried out by directly depositing the Am-

Please cite this article in press as: C.M. Pandey, et al., Controlled deposition of functionalized silica coated zinc oxide nano-assemblies at the air/water interface for blood cancer detection, Analytica Chimica Acta (2016), http://dx.doi.org/10.1016/j.aca.2016.07.024

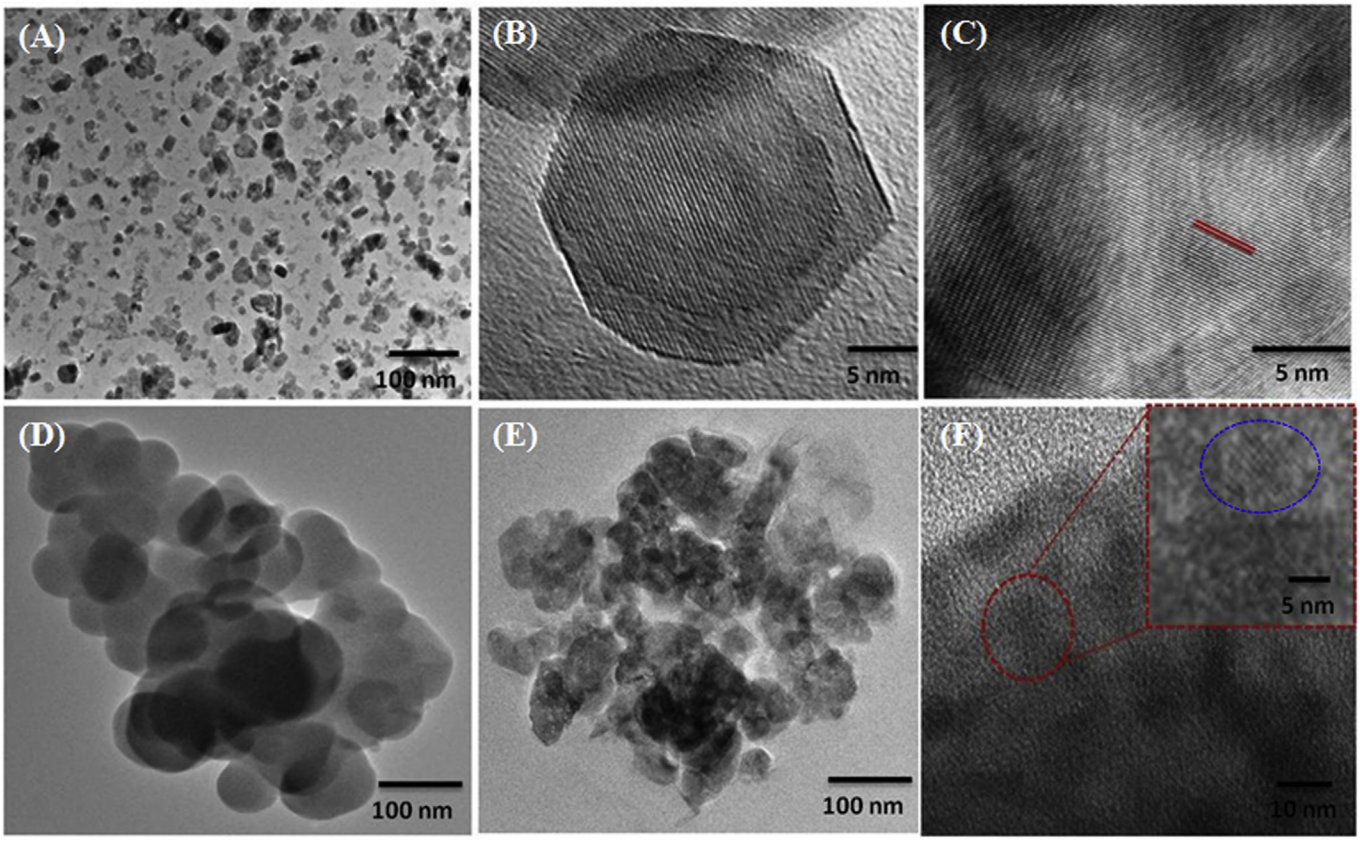


Fig. 2. (A) TEM image of ZnO NPs (B) Magnified image showing hexagonal structure of ZnONPs (C) HRTEM image of ZnONPs (D) TEM image of Silica NPs (E) TEM image of Si@ZnO NPs (F) HRTEM image of Si@ZnO NPs.

Si@ZnO onto ITO coated glass substrate (Fig. 4(E)). It was observed that aggregation of the nanocomposite occurred on the electrode that upon immobilization of pDNA showed an uneven distribution of the pDNA (Fig. 4(F)).

3.8. Electrochemical characterization

3.8.1. Electrochemical studies of the monolayers

Electrochemical impedance spectroscopic (EIS) studies were conducted to evaluate the electrical properties of the multilayer assembly to provide the information during the step deposition of the Am-Si@ZnO LB layers. Impedance spectra were recorded after deposition of each layer of Am-Si@ZnO LB film to investigate the effect of the structure and thickness of the multilayer on the overall interfacial properties. The impedance spectra seen in the Nyquist plot consists of a semicircle portion observed at higher frequencies indicating electron transfer process, whereas the linear part at low frequencies corresponds to the diffusion controlled process [11]. The modified Randles equivalent circuit (inset Fig. 5(B)) was employed to fit the impedance spectra of the fabricated biosensor. The circuit consists of the electrolyte resistance (Rs) between the working and the reference electrode, the Warburg impedance (Z_W), associated with the diffusion process of redox probe ions from the bulk solution to the electrode–solution interface, the electron transfer resistance (Rct) and the constant phase element CPE (related to the double layer capacitance) [24]. The impedance measurements were carried out at the open circuit voltage. The tested frequency range was from 1 Hz to 100 kHz with an amplitude of ±5 mV. With increase in the number of layers of Am-Si@ZnO from two to six, the R_{CT} value decreases (Fig. 5(A)) correspondingly. Changes can be clearly seen in the spectra during the stepwise formation of the multilayer assemblies (2 layers (curve iii), 4 layers (curve ii) and 6 layers (curve i)). The diameter of the semicircle decreases with an increasing number of Am-Si@ZnO LB film, which is due to increase in the film thickness and change in the apparent charge transfer resistance. The interfacial properties of the electrode after each different monolayer (2, 4, 6 layers) were investigated as shown in Table 1. It was found that with increase in the number of Am-Si@ZnO monolayer there was an increase in the exchange current per unit geometric area and the apparent electron transfer rate constant (K_{app}) and it was maximum for 6 layers. To avoid any non-specific adsorption of the cDNA, the optimization of the pDNA on the Am-Si@ZnO/ITO electrode was conducted by varying the pDNA concentration from 10^{-5} M to 10^{-10} M. As shown in Fig. S5, the R_{CT} value leveled off at 10^{-6} M pDNA concentration suggesting that maximum immobilization was achieved at this concentration.

Cyclic voltammetry studies were performed, using a three-electrode system in PBS solution (100 mM, pH 7.0, 150 mM NaCl) containing 5 mM $[Fe(CN)6]^{-3/-4}$. The results of cyclic voltammetric studies, obtained as a function of scan rate (υ, 10–300 mV s^{-1}), for Am-Si@ZnO/ITO electrode and pDNA/Am-Si@ZnO/ITO bioelectrode are shown in Figs. S6(A) and (B), respectively. The observed positive and negative peaks correspond to the oxidation and reduction reactions of the $[Fe(CN)_6]^{-3/-4}$ redox pair, respectively. The peak currents (*Ip*) for both oxidation and reduction follow a linear relation with respect to square root of the scan rate (inset (i), Fig. S6(A), (B)) indicating the existence of diffusion-controlled electrochemical reaction rates for the redox pair at the electrode. It was observed that the oxidation peak shifted to a more positive value

Please cite this article in press as: C.M. Pandey, et al., Controlled deposition of functionalized silica coated zinc oxide nano-assemblies at the air/water interface for blood cancer detection, Analytica Chimica Acta (2016), http://dx.doi.org/10.1016/j.aca.2016.07.024

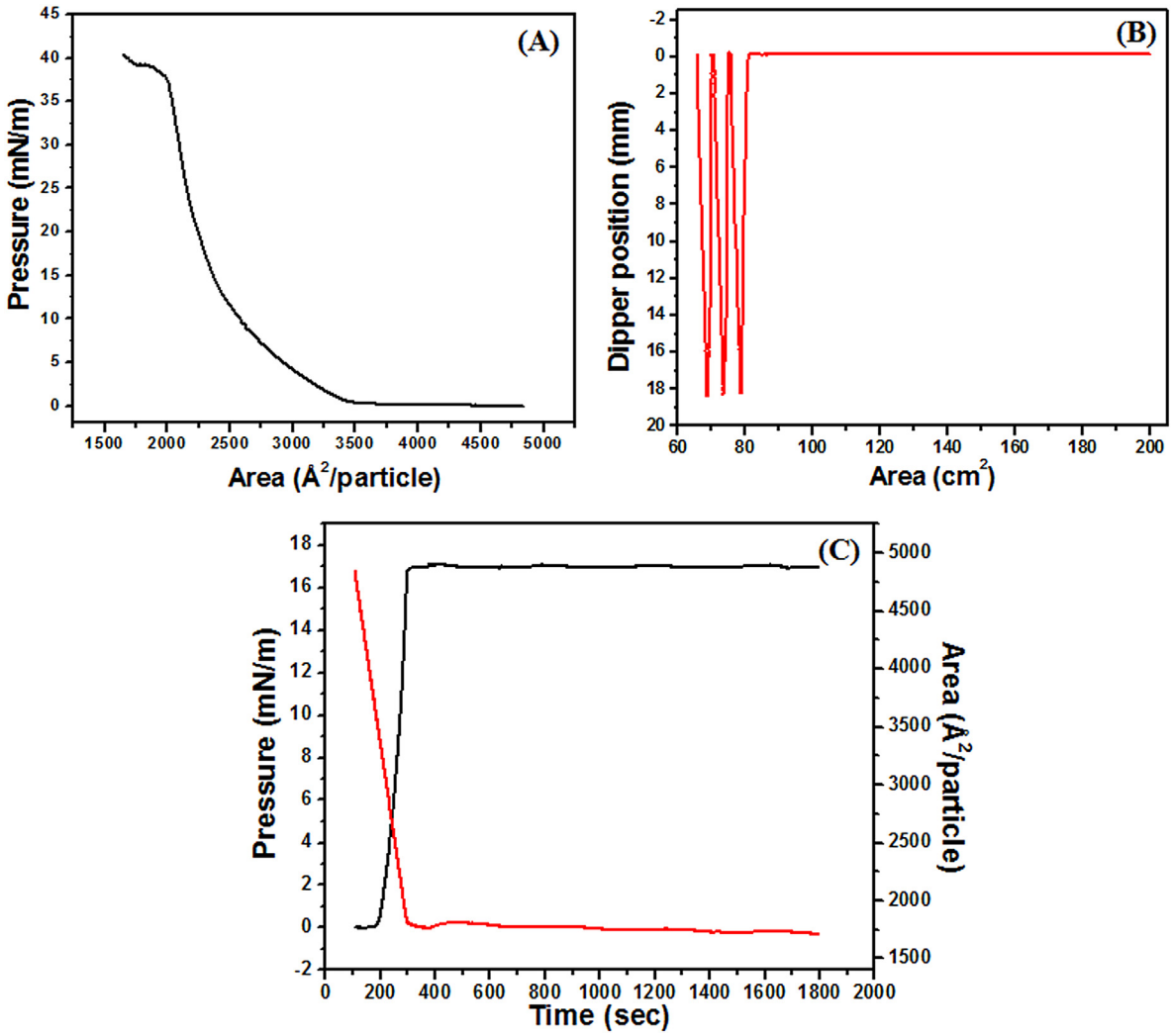


Fig. 3. (A) Surface pressure–area isotherm of Am-Si@ZnO NPs (B) Deposition curve of Am-Si@ZnO NPs on ITO substrate (C) Kinetic measurements showing variation in the particulate surface area at the air–water interface as a function of time at a constant surface pressure.

and the reduction peak to more negative values where both the peak potentials were linearly dependent on the log of the scan rate (inset (ii), Fig. S6(A), (B)). Using Laviron's equations, the value of electron transfer coefficient (α), for n number of electrons, was determined from the slope of two straight lines with anodic and cathodic slopes of $2.303RT/(1-\alpha)nF$ and $-2.303RT/\alpha nF$, respectively [42]. The diffusion coefficient (D) was determined by a concentration gradient of $[Fe(CN)_6]^{3-/4-}$ ions between bulk and interface and was calculated via the Randles–Sevick equation (1):

$$Ip = \left(2.69 \times 10^5\right)\alpha^{1/2} n^{3/2} ACD^{1/2}\upsilon^{1/2} \quad (1)$$

where C is the molar concentration of $[Fe(CN)_6]^{3-/4-}$, and A is the electrode surface area that is immersed in the electrolyte solution (0.5 cm^2). The D value for Am-Si@ZnO/ITO electrode was found to be greater than that of the pDNA/Am-Si@ZnO/ITO electrode. By using the calculated diffusion coefficient, the electroactive surface area (A_e) for the Am-Si@ZnO/ITO electrode and pDNA/Am-Si@ZnO/ITO electrode was calculated to be 1.1685 mm^2 and 0.9239 mm^2, respectively (Table 2) [42].

3.8.2. Electrochemical response studies

For the electrochemical response studies, 6 layers of Am-Si@ZnO LB film were used. When pDNA was immobilized onto the Am-Si@ZnO/ITO electrode, an increase in R_{CT} value was observed due to the negatively charged phosphate backbone of pDNA exposed to the electrolyte, which in turn perhaps repelled $[Fe(CN)_6]^{-3/-4}$ (Fig. 5(B); curve ii). When the pDNA was incubated with its complementary target DNA sequence (cDNA), the hybridization reaction occured and more negatively charged phosphate backbones were introduced. Hence, the R_{CT} value increased following the formation of double-stranded DNA (Fig. 5(B); curve iii). Thus with a change in negative charge and conformation transition, there was a change in the interfacial properties. The difference between the value of R_{CT} for the pDNA immobilized electrode and after hybridization with cDNA ($\Delta R_{CT} = R_{CT}$cDNA- R_{CT}pDNA) was used as the measurement signal. The analytical signal (in terms of ΔR_{CT}) showed a linear relationship with the logarithmic value of the complementary target DNA concentration ranging from 10^{-16} to 10^{-6} M (Fig. 5(D); curve (i)) and follows the following equation:

$$\Delta R_{CT} = 1840.18 + 105.26[\log(\text{concentration of cDNA})] \quad (2)$$

with a linear regression coefficient of 0.9960. The detection limit was calculated using the expression, 3σ/sensitivity, where σ is the standard deviation of the blank electrode. The detection limit for

Please cite this article in press as: C.M. Pandey, et al., Controlled deposition of functionalized silica coated zinc oxide nano-assemblies at the air/water interface for blood cancer detection, Analytica Chimica Acta (2016), http://dx.doi.org/10.1016/j.aca.2016.07.024

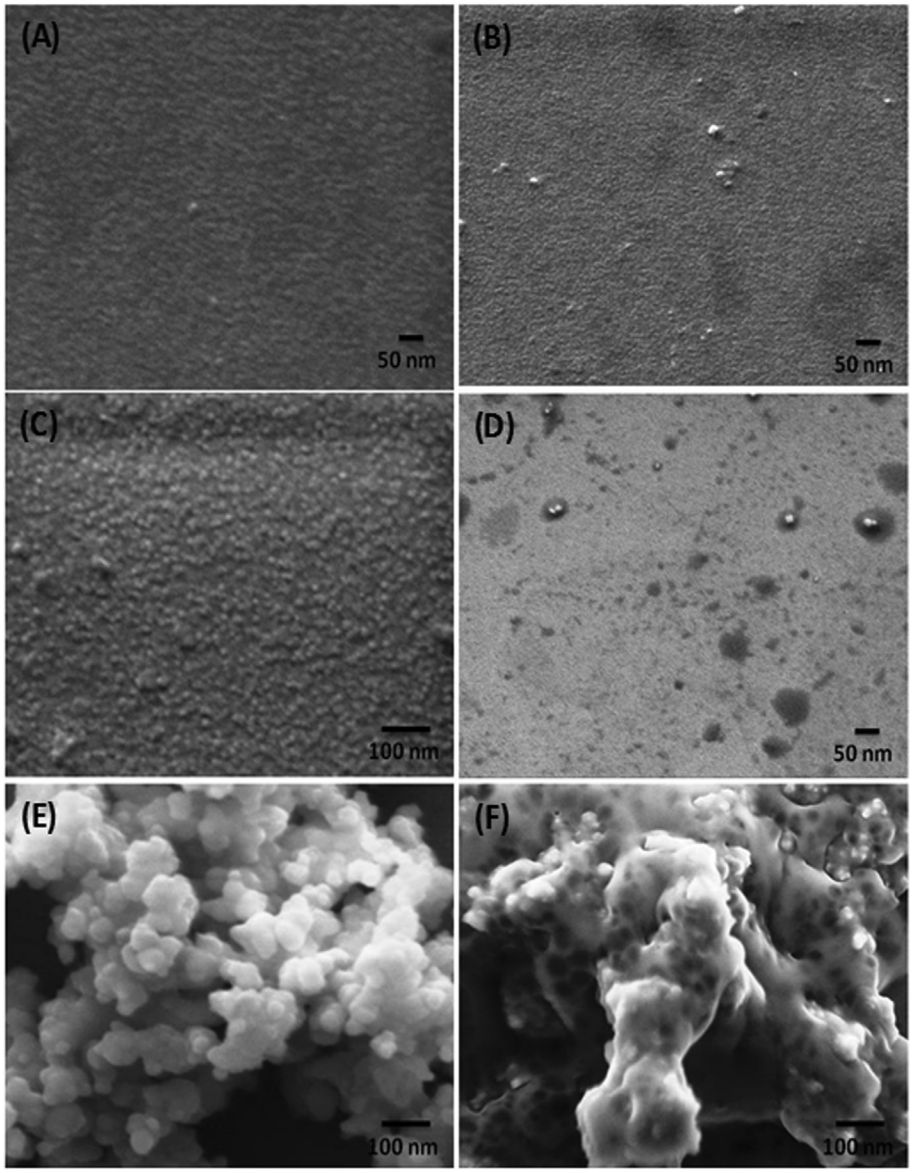


Fig. 4. SEM image of (A) 4 layered LB film of Am-Si@ZnO/ITO, (B) 6 layered LB film of Am-Si@ZnO/ITO. (C) Magnified SEM image of 6 layered LB film of Am-Si@ZnO/ITO. SEM image of (D) pDNA immobilized on 6 layered LB film of Am-Si@ZnO/ITO; (E) Self assembled layers of Am-Si@ZnO on ITO substrate (F) pDNA immobilization on Am-Si@ZnO/ITO (self assembled).

pDNA/Am-Si@ZnO/ITO electrode was found to be 1×10^{-16} M, which is quite higher in comparison to pDNA/ZnO/ITO electrode (1×10^{-13} M, Fig. 5(D); curve (ii)). The enhanced sensitivity is probably due to the favourable orientation of the pDNA onto Am-Si@ZnO LB films. The reproducibility of the fabricated pDNA/Am-Si@ZnO/ITO electrode was investigated by using the interassays coefficient of variation, which was evaluated by analysis of the same concentration of cDNA (10^{-16} M and 10^{-12} M) using five equally prepared electrodes [46]. Five independently made genosensor exhibited similar R_{CT} response and the interassay variation coefficient of interassays was 5.1% (10^{-16} M) and 4.4% (10^{-12} M). The low relative standard deviation indicates that the proposed Am-Si@ZnO LB film based nucleic acid sensor has good repeatability. Further, Langmuir isotherm approach was used to determine the association constant (K_a) for binding interaction assuming equal binding energy for all binding sites [47]. The K_a was estimated from the slope of the regression equation and found to be 0.584 M [46,47]. The fabricated pDNA/Am-Si@ZnO/ITO bioelectrode showed enhanced sensitivity and linearity range as compared to other biosensors reported for CML detection (Table ST1).

3.8.3. *Specificity studies of the bioelectrode*

The specificity of the pDNA/Am-Si@ZnO/ITO bioelectrode towards different target DNA sequences (complementary, non-complementary and one base mismatch) was studied using EIS (Fig. S7). On incubation of the bioelectrode with non-complementary DNA (Fig. S7, curve ii), there was a slight or negligible change in the Rct value with respect to the pDNA (curve i). Since the non-complementary DNA bases do not match with the pDNA bases it is expected that there is no hybridization taking place and hence the Rct should result in a semicircle diameter similar to that of pDNA/Am-Si@ZnO/ITO bioelectrode. When the pDNA/Am-Si@ZnO/ITO bioelectrode was immobilized with one-base mismatch DNA sequence, there was a slight increase in semicircle

Please cite this article in press as: C.M. Pandey, et al., Controlled deposition of functionalized silica coated zinc oxide nano-assemblies at the air/water interface for blood cancer detection, Analytica Chimica Acta (2016), http://dx.doi.org/10.1016/j.aca.2016.07.024

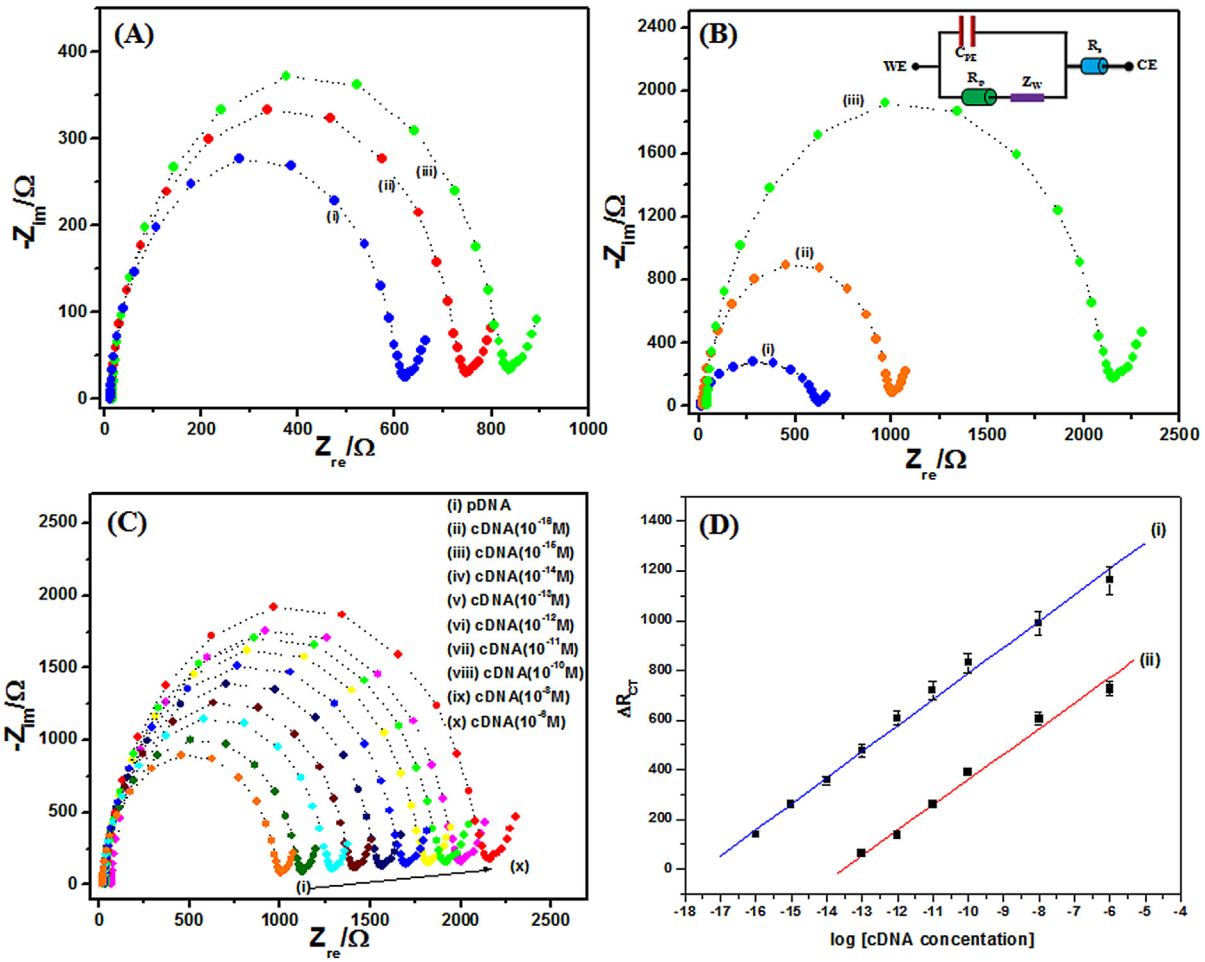


Fig. 5. (A) Nyquist diagram (Z_{im} versus Z_{re}) for the Faradic impedance of (i) 6, (ii) 4, (iii) 2 LB layers of Am-Si@ZnO/ITO. (B) Nyquist diagram (Z_{im} versus Z_{re}) for the Faradic impedance of (i) 6 layers of Am-Si@ZnO/ITO, (ii) pDNA/Am-Si@ZnO/ITO (iii) cDNA/pDNA/Am-Si@ZnO/ITO. (C) Nyquist diagram (Z_{im} versus Z_{re}) for the Faradic impedance of cDNA (10^{-6} M – 10^{-16} M) on pDNA/Am-Si@ZnO/ITO. (D) Linearity relation curve between ΔR_{CT} and log of concentrations of cDNA for (i) pDNA/Am-Si@ZnO/ITO electrode and, (ii) pDNA/ZnO/ITO electrode.

Table 1
Kinetic parameters calculated for the different Am-Si@ZnO LB layers deposited on ITO electrode using EIS.

No. of Layers	R_{CT} (Ω)	K_{app} (cm/s)	I_o (A/cm^2)
6 layers	606.880	1.75×10^{-7}	4.23×10^{-5}
4 layers	731.853	1.45×10^{-7}	3.51×10^{-5}
2 layers	819.643	1.29×10^{-7}	3.13×10^{-5}
pDNA	986.864	1.07×10^{-7}	2.604×10^{-5}

diameter in comparison to that of the pDNA/Am-Si@ZnO/ITO bioelectrode (curve iii). This explains partial hybridization of pDNA with the complementary bases of the one-base mis-match DNA resulting in increased negative charge of the electrode surface which repelled the marker ion [42]. These results reveal selectivity of the pDNA/Am-Si@ZnO/ITO bioelectrode towards different target DNA sequences. The negligible change in the value of R_{CT} was observed when pDNA/Am-Si@ZnO/ITO bioelectrode was treated with non-complementary DNA and one-base mismatch, which shows that fabricated bioelectrode is highly specific for CML detection.

3.9. Validation of the biosensor with patient samples

To test real application of the fabricated DNA biosensor, positive real samples of CML patient, were procured from Rajiv Gandhi Cancer Institute and Research Centre, Delhi, India after PCR amplification. Prior to performing the electrochemical assay with PCR amplicons of BCR-ABL fusion gene, the samples were ultrasonicated to allow shearing. Gel electrophoresis experiment of the

Table 2
Kinetic parameter calculated for the Am-Si@ZnO/ITO electrode and pDNA/Am-Si@ZnO/ITO electrode.

Name of electrode	Electron transfer coefficient (α)	Charge transfer rate constant (ks; s^{-1})	Diffusion coefficient (D; cm^{2}s^{-1})	Electroactive surface area (A; mm^2)	Average surface concentration (Γ; mol cm^2)
Am-Si@ZnO/ITO	0.596	0.0121	3.08×10^{-11}	1.1685	3.55×10^{-8}
pDNA/Am-Si@ZnO/ITO	0.5158	0.0738	1.89×10^{-11}	0.9239	2.56×10^{-8}

Please cite this article in press as: C.M. Pandey, et al., Controlled deposition of functionalized silica coated zinc oxide nano-assemblies at the air/water interface for blood cancer detection, Analytica Chimica Acta (2016), http://dx.doi.org/10.1016/j.aca.2016.07.024

fragmented cDNA samples was performed to obtain an estimation of fragments length with respect to the sonication time (Fig. S7). It was revealed that fragmentation in the length range of about 50 bases occurred after 15 min of sonication (Fig. S7; panel iii). The R_{CT} value of the positive real sample gave a mean average of 2.3 KΩ and 2.45 KΩ (Fig. S8; curve v and vi), which were similar to that of the cDNA (curve iv). The analysis of EIS results shows that the fabricated nucleic acid sensor performed equally well despite the fact that BCR-ABL from real sample is much longer than that of the synthetic target DNA [48].

4. Conclusions

An impedimetric nucleic acid sensor based on covalently immobilized CML specific DNA onto Am-Si@ZnO LB films has been developed. The sensing results carried out using EIS studies reveal that the pDNA/Am-Si@ZnO/ITO nucleic acid sensor shows linear range, 10^{-16} M-10^{-6} M with an increased sensitivity of 10^{-16} M for CML detection. This LB based nucleic acid sensor has been successfully used to distinguish CML positive patient samples. Efforts are being made to integrate the Am-Si@ZnO LB film with the microfluidic techniques to execute on-chip electrochemical DNA sensor in a single platform. Thus this platform holds great promise for development of ultrasensitive bioassay for cancer monitoring.

Acknowledgement

We thank Director, CSIR-NPL, New Delhi, India for his interest and support in this work. We thank Dr. R.K.Kotnala (CSIR-NPL) for interesting discussions. C.M. Pandey acknowledges the financial support received from Department of Science and Technology, India under DST-INSPIRE Faculty project (Grant No. DST/INSPIRE/04/2015/000932).

Appendix A. Supplementary data

Supplementary data related to this article can be found at http://dx.doi.org/10.1016/j.aca.2016.07.024.

References

[1] A.A. Ensafi, M. Taei, H.R. Rahmani, T. Khayamian, Sensitive DNA impedance biosensor for detection of cancer, chronic lymphocytic leukemia, based on gold nanoparticles/gold modified electrode, Electrochim. Acta 56 (2011) 8176–8183.
[2] M.W.N. Deininger, J.M. Goldman, J.V. Melo, The molecular biology of chronic myeloid leukemia, Blood 96 (2000) 3343–3356.
[3] F. Morel, C. Ka, M.J. Le Bris, A. Herry, P. Morice, P. Bourquard, J.F. Abgrall, C. Berthou, M. De Braekeleer, Deletion of the 5[prime] abl region in Philadelphia chromosome-positive chronic myeloid leukemia, Leukemia 17 (2003) 473–474.
[4] J.P. Radich, T. Gooley, E. Bryant, T. Chauncey, R. Clift, L. Beppu, S. Edmands, M.E.D. Flowers, K. Kerkof, R. Nelson, F.R. Appelbaum, The significance of bcr-abl molecular detection in chronic myeloid leukemia patients "late," 18 months or more after transplantation, Blood 98 (2001) 1701–1707.
[5] S. Slavin, A. Nagler, E. Naparstek, Y. Kapelushnik, M. Aker, G. Cividalli, G. Varadi, M. Kirschbaum, A. Ackerstein, S. Samuel, A. Amar, C. Brautbar, O. Ben-Tal, A. Eldor, R. Or, Nonmyeloablative stem cell transplantation and cell therapy as an alternative to conventional bone marrow transplantation with lethal cytoreduction for the treatment of malignant and nonmalignant hematologic diseases, Blood 91 (1998) 756–763.
[6] M.A. Tainsky, Genomic and proteomic biomarkers for Cancer: a multitude of opportunities, Biochim. Biophys. Acta 1796 (2009) 176–193.
[7] R.W. McKenna, Multifaceted approach to the diagnosis and classification of acute leukemias, Clin. Chem. 46 (2000) 1252–1259.
[8] K.J. Odenthal, J.J. Gooding, An introduction to electrochemical DNAbiosensors, Analyst 132 (2007) 603–610.
[9] T.G. Drummond, M.G. Hill, J.K. Barton, Electrochemical DNA sensors, Nat. Biotech. 21 (2003) 1192–1199.
[10] X. Chen, L. Wang, S. Sheng, T. Wang, J. Yang, G. Xie, W. Feng, Coupling a universal DNA circuit with graphene sheets/polyaniline/AuNPs nanocomposites for the detection of BCR/ABL fusion gene, Anal. Chim. Acta 889 (2015) 90–97.
[11] C.M. Pandey, G. Sumana, B.D. Malhotra, Microstructured cystine dendrites-based impedimetric sensor for nucleic acid detection, Biomacromolecules 12 (2011) 2925–2932.
[12] L. Wang, E. Hua, M. Liang, C. Ma, Z. Liu, S. Sheng, M. Liu, G. Xie, W. Feng, Graphene sheets, polyaniline and AuNPs based DNA sensor for electrochemical determination of BCR/ABL fusion gene with functional hairpin probe, Biosens. Bioelectron. 51 (2014) 201–207.
[13] W. Zhang, Electrochemically reduced graphene oxide supported poly(indole-5-carboxylic acid) nanocomposite for genosensing application, RSC Adv. 5 (2015) 103649–103655.
[14] P.R. Solanki, A. Kaushik, V.V. Agrawal, B.D. Malhotra, Nanostructured metal oxide-based biosensors, NPG Asia Mater 3 (2011) 17–24.
[15] A. Sharma, C.M. Pandey, Z. Matharu, U. Soni, S. Sapra, G. Sumana, M.K. Pandey, T. Chatterjee, B.D. Malhotra, Nanopatterned cadmium selenide Langmuir–-blodgett platform for leukemia detection, Anal. Chem. 84 (2012) 3082–3089.
[16] J. Drbohlavova, V. Adam, R. Kizek, J. Hubalek, Quantum dots-characterization, preparation and usage in biological systems, Int. J. Mol. Sci. 10 (2009) 656–673.
[17] M.A. Walling, J.A. Novak, J.R.E. Shepard, Quantum dots for live cell and in vivo imaging, Int. J. Mol. Sci. 10 (2009) 441–491.
[18] X.-H. Lin, P. Wu, W. Chen, Y.-F. Zhang, X.-H. Xia, Electrochemical DNA biosensor for the detection of short DNA species of Chronic Myelogenous Leukemia by using methylene blue, Talanta 72 (2007) 468–471.
[19] A.A. Ensafi, H. Karimi-Maleh, Modified multiwall carbon nanotubes paste electrode as a sensor for simultaneous determination of 6-thioguanine and folic acid using ferrocenedicarboxylic acid as a mediator, J. Electroanal. Chem. 640 (2010) 75–83.
[20] D. Grieshaber, R. MacKenzie, J. Vörös, E. Reimhult, Electrochemical biosensors - sensor principles and architectures, Sens. (Basel, Switzerland) 8 (2008) 1400–1458.
[21] Q.M. Zhang, M.J. Serpe, Versatile method for coating surfaces with functional and responsive polymer-based films, ACS Appl. Mater. Interfaces 7 (2015) 27547–27553.
[22] C.M. Pandey, R. Singh, G. Sumana, M. Pandey, B. Malhotra, Electrochemical genosensor based on modified octadecanethiol self-assembled monolayer for Escherichia coli detection, Sens. Actuator B-Chem. 151 (2011) 333–340.
[23] T. Hosokai, A. Hinderhofer, F. Bussolotti, K. Yonezawa, C. Lorch, A. Vorobiev, Y. Hasegawa, Y. Yamada, Y. Kubozoro, A. Gerlach, S. Kera, F. Schreiber, N. Ueno, Thickness and substrate dependent thin film growth of picene and impact on the electronic structure, J. Phys. Chem. B 119 (2015) 29027–29037.
[24] A. Kaushik, P.K. Vabbina, V. Atluri, P. Shah, A. Vashist, R.D. Jayant, A. Yandart, M. Nair, Electrochemical monitoring-on-chip (E-MoC) of HIV-infection in presence of cocaine and therapeutics, Biosens. Bioelectron. 86 (2016) 426–431.
[25] M.A. Karymov, A.A. Kruchinin, Y.A. Tarantov, I.A. Balova, L.A. Remisova, N.G. Sukhodolov, A.I. Yanklovich, A.M. Yorkin, Langmuir-Blodgett film based membrane for DNA-probe biosensor, Sens. Actuator B-Chem. 6 (1992) 208–210.
[26] S.L. Selektor, M.A. Shcherbina, A.V. Bakirov, P. Batat, C. Grauby-Heywang, S. Grigorian, V.V. Arslanov, S.N. Chvalun, Cation-controlled Excimer packing in Langmuir–blodgett films of hemicyanine amphiphilic chromoionophores, Langmuir 32 (2016) 637–643.
[27] P.R. Solanki, A. Kaushik, V.V. Agrawal, B.D. Malhotra, Nanostructured metal oxide-based biosensors, NPG Asia Mater. 3 (2011) 17–24.
[28] Y.V. Stebunov, O.A. Aftenieva, A.V. Arsenin, V.S. Volkov, Highly sensitive and selective sensor Chips with graphene-oxide linking layer, ACS Appl. Mater. Interfaces 7 (2015) 21727–21734.
[29] A.F.D. Cruz, N. Norena, A. Kaushik, S. Bhansali, A low-cost miniaturized potentiostat for point-of-care diagnosis, Biosens. Bioelectron 62 (2014) 249–254.
[30] W. Zhong Lin, Zinc oxide nanostructures: growth, properties and applications, J. Phys. Condens. Matter 16 (2004) R829.
[31] S.S. Low, M.T.T. Tan, H.-S. Loh, P.S. Khiew, W.S. Chiu, Facile hydrothermal growth graphene/ZnO nanocomposite for development of enhanced biosensor, Anal. Chim. Acta 903 (2016) 131–141.
[32] S.K. Arya, S. Saha, J.E. Ramirez-Vick, V. Gupta, S. Bhansali, S.P. Singh, Recent advances in ZnO nanostructures and thin films for biosensor applications: Review, Anal. Chim. Acta 737 (2012) 1–21.
[33] E.A. Meulenkamp, Synthesis and growth of ZnO nanoparticles, J. Phys. Chem. B 102 (1998) 5566–5572.
[34] Y. Lv, L. Guo, H. Xu, L. Ding, C. Yang, J. Wang, W. Ge, S. Yang, Z. Wu, Low temperature synthesis and optical properties of small-diameter ZnO nanorods, J. Appl. Phys. 99 (2006) 114302.
[35] D. JapiÄ, I. Djerdj, M. MarinÅ¡ek, Z.C. Orel, In situ and ex situ TEOS coating of ZnO nanoparticles and the preparation of composite ZnO/PMMA for UV-VIS Absorbers, Acta Chim. Slov. 60 (2013) 797–808.
[36] B. Liu, H.C. Zeng, Hydrothermal synthesis of ZnO nanorods in the diameter regime of 50 nm, J. Am. Chem. Soc. 125 (2003) 4430–4431.
[37] K.D. Kim, D.W. Choi, Y.-H. Choa, H.T. Kim, Optimization of parameters for the synthesis of zinc oxide nanoparticles by Taguchi robust design method, Colloids Surf. A 311 (2007) 170–173.
[38] N.V. Konduru, K.M. Murdaugh, A. Swami, R.J. Jimenez, T.C. Donaghey, P. Demokritou, J.D. Brain, R.M. Molina, Surface modification of zinc oxide nanoparticles with amorphous silica alters their fate in the circulation,

Nanotoxicology (2015) 1–8.
[39] J. Tao, Z. Xiaofeng, Z. Jian, S. Yanling, L. Tianxing, A Zinc Oxide Modified Porous Silicon Humidity Sensor, Information Acquisition, 2006 IEEE International Conference on, 2006, pp. 1158–1162.
[40] H.-L. Xia, F.-Q. Tang, Surface synthesis of zinc oxide nanoparticles on silica Spheres: preparation and characterization, J. Phys. Chem. B 107 (2003) 9175–9178.
[41] G.A. Farzi, R. Tayebee, S. Naghibinasab, Surface modification of ZnO nanoparticles with Trimetoxyvinyl Silane and Oleic Acid and studying their dispersion in organic media, Int. J. Nano Dimens. 6 (2015) 67–75.
[42] C.M. Pandey, A. Sharma, G. Sumana, I. Tiwari, B.D. Malhotra, Cationic poly(lactic-co-glycolic acid) iron oxide microspheres for nucleic acid detection, Nanoscale 5 (2013) 3800–3807.
[43] Z. Matharu, G. Sumana, S.K. Arya, S.P. Singh, V. Gupta, B.D. Malhotra, Polyaniline Langmuir–Blodgett film based cholesterol biosensor, Langmuir 23 (2007) 13188–13192.
[44] M. Ramasamy, Y.J. Kim, H. Gao, D.K. Yi, J.H. An, Synthesis of silica coated zinc oxide–poly(ethylene-co-acrylic acid) matrix and its UV shielding evaluation, Mater. Res. Bull. 51 (2014) 85–91.
[45] Y. Xu, L. Axe, Synthesis and characterization of iron oxide-coated silica and its effect on metal adsorption, J. Colloid Interface Sci. 282 (2005) 11–19.
[46] C. Mouli Pandey, G. Sumana, I. Tiwari, Nanostructuring of hierarchical 3D cystine flowers for high-performance electrochemical immunosensor, Biosens. Bioelectron. 61 (2014) 328–335.
[47] S.K. Arya, T.S. Pui, C.C. Wong, S. Kumar, A.R.A. Rahman, Effects of the electrode size and modification protocol on a label-free electrochemical biosensor, Langmuir 29 (2013) 6770–6777.
[48] A. Sharma, C.M. Pandey, G. Sumana, U. Soni, S. Sapra, A. Srivastava, T. Chatterjee, B.D. Malhotra, Chitosan encapsulated quantum dots platform for leukemia detection, Biosens. Bioelectron. 38 (2012) 107–113.

Please cite this article in press as: C.M. Pandey, et al., Controlled deposition of functionalized silica coated zinc oxide nano-assemblies at the air/water interface for blood cancer detection, Analytica Chimica Acta (2016), http://dx.doi.org/10.1016/j.aca.2016.07.024

IJARCCE

ISSN (Online) 2278-1021
ISSN (Print) 2319 5940

International Journal of Advanced Research in Computer and Communication Engineering
Vol. 5, Issue 6, June 2016

Dezert- Smarandache Theory based Classification of EMG Signals

Preeti Meena[1], Malti Bansal[2]

Department of ECE, Delhi Technological University, Delhi, India[1, 2]

Abstract: This research paper proposes an intellectual method for the classification of different types of Electromyography (EMG) signals like normal, myopathy and neuropathy signals. Inside the human body, contraction of muscles and nerves occur at every second. And, EMG is a techniqueused to measure this electrical activity. For the analysis of EMG signals, so many methods have been already used.With this research, a new method is proposed in which Dezert-Smarandache Theory (DSmT) based classification technique is utilizedfor the EMG signals analysis. In this, discrete wavelet transform with some features likeenergy, mean and standard deviation are exploited for the features extraction of the EMG signals. After that, classifiers are used in the analysis for the modelling purpose. Then, using these classifiers, DSmT based technique helps in improving the accuracy of the results.It can be seen in the results that DSmT based classification gives the best accuracy (approximately 97%) in comparison to the other classifiers used during this research.

Keyword: DSmT, Electromyography, Wavelet Transform, SVM, SVM-kNN.

I. INTRODUCTION

For the analysis of Electromyography (EMG), it should be a well-known fact that muscles and nerves exists in the human body and contraction of these two may cause pain in the body. EMG is utilized to record these changes in the form of a graph occurred due to contraction of musclesEarly diagnosis is required for dealingwith such diseases. Classification of EMG signals is a vitalexploration. Asystematizedstudy on their classification is required for the proper analysis of the diseases.Hence, a number of methods, most ofthem were computer based, have been proposed. Amongst these EMG analysis algorithms, features of the EMG were extracted using the techniques like Discrete wavelet transform (Daubechies-6) [2], AR modelling [3], autoregressive cepstral analysis [4], PSO [5], wavelet packet energy [6] etc. With these feature extraction techniques, training of different classifiers are done for their modeling.

Classifiers already utilized in the classification of EMG signals are as follows: Fuzzy [6], Artificial neural networks (ANN) [7], Fuzzy-genetic [8], Neuro-fuzzy [9], Deep fuzzy neural network [2], SVM [10], SVM-kNN [1]etc. Using these methods of features extraction and classifiers for classification, good results were obtained in the EMG classification. Nevertheless, performance of these results can be enhanced using a technique called as Dezert-Smarandache Theory (DSmT) [14] for the much better accuracy in terms of results.

In the research paper, a new method for the classification of EMG signals is proposed. The brief outline for the method is represented in the block diagram in Fig.1. From the block diagram, it is seen that firstly, EMG signals are taken as the dataset. Then wavelet transform for these signals are computed as Detail coefficients. For the D_4 coefficient only, features like energy, mean and standard deviation are found out. Later, classification of these signals is performed based on the calculated feature values.

This research paper is organized in different sections which are as follows: Section II gives an overview for the method proposed as a block diagram. Section III gives a detailedview of the dataset used and explanations for the methods and classifiers used. Section IV provides the idea about the overall simulation technique explained using the block diagram for the proposed method. Section Vcomprisesof the classification results trailed by conclusion in Section VI.

II. BLOCK DIAGRAM

The brief outline for the method is represented in the block diagram in Fig.1.In this, anovelmethod is proposed for the classification of EMG signals.

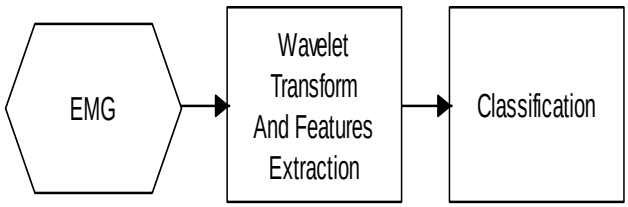


FIG.1.EMG SIGNALS CLASSIFICATION

From the block diagram, it is seen that firstly, EMG signals are taken as the dataset. Then wavelet transform for these signals are computed as Detail coefficients. For the D_4 coefficient only, features like energy, mean and standard deviation are found out. Later, classification of these signals is performed based on the calculated feature values.

Copyright to IJARCCE

IJARCCE

ISSN (Online) 2278-1021
ISSN (Print) 2319 5940

International Journal of Advanced Research in Computer and Communication Engineering
Vol. 5, Issue 6, June 2016

III. PROPOSED METHOD

A. Data Set Used

MIT-BIH database is used to load the Data set of EMG signals. A description of the data set is shown in the Table I.

TABLE I
DESCRIPTION OF DATASET USED

EMG Signals	Total
Normal	500
Myopathy	500
Neuropathy	500

From the sample of dataset used, waveforms of three types of EMG signals are taken and shown in the Fig. 2. These waveforms represent the normal, myopathy and neuropathy signals.

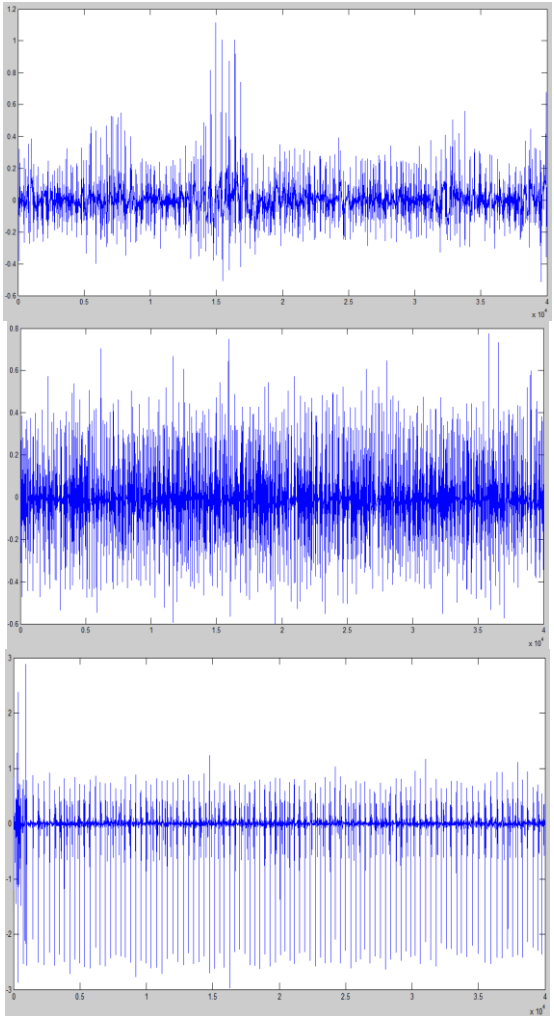


FIG.2. EMG SIGNALS – NORMAL, MYOPATHY AND NEUROPATHY

B. Wavelet Transform

Wavelet transformis the simultaneous representation of the signal in real-time and frequency domain[10]. Hence, it cangive time and frequency information of the signal at the same point of time. Hence, the wavelet transform can be defined as:

$$T(m,n) = \int_{-\infty}^{\infty} x(\tau)\frac{1}{\sqrt{m}}\psi\left(\frac{\tau - n}{m}\right)d\tau \quad (1)$$

Here, ψ representsthe transforming function known as the mother wavelet function. It can be observed from the equation that the transformation is a function of the variables, m and n, wherem is the translation parameter and n is the scale parameter.

For such transformation, signal is distributed from various high-pass h[p] and low-pass l[p] filters. For the proper decomposition of the signal, process is made repetitive for the either h[p] output or l[p] output or for both of the outputs.Such decomposition's first level establishes one level of decomposition and it can be given as:

$$y_{hi}(r) = \sum_{p} x(p).h(2r - p) \quad (2)$$

$$y_{lo}(r) = \sum_{p} x(p).l(2r - p) \quad (3)$$

Here,$y_{hi}[r]$ is the output from the high-pass filter and $y_{lo}[r]$ is the outputfrom the low-pass filter after sub-sampling by 2. It is shown in the Fig.3.

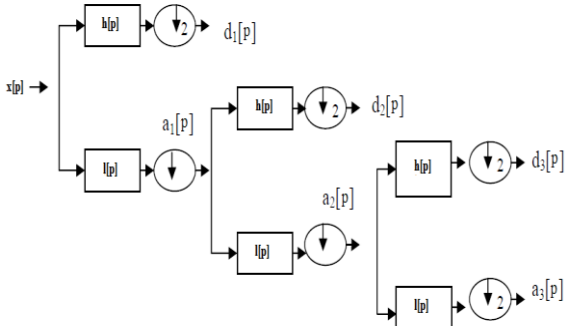


FIG. 3. SUB-BAND DECOMPOSITION OF DWT IMPLEMENTATION;
H[P] IS THE HIGH PASS FILTER, l[P] THE LOW PASS FILTER.

In the Fig.3 shown is the Sub-band decomposition of DWT in which x[p] is the original signal that needs to be decomposed,l[p] and h[p] are low-pass and high-pass filters, respectively. Thisdecomposition of the x[p] will results in the detail and the approximation coefficients. The approximationor the detail coefficients may further be decomposedby sub-level of decomposition as shown in the process Fig.4.

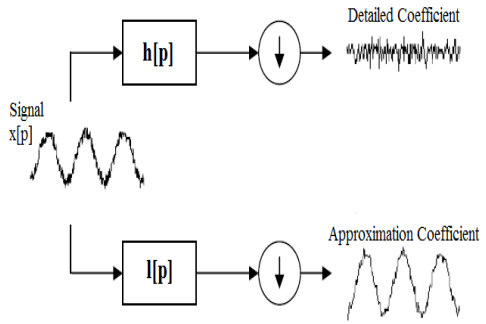


FIG. 4. EMG SIGNAL AND ITS WAVELET DECOMPOSITION INTO APPROXIMATION AND DETAILED COEFFICIENTS.

IJARCCE

ISSN (Online) 2278-1021
ISSN (Print) 2319 5940

International Journal of Advanced Research in Computer and Communication Engineering
Vol. 5, Issue 6, June 2016

For the EMG signal, Coiflet 5 (coif5) wavelet transform is utilized to compute the approximation and detail coefficients.These wavelet coefficients computed gives the EMG signal's representation in time and frequency domain simultaneously.

Now, from the computed detail coefficients of the EMG signals, the coefficient which highly in resemblance with its original signal is selected. From the results, it will be shown that this coefficient is the D_4 coefficient. And in the Fig. 5, it can be observed that D_4 coefficient resembles its original signal.

C. Features Extraction

Now, features are extractedfor the EMG signals. As from the wavelet transform of the EMG signal, D_4 coefficient is already computed and it contains the maximum information of the original signal. Hence, D_4 coefficient is utilized to extract the features for the EMG signals and that areenergy, mean and standard deviation [13]. These feature are briefly discussed:

(a) Mean of the absolute values of the D_4 coefficient in each sub-band.

$$Mean = \frac{\sum_q y_q}{q} = \mu \qquad (4)$$

(b) Energy of the wavelet coefficient 4 in each sub-band.Energy of the sub-signal $y_{qv}(\tau)$ is calculated by

$$Energy = \sum_q \sum_k \left| D_k^q \right|^2 \qquad (5)$$

(c) Standard deviation of the D_4 coefficient in each sub-band of the signal.

$$\text{Standard_Deviation} = \sqrt{\frac{\sum_q (y_q - \mu)^2}{q}} \qquad (6)$$

The features extracted as energy,mean and standard deviation are now exploited to train and test on the classifiers.

D. SVM

Now, the Classifiers are used which are trained using the computed features.In the previous sub-section that coiflet wavelet transform's D_4 coefficient of the EMG signals and features like energy,mean and standard deviation were collected. Here, the SVM model is trained using these features and then the same trained model is utilized to test for the classification of the EMG signals. Support Vector Machine is a classifier in which supervised learning technique is used whichincludes training is provided to the model and then samples are tested on that model. This technique providesmuch efficient results compared to theunsupervised learning based classifiers. This classifier is modest and informal to recognize. This is because it builds a hyperplane between the different classes which need to be classified using the classifier.In this, after plotting the samples in a space, a hyperplane is drawn according to the condition that margin between the support vectors and the hyperplane need to be maximized. It can be seen in [10].For this,the classifier used may be linear or non-linear. Samples which are able to classify only using a straight line are the linearly separable or linear SVM. But in practical situations, it is very difficult for a straight line hyperplaneto classify each and every sample. For such cases, non-linear classifier is used.In this, a non-linear operator maps the inputs to the classifier into a higher dimensional space so that samples can be classified easily.

If a linear function is given by the equation

$$h(y) = cy + d \qquad (7)$$

Then its dimensionality can be increased by using the equation as

$$h(y) = c.\psi(y) + d \qquad (8)$$

In (8), kernel functionis used to raise the dimensionality of the mapping. If the samples are not distinguishable in lower dimensional space, then kernel functions are used.

Though, the classification using SVM faces some complications in the complex applications which lowers its classification accuracy. It is also difficultto choose the kernel function parameters. So, for better classification results, SVM-kNN is used.

E. SVM-KNN

SVM-kNN is a hybrid classifier. It is the hybrid of Support Vector Machine and k-Nearest Neighbour classifiers. In the previous section studies, it was observed that SVM is a 1NN classifier [10] because SVM utilizes only a single representative point for each classaccording to the nearest neighbour approach. Nevertheless in the combination of the SVM andkNN, more than one vector points are preferred from the sample points. Say k-points are chosen and hence, the class is decided for the tested samples.

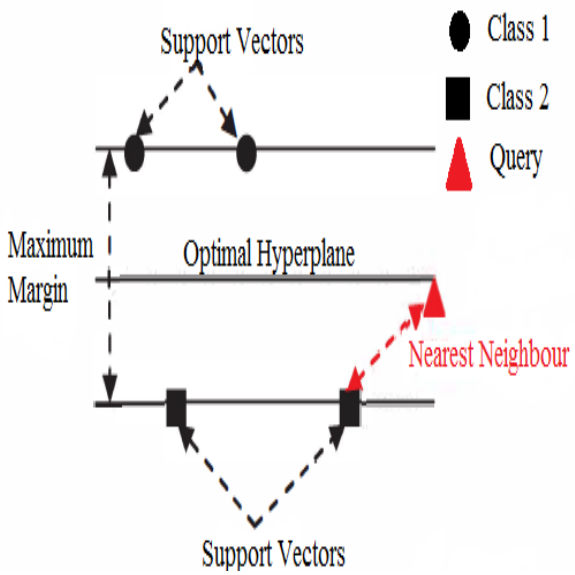


FIG.5. SVM-KNN CLASSIFICATION

IJARCCE
ISSN (Online) 2278-1021
ISSN (Print) 2319 5940
International Journal of Advanced Research in Computer and Communication Engineering
Vol. 5, Issue 6, June 2016

In the Fig.5 it can be observed that this hybrid algorithm of SVM-KNNconsiders more than one support vectors as the representative vector points for a class. This is a much better classifier than the SVM as in that only sample pointthat is present nearest to the hyperplane represents the support vector. In SVM-kNN, all support vectors are considered as representative vector points for the class and hence, maximum of information of a class is utilized in the classification process.During thismodel approach of the signals, nearest neighbour (that is, support vector) is computed as the query point using k-nearest neighbour algorithm. In the next sub-section, DSmT is explained.

F. DSMT

For the classification purpose, more than two classes classification problem is formulated as a m-class problem in which classes are associated to pattern classes such as ψ_0, ψ_2,ψ_3……., ψ_m.In this, parallel combination of two classifiers, which will be treated as the information sources, are formulated through Dezert-Smarandache Theory (DSmT) using the PCR6 combination rule.

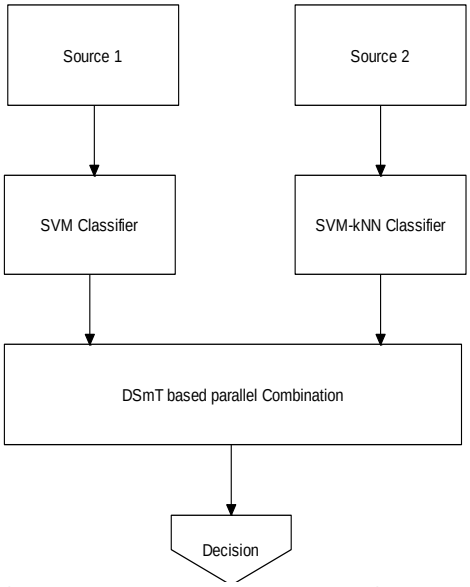


FIG.6. STRUCTURE OF THE COMBINATION SCHEME USING DSMT

DSMT is a fusion process of which allows to combine independent sources of information which are formulated as the belief functions. It is able to solve complex and multi-class problems with efficient results.

IV. EXPERIMENTAL VIEW

EMG Dataset:MIT-BIH Database is loaded as the Data set of EMG signals. It is shown in the tableshown in Table II.

TABLE II
DESCRIPTION OF DATASET USED

EMG Signals	Training	Testing	Total
Normal	350	150	500
Myopathy	350	150	500
Neuropathy	350	150	500

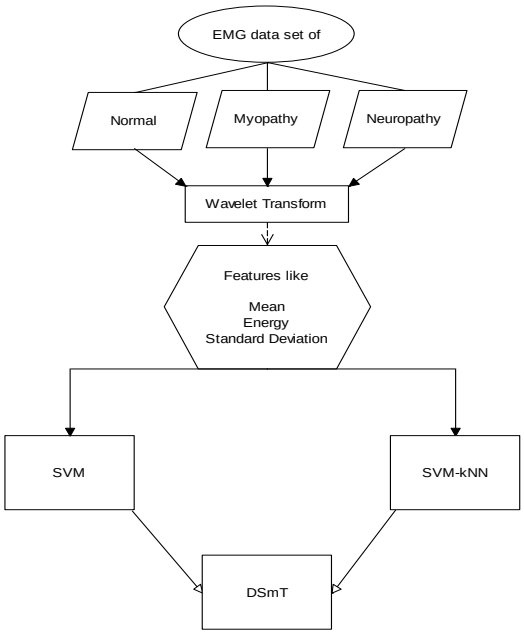


FIG.7. BLOCK DIAGRAM OF EMG SIGNALS CLASSIFICATION

Computing the wavelet transform and their features:Discrete wavelet transform (DWT) of the EMG signals are computed using the coiflet wavelet transform of the order of 5. Then, Features such as Energy, Mean and Standard Deviation for the D_4 coefficient are computed for each and every sample of data set of the different types of EMG signals used during the research. These calculated features in the form of energy, mean and standard deviation serve as an input to train and test the various classifiers.

Classification: During the classification, computed features of the EMG signals in the second stage are exploited by the classifiers like SVM, SVM-kNNand DSmTto determine the corresponding class of the samples. This feature set consists of mean, energy and standard deviation of the D_4 coefficient of the coiflet wavelet transform that should efficiently characterize the variations in the input signals for accurate detection and classification of the EMG signals. The calculated features will be applied to the classifiers like SVM, SVM-kNN and DSmT classifiers as training and testing data to classify the EMG signals in their corresponding classes.

V. RESULTS

In this study, SVM, SVM-kNNand DSmTclassifiers are used for the classification of the different types of EMG (Normal, Myopathy and Neuropathy)signals. As the features required to train the classifiers, D4 coefficient of the coiflet wavelettransform is used. Then, as the features, energy, mean and standard deviation is used.

Now, data set utilized for this research is shown in the Table II. Firstly, onthis data set of the EMG signals, wavelet transform is applied. Coiflet family of order 5 is used in the wavelet transform. The results for the wavelet transform of each type of data set used is represented in the figures 8, 9 and 10.

Copyright to IJARCCE
DOI 10.17148/IJARCCE.2016.5655

IJARCCE

ISSN (Online) 2278-1021
ISSN (Print) 2319 5940

International Journal of Advanced Research in Computer and Communication Engineering
Vol. 5, Issue 6, June 2016

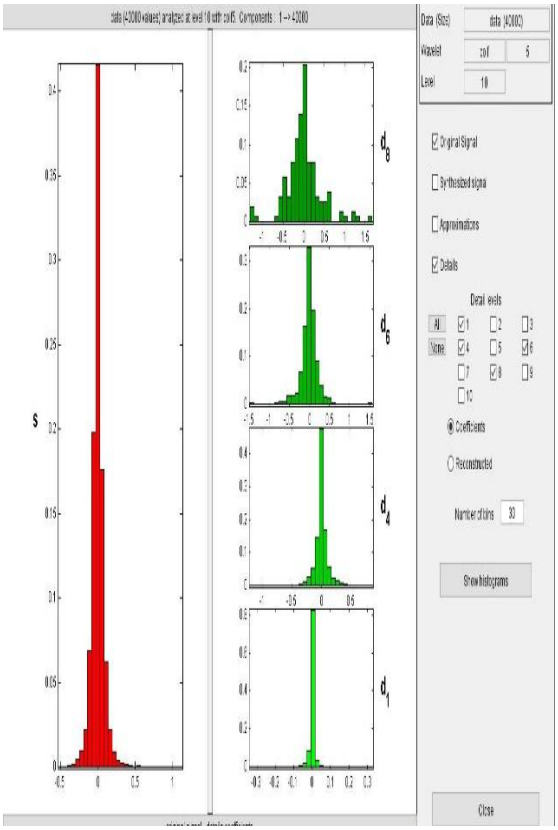


FIG.8. HISTOGRAM OF WAVELET TRANSFORM OF NORMAL PERSON EMG

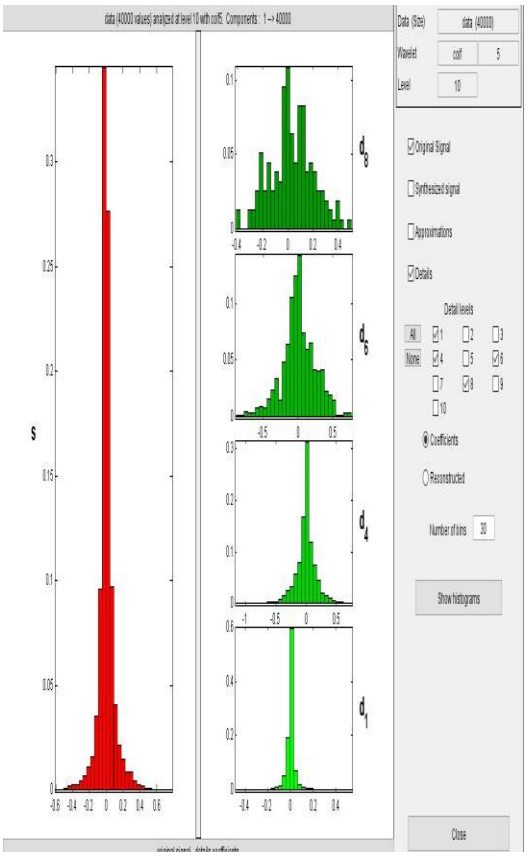


FIG.9. HISTOGRAM OF WAVELET TRANSFORM OF MYOPATHY PERSON EMG

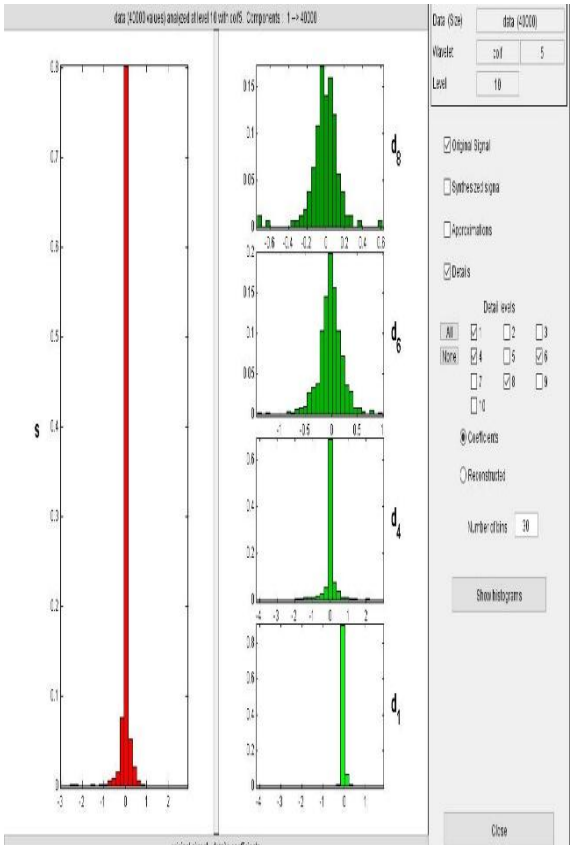


FIG 10. HISTOGRAM OF WAVELET TRANSFORM OF MYOPATHY PERSON EMG

In these figures, wavelet transformof the EMG signals is represented in the form of histograms. And it can be seen from the figures that histogram of D_4 coefficient greatly resembles its original signal's histogram. This implies D4 coefficient is sufficient to give the maximum features alone. Therefore, energy, mean and standard deviation is computed for D_4 coefficient only. Sample values for these features are shown in the Table III.

TABLE III
SAMPLE VALUES OF FEATURES FOR EMG SIGNALS

EMG Signal	Mean	Energy	Standard Deviation
Normal	6.85	46.55	2.173
Myopathy	4.97	24.49	0.574
Neuropathy	8.85	75.35	5.546

Table III shows the sample values for the EMG signals as the features computed (like energy, mean and standard deviation) for the D_4 coefficients of the coiflet of order 5. These features are computed for each and every sample of data set for the thre types of EMG signals exploited.
Hence, from these EMG features computed, features of 1050 samples (Normal-350, Myopathy-350 and Neuropathy-350)are chosenfrom each class and utilized to train the SVM. After that, remaining 450 samples (Normal-150, Myopathy-150 and Neuropathy-150) are tested on the same trained SVM. Its classification results are shown in the Table IV in the form of a confusion matrix.

Copyright to IJARCCE

TABLE IV
CONFUSION MATRIX OF SVM CLASSIFICATION

Targets → / Outputs ↓	Normal	Myopathy	Neuropathy	Accuracy
Normal	141/150	3/150	6/150	94%
Myopathy	11/150	134/150	5/150	89.33%
Neuropathy	7/150	4/150	139/150	92.67%

The confusion matrix shown in the Table IV shows a good result in terms of classifying the EMG signals into their respective classes. SVM gives 92% of accuracy in classifying these signals. This is quite good but SVM-kNNis utilized further to increase this percent of accuracy in classification of EMG signals.

Next, SVM-kNN classifier is used for the EMG signals classification. In this also, features of 1050 samples (Normal-350, Myopathy-350 and Neuropathy-350) are utilized to train the SVM-kNN. Then, the remaining samples are used to test on the same trained SVM-kNN.

TABLE V
CONFUSION MATRIX OF SVM-KNN CLASSIFICATION

Targets → / Outputs ↓	Normal	Myopathy	Neuropathy	Accuracy
Normal	147/150	2/150	1/150	98%
Myopathy	8/150	137/150	5/150	91.33%
Neuropathy	3/150	5/150	142/150	94.67%

And, this can be observed from the Table V that increase in the accuracy of classification is observed. Table V shows the confusion matrix of SVM-kNN classification and from this classifier an accuracy of approximately 95% is observed.

However, these results are improved using a technique known as DSmT technique. This technique utilizes features of both the classifiers used i.e. SVM and SVM-kNN. And, raise the accuracy of classifying the EMG signals.

TABLE VI
CONFUSION MATRIX OF DSMT BASED CLASSIFICATION

Targets → / Outputs ↓	Normal	Myopathy	Neuropathy	Accuracy
Normal	148/150	2/150	0/150	98.67%
Myopathy	3/150	144/150	4/150	96%
Neuropathy	2/150	3/150	146/150	97.33%

Here also, it can be clearly seen in the confusion matrix shown in the Table VI that an accuracy of 97.33% is reached using the DSmT in this classification compared to the other classifiers results.

VI. CONCLUSION

It can be conclude from the research that themethodpresented is a novel and very efficient method for the classification of the three different types of EMG signals (i.e. Normal, Myopathy and Neuropathy) using theDSmT based classifier.In this method, the extraction of features like energy, mean and standard deviation is done for the coiflet family of wavelet transform of the order of 5 for the EMG signals. Results achieved from the classification showsan alternative approach, which when compared to the other methods, for extracting relevant features and classification for EMG signals shows results with higher accuracy.

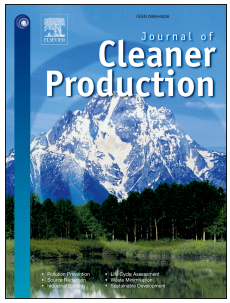
Classification results with accuracy of 97.33% with only a small number of features is only possible because of the use of DSmT based technique.Therefore, now,it can be concluded thatthe costly tests of diagnosing the EMG diseasescan beswitched by this automatic technique of classifying EMG signals.

REFERENCES

1. PreetiMeena, Malti Bansal, "Classification of EMG Signals using SVM-kNN", Int Journal of Advanced Research in Electronics and Communication Engineering", vol. 5, issue 6, pp. 1718-1724, 2016.
2. Subasi, A., "Classification of EMG signals using combined features and soft computing techniques," Applied Soft Computing, vol. 12, pp 2188- 2198, 2012.
3. Kaur, G. Shatru-Aurora, A., Kumar-Jain, Vijendra., "EMG Diagnosis via AR Modeling and Binary Support Vector Machine Classification," Int Journal Of Eng. Science and Tech., vol. 2, pp. 1767-1772. 2010
4. C.S. Pattichis, A.G. Elia, Autoregressive cepstral analyses of motor unit action potentials, Medical Engineering & Physics 21 (1999) 405–419.
5. Subasi, A., "Classification of EMG signals using PSO optimized SVM for diagnosis of neuromuscular disorders," Computers in Biology and Medicine, vol. 43, pp 576-586, 2013.
6. Khushaba RN, Al-Jumaily A, Al-Ani, "A. Novel feature extraction method based on fuzzy entropy and wavelet packet transform for myoelectric Control," 2007 IntSympCommunInf Technol., pp. 352– 357, 2007.
7. Y. Becerikli, On three intelligent systems: dynamic neural, fuzzy and wavelet networks for training trajectory, Neural Computing & Applications 13 (4) (2004) 339–351.
8. C.A. Pena-Reyes, M. Siper, A fuzzy-genetic approach to breast cancer diagnosis, Artificial Intelligence in Medicine 17 (1999) 131–155.
9. S.E. Hussein, M.H. Granat, Intention detection using a neuro-fuzzy EMG classifier, IEEE Engineering in Medicine and Biology November/December (2002) 123–129.
10. Subasi, A., "Classification of EMG signals using PSO optimized SVM for diagnosis of neuromuscular disorders," Computers in Biology and Medicine, vol. 43, pp 576-586, 2013.
11. C. Parameswariah, S. Member, M. Cox, and S. Member, "Frequency Characteristics of Wavelets," vol. 17, no. 3, pp. 800–804, 2002
12. Sepulveda-Cano LM, Acosta-Medina CD, Castellanos-Dominguez G "Relevance Analysis of Stochastic Biosignals for Identification of Pathologies," 2011 EURASIP J. Adv. Sig. Proc. 2011.
13. Phinyomark, a. Quaine, F., Charbonnier, S., Serviere, C., Tarpin-Bernard, F., Laurillau, Y., "EMG feature evaluation for improving myoelectric pattern recognition robustness", Expert systems with applications, vol. 40, pp. 4832-4840, 2013.
14. Nassim Abbas et. al., "The effective use of the DSmT for multi-class classification", Proceedings of the 5th International Symposium on Signal Processing, 2012.

DOI 10.17148/IJARCCE.2016.5655

Accepted Manuscript



Disposition decisions in reverse logistics: Graph theory and matrix approach

Saurabh Agrawal, Rajesh K. Singh, Qasim Murtaza

PII: S0959-6526(16)30933-7

DOI: 10.1016/j.jclepro.2016.07.045

Reference: JCLP 7617

To appear in: *Journal of Cleaner Production*

Received Date: 2 November 2015

Revised Date: 27 June 2016

Accepted Date: 7 July 2016

Please cite this article as: Agrawal S, Singh RK, Murtaza Q, Disposition decisions in reverse logistics: Graph theory and matrix approach, *Journal of Cleaner Production* (2016), doi: 10.1016/j.jclepro.2016.07.045.

This is a PDF file of an unedited manuscript that has been accepted for publication. As a service to our customers we are providing this early version of the manuscript. The manuscript will undergo copyediting, typesetting, and review of the resulting proof before it is published in its final form. Please note that during the production process errors may be discovered which could affect the content, and all legal disclaimers that apply to the journal pertain.

ACCEPTED MANUSCRIPT

Disposition Decisions in Reverse Logistics: Graph Theory and Matrix Approach

Author Details

Author 1 Name: **Saurabh Agrawal**

Department: **Mechanical, Production & Industrial Engineering Department**

University/Institution: **Delhi Technological University**

Town/City: **Delhi**

Country: **India-110042**

Email: agrawals.iit@gmail.com

Author 2 Name: **Dr. Rajesh K Singh**

Department: **Operations Management**

University/Institution: **Management Development Institute**

Town/City: **Gurgaon**

Country: **India-122 007**

Email: rksdce@yahoo.com

Author 3 Name: **Dr. Qasim Murtaza**

Department: **Mechanical, Production & Industrial Engineering Department**

University/Institution: **Delhi Technological University**

Town/City: **Delhi**

Country: **India-110042**

Email: qasimmurtaza@gmail.com

Corresponding author: Saurabh Agrawal

Corresponding Author's Email: agrawals.iit@gmail.com

ACCEPTED MANUSCRIPT

ACCEPTED MANUSCRIPT

Disposition Decisions in Reverse Logistics: Graph Theory and Matrix Approach

Abstract

Reverse logistics has become an essential part of business because of legislation, environmental concerns, and corporate social responsibility. Reverse logistics activities involve the collection of returned products, inspection and sorting out into different categories, and disposition them for reuse, repair, remanufacturing or recycling. One of the important decisions is to disposition returned products appropriately for the success of reverse logistics. Disposition decision plays an important role in the performance of reverse logistics. Perusal of previous literature indicates that there are very few studies related to disposition of returned products in reverse logistics. This paper attempts to explore the various disposition alternatives and develop an approach for the selection of best disposition alternative using graph theory and matrix approach. A case of mobile manufacturing firm is discussed for the illustration of this approach. The firm has to select best disposition alternative among four identified alternatives such as returned products for repair or reuse and resell as new; or repair or refurbish and resell; or re-manufacture and sell; or recycle. Different disposition attributes are identified based on literature review and experts opinion. Graph theory and matrix approach has been applied to select the best alternative. Permanent function value, referred as "Disposition Index" was evaluated for each alternative with the help of C++ program and alternatives were prioritized based on these values. The results show that firm must repair or reuse and resell the returned mobile phones as new in present business scenario in India. In addition, recycling must be preferred over remanufacturing of returned mobile phones. The study prioritized alternatives for disposition of returned products in reverse logistics appropriately. The findings of the study will provide useful insight to the supply chain managers and researchers for disposition decision-making in reverse logistics.

ACCEPTED MANUSCRIPT

ACCEPTED MANUSCRIPT

Keywords: Disposition; Supply Chain Management; Reverse Logistics; Graph Theory; Logistics

1. Introduction

In last few years, firms are offering more consumer friendly and relaxed consumer return policies because of business competitiveness and advent of e-commerce business. Managing product returns in supply chain is becoming more important for the success of business with the increased volume of returned products (Guide Jr et al., 2006). Product returns may be commercial returns, service returns, distribution returns or end of life returns. The customer may return the products because of many known or unknown reasons including defects, damage, or customer dissatisfaction (Barsky and Ellinger, 2001). Products are also returned because of liberal returns policies and allowances offered by the firms as a part of business strategy for better customer satisfaction (Reda, 1998). Some firms are also forced to deal with product returns because of environmental regulations in many countries requiring remanufacturing or recycling of used products (Guide and Wassenhove, 2002). According to Govindan and Popiuc (2014), these returns can generate new profits in business. However, very few firms realized higher margins on remanufactured products in comparison to the new products (Stock et al., 2002). Still, product returns are eminent in a competitive business environment, and firms need to manage them efficiently. One of the ways of dealing with these product returns is to adopt and implement reverse logistics programs. Reverse logistics can manage both bad and good product returns effectively and it can make significant contributions to the sustainability efforts of an organization (Narayana et al., 2014).

Reverse logistics activities involve all functions that start with the collection of returned products through their acquisition and end with the extraction of all possible value from those products. The customer, returning the products may expect a credit or replacement

ACCEPTED MANUSCRIPT

as quickly as possible while reverse logistics may be more interested in disposition of these returned products to recapture the maximum value (Hall et al., 2013). Therefore, it is important to disposition products effectively for maximum recapturing value along with customer satisfaction. According to Attia (2015), returned product disposition strategies are positively correlated with the reverse logistics performance and hence, with the performance of an organization. For disposition of returned products, various disposition alternatives are available to the manufacturers. The disposition alternatives include simply reusing the product, or repair or remanufacture or recycle the products or properly dispose them (Thierry et al., 1995; Blackburn et al., 2004; Carter and Ellram, 1998; Krikke et al., 2003). Disposition alternatives are often industry or product-specific and depend upon characteristics of the product such as price / value, transportation cost, shelf life of the product, and market demand patterns (Skinner et al., 2008). Recently, in a literature review, Agrawal et al. (2015) observed that there are very few studies focusing on the disposition decisions in reverse logistics. It is also evident from the recent comprehensive review of reverse logistics articles by Govindan et al. (2015). The objective of the proposed study is to develop an approach for the selection of best disposition alternative. Since, Graph Theory and Matrix Approach (GTMA) maintain the hierarchical structure and at the same time utilize interdependencies among attributes; this approach is well suited for the proposed study. A case of mobile manufacturing firm is discussed for the illustration of the approach. The disposition attributes were identified based on past literature review and discussion with the experts, and "Disposition Index" was determined for the various disposition alternatives. "Disposition Index" is the value of permanent function obtained through GTMA in such a way that higher the disposition index, better is the disposition alternative. The disposition index values of various disposition alternatives were compared and best disposition alternative was selected.

ACCEPTED MANUSCRIPT

The remainder of the paper is organized as follows: Section 2 consists of literature review of reverse logistics, disposition alternatives, and previous approaches utilized for the selection of best disposition alternative. In section 3, GTMA along with development of step by step approach are discussed for the determination of disposition index. Subsequently, the proposed approach is validated through a case illustration of a mobile manufacturing firm in section 4, and results are discussed in this section. Finally, section 5 summarizes all the findings and concludes the study along with future scope of research.

2. Literature Review

According to Rogers and Tibben (1999), reverse logistics is defined "*as the process of planning, implementing, and controlling the efficient, cost effective flow of raw materials, in process inventory, finished goods and related information from the point of consumption to the point of origin for the purpose of recapturing value or proper disposal"*. Srivastava (2008) clarified reverse logistics as the process of planning, implementing and controlling the efficient, effective inbound flow, inspection, and disposition of returned products and related information for recovering value. Products after acquisition are supposed to be collected and delivered to the facilities for inspection, sorting, and disposition. Rogers and Tibben-Lembke (1999) observed that the customer may return the products because of many known or unknown reasons and the condition of returned products may differ greatly. Therefore, a separate inspection of each item is required for sorting the products. Its overall appearance and state of the constituting elements need to be evaluated. Products and components are sorted into the different categories based on such evaluations (De Brito and Dekker, 2002). Once products are sorted out into different categories, diagnostic tests are performed to determine that what action may recover the most possible value from the returned products, and products are disposition accordingly. Khor and Udin (2012) examined the impact of

ACCEPTED MANUSCRIPT

disposition decision on the economic and environmental performance of the organizations. They collected the data through survey of electronics industry in Malaysia and found that disposition decisions significantly influence the performances of the organizations. Thierry et al. (1995) illustrated three disposition alternatives as product reuse, product recovery, and waste management. Krikke et al. (2003), and Tibben-Lembke and Rogers (2002) further modified these alternatives as reuse, product upgrade, material recovery and waste management. Norek (2003) stated that firms mostly have five recovery alternatives including sell as new; repair or repackage and resell as new; repair or repackage and resell as used; resell at a lower value to a salvage house; and sell by the weight to a salvage house. Previous studies discussed about number of alternatives available for the disposition of returned products. Each study emphasized slightly different alternatives and definitions of disposition. Five common disposition alternatives, which are frequently discussed in the past literature are direct reuse; repair; remanufacture; recycle; and disposal (Fleischmann et al., 1997; Thierry et al., 1995; De Brtio and Dekker, 2002; Hazen, 2011; Agrawal et al., 2014; Govindan and Soleimani, 2016). These disposition alternatives are explained as follows.

(i) Reuse

When a customer returns the new product as it is, product is reinserted back into the supply chain. Reuse of returned product requires only minor inspection, cleaning and minor maintenance; and products are generally returned back to the forward logistics chain for redistribution (Fleischmann et al., 2000). This process includes unused product, packaging, bottling etc. If product requires any upgrade then it may go for other alternatives.

ACCEPTED MANUSCRIPT

(ii) Repairing

If a product cannot be directly reused then the next alternative is repairing. It is concerned with repairing and servicing of products and retuning those products to the customers (Krikke et al., 2004).

(iii) Remanufacturing

It is generally concerned with product / module / component recovery from high value products (Blackburn et al., 2004). In most of the cases, the manufacturers carry out remanufacturing because they know the product better. Uncertainty in terms of quality, quantity and timing of product returns are important factor for the success of remanufacturing (Rogers and Tibben-Lembke, 1999).

(iv) Recycling

It is generally concerned with the material recovery from rather low value product / module / component (Blackburn et al., 2004). If a product, module or component cannot be reused in any form then there is alternative of extracting material through recycling and use of it as raw material. In many cases, investment cost is high due to requirement of advanced technological equipment for recycling. Low recovery value and high investments require higher processing volume to make it economically viable (Fleischmann et al., 2000).

(v) Disposal

In case, a product cannot be reused, repaired, remanufactured, or recycled then the last alternative is disposal of those products. There are two alternatives either incineration or disposal to landfill. Landfill is not preferred because of regulatory restrictions in many countries.

Secondary market is also considered as one of the alternatives for returned product disposition. For some firms, selling through the secondary market such as a factory outlet store, owned and operated by the manufacturer can be more profitable than their sell through

ACCEPTED MANUSCRIPT

distributors or retailers (Rogers and Tibben-Lembke 1999). Louwers et al. (1999) considered the disposition of old carpets into secondary market for recycling and reusing. Abraham (2011) explored the reverse logistics systems of the apparel aftermarket in India and discussed about the exchange of old cloths with utensils in secondary market. Matar et al. (2014) developed a cost based model for plastic beverage bottles considering secondary market. Huang et al. (2014) developed a generic model for retailers' inventory decision considering secondary market to salvage the returns and the leftovers from the initial sales. Alumur et al. (2012) developed a model for washing machines and observed that there is more profit in selling remanufactured products to the secondary market. Secondary market can play an important role in the success of reverse logistics if explored properly. However, selling through secondary markets can be more complicated than marketing new product. Suppliers are often concerned about brand equity, and may not prefer to enter into the secondary market (Rogers et al., 2012).

Selection of the disposition alternative depends on the number of attributes. Most of the earlier attributes for the selection of disposition alternatives were based on the operational requirements. Later on authors started considering disposition as strategic issues. Tan and Kumar (2006) developed a system dynamics model for disposition of products for remanufacturing or refurbishing. They found that part replacements from suppliers are more profitable than refurbished computer parts. Skinner et al. (2008) empirically examined the different disposition strategies and found that “if adequate resource support for reverse logistics is not available then choose to destroy the product because other disposition alternatives like recycling or remanufacturing require significant resources for recapturing value”. Gobbi (2011) considered product recovery value and found that low product recovery value is associated with recycling and energy recovery, and high product recovery value is associated with reprocessing and reuse. When the recovery alternative is recycling, time is

ACCEPTED MANUSCRIPT

not relevant; the primary objective is cost reduction. When the recovery alternative is reprocessing, time is primarily relevant, trade-offs between cost and time efficiency are necessary. Guide et al. (2008) developed a model for the optimal disposition of returned product considering the time value of the return, the condition of the product, and the congestion effect at the remanufacturing facility. This model is helpful in extracting value from product return processes. Hazen (2011) identified seven reverse logistics components of disposition decision by utilizing a problem-driven content analysis methodology. This study considers disposition strategies ranging from corporate strategy to business level strategy along with external factors for disposition decision-making. Karamouzian et al. (2014) worked on queuing theory based optimal disposition decision model. It utilized an acquisition policy by grading the return products. The objective of the study was to maximize the product recovery value. Wadhwa et al. (2009) developed fuzzy-set theory based flexible decision model for the selection of best alternative. Dehghanbaghi et al. (2016) also developed a fuzzy rule-based decision-making approach using fuzzy AHP for ranking the recovery / disposal strategies for brown products. Senthil et al. (2012) proposed a hybrid methodology model, based on AHP and TOPSIS under fuzzy environment for the selection and evaluation of alternatives including manufacturer's operation, third party operation or joint operation. These studies provide a great insight of the disposition issues in the reverse logistics.

3. Research Methodology

Selection of the disposition alternative depends on the number of attributes and available alternatives for the disposition of returned products. Various multi criteria approaches like TOPSIS, AHP, ANP, and DEA are available for providing solutions to such type of problems. TOPSIS and AHP are applied if the attributes are independent (Rao and Padmanabhan, 2006), which is not the case of proposed problem. While ANP does not

ACCEPTED MANUSCRIPT

represent hierarchical relationship among attributes, DEA requires more computation and if the number of attributes are large, then DEA may be a poor discriminator of good and poor performers (Rao and Padmanabhan, 2006). Graph Theory and Matrix Approach (GTMA) does not have such limitations.

GTMA is a systematic and logical decision making approach. Matrix approach is useful in analyzing the directional graphs particularly when numbers of nodes are large and graphs become complex to visualize. There are many software tools available for computing and analyzing matrices easily. GTMA enables a more critical analysis and there is no restriction on number of attributes for the analysis. The permanent concept fully characterizes the considered selection problem, as it contains all possible structural components of the attributes and their relative importance. In permanent function, even a small variation in attributes leads to a significant difference in the disposition index, and it is easy to rank the alternatives in the descending order with clear-cut difference in the selection index. Further, the measures of the attributes and their relative importance are used together to rank the alternatives which provides a better evaluation of the alternatives. Because of all these advantages discussed above, the proposed study has applied GTMA for the selection of disposition alternative. In past, researchers have utilized the advanced theory of graphs for modeling and analysis of various systems, and proved beneficial for solving real life problems in the field of science and technology (Chen, 1997; Jense and Gutin, 2000). Rao (2006) used this approach for the material selection by determining material suitability index. Kulkarni (2005) utilized GTMA for the evaluation of total quality management performance of an industry. Darvish et al. (2009) applied the approach for contractor ranking in construction industry. Muduli et al. (2013) identified and ranked the barriers to green supply chain in Indian mining industry. Faisal (2012) utilized this approach to quantify supply chain sustainability for small and medium scale industry. Sabharwal and Garg (2013) used this

ACCEPTED MANUSCRIPT

approach for determining minimum and maximum cost effectiveness index for remanufacturing. This index is helpful in deciding the disposition of returned products for remanufacturing. Rao and Padmanabhan (2010) proposed end of life scenario (EOL) index for end of life products and applied GTMA for the selection of best product EOL scenario based on this index. They used permanent function value for the calculation of EOL scenario index and compared these indexes for the selection of best alternative. Similarly, Gupta and Singh (2015) evaluated supply chain management environment index by using this approach. Agrawal et al. (2016) utilized GTMA along with sustainable balanced scorecard for the outsourcing decisions in reverse logistics.

In GTMA, nodes and edges are two basic elements, which represent the inter-relationship between nodes (different attributes) in the form of directional graph (also known as digraph) and in the form of matrix. These nodes represent the attributes. Attribute is defined as a factor that influences the disposition decision for a given product. Once the attributes are decided, a diagraph showing these attributes and their interdependence is prepared. Numbers of nodes (M) in the diagraph are equal to the number of attributes considered for the study, and arrow or directed edge connecting two nodes represents their relative importance. A systematic approach, based on the approach discussed by Rao and Padmanabhan (2006) is developed for the study.

The digraph consists of a set of nodes $N = \{n_i\}\ where\ i = 1,2,3 \dots \dots M$ and a set of directed edge $E = \{a_{ij}\}$. A node n_i represents an i^{th} attribute for the selection of disposition alternative and edges represent the relative importance of these attributes. For example, if the attribute "i" is more important than the attribute "j" while comparing two attributes for their relative importance, then arrow or edge is directed from node "i" to node "j". The value of importance is represented by a_{ij}. If the attribute "j" is more important than the attribute "i" , then arrow or edge is directed from node "j" to node "i". The value of importance is

represented by a_{ji}. The digraph, graphical representation of the attributes makes it helpful in visualizing the relative importance of attributes easily and quickly. However, as number of attributes (nodes) increases, it becomes complicated and difficult to analyze the digraph visually. In such cases, the digraph is transformed into the form of a matrix.

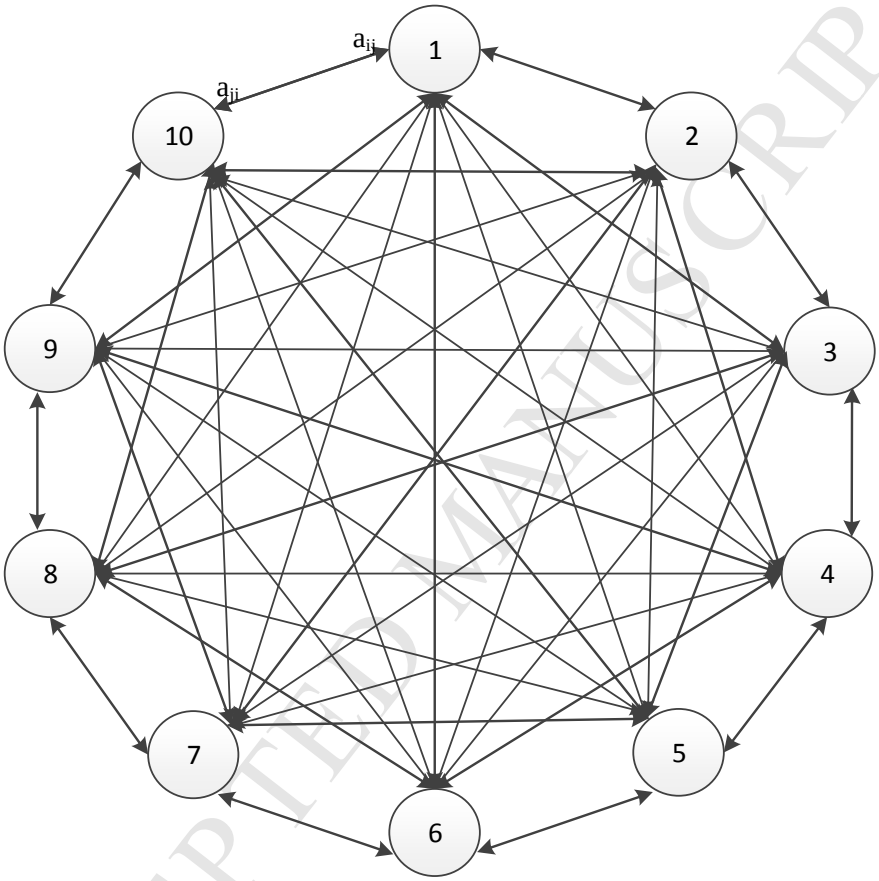


Figure 1. Digraph of inter-relationship among disposition attributes

Diagraph is transformed into a square matrix, called relative importance matrix in which the off-diagonal elements represent the relative importance of one attribute over other. The diagonal elements represent the importance of the attributes for a particular disposition alternative. Since diagraph or matrix may change with change in number of attributes, a standard form of matrix function, known as permanent function is computed rather than the determinant of the matrix. In case of determinant function of a matrix, some information

may be lost due to the presence of negative signs. Therefore, researchers preferred to use the permanent function of a matrix in order to provide the complete information without any loss (Rao and Gandhi, 2001, 2002, Rao and Padmanabhan, 2006). The study selected ten attributes for the selection of disposition alternative. The attributes, selected for the proposed study (discussed later in section 4) are Customer behavior (CBH), Market conditions, (MCD), Existing regulation, (EXR), Environmental impact (EVI), Supply chain capabilities (SCC), Product Value (PRV), Processing Cost (PRC), No. of Returned Products (NRP), Quality of Returned Products (QRP), and Recapturing Value (RCV). Digraph for the 10 number of attributes is shown in figure 1. It is difficult to represent them on a digraph so a matrix, $[A]$ is prepared as shown below. It is an M x M matrix for 10 number of attributes which consists of diagonal elements, represented as D_{ij} , $where\ i = j$ and off-diagonal elements represented as a_{ij} , $where\ i \neq j$. The off-diagonal elements indicate the relative importance of attributes; these values are same for all the alternatives or disposition alternatives. The diagonal elements indicate the importance of each attribute for a given alternative, and these values may be different for each disposition alternative.

[*A*]=

	CBH	MCD	EXR	EVI	SCC	PRV	PRC	NRP	ORP	RCV
CBH	D_1	a_{12}	a_{13}	a_{14}	a_{15}	a_{16}	a_{17}	a_{18}	a_{19}	a_{110}
MCD	a_{21}	D_2	a_{23}	a_{24}	a_{25}	a_{26}	a_{27}	a_{28}	a_{29}	a_{210}
EXR	a_{31}	a_{32}	D_3	a_{34}	a_{35}	a_{36}	a_{37}	a_{38}	a_{39}	a_{310}
EVI	a_{41}	a_{42}	a_{43}	D_4	a_{45}	a_{46}	a_{47}	a_{48}	a_{49}	a_{410}
SCC	a_{51}	a_{52}	a_{53}	a_{54}	D_5	a_{56}	a_{57}	a_{58}	a_{59}	a_{510}
PRV	a_{61}	a_{62}	a_{63}	a_{64}	a_{65}	D_6	a_{67}	a_{68}	a_{69}	a_{610}
PRC	a_{71}	a_{72}	a_{73}	a_{74}	a_{75}	a_{76}	D_7	a_{78}	a_{79}	a_{710}
NRP	a_{81}	a_{82}	a_{83}	a_{84}	a_{85}	a_{86}	a_{87}	D_8	a_{89}	a_{810}
QRP	a_{91}	a_{92}	a_{93}	a_{94}	a_{95}	a_{96}	a_{97}	a_{98}	D_9	a_{910}
RCV	a_{101}	a_{102}	a_{103}	a_{104}	a_{105}	a_{106}	a_{107}	a_{108}	a_{109}	D_{10}

The permanent function of this matrix is written as follows:

$$\textbf{per(A)} = \prod_{i=1}^{M} D_i + \sum_{i=1}^{M-1}\sum_{j=i+1}^{M} \dots\dots\dots \sum_{M=t+1}^{M}(a_{ij}a_{ji})D_kD_1D_mD_nD_o \dots\dots D_tD_M \quad \text{....M} \neq \text{pus}$$

$$+ \sum_{i=1}^{M-2}\sum_{j=i+1}^{M-1}\sum_{k=j+1}^{M} \dots\dots \sum_{M=t+1}^{M}(a_{ij}a_{jk}a_{ki} + a_{ik}a_{kj}a_{ji})D_1D_mD_nD_0 \dots\dots D_tD_M \quad \text{k....M} \neq \text{pus}$$

$$+ \sum_{i=1}^{M-3}\sum_{j=i+1}^{M}\sum_{k=i+2}^{M-1}\sum_{l=i+2}^{M} \dots\dots \sum_{M=t+1}^{M}(a_{ij}a_{ji})(a_{kl}a_{lk})D_mD_nD_o \dots\dots D_tD_M \quad \text{k,l ....M} \neq \text{pus}$$

$$+ \sum_{i=1}^{M-3}\sum_{j=i+1}^{M+1}\sum_{k=i+1}^{M}\sum_{l=i+1}^{M} \dots\dots\dots \sum_{M=t+1}^{M}(a_{ij}a_{jk}a_{kl}a_{li} + a_{il}a_{lk}a_{kj}a_{ji})D_mD_nD_o\dots\dots D_tD_M$$

$$\text{k,l ...M} \neq \text{pus}$$

$$+$$

$$\sum_{i=1}^{M-2}\sum_{j=i+1}^{M-1}\sum_{k=j+1}^{M}\sum_{l=1}^{M-1}\sum_{m=l+1}^{M} \dots\dots \sum_{M=t+1}^{M} (a_{ij}a_{jk}a_{ki} + a_{ik}a_{kj}a_{ji})\ (a_{lm}a_{ml})D_nD_o \dots D_tD_M$$

$$\text{k,l,m.....M} \neq \text{pus}$$

$$+$$

$$\sum_{i=1}^{M-4}\sum_{j=i+1}^{M-1}\sum_{k=i+1}^{M}\sum_{l=i+1}^{M}\sum_{m=j+1}^{M} \dots\dots \sum_{M=t+1}^{M}(a_{ij}a_{jk}a_{kl}a_{lm}a_{mi} +$$

$$a_{im}a_{ml}a_{lk}a_{kj}a_{ji})D_nD_o \dots D_tD_M$$

$$\text{k,l,m.....M} \neq \text{pus}$$

$$+ \sum_{i=1}^{M-5}\sum_{j=i+1}^{M-1}\sum_{k=j+1}^{M}\sum_{l=1}^{M-2}\sum_{m=l+1}^{M-1}\sum_{n=m+1}^{M} \dots \sum_{M=t+1}^{M}(a_{ij}a_{jk}a_{ki} + a_{ik}a_{kj}a_{ji})(a_{lm}\ a_{mn}a_{nl} +$$

$$a_{lm}a_{nm}a_{ml})D_o \dots\dots D_tD_M \quad \text{k,l,m,n.....M} \neq \text{pus}$$

$$+$$

$$\sum_{i=1}^{M-5}\sum_{j=i+1}^{M}\sum_{k=i+1}^{M-3}\sum_{l=i+2}^{M}\sum_{m=k+1}^{M-1}\sum_{n=k+2}^{M} \dots\dots \sum_{M=t+1}^{M}(a_{ij}a_{ji})(a_{kl}a_{lk})(a_{mn}a_{nm})D_o \dots\dots D_tD_M$$

$$\text{k,l,m,n.....M} \neq \text{pus}$$

$$+\sum_{i=1}^{M-5}\sum_{j=i+1}^{M-1}\sum_{k=i+1}^{M}\sum_{l=i+1}^{M}\sum_{m=i+1}^{M}\sum_{n=j+1}^{M} \dots\dots \sum_{M=t+1}^{M}(a_{ij}a_{jk}a_{kl}a_{lm}a_{mn}a_{in} +$$

$$a_{ni}a_{nm}a_{ml}a_{lk}a_{kj}a_{ji})D_o \dots\dots D_tD_M \quad \text{k,l,m,n.....M} \neq \text{pus}$$

In general, the permanent of an M×M matrix, [*A*] with attributes a_{ij} defined by Forbert and Marx (2003) as

$$Per\ (A) = \sum_{p}\prod_{i=1}^{N} a_i\ , P(i)$$

ACCEPTED MANUSCRIPT

Where, the sum is overall permutations P. In order to calculate the permanent function value, a computer program for M × M matrix was written in C++ language. The program takes few minutes to run the program and compute the value of permanent function. The logical flow diagram for writing program is attached in appendix (A1). The value of permanent function is referred as "Disposition Index" for the proposed study. A step by step approach for applying GTMA is enumerated as follows:

Step 1

Identify the disposition alternatives and attributes for the selection of best disposition alternatives.

Step 2

Find out the relative importance of disposition attributes on a suitable scale. The scale shown in table 1 is utilized for the proposed study. The values of off-diagonal elements of the matrix $[A]$ will be selected from this table.

Table 1. Scale for the relative importance of attributes

Description	aij	1-aij
Two attributes are equally important	0.5	0.5
One attribute (i) is slightly more important over the other (j)	0.6	0.4
One attribute (i) is strongly more important over the other (j)	0.7	0.3
One attribute (i) is very strongly important over the other (j)	0.8	0.2
One attribute (i) is extremely important over the other (j)	0.9	0.1
One attribute (i) is exceptionally more important over the other (j)	1	0

Step 3

Find out the importance of attributes for each disposition alternative on a suitable scale. The scale shown in table 2 is utilized for the proposed study. The values of diagonal elements for the respective alternative will be selected from this table.

ACCEPTED MANUSCRIPT

Table 2. Scale for the importance of attributes for each disposition alternative

Qualitative measure of attributes	Assigned Value of Dij
Exceptionally low	0.0
Extremely low	0.1
Very low	0.2
Low	0.3
Below average	0.4
Average	0.5
Above average	0.6
High	0.7
Very high	0.8
Extremely high	0.9
Exceptionally high	1.0

Step 4

Develop the matrix for the selection of disposition alternative. This is an M x M matrix represented as matrix [*A*]. The matrix must be developed by entering the value of off-diagonal elements, which are values of relative importance of attributes selected from the table 1. The value of diagonal elements of the matrix should be selected from the table 2 for each of alternatives. Thus, number of matrices will be equal to number of alternatives.

Step 5

Obtain the permanent function for each of the disposition alternatives by using the matrix [*A*].

Step 6

Determine the value of permanent function for each of the disposition alternatives by using the permanent function **per(A)** discussed above. It may be determined manually or may be determined by entering the values of diagonal and off-diagonal elements for each alternative

ACCEPTED MANUSCRIPT

in C++ program written for proposed problem. The value of permanent function may be determined by running the program on C++ compiler like turbo C++. After the determination of permanent function for each of the alternatives, the alternatives may be compared and the best alternative may be selected based on these values.

4. Case Illustration

ABC Limited is one of the leading consumer electronics firm headquartered in NCR, Delhi (Gurgaon), India. This firm has approximately 900 employees and generates USD 2.3b annual revenue in last financial year. The firm is the largest domestic mobile phone firm in low cost market segment. The firm is currently the 2nd largest mobile phone firm in India having 16% market share in smart phone market and 13 % market share in overall mobile phone segment. The firm has manufacturing plant in Rudraprayag, UttraKhand, India where it manufactures mobile phone devices. This firm procures some of the components and parts from china and assembles them at this facility. The firm has excellent supply chain network in India and sells approximately 2.3 million handsets monthly with the help of 125,000 retails outlet in 560 towns throughout India. Recently, the firm has started selling mobile phones in Russia also.

In order to apply proposed approach, possible disposition alternatives associated with mobile phone hand set for the ABC Ltd were identified. These alternatives are repair or reuse and resell as new; repair or refurbish and resell in secondary market; re-manufacture and sell in the secondary market; recycle; and disposal. The last alternative, disposal is not allowed because of regulatory restrictions by the Government of India. In addition, consumers have become more environmental conscious, want to ensure that products are disposition appropriately, and do not end up in landfills (Hazen et al., 2015). Therefore, it is not considered as possible disposition alternative for the study. The first alternative, repair or

ACCEPTED MANUSCRIPT

reuse and resell is concerned with those mobile phones which are returned directly to the firm rather than customer going to the retailer or service center for returning those products. These mobile phones are mostly sold through e-business or e-retailers and they are almost new because only minor repair or reuse is required or customer returns them because of their choice. The second alternative, repair or refurbish, and resell is concerned with mobile phones, which require major repair or refurbishment and they cannot be sold as new. The ABC Ltd may sell them in secondary market. The third alternative, re-manufacture and sell are concerned with remanufacturing of mobile phones through disassembly and use their parts and components. The fourth alternative is recycling of mobile phones. In order to assign the values of diagonal and off-diagonal elements, total eleven experts participated in the study. The experts were selected from the firm and from the electronics industry. The experts have an average experience of approximately 8 years in manufacturing, marketing, and finance department. In addition, one expert was selected from the academia involved in the area of reverse logistics. The experts are at the key responsible position in their respective organization, and their knowledge is assumed to be sufficient for the proposed study. In order to determine the disposition index for the selection of best disposition alternative, the steps of methodology discussed in section 3 were carried out as follows:

Step 1

First step involves the selection of attributes for the study. Based on the past literature review and discussion with the experts, disposition decision is dependent on the number of attributes such as Customer behavior (CBH), Market conditions, (MCD), Existing regulation, (EXR), Environmental impact (EVI), Supply chain capabilities (SCC), Product Value (PRV), Processing Cost (PRC), No. of Returned Products (NRP), Quality of Returned Products (QRP), and Recapturing Value (RCV). All these attributes for the selection of best disposition alternative are reviewed in table 4.

ACCEPTED MANUSCRIPT

Table 4. Attributes for the selection of best disposition alternative

Attribute	Authors	Description
Customer behavior (CBH)	Hazen et al. (2012), Jack et al. (2010), Amini et al. (2005), Inderfurth (2005), Kara and Onut (2010), Geyer et al. (2007), Vorasayan and Ryan (2006).	Customer behavior plays bigger role in reverse logistics as compared to the forward supply chain. Quality, quantity and timing of returned products are uncertain and difficult to predict and dependent on the customer behavior. In addition, the demand for remanufactured products or recycled material largely depends on customer behavior and plays an important role in disposition decision making.
Market conditions, (MCD)	Richey et al. (2005), Lambert et al. (2011), Franke et al. (2006)	It is considered from the competitive perspective. It is important to notice that what and how competitors are handling the returned products. Selling remanufactured products in the market may be utilized as green strategy at the same time it may affect the brand image of a product depending on the market conditions.
Existing regulation, (EXR)	Hazen et al. (2012), Subramanian et al. (2014)	Government rules and regulations, which may affect the disposition of returned products and may impose restrictions on some of the disposition decisions for example disposal of end of life products is not allowed in many countries.
Environmental impact (EVI)	Shih (2001), Dowlatshahi (2005), Wu and Dunn (1995), Hoek (1999)	It is defined as impact of reverse logistics on environment and its contribution to reduce negative impact on environment. Environmental impacts of reverse logistics has been considered in many studies.
Supply chain capabilities (SCC)	Hazen et al. (2012), Bell et al. (2013), Defee et al. (2009)	It is defined as a firm's supply chain capability to integrate reverse logistics into existing system and making resources available to the reverse logistics activities (Hazen, 2011).
Product Value (PRV)	Ferrer and Whybark (2000), Chunga and Weeb (2011), Sharma et al. (2016)	In general, rather low value product / module / components are recycled for material recovery (Blackburn et al., 2004). It may be expensive to remanufacture them and at the same time, customers may like to buy new product because of low value.
Processing Cost (PRC)	Jamal et al. (2004), Li et al. (2009), Kongar and Gupta (2001), Sabharwal and Garg (2013)	It is defined as cost involved in reuse / repair / remanufacture / recycle of returned products. It includes the transportation cost, operating cost, inventory cost, and recovery cost.
No. of Returned Products (NRP)	Savaskan et al. (2004), Rubio and Corominas (2008), Sabharwal and Garg (2013)	Numbers of returned products are highly uncertain and difficult to predict. Knowing numbers of returned products available for disposition at a particular point of time is very important for disposition decision-making.

ACCEPTED MANUSCRIPT

Quality of Returned Products (QRP)	Aras et al. (2004), Guide and Wassenhove (2001), Ardeshirilajimi and Azadivar (2015), Sabharwal and Garg (2013)	Quality of returned products is also important factor for disposition decision-making. A good quality returned product offers better value to the remanufacturer and a low quality may be a better candidate for recycling.
Recapturing Value (RCV)	Ravi et al. (2005), Gobbi (2011), Rogers and Tibben-Lemke (2001), Kumar and Saravanan (2014) , Madaan et al. (2015)	Recapturing value from used product may be the primary economic objective of most of reverse logistics system and greatly affects the disposition decisions in reverse logistics.

Based on the discussion with the experts, following four alternatives for disposition of returned products are considered for the study.

Disposition Alternative 1 **($ALT-1$):** Repair or reuse and resell as new;

Disposition Alternative 2 **($ALT-2$):** Repair or refurbish and resell;

Disposition Alternative 3 **($ALT-3$):** Re-manufacture and sell;

Disposition Alternative 4 **($ALT-4$):** Recycle

Step 2

Quantitative values of relative importance are assigned by comparing them on scale discussed in section 3. The group of experts was asked to select the values for the off-diagonal elements on the basis of scale shown in table 1. The responses were examined and highest mode value was selected based on consensus. The values are shown in matrix [B]. The values of diagonal elements are discussed in the next step.

$$[B] = \begin{array}{c} \\ \text{CBH} \\ \text{MCD} \\ \text{EXR} \\ \text{EVI} \\ \text{SCC} \\ \text{PRV} \\ \text{PRC} \\ \text{NRP} \\ \text{QRP} \\ \text{RCV} \end{array} \begin{array}{c} \begin{array}{cccccccccc} \text{CBH} & \text{MCD} & \text{EXR} & \text{EVI} & \text{SCC} & \text{PRV} & \text{PRC} & \text{NRP} & \text{QRP} & \text{RCV} \end{array} \\ \begin{bmatrix} D_{11} & 0.5 & 0.3 & 0.5 & 0.6 & 0.7 & 0.5 & 0.5 & 0.5 & 0.7 \\ 0.5 & D_{22} & 0.6 & 0.6 & 0.5 & 0.4 & 0.6 & 0.5 & 0.6 & 0.5 \\ 0.7 & 0.4 & D_{33} & 0.6 & 0.7 & 0.8 & 0.7 & 0.6 & 0.7 & 0.6 \\ 0.5 & 0.4 & 0.4 & D_{44} & 0.6 & 0.7 & 0.6 & 0.6 & 0.4 & 0.5 \\ 0.4 & 0.5 & 0.3 & 0.4 & D_{55} & 0.5 & 0.5 & 0.6 & 0.5 & 0.4 \\ 0.3 & 0.6 & 0.2 & 0.3 & 0.5 & D_{66} & 0.5 & 0.5 & 0.6 & 0.5 \\ 0.5 & 0.4 & 0.3 & 0.4 & 0.5 & 0.5 & D_{77} & 0.5 & 0.5 & 0.5 \\ 0.5 & 0.5 & 0.4 & 0.4 & 0.4 & 0.5 & 0.5 & D_{88} & 0.5 & 0.4 \\ 0.5 & 0.4 & 0.3 & 0.6 & 0.5 & 0.4 & 0.5 & 0.5 & D_{99} & 0.3 \\ 0.3 & 0.5 & 0.4 & 0.5 & 0.6 & 0.5 & 0.5 & 0.6 & 0.7 & D_{1010} \end{bmatrix} \end{array}$$

Step 3

The experts were also asked to select quantitative values of diagonal elements on the basis of scale shown in table 2. The experts assigned these values for all four alternatives considered for the study. These values are shown in table 5.

Table 5. Diagonal elements values for each disposition alternative

Attributes	$\boldsymbol{ALT-1}$	$\boldsymbol{ALT-2}$	$\boldsymbol{ALT-3}$	$\boldsymbol{ALT-4}$
Customer behavior (CBH)	0.6	0.5	0.3	0.7
Market conditions, (MCD)	0.7	0.5	0.2	0.6
Existing regulation, (EXR)	0.6	0.6	0.6	0.6
Environmental impact (EVI)	0.7	0.7	0.7	0.7
Supply chain capabilities (SCC)	0.9	0.8	0.6	0.9
Product Value (PRV)	0.7	0.7	0.6	0.4
Processing Cost (PRC)	0.8	0.7	0.4	0.6
No. of Returned Products (NRP)	0.4	0.6	0.3	0.7
Quality of Returned Products (QRP)	1	0.9	0.6	0.1
Recapturing Value (RCV)	0.9	0.8	0.5	0.4

Step 4

The diagonal values for each alternative were entered into the matrix $[B]$. Four matrices were developed for all four alternatives and these matrices are represented as $[ALT-1]$, $[ALT-2]$, $[ALT-3]$, and $[ALT-4]$. These matrices are as follows.

$[ALT-1]$ =

	CBH	MCD	EXR	EVI	SCC	PRV	PRC	NRP	QRP	RCV
CBH	0.6	0.5	0.3	0.5	0.6	0.7	0.5	0.5	0.5	0.7
MCD	0.5	0.7	0.6	0.6	0.5	0.4	0.6	0.5	0.6	0.5
EXR	0.7	0.4	0.6	0.6	0.7	0.8	0.7	0.6	0.7	0.6
EVI	0.5	0.4	0.4	0.7	0.6	0.7	0.6	0.6	0.4	0.5
SCC	0.4	0.5	0.3	0.4	0.9	0.5	0.5	0.6	0.5	0.4
PRV	0.3	0.6	0.2	0.3	0.5	0.7	0.5	0.5	0.6	0.5
PRC	0.5	0.4	0.3	0.4	0.5	0.5	0.8	0.5	0.5	0.5
NRP	0.5	0.5	0.4	0.4	0.4	0.5	0.5	0.4	0.5	0.4
QRP	0.5	0.4	0.3	0.6	0.5	0.4	0.5	0.5	1	0.3
RCV	0.3	0.5	0.4	0.5	0.6	0.5	0.5	0.6	0.7	0.9

$[ALT-2]$ =

	CBH	MCD	EXR	EVI	SCC	PRV	PRC	NRP	QRP	RCV
CBH	0.5	0.5	0.3	0.5	0.6	0.7	0.5	0.5	0.5	0.7
MCD	0.5	0.5	0.6	0.6	0.5	0.4	0.6	0.5	0.6	0.5
EXR	0.7	0.4	0.6	0.6	0.7	0.8	0.7	0.6	0.7	0.6
EVI	0.5	0.4	0.4	0.7	0.6	0.7	0.6	0.6	0.4	0.5
SCC	0.4	0.5	0.3	0.4	0.8	0.5	0.5	0.6	0.5	0.4
PRV	0.3	0.6	0.2	0.3	0.5	0.7	0.5	0.5	0.6	0.5
PRC	0.5	0.4	0.3	0.4	0.5	0.5	0.7	0.5	0.5	0.5
NRP	0.5	0.5	0.4	0.4	0.4	0.5	0.5	0.6	0.5	0.4
QRP	0.5	0.4	0.3	0.6	0.5	0.4	0.5	0.5	0.9	0.3
RCV	0.3	0.5	0.4	0.5	0.6	0.5	0.5	0.6	0.7	0.8

ACCEPTED MANUSCRIPT

$[ALT-3]$ =

RCV	CBH	MCD	EXR	EVI	SCC	PRV	PRC	NRP	QRP
CBH	0.3	0.5	0.3	0.5	0.6	0.7	0.5	0.5	0.5	0.7
MCD	0.5	0.2	0.6	0.6	0.5	0.4	0.6	0.5	0.6	0.5
EXR	0.7	0.4	0.6	0.6	0.7	0.8	0.7	0.6	0.7	0.6
EVI	0.5	0.4	0.4	0.6	0.6	0.7	0.6	0.6	0.4	0.5
SCC	0.4	0.5	0.3	0.4	0.7	0.5	0.5	0.6	0.5	0.4
PRV	0.3	0.6	0.2	0.3	0.5	0.6	0.5	0.5	0.6	0.5
PRC	0.5	0.4	0.3	0.4	0.5	0.5	0.4	0.5	0.5	0.5
NRP	0.5	0.5	0.4	0.4	0.4	0.5	0.5	0.3	0.5	0.4
QRP	0.5	0.4	0.3	0.6	0.5	0.4	0.5	0.5	0.6	0.3
RCV	0.3	0.5	0.4	0.5	0.6	0.5	0.5	0.6	0.7	0.5

$[ALT-4]$ =

	CBH	MCD	EXR	EVI	SCC	PRV	PRC	NRP	QRP	RCV
CBH	0.7	0.5	0.3	0.5	0.6	0.7	0.5	0.5	0.5	0.7
MCD	0.5	0.6	0.6	0.6	0.5	0.4	0.6	0.5	0.6	0.5
EXR	0.7	0.4	0.6	0.6	0.7	0.8	0.7	0.6	0.7	0.6
EVI	0.5	0.4	0.4	0.7	0.6	0.7	0.6	0.6	0.4	0.5
SCC	0.4	0.5	0.3	0.4	0.9	0.5	0.5	0.6	0.5	0.4
PRV	0.3	0.6	0.2	0.3	0.5	0.4	0.5	0.5	0.6	0.5
PRC	0.5	0.4	0.3	0.4	0.5	0.5	0.6	0.5	0.5	0.5
NRP	0.5	0.5	0.4	0.4	0.4	0.5	0.5	0.7	0.5	0.4
QRP	0.5	0.4	0.3	0.6	0.5	0.4	0.5	0.5	0.1	0.3
RCV	0.3	0.5	0.4	0.5	0.6	0.5	0.5	0.6	0.7	0.4

ACCEPTED MANUSCRIPT

ACCEPTED MANUSCRIPT

Step 5

The permanent function for the selection of disposition alternative may be written with the help of matrix developed in step 4. Since, a computer program is written in C++ for calculating the permanent function value of this matrix, step 5 can be skipped.

Step 6

The permanent function value, decision index values for four alternatives were determined by using the computer program. These values are listed in descending order as follows:

Disposition Index for Disposition Alternative-1 ($ALT-1$) = 5032.64

Disposition Index for Disposition Alternative-2 ($ALT-2$) = 4568.91

Disposition Index for Disposition Alternative-4 ($ALT-4$) = 3631.36

Disposition Index for Disposition Alternative-3 ($ALT-3$) = 3057.34

From these values of Disposition Index, disposition alternative-1, repair or reuse and resell as new (Disposition Index value = 5032.64) is the best choice among all considered alternatives for the mobile handset of ABC Limited. In a study of US and UK market, Geyer and Blass (2010) found that mobile phone reuse has healthier profit margin and recycling is the by-product. In last few years, mobile phone returns have increased considerably with the increase in huge product demand and e-business in India (Jena and Sarmah, 2015). Offers like cash on delivery and change in mind of customer during the delivery may influence the increase in these numbers. Second disposition alternative, repair or refurbish and resell

ACCEPTED MANUSCRIPT

(Disposition Index value = 4568.91) is the next best alternative. This alternative is related to mobile phones, which require refurbishment or major repairing. The firm can reconditioned them without requiring dedicated remanufacturing facility. The fourth alternative, recycle (Disposition Index value = 3057.34) is preferred over third alternative, re-manufacture and sell (Disposition Index value = 3631.36). Govindan et al. (2016) stated that remanufacturing in India is motivated by the potential for profit. In a study of Indian mobile phone remanufacturing business, Rathore et al. (2011) observed that remanufacturing in India is in learning stage and the firms have not adopted remanufacturing as a professional business activity. They also observed that the customers are not interested in second hand mobiles. Although remanufacturing is more viable alternative from the economic and environment perspective because of reducing size and weight of mobile phones (Gehin et al., 2008; Andrew et al., 2006); recycling is preferred over remanufacturing for the firm in current market conditions because of customer attitude, remanufacturing capability, competitiveness, and lower cost model of the firm. Sale of remanufactured products in the market may also affect the price and sales volume of new products (Atasu et al., 2010). Therefore, recycling is preferred option in comparison to remanufacturing for the firm. In a review of mobile phone waste management related articles, Sarath et al. (2015) stated that more than 80% of the material used in mobile phones could easily be recycled.

5. Conclusion

In proposed study, the GTMA is utilized for the selection of best disposition alternative based on various disposition attributes. Attributes are selected based on past literature review and discussion with the experts. These attributes are selected from the economic, environmental, and operational aspects of reverse logistics. GTMA has been applied because it allows interaction among attributes, and computation is easy because of matrices. This approach

ACCEPTED MANUSCRIPT

involves the determination of permanent function for the matrices of various disposition alternatives considered for the study. The permanent function is referred as disposition index for the proposed study. A firm, for a particular product may repeatedly calculate the disposition index and over a period, the value of this index may be benchmarked. These values may be utilized in decision-making for the selection of best disposition alternative. A case of mobile phone manufacturing firm was discussed for the illustration of the approach. The results indicate that recycling is preferred to remanufacturing for the disposition of returned mobile handset. The findings of the study will help in improving the overall reverse logistic performance. The proposed approach may help managers and researchers in disposition decision-making and further development on this issue while dealing with product returns, and the reverse logistics. The study contributes to the limited literature available for the disposition decision-making in reverse logistics. However, these results may not be generalized because it is illustration of an approach for a firm, but may be used as methodology for future research in context of other products and sectors. Further, other approaches may also be applied to solve this problem and results may be compared with the findings of this study. One of the limitations of the study is that the limited numbers of disposition alternatives were examined. Therefore, other disposition alternatives such as donation to community, selling in secondary markets may also be explored as a future scope of this study.

Acknowledgements

We greatly acknowledge the contributions of the subject editor, language expert, and reviewers for helping us in improving the quality of this article.

References

ACCEPTED MANUSCRIPT

- Agrawal, S., Singh, R.K., Murtaza, Q., 2016. Outsourcing decisions in reverse logistics: Sustainable balanced scorecard and graph theoretic approach. Resour. Conserv. Recycl. 108, 41-53.
- Agrawal, S., Singh, R.K., Murtaza, Q., 2015. A literature review and perspectives in reverse logistics. Resour. Conserv. Recycl. 97, 76-92.
- Agrawal, S., Singh, R.K., Murtaza, Q., 2014. Forecasting product returns for recycling in Indian electronics industry. J. Adv. Manag. Res. 11(1), 102-114.
- Abraham, N., 2011. The apparel aftermarket in India - a case study focusing on reverse logistics. J. Fashion Mark. Manag. 5(2), 211-227.
- Alumur, S.A., Nickel, S., Saldanha-da-Gama, F., Verter, V., 2012. Multi-period reverse logistics network design. Eur. J. Oper. Res. 220(1), 67-78.
- Amini, M.M., Retzlaff-Roberts, D., Bienstock, C.C., 2005. Designing a reverse logistics operation for short cycle time repair services. Int. J. Prod. Econ. 96(3), 367-380.
- Andrew, M.K., Burges, S., Ijomah, W., McMahon, C., 2006. Reducing waste: repair, recondition, remanufacture or Recycle? Sustainable Development, 14 (4), 257-267.
- Aras, N., Boyaci, T., Verter, V., 2004. The effect of categorizing returned products in remanufacturing. IIE Trans. 36(4), 319-331.
- Ardeshirilajimi, A., Azadivar, F., 2015. Reverse supply chain plan for remanufacturing commercial returns. Int. J. Adv. Manuf. Tech. 77(9-12), 1767-1779.
- Atasu, A., Guide, Jr. V.D.R., Van Wassenhove L.N., 2010. So what if remanufacturing cannibalizes my new product sales? Calif. Manag. Rev. 52(2), 1-21.
- Attia, A., 2015. The Impact of Returned Product Disposition Strategies on Organizational Performance Applied to the Egyptian Household Appliance Industry. Int. J. Bus. Manag. 10(9), 143.

ACCEPTED MANUSCRIPT

- Barsky, N.P., Ellinger, A.E., 2001. Unleashing the value in the supply chain. Strat. Fin. 82(7), 32-7.
- Bell, O.E., Mollenkopf, D.A., Stolze, H.J., 2013. Natural resource scarcity and the closed-loop supply chain: a resource-advantage view. Int. J. Phys. Distrib. Logist. Manag. 43(5/6), 351-379.
- Blackburn, J.D., Guide, Jr. V.D.R., Souza, G.C., Wassenhove, L.N.W., 2004. Reverse Supply Chains for commercial returns. Calif. Manag. Rev. 46 (2), 6-22.
- Carter, C.R., Ellram, L.M., 1998. Reverse logistics: a review of the literature and framework for future investigation. J. Bus. Logist. 19 (1), 85-102.
- Chen,W.K., 1997. Digraph theory and its engineering applications. Chicago: University of Illinois.
- Chunga, C.J., Weeb, H.M., 2011. Short life-cycle deteriorating product remanufacturing in a green supply chain inventory control system. Int. J. Prod. Econ. 129(1), 195-203.
- Darvish, M., Yasaei, M., Saeedi, A., 2009. Application of the graph theory and matrix methods to contractor ranking. Int. J. Proj. Manag. 27(6), 610-619.
- De Brito, M.P., Dekker, R., 2002. Reverse logistics: A framework. Econometric Institute Report EI, 2002-38.
- Defee, C.C., Esper, T., Mollenkopf, D., 2009. Leveraging closed-loop orientation and leadership for environmental sustainability. Supply Chain Manag. 14(2), 87-98.
- Dehghanbaghi M, Hosseininasab H, Sadeghieh A., 2016. A hybrid approach to support recovery strategies (A case study). J. Clean. Prod. 113, 717-29.
- Dowlatshahi, S., 2005. A strategic framework for the design and implementation of remanufacturing operations in reverse logistics. Int. J. Prod. Res. 43(16), 3455-3480.
- Faisal, M.N., 2012. Sustainability metrics for a supply chain: the case of small and medium enterprises. Int. J. Services Oper. Manag. 13(3), 392- 414.

ACCEPTED MANUSCRIPT

- Ferrer, G. Whybark, D.C., 2000. From garbage to goods: Successful remanufacturing systems and skills. Bus. Horizons 43(6), 55-64.
- Fleischmann, M., Krikke, H.R., Dekker, R. Flapper, S.D.P., 2000. A characterization of logistics networks for product recovery. Omega 28 (6), 653-666.
- Fleischmann, M., Van Wassenhove, L.N., Van Nunen, J.A.E.E., van der Laan, E.A., Dekker, R. Bloemhof-Ruwaard, J.M., 1997. Quantitative models for reverse logistics: a review. Eur. J. Oper. Res. s103 (1), 1-17.
- Forbert, H., Marx, D., 2003. Calculation of the permanent of a sparse positive matrix. Comp. Phys. Comm. 150(3), 267-273.
- Franke, C., Basdere, B., Ciupek, M. Seliger, S., 2006. Remanufacturing of mobile phones-capacity, program and facility adaptation planning. Omega 34(6), 562-570.
- Geyer, R., Van Wassenhove, L.N., Atalay, A., 2007. The Economics of Remanufacturing Under Limited Component Durability and Finite Product Life Cycles. Manag. Sci. 53(1), 88-100.
- Geyer, R., Blass, V.D., 2010. The economies of cell phone reuse and recycling. Int. J. Adv. Manuf. Tech. 47, 515-525.
- Gehin, A., Zwolinski, P., Brissaud, D., 2008. A tool to implement sustainable end-of life strategies in the product development phase. J. Clean. Prod. 16(5), 566-576.
- Gobbi, C., 2011. Designing the Reverse Supply Chain: the impact of the product residual value. Int. J. Phys. Distrib. Logist. Manag. 41(8), 768-796.
- Govindan, K., Popiuc, M.N., 2014. Reverse supply chain coordination by revenue sharing contract: A case for the personal computers industry. Eur. J. Oper. Res. 233(2), 326-336.
- Govindan, K., Soleimani, H., 2016. A review of reverse logistics and closed-loop supply chains: a Journal of Cleaner Production focus. J. Clean. Prod. *Article in Press.*

ACCEPTED MANUSCRIPT

- Govindan K, Shankar KM, Kannan D., 2016. Application of fuzzy analytic network process for barrier evaluation in automotive parts remanufacturing towards cleaner production–a study in an Indian scenario. J. Clean. Prod. 114, 199-213.
- Govindan, K., Soleimani, H., Kannan, D., 2015. Reverse logistics and closed-loop supply chain: A comprehensive review to explore the future. Eur. J. Oper. Res. 240(3), 603-626.
- Guide, Jr. V.D.R., Gunes, E.D., Souza, G.C., VanWassenhove L.N., 2008. The optimal disposition decision for product returns. Oper. Manag. Res. 1(1), 6-14.
- Guide, V.D.R., Souza, Jr., G.C., Van Wassenhove, L.N., Blackburn, J.D., 2006. Time value of commercial product returns. Manag. Sci. 52, 1200-1214.
- Guide, V.D.R., Jr., Van Wassenhove, L.N., 2002. The reverse supply chain. Harv. Bus. Rev. 80(2), 25-26.
- Guide, V.D.R., Van Wassenhove, L.N., 2001. Managing product returns for remanufacturing. Prod. Oper. Manag. 10(2), 142-155.
- Gupta, T.K., Singh, V., 2015. A systematic approach to evaluate supply chain management environment index using graph theoretic approach. Int. J. Logis. Syst. Manag. 21(1), 1-45.
- Hall, D.J., Huscroft, J.R., Hazen, B.T., Hanna, J.B., 2013. Reverse logistics goals, metrics, and challenges: perspectives from industry. Int. J. Phys. Distrib. Logist. Management, 43(9), 768-785.
- Hazen, B.T., 2011. Strategic reverse logistics disposition decisions: from theory to practice. International Journal of Logistics Systems and Management, 10(10), 275-292.
- Hazen, B.T., Hall, D.J. Hanna, J.B., 2012. Reverse logistics disposition decision making: Developing a decision framework via content analysis. Int. J. Phys. Distrib. Logist. Manag. 42 (3), 244-274.

ACCEPTED MANUSCRIPT

- Hazen, B.T., Overstreet, R.E., Hall, D.J., Huscroft, J.R., Hanna, J.B., 2015. Antecedents to and outcomes of reverse logistics metrics. Indust. Marketing Manag. 46, 160-170.
- Hoek, R.V., 1999. From reversed logistics to green supply chains. Supply Chain Manag. 4(3), 129-135.
- Huang, X., Gu, J.W., Ching, W.K. Siu, T.K., 2014. Impact of secondary market on consumer return policies and supply chain coordination. Omega, 45, 57-70.
- Inderfurth, K., 2005. Impact of uncertainties on recovery behavior in a remanufacturing environment: A numerical analysis. Int. J. Phys. Distrib. Logist. Manag. 35(5), 318-336.
- Jack, E.P., Powers, T.L., Skinner, L., 2010. Reverse logistics capabilities: antecedents and cost savings. Int. J. Phys. Distrib. Logist. Manag. 40(3), 228-246.
- Jamal, A.M.M., Sarker, B.R., Mondal, S., 2004. Optimal manufacturing batch size with rework process at a single-stage production system. Comp. Indust. Eng. 47(1), 77-89.
- Jena, S.K., Sarmah, S.P., 2015. Measurement of consumers' return intention index towards returning the used products. J. Clean. Prod. 108, 818-829.
- Jense, J.B., Gutin, G., 2000. Digraph theory, algorithms, and applications. London: Springer.
- Kara, S.S., Onut, S., 2010. A two-stage stochastic and robust programming approach to strategic planning of a reverse supply network: The case of paper recycling. Expert Syst. Appl. 37(9), 6129-6137.
- Karamouzian, A., Naini, S.G.J., Mazdeh, M., 2014. Management of returned products to a remanufacturing facility considering arrival uncertainty and priority processing. Int. J. Oper. Res. 20(3), 331-340.

ACCEPTED MANUSCRIPT

- Khor KS, Udin Z.M., 2012. Impact of reverse logistics product disposition towards business performance in Malaysian E&E companies. J. Supply Chain Customer Relationship Manag. 1.
- Kongar, E., Gupta, S.M., 2001, February. Goal programming approach to the remanufacturing supply-chain model. In Intelligent Systems and Smart Manufacturing (pp. 167-178. International Society for Optics and Photonics.
- Krikke, H., Le Blanc, L., Van de Velde, S., 2004. Product modularity and the design of closed-loop supply chains. Calif. Manag. Rev. 46(2), 23-39.
- Krikke, H.R., Bloemhof-Ruwaard, J., Van Wassenhove, L.N., 2003. Concurrent product and closed-loop supply chain design with an application to refrigerators. Int. J. Prod. Res. 41 (16), 3689-3719.
- Kulkarni, S., 2005. Graph theory and matrix approach for performance evaluation of TQM in Indian industries. The TQM Magazine, 17(6), 509-526.
- Kumar, B.M., Saravanan, R., 2014. Network Design for Reverse Logistics–A Case of Recycling Used Truck Tires. Applied Mechanics Mater. 592, 2677-2688.
- Lambert, S., Riopel, D., Kader, W.A., 2011. A reverse logistics decisions conceptual framework. Comp. Indust. Eng. 61(3), 561-581.
- Li, J., González, M., Zhu, Y., 2009. A hybrid simulation optimization method for production planning of dedicated remanufacturing. Int. J. Prod. Econ. 117(2), 286-301.
- Louwers, D., Kip, B.J., Peters, E., Souren, F., Flapper, S.D.P., 1999. A facility location allocation model for reusing carpet materials. Comp. Indust. Eng. 36(4), 855-869.
- Madaan, J., Chan, F.T., Niu, B., 2015. Strategies for evaluating performance of flexibility in product recovery system. Int. J. Prod. Res. 1-12.
- Matar, N., Jaber, M.Y., Searcy, C., 2014. A reverse logistics inventory model for plastic bottles. Int. J. Logist. Manag. 25(2), 315-333.

ACCEPTED MANUSCRIPT

- Muduli, K., Govindan, K., Barve, A., Geng, Y., 2013. Barriers to green supply chain management in Indian mining industries: a graph theoretic approach. J. Clean. Prod. 47, 335-344.
- Narayana, S.A., Elias, A.A., Pati, R.K., 2014. Reverse logistics in the pharmaceuticals industry: a systemic analysis. Int. J. Logist. Manag. 25(2), 379-398.
- Norek, C.D., 2003. Throwing it into reverse. DC Velocity 1(1), 54-8.
- Rao R.V., Gandhi O.P., 2001. Digraph and matrix method for selection, identification and comparison of metal-cutting fluids. J. Eng. Trib. 215, 25-33.
- Rao R.V., Gandhi O. P., 2002. Digraph and matrix methods for machinability evaluation of work materials. Int. J. Machine Tools Manuf. 212, 321-30.
- Rao, R.V., 2006. A material selection model using graph theory and matrix approach. Materials Sci. Eng. A 431(1–2), 248-255.
- Rao, R.V., 2007. Decision Making in the Manufacturing Environment: Using Graph Theory and Fuzzy Multiple Attribute Decision Making Methods. Springer Publication, London, 7–25.
- Rao, R.V., Padmanabhan, K.K., 2006. Selection, identification and comparison of industrial robots using digraph and matrix methods. Robot. Computer-Integrated Manuf. 22(4), 373-383.
- Rao, R.V., Padmanabhan, K.K., 2010. Selection of best product end-of-life scenario using digraph and matrix methods. J. Eng. Design 21(4), 455-472.
- Ravi, V., Shankar, R., Tiwari, M.K., 2005. Productivity improvement of a computer hardware supply chain. Int. J. Prod. Perf. Manag. 54(4), 239-255.
- Rathore, P., Kota, S., Chakrabarti, A., 2011. Sustainability through remanufacturing in India: a case study on mobile handsets. J. Clean. Prod. 709-1722.
- Reda, S., 1998. Getting a handle on returns. Stores, 80(12), 22-26.

ACCEPTED MANUSCRIPT

- Richey, R.G., Chen, H., Genchev, S.E., Daugherty, P.J., 2005. Developing effective reverse logistics programs. Indust. Mark. Manag. 34(8), 830-840.
- Rogers, D.S., Tibben-Lembke, R., 1999. Going backwards: reverse logistics trends and practices, Reno, NV: Reverse Logistics Executive Council.
- Rogers, R.S., Tibben-Lembke, D.S., 2001. An examination of reverse logistics practices. J. Bus. Logist. 22(2), 129-148.
- Rogers, D.S., Melamed1, B., Lembke, R.S., 2012. Modeling and Analysis of Reverse Logistics. J. Bus. Logist. 33(2), 107-117.
- Rubio, S., Corominas, A., 2008. Optimal manufacturing–remanufacturing policies in a lean production environment. Comp. Indust. Eng. 55(1), 234-242.
- Sabharwal, S., Garg, S., 2013. Determining cost effectiveness index of remanufacturing: A graph theoretic approach. Int. J. Prod. Econ. 144(2), 521-532.
- Sarath P, Bonda S, Mohanty S, Nayak SK., 2015. Mobile phone waste management and recycling: Views and trends. Waste Manag. 46, 536-45.
- Savaskan, R.C., Bhattacharya, S., Wassenhove, L.N.V., 2004. Closed-Loop Supply Chain Models with Product Remanufacturing. Manag. Sci. 50(2), 239-252.
- Senthil, S., Srirangacharyulu, B., Ramesh, A., 2012. A decision making methodology for the selection of reverse logistics operating channels. Proce. Eng. 38, 418-428.
- Sharma, V., Garg, S.K., Sharma, P.B., 2016. Identification of major Drivers and Roadblocks for Remanufacturing in India. J. Clean. Prod. 112, 1882-1892.
- Shih, L.H., 2001. Reverse logistics system planning for recycling electrical appliances and computers in Taiwan. Resour. Conserv. Recycl. 32(1), 55-72.
- Skinner, L.R., Bryant, P.T., Richey, R.G., 2008. Examining the impact of reverse logistics disposition strategies. Int. J. Phys. Distrib. Logist. Manag. 38 (7), 518-539.
- Srivastava, S., 2008. Network design for reverse logistics. Omega, 36(4), 535-48.

ACCEPTED MANUSCRIPT

- Stock, J., Speh, T., Shear, H., 2002. Many happy (product) returns. Harv. Bus. Rev. 80(7), 16-17.
- Subramanian, N., Gunasekaran, A., Abdulrahman, M.D., Liu, C., Su, D., 2014. Reverse logistics in the Chinese auto-parts firms: implementation framework development through multiple case studies. Int. J. Sust. Development World Ecology 21(3), 223-234.
- Tan, A.W.K., Kumar, A., 2006. A decision-making model for reverse logistics in the computer industry. The International Journal of Logistics Management, 17(3), 331-354.
- Thierry, M.C., Salomon, M., Van Nunen, J.A.E.E., Van Wassenhove, L.N., 1995. Strategic issues in product recovery management. Calif. Manag. Rev. 37(2), 114-135.
- Tibben-Lembke, R.S., Rogers, D.S., 2002. Differences between forward and reverse logistics in a retail environment. Supply Chain Manag. 7(5), 271-282.
- Vorasayan, J., Ryan, S.M., 2006. Optimal price and quantity of refurbished products. Prod. Oper. Manag. 15(3), 369-384.
- Wadhwa, S., Madaan, J., Chan, F.T.S., 2009. Flexible decision modeling of reverse logistics system: a value adding MCDM approach for alternative selection. Robot. Computer-Integrated manuf. 25(2), 460-469.
- Wu, H.J., Dunn, S.C., 1995. Environmentally responsible logistics systems. Int. J. Phys. Distrib. Logist. Manag. 25(2), 20-38.

ACCEPTED MANUSCRIPT

ACCEPTED MANUSCRIPT

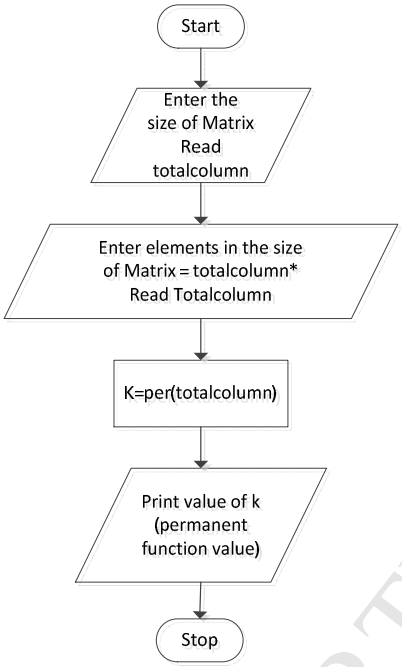
ACCEPTED MANUSCRIPT

ACCEPTED MANUSCRIPT

Appendix [A1]

Logical flow diagrams for determining “permanent function”

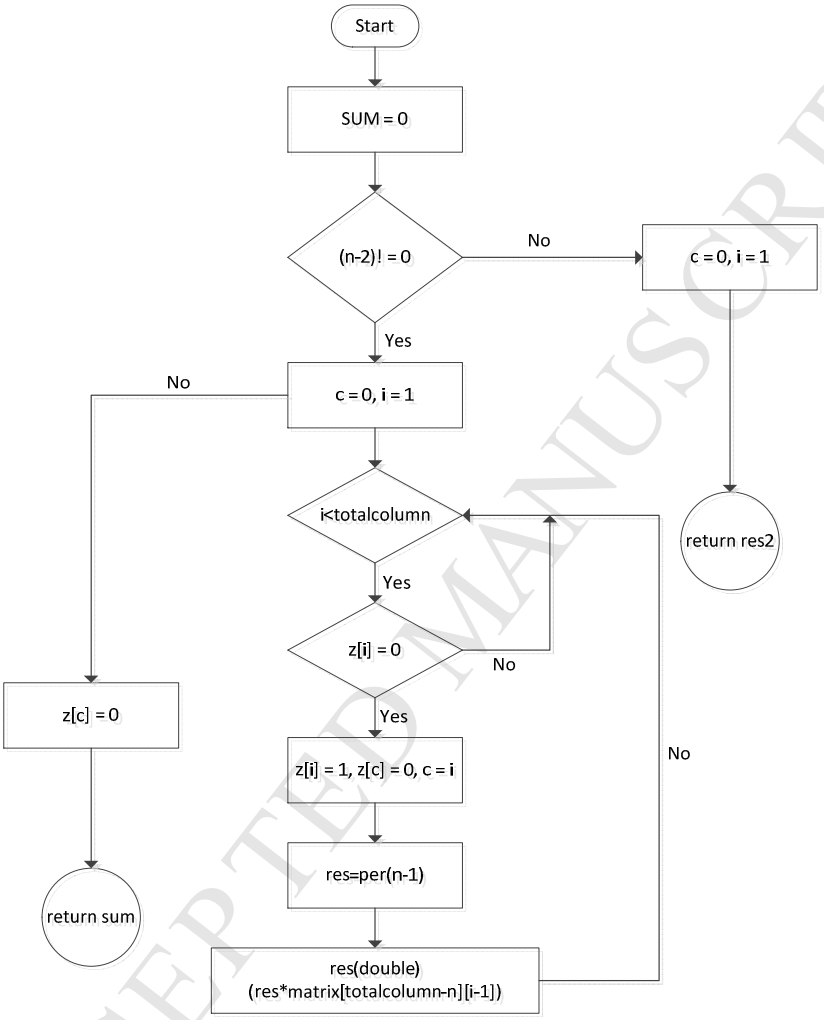
(i) Main Body



ACCEPTED MANUSCRIPT

ACCEPTED MANUSCRIPT

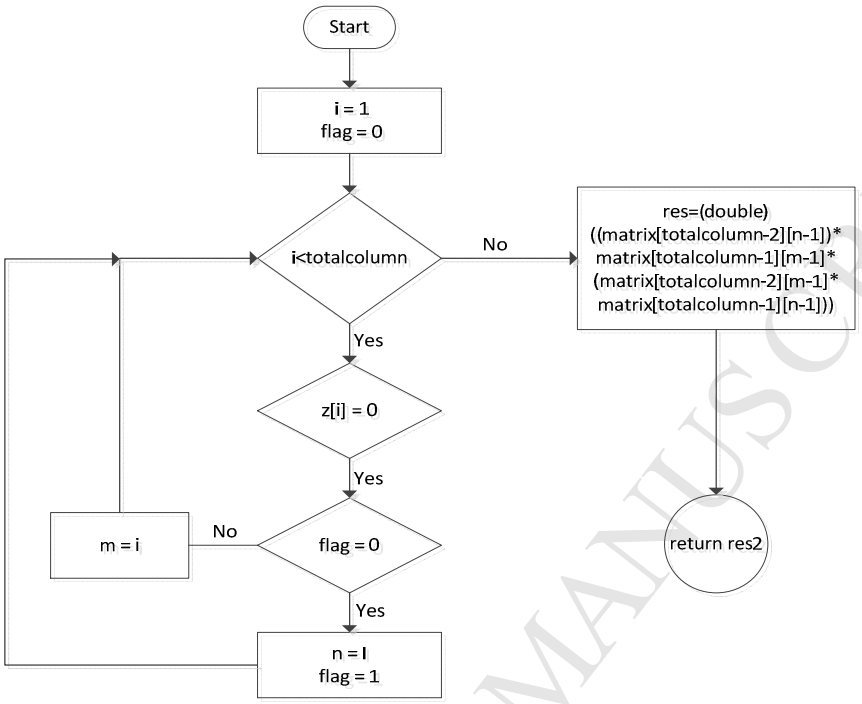
(ii) Per(Int n)



ACCEPTED MANUSCRIPT

ACCEPTED MANUSCRIPT

(iii) Perof2()



ACCEPTED MANUSCRIPT

ACCEPTED MANUSCRIPT

Highlights

- Explored the disposition of returned products in reverse logistics
- Reviewed various disposition decision attributes, and approaches
- Proposed a graph theory and matrix approach to select the best alternative
- A case of mobile manufacturing firm is discussed for the illustration of approach
- The approach will help managers to disposition returned products appropriately

ACCEPTED MANUSCRIPT

IJIREEICE

ISSN (Online) 2321 – 2004
ISSN (Print) 2321 – 5526

INTERNATIONAL JOURNAL OF INNOVATIVE RESEARCH IN ELECTRICAL, ELECTRONICS, INSTRUMENTATION AND CONTROL ENGINEERING
Vol. 4, Issue 7, July 2016

ECG Peaks Detection using Principal Component Analysis

Sahil Dalal[1], Rajesh Birok[2]

Department of ECE, Delhi Technological University, Delhi, India[1]

Associate Professor, Department of ECE, Delhi Technological University, Delhi, India[2]

Abstract: In this research paper, a novel method is proposed for the delineation of the ElectroCardioGraphy (ECG) signals. ECG signals are utilized to measure the heart activity of the subject. So, for the proper analysis of the ECG, knowledge of these peaks should be there. Hence, for the same, principal component analysis is exploited. Using this analysis, peaks of the ECG signals are obtained for the different types of ECG signals i.e. Apnea, Ischemia, Normal and Tachycardia. Then these results are compared representing differentiability among different ECG signals on the basis of ECG peaks. And, using this method, principal component analysis comes out to be a very efficient and a quality detection technique in identifying the ECG peaks of the different types of ECG signals used.

Keywords: Apnea, ECG, Ischemia, PCA, Tachycardia.

I. INTRODUCTION

ElectroCardioGraphy (ECG) is a technique utilized for measuring the electrical activity of the heart. There are so many heart related diseases present in this world among the human beings. So many dies because of problems in their heart. And Doctors exploits ECG to diagnose and treatment for the related problems.

This diagnosis can be made automatic if these ECG signals obtained for different subjects can be differentiated on the basis of some pattern. A standard ECG waveform is shown in the Fig.1.

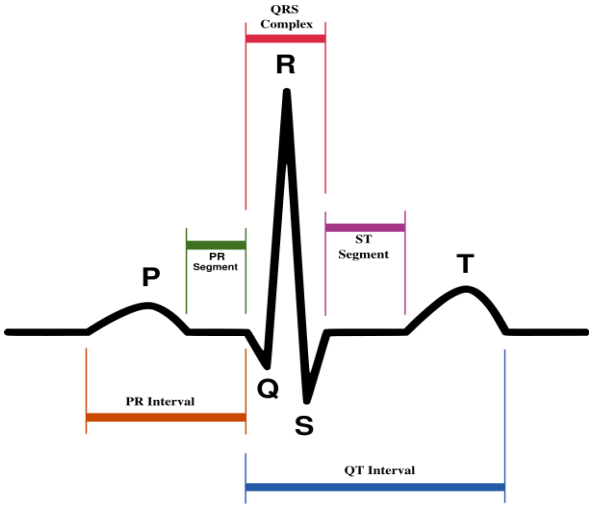


Fig.1. ECG waveform with its characteristic points

In the figure, P-QRS-T waveform is represented and these points can be used as the characteristic points for the ECG signal. For various signals in ECG, variation in the P-QRS-T waveform can be observed. There are so many algorithms already developed for the delineation of the ECG signals. Among these algorithms, real time QRS algorithm [1-3], software based algorithm [4-7], CWT [8], matched filters [9], linear predictive coding [10], ECG slope criteria [11], power spectral density [12], second order derivatives [13], DWT [14], wavelet transforms [15-16] are studied. In [17], ischemia beats were detected using a rule mining based technique. And similarly some other beats are selected in other researchers.

Now, in this research paper, a novel method is proposed for the delineation of the different types of ECG signals i.e. Apnea, Ischemia, Normal and Tachycardia. In this, PCA algorithm is utilized to identify the ECG characteristic points.

This research paper is organised in the following sections as: Section II tells about the overview of the complete work using a block diagram. Section III tells about the different types of ECG signals used and the proposed method. Section IV gives an idea about the experimental work exploited in the method proposed. Then in section V, results are discussed followed by conclusion in section VI.

II. BLOCK DIAGRAM

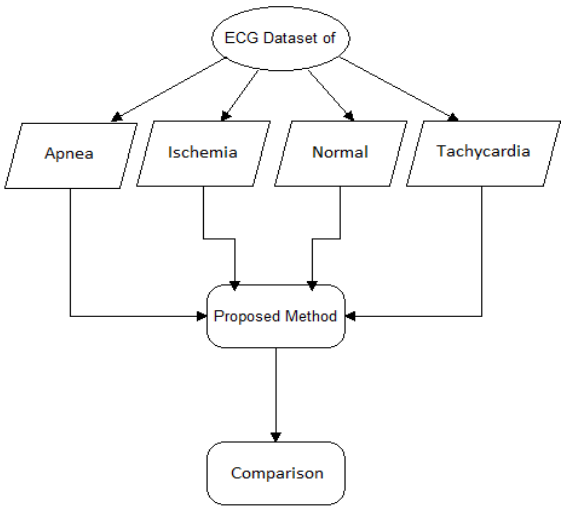


Fig.2. Block Diagram of the proposed method

Copyright to IJIREEICE

IJIREEICE
ISSN (Online) 2321 – 2004
ISSN (Print) 2321 – 5526
INTERNATIONAL JOURNAL OF INNOVATIVE RESEARCH IN ELECTRICAL, ELECTRONICS, INSTRUMENTATION AND CONTROL ENGINEERING
Vol. 4, Issue 7, July 2016

In the the Fig. 2 shown is the block diagram representing the overview of the work done during this research. In this, four different types of ECG waveforms are taken namely Apnea, Ischemia, Normal and Tachycardia. Then, as shown in the block diagram, propsed method i.e PCA is applied on these signals and their characteristic points are computed. After that, on the basis of these characteristic points, ECG signals are compared.

III.PROPOSED METHOD

A. Data-Set

Dataset is taken from the MIT-BIH database for the different types of ECG signals utilized during this research. Among these signals, Apnea, Ischemia and Tachycardia are the three types of situations in the subjects having heart related problems with normal signal as the fourth type. These signals are explained in brief in the sub-sections.

a. Normal ECG

Fig.3 represents an ECG waveform showing the heart condition of a normal human being. Comparing with the Fig.1, P-QRS-T points are observable in the Fig.3.

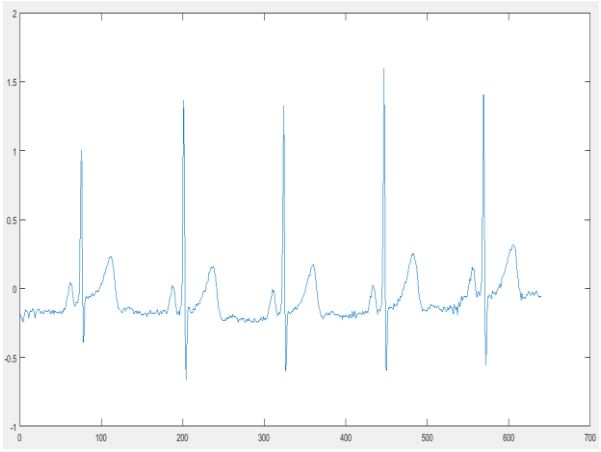


Fig.3. Normal ECG Signal Waveform

TABLE I DIFFERENT PHASES IN NORMAL ECG

Section of ECG	Source
P-Wave	Record the electrical activity through the upper heart chambers (Atria Excitation)
QRS-Complex	Record the movement of electrical impulses through the lower heart chambers. (Atria repolarization + Ventricle depolarization)
T-Wave	Corresponds to the period when the lower heart chambers are relaxing electrically and preparing for their next muscle contraction. (Ventricle repolarization)
ST Segment	Corresponds to the time when the ventricle is contracting but no electricity is flowing through it.

In the Table I, normal ECG signal is explained that how the peaks in ECG are obtained depending on the different situations in the heart.

b. Apnea

Apnea is defined as ECG waveform obtained during the intermittent halt of breathing in the subject. It is due to the irregular sleep and related to the accrued risks of high pressure level. It is shown in the Fig.4.

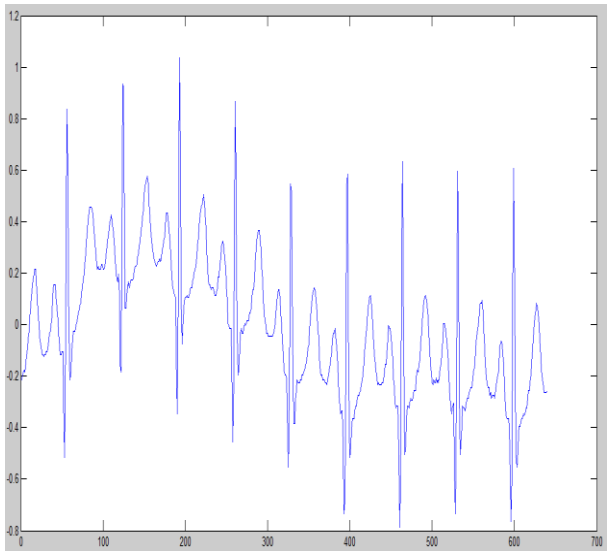


Fig.4. Apnea Signal Waveform

c. Ischemia

Ischemia is a type of ECG signal in which T wave is inverted. In this, sometimes, decrease in the amplitude and disappearance of the R wave may also occur. This type also includes a shift of the ST segment. It is shown in the Fig.5.

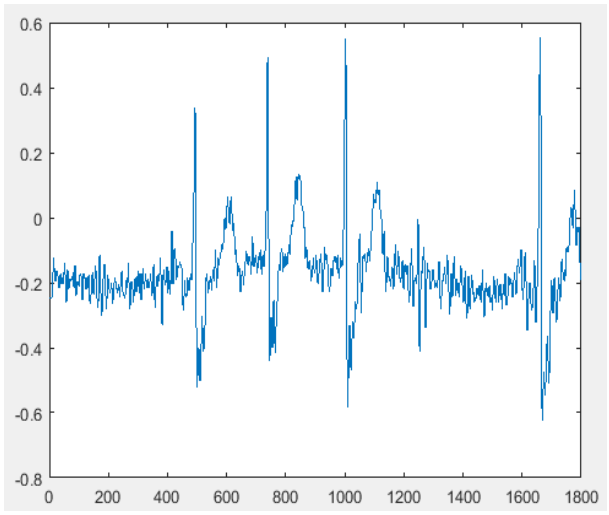


Fig.5. Ischemia Signal Waveform

d. Tachycardia

Tachycardia is a condition in the ECG in which atrial and ventricular rates are accelerated exceeding the normal ECG rate. Beats in the tachycardia are regular but comparatively faster. It is also observed by the presence or absence of the P or flutter waves in the signal.

Copyright to IJIREEICE
DOI 10.17148/IJIREEICE.2016.4718

IJIREEICE
ISSN (Online) 2321 – 2004
ISSN (Print) 2321 – 5526
INTERNATIONAL JOURNAL OF INNOVATIVE RESEARCH IN ELECTRICAL, ELECTRONICS, INSTRUMENTATION AND CONTROL ENGINEERING
Vol. 4, Issue 7, July 2016

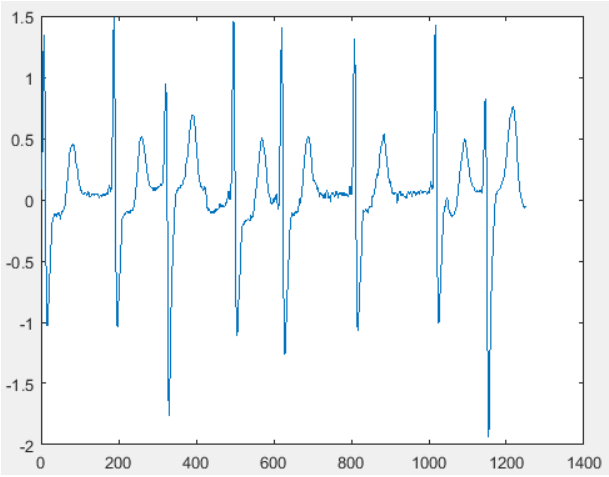


Fig.6. Tachycardia Signal Waveform

B. PCA

PCA is an orthogonal linear transformation. It transfers the data to a new frame of reference such the largest variance of any projection of the information involves lie on the first coordinate (first principal component), the second largest variance lies on the second coordinate (second principal component), and so on. Linear projection method to reduce the number of parameters. Map the data into a space of lower dimensionality.

PCA Algorithm:

Let X be an input data set.

Now, Perform the following steps:

Calculate the mean:

$$m[p] = \frac{1}{Q}\sum_{q=1}^{Q} X[p,q] \qquad (1)$$

Calculate the mean deviation and keep the data in the matrix $D_m[P \times Q]$:

$$D_m = X - m.h \qquad (2)$$

where h is a 1 × Q row vector of all 1's:

h[q] = 1 for n = 1, …....Q

Find the covariance matrix Cv:

$$Cv = D_m.D_m^{T} \qquad (3)$$

Find the eigenvectors and eigenvalues of the covariance matrix $V^{-1}CvV$ where V is the eigenvectors matrix. D is the diagonal matrix of eigenvalues of Cv.

$$D[m,n] = \lambda_p \qquad (4)$$

for m = n = p is the m^{th} eigen value of the covariance matrix Cv.

Rearrange the eigenvalues

$$\lambda_1 \geq \lambda_2 \geq \lambda_3 .... \geq \lambda_Q \qquad (5)$$

Choosing components and forming a feature vector: save the first L columns of V as the M × L matrix W,

$$W[m,n] = V[m,n], \qquad (6)$$

for m = 1, . . . ,P

n = 1, . . . , L where $1 \leq L \leq P$.

Deriving the new data set: The eigenvectors with the maximum eigenvalues are projected into space. This projection results in a vector represented by fewer dimension (L < P) containing the essential coefficients only.

IV. RESULTS DISCUSSION

Now, in the results, Eigen values computed from the PCA algorithm are utilized to detect the characteristic points in the ECG signals. These characteristic points includes Q, R,S and T peaks of the different types of ECG signals viz. Apnea, Ischemia Normal and Tachycardia signals.

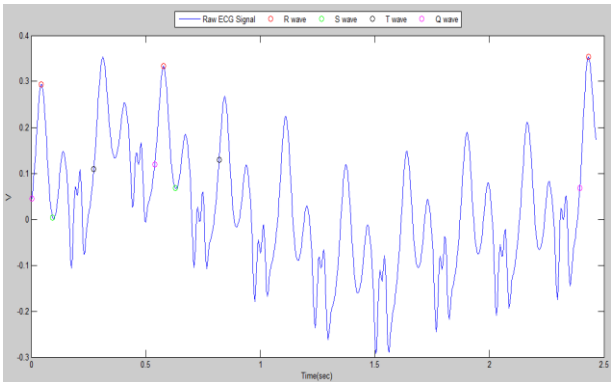


Fig.7. Apnea ECG Peaks Detection

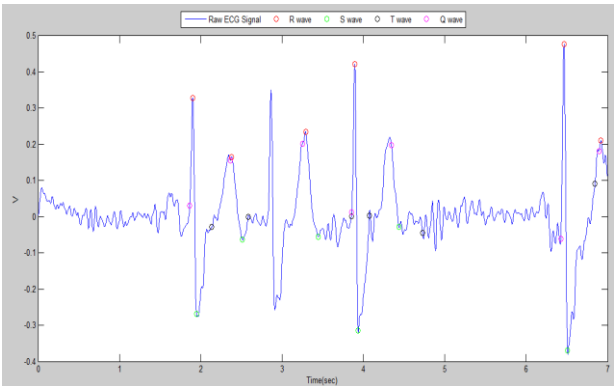


Fig.8. Ischemia ECG Peaks Detection

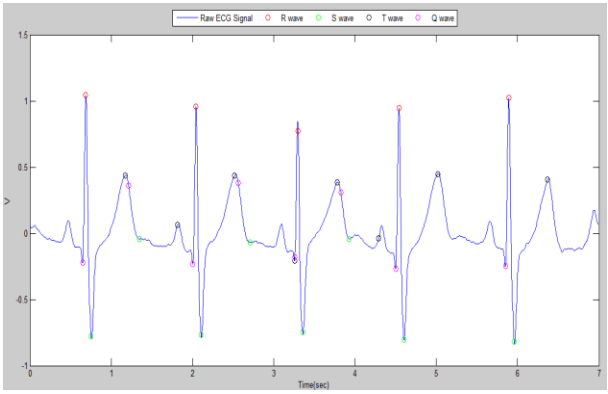


Fig.9. Normal ECG Peaks Detection

IJIREEICE

ISSN (Online) 2321 – 2004
ISSN (Print) 2321 – 5526

INTERNATIONAL JOURNAL OF INNOVATIVE RESEARCH IN ELECTRICAL, ELECTRONICS, INSTRUMENTATION AND CONTROL ENGINEERING
Vol. 4, Issue 7, July 2016

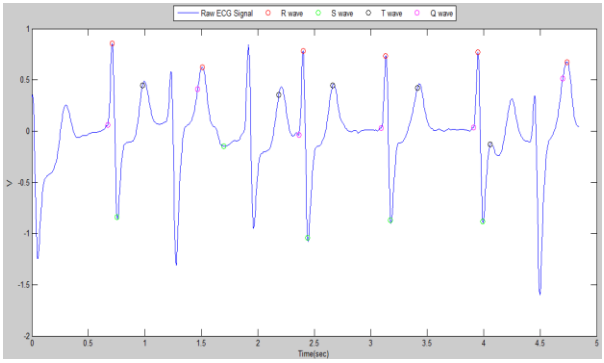


Fig.10. Tachycardia ECG Peaks Detection

In the Fig.7-10 shows the parameter detection in the ECG signals selected as sample from the datasets. It can be observed from the signals figures that variation among the signals can be observed. And this variation is also shown in the Table II.

This table shows the parameter values for the different types of ECG signals used during this work i.e. Apnea, Ischemia, Normal and Tachycardia signals. As feature values, parameters extracted are the amplitudes of Q,R,S and T peaks with their index values which contain their interval values.

TABLE III ECG PARAMETERS CHARACTERISTIC POINTS

ECG	Parameters	Sample values
Apnea	R_i	260.667
	R_amp	0.3271
	S_i	92.5
	S_amp	0.0359
	T_i	140
	T_amp	0.1194
	Q_i	250.667
	Q_amp	0.0771
Ischemia	R_i	1067.6
	R_amp	0.2907
	S_i	971.667
	S_amp	-0.1832
	T_i	1033.2
	T_amp	0.0040
	Q_i	1060.4
	Q_amp	0.1028
Normal	R_i	770
	R_amp	0.7243
	S_i	792.1250
	S_amp	-0.5091
	T_i	903.25
	T_amp	0.2410
	Q_i	763.75
	Q_amp	-0.0117
Tachycardia	R_i	701.5
	R_amp	0.7406
	S_i	617.6
	S_amp	-0.7577
	T_i	681.2
	T_amp	0.3809
	Q_i	691.5
	Q_amp	0.1688

Copyright to IJIREEICE
DOI 10.17148/IJIREEICE.2016.4718

IJIREEICE
ISSN (Online) 2321 – 2004
ISSN (Print) 2321 – 5526
INTERNATIONAL JOURNAL OF INNOVATIVE RESEARCH IN ELECTRICAL, ELECTRONICS, INSTRUMENTATION AND CONTROL ENGINEERING
Vol. 4, Issue 7, July 2016

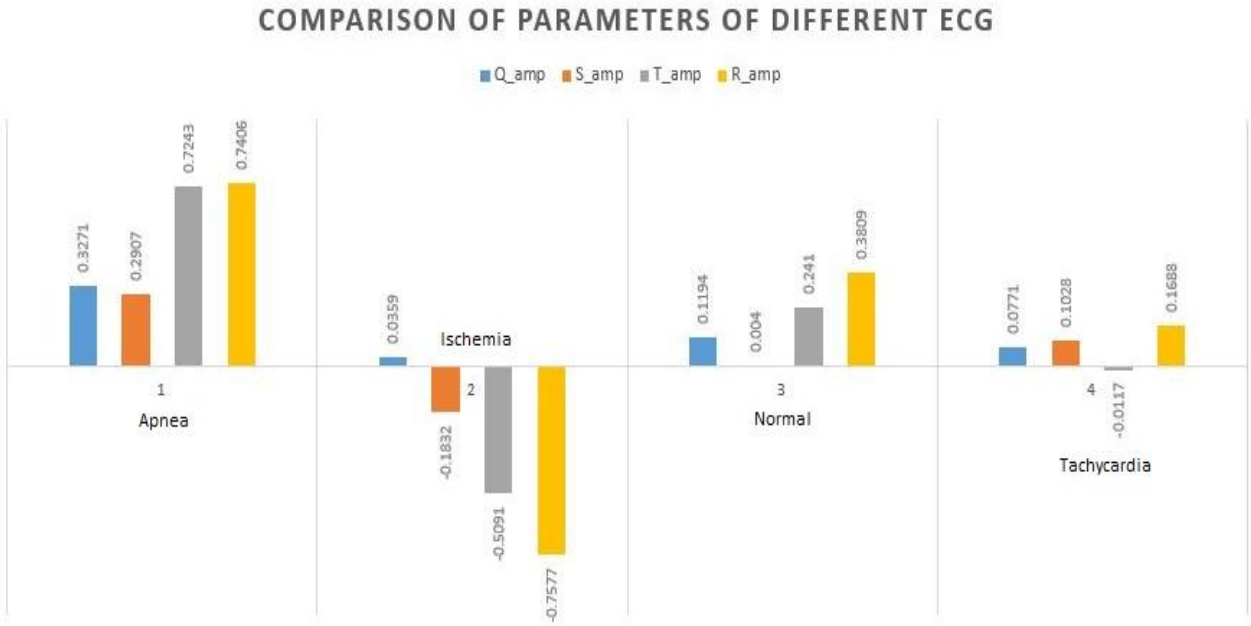


Fig.11. Comparison of characteristic points of different ECGs

Next in the Fig.11 shows is the graph representing the comparison among the feature values extracted using the Principal Component Analysis (PCA) algorithm. And it can be observed from the figure that there is difference among the characteristic points i.e. Q, R, S and T peaks.

V. CONCLUSION

The proposed method in this research paper utilizes Principal Component Analysis (PCA) algorithm to identify the characteristic points i.e. Q, R, S and T peaks. And it can be observed from the results that the different types of ECG signals viz. Apnea, Ischemia, Normal and Tachycardia signals, used during this research have different characteristic points.

As the future work, due to the difference in these characteristic points, these can be exploited to classify the ECG signals.

REFERENCES

[1] B.U. Kohler, C. Hennig, R. Orglmeister, The principles of software QRS detection, IEEE Eng. Med. Biol. Mag. 21 (1) (2002) 42–57.
[2] C. Saritha, V. Sukanya, Y. Narasimha Murthy, ECG analysis using wavelets, Bulg. J. Phys. 35 (2008) 68–77.
[3] P. Ranjith, ECG analysis using wavelet transform: application to myocardial ischemia detection, ITBM-RBM 24 (January) (2003) 44– 47.
[4] J. Pan, W.J. Tomkins, A real time QRS detection algorithm, IEEE Trans. Biomed. Eng. 32 (3) (1985).
[5] O. Pahlm, L. Sörnmo, Software QRS detection in ambulatory monitoring – a review, Med. Biol. Eng. Comput. 22 (July) (1984) 289–297.
[6] F. Gritzali, Toward a generalized scheme for QRS detection in ECG waveforms, Signal Process. 15 (September) (1988) 183–192.
[7] G.M. Friesen, T.C. Jannett, M.A. Jadallah, S.L. Yates, S.R. Quint, H.T. Nagle, A comparison of the noise sensitivity of nine QRS detection algorithms, IEEE Trans. Biomed. Eng. 37 (January) (1990) 85–98.
[8] A. Ghaffari, H. Golbayani, M. Ghasemi, A new mathematical based QRS detector using continuous wavelet transform, Comput. Electr. Eng. 34 (2) (2008) 81–91.
[9] A.S.M. Koeleman, H.H. Ros, T.J. van den Akker, Beat-to-beat interval measurement in the electrocardiogram, Med. Biol. Eng. Comput. 23 (August) (1985) 213–219.
[10] Kang-Ping Lin, Walter H. Chang, QRS feature extraction using linear prediction, IEEE Trans. Biomed. Eng. 36 (10) (1989).
[11] I.K. Daskalov, I.A. Dotsinsky, I.I. Christov, Developments in ECG acquisition, preprocessing, parameter measurement and recording, IEEE Eng. Med. Biol. Mag. 17 (September) (1998) 50–58.
[12] Abdulnasir Hossen, Bader Al-Ghunaimi, A wavelet-based soft decision technique for screening of patients with congestive heart failure, Biomed. Signal process. Control 2 (May) (2007) 135–143.
[13] J.G.C. Kemmelings, A.C. Linnenbank, S.L.C. Muilwijk, A. Sippens-Groenewegen, A. Peper, C.A. Grimbergen, Automatic QRS onsetand offset detection for body surface QRS integral mapping of ventricular tachycardia, IEEE Trans. Biomed. Eng. 41 (September) (1994) 830–836.
[14] E.S. Jayachandran, K. Paul Joseph, R. Acharya U, Analysis of myocardial infarction using discrete wavelet transform, J. Med. Syst. 34 (October) (2010) 985–992.
[15] C. Li, C. Zheng, C. Tai, Detection of ECG characteristic points using wavelet transforms, IEEE Trans. Biomed. Eng. 42 (January) (1995) 21–28.
[16] J.S. Sahambi, S. Tandon, R.K.P. Bhatt, Using wavelet transform for ECG characterization, IEEE Eng. Med. Biol. 16 (1) (1997) 77–83.
[17] Themis P. Exarchos et al., Association rule-mining based methodology for automated detection of ischemic ECG beats, IEEE Trans. Biomed. Eng. 53 (8) (2006).

ISSN: 2278 – 909X
International Journal of Advanced Research in Electronics and Communication Engineering (IJARECE)
Volume 5, Issue 7, July 2016

ECG Signals Analysis using PCA with Neural Network and Fuzzy Logic

Sahil Dalal, Rajesh Birok

***Abstract*— In the paper, a method is proposed for the analysis of the ElectroCardioGraphy (ECG) signals. ECG signals are exploited to measure the heart activity of the person. So, for the proper analysis of the ECG, a knowledge of its peaks should be there. Hence, the purpose of this research is to address in identifying the Normal, Apnea, Tachycardia and Ischemia signals using the method of Principal Component Analysis (PCA) and various classifiers i.e. Support Vector Machine (SVM), Artificial Neural Networks (ANN) and Fuzzy Logic. PCA algorithm is used to extract the relevant information from the ECG input data which are their P-QRS-T parameters values. Then the extracted features data is analyzed and classified using Support Vector Machine (SVM), Artificial Neural Networks (ANN) and Fuzzy Logic classifiers. Then these classification results are compared and observed a good accuracy of around 92% in the classification.**

***Index Terms*— ANN, Apnea, ECG, Fuzzy, Ischemia, PCA, SVM, Tachycardia.**

I. INTRODUCTION

ElectroCardioGraphy (ECG) is a way exploited for measuring the electrical activity of the heart. There can be so many heart related diseases present in this world among the human beings. So, because of problems in the heart, many people die every year. And Doctors exploits ECG to diagnose and treatment for the related problems.

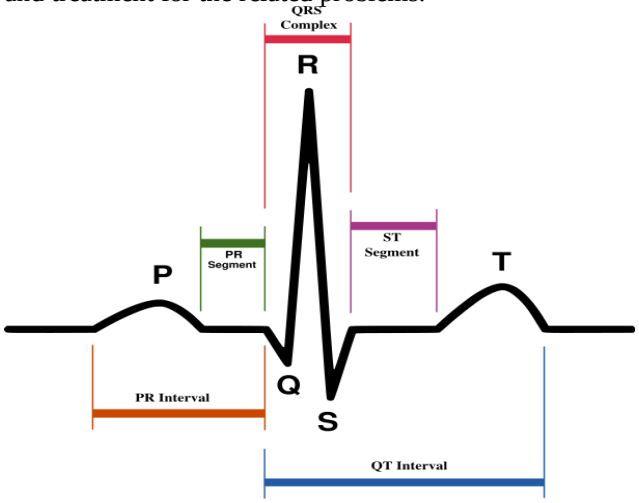


Fig.1. ECG waveform with its characteristic points

This diagnosis can be made automatic if these ECG signals obtained for different subjects can be differentiated on the basis of some pattern. A standard ECG waveform is shown in the Fig.1. In the figure, P-QRS-T waveform is represented and these points can be used as the characteristic points for the ECG signal. For various signals in ECG, variation in the P-QRS-T waveform can be observed. There are so many algorithms already developed for the delineation of the ECG signals.

TABLE.I

SUMMARY OF THE EARLIER PROPOSED METHODS

STUDY	TECHNIQUE	ACCURACY
Shen [2]	HB + WED + NNC	95.3%
Chan et al. [3]	CCORR + NC	90.8%
Chiu et al. [4]	DWT + NC, ED	95.71%
Yao and Wan [5]	DWTMRRS + PCA	91.5%
Boumbarov et al. [6]	PCA + RBFNN	86%
Homer et al. [7]	RARMA + NNC	85.2%
Agrafioti and Hatzinakos [8]	AC + WT + NNC	92.3%
Lourenco et al. [9]	MANRHB + NC	94.3%

Among these algorithms, real time QRS algorithm [10-12], software based algorithm [13-16], CWT [17], matched filters [18], linear predictive coding [19], ECG slope criteria [20], power spectral density [21], second order derivatives [22], DWT [23], wavelet transforms [24-26] are studied. In [1], ECG beats were detected using principal component based technique. And similarly some other beats are selected in other researchers.

Now, in this research paper, a novel method is proposed for the classification of the different types of ECG signals i.e. Apnea, Ischemia, Normal and Tachycardia. In this, PCA algorithm is utilized to identify the ECG signals.

This research paper is organized in the following sections as: Section II tells about the overview of the complete work using a block diagram. Section III tells about the different types of ECG signals used and the proposed method. Then in section IV, results are discussed followed by conclusion in section V.

***Sahil Dalal**, Department of Electronics & Communication Engineering, Delhi Technological University, Delhi, India..*

***Rajesh Birok**, Associate Professor, Department of Electronics & Communication Engineering, Delhi Technological University, Delhi, India*

All Rights Reserved © 2016 IJARECE

II. Block Diagram

In the the Fig. 2 shown is the block diagram representing the overview of the work done during this research. In this, four different types of ECG waveforms are taken namely Apnea, Ischemia, Normal and Tachycardia. Then, as shown in the block diagram, propsed method i.e PCA is applied on these signals and their characteristic points are computed. After that, on the basis of these characteristic points, ECG signals are classified using the three different classifiers i.e. SVM, ANN and Fuzzy classifiers.

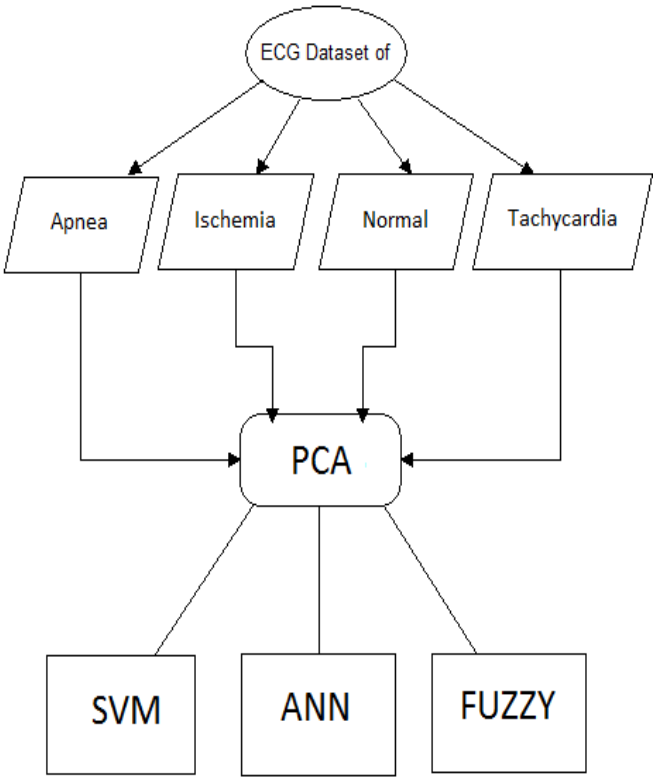


Fig.2. Block Diagram of the Proposed method

III. Proposed Method

A. *Data-Set*

Dataset is taken from the MIT-BIH database for the different types of ECG signals utilized during this research. Among these signals, Apnea, Ischemia and Tachycardia are the three types of situations in the subjects having heart related problems with normal signal as the fourth type. Dataset for ECG detection is loaded from the MIT-BIH database of Physiobank ATM. It is shown below in the Table II.

TABLE II

DESCRIPTION OF DATASET USED

ECG Signals	Training	Testing	Total
Apnea	18	12	30
Normal	18	12	30
Ischemia	18	12	30
Tachycardia	18	12	30

These signals are explained in brief in the sub-sections.

a. Normal ECG

Fig.3 represents an ECG waveform showing the heart condition of a normal human being. Comparing with the Fig.1, P-QRS-T points are observable in the Fig.3.

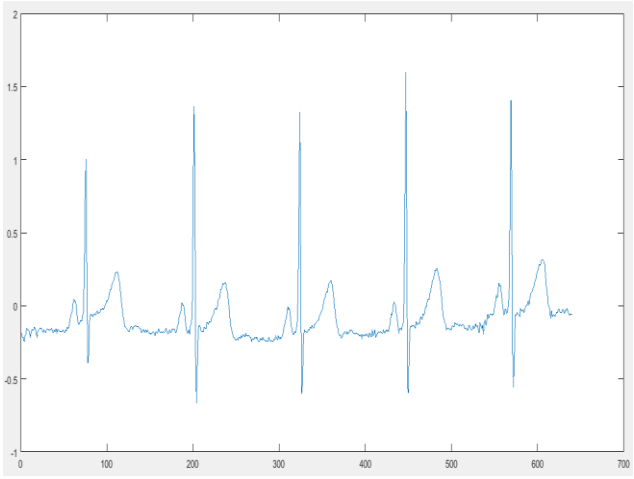


Fig.3. Normal ECG Signal Waveform

TABLE III

DIFFERENT PHASES IN NORMAL ECG

Section of ECG	Source
P-Wave	Record the electrical activity through the upper heart chambers (Atria Excitation)
QRS-Complex	Record the movement of electrical impulses through the lower heart chambers. (Atria repolarization + Ventricle depolarization)
T-Wave	Corresponds to the period when the lower heart chambers are relaxing electrically and preparing for their next muscle contraction. (Ventricle repolarization)
ST Segment	Corresponds to the time when the ventricle is contracting but no electricity is flowing through it.

In the Table III, normal ECG signal is explained that how the peaks in ECG are obtained depending on the different situations in the heart.

b. Apnea

Apnea is defined as ECG waveform obtained during the intermittent halt of breathing in the subject. It is due to the irregular sleep and related to the accrued risks of high pressure level. It is shown in the Fig.4.

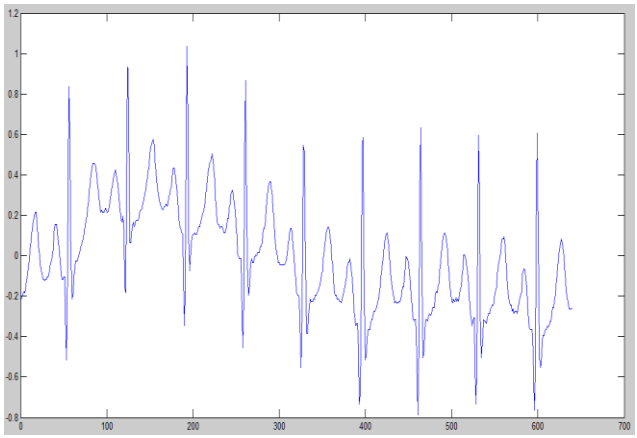


Fig.4. Apnea Signal Waveform

c. Ischemia

Ischemia is a type of ECG signal in which T wave is inverted. In this, sometimes, decrease in the amplitude and disappearance of the R wave may also occur. This type also includes a shift of the ST segment. It is shown in the Fig.5.

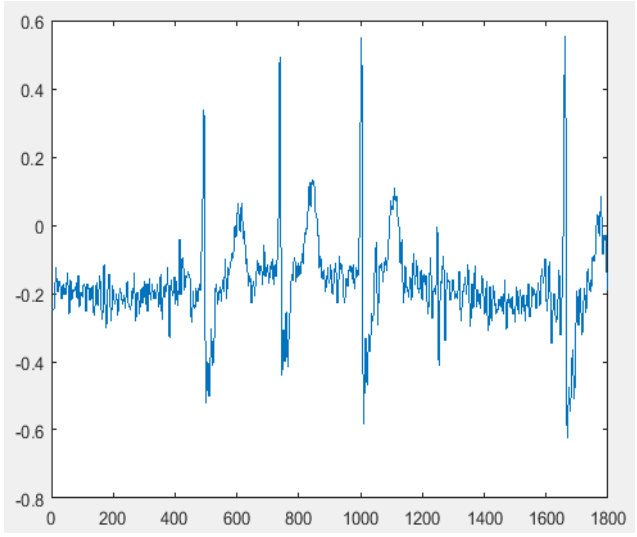


Fig.5. Ischemia Signal Waveform

d. Tachycardia

Tachycardia is a condition in the ECG in which atrial and ventricular rates are accelerated exceeding the normal ECG rate. Beats in the tachycardia are regular but comparatively faster. It is also observed by the presence or absence of the P or flutter waves in the signal.

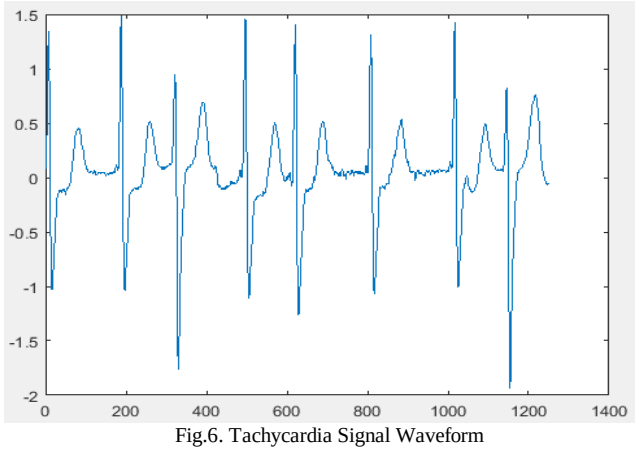


Fig.6. Tachycardia Signal Waveform

B. PCA

PCA is an orthogonal linear transformation. It transfers the data to a new frame of reference such the largest variance of any projection of the information involves lie on the first coordinate (first principal component), the second largest variance lies on the second coordinate (second principal component), and so on. Linear projection method to reduce the number of parameters. Map the data into a space of lower dimensionality.

PCA Algorithm:

Let X be an input data set.

Now, Perform the following steps:

Calculate the mean:

$$m[p] = 1/Q \sum_{q=1}^{Q} X[p,q] \quad (1)$$

Calculate the mean deviation and keep the data in the matrix $D_m[P \times Q]$:

$$D_m = X - m.h \quad (2)$$

where h is a 1 × Q row vector of all 1's:

h[q] = 1 for n = 1, …....Q

Find the covariance matrix Cv:

$$Cv = D_m . D_m^T \quad (3)$$

Find the eigenvectors and eigenvalues of the covariance matrix $V^{-1}CvV$ where V is the eigenvectors matrix. D is the diagonal matrix of eigenvalues of Cv.

$$D[m,n] = \lambda_p \quad (4)$$

for m = n = p is the m^{th} eigen value of the covariance matrix Cv.

Rearrange the eigenvalues

$$\lambda_1 \geq \lambda_2 \geq \lambda_3 .... \geq \lambda_Q \quad (5)$$

Choosing components and forming a feature vector: save the first L columns of V as the M × L matrix W,

$$W[m, n] = V[m, n], \quad (6)$$

for m = 1, . . . ,P

n = 1, . . . , L

where 1 ⩽ L ⩽P.

Deriving the new data set: The eigenvectors with the maximum eigenvalues are projected into space. This projection results in a vector represented by fewer dimension (L < P) containing the essential coefficients only.

All Rights Reserved © 2016 IJARECE

C. SVM

SVM i.e. Support Vector Machine classifier is utilized for ECG signals classification because of its multi-classification ability in differentiating various classes. SVM is explained using the equations in which margin between the support vectors is to be maximized. For this compute the parameters f, f_0 of the hyperplane so that to:

$$\underset{\text{minimize}}{J(f, f_0) \equiv \frac{1}{2}\|f\|^2} \quad (7)$$

subject to langrangian equations.

Clearly, making the norm minimum will makes themargin maximum. This is a nonlinear (quadratic) optimization task subject to a set of linear inequality constraints. Hence, the SVM decision function is expressed as equations

$$f = \sum_{i=1}^{N} c_i . z_i . x_i \quad (8)$$

$$\sum_{i=1}^{N} c_i . z_i = 0 \quad (9)$$

D. ANN

With SVM, ECG classification is also done using Artificial Neural Network (ANN). In this also, train the network first by using some training data. A suitable training algorithm results in an ANN which is capable of generating a non-linear mapping function with the proficiency of demonstrating relationships between given ECG features and cardiac disorders.

$$u_k = \sum_{j=1}^{n} x_j . w_{kj} \quad (10)$$

$$v_k = u_k + b_k \quad (11)$$

A well designed ANN will exhibit good generalization when a correct input output mapping is obtained even when the test input is slightly different from the data used to train the network.

E. FUZZY

Zong and Jiang (1998) described the method of fuzzy logic approach single channel ECG beat and rhythm detection. The method summarized and makes use of the medical knowledge and diagnostic rules of cardiologists. Linguistic variables have being used to represent beat features and fuzzy conditional statements perform reasoning. The algorithm can identified rhythms as well as individual beats. This method also handling the beat features and reasoning process is heuristic and seems more reasonable as stated in their paper. It also presented that this method may be of great utility in clinical applications such as multi-parameter patient monitoring systems, where many physiological variables and diagnostic rules exist.

IV. Results & Discussion

Now, in the results, Eigen values computed from the PCA algorithm are utilized to detect the characteristic points in the ECG signals. These characteristic points includes Q, R,S and T peaks of the different types of ECG signals viz. Apnea, Ischemia Normal and Tachycardia signals.

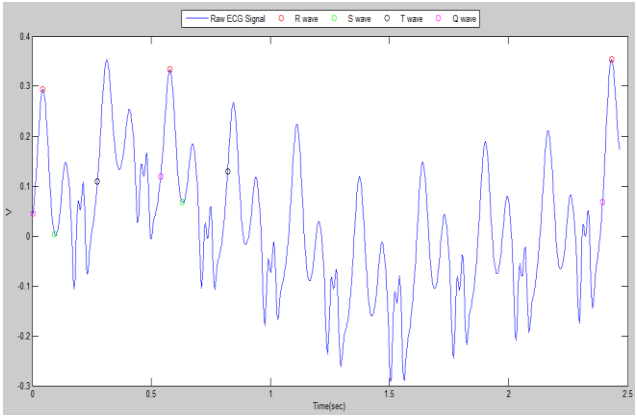


Fig.7. Apnea ECG Peaks Detection

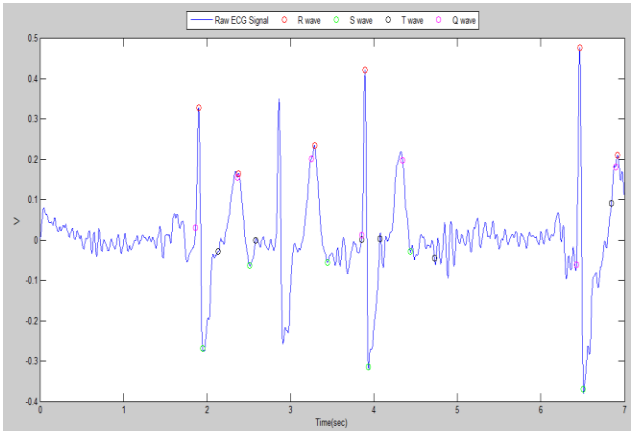


Fig.8. Ischemia ECG Peaks Detection

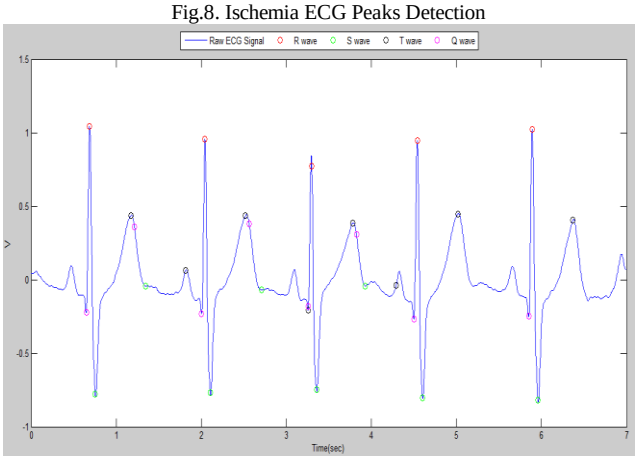


Fig.9. Normal ECG Peaks Detection

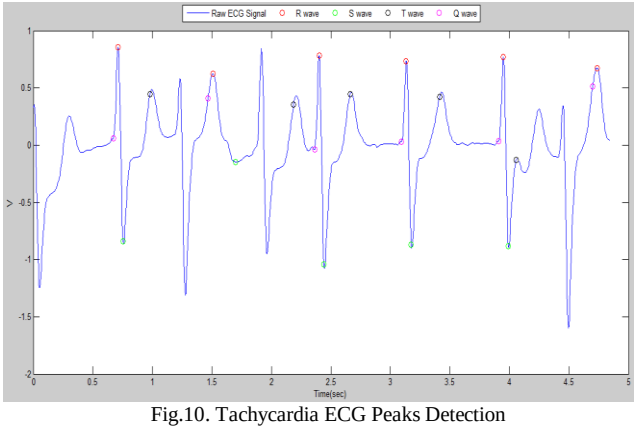


Fig.10. Tachycardia ECG Peaks Detection

In the Fig.7-10 shows the parameter detection in the ECG signals selected as sample from the datasets. It can be observed from the signals figures that variation among the signals can be observed.

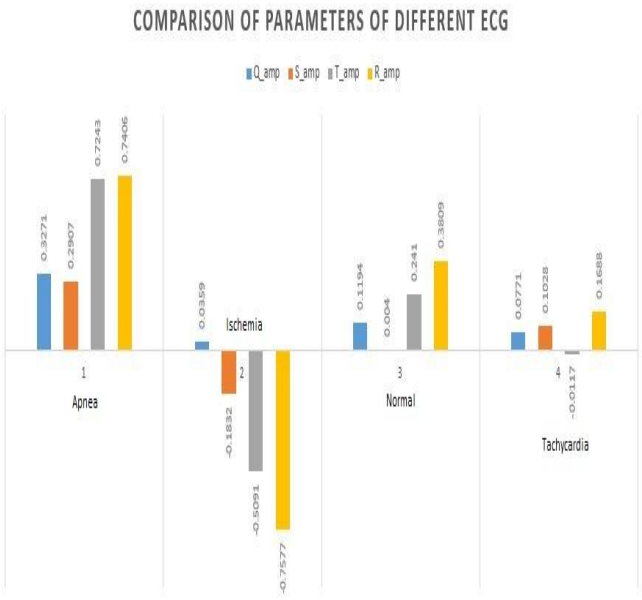


Fig.11. Comparison of characteristic points of different ECGs

Next in the Fig.11 shows is the graph representing the comparison among the feature values extracted using the Principal Component Analysis (PCA) algorithm. And it can be observed from the figure that there is difference among the characteristic points i.e. Q, R, S and T peaks.

TABLE IV

CONFUSION MATRIX FROM SVM

Targets / Outputs	AP	IS	NR	TC	Accuracy
AP	10/12	1/12	1/12	0/12	83.33%
IS	1/12	10/12	1/12	0/12	83.33%
NR	0/12	0/12	12/12	0/12	100%
TC	0/12	1/12	2/12	9/12	75%

Now, these parameters obtained, are used in the classifiers for the classification of these ECG signals. For the classification, firstly SVM is used. In this classifier, 120 subjects dataset is used in total. Among these, 72 subjects are used to train the SVM and remaining are tested on this trained classifier. The results from the SVM classifier are shown in the Table IV which shows a confusion matrix of the tested dataset. In this table, AP, IS, NR and TC represents Apnea, Ischemia, Normal and Tachycardia respectively.

In the Table IV, it can be seen that this classifier doesn't give us a satisfactory results with just 85.4% of accuracy. Hence, for an improvement in the results next classifier is used i.e. ANN.

ANN applied on the dataset gives the neural network as shown in the Fig. 12 in which 72 subject parameter values are used for the training and 48 for the testing.

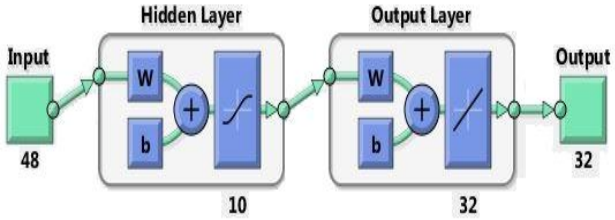


Fig.12. Neural Network

TABLE V

CONFUSION MATRIX FROM ANN

Targets / Outputs	AP	IS	NR	TC	Accuracy
AP	9/12	1/12	0/12	2/12	75%
IS	0/12	11/12	0/12	1/12	91.67%
NR	0/12	0/12	12/12	0/12	100%
TC	0/12	1/12	1/12	10/12	83.33%

Then next shown is the Table V showing the confusion matrix of these ECG signals obtained by classification using this classifier.

According to this table, an accuracy of 87.5% is observed which is very good and gives a much better results compared to SVM in which only 85.4% accuracy was observed. Next, Fuzzy is applied on these feature values obtained using these ECG datasets.

Now, the dataset is applied on the Fuzzy logic for the classification purpose. Fig.13 shows the modelling of Fuzzy Logic which helps in the classification of the ECG signal classes.

All Rights Reserved © 2016 IJARECE

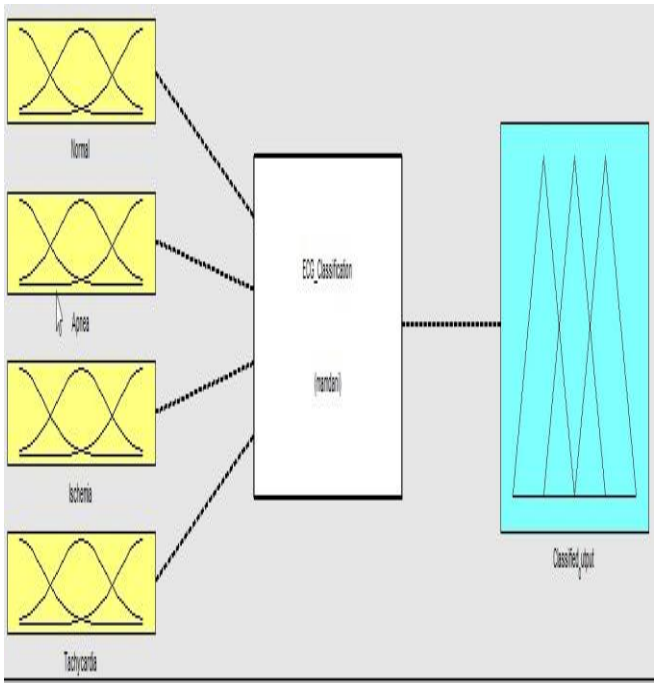


Fig.13. Fuzzy Rule Based Model

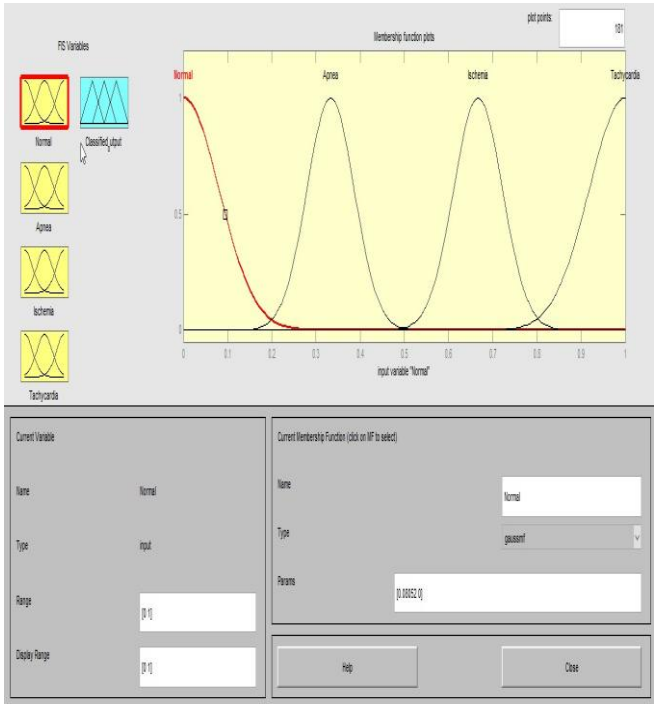


Fig.14. Membership_functions for Inputs

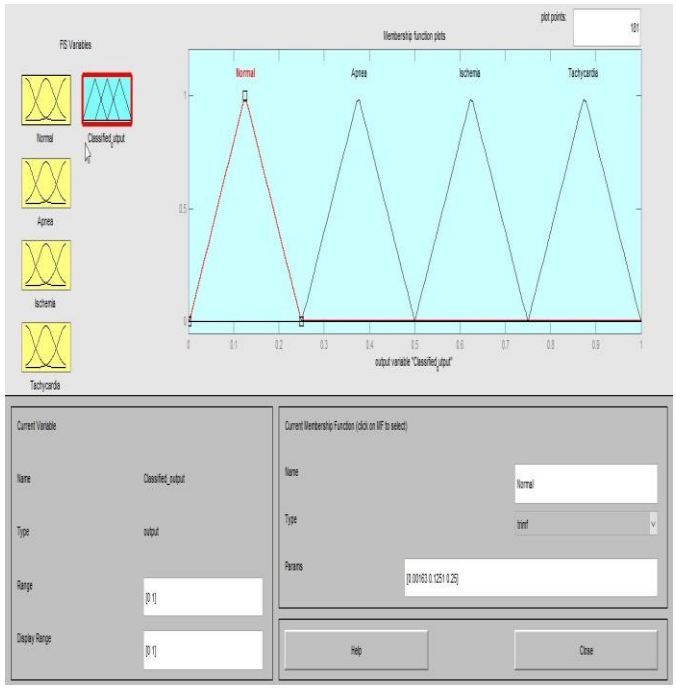


Fig.15. Membership Function for Output

TABLE VI

CONFUSION MATRIX FROM FUZZY

Targets / Outputs	AP	IS	NR	TC	Accuracy
AP	10/12	0/12	0/12	2/12	83.33%
IS	0/12	11/12	0/12	1/12	91.67%
NR	0/12	0/12	12/12	0/12	100%
TC	0/12	0/12	1/12	11/12	91.67%

Then the Fig.14-15 shows the membership functions for the inputs (Gaussian) and outputs (Triangular) respectively. In the Table VI shown is the confusion matrix for the Fuzzy classifier. The table shows good accuracy in classifying the different types of ECG signals used during this project. An accuracy of 91.70% is achieved using this classifier.

V. CONCLUSION

The proposed method in this research paper utilizes Principal Component Analysis (PCA) algorithm to classify the different types of ECG signals viz. Apnea, Ischemia, Normal and Tachycardia signals, used during this research which have different characteristic points obtained using the principal component analysis algorithm. Accuracy obtained with these classifiers is upto 92% (approx..) and hence, this method can also be utilized by the doctors to classify various ECG signals.

This accuracy in classifying these ECG signals can be improved by using the hybrid of the different classifiers as the future work in this.

REFERENCES

[1] Sahil Dalal, Rajesh Birok, ECG Peaks Detection using Principal Component Analysis, International Journal of Innovative Research in Electrical, Electronics, Instrumentation and Control Engineering (under publication).
[2] T.-W. D. Shen, W. J. Tompkins, and Y. H. Hu, "Implementation of a one-lead ECG human identification system on a normal population," *J. Eng. Comput. Innovations*, vol. 2, no. 1, pp. 12–21, Jan. 2011.
[3] A. D. C. Chan, M. M. Hamdy, A. Badre, and V. Badee, "Wavelet distance measure for person identification using electrocardiograms," *IEEE Trans. Instrum. Meas.*, vol. 57, no. 2, pp. 248–253, Feb. 2008.
[4] C.-C. Chiu, C.-M. Chuang, and C.-Y. Hsu, "A novel personal identity verification approach using a discrete wavelet transform of the ECG signal," in *Proc. 2nd Int. Conf. Multimedia and Ubiquitous Engineering*, Busan, Korea, 2008.
[5] J. Yao and Y. Wan, "A wavelet method for biometric identification using wearable ECG sensors," in *Proc. 5th Int. Summer School and Symp. Medical Devices and Biosensors, 2008 (ISSS-MDBS 2008)*, pp. 297–300.
[6] O. Boumbarov, Y. Velchev, and S. Sokolov, "ECG personal identification in subspaces using radial basis neural networks," in *Proc. IEEE Int. Workshop on Intelligent Data Acquisition and Advanced Computing Systems: Technology and Applications, 2009 (IDAACS 2009)*, Sept. 2009, pp. 446–451.
[7] M. Homer, J. M. Irvine, and S. Wendelken, "A model-based approach to human identification using ECG," in *Proc. SPIE*, Orlando, FL, 2009, vol. 7306.
[8] F. Agrafioti and D. Hatzinakos, "Signal validation for cardiac biometrics," in *Proc. 2010 IEEE Int. Conf. Acoustics Speech and Signal Processing (ICASSP)*, Mar. 2010, pp. 1734–1737.
[9] A. Lourenço, H. Silva, and A. Fred, "Unveiling the biometric potential of finger-based ECG signals," *Computat. Intell. Neurosci.*, vol. 2011, no. 720971, 2011.
[10] B.U. Kohler, C. Hennig, R. Orglmeister, The principles of software QRS detection, IEEE Eng. Med. Biol. Mag. 21 (1) (2002) 42–57.
[11] C. Saritha, V. Sukanya, Y. Narasimha Murthy, ECG analysis using wavelets, Bulg. J. Phys. 35 (2008) 68–77.
[12] P. Ranjith, ECG analysis using wavelet transform: application to myocardial ischemia detection, ITBM-RBM 24 (January) (2003) 44–47.
[13] J. Pan, W.J. Tomkins, A real time QRS detection algorithm, IEEE Trans. Biomed. Eng. 32 (3) (1985).
[14] O. Pahlm, L. Sörnmo, Software QRS detection in ambulatory monitoring – a review, Med. Biol. Eng. Comput. 22 (July) (1984) 289–297.
[15] F. Gritzali, Toward a generalized scheme for QRS detection in ECG waveforms, Signal Process. 15 (September) (1988) 183–192.
[16] G.M. Friesen, T.C. Jannett, M.A. Jadallah, S.L. Yates, S.R. Quint, H.T. Nagle, A comparison of the noise sensitivity of nine QRS detection algorithms, IEEE Trans. Biomed. Eng. 37 (January) (1990) 85–98.
[17] A. Ghaffari, H. Golbayani, M. Ghasemi, A new mathematical based QRS detector using continuous wavelet transform, Comput. Electr. Eng. 34 (2) (2008) 81–91.
[18] A.S.M. Koeleman, H.H. Ros, T.J. van den Akker, Beat-to-beat interval measurement in the electrocardiogram, Med. Biol. Eng. Comput. 23 (August) (1985) 213–219.
[19] Kang-Ping Lin, Walter H. Chang, QRS feature extraction using linear prediction, IEEE Trans. Biomed. Eng. 36 (10) (1989).
[20] I.K. Daskalov, I.A. Dotsinsky, I.I. Christov, Developments in ECG acquisition, preprocessing, parameter measurement and recording, IEEE Eng. Med. Biol. Mag. 17 (September) (1998) 50–58.
[21] Abdulnasir Hossen, Bader Al-Ghunaimi, A wavelet-based soft decision technique for screening of patients with congestive heart failure, Biomed. Signal process. Control 2 (May) (2007) 135–143.
[22] J.G.C. Kemmelings, A.C. Linnenbank, S.L.C. Muilwijk, A. Sippens-Groenewegen, A. Peper, C.A. Grimbergen, Automatic QRS onsetand offset detection for body surface QRS integral mapping of ventricular tachycardia, IEEE Trans. Biomed. Eng. 41 (September) (1994) 830–836.
[23] E.S. Jayachandran, K. Paul Joseph, R. Acharya U, Analysis of myocardial infarction using discrete wavelet transform, J. Med. Syst. 34 (October) (2010) 985–992.
[24] C. Li, C. Zheng, C. Tai, Detection of ECG characteristic points using wavelet transforms, IEEE Trans. Biomed. Eng. 42 (January) (1995) 21–28.
[25] J.S. Sahambi, S. Tandon, R.K.P. Bhatt, Using wavelet transform for ECG characterization, IEEE Eng. Med. Biol. 16 (1) (1997) 77–83.
[26] Themis P. Exarchos et al., Association rule-mining based methodology for automated detection of ischemic ECG beats, IEEE Trans. Biomed. Eng. 53 (8) (2006).

All Rights Reserved © 2016 IJARECE

Energy and Exergy Analysis of Solar Triple Effect Refrigeration Cycle

Manoj Dixit, S. C. Kaushik, and Akhilesh Arora

***Abstract*—In this paper solar driven triple effect refrigeration cycle is investigated from the viewpoint of both energy and exergy concepts of thermodynamics. In this cycle ejector organic Rankine cycle, absorption refrigeration cycle and transcritical CO_2 refrigeration cycles are integrated in order to obtain a range of temperature for varied simultaneous use. Parabolic trough collectors are used to utilize solar thermal energy for driving the refrigeration cycles. Exergy analysis determines the destruction and losses of exergy in various components and hence in overall system. Exergy efficiencies provide measure of approach to ideality while exergy destruction and losses provide measure of the deviation from ideality. Energy efficiency is found to be around 16.42% while exergy efficiency is 1.64%. The maximum thermodynamic irreversibility occurs in parabolic trough collector, followed by generator of absorption refrigeration system, heat recover vapour generator and ejector.**

***Index Terms*—Absorption refrigeration, exergy, solar energy, triple effect.**

I. Introduction

Energy plays a significant role in the development of the world. Refrigeration and air conditioning systems alone accounts for around 30% of the global energy consumption [1]. Also, 45% of the total residential energy consumption is due to air conditioning systems [2]. There are many commercial and industrial applications where cooling is required at different temperatures simultaneously. For example, supermarkets where air conditioning can be provided by absorption refrigeration system, cooling temperatures of 0 to -10 ℃ can be provided by ejector refrigeration system and lower temperatures of around -10 to -30 ℃ can be provided by vapour compression refrigeration system. The integration of these three cooling technologies can provide the different temperatures at different magnitudes simultaneously.

In this paper absorption refrigeration, organic Rankine, ejector refrigeration and transcritical vapour compression refrigeration cycles are combined. The solar heat is used to operate ORC and ARC directly while ERC and VCR cycle are operated by turbine exhaust ant turbine power respectively. For the utilization of solar energy parabolic trough collectors (PTC) are used. For thermodynamic performance both energy and exergy analysis is carried out. Exergy analysis provides more meaningful information as compared to energy analysis. It helps in identifying site, quantity and source of thermodynamic inefficiency. Exergy destruction in each component is evaluated in order to find out the direction for potential improvement. Parametric analysis is done to examine the influence of various operating parameters on the system [3]-[14].

Manuscript received October 12, 2015; revised March 8, 2016.

Manoj Dixit and S. C. Kaushik are with the Centre for Energy Studies, Indian Institute of Technology Delhi, New Delhi, 110016, India (e-mail: mandix@ces.iitd.ac.in, kaushik@ces.iitd.ac.in).

A. Arora is with the Mechanical Engineering Department, Delhi Technological University, Delhi, 110042, India (e-mail: aroraakhilesh@yahoo.com).

II. System Description

The solar driven triple effect cycle consists of parabolic trough collector, absorption refrigeration cycle, organic Rankine cycle, ejector refrigeration cycle and transcritical vapour compression refrigeration cycle as shown in Fig. 1.

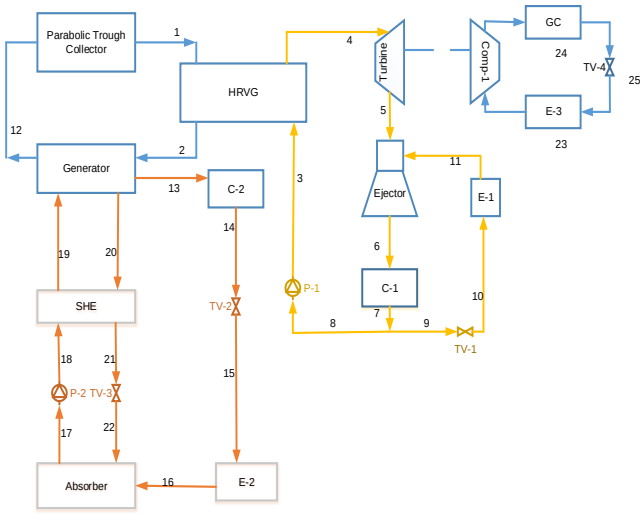


Fig. 1. PTC integrated triple effect refrigeration cycle.

The PTC are suitably employed to harness the maximum available solar energy. The parabolic trough collectors perform better with efficient tracking system. It allows focusing the entire available energy on the metallic tube (receiver) Therminol VP-1 oil is used as the working fluid in the present case. The oil transfers its heat to HRVG (1-2) and generator (2-12). The working substance used in ejector organic Rankine cycle (EORC) is R-141b. The superheated vapour of R-141b (4) is generated in HRVG and expanded in turbine. The turbine exhaust (5) act as a primary motive fluid for ERC (5-6-7-9-10-11). At the exit of the nozzle section of the ejector, the high velocity primary refrigerant vapours create vacuum at the inlet of the mixing chamber and thereby extracting secondary refrigerant vapour (11) from evaporator-1 and causes cooling effect.

The mixture of primary and secondary fluid (6) is condensed in condenser-1. The work output of turbine is fed to compressor of transcritical VCR cycle (23-24-25-26). The

doi: 10.18178/jocet.2017.5.3.373

refrigerant used in the cycle is nitrous oxide (N_2O). The single effect LiBr-H_2O absorption refrigeration cycle (13-14-15-16-17-18-19-20-21-22) consists of generator, condenser-2, evaporator-2, absorber, solution heat exchanger (SHE), pump-2 (P-2) and throttle valves (TV-2 and TV-3). The description of ARC cycle is given elsewhere [15].

III. Thermodynamic Analysis

Principle of mass conservation together with first and second law of thermodynamics is applied in order to carry out the thermodynamic analysis of PTC integrated triple effect cooling system. The general equations are:

$$\sum \dot{m}_i - \sum \dot{m}_o = 0 \tag{1}$$

$$\sum \dot{m}_i x_i - \sum \dot{m}_o x_o = 0 \tag{2}$$

$$\sum \dot{Q} - \sum \dot{W} = \sum \dot{m}_o h_o - \sum \dot{m}_i h_i \tag{3}$$

The second law of thermodynamics facilitates in assessing the performance of the system based on exergy, which always decreases owing to irreversibility.

For a control volume, the exergy flow rate of a fluid, considering only physical exergy, is expressed as:

$$\dot{E} = \dot{m}[(h - h_0) - T_0(s - s_0)] \tag{4}$$

Exergy destruction rate for each component is calculated using equation (4)

$$\dot{E}D = \sum \dot{m}_i \psi_i - \sum \dot{m}_o \psi_o + \left[\sum (\dot{Q}(1 - T_0/T))_i - (Q(1 - T_0/T))_o \right] + \sum \dot{W} \tag{5}$$

TABLE I: Parameters Used in the Modelling

Parameters	Value
Environment temperature (℃)	15
Environment pressure (kPa)	101.35
PTC oil temperature (℃)	160-180
Turbine inlet pressure (kPa)	900-1700
Turbine back pressure (kPa)	220-300
Turbine isentropic efficiency (%)	85
ERC evaporator temperature (℃)	-5
ARC evaporator temperature (℃)	5
VCR evaporator temperature (℃)	-35
Condenser-2 temperature (℃)	35
Gas cooler temperature (℃)	40
Gas cooler pressure (MPa)	8-11
Absorber temperature (℃)	35
Pump isentropic efficiency (%)	70
HRVG efficiency (%)	100
Pinch point temperature difference (℃)	10
Nozzle efficiency (%)	90
Mixing chamber efficiency (%)	85
Diffuser efficiency (%)	85
Length of PTC module (m)	12.27
Width of PTC module (m)	5.76
Total area of PTC field (m^2)	5540
Focal length (m)	1.71
Incidence angle (N-S axis orientation, ٩)	9.48
Receiver tube outer diameter (m)	0.07
Receiver tube inner diameter (m)	0.065
Glass envelope outer diameter (m)	0.115
Glass envelope inner diameter (m)	0.109
Solar beam radiation (W/m^2)	850
Intercept factor (IF)	0.92
Mirror reflectivity (γ_r)	0.92
Glass transmissivity (τ_g)	0.945
Solar absorptivity (α_a)	0.94
Losses due to shading (η_d)	0.98
Heat removal factor (F_r)	0.90
Temperature of sun (K)	5600

The input solar power to the system is the solar power collected by the collectors or mirrors of the PTC and is given as [16]:

$$\dot{Q}_I = I_b A_{sc} \cos\theta \tag{6}$$

where I_b is direct normal radiation (DNI) and θ is the angle of incidence.

The total exergetic solar power input to PTC is given as [17]:

$$\dot{E}_I = \dot{Q}_I \left[1 - \frac{4}{3}\left(\frac{T_a}{T_s}\right) + \frac{1}{3}\left(\frac{T_a}{T_s}\right)^4 \right] \tag{7}$$

where T_s is the apparent black body temperature of the sun and T_a is the ambient temperature.

The solar power absorbed by receiver/absorber of PTC can be estimated by the following equation [16].

$$\dot{Q}_r = I_b.A_{sc}.K(\theta).\gamma_r\tau_g.\alpha_a.\text{IF}.\eta_d.\text{End Loss} \tag{8}$$

TABLE II: Energy and Exergy Relations for the Various Components of Triple Effect Refrigeration Cycle

Component	Energy relations	Exergy relations
HRVG	$\dot{m}_1(h_1 - h_2) = \dot{m}_3(h_4 - h_3)$	$\dot{E}D_{HRVG} = T_0(\dot{m}_2 s_2 - \dot{m}_1 s_1 + \dot{m}_4 s_4 - m_3 s_3)$
Turbine	$\dot{W}_T = \dot{m}_4(h_4 - h_5)$	$\dot{E}D_T = T_0(s_5 - s_4)$
Ejector	$\dot{m}_5 h_5 + \dot{m}_{11} h_{11} = (m_5 + m_{11})h_6$ $\mu = \left[\eta_n \eta_m \eta_d (h_{pf,n1} - h_{pf,n2,s}) / (h_{mf,d,s} - h_{mf,m}) \right]^{0.5} - 1$	$\dot{E}D_{ej} = T_0(\dot{m}_6 s_6 - \dot{m}_5 s_5 - m_{11} s_{11})$

Condenser-1	$\dot{Q}_{c1} = \dot{m}_6(h_6 - h_7)$	$\dot{E}D_{c1} = \dot{m}_6(h_6 - T_0 s_6) - m_7(h_7 - T_0 s_7)$
Evaporator-1	$\dot{Q}_{e1} = \dot{m}_{11}(h_{11} - h_{10})$	$\dot{E}D_{e1} = T_0(\dot{m}_{11}s_{11} - \dot{m}_{10}s_{10} - \dot{Q}_{e1}/T_{e1})$
Generator	$\dot{Q}_g = \dot{m}_f(h_2 - h_{12}) = \dot{m}_{13}h_{13} + m_{20}h_{20} - m_{19}h_{19}$	$\dot{E}D_g = T_0(\dot{m}_{20}s_{20} + \dot{m}_{13}s_{13} + \dot{m}_{12}s_{12} - m_{19}s_{19} - m_2 s_2)$
Absorber	$\dot{Q}_a = \dot{m}_{16}h_{16} + \dot{m}_{22}h_{22} - m_{17}h_{17}$	$\dot{E}D_a = T_0(\dot{m}_{17}s_{17} - \dot{m}_{16}s_{16} - m_{22}s_{22} - \dot{Q}_a/T_a)$
Condenser-2	$\dot{Q}_{c2} = \dot{m}_{13}(h_{13} - h_{14})$	$\dot{E}D_{c2} = T_0(\dot{m}_{14}s_{14} - \dot{m}_{13}s_{13} - \dot{Q}_{c2}/T_{c2})$
Evaporator-2	$\dot{Q}_{e2} = \dot{m}_{16}(h_{16} - h_{15})$	$\dot{E}D_{e2} = T_0(\dot{m}_{16}s_{16} - \dot{m}_{15}s_{15} - \dot{Q}_{e2}/T_{e2})$
Compressor	$\dot{W}_{comp1} = \dot{m}_{24}(h_{24} - h_{23})$	$\dot{E}D_{comp} = T_0\dot{m}_{24}(s_{24} - s_{23})$
Evaporator-3	$\dot{Q}_{e3} = \dot{m}_{23}(h_{23} - h_{26})$	$\dot{E}D_{e3} = T_0(\dot{m}_{23}s_{23} - \dot{m}_{26}s_{26} - \dot{Q}_{e3}/T_{e3})$
GC	$\dot{Q}_{gc} = \dot{m}_{24}(h_{24} - h_{25})$	$\dot{E}D_{gc} = T_0(\dot{m}_{25}s_{25} - \dot{m}_{24}s_{24} - \dot{Q}_{gc}/T_{gc})$
SHE	$\dot{m}_{20}h_{20} - \dot{m}_{21}h_{21} = \dot{m}_{19}h_{19} - m_{18}h_{18}$	$\dot{E}D_{she} = T_0[\dot{m}_{19}(s_{19} - s_{18}) + m_{21}(s_{21} - s_{20})]$
TV-1	$h_9 = h_{10}$	$\dot{E}D_{tv1} = T_0\dot{m}_{10}(s_{10} - s_9)$
TV-2	$h_{14} = h_{15}$	$\dot{E}D_{tv2} = T_0\dot{m}_{15}(s_{15} - s_{14})$
TV-3	$h_{21} = h_{22}$	$\dot{E}D_{tv3} = T_0\dot{m}_{22}(s_{22} - s_{21})$
TV-4	$h_{26} = h_{27}$	$\dot{E}D_{tv4} = T_0\dot{m}_{27}(s_{27} - s_{26})$
Pump-1	$\dot{W}_{p1} = \dot{m}_3(h_3 - h_8)$	$\dot{E}D_{p1} = T_0\dot{m}_3(s_3 - s_9)$
Pump-2	$\dot{W}_{p2} = \dot{m}_{18}(h_{18} - h_{17})$	$\dot{E}D_{p2} = T_0\dot{m}_{18}(s_{18} - s_{17})$

The End Losses are the function of the focal length of collector (f), the length of the collector (L) and the incident angle [18].

$$\text{End Loss} = 1 - f.\tan\theta / L \quad (9)$$

The incident angle affects the direct normal irradiation on the mirror aperture. This effect is accounted for by the incident angle modifier ($K(\theta)$) which is given by [19].

$$K(\theta) = \cos\theta - 2.859621\times10^{-5}.\theta^2 - 5.25097\times10^{-4}.\theta \quad (10)$$

The total exergetic solar power absorbed by the receiver /absorber of PTC is given by

$$\dot{E}_r = Q_r(1 - T_a/T_r) \quad (11)$$

The useful thermal power gain (Q_u) by thermic fluid is given by

$$\dot{Q}_u = m_f C_{pf}(T_{f,o} - T_{f,i}) \quad (12)$$

The useful thermal power gain can also be expressed as:

$$\dot{Q}_u = F_r[\dot{Q}_r - U_l A_r(T_{f,i} - T_a)] \quad (13)$$

The useful exergetic gain (Ex_u) by thermic fluid is given by

$$\dot{E}_u = \dot{m}_f[(h_{f,o} - h_{f,i}) - T_0(s_{f,o} - s_{f,i})] \quad (14)$$

In order to carry out thermodynamic analysis of such complex system, certain assumptions are required to simplify the analysis. The system operates under steady state condition, Pressure loss and pump work are neglected, the states of fluid at the exit of condenser and evaporator are saturated liquid and saturated vapor respectively, only physical exergy is considered and Lithium bromide solution in the absorber and generator are in equilibrium state at their respective pressure and temperature. The required operating parameters for the thermodynamic analysis are given in Table I. The relations obtained by the application of energy and exergy balance to each component of ARC, EORC and VCRC are outlined in Table II.

The performance of the system, based on first law of thermodynamics, can be evaluated using thermal efficiency (η_{th}) which is defined as the ratio of the desired cooling effect to the heat input. The thermal efficiency of solar triple effect system is expressed as:

$$\eta_{th} = (\dot{Q}_{e1} + \dot{Q}_{e2} + \dot{Q}_{e3}) / Q_I \quad (15)$$

where $\dot{Q}_I$ is the total solar power input to the system and $\dot{Q}_{e1}$, $\dot{Q}_{e2}$ and $\dot{Q}_{e3}$ are the refrigeration effect in ERC, ARC and VCRC respectively.

The exergy efficiency is expressed on the basis of second law of thermodynamics as

$$\eta_{ex} = (\Delta\dot{E}_{e1} + \Delta\dot{E}_{e2} + \Delta\dot{E}_{e3}) / E_I \quad (16)$$

where $\dot{E}_I$ is the total exergetic solar power input to the system and $\Delta\dot{E}_{e1}$, $\Delta\dot{E}_{e2}$, and $\Delta\dot{E}_{e3}$ are the exergy change in evaporator-1 of ERC, evaporator-2 of ARC and evaporator-3 of VCRC respectively, which are expressed as:

$$\Delta \dot{E}_{e1} = \dot{E}_{11} - E_{10} \quad (17)$$

$$\Delta \dot{E}_{e2} = \dot{E}_{16} - E_{15} \quad (18)$$

$$\Delta \dot{E}_{e3} = \dot{E}_{34} - E_{33} \quad (19)$$

IV. Results and Discussion

Based on the thermodynamic relations, a program is developed in Engineering Equation Solver (EES) [20]. The results thus obtained are presented and discussed in this section. For the base case calculations, oil temperature at PTC outlet is considered as 170 ℃, turbine inlet pressure is 900 kPa, turbine back pressure is 220 kPa and gas cooler pressure is 9320 kPa. In order to carry out the parametric analysis, one parameter is varied while others remain constant.

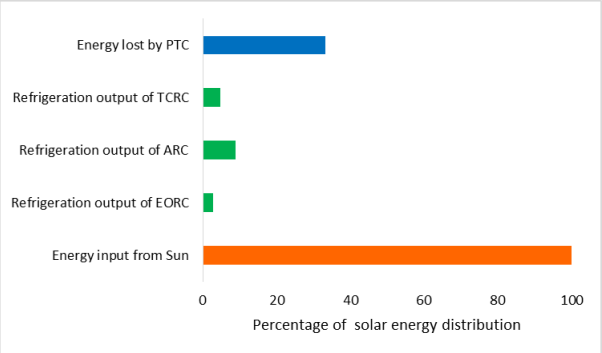


Fig. 2. Percentage of solar energy distribution for solar triple effect refrigeration cycle.

Fig. 2 shows the distribution of total solar energy falling on PTC for the base case. Out of the total energy input to the system, only 16.42% is obtained as desired refrigeration output, while rest of the solar energy is wasted. The refrigeration output of EORC, ARC and VCRC are respectively 2.85%, 8.82% and 4.75 % of the total solar energy input. PTC is a major component of input energy loss as around 33% of input solar energy is wasted by it.

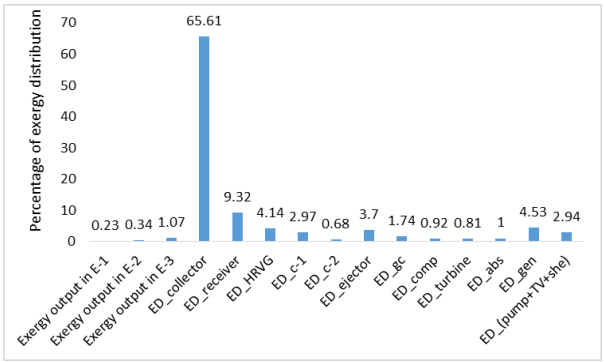


Fig. 3. Percentage of solar exergy distribution in output and destruction for solar triple effect refrigeration cycle.

Application of exergy analysis to the system provides valuable information on exergy distribution and destruction, as shown in Fig. 3. It is clear from the figure that out of the total solar exergy available to the system, only 1.64% is obtained as desired refrigeration output while remaining 98.36% undergoes destruction and loss. The collection subsystem of PTC is the major source of thermodynamic inefficiency as it accounts for 65.61% destruction of solar exergy input to the system, followed by receiver of PTC, generator, HRVG, ejector and condenser-1. Thus, exergy analysis makes it clear that special attention needs to be given to these components while selecting their design and operating parameters, so as to enhance the performance of the complete system.

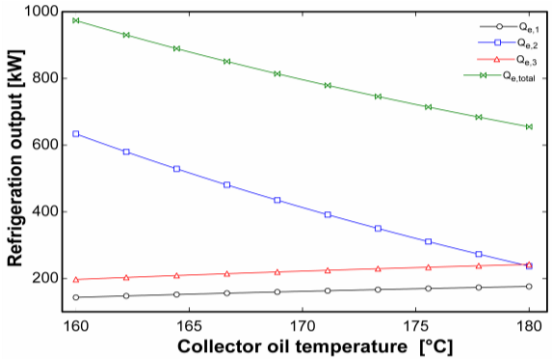


Fig. 4. Effect of collector oil temperature on refrigeration output.

Fig. 4 shows the variation of refrigeration output of EORC, ARC and VCRC with the increase in temperature of oil at PTC outlet (point 1). It is found in the analysis that refrigeration output of ARC decreases while that of EORC and VCRC increases with the increase in oil temperature. As oil temperature increases from 160 ℃ to 180 ℃, the refrigeration output of both EORC and VCRC increases by almost 23%. Increased temperature results in better quality of refrigerant vapour at turbine inlet, thus more power is available from turbine to VCRC. This causes increased mass flow rate of refrigerant through evaporator-3, resulting in increased refrigerating effect in VCRC. Also, improved quality of vapour refrigerant at turbine inlet results in better quality of refrigerant at the exit of turbine. This causes increase in velocity of primary motive fluid at nozzle exit, which creates greater vacuum at secondary vapour entrance to ejector. This causes more secondary refrigerant to flow through evaporato-3 and hence higher refrigerating effect in EORC. The cooling capacity of ARC reduces by 62.62% with the increase in oil temperature within the given range. The fall in cooling capacity of ARC is because of the decrease in oil temperature at the exit of HRVG (point 2). Thus input heat to ARC decreases which causes lesser refrigerant (water) generation in the generator. The magnitude of refrigeration output of ARC is much more than that of EORC and VCRC, therefore, the total refrigeration output follows the trend of variation of refrigeration output of ARC. The total cooling capacity of the system registers a decline of 32.72% with the increase in oil temperature from 160 ℃ to 180 ℃.

Fig. 5 represents the variation of first law based thermal efficiency and second law based exergy efficiency with oil temperature. Appreciable drop in thermal efficiency of the system is observed with the rise in temperature of oil, whereas exergy efficiency remains almost constant with the change in temperature. The decrease in thermal efficiency is around 32%, and it is so because of drastic fall in overall cooling capacity with the increase in oil temperature.

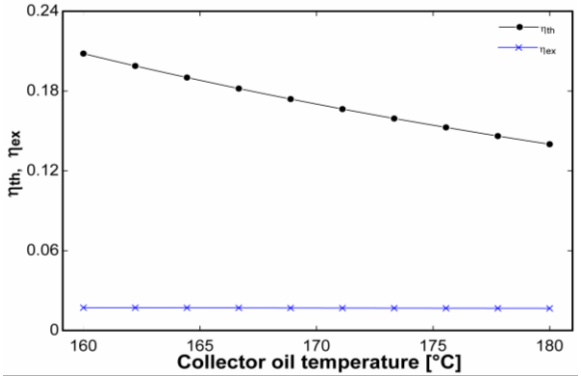


Fig. 5. Variation of efficiency with collector oil temperature.

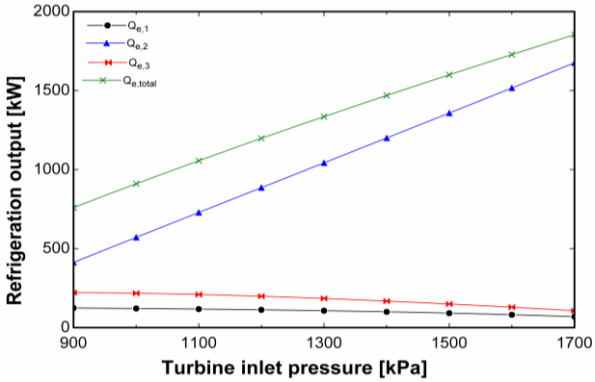


Fig. 6. Variation of refrigeration output with turbine inlet pressure.

Fig. 6 shows the effect of turbine inlet pressure on cooling capacities of EORC, ARC and VCRC and on total cooling capacity. Increase in turbine inlet pressure from 900 kPa to 1700 kPa causes reduction in cooling capacities of EORC and VCRC by 43.79% and 51.67% respectively. Contrary to this, the cooling capacity of ARC increases with increase in turbine inlet pressure. It is more than three times at 1700 kPa than at 900 kPa. Consequently, total cooling capacity registers an increase of 144%. Thus it can be said that turbine inlet pressure has profound effect on cooling capacity. The rise of turbine inlet pressure reduces the mass flow rate of refrigerant (R141b) vapours generated in HRVG. Thus, heat input to EORC decreases whereas heat input to ARC increases. Lower mass flow rate and lower heat input in EORC results in lower refrigeration and power output. Lower power generation in EORC causes lower power input to VCRC and thus lower refrigeration output of VCRC. Increase in availability of heat to ARC results in increase in cooling capacity of ARC.

Fig. 7 shows the variation of energy and exergy efficiency of solar driven triple effect refrigeration system with increase in turbine inlet pressure. The thermal efficiency increases significantly as compared to exergetic efficiency. The increase in thermal and exergetic efficiency, with the increase in turbine inlet pressure, is 144% and 24% respectively.

The effect of gas cooler pressure on refrigeration output is shown in Fig. 8. The gas cooler pressure is varied between 8000 kPa and 11000 kPa. The increase in gas cooler pressure affects only the output of VCRC, the outputs of ARC and EORC remains unaffected. With the increase in gas cooler pressure, refrigeration output of VCRC first increases and then starts decreasing. Therefore, there is a particular value of gas cooler pressure corresponding to which cooling capacity of VCRC and hence total cooling capacity is maximum. The gas cooler pressure corresponding to maximum cooling capacity for the base case is 9333 kPa.

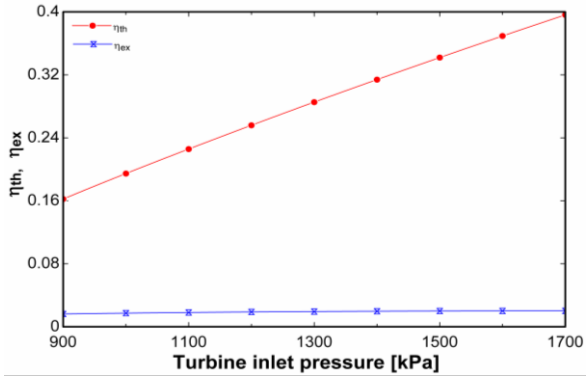


Fig. 7. Variation of efficiency with turbine inlet pressure.

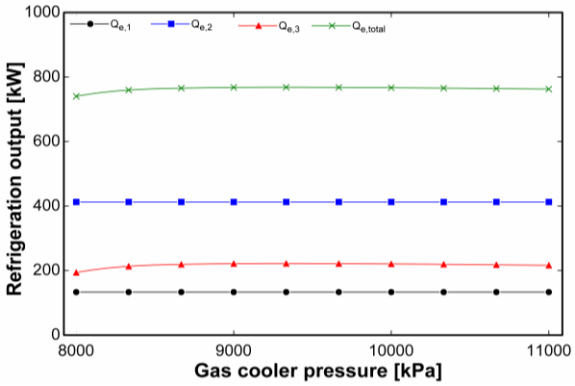


Fig. 8. Variation of refrigeration output with gas cooler pressure.

Fig. 9 shows the variation of thermal efficiency and exergy efficiency with increase in gas cooler pressure. Like cooling capacity, both thermal and exergetic efficiencies attains a maximum value at a particular gas cooler pressure. The gas cooler pressure corresponding to maximum thermal efficiency and maximum exergetic efficiency is same. The maximum values of thermal and exergetic efficiencies, for the base case, are 16.43% and 1.64% respectively and the corresponding gas cooler pressure is 9333 kPa. Thus, it can be concluded that maximum refrigeration output, maximum thermal efficiency and maximum exergetic efficiency are obtained at same gas cooler pressure, other conditions being constant.

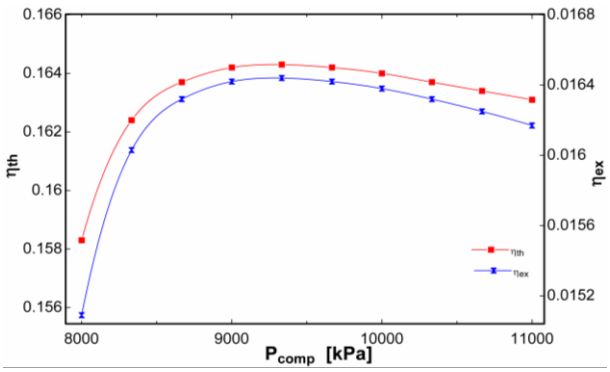


Fig. 9. Variation of efficiency with gas cooler pressure.

V. Conclusion

Based on the energy and exergy analysis of solar triple

effect refrigeration cycle, following conclusions can be made.

1) Irreversibility is maximum due to PTC, generator, HRVG and ejector. Therefore, design of these components requires extra attention for better performance of the system.
2) Exergy output of solar triple effect cycle is much less than energy output. About 16.82% is obtained as desired energy output while only 1.64% is obtained as desired exergy output.
3) The exergy output of VCRC is much more than the exergy output of ARC and EORC for a given solar energy source. It is 1.07% for VCRC while for ARC it is 0.34% and for EORC it is merely 0.23%.
4) Maximum energy and exergy efficiency occurs at a particular gas cooler pressure for given set of conditions.

ACKNOWLEDGMENT

The support of Ministry of New and Renewable Energy (MNRE), Government of India, is duly acknowledged.

REFERENCES

[1] L. O. S. Buzelin, S. C. Amico, J. V. C. Vargas, and J. A. R. Parise, "Experimental development of an intelligent refrigeration system," *International Journal of Refrigeration*, vol. 28, pp. 165–175, 2005.
[2] B. Choudhury, P. K. Chatterjee, and J. P. Sarkar, "Review paper on solar-powered air conditioning through adsorption route," *Renewable and Sustainable Energy Reviews*, vol. 14, pp. 2189-2195, 2010.
[3] B. F. Tchanche, G. Lambrinos, A. Frangoudakis, and G. Papadakis, "Low-grade heat conversion into power using organic Rankine cycle – a review of various applications," *Renewable and Sustainable Energy Reviews*, vol. 15, no. 8, pp. 3963-3979, 2011.
[4] D. Sun, I. W. Eames, and S. Aphornratana, "Evaluation of a novel combined ejector refrigeration cycle-I: computer simulation," *International Journal of Refrigeration*, vol. 19, pp. 172-180, 1996.
[5] D. Hong, G. Chen, L. Tong, and Y. He, "A novel ejector-absorption combined refrigeration cycle," *International Journal of Refrigeration*, vol. 34, pp. 1596-1603, 2011.
[6] J. Wang, Y. Dai, and Z. Sun, "A theoretical study on a novel combined power and ejector refrigeration cycle," *International Journal of Refrigeration*, vol. 32, pp. 1186-1194, 2009.
[7] Y. Dai, J. Wang, and L. Gao, "Exergy analysis, parametric analysis and optimization for a novel combined power and ejector refrigeration cycle," *Applied Thermal Engineering*, vol. 29, pp. 1983-1990, 2009.
[8] D.Y. Goswami and F. Xu, "Analysis of a new thermodynamic cycle for combined power and cooling using low and mid temperature solar collectors," *Journal of Solar Energy Engineering*, vol. 121, no. 2, pp. 91-97, 1999.
[9] A. A. Hasan, D. Y. Goswami, and S. Vijayaraghavan, "First and second law analysis of new power and refrigeration thermodynamic cycle using solar heat source," *Solar Energy*, vol. 73, no. 5, pp. 385-393, 2002.
[10] C. Martin and D. Y. Goswami, "Effectiveness of cooling production with a combined power and cooling thermodynamic cycle," *Applied Thermal Engineering*, vol. 26, pp. 576-582, 2006.
[11] N. Zhang and N. Lior, "Methodology for thermal design of novel combined refrigeration/power binary fluid systems," *International Journal of Refrigeration*, vol. 30, no. 6, pp. 1072-1085, 2007.
[12] B. K. Agrawal and M. N. Karimi, "Thermodynamic performance assessment of a novel waste heat based triple effect refrigeration cycle," *International Journal of Refrigeration*, vol. 35, pp. 1647–1656, 2012.
[13] A. Khaliq, R. Kumar, I. Dincer, and F. Khalid, "Energy and exergy analyses of a new triple-staged refrigeration cycle using solar heat source," *Journal of Solar Energy Engineering*, vol. 136, no. 1, 2013.
[14] A. Khaliq, "Performance analysis of a waste-heat-powered thermodynamic cycle for multi-effect refrigeration: Waste-heat-driven multi-effect cooling cycle," *International Journal of Energy Research*, vol. 39, pp. 529-542, 2015.
[15] K. E. Herold, R. Radermacher, and S. A. Klein, *Absorption Chillers and Heat Pumps*, USA: CRC Press, 1996.
[16] V. S. Reddy, S. C. Kaushik, and S. K. Tyagi, "Exergetic analysis and performance evaluation of parabolic trough concentrating solar thermal power plant (PTCSTPP)," *Energy*, vol. 39, no. 1, pp. 258–273, 2012.
[17] R. Petela, "Exergy of heat radiation," *Journal of Heat Transfer*, vol. 86, pp. 187-192, 1964.
[18] F. Lippke, "Simulation of the part-load behaviour of a 30 MWe SEGS plant," Report No. SAND95-1293, SNL, Alburquerque, NM, USA, 1995.
[19] M. J. Montes, A. Abanades, J. M. Martinez-Val, and M. Valdes, "Solar multiple optimization for a solar only thermal power plant using oil as heat transfer fluid in the parabolic trough collectors," *Solar Energy*, vol. 83, pp. 2165-2176, 2009.
[20] S. A. Klein and F. Alvarado, *Engineering Equation Solver (EES)*, WI: F-Chart Software, 2005.



Manoj Dixit is a Ph.D. research scholar in the Centre for Energy Studies at Indian Institute of Technology (IIT), Delhi, India. He completed his M.Tech. degree in thermal engineering from Delhi Technological University (erstwhile Delhi College of Engineering), Delhi in 2012. His research areas of interest are solar cooling, thermal system design, analysis, and optimization and energy conservation, and heat recovery.



S. C. Kaushik is a professor in the Centre for Energy Studies at Indian Institute of Technology (IIT), Delhi. He received his Ph.D. in plasma science from IIT Delhi after his distinguished first position in master's degree in science (electronics) from Meerut University. His research fields of activities include thermal science and engineering, energy conservation and heat recovery, solar refrigeration and airconditioning, solar architecture, and thermal storage and power generation. He has made significant contributions in these fields as evident by his above 300 research publications in journals of repute at national and international levels. He is a pioneer researcher on exergy analysis and finite time thermodynamics of energy systems at national & international level and a leading expert on alternative refrigeration and air conditioning technologies. He has co-authored/ edited several books on energy related topics in his academic carrier.



Akhilesh Arora is working as an assistant professor in the Department of Mechanical Engineering at Delhi Technological University (erstwhile Delhi College of Engineering) Delhi since 2004. Prior to joining Delhi College of Engineering, he has also worked at the College of Military Engineering, Pune in the capacity of lecturer for two years. He obtained his Ph.D. and master degrees from the Indian Institute of Technology, Delhi, in 2010 and 1997 respectively. His research area is refrigeration and air-conditioning, thermal science and engineering, energy conservation and heat recovery. He has published number of research papers in international and national journals.

Wind Energy

IJAPIE-2016-07-307,VOL 1(3), 32-36

INTERNATIONAL JOURNAL OF ADVANCED PRODUCTION AND INDUSTRIAL ENGINEERING

(A Blind Peer Reviewed Journal)

Friction Stir Processed Copper Studies with Carbon Nanotubes

V.Jeganathan Arulmoni[1], R.S. Mishra[2]

[1,2] *(Mechanical Engineering, Delhi Technological University, Delhi, India)*

Email: v.jeganathan.dce@gmail.com

Abstarct : *FSP has been successfully applied to various cast aluminium and magnesium and copper alloys to eliminate casting defects and thereby improve their mechanical properties. Processing parameters such as tool geometry, tool rotational speed, tool tilt angle, processing speed, axial load and groove width &depth have been studied along with their effect. The hardness number comes out to be highest for third pass in comparing with single and double passes. Microstructure obtained gets more compact and defect free as number of passes increases.*

Keywords: *Friction stir processing, copper, carbon nanotubes, microstructure, wear, mechanical properties.*

INTRODUCTION

Friction stir processing (FSP) is used to enhance ductility, induces super plasticity and improve corrosion resistance properties. Friction stir processing (FSP) was developed for microstructural modification of metallic materials where the tool consists of a shoulder and a pin. One of the main function of the tool is to 'stir' and 'move' the material. Tool rotational speed and feed depends upon the hardness of the material. An increase in traverse speed and decrease in rotation of the FSP tool may cause reduction in the grain size of the stir zone for the specimen friction stir processed without any metal particles. Higher traverse speed affect microhardness. Addition of metal powder non-metallic powder and nano materials found increasing the wear resistance of the material. Axial load is the force acting upon the FSP tool which helps the tool pin plunge into the material. Groove width and depth depends upon the amount of metal powder non-metallic powder and nano materials to be used to make the metal matrix also it depends upon the depth of composite material.

The main objective of this paper is to discuss the study of FSP of copper with use of carbon nanotubes. The effect of FSP parameters such as tool rotational speed, processing speed, axial load, groove width and depth on microstructure and micro hardness investigated. Carbon nanotube particle were used in the processing and its effect on process parameters of FSP is determined. Microstructure of processed copper with and without CNT in multiple passes are discussed.

II. EXPERIMENTAL RESULTS

The experiments have been performed on friction stir processing machine shown in figure1. The experimental work is conducted as per the following steps:

1. Preparation of the work piece and tool
2. Filling carbon nanotube material in the groove
3. Friction stir Processing
4. Preparation of specimens for tests
5. Tensile, Hardness and microstructure tests conducted



Fig. 1. Friction stir welding / processing machine

Dimension of the work piece produced are as follows:

Length (mm)	200 mm
Breadth (mm)	75 mm
Thickness (mm)	8 mm

Dimension of groove are as follows:

Depth of cut (mm)	2.5 mm
Width (mm)	1.0 mm

For making the groove of 1mm width, cutter of 1mm thickness is used. Material of cutter is High Speed Steel (HSS). The Tool used for friction stir processing is a Cylindrical Threaded Tool made up of High Speed Steel (HSS). Tool is "Vacuum Hardened" to 60 BHN.

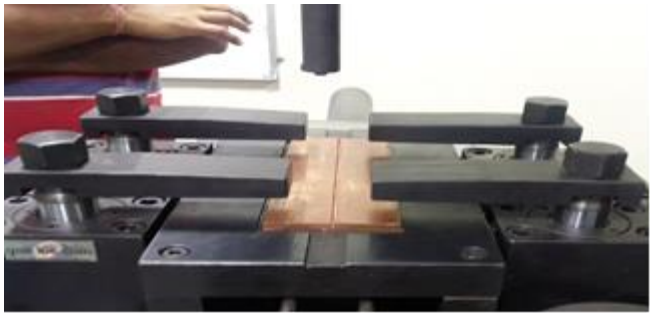


Fig. 2. Work piece fitted on the FSP Machine



Fig. 3. Tools used during Friction stir processing



Fig. 4. Cylindrical Threaded Tool Probe

Dimension of the tool are as follows:

Length of tool	120mm
Diameter of the tool	19.95mm
Length of the probe	3mm
Diameter of the probe	7mm

Cylindrical threaded tool have certain advantages over the cylindrical tool are as:

1) Better processing results
2) Reduce weld force
3) Enable easies flow of plasticized material
4) Increase interface between the pin and the plasticized material, thereby increasing heat generation.

Properties of Carbon Nano tube powder are as follows:

Diameter	50-85nm
Length	10-15 micrometer
Nitrogen surface area	10-90 m2/gm
Volume resistivity	2i<< 5*10-4ohm-cm
Carbon content	>94%

Advantages of using Carbon Nano tube powder in the Processing:

- Develop High Tensile strength in the material upto 63 GPascals.
- Leads to strong interfacial adhesion
- Increases stiffness and strength of the material.

The parameters used during processing are as follows:

Load (Kg)	1000 kg
Feed (mm/min)	20 mm/min
Rotational speed of tool (rpm)	1100rpm

These parameters are kept constant during the processing. For Analysis of the micro structure and mechanical properties, the processing is done in “Multiple Passes” on the work pieces.



Fig. 5. Tensile test specimens cut from processed Area

Tensile test determines the strength of the material subjected to a simple stretching operation. The primary use the testing machine is to create the stress-strain graph. The aim of the test is to asses some mechanical characteristics of the testing material. The results of the tensile tests are used in selecting materials for engineering applications. Tensile properties

frequently are included in material specifications to ensure quality.

In this project we are determining the tensile strength of specimens of multi passed friction stir processed copper.

A universal testing machine (UTM) is used to test the tensile strength and compressive strength of the materials. The result of tensile test is shown in table1.

Table 1: Specimen Details and output Results during Tensile Tests

Output(Generic metals tensile from position)	**Without processing**	**Single pass without CNT**	**Single pass with CNT**	**Two pass with CNT**	**Three pass with CNT**
Width(mm)	5.98	6.01	6.01	6.01	6.0
Thickness(mm)	5.87	5.81	5.81	5.66	5.79
Gauge Length (initial)(mm)	25	25	25	25	25
Gauge Length(final) (mm)	32.9	46.4	31.5	28.7	29.1
Area (mm^2)	35.1	34.9	34.9	34	34.7
Ultimate Force(N)	8560	6840	2520	2570	4340
Ultimate Stress(MPa)	244	196	72.1	75.5	125
Offset @ 0.2%(N)	7600	4120	1610	2340	3760
Offset @ 0.2% (MPa)	217	118	46.2	68.7	108
TE(Auto)(%)	30.5	91	24.6	13.3	16.0

The stress-strain curves for respective specimens are shown as:-

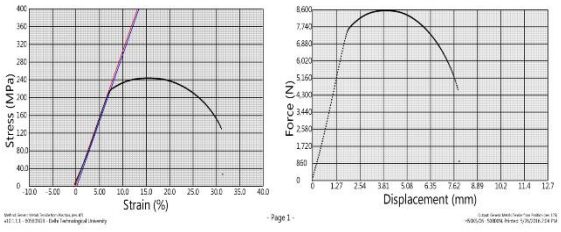


Fig 6: Stress-Strain and Displacement curve for Specimen without processing

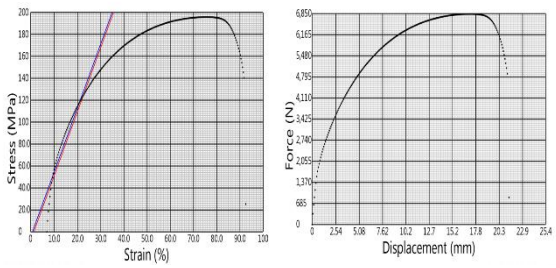


Fig 7: Stress-Strain and Displacement curve for Specimen without CNT processing

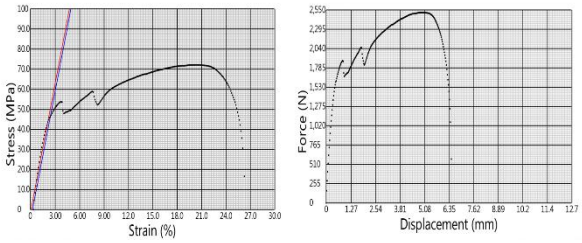


Fig 8: Stress-Strain and Displacement curve for Specimen without CNT processing

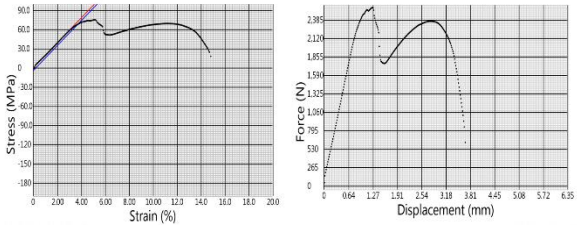


Fig 9: Stress-Strain and Displacement curve for Specimen with CNT double pass processing

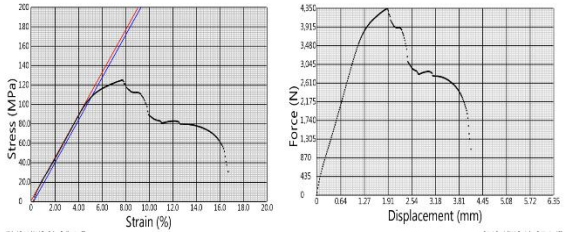
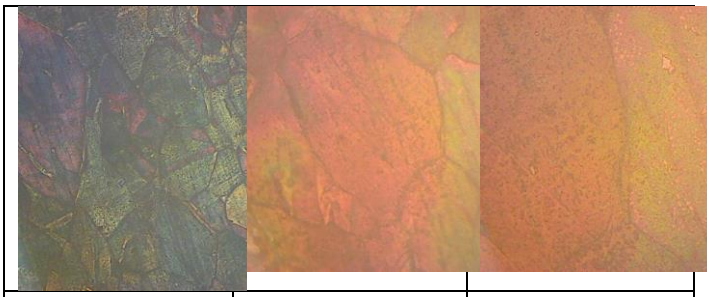


Fig 10: Stress-Strain and Displacement curve for Specimen with CNT triple pass processing

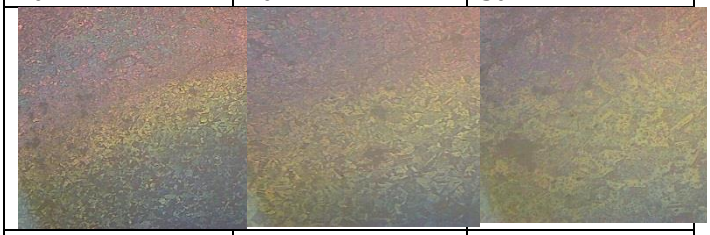
Table 2: Rockwell hardness test results

Sr. No.	Specimen	Rockwell hardness test (HRB)	Brinell hardness number(BHN)
1.	Base metal	32-36	147
2.	Specimen Processed without CNT	95	210
3.	Processed with CNT single pass	102	253
4.	Processed with CNT double pass	112	371
5.	Processed with CNT triple pass	118	487

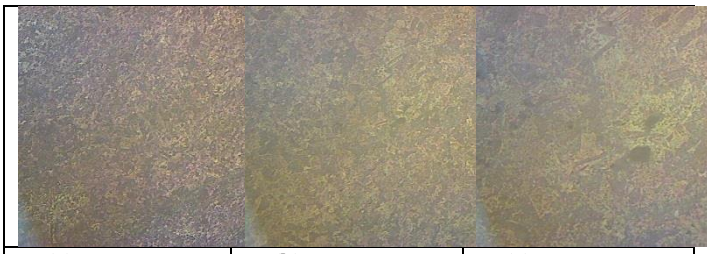
Output result from the hardness test is shown table 2. Test was performed on Rockwell hardness machine, corresponding result is converted to Brinell hardness number. In the above result as the processes increases with multiple passes hardness also increases.



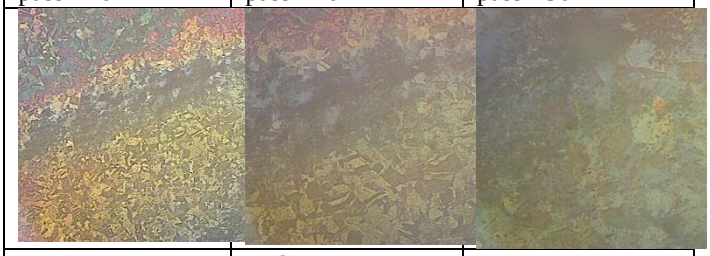
11(a) Specimen at 10x	11(b) Specimen at 20x	11(c) Specimen at 50x



12(a) Specimen without CNT with singlepass- Specimen at 10x	12(b) Specimen without CNT with singlepass- Specimen at 20x	12(c) Specimen without CNT with singlepass- Specimen at 50x



13(a) Specimen with CNT single pass- 10x	13(b) Specimen with CNT single pass- 20x	13(c) Specimen with CNT single pass- 50x



14(a) Specimen with CNT double pass- 10x	14(b) Specimen with CNT double pass- 20x	14(c) Specimen with CNT double pass- 50x



15(a) Specimen with CNT triple pass- 10x	15(b) Specimen with CNT triple pass- 20x	15(c) Specimen with CNT triple pass- 50x

CONCLUSION

In this study the following conclusions are made on the basis of tests performed:

The ultimate tensile strength of the processed material comes out to be lesser than the parent material.

Hardness of the processed specimens increases as the number of passes are increased due to more compact microstructure. The hardness number comes out to be highest for third pass in comparing with single and double passes.

Microstructure obtained gets more compact and defect free as number of passes increases.

In tensile testing, the ultimate force decreases from 8560 to 6840 N from base material to single pass specimen without CNT. But in case Specimens with CNT with single, double and triple passes the ultimate force increases.

REFERENCES

[1] H. Sarmadi , A.H.Kokabi,S.M.Seyed Reihani, [2013] Friction and wear performance of copper–graphite surface composites fabricated by friction stir processing (FSP),Wear, 304, pp1–12

[2] I. Galvao, A. Loureiro and D. M. Rodrigues,[2012] Influence of process parameters on the mechanical enhancement of copper-DHP by FSP, Advanced Materials Research, 445, pp 631-636

[3] I. Galvao, R.M. Leal, D.M. Rodrigues, A. Loureiro, [2013] Influence of tool shoulder geometry on properties of friction stir welds in thin copper sheets,Journal of Materials Processing Technology , 213, pp129–135

[4] R. Sathiskumar , N. Murugan , I. Dinaharan , S.J. Vijay, [2014] Prediction of mechanical and wear properties of copper surface composites fabricated using friction stir processing,Materials and Design , 55, pp224–234

[5] R. Sathiskumar, N. Murugan, I. Dinaharan, S.J. Vijay, [2013] Characterization of boron carbide particulate reinforced in situ copper surface composites synthesized using friction stir processing,Materials Characterization, 84, pp1 6 – 2 7

[6] R Sathiskumar, N Murugan, I Dinaharan and S J Vijay, [2013] Role of friction stir processing parameters on microstructure and microhardness of boron carbide particulate reinforced copper surface composites, Indian Academy of Sciences, Sadhana, 38(6), pp. 1433–1450

[7] Ranganath. M. S, R. C. Singh , Rajiv Chaudhary, R.K. Pandey, Experimental Investigation of Friction and Wear Behavior at the Interface of Aluminium and Mild Steel, International Journal of Advance Research and Innovation, 2(4), 2014, 775-780

[8] S. Mukherjee, A.K. Ghosh, [2011] Friction stir processing of direct metal deposited copper–nickel 70/30,Materials Science and Engineering A , 528, pp3289–3294

[9] Salar Salahi and Vahid Rezazadeh, [2013] Fracture Mechanism in Friction Stir Processed Annealed Pure Copper Samples,World Applied Sciences Journal , 23(12), pp54-58

[10] V.Jeganathan Arulmoni, R S Mishra, Friction Stir Processing of Aluminum alloys for Defence Applications, International Journal of Advance Research and Innovation, Volume 2, Issue: 2 , 2014 pp 337-341 , ISSN 2347 - 3258

[11] V.Jeganathan Arulmoni, Ranganath M S , R S Mishra, Effect of Process Parameters on Friction Stir Processed Copper and Enhancement of Mechanical Properties of the Composite Material: A Review on Green Process Technology, International Research Journal of Sustainable

Science & Engineering, Volume 2, Issue: 4 , 2014 pp 1-10 , 2347-6176 ,IRJSSE

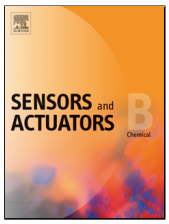
[12] V.Jeganathan Arulmoni, Ranganath M. S, R. S. Mishra, [2014] Experimental Investigations on Friction Stir Processed Copper and Enhancement of Mechanical Properties of the Composite Material, International Journal of Advance Research and Innovation vol 2(3), pp 557-563

[13] V.Jeganathan Arulmoni, Ranganath M. S. R.S. Mishra: 'Friction Stir Processed Copper: A Review', International Research Journal Of Sustainable Science & Engineering, 2015, Vol 3(8), pp 1-11

[14] V. Jeganathan Arulmoni, R.S. Mishra, Ranganath M. S: 'Material Flow and Microstructural Studies in Friction Stir Welding /Processing of Aluminium: A Literature Review', Int. J. Adv. Res. And Inno, 2015, Vol 3 (2), pp 500–511

[15] V. Jeganathan Arulmoni, Ranganath M. S., R. S. Mishra, Effect of Single and Multiple-Pass Friction Stir Processing on Microstructure, Hardness and Tensile Properties of a 99.99% Cu with Carbon Nano Tubes, International Journal of Advance Research and Innovation, Volume 3, Issue: 1 , 2015 pp 189-196 , ISSN 2347 -3258

Accepted Manuscript



Title: Highly Sensitive Electrochemical Immunosensor based on Graphene-Wrapped Copper Oxide-Cysteine Hierarchical Structure for Detection of Pathogenic Bacteria

Author: Chandra Mouli Pandey Ida Tiwari Vidya Nand Singh K.N. Sood Gajjala Sumana Bansi Dhar Malhotra

PII: S0925-4005(16)31165-0
DOI: http://dx.doi.org/doi:10.1016/j.snb.2016.07.121
Reference: SNB 20619

To appear in: *Sensors and Actuators B*

Received date: 11-4-2016
Revised date: 12-7-2016
Accepted date: 21-7-2016

Please cite this article as: Chandra Mouli Pandey, Ida Tiwari, Vidya Nand Singh, K.N.Sood, Gajjala Sumana, Bansi Dhar Malhotra, Highly Sensitive Electrochemical Immunosensor based on Graphene-Wrapped Copper Oxide-Cysteine Hierarchical Structure for Detection of Pathogenic Bacteria, Sensors and Actuators B: Chemical http://dx.doi.org/10.1016/j.snb.2016.07.121

This is a PDF file of an unedited manuscript that has been accepted for publication. As a service to our customers we are providing this early version of the manuscript. The manuscript will undergo copyediting, typesetting, and review of the resulting proof before it is published in its final form. Please note that during the production process errors may be discovered which could affect the content, and all legal disclaimers that apply to the journal pertain.

ACCEPTED MANUSCRIPT

Highly Sensitive Electrochemical Immunosensor based on Graphene-Wrapped Copper Oxide-Cysteine Hierarchical Structure for Detection of Pathogenic Bacteria

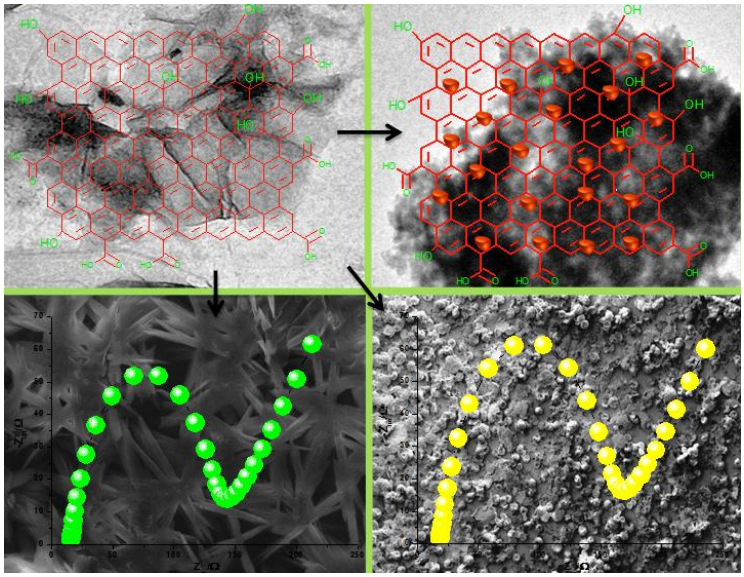
Chandra Mouli Pandey[a,b,c], Ida Tiwari[b], Vidya Nand Singh[a], K.N. Sood[a], Gajjala Sumana[a*], Bansi Dhar Malhotra[c]

[a]Biomedical Instrumentation Section, CSIR-National Physical Laboratory, New Delhi-110012, India

[b]Department of Chemistry, Faculty of Science, Banaras Hindu University, Varanasi-221005, India

[c]Nanobioelectronics Laboratory, Department of Biotechnology, Delhi Technological University, Delhi-110042, India

ACCEPTED MANUSCRIPT



Graphene wrapped copper (II) assisted cysteine hierarchical structures as sensing layer for ultrasensitive label-Free Electrochemical Immunosensor for detection of *Escherichia coli* O157:H7 in water.

ACCEPTED MANUSCRIPT

Highlights

- Facile and eco-friendly synthesis of rGO-CysCu hierarchical structures.
- The thin structure of the GO exhibit higher electro-chemical performance as sensing layer.
- Fabricated immunosensor shows high selectivity and sensitivity for *E. coli* O157:H7 detection.
- The rGO-CysCu based immunosensor can be used to differentiate the *E. coli* O157:H7 cells from the non-pathogenic *E. coli* (DH5α) and other bacterial cells in synthetic samples.

ACCEPTED MANUSCRIPT

Abstract

We report results of the studies relating to fabrication of the graphene wrapped copper (II) assisted cysteine hierarchical structure (rGO-CysCu, 10 μm) synthesised using facile, aqueous and environmental-friendly conditions. The results of electrochemical impedance spectroscopic investigations indicate that self-assembly of rGO-CysCu molecules onto gold electrode provides a high surface area and high electron transfer rate constant (1.82×10^{-6} cm/s). Further, an ultrasensitive label-free electrochemical immunosensor for quantitative determination of *Escherichia coli* O157: H7 (*E. coli*) has been developed using rGO-CysCu as the sensing layer. Under optimal conditions, the calibration plot pertaining to sensing characteristics of the fabricated immunoelectrode for *E. coli* O157: H7 was approximately linear in the wide detection range of 10 CFU mL^{-1} to 10^8 CFU mL^{-1} with a detection limit of 3.8 CFU mL^{-1}. Moreover, the proposed method was successfully used to differentiate the *E. coli* O157: H7 cells from the non-pathogenic *E. coli* (DH5α) and other bacterial cells in the synthetic samples.

Keywords: Graphene Oxide, Hierarchical structures, Cysteine, Electrochemical immunosensor, *Escherichia coli* O157: H7.

Corresponding author: sumanagajjala@gmail.com; Tel.: +91-11-45609152; Fax: +91-11-45609312

1. Introduction

To meet the emerging challenges of green analytical chemistry, electrochemical devices present unique opportunities by providing an efficient monitoring route without causing any harmful effect on the environment [1-3]. Advantages of these electrochemical systems include high sensitivity, selectivity, wide linear range, low-cost instrumentation, minimal space and power requirements [4-6]. The recent breakthrough in the science and technology of advanced electrode materials has had a significant impact on the development

ACCEPTED MANUSCRIPT

of electrochemical-based devices [7, 8]. In this context, the emergence of nanotechnology provides excellent opportunities to obtain improved performance of these systems by fabrication of novel multifunctional nanostructured materials [9-11].

The development of multi-functional composite materials of hierarchical nano- and micro-scale structures is of great interest because these structures provide a large surface area, good conductivity, and permeability due to their spatial arrangement and size dependent properties [10, 12, 13]. Keeping this in view, the fabrication of three-dimensional (3D) architectures based on integrating two-dimensional graphene with nanoparticles has led to increased attention of many researchers [14, 15]. These 3D graphene-based materials possess a high surface area (>2600 m^2 g^{-1}) and high electrical/thermal conductivity as well as excellent mechanical properties [16, 17]. In spite of these interesting characteristics, the main drawback lies in the synthesis is the chemical reduction process of GO to rGO that usually results in the environmental health risks due to the use of toxic or hazardous chemical reduction [18, 19]. Therefore, to fabricate an efficient sensing layer for application to electrochemical immunosensor, it is crucial to develop an environment-friendly pathway to synthesize new bio-molecule-assisted materials that are biocompatible and have high electron transfer efficiency [20, 21].

With the development of new green synthesis methods, a new generation of nanomaterials synthesized by the template of cysteine (Cys) has attracted much attention [22, 23]. We recently reported the formation of the hexagonal shaped structure of Cys bio-molecules in the presence of copper oxide and their rearrangements into flower-like structures that exhibit exposed facets and increased active surface area [12, 24]. In this work, GO has been added to the aqueous Cys solution in the presence of Cu (II). To delineate the reaction mechanism, comparative studies were conducted wherein Cu (II) was not added to rGO-Cys hierarchical structures. The synthesised rGO-CysCu showed excellent

ACCEPTED MANUSCRIPT

electrochemical properties when self-assembled onto the gold (Au) electrode. This rGO-CysCu modified Au electrode was used in the fabrication of immunosensor for the detection of *E. coli* O157: H7 cells in drinking water samples and synthetic samples. The conventional methods used for the detection of *E. coli* O157: H7 include culture and colony counting methods, and immunology-based methods [25,26]. These methods are time-consuming and often require initial sample preparation and enrichment steps to detect low *E. coli* O157: H7 concentration [25]. The electrochemical impedance based biosensing is an attractive alternative for performing simple, sensitive, fast, selective and reliable measurements of the pathogenic bacteria, being at the same time cost-effective and applicable to real-time monitoring [26]. Many fabricated impedimetric immunosensors have been proposed for detection of *E. coli* O157: H7 ranging from $10–10^3$ CFU mL^{-1} [27-29]. However, the the lower limit of detection is urgently required for bacterial analysis of water or clinical samples as the infectious doses of *E. coli* O157: H7 can be lower than ten cells [30,31]. In this work we report results of the studies relating to the one-step synthesis of rGO-CysCu which is cost-effective, and eco-friendly. Further, this biosensing platform has been used for the detection of water-borne pathogen (*E. coli* O157: H7). It is found that the unique 3D architecture and high hydrophilicity of rGO-CysCu perhaps strengthen the adhesive force between the antibody and the substrate. And the Cys layer not only serves as a multifunctional interface to be easily functionalized with targeting molecules but also maintains bioactivity of antibodies and improved water-solubility of the synthesized material [13, 32]. Moreover, this strategy of structurally integrating hierarchical structure of Cys, GO, and bio-recognition molecules provide new insights into the design of the rGO-CysCu based immunosensor for *E. coli* O157: H7 detection, which may open up new channels in the fabrication of immunosensors for clinical diagnosis of pathogenic diseases.

2. Experimental

ACCEPTED MANUSCRIPT

2.1. Chemicals

Graphite powder, copper(II) chloride dihydrate ($CuCl_2.2H_2O$), sodium hydroxide (NaOH), N,N-dimethylacetamide (DMAC), L-Cysteine (Cys), N-hydroxysuccinimide (NHS), N-ethyl-N-(3-dimethylaminopropyl carbodimide (EDC), and all other reagents and solvents were of analytical grade and were procured from Sigma-Aldrich (India). Monoclonal antibodies and the target cells of *E. coli* (O157: H7) were purchased from Kirkegaard & Perry Laboratories, Gaithersburg MD, USA, respectively. Phosphate buffer saline (PBS) was prepared by mixing phosphate buffer with 0.9% NaCl. Ultrapure water (Mill-Q, Millipore, 18.2 MΩ resistivity) was used throughout the experiments.

2.2. Synthesis of Graphene Oxide

The modified hummer's method was used to prepare GO from natural graphite powder using H_2SO_4, $NaNO_3$, and H_2O_2 (30%). The synthesised GO was dispersed in distilled water (0.1 mg mL^{-1}) and sonicated for further use.[33, 34]

2.3. Synthesis of GO Wrapped CysCu and Cys Microstructures

For the synthesis of GO wrapped Cys microstructure, firstly aqueous solution of $CuCl_2$ (1M) was added to the different concentration of L- Cys solution (1, 10 and 100 mM) and the solution was sonicated for 5 min. Subsequently, 0.1 mg mL^{-1} GO dispersion was added to different concentrations of Cys-containing Cu (II), and the solution was sonicated for 10 min until the color was changed from brown to deep blue-gray. The control experiments were carried out under similar conditions in the absence of Cu (II). The growth process of both the rGO-Cys and rGO-CysCu was observed after six hours of reaction time at 25^oC [20, 35].

2.4. Pre-treatment and Self-assembly of rGO-Cys and rGO-CysCu on the Gold Surface

The Au plate (0.25 cm^2 diameter, 100 nm thick) was washed in boiling 2.0 M KOH for about 1 h, followed by ultra-sonication in Piranha solution (3:1; H_2SO_4/H_2O_2) for 10 min

ACCEPTED MANUSCRIPT

and the electrode was subsequently washed five times with deionized water [36]. For the fabrication of rGO-CysCu hierarchical structures, the Au electrode was dipped in the rGO-Cys and rGO-CysCu solution for 6 h (for self-assembly) after which the electrode was repeatedly rinsed with deionized water.

2.5. Bacterial Strains and Growth Conditions

The *E. coli* O157: H7 and *E. coli* DH5α strains were used in this study. The bacterial culture was routinely grown at 37 °C in the Luria-Bertani medium for 12 h. Mac-Conkey agar plating was used to determine the viable cell counts [37]. After overnight incubation, the colonies were counted. Colony-forming units (CFU) were counted as 1×10^{8} CFU mL^{-1} in 0.01 mol L^{-1} PBS buffer (pH 7.4) containing 0.1% NaN_3, and the colonies were stored at 4 °C until further use. The bacterial cells are stored in 50% aqueous glycerol solution and the serial dilutions (10 to 1×10^{8} CFU mL^{-1}) were prepared in PBS buffer and stored at -20 ^{o}C before use. *E. coli* O157: H7 specific monoclonal antibody solution was prepared in PBS buffer; pH 7.4 containing 0.1% sodium azide.

2.6. Fabrication of Immunosensor

Both the rGO-Cys/Au and rGO-CysCu/Au electrodes were treated with a mixture of 2 mM EDC and 5 mM NHS for 1 h at 27 ^{o}C, in dark condition to activate the –COOH groups present on the electrode surface. Further, the modified electrodes were incubated with monoclonal antibodies (Ec_{Ab}, 20 µl; 0.1 mg ml^{-1}) solution in a humid chamber overnight at room temperature (27 ^{o}C). Finally, the electrodes were rinsed with PBS solution to wash away the excess unbound antibodies. The antibodies-immobilized electrodes were subsequently treated with 1% bovine serum albumin (BSA) to block the unspecific binding sites followed by washing with PBS. Figure 1 show the different steps involved in the synthesis, self-assembly of rGO-CysCu and rGO-CysCu to the Au electrode and the subsequent immunosensor fabrication.

ACCEPTED MANUSCRIPT

2.7. Characterization

The morphological investigations of the modified graphene Cys hierarchical structures were carried out using transmission electron microscopy (TEM, Hitachi Model, H-800). The scanning electron microscopy (SEM) images of the rGO-Cys/Au and rGO-CysCu/Au electrode were recorded using a JEOL-JSM-6700F field-emitting scanning electron microscope (FESEM, 15 kV). To investigate the formation of rGO-CysCu and GO, Fourier transform infra-red (FT-IR) spectroscopy measurements were carried out using Perkin-Elmer spectrometer (Model Spectrum BX) at 25^{o}C. The FT-IR spectra of rGO-CysCu and rGO-Cys were recorded using KBr in the frequency region of 400cm^{-1} - 4000 cm^{-1}. The FTIR signal was obtained by averaging 64 scans at the resolution of 4 cm^{-1}. The electrochemical studies were performed using Autolab potentiostat/galvanostat (Eco Chemie, Netherlands) using a three-electrode cell, with Au as working electrode, platinum as auxiliary electrode and Ag/AgCl as reference electrode in phosphate buffer (PBS, 100 mM, pH 7.0, 0.9% NaCl) containing 5 mM $[Fe(CN)_6]^{3-/4-}$.

3. Results and discussion

3.1. FTIR studies

The results of FTIR spectroscopy measurements of GO show characteristic peaks at 1626, 3410 and 1399 cm^{-1} corresponding to C=O stretching vibration, O–H stretching and deformation, respectively (Fig. 2 (A)). The peaks corresponding to the presence of epoxy C–O stretching vibration and the alkoxy C–O stretching vibration are observed at 1244 and 1038 cm^{-1}, respectively indicating the presence of GO [38]. The FTIR spectrum of rGO-CysCu exhibits peaks at 2861 cm^{-1} and 2926 cm^{-1} pertaining to stretching vibrations of alkane group (Fig. 2 (B)). The presence of Cys on the graphene sheets introduced secondary amide groups as indicated by the emergence of the secondary amine peak at about 1542 cm^{-1} [39]. A shift

ACCEPTED MANUSCRIPT

in the position of COO^- and NH^{3+} stretching is perhaps due to a change in their dipole moment when CysCu binds with the rGO surface having high electron density [35, 40].

The UV-Visible spectrum clearly shows the formation of GO where a π–π* absorption band at 222 nm was observed (Fig. S1 (A); curve (i)). Whereas, the peak shifted to 230 nm in the case of rGO-CysCu, and a shoulder n–π* absorption band at 305 nm was observed. This absorption peak indicates that some groups on the GO surface were perhaps removed, which may result in the formation of conjugated structure (Fig. S1(A); curve (ii)) [39, 41, 42].

Raman spectroscopic analysis was employed to study the Raman scattering in rGO-CysCu (Fig. S1 (B)). For GO, the G-band is found at ~1602 cm^{-1} while an intense D-band peak appears at ~1373 cm^{-1}, which corresponds to sp^3 carbon and defects associated with vacancies and grain boundaries (Fig. S1 (B); curve (i)) [42]. The results of successive reduction of GO and synthesis of rGO-CysCu nanocomposites are shown in Fig. S1 (B); curve (ii). The shift of G band of rGO-CysCu nanocomposite (curve ii) to 1613 cm^{-1} is attributed to the high ability for recovery of the hexagonal network of the carbon atom. It is found that rGO-CysCu nanocomposite shows the relatively higher intensity of D to G band (1.32) than that of GO (0.76) suggesting the formation of new graphitic domains structure [43].

3.2. Contact angle studies

Contact angle (CA) measurements have been carried out using the sessile drop method to investigate hydrophilicity of the fabricated rGO-Cys/Au and rGO-CysCu/Au electrode, which in turn can be related to assembly of the rGO composite and Ec_{Ab} immobilization on the Au surface (Fig. S2). It has been observed that the value of the CA decreases from 110.26° (bare Au, Fig. S2 (A)) to 50° for rGO-Cys/Au electrode (Fig. S2 (B)) and 36.42° rGO-CysCu/Au electrode (Fig. S2 (D)), indicating self-assembly of rGO-Cys and

ACCEPTED MANUSCRIPT

rGO-CysCu at the Au surface. Moreover, the lower CA value obtained for the rGO-CysCu/Au electrode suggests a larger surface coverage by rGO-CysCu compared to that of rGO-Cys/Au electrode. After immobilization of the Ec_{Ab}, there was a further decrease in the value of the CA to 29.56° (Fig. S2 (C)) and 18.62° (Fig. S2 (E)) for rGO-Cys/Au and rGO-CysCu/Au electrode, respectively. This indicates the hydrophilic nature of the surface and immobilization of the Ec_{Ab}. All the measurements were repeated in triplicate on different electrodes, and the variation in the results was found within ±3° [43].

3.3. Microscopic analysis of the nanocomposite

The TEM image of GO sheet reveals a typical ripped and crumpled morphology (Fig. 3 (A)). Whereas the TEM analysis of pristine CuO reveals the presence of uniform grains of average size 5 nm (Fig. 3 (B)). It is found that there are non-uniform distribution and aggregation of CuO nanoparticles on the rGO surface irrespective of the Cu (II) concentration of 0.1M (Fig. 3 (C)) and 1.0 M (Fig. 3 (D)). The morphological investigations of rGO-CysCu composites were carried out using TEM to study the influence of Cys concentration on the microstructures by keeping the concentration of rGO and Cu (II) constant. It was observed that at relatively low Cys concentration (1 mM), spindle-like structures were formed (Fig. S3 (A)), whereas after incorporation of GO, these structures were covered by the rGO sheet (Fig. 4 (A)). Interestingly, at a moderate concentration of Cys (10 mM) the spindles were formed in a large number (Fig. S3 (C)) and were wrapped by the rGO sheets (Fig. 4 (B)). However, at high concentration of Cys (100 mM), there was perhaps the formation of disoriented flower-like structure formed underneath the rGO sheet (Fig. 4 (C)). The time for the formation of all these microstructure was less than 1 h. To understand the influence of Cu (II) on the growth of rGO-CysCu composite, further experiments were conducted in the absence of Cu (II) precursor. It appears that fewer Cys hierarchical structures were formed when the solution was kept for 1 h. With the increase in the reaction

ACCEPTED MANUSCRIPT

time (8 h), the formation of flower-like structure occurred that was well covered by rGO (Fig. 4 (D)).

3.4. Morphological characterization of the bioelectrode

Figure 5A shows self-assembly of the rGO-CysCu molecules at the Au surface. It appears that at a lower concentration of Cys (1 and 10 mM) dendritic structure wrapped with rGO were self-assembled at the Au electrode (Fig. S4 (B) and (C)). And when the concentration of Cys was increased to 100 mM, disordered semi-flower structure formed beneath the rGO sheet was observed on the Au electrode (Fig. S5 (A)). The SEM micrograph indicated the formation of cauliflower-like structure in case of rGO-Cys, wherein multilayer of the rGO sheet was attached to these structures (Fig. 5 (B)). At a concentration of 100 mM the pristine Cys flakes tended to have a hexagonal/quasi-hexagonal shape having thickness from ~200 to ~500 nm (Fig. S5 (A)). When GO was used as the growth template, no hexagonal shape of Cys flakes was obtained, suggesting that the growth of Cys could have been considerably affected by the crystal quality of graphene underneath (Fig. S5 (B)) [44, 22, 45, 46]. EDAX analysis of Cys revealed the presence of C, N, O, S elements (Fig. S6 (A)) while the self-assembly of rGO-CysCu on Au electrode consisted of elements such as C, N, O, S, and Cu (Fig. S6 (B)). Further, uniform surface coverage can be seen after the immobilization of antibodies onto rGO-CysCu/Au electrode which may be due to covalent linking of the amino-terminated antibodies with the –COOH group of Cys (Fig. 5 (C)). On the other hand, in the case of rGO-Cys/Au electrode, the antibodies occupied the pores of the flower (Fig. 5 (D)) formed between the Cys sheets (Fig. 5 (D); inset).

3.5. Electrochemical Characterization

The electrochemical impedance spectroscopy (EIS) is a widely used electrochemical technique, due to its fast and sensitive response occurring at the electrode-electrolyte interface [47, 48]. EIS mainly includes a semicircle portion, observed at higher frequencies,

ACCEPTED MANUSCRIPT

which corresponds to the electron transfer limited process, followed by a linear part characteristic of the lower frequency attributed to a diffusion limited electron transfer [49]. Semicircle diameter of EIS spectra gives the value of charge transfer resistance (R_{ct}). The increase in the diameter of the semicircle reflects an increase in the R_{ct} and the numerical values of R_{ct} can be derived from experimental impedance spectra by fitting an equivalent circuit model based on modified Randles and Ershler model to the data [50]. The change in R_{ct} value after each modification step was analysed using phosphate buffer (PBS, 100 mM, pH 7.0, 0.9% NaCl) containing 5 mM $[Fe(CN)_6]^{3-/4-}$ as the redox probe. Under the optimum conditions, the bare Au electrode showed almost a straight line characteristic of mass diffusion limiting process having the R_{ct} value of 30 Ω (Fig. S7, curve (i)). After self-assembly of the Cys (curve (v)), CysCu (curve (iv)), rGO-Cys (curve (iii)) rGO-CysCu (curve (ii)) and on the Au electrode (i), R_{ct} was found to be 246.9, 186.58. 141.8, and 119.4 Ω, respectively. This decrease in the R_{ct} value clearly indicated that doping the rGO-Cys system with Cu significantly changed the reactivity leading to stronger physical or chemical interactions between GO and Cys as compared to that of pristine GO. This strong chemisorption arising due to structural change in the Cu-doped rGO-Cys, facilitated strong adsorption leading to faster electron transfer kinetics in comparison to that of the electrode without GO [51, 52]. However, the covalent binding of Ec_{Ab} followed by removal of the physically adhered antibodies and blocking of exposed carboxyl groups on the modified Au electrode with blocking agent BSA resulted in an increase of R_{ct} in each case. This could perhaps be attributed to the binding of the non-conducting antibodies, which retarded the charge transfer process (curve (ii); Fig. 6 (A) and (B)). When the target Ec_{cells} were incubated to the antibody modified electrode surface, the formation of antibody–antigen complex occured. This complex formation created increased barrier due to cell membrane thickness (5–10 nm) and resistance (10^2–10^5 Ω cm^2) for the electrochemical transduction process,

ACCEPTED MANUSCRIPT

thereby hindering the access of the redox probe to the electrode surface, resulting in further increase in R_{ct} (curve (iii); Fig. 6 (A) and (B)) [53]. The fitting values for the various equivalent circuit elements and the change in the R_{ct} value for the two electrodes are illustrated by the histogram (Fig. 6 (C)). It can, thus, be inferred that the solution resistance (R_s) and Warburg resistance (Z_W) are constant, as they depict the properties of solution and diffusion of $[Fe(CN)_6]^{3-/4-}$ through the interface, respectively. In the impedance spectra the electrode reaction is totally controlled by the electron–transfer kinetics. Thus, the exchange current per geometric unit area is given as:

$$R_{ct} = 1\ RT/i_o\ F \quad (1)$$

and the apparent electron transfer rate constant (k_{app}) is derived from Eqn (2):

$$k_{app} = RT/n^2F^2AR_{ct}C \quad (2)$$

where n is the number of electrons transferred, F is the Faraday constant, R is gas constant, T is temperature in Kelvin, A is experimentally-determined area of the electrode, the R_{ct} value is obtained from the fitted Nyquist plots, C is concentration of the $[Fe(CN)_6]^{3-/4-}$ (mol cm^{-3}). The values of k_{app} are 1.18×10^{-6} and 1.82×10^{-6} cm/s for the rGO-Cys/Au electrode and rGO-CysCu/Au electrode, respectively. The value of i_o after antibody immobilization is estimated to be as 1.32×10^{-4} A/cm^2 which is attributed to slow diffusion of the $[Fe(CN)_6]^{3-/4-}$ ions through interface layer when compared to that of the non-immobilized rGO-CysCu/Au electrode (2.1×10^{-4} A/cm^2). Besides this, the peak current of cyclic voltammetry varies as a function of the square root of scan rate (Fig. 6 (D)), revealing linear dependence of peak currents with respect to the scan rate. This indicates that the electron transfer from rGO-Cys/Au and rGO-CysCu/Au electrodes is a surface-controlled process. All the experiments were repeated five times and the imprecision of the data was found to be within 5%.

3.6. Electrochemical Response Studies of Ec_{Ab}/rGO-CysCu/Au and Ec_{Ab}/rGO-Cys/Au bioelctrodes

ACCEPTED MANUSCRIPT

EIS was used for the quantitative determination of *E. coli* cells, as it provides an instant response (electronic shielding effect from the cell membrane), showing the efficiency of electron transfer between the electrode surface and the electro-active substances [54]. We observed a linear increase in impedance with an increase in the concentration of *E. coli* O157: H7 cells, indicating the generation of a resistant and capacitive double layer between the surface and electrolyte [24]. The sensing response characteristics of the Ec_{Ab}/rGO-CysCu/Au bioelectrode (Fig. 7 (A)) indicated that more cells could be detected (10–10^8 CFU mL^{-1}) in comparison to that of Ec_{Ab}/rGO-Cys/Au bioelectrode (50–10^8 CFU mL^{-1}; Fig. 7 (C)) due to generation of the higher blocking effect. Moreover, the R_{ct} values of these impedance signals display good linearity with respect to concentration of the target *E. coli* cells and linear equation for Ec_{cell}/Ec_{Ab}/rGO-CysCu/Au electrode (Fig. 7 (B)) was calculated as:

$$Y(\Omega) = -14.46 + 69.71X \text{ (log CFU } mL^{-1}\text{)}; R=0.9989 \quad (3)$$

Similarly, for the Ec_{cell}/Ec_{Ab}/rGO-Cys/Au electrode (Fig. 7 (D)), the linear equation in the concentration range of Ec_{cell} obtained is:

$$Y(\Omega) = -34.67 + 54.09X \text{ (log CFU } mL^{-1}\text{)}; R=0.9980 \quad (4)$$

The limit of detection calculated using the expression 3σ/sensitivity, where σ is the standard deviation of the blank electrode [24], for the Ec_{Ab}/rGO-CysCu/Au bioelectrode (3.8 CFU mL^{-1}) is much less in comparison to that of Ec_{Ab}/rGO-Cys/Au bioelectrode (32 CFU mL^{-1}). The imprecision of the data indicated by error bars in Figure 7 (B) and (D) was found to be <4%. This improved EIS detection performance was largely due to the enhanced electron transfer rate from rGO-CysCu and highly specific antigen−antibody immune reaction. In case of the rGO-Cys electrode, the antibodies were less accessible for the formation of antigen-antibody complex, resulting in a decrease in the sensitivity [55]. For all the sensing experiments, R_{ct} of antibodies-immobilized on the modified electrode with PBS

ACCEPTED MANUSCRIPT

solution was taken as the control signal. The fabricated rGO-CysCu based immunosensor had higher sensitivity in comparison to other immunosensor reported in the literature for *E. coli* detection (Table ST1). The enhanced analytical performance of rGO-CysCu/Au electrode can be attributed to the good conductivity, stability, and biocompatibility of Cys due to increased local topographic interactions with the cellular surface, and the electrostatic adhesion with Ec_{cell} [47].

3.7. Interference Studies

To investigate selectivity of the proposed immunosensor, the response characteristics of the bioelectrode were studied using cultured cells of other water-borne pathogens (*Salmonella typhi*, *Shigella dysenteriae* and *Neisseria meningitides*) as a function of concentration [12]. The cells of these bacterial pathogens were incubated on the fabricated immunosensor for 1 h, and EIS was used for the detection. Meanwhile, the cultured *E. coli* O157: H7 cells were immobilized under similar experimental conditions. Figure S8 (A) shows a sharp increase in ΔR_{ct} value with increase in the log (*E. coli* O157:H7 concentration) suggesting the formation of immuno-complex, while in case of cells of other waterborne pathogens incubated on the immunosensor, there was a slight change in the ΔR_{ct} value when the concentration approached the higher range (10^8 CFU ml^{-1}). This slight change in the ΔR_{ct} value could perhaps be due to non-specific adsorption (less than 8%) of the cells on the immunosensor surface.

The specificity of the immunosensor was determined by incubating the bioelectrode with non-pathogenic *E. coli* DH5α bacteria cells that closely resembled the *E. coli* O157: H7. Figure S8 (B) shows that the change in ΔR_{ct} is similar to that of the control signifying that DH5α does not form the immuno-complex. Further, a known concentration (1×10^6 CFU mL^{-1}) of *E. coli* O157:H7 was mixed with *Salmonella typhii* and *E. coli* DH5α. The ΔR_{ct}

ACCEPTED MANUSCRIPT

signals thus obtained for the mixture of pathogens are similar to that of *E. coli* O157: H7 showing that this immunosensor can specifically detect *E. coli* O157: H7.

3.8. Precision, Stability, and Regeneration of Immunosensor

To assess reproducibility and the reliability of the proposed immunosensor, the coefficient of variation (C_oV) of inter-assay precision was used with two samples containing $1x10^1$ CFU mL^{-1} and $1x10^3$ CFU mL^{-1} of Ec_{cells}. The inter-assay C_oV was evaluated by analysis of the same concentration of Ec_{cells} (10^1 CFU mL^{-1} and 10^3 CFU mL^{-1}) using five equally prepared electrodes. Five independently made immunosensors exhibited similar current response and the inter-assay C_oV was determined to be 4.3% (10^1 CFU mL^{-1}) and 3.2% (10^3CFU mL^{-1}). The observed low value of relative standard deviation indicated that the proposed immunosensor displayed good repeatability. In addition, the storage stability of the immunosensor was tested by putting the Ec_{Ab}/rGO-CysCu/Au electrode in a refrigerator (4 ^oC) and measuring its response towards *E. coli* O157:H7 detection every five days (Fig. S9 (A)). After 40 days, the impedimetric response of the sensor remained 90.2 % of the initial value indicating that the immunosensor had acceptable reliability and increased stability could be assigned to biocompatibility of the Cys, which maintain the bioactivity of antibodies and other biomolecules.

The regeneration step was performed by immersion of the working electrode (10^8 CFU mL^{-1}) for 10 min in glycine-HCl buffer (0.1 M, pH = 2.2) and washed with PBS solution to interrupt the antigen−antibody immune complexes [56]. It was found that there was a gradual decrease in ΔR_{ct} with an increase of the regeneration time and it decreased after regenerating the immunosensor for 8 times (Fig. S9 (B). This could be due to gradual shelling and denaturation of Ec_{cells}/antibodies or the structure of rGO-CuCys during continuous processed by a glycine-HCl buffer and cleaning with the increase of regeneration times [57].

ACCEPTED MANUSCRIPT

The results demonstrate that this immunosensor could be regenerated and used, for at least 8 times with relative standard deviation of 7.3%.

3.9. Real Sample Analysis

The cultured *E. coli* O157: H7 cells were inoculated in water to determine accuracy of the fabricated immunosensor by comparing the quantitative analysis of the water samples with the plate count method. Five measurements were made for every *E. coli* sample, and it was found that the average values were similar to those obtained using the plate count method (Table 1), and the relative error maximum was less than 8.00%.

The validation of the bioelectrode was carried out using the synthetic samples (*E. coli* O157: H7 spiked tap water, juices and skimmed milk) at 1×10^{6} CFU mL^{-1} and 1×10^{8} CFU mL^{-1}concentration, respectively via standard addition method. The immunosensing response studies indicated that response of the bioelectrodes in all the *E. coli* O157: H7 synthetic samples was comparable with that of the conventional calibration curve obtained using standard samples at physiological conditions with less than 10% variation (Table 2). Therefore, the developed impedimetric immunosensor can be used for rapid and sensitive determination of *E. coli* O157: H7 in real samples.

4. Conclusions

A highly sensitive electrochemical impedance based immunosensor has been fabricated for the detection of *E. coli* O157: H7 using 3D hierarchical structure of rGO wrapped Cys. Environmental friendly route has been used to synthesize the GO wrapped Cys 3D structure, which shows excellent conductivity, stability, and performs as an appropriate sensing layer. With covalent conjugation of *E. coli* O157: H7 antibody, a broader detection range ($10–10^{8}$ CFU mL^{-1}) and a much lower detection limit (3.8 CFU mL^{-1}) with high

ACCEPTED MANUSCRIPT

specificity of Ec_{Ab}/rGO-CyCu/Au electrode towards *E. coli* cell O157:H7 detection has been achieved. This fabricated immunosensor is selective for *E. coli* O157: H7 and can successfully detect the presence of *E. coli* O157: H7 in the synthetic food samples. With simple operation and rapid response using EIS, this immunosensor can be used as a sensitive laboratory method for the detection of low concentrations of pathogenic bacteria. It is thus a promising alternative to standard and conventional detection methods currently being used for bacterial detection.

Acknowledgements

We thank Director, CSIR-NPL, New Delhi, India for his interest in this work. C.M. Pandey acknowledges University Grant Commission, India for providing Dr. D. S. Kothari Postdoctoral Fellowship (No.F.4-2/2006 (BSR)/CH/14-15/0164). We thank Mrs. Pragya Mishra (Rice Genome, IARI) for providing the *E. coli* culture sample, Dr. A.K.Pandey (PGIMER, Chandigarh), and Mrs. Shipra Solanki, (CSIR-NPL, New Delhi) for interesting discussions.

References

[1] J. Wang, Real-Time Electrochemical Monitoring: Toward Green Analytical Chemistry, Acc. Chem. Res., 35 (2002) 811-816.

[2] P.T. Anastas, Green Chemistry and the Role of Analytical Methodology Development, Crit. Rev. Anal. Chem., 29 (1999) 167-175.

[3] L. Li, Q. kong, Y. Zhang, C. Dong, S. Ge, J. Yu, A 3D electrochemical immunodevice based on a porous Pt-paper electrode and metal ion functionalized flower-like Au nanoparticles, Journal of Materials Chemistry B, 3 (2015) 2764-2769.

[4] O. Lazcka, F.J.D. Campo, F.X. Muñoz, Pathogen detection: A perspective of traditional methods and biosensors, Biosens. Bioelectron., 22 (2007) 1205-1217.

[5] A. Kaushik, A. Yndart, R.D. Jayant, V. Sagar, V. Atluri, S. Bhansali, M. Nair, Electrochemical sensing method for point-of-care cortisol detection in human immunodeficiency virus-infected patients, International Journal of Nanomedicine, 10 (2015) 677-685.

ACCEPTED MANUSCRIPT

[6] L.D. Mello, L.T. Kubota, Review of the use of biosensors as analytical tools in the food and drink industries, Food Chem., 77 (2002) 237-256.

[7] S. Gao, S. Yang, J. Shu, S. Zhang, Z. Li, K. Jiang, Green Fabrication of Hierarchical CuO Hollow Micro/Nanostructures and Enhanced Performance as Electrode Materials for Lithium-ion Batteries, J. Phys. Chem. C, 112 (2008) 19324-19328.

[8] Z. Wen, J. Li, Hierarchically structured carbon nanocomposites as electrode materials for electrochemical energy storage, conversion and biosensor systems, J. Mater. Chem., 19 (2009) 8707-8713.

[9] J.-S. Hu, L.-S. Zhong, W.-G. Song, L.-J. Wan, Synthesis of Hierarchically Structured Metal Oxides and their Application in Heavy Metal Ion Removal, Adv. Mater., 20 (2008) 2977-2982.

[10] P. Zhang, S. Wang, Designing Fractal Nanostructured Biointerfaces for Biomedical Applications, Chemphyschem, 15 (2014) 1550-1561.

[11] Q. Xu, L. Wang, J. Lei, S. Deng, H. Ju, Platinum nanodendrite functionalized graphene nanosheets as a non-enzymatic label for electrochemical immunosensing, J. Mater. Chem. B, 1 (2013) 5347-5352.

[12] C.M. Pandey, G. Sumana, I. Tiwari, Copper oxide assisted cysteine hierarchical structures for immunosensor application, Appl. Phys. Lett. 105 (2014) -.

[13] Y. Lei, S. Song, W. Fan, Y. Xing, H. Zhang, Facile Synthesis and Assemblies of Flowerlike SnS2 and In3+-Doped SnS2: Hierarchical Structures and Their Enhanced Photocatalytic Property, J. Phys. Chem. C, 113 (2009) 1280-1285.

[14] K. Rana, J. Singh, J.-T. Lee, J.H. Park, J.-H. Ahn, Highly Conductive Freestanding Graphene Films as Anode Current Collectors for Flexible Lithium-Ion Batteries, ACS Appl. Mater. Interfaces, 6 (2014) 11158-11166.

[15] W. Wang, S. Guo, I. Lee, K. Ahmed, J. Zhong, Z. Favors, F. Zaera, M. Ozkan, C.S. Ozkan, Hydrous Ruthenium Oxide Nanoparticles Anchored to Graphene and Carbon Nanotube Hybrid Foam for Supercapacitors, Sci. Rep., 4 (2014).

[16] M.S. Artiles, C.S. Rout, T.S. Fisher, Graphene-based hybrid materials and devices for biosensing, Adv. Drug Del. Rev., 63 (2011) 1352-1360.

[17] L.I. Alexander, Graphene-based and graphene-like materials, Russ. Chem. Rev. 81 (2012) 571.

[18] L. Zhang, L. Zhao, J. Lian, Nanostructured Mn3O4-reduced graphene oxide hybrid and its applications for efficient catalytic decomposition of Orange II and high lithium storage capacity, RSC Advances, 4 (2014) 41838-41847.

ACCEPTED MANUSCRIPT

[19] I. Uysal Unalan, G. Cerri, E. Marcuzzo, C.A. Cozzolino, S. Farris, Nanocomposite films and coatings using inorganic nanobuilding blocks (NBB): current applications and future opportunities in the food packaging sector, RSC Advances, 4 (2014) 29393-29428.

[20] Y. Zhang, J. Tian, H. Li, L. Wang, X. Qin, A.M. Asiri, A.O. Al-Youbi, X. Sun, Biomolecule-Assisted, Environmentally Friendly, One-Pot Synthesis of CuS/Reduced Graphene Oxide Nanocomposites with Enhanced Photocatalytic Performance, Langmuir, 28 (2012) 12893-12900.

[21] Q. Huang, L. Zhou, X. Jiang, Y. Zhou, H. Fan, W. Lang, Synthesis of Copper Graphene Materials Functionalized by Amino Acids and Their Catalytic Applications, ACS Appl. Mater. Interfaces, 6 (2014) 13502-13509.

[22] K. Chang, W. Chen, l-Cysteine-Assisted Synthesis of Layered MoS2/Graphene Composites with Excellent Electrochemical Performances for Lithium Ion Batteries, ACS Nano, 5 (2011) 4720-4728.

[23] Q. Lu, F. Gao, S. Komarneni, Biomolecule-Assisted Synthesis of Highly Ordered Snowflakelike Structures of Bismuth Sulfide Nanorods, J. Am. Chem. Soc., 126 (2003) 54-55.

[24] C. Mouli Pandey, G. Sumana, I. Tiwari, Nanostructuring of hierarchical 3D cystine flowers for high-performance electrochemical immunosensor, Biosens. Bioelectron., 61 (2014) 328-335.

[25] J.W.-F. Law, N.-S. Ab Mutalib, K.-G. Chan, L.-H. Lee, Rapid methods for the detection of foodborne bacterial pathogens: principles, applications, advantages and limitations, Frontiers in Microbiology, 5 (2014) 770.

[26] A.K. Deisingh, M. Thompson, Strategies for the detection of Escherichia coli O157:H7 in foods, J. Appl. Microbiol., 96 (2004) 419-429.

[27] J.-T. Liu, K. Settu, J.-Z. Tsai, C.-J. Chen, Impedance sensor for rapid enumeration of E. coli in milk samples, Electrochim. Acta, 182 (2015) 89-95.

[28] N. Baram, D. Starosvetsky, J. Starosvetsky, M. Epshtein, R. Armon, Y. Ein-Eli, Enhanced inactivation of E. coli bacteria using immobilized porous TiO2 photoelectrocatalysis, Electrochim. Acta, 54 (2009) 3381-3386.

[29] W. Dou, W. Tang, G. Zhao, A disposable electrochemical immunosensor arrays using 4-channel screen-printed carbon electrode for simultaneous detection of Escherichia coli O157:H7 and Enterobacter sakazakii, Electrochim. Acta, 97 (2013) 79-85.

[30] N.A. Cornick, A.F. Helgerson, Transmission and Infectious Dose of Escherichia coli O157:H7 in Swine, Appl. Environ. Microbiol., 70 (2004) 5331-5335.

ACCEPTED MANUSCRIPT

[31] A.-M.J. Haque, H. Park, D. Sung, S. Jon, S.-Y. Choi, K. Kim, An Electrochemically Reduced Graphene Oxide-Based Electrochemical Immunosensing Platform for Ultrasensitive Antigen Detection, Anal. Chem., 84 (2012) 1871-1878.

[32] X. Chen, H. Li, S. Wang, M. Yang, Y. Qi, Biomolecule-assisted hydrothermal synthesis of molybdenum disulfide microspheres with nanorods, Mater. Lett., 66 (2012) 22-24.

[33] J. Chen, B. Yao, C. Li, G. Shi, An improved Hummers method for eco-friendly synthesis of graphene oxide, Carbon, 64 (2013) 225-229.

[34] D.C. Marcano, D.V. Kosynkin, J.M. Berlin, A. Sinitskii, Z. Sun, A. Slesarev, L.B. Alemany, W. Lu, J.M. Tour, Improved Synthesis of Graphene Oxide, ACS Nano, 4 (2010) 4806-4814.

[35] Y. Zhao, X. Song, Q. Song, Z. Yin, A facile route to the synthesis copper oxide/reduced graphene oxide nanocomposites and electrochemical detection of catechol organic pollutant, CrystEngComm, 14 (2012) 6710-6719.

[36] C.M. Pandey, I. Tiwari, G. Sumana, Hierarchical cystine flower based electrochemical genosensor for detection of Escherichia coli O157:H7, RSC Advances, 4 (2014) 31047-31055.

[37] Y.M. Ibrahim, A.R. Kerr, J. McCluskey, T.J. Mitchell, Control of Virulence by the Two-Component System CiaR/H Is Mediated via HtrA, a Major Virulence Factor of Streptococcus pneumoniae, J. Bacteriol., 186 (2004) 5258-5266.

[38] M. Naebe, J. Wang, A. Amini, H. Khayyam, N. Hameed, L.H. Li, Y. Chen, B. Fox, Mechanical Property and Structure of Covalent Functionalised Graphene/Epoxy Nanocomposites, Sci. Rep., 4 (2014).

[39] B. Jiang, Y. Liang, Q. Wu, H. Jiang, K. Yang, L. Zhang, Z. Liang, X. Peng, Y. Zhang, New GO-PEI-Au-l-Cys ZIC-HILIC composites: synthesis and selective enrichment of glycopeptides, Nanoscale, 6 (2014) 5616-5619.

[40] M. Schriver, W. Regan, W.J. Gannett, A.M. Zaniewski, M.F. Crommie, A. Zettl, Graphene as a Long-Term Metal Oxidation Barrier: Worse Than Nothing, ACS Nano, 7 (2013) 5763-5768.

[41] J.I. Paredes, S. Villar-Rodil, A. Martínez-Alonso, J.M.D. Tascón, Graphene Oxide Dispersions in Organic Solvents, Langmuir, 24 (2008) 10560-10564.

[42] K.N. Kudin, B. Ozbas, H.C. Schniepp, R.K. Prud'homme, I.A. Aksay, R. Car, Raman Spectra of Graphite Oxide and Functionalized Graphene Sheets, Nano Lett., 8 (2007) 36-41.

ACCEPTED MANUSCRIPT

[43] R. Thiramanas, K. Jangpatarapongsa, U. Asawapirom, P. Tangboriboonrat, D. Polpanich, Sensitivity and specificity of PS/AA-modified nanoparticles used in malaria detection, Microb. Biotechnol. 6 (2013) 406-413.

[44] L. Liu, W. Liu, T. Hong, X. Weng, Q. Zhai, X. Zhou, Ag+ and cysteine detection by Ag+-guanine interaction based on graphene oxide and G-quadruplex DNA, Anal. Methods, 4 (2012) 1935-1939.

[45] F. Ma, Z. Zhang, H. Jia, X. Liu, Y. Hao, B. Xu, Adsorption of cysteine molecule on intrinsic and Pt-doped graphene: A first-principle study, J. Mol. Struct. 955 (2010) 134-139.

[46] L. Huijuan, L. Hejun, F. Qiangang, C. Yanhui, C. Xiaoyu, S. Can, Y. Xiaoyan, L. Lei, Density functional theory study on the interactions of l-cysteine with graphene: adsorption stability and magnetism, Nanotechnol. 24 (2013) 495702.

[47] I. SzymaÅ„ska, H. Radecka, J. Radecki, R. Kaliszan, Electrochemical impedance spectroscopy for study of amyloid Î²-peptide interactions with (âˆ’) nicotine ditartrate and (âˆ’) cotinine, Biosens. Bioelectron., 22 (2007) 1955-1960.

[48] P. Geng, X. Zhang, W. Meng, Q. Wang, W. Zhang, L. Jin, Z. Feng, Z. Wu, Self-assembled monolayers-based immunosensor for detection of Escherichia coli using electrochemical impedance spectroscopy, Electrochim. Acta, 53 (2008) 4663-4668.

[49] A. Ramanavicius, A. Finkelsteinas, H. Cesiulis, A. Ramanaviciene, Electrochemical impedance spectroscopy of polypyrrole based electrochemical immunosensor, Bioelectrochemistry, 79 (2010) 11-16.

[50] J.E.B. Randles, Kinetics of rapid electrode reactions, Discuss. Faraday Soc., 1 (1947) 11-19.

[51] Z. Zhong, W. Wu, D. Wang, D. Wang, J. Shan, Y. Qing, Z. Zhang, Nanogold-enwrapped graphene nanocomposites as trace labels for sensitivity enhancement of electrochemical immunosensors in clinical immunoassays: Carcinoembryonic antigen as a model, Biosens. Bioelectron., 25 (2010) 2379-2383.

[52] M.S. Goh, M. Pumera, The Electrochemical Response of Graphene Sheets is Independent of the Number of Layers from a Single Graphene Sheet to Multilayer Stacked Graphene Platelets, Chemistry – An Asian Journal, 5 (2010) 2355-2357.

[53] Y. Xie, A. Chen, D. Du, Y. Lin, Graphene-based immunosensor for electrochemical quantification of phosphorylated p53 (S15), Anal. Chim. Acta, 699 (2011) 44-48.

[54] L. Yang, Y. Li, G.F. Erf, Interdigitated Array Microelectrode-Based Electrochemical Impedance Immunosensor for Detection of Escherichia coli O157:H7, Anal. Chem., 76 (2004) 1107-1113.

ACCEPTED MANUSCRIPT

[55] M. He, A.E. Herr, Automated microfluidic protein immunoblotting, Nat. Protocols, 5 (2010) 1844-1856.

[56] V.B. Kandimalla, N.S. Neeta, N.G. Karanth, M.S. Thakur, K.R. Roshini, B.E.A. Rani, A. Pasha, N.G.K. Karanth, Regeneration of ethyl parathion antibodies for repeated use in immunosensor: a study on dissociation of antigens from antibodies, Biosens. Bioelectron., 20 (2004) 903-906.

[57] W. Yi, W. Liang, P. Li, S. Li, Z. Zhang, M. Yang, A. Chen, B. Zhang, C. Hu, Application of a Fab fragment of monoclonal antibody specific to N-terminal pro-brain natriuretic peptide for the detection based on regeneration-free electrochemical immunosensor, Biotechnol. Lett, 33 (2011) 1539-1543.

ACCEPTED MANUSCRIPT

Biographies

Chandra Mouli Pandey received his Ph.D. degree from Banaras Hindu University, Varanasi, India in collaboration with Biomedical Instrumentation Section at National Physical Laboratory, New Delhi, India (2015). He has published 18 research papers in peer-reviewed journals. He is currently working as a DST-INSPIRE Faculty in Department of Applied Chemistry, Delhi Technological University, Delhi, India. His main interest of research is development of biosensor for health care based on nano-materials and bionanocomposites.

Ida Tiwari received her doctrait in 2001 in the field of electroanalytical sensors from Banaras Hindu University, Varanasi, India. There after she was awarded Research Associateship from C.S.I.R., New Delhi, India in which she worked on sensors. She joined Analytical Chemistry Division, Department Of Chemistry, Faculty of Science, Banaras Hindu University, Varanasi, India as Assistant Professor in 2004 and has 15 years research experience in field of sensors, biosensors, composite materials, nanotechnology.

Vidya Nand Singh received his Ph.D. degree from the IIT Delhi, Delhi, India in 2005. He is working as scientist in Compound Semiconductor Solar Cell, Physics of Energy Harvesting Division, CSIR- National Physical Laboratory, New Delhi 110012, India. He has published more than 60 research papers and the main area of his research is on improving the efficiency of the different types of solar cells.

K.N. Sood is working as Senior Technical Officer in Electron Microscope Section, Division of Materials Characterization, CSIR-National Physical Laboratory, New Delhi-110012, India. He is involved

Gajjala Sumana received her Ph.D. (1998) from Jiwaji University in Chemistry, India. She is currently working as a scientist with the DST Centre on Biomolecular Electronics at the National Physical Laboratory, New Delhi, India. She has a research experience of 20 years in controlled drug delivery, liquid crystal polymers, polymer dispersed liquid crystals and biosensors. She has published more than 70 publications in the area of biomedical applications.

Bansi D. Malhotra received his Ph.D. degree from the University of Delhi, Delhi, India in 1980. He has published more than 280 papers in peer-reviewed journals, filed 10 patents, and edited/co-edited books on biosensors and polymer electronics. After his stint as Chief Scientist and Head of the DST Centre on Biomolecular Electronics at the CSIR-National Physical Laboratory, New Delhi, India, he moved to the Delhi Technological University (DTU), India and is currently a Professor. He has nearly 30 years of research experience in the field of biomolecular electronics and has guided 25 Ph.D. students to date. His current activities include biosensors, nanobiomaterials, conducting polymers, and ordered molecular assemblies including Langmuir-Blodgett films and self-assembled monolayers among others. Dr. Malhotra is a Fellow of the Indian National Science Academy (INSA), the National Academy of Sciences, India (NASI), and an academician of the Asia-Pacific Academy of Materials (APAM).

ACCEPTED MANUSCRIPT

Figure Captions

Figure 1. Schematic illustration for the synthesis and self-sssembly of rGO-CysCu and rGO-Cys on to the gold electrode and subsequent immunosensor fabrication.

Figure 2. FTIR spectra of (A) GO and (B) rGO-CysCu.

Figure 3. Transmission electron microscopic image (A) GO (B) CuO nanoparticles (C) CuO (0.1 M) assembly on GO and (D) CuO (1.0 M) assembly on GO.

Figure 4. Transmission electron microscopic image of rGO wrapped CysCu as a function of Cys concentration (A) 1 mM (B) 10 mM and (C) 100 mM (D) TEM image of rGO wrapped Cys without Cu (II).

Figure 5. Scanning electron microscopic images of (A) rGO-CysCu/Au electrode (B) rGO-Cys/Au electrode (C) Ec_{Ab}/rGO-CysCu/Au electrode and (D) Ec_{Ab}/rGO-Cys/Au electrode.

Figure 6. Nyquist diagram (Z_{im} versus Z_{re}) for the Faradic impedance measured in PBS solution (pH 7.4) containing 5 mM $[Fe(CN)_6]^{3-/4-}$, in the frequency range from 10^6 to 10^{-2} Hz for **(A)** (i) rGO-Cys electrode (ii) Ec_{Ab}/rGO-Cys/Au electrode, (ii) Ec_{cell}/Ec_{Ab}/rGO-Cys/Au electrode, and **(B)** (i) rGO-CysCu electrode (ii) Ec_{Ab}/rGO-CysCu/Au electrode, (iii) Ec_{cell}/Ec_{Ab}/rGO-CysCu/Au electrode.

(C) Histogram showing the change in R_{ct} for the rGO-Cys electrode and rGO-CysCu electrode after modification with antibody and target cell. (D) Cyclic voltammetric analysis showing the variation of current with square root of scan rate (10-300 mV) for (i) rGO-CysCu electrode and (ii) rGO-Cys electrode.

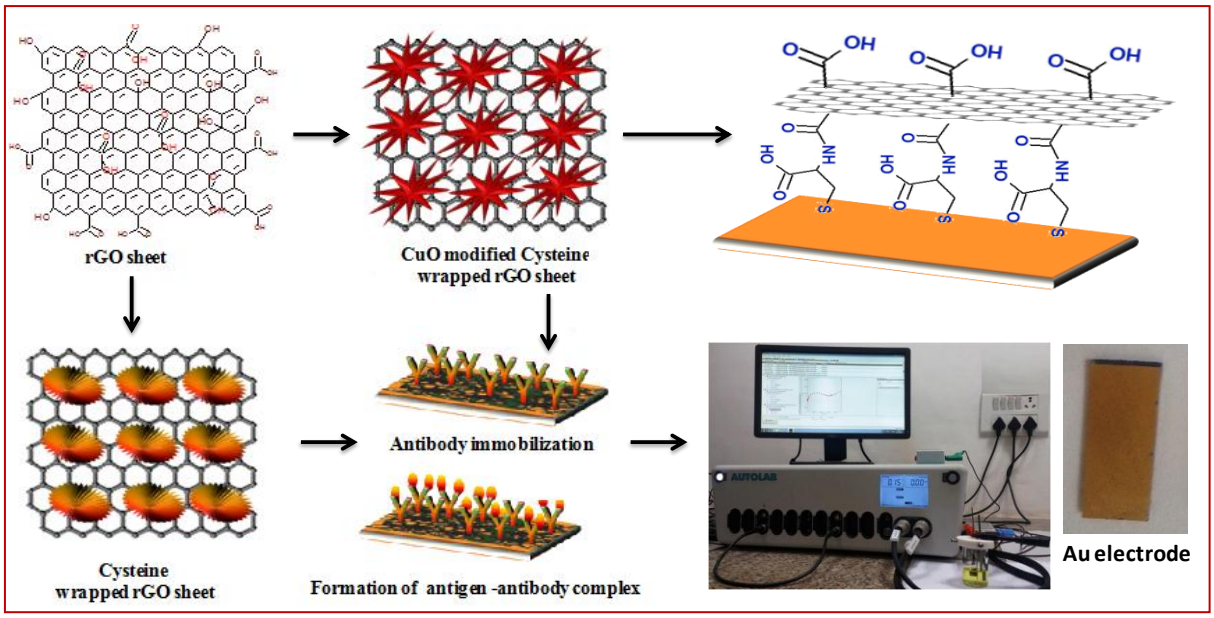
Figure 7. EIS showing the immunosensing response for (A) Ec_{Ab}/rGO-CysCu/Au electrode, and (B) the linearity plot with variation in the concentration of *E. coli* cells (10 to 1 x 10^8 CFU mL^{-1}). (C) Immunosensing response of Ec_{Ab}/rGO-Cys/Au electrode and (D) the linearity plot with variation in the concentration of *E. coli* cells (50 to 1 x 10^8 CFU mL^{-1}).

Table 1. Comparison of analytical results obtained from the EIS system and plate count method.

Table 2. Analytical results obtained using the EIS when the immunosensor was exposed to synthetic samples (*E. coli* O157:H7 spiked tap water, juices and skimmed milk).

ACCEPTED MANUSCRIPT

Figure 1.



ACCEPTED MANUSCRIPT

Figure 2.

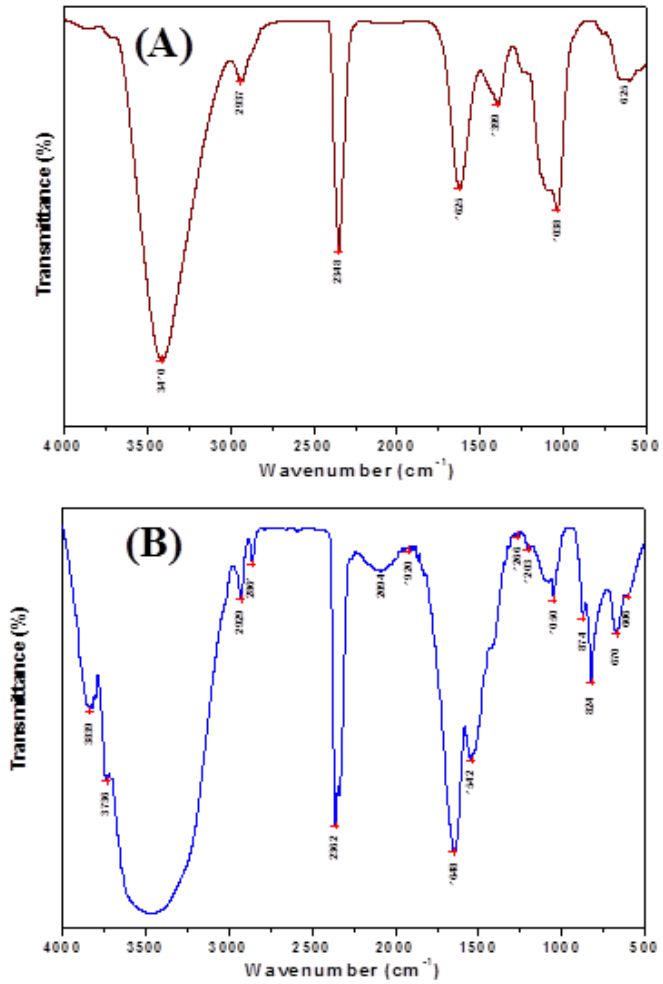
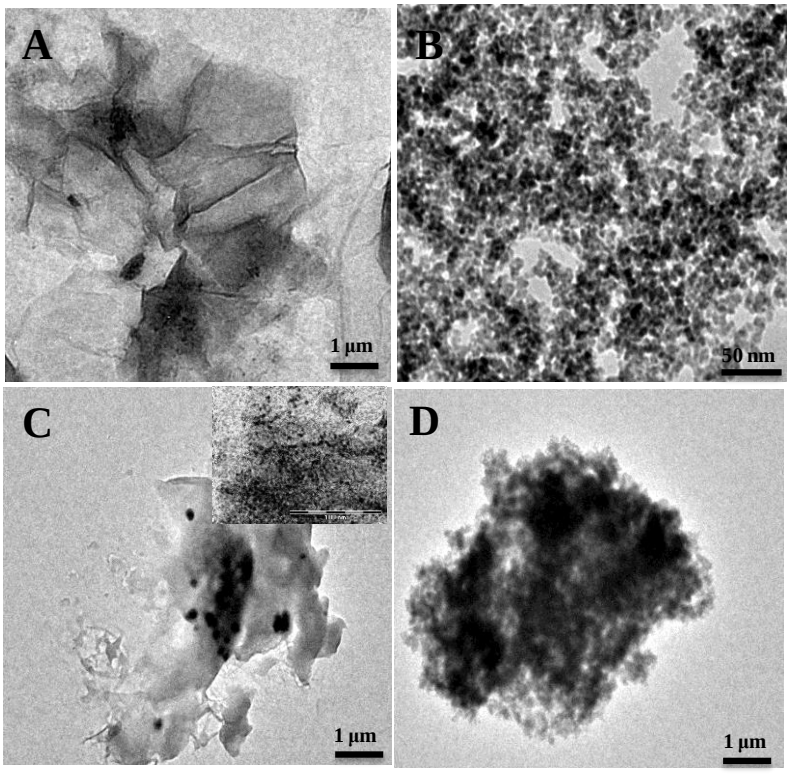


Figure 3.



ACCEPTED MANUSCRIPT

Figure 4.

Figure 4.

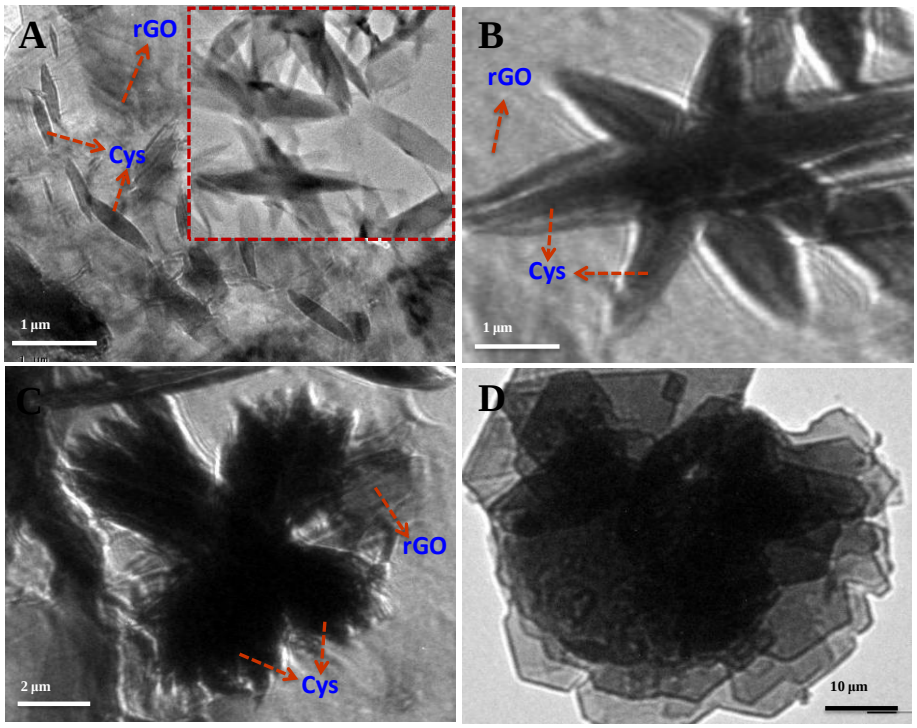
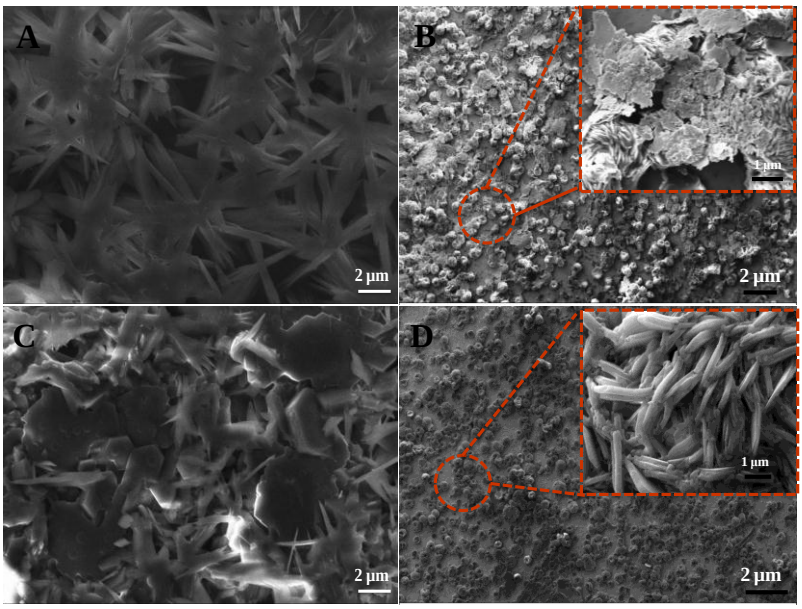


Figure 5.



ACCEPTED MANUSCRIPT

Figure 6.

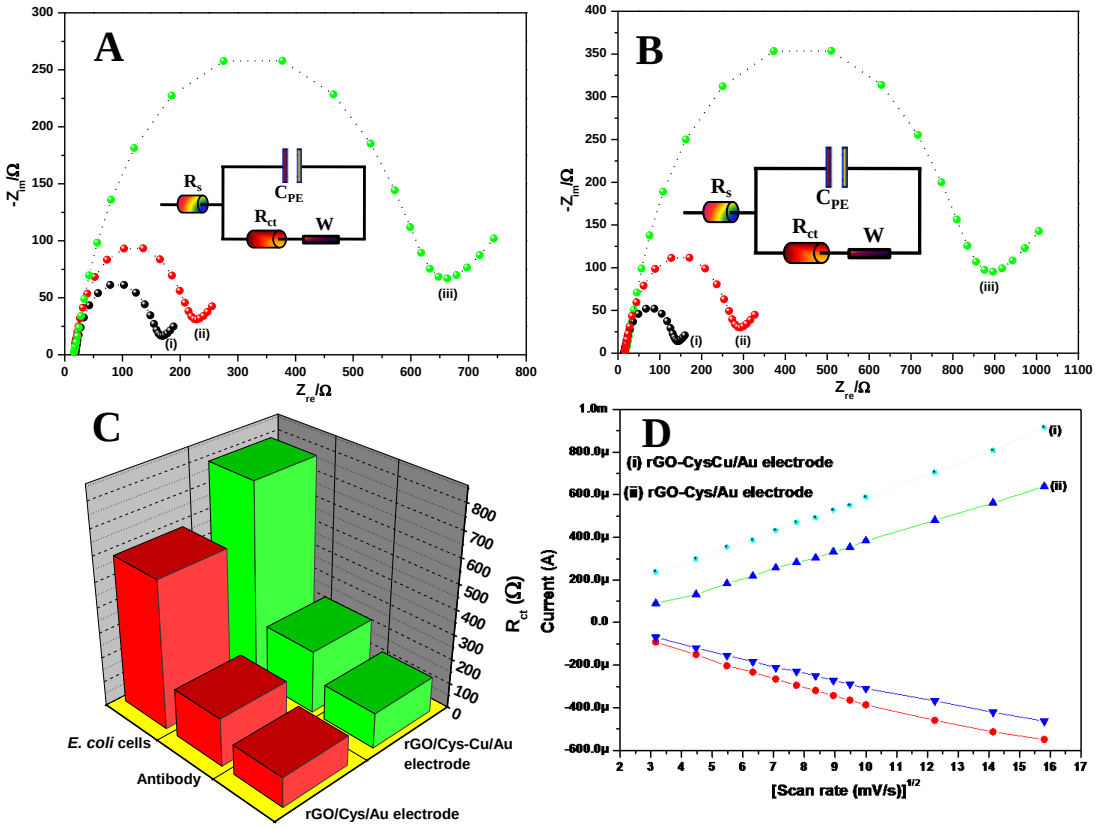


Figure 7.

ACCEPTED MANUSCRIPT

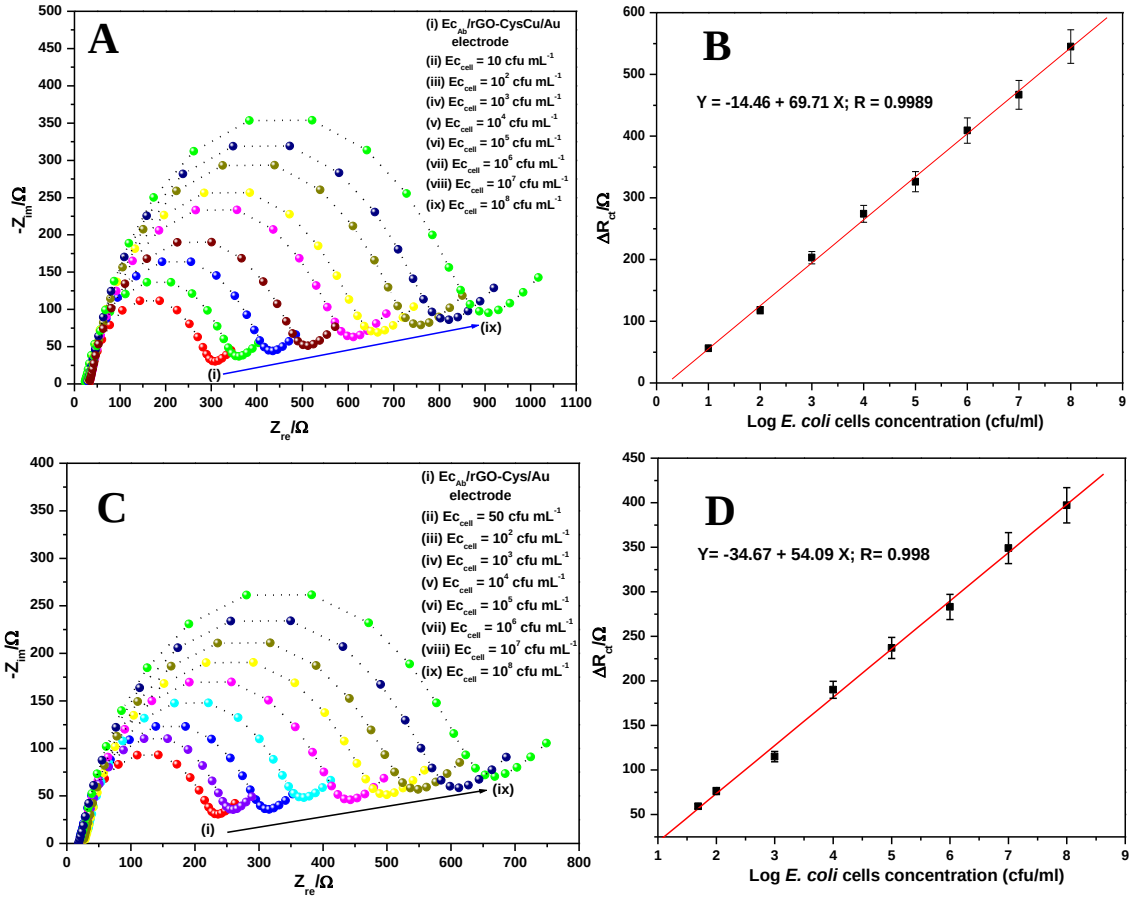


Table 1.

ACCEPTED MANUSCRIPT

Samples	Immunosensor (CFU ml^{-1})	Plate count method (CFU ml^{-1})	Relative error (%)
1	$3.6x10^{1}$	$3.4x10^{1}$	5.88
2	$2.1x10^{2}$	$2.2x10^{2}$	4.54
3	$6.5x10^{3}$	$6.3x10^{3}$	3.17
4	$3.2x10^{3}$	$3.3x10^{3}$	3.03
5	$5.4x10^{4}$	$5.2x10^{4}$	3.84
6	$2.1x10^{4}$	$2.2x10^{4}$	4.54
7	$1.2x10^{5}$	$1.3x10^{5}$	7.69
8	$6.0x10^{6}$	$6.4x10^{6}$	6.25
9	$1.2x10^{5}$	$1.3x10^{5}$	7.68

Table 2.

ACCEPTED MANUSCRIPT

Synthetic Samples	**added cells**	**R_{ct} value obtained using EIS (Ω)**	**% Error**
Tap water	1X 10^8	810	3.01
Tap water	1X 10^6	690	4.54
Fruit juice	1X 10^8	812	1.75
Fruit juice	1X 10^6	630	4.5
Milk sample	1X 10^8	830	8.27
Milk sample	1X 10^6	700	10.06

Appl. Phys. A (2016)122:717
DOI 10.1007/s00339-016-0239-9

Applied Physics A
Materials Science & Processing

Influence of gate metal engineering on small-signal and noise behaviour of silicon nanowire MOSFET for low-noise amplifiers

Neha Gupta[1] · **Rishu Chaujar**[1]

Received: 12 April 2016 / Accepted: 24 June 2016
© Springer-Verlag Berlin Heidelberg 2016

Abstract In this paper, we have investigated the small-signal behaviour and RF noise performance of gate electrode workfunction engineered (GEWE) silicon nanowire (SiNW) MOSFET, and the results so obtained are simultaneously compared with SiNW and conventional MOSFET at THz frequency range. This work examines reflection and transmission coefficients, noise conductance, minimum noise figure and cross-correlation factor. Results reveal significant reduction in input/output reflection coefficient and an increase in forward/reverse transmission coefficient owing to improved transconductance in GEWE-SiNW in comparison with conventional counterparts. It is also observed that minimum noise figure and noise conductance of GEWE-SiNW is reduced by 17.4 and 31.2 %, respectively, in comparison with SiNW, thus fortifying its potential application for low-noise amplifiers (LNAs) at radio frequencies. Moreover, the efficacy of gate metal workfunction engineering is also studied and the results validate that tuning of workfunction difference results further improvement in device small-signal behaviour and noise performance.

✉ Rishu Chaujar
rishu.phy@dce.edu

Neha Gupta
nehagupta@dtu.ac.in

[1] Microelectronics Research Lab, Department of Engineering Physics, Delhi Technological University, Bawana Road, Delhi 110042, India

1 Introduction

Aggressive scaling of CMOS dimensions had led to enhancement of cut-off frequency and maximum oscillator frequency which leads to a promising candidate for RFICs which was previously overlooked by other active devices [1, 2]. However, conventional CMOS shows shortcomings such as DIBL, hot-carrier effects and mobility degradation as device dimensions go in sub-micrometre. According to ITRS [3], amalgamation of new technologies is becoming crucial for deep sub-micron CMOS devices as recently reported in the literature [4–6]. Si nanowire FETs are more attractive than the conventional dual-gate (DG), SOI, III–V-based FETs and FinFETs because of higher on-current conduction due to stronger quantum confinement which results in higher mobility than bulk silicon, and also its properties such as concentration and dopant type can be changed during synthesis. In addition, the radius of the nanowire can readily be reduced to a few nanometres in size that limits the scaling of conventional MOSFET and also because of their adoptability for high-density integration including that of 3D [7, 8]. It was also found that gate-all-around (GAA) silicon nanowire transistors (SiNWTs) have cut-off frequency larger than that of planar Si MOSFET [9–11]. However, as with many novel device architectures, the SiNW MOSFET has problems of its own. One major problem facing nanowire MOSFETs with SiO_2 gate stack is the lower threshold voltage than desired. But, channel doping to correct the threshold voltage is difficult due to the narrow radius of nanowire. In addition, carrier mobility is also impacted with higher channel doping. Hence, there is a need of integration of some engineering schemes to overcome such effect. Gate workfunction tuning would thus make a better solution [12]; it is the most promising engineering scheme as it improves the transport

Published online: 05 July 2016

efficiency of carriers by modifying electric field in the channel and surface potential along the channel which results in enhanced transconductance and reduced SCEs [13]. It has already been demonstrated in our previous work that incorporation of GEWE engineering scheme onto silicon nanowire MOSFET alleviates short channel effects such as hot-carrier effects and DIBL [14, 15]. Also, improvement in cut-off and maximum oscillator frequency has also reported in our previous work [16, 17]. The most appropriate method to examine small-signal behaviour of MOSFET at high frequencies involves *S*-parameter measurements. *S*-parameters are most commonly employed for those networks that are operating at RF and microwave frequencies where signal power and energy analysis are more easily computed than voltages and currents. Since, at high frequency it is very difficult to estimate current and voltages. Short and open circuits (used by definitions of most n-port parameters) are hard to realize at high frequencies. As a result, microwave engineers work with so-called *S*-parameters, which utilize waves and matched terminations (normally 50 Ω). This approach also minimizes reflection problems [18]. Moreover, it has been scrutinized that short channel MOSFETs have comparatively higher channel thermal noise than long channel MOSFET devices in the strong inversion and saturation region [19–21]. This appearance is due to short channel effects (SCEs) associated with channel length modulation (CLM), velocity saturation (VS) and hot-carrier effect. As a result of accounting for these effects, it was shown that the major contribution to the drain current noise mainly comes from the linear channel region [19]. However, this issue of surplus noise is still an active area of investigation [22, 23] for RF amplifiers and receivers for communication.

In this paper, the small-signal behaviour and noise FOMs of GEWE-SiNW MOSFET is discussed at the simulation point of view. Additionally, owing to the increased demand for high-speed and low-noise devices, an accurate investigation of the MOSFET at high frequencies (HF) is necessary to represent the behaviour of device in microwave circuits and systems [24]. The complete work in this paper is systematized as follow: Sect. 2 describes the 3D device architecture of GEWE-SiNW MOSFET and its default parameters and simulation models used in this analysis. Further, we calibrate our simulation models and then evaluate the small-signal behaviour of our device in terms of scattering parameter (*S*-parameter). Further, we examine the noise analysis of *n*-channel GEWE-SiNW MOSFET at high frequency for the first time. In addition, the effect of GEWE scheme on small-signal parameters and RF FOMs also studied in this work. Finally, the conclusions are drawn in Sect. 4.

2 Device structure and physical models

Figure 1a–c shows the schematic cross-sectional view of the simulated device structure of n-type conventional, SiNW and GEWE-SiNW MOSFET, respectively. GEWE-SiNW consists of gate metals M1 and M2 of length L1 and L2 of 15 nm each, respectively, as shown in Fig. 1c which is towards the 45 nm node CMOS technology as stated in ITRS [25]. The radius of silicon nanowire is 5 nm. The oxide thickness is 1.5 nm; the source and drain region are of n-type with uniform doping profiles of 5×10^{19} cm^{-3} of length 5 nm for all device designs. The metal gate workfunction is 4.8 eV for conventional and SiNW and for GEWE, metal gate workfunction at the source end (Φ_{M1}) is 4.8 eV (Au) and metal gate workfunction at the drain end (Φ_{M2}) is 4.4 eV (Ti). All the device parameters are by default unless stated otherwise. All the simulations have been performed using physical models accounting for the electric field-dependent and concentration-dependent carrier mobilities, Shockley–Read–Hall recombination/generation with doping-dependent carrier lifetime, inversion layer Lombardi CVT mobility model, wherein concentration-dependent mobility, high field saturation model are all included [26]. To incorporate all non-local effects, we have adopted the quantum mechanical models which are more accurate than drift–diffusion method. The detailed description of default parameters used in the simulations is shown in Table 1. To characterize the device performance accurately, it is very important to define the carrier transport with proper models.

The quantum confinement effect in the deep scaled device may not be negligible [27]. Since the inversion charge layer thickness in the conducting silicon nanowire channel is comparable to the nanowire dimension, the effect of quantum confinement in sub-nanometre device may not be negligible. The Bohm quantum potential (BQP) model [28] can also be used with energy balance and hydrodynamic models, where the semi-classical potential is modified by the quantum potential in a similar way as for the continuity equations. The model introduces a position-dependent quantum potential, Q, which is added to the Potential Energy of a given carrier type. This quantum potential is derived using the Bohm interpretation of quantum mechanics [29] and is described below:

Time-independent Schrodinger equation can be written as:

$$\left(\frac{-\hbar}{2m^*}\nabla^2 - V\phi\right)\psi_j = E_j\psi_j \tag{1}$$

According to Bohm's interpretation of quantum mechanics, the wave function in a polar representation can be written as:

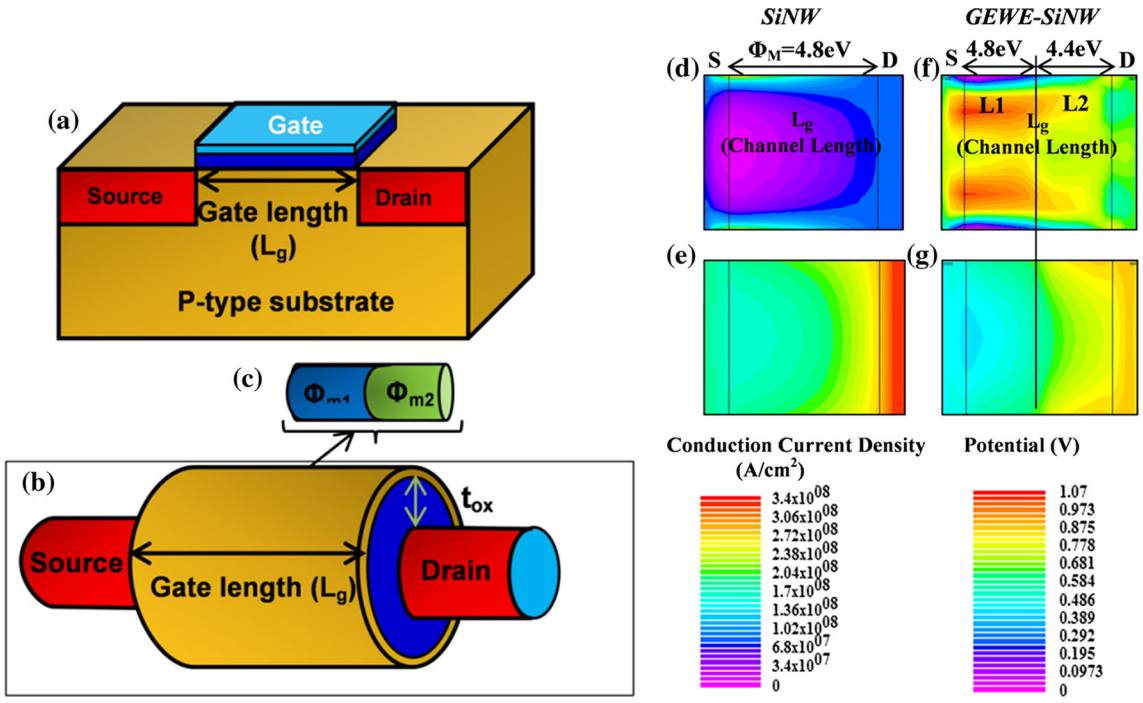


Fig. 1 Schematic cross-sectional view of **a** conventional MOSFET, **b** SiNW MOSFET and **c** GEWE-SiNW MOSFET, **d–f** contours distribution of conduction current density and **e–g** surface potential along the channel for SiNW and GEWE-SiNW MOSFET, respectively

Table 1 Physical models invoked during simulations at room temperature (300 K)

S. no.	Physical models	Description
1.	Mobility models	Lombardi CVT and constant low field mobility model
2.	Recombination model	Shockley–Read–Hall (SRH) recombination is included to incorporate minority recombination effects with carrier lifetime = 1×10^{-7} s
3.	Statistics	Boltzmann transport model, The use of Boltzmann statistics is normally justified in semiconductor device theory, but Fermi–Dirac statistics are necessary to account for certain properties of very highly doped (degenerate) materials
4.	Impact ionization and tunnelling model	No such model is used in current work as we are not interested in evaluating hot-carrier performance
5.	Energy transport model	Hydrodynamic model is used as it includes all non-local effects and is more accurate than the drift–diffusion method. Drift–diffusion model shows short comings as channel length scales down to 50 nm
6.	Quantum mechanical model	Quantum mechanical model plays an important role in determining the performance of surrounding gate MOSFET

$$\psi = R.\ \exp\left(\frac{iS}{\hbar}\right) \tag{2}$$

where R is probability density per unit volume, S has dimensions of action (energy × time).

By substituting Eq. 2 in 1, the Schrodinger equation can be written as:

$$\frac{\hbar^2}{2}\nabla\left\{M^{-1}\nabla\left[R.\exp\left(\frac{iS}{\hbar}\right)\right]\right\} + V.\mathrm{R}exp\left(\frac{iS}{\hbar}\right) = E.R.\exp\left(\frac{iS}{\hbar}\right) \tag{3}$$

where M^{-1} is the inverse of effective mass tensor and $M^{-1}\nabla S$ is local velocity of particle associated with wave function. Real part of Eq. 3 is interpreted as continuity equation of probability density while imaginary part states that the total energy, E is conserved and equal to sum of potential (V) and kinetic energy ($0.5\ M^{-1}\nabla S$). Therefore, quantum potential is defined as:

$$V = \frac{-\hbar^2}{2}\frac{\nabla(M^{-1}\nabla R)}{R} \tag{4}$$

Potential V is obtained by the single particle Schrodinger equation and use "*mean field approximation*" and consider an effective Bohm quantum potential defined as the weighted average potential for all carriers constrained in confining potential. Effective quantum potential is written as:

$$Q_{\text{eff}} = \frac{-\hbar^2}{2}\gamma\nabla\frac{[M^{-1}\nabla(n^{\alpha})]}{n^{\alpha}} \tag{5}$$

where α and γ are two adjustable parameters, M^{-1} is the inverse effective mass tensor, n is the electron (or hole) density and h is a Planck's constant.

Bohm quantum potential (BQP) model with $\alpha = 0.5$ and $\gamma = 1.2$ was used to take quantum mechanical effects into consideration. Additionally, numerical methods such as bi-conjugate gradient stabilized (BICGST) have been considered to obtain the solutions with improved convergence in 3D device structure [26]. Default simulator coefficients for all parameters have been employed. In order to fairly analyse the device performances, all the three devices are optimized to have the same threshold voltage, i.e. 0.32 V by changing channel doping and keeping the doping of source and drain constant of uniform doping i.e. 5×19 cm^{-3}. Threshold voltage is defined as minimum gate to source voltage (V_{gs}) at which current starts flowing between source and drain or it is defined as the that voltage at which I_{on}=10^{-8} A. Figure 1d–g shows the contour plot of conduction current density and surface potential along the channel of SiNW and GEWE-SiNW, respectively. It is evident from contours that with the incorporation of GEWE scheme, conduction density of electron enhances which results in higher current driving capability in comparison with SiNW MOSFET.

2.1 Calibration

The calibration of model parameters used in the simulation has been performed according to the experimental results [30] using above-mentioned models. Figure 2a shows the simulated I_d–V_{gs} characteristics of 30 nm short channel cylindrical gate silicon nanowire MOSFET at $V_{ds} = 1.0$ V and the transfer characteristics of extracted data of [30]. The results are in close proximity, thus validating the choice of models parameters taken in simulation. Figure 2b shows the transfer characteristics of GEWE-SiNW and SiNW MOSFET at 0.2 V drain voltage. It is evident from the figure that with the integration of gate engineering scheme, the on-current of GEWE-SiNW increases 2.2 times in comparison with silicon nanowire MOSFET due to redistribution of electric field in the channel which enhances the mobility and hence imparts the driving current capability of a device.

The MOSFET transconductance is defined by, $g_m = -\partial I_{ds}/\partial V_{gs}$ where I_{ds} drain current and V_{gs} is gate voltage. It is typically measured in the linear regime and used as indirect monitor of inversion carrier mobility. Transconductance is useful in designing linear amplifiers, and larger the transconductance for a device, the greater the gain (amplification) it is capable of delivering, when all other factors are held constant. As is evident from Fig. 2b, the transconductance is much higher in case of GEWE-SiNW MOSFET owing to enhancement in drain current. Moreover, noteworthy improvement in DIBL (or barrier lowering) is also observed in GEWE-SiNW due to step potential profile at the interface of dissimilar metal gates as is shown in contours of Fig. 1e–g. Subthreshold swing (SS) also reduces in case of GEWE-SiNW as shown in Fig. 2b and thus implies that GEWE-SiNW is immune to SCEs in comparison with SiNW MOSFET

2.2 Fabrication feasibility

The fabrication feasibility of SiNW MOSFET has been reported in the literature using several integration schemes. Yang et al. [31] fabricated vertical gate-all-around silicon nanowire MOSFET. Rustagi et al. [32] in 2007 reported the fabrication of CMOS inverter-based GAA SiNW MOSFETs using top-down approach. Moreover, for the

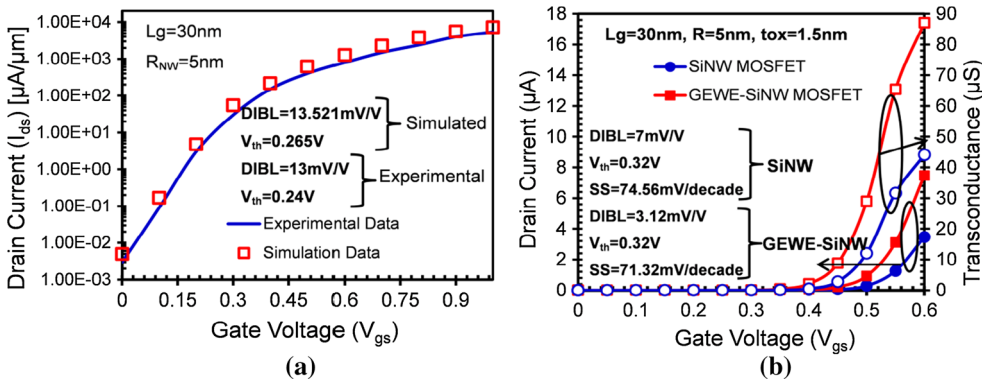
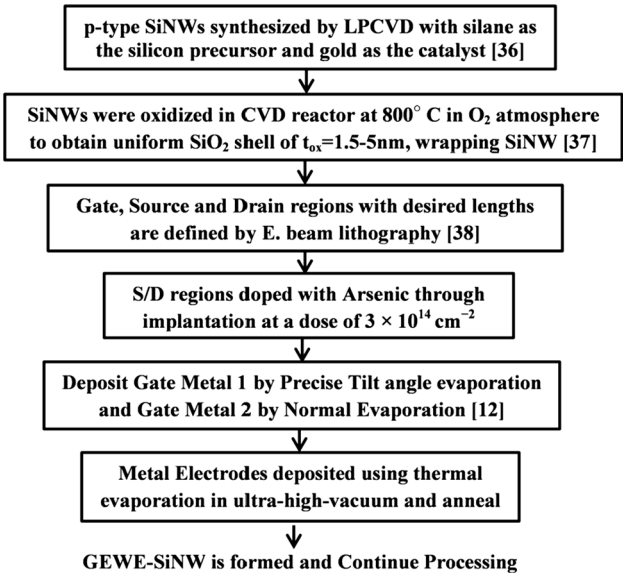


Fig. 2 **a** Calibration with the experimental results. I_{ds}–V_{gs} characteristics of 5 nm radius with 30 nm short channel cylindrical gate silicon nanowire MOSFET with $t_{ox} = 2$ nm and TiN as metal gate at $V_{ds} = 1.0$ V, **b** I_{ds}–V_{gs} and transconductance characteristics of GEWE silicon nanowire MOSFET at $V_{ds} = 0.2$ V

Table 2 Summary of the standard process flow of GEWE-SiNW



realization of GEWE architecture, numerous schemes have been suggested such as tilt angle evaporation metal gate deposition [12], metal interdiffusion process [33] and fully silicided (FUSI) metal gate [34]. Further, CMOS with dual metal gate has also been successfully fabricated using poly-Si gate doping control of the source and drain side gate individually [35]. Thus, the proposed device (GEWE-SiNW MOSFET) can be fabricated using the above design schemes, in which the advantages of GEWE scheme are amalgamated with SiNW MOSFET making it a promising design for system on chip and RF/microwave applications. A proposed summary of the process flow, outlining the fabrication process of GEWE-SiNW MOSFET and its integration with the standard CMOS process, is shown in Table 2.

3 Results and discussion

In this section, we investigate the small-signal behaviour of GEWE-SiNW MOSFET in terms of scattering (reflection and transmission coefficients) parameters. Further, the efficacy of gate metal engineering also studied on *S*-parameters at THz range by keeping the workfunction at the source side constant (4.8 eV) and varying the workfunction of metal gate at the drain end.

3.1 Small-signal behaviour of GEWE-SiNW MOSFET

S_{11} and S_{22} are defined as input and output reflection coefficient at port 1 and port 2, respectively, and is a measure of quality of match between the port and terminating impedance. S_{11} is the most commonly used parameter to characterize small-signal behaviour of active device at high frequency. Matching is generally required in RF circuits. When there is a perfect match, there is no reflected wave and reflection coefficient is zero. Figure 3a, b shows the real part of input and output reflection coefficient of conventional, SiNW and GEWE-SiNW MOSFET. As is evident from figure, both input and output coefficients decrease with increase in frequency and decrement in reflection coefficient is more in GEWE-SiNW as compared to its counterparts.

Due to the incorporation of two dissimilar metals on cylindrical gate, current driving capability increases due to redistribution of the electric field at the interface of two metals owing to step potential which causes enhancement in carrier velocity, and thus, current driving capability increases that results in increased transconductance and hence leading to improvement in reflection coefficient. As the matching between the ports and characteristics impedance improve, reflection coefficient decreases due to smaller reflected power. The reverse isolation parameter S_{12} determines the measure of feedback from the output of an amplifier to the input and thus supremacies its stability at high frequency [39]. Figure 3c shows the variation of real part of reverse transmission coefficient of conventional, SiNW and GEWE-SiNW MOSFET. Result unveils the reverse transmission coefficient of GEWE-SiNW increases to 5.07 and 4.2 times at 3.4 THz due to enhancement of transconductance in comparison with conventional and SiNW MOSFET, respectively. Figure 3d shows the forward transmission coefficient as a function of frequency also defined as a forward gain of two port device. The S_{21} (voltage gain) increases to 7.14 times in SiNW and 13.5 times in GEWE-SiNW MOSFET compared to conventional MOSFET as depicted in Fig. 3d. This enhancement is due to cylindrical gate designs and GEWE engineering scheme which enhances device performance and alleviates SCEs.

Further, we investigate the effect of metal gate workfunction on small-signal behaviour of GEWE-SiNW MOSFET at THz frequency range. Figure 4a, b shows the input and output reflection coefficient at different metal gate workfunction of drain end. As is evident from Fig. 4a, the effect of workfunction difference is very less on input reflection coefficient and also its value increases with increase in workfunction difference which is not desirable. Further, output reflection coefficient decreases with increase in workfunction difference which is desirable for RF amplifiers and receivers. This is due to excellent gate control which results in higher transconductance and hence improves reflection coefficient. As we increase the metal gate workfunction difference to 0.7 eV, reverse

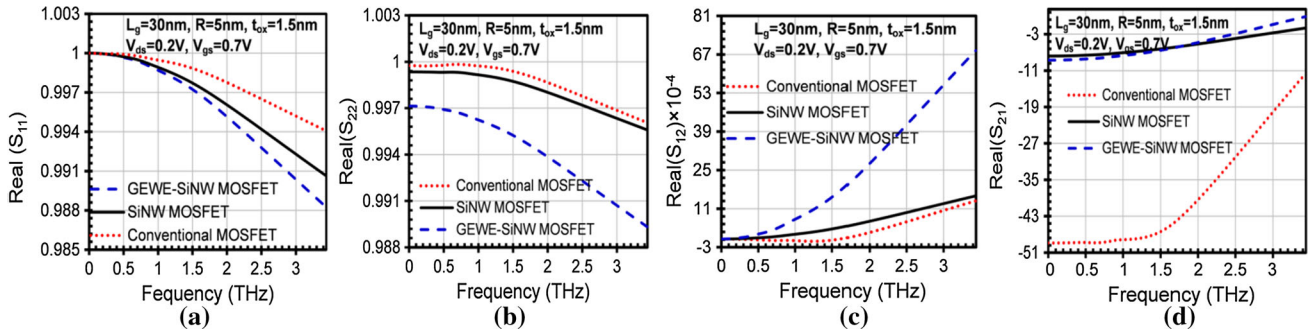


Fig. 3 **a–b** Real part of input output reflection coefficient, **c–d** real part of reverse and forward transmission coefficient as a function of frequency for conventional, SiNW and GEWE-SiNW MOSFET at $V_{gs} = 0.7$ V and $V_{ds} = 0.2$ V

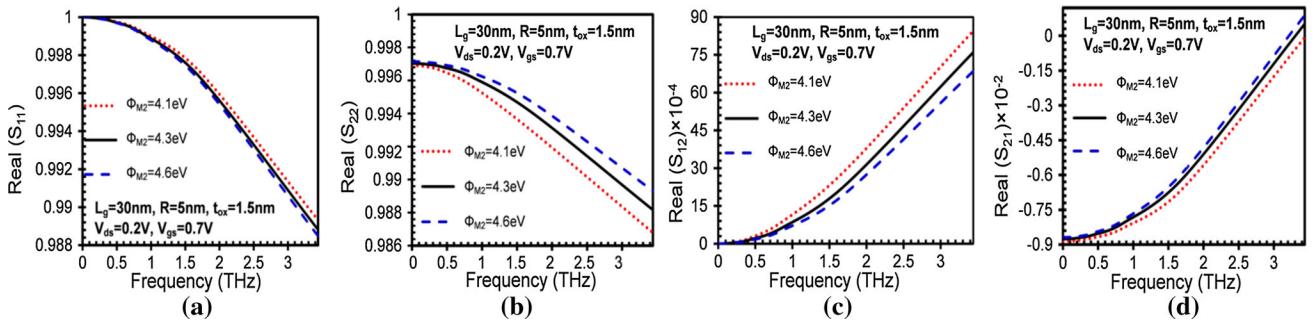


Fig. 4 **a–b** Real part of input and output reflection coefficient, **c–d** real part of reverse and forward transmission coefficient as a function of frequency for different metal gate workfunction at the drain side at $V_{gs} = 0.7$ V and $V_{ds} = 0.2$ V

transmission coefficients increase to 1.25 times at 3.4 THz compared to other workfunction difference due to improvement in on-current and reduced short channel effects owing to improvement of screening effect with an increase in metal workfunction difference as is evident from Fig. 4c, whereas forward transmission coefficient decreases as we increase the workfunction difference which is not desirable at THz. But the deprivation is very less as is shown in Fig. 4d. Thus, there is need to optimize the value of metal gate workfunction for optimal small-signal performance for RF amplifier and high-speed applications.

3.2 Noise metrics

For the design of CMOS RF circuits, investigation of noise conductance and noise figure (NF) is of paramount importance at high frequency. The effectiveness of low-noise amplifier (LNA) is determined by an important metric called noise figure. Noise conductance is generally used to estimate the power spectral density of noise current generators. Low-noise conductance is required in RF amplifiers and LNAs. Figure 5a depicts the noise conductance as a function of frequency for conventional, SiNW, GEWE-SiNW MOSFET. In GEWE-SiNW MOSFET, noise conductance decreases due to reduced hot-carrier phenomenon which results in lower impact ionization of carriers at the Si–SiO_2 interface and thus reduces noise. Additionally, as silicon nanowire phonon–phonon scattering is less observed, noise conductance also decreases. Hence, its dominance, for low-power and low-noise applications where noise is a major concern, is significant. Noise figure is an estimation of deterioration of signal-to-noise ratio caused by a component in RF signal chains. It is generally used to evaluate the performance of an amplifier or a radio receiver, with lower values specifying better performance.

Figure 5b shows the variation of NF_{MIN} as a function of frequency. As is evident from the figure, minimum noise figure decreases with increase in frequency, but this decline is more prominent in GEWE-SiNW MOSFET. The minimum noise figure is proportional to intrinsic gate resistance and inversely proportional to transconductance [40]. In GEWE-SiNW, there is a step potential created at the interface of two dissimilar metals workfunction which redistributes the electric field in the channel and hence increases the carrier efficiency which results in improved transconductance and low noise figure in comparison with its conventional counterparts. A low noise figure reflects that a very little noise is being added by the network. Thus,

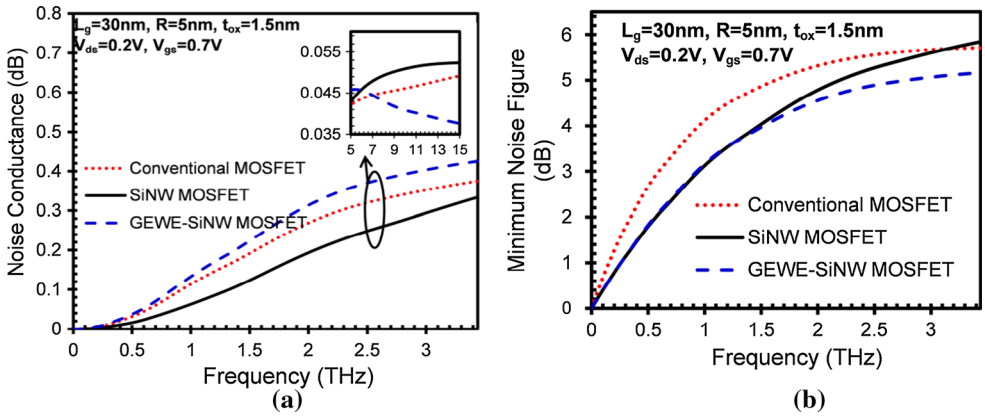


Fig. 5 **a** Noise conductance and **b** minimum noise figure as a function of frequency for conventional, SiNW and GEWE-SiNW MOSFET at $V_{gs} = 0.7$ V and $V_{ds} = 0.2$, respectively

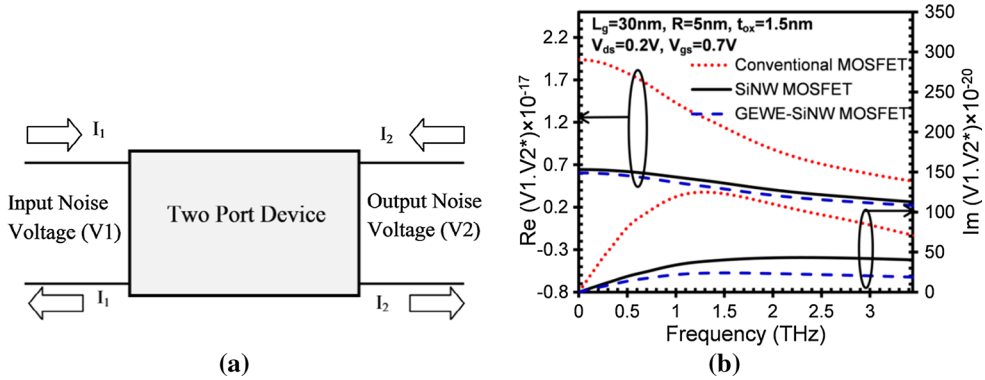


Fig. 6 **a** MOSFET as a two port device where the input noise is replaced by a voltage V1 and the noise received at output is replaced by V_2, **b** cross-correlation as a function of frequency for conventional, SiNW and GEWE-SiNW MOSFET at $V_{gs} = 0.7$ V and $V_{ds} = 0.2$ V

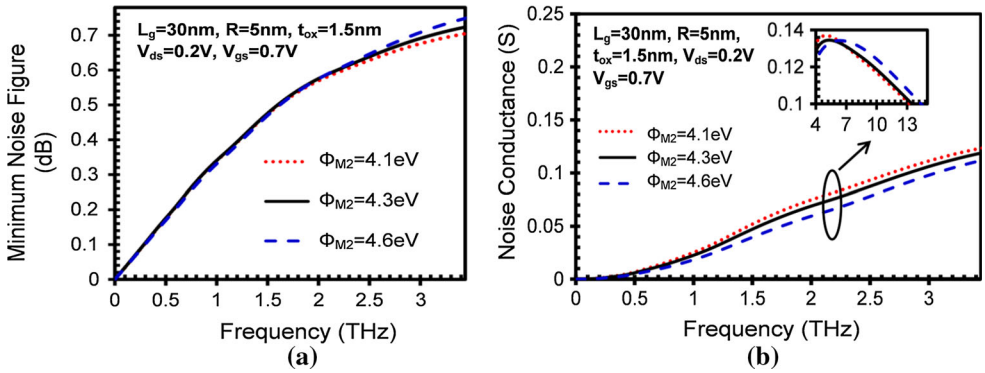


Fig. 7 **a** Minimum noise figure and **b** noise conductance as a function of frequency for GEWE-SiNW MOSFET for different gate metal workfunction values at drain end

GEWE-SiNW MOSFET is a reliable candidate for low-noise amplifiers (LNAs).

Figure 6a depicts MOSFET as a two port device where noise induced at the gate terminal is separated from the MOSFET and is depicted by V1 and the noise received at the output is depicted by V2 [41]. Figure 6b shows that real and imaginary part of cross-correlation is reduced in comparison with conventional devices with change in frequency. Since, with the incorporation of GEWE scheme, electric field reduces at the drain end, less isotropic scattering is observed. Due to this reduced isotropic scattering, the scattering mechanism is not so effective in breaking the correlation between gate current and drain current [41]. Thus, cross-correlation (i.e. V1.V2*) reduces in GEWE-SiNW MOSFET at higher frequencies.

Moreover, the noise performance of GEWE-SiNW MOSFET further enhanced by tuning the workfunction difference by keeping the workfunction at the source side constant and varying the workfunction at the drain end. As we increase the workfunction difference to 0.7 eV, minimum noise figure decreases in comparison with 0.2 eV as is evident from Fig. 7a. It is very clear that change is observable at very high frequency (around 2.5–3 THz); around 7.82 % decrement is observed when workfunction

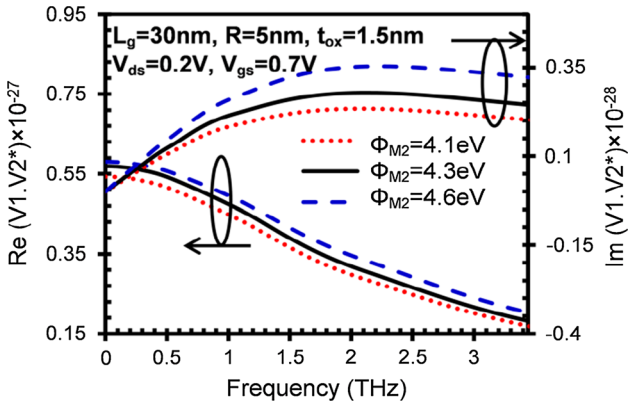


Fig. 8 Cross-correlation as a function of frequency for GEWE-SiNW MOSFET for different gate metal workfunction values at drain end

at the drain end is 4.1 eV owing to enhancement in transconductance and carrier transport efficiency. Moreover, noise conductance also decreases with increase in workfunction difference but more prominent at high frequency as is evident from the inset of Fig. 7b. Therefore, noise FOMs are not affected much with change in workfunction difference. Another parameter which decides the noise performance of a device is cross-correlation factor. Figure 8 shows the cross-correlation factor of GEWE-SiNW MOSFET of different metal gate workfunction at drain end and the result shows that with workfunction 4.1 eV, electric field reduces at the drain end which results in less scattering of carriers, and thus, correlation between input and output is less observed which is desirable for RF communication.

4 Conclusion

In this paper, a comprehensive small-signal behaviour and noise analysis of GEWE-SiNW MOSFET is explained in terms of *S*-parameters and noise FOMs at THz frequency range. The simulation results obtained shows that with the incorporation of GEWE scheme into SiNW, reflection coefficient decreases and transmission coefficient increases in comparison with SiNW and conventional MOSFET. Prominent reduction in noise metrics such as minimum noise figure, noise conductance and cross-correlation of GEWE-SiNW MOSFET in comparison to SiNW and Conventional MOSFET. This makes GEWE-SiNW MOSFET appropriate for microwave amplifier and oscillator designs. Moreover, tuning of gate workfunction difference noise metrics improves due to reduction in SCEs and improvement in transconductance, whereas forward gain degrades. Thus, we have to choose the optimum value of gate metal workfunction for better device performance at HF communication circuits and LNAs.

Acknowledgments The authors would like to thank Department of Science and Technology (DST), Government of India (SERB), and one of the authors (Neha Gupta) is grateful to the University Grant Commission (UGC) for providing the necessary financial assistance to carry out this research work.

References

1. C. Enz, An MOS transistor model for RF IC design valid in all regions of operation. IEEE Trans. Microw. Theory Tech. **50**(1), 342–359 (2002)
2. Q. B. Chen, Compact modeling of multi-gate MOSFETs for RF designs. in *IEEE International Wireless Symposium (IWS)*, pp. 1–4 (2013). doi:10.1109/IEEE-IWS.2013.6616743
3. ITRS, International Technology Roadmap for Semiconductors (2011)
4. A. Kumar, N. Gupta, R. Chaujar, Analysis of novel transparent gate recessed channel (TGRC) MOSFET for improved analog behaviour. Microsyst. Technol. **21**(5) (2015). doi:10.1007/s00542-015-2554-z
5. A. Kumar, N. Gupta, R. Chaujar, Novel design: transparent gate recessed channel (TGRC) MOSFET for improved reliability applications. in *IEEE 1st International Conference on Microelectronics, Circuits and Systems*, pp. 1–5 (2014)
6. A. Kumar, R. Chaujar, Monica, Thermal behavior of novel transparent gate recessed channel (TGRC) MOSFET: TCAD analysis. in *Tech-Connect World Innovation Conference & Expo* (2014)
7. H. Iwai, Roadmap for 22 nm and beyond (Invited Paper). Microelectron. Eng. **86**, 1520–1528 (2009)
8. D. W. Kim et al., Fabrication and electrical characteristics of self-aligned (SA) gate-all-around (GAA) Si nanowire MOSFETs (SNWFET). in IEEE International Conference on IC Design and Technology (ICICDT), pp. 63–66 (2010)
9. R. Wang et al., Analog/RF performance of Si nanowire MOSFETs and the impact of process variation. IEEE Trans. Electron Devices **54**(6), 1288–1294 (2007)
10. A. Sarkar, S. De, A. Dey, C.K. Sarkar, Analog and RF performance investigation of cylindrical surrounding-gate MOSFET with an analytical pseudo-2D model. J. Comput. Electron. **11**(2), 182–195 (2012)
11. S. Cho, K.R. Kim, B.G. Park, I.M. Kang, RF performance and small-signal parameter extraction of Junctionless silicon nanowire MOSFETs. IEEE Trans. Electron Devices **58**(5), 1388–1396 (2011)
12. W. Long, H. Ou, J.M. Kuo, K.K. Chin, Dual-material gate (DMG) field effect transistor. IEEE Trans. Electron. Devices **46**(5), 865–870 (1999)
13. C. Y. Zheng, The using of dual-material gate MOSFET in suppressing short-channel effects: a review. in IEEE International Conference on Electronics, Communications and Control (ICECC), pp. 2979–2982 (2011)
14. N. Gupta, A. Kumar, R. Chaujar, Oxide bound impact on hot-carrier degradation for gate electrode workfunction engineered (GEWE) silicon nanowire MOSFET, Microsyst. Technol. 1–10 (2015). doi:10.1007/s00542-015-2557-9
15. N. Gupta, R. Chaujar, Implications of transport models on the analog performance of gate electrode workfunction engineered (GEWE) SiNW MOSFET. in IEEE 2nd International Conference on Devices, Circuits and Systems (ICDCS), pp. 1–5 (2014)
16. N. Gupta, A. Kumar, R. Chaujar, Impact of device parameter Variation on RF performance of gate electrode workfunction engineered (GEWE)-silicon nanowire (SiNW) MOSFET. J. Comput. Electron. **14**(3), 798–810 (2015)

17. N. Gupta, A. Kumar, R. Chaujar, Investigation of frequency dependent Parameter of GEWE-SINW MOSFET for microwave and RF applications. Int. J. Adv. Technol. Eng. Sci. **2**(1), 35–40 (2015)
18. J.J. Liou, F. Schwierz, RF MOSFET: recent advances, current status and future trends. Solid-State Electron. **47**(11), 1881–1885 (2003)
19. C.H. Chen, M.J. Deen, Channel noise modeling of deep submicron MOSFETs. IEEE Trans. Electron Devices **49**(8), 1484–1487 (2009)
20. S. Asgaran, M.J. Deen, C.H. Chen, Analytical modeling of MOSFETs channel noise and noise parameters. IEEE Trans. Electron Devices **51**(12), 2109–2114 (2004)
21. K. Han, H. Shin, K. Lee, analytical drain thermal noise current model valid for deep submicron MOSFETs. IEEE Trans. Electron Devices **51**(2), 261–269 (2004)
22. Y. Tsividis, C. McAndrew, *Operation and Modeling of the MOS Transistor*, 3rd edn. (Oxford University Press, Oxford, 2013)
23. S.D. Yu, A unified channel thermal noise model for short channel MOS transistors. J. Semicond. Technol. Sci. **13**(3), 213–223 (2013)
24. C.H. Doan, S. Emami, S.M. Niknejad, R.W. Brodersen, Millimeter-wave CMOS design. IEEE J. Solid-State Circuits **40**(1), 144–155 (2005)
25. C. Hu, *Modern Semiconductor Device for Integrated Circuit* (Prentice Hall, Upper Saddle River, 2009), pp. 261–274
26. ATLAS User's Manual (SILVACO Int., Santa Clara, 2014)
27. A. Chaudhry, J.N. Roy, Mosfet models, quantum mechanical effects and modeling approaches: a review. J. Semicond. Technol. Sci. **10**, 20–27 (2010)
28. V. S. Patnaik, A. Gheedia, M. J. Kumar, 3D simulation of nanowire FETs using quantum models (2008)
29. G. Iannaccone, G. Curatola, G. Fiori, Effective Bohm Quantum Potential for device simulators based on drift-diffusion and energy transport. in *Simulation of semiconductor processes and devices (SISPAD)*, pp. 275–278 (2004)
30. S. D. Suk et al, High performance 5 nm radius twin silicon nanowire MOSFET (TSNWFET): fabrication on bulk Si wafer, characteristics, and reliability. in *IEEE International Electron Devices Meeting Technical Digest*, pp. 717–720 (2005). doi:10.1109/IEDM.2005.1609453
31. B. Yang, K.D. Buddharaju, S.H.G. Teo, N. Singh, G.Q. Lo, D.L. Kwong, Vertical silicon-nanowire formation and gate-all around MOSFET. IEEE Electron Device Lett. **29**(7), 791–794 (2008)
32. S.C. Rustagi et al., CMOS inverter based on gate-all-around silicon-nanowire MOSFETs fabricated using top-down approach. IEEE Electron Device Lett. **28**(11), 1021–1024 (2007)
33. I. Polishchuk, P. Ranade, T.J. King, C. Hu, Dual work function metal gate CMOS technology using metal interdiffusion. IEEE Electron Device Lett. **22**(9), 444–446 (2001)
34. J. Liu, H.C. Wen, J.P. Lu, D.L. Kwong, Dual-work-function metal gates by full silicidation of Poly-Si with Co-Ni bi-layers. IEEE Electron Device Lett. **26**(4), 228–230 (2005)
35. K.Y. Na, Y.S. Kim, Silicon complementary metal-oxide semiconductor field-effect transistors with dual work function gate. Jpn. J. Appl. Phys. **45**(12), 9033–9036 (2006)
36. O. Shirak, O. Shtempluck, V. Kotchtakov, G. Bahir, Y.E. Yaish, High performance horizontal gate-all-around silicon nanowire field-effect transistors. Nanotechnology **23**, 395202 (2012)
37. D. Moon, S.-J. Choi, J.P. Duarte, Y.-K. Choi, Investigation of silicon nanowire gate-all-around junctionless transistors built on a bulk substrate. IEEE Trans. Electron Devices **60**, 1355–1360 (2013)
38. J.-H. Lee, B.-S. Kim, S.-H. Choi, Y. Jang, S.W. Hwangc, D. Whang, A facile route to Si nanowire gate-all-around field effect transistors with a steep subthreshold slope. Nanoscale **5**, 8968–8972 (2013)
39. L. Belostotski, J.W. Haslett, Two-port noise figure optimization of source-degenerated cascade CMOS LNAs. Analog Integr. Circ. Sig. Process **55**(2), 125–137 (2008)
40. M. Golio, *Microwave and RF product applications*, 1st edn. (CRC-Press, Boca Raton, 2003)
41. D.M. Pozar, *Microwave engineering*, 4th edn. (Wiley, New York, 2012)

ResearchGate

See discussions, stats, and author profiles for this publication at: https://www.researchgate.net/publication/303914805

In-situ electrosynthesized Nanostructured Mn3O4-Polyaniline Nanofibers- Biointerface for Endocrine Disrupting Chemical Detection

Article *in* Sensors and Actuators B Chemical · June 2016

DOI: 10.1016/j.snb.2016.06.050

READS

97

8 authors, including:



Prabhakar Rai

Indian Institute of Technology Kanpur

44 PUBLICATIONS **501** CITATIONS

SEE PROFILE



Ashutosh Sharma IITK

Indian Institute of Technology Kanpur

360 PUBLICATIONS **8,189** CITATIONS

SEE PROFILE



Bansi Malhotra

Delhi Technological University

361 PUBLICATIONS **10,391** CITATIONS

SEE PROFILE



Renu John

Indian Institute of Technology Hyderabad

56 PUBLICATIONS **846** CITATIONS

SEE PROFILE

All in-text references underlined in blue are linked to publications on ResearchGate, letting you access and read them immediately.

Available from: Nawab Singh
Retrieved on: 20 July 2016

Sensors and Actuators B 236 (2016) 781–793

Contents lists available at ScienceDirect

Sensors and Actuators B: Chemical

journal homepage: www.elsevier.com/locate/snb

In-situ electrosynthesized nanostructured Mn_3O_4-polyaniline nanofibers- biointerface for endocrine disrupting chemical detection

Nawab Singh [a], Md. Azahar Ali [b], Kali Suresh [c], Ved Varun Agrawal [d], Prabhakar Rai [e], Ashutosh Sharma [e,*], B.D. Malhotra [f,*], Renu John [a,*]

[a] Department of Biomedical Engineering, Indian Institute of Technology Hyderabad, Kandi, Sangareddy-502285 Telangana, India
[b] Department of Electrical and Computer Engineering, Iowa State University, Ames, IA-50011, USA
[c] Centre for Nanotechnology, Hyderabad Central University, Hyderabad Telangana-500046, India
[d] Centre on Biomolecular Electronics, Biomedical Instrumentation Section, CSIR-National Physical Laboratory, Dr. K. S. Krishnan Marg, New Delhi-110012, India
[e] Department of Chemical Engineering, Indian Institute of Technology Kanpur, Kanpur, 208016, India
[f] Department of Biotechnology, Delhi Technological University, Shahbad Daulatpur, Main Bawana Road, Delhi-110042, India

ARTICLE INFO

Article history:
Received 9 March 2016
Received in revised form 31 May 2016
Accepted 7 June 2016
Available online 8 June 2016

Keywords:
Nanofibers
Mn_3O_4 nanoparticles
Polyaniline
Bisphenol A
Tyrosinase

ABSTRACT

We report results of the studies relating to fabrication of an electrochemical biosensor platform bas on *in-situ* electrosynthesized manganese oxide (Mn_3O_4)-polyaniline (PANI) nanofibers for detection bisphenol A (BPA), an endocrine disrupting chemical. The spherical Mn_3O_4 nanoparticles synthesiz using cetyltrimethylammoniumbromide were modified with PANI in presence of polyvinyl sulpho acid and glutaraldehyde. The tyrosinase (Tyrs) molecules covalently immobilized on the PANI-modif Mn_3O_4 nanofibers surface were characterized using X-ray diffraction, electron microscopy and Four transform infrared spectroscopy. This electrochemical biosensor exhibits a response time of 20 s, s sitivity of 0.776 mA μM^{-1} L cm^{-2}, respectively, and 0.134 mA μM^{-1} L cm^{-2} in the concentration rang 0.004–0.09 $\times 10^{-6}$ mol L^{-1} and 0.2–0.8 $\times 10^{-6}$ mol L^{-1} of BPA.

© 2016 Elsevier B.V. All rights reserv

1. Introduction

Polymeric materials are currently in increased demand in our daily lives due to their reusability, recoverability and stability [1]. Along with widespread applications of polymeric compounds in food, drinking water and packaging industry, questions have been posed on the harmfulness of these chemicals on human beings and animals. Bisphenol A (2, 2-bis (4-hydroxyphenyl) propane ($C_{15}H_{16}O_2$); BPA) is such a chemical that is used in manufacturing drinking water bottles, baby feeding bottles and food packaging industries [2]. It is also used for the synthesis of epoxy resins, polystyrene resins, polycarbonate, inner coating of food cans, dental sealants, food packaging and drug delivery systems [3]. BPA and other similar phenolic compounds are, therefore, a natural threat to our precious environment including drinking water. BPA is considered as an endocrine disrupting compound (EDC) since it may trigger secretion of natural estrogen by the human endocrine system, resulting in elevated estrogenic activity in t human body. EDCs are pollutants chemical that are known to affe the hormonal balance of various species including humans [4, BPA has been reported to have adverse effects such as can [6], decreased semen quality, reduced immunity, heart diseas obesity and impaired reproduction in human beings and anim [7–9]. Hence the detection of BPA in drinking water and food ev at very low concentration is very crucial from a public hea perspective. Several techniques such as high-performance liqu chromatography, gas chromatography, capillary electrophores chemiluminescence, [2,10,11] and ELISA have been employed the detection of BPA in a given environment. However, these met ods are expensive, time consuming, and require special expert for handling the complex procedure. Some immunosensors ha been reported for detection of BPA using BIACORE 3000 sensor ch [12] waveguide-based evanescent immunosensor, [13] and piez electric immunosensor [14]. In spite of these developments, the is enough scope for the development of an improved biosensi device that can be used for BPA detection.

Manganese oxide (Mn_3O_4) is one of the most stable tran tion metal oxides with a spinel structure. It is being explor for the development of rechargeable lithium ion batteries, cat

* Corresponding authors.
E-mail addresses: ashutos@iitk.ac.in (A. Sharma), bansi.malhotra@gmail.com (B.D. Malhotra), renujohn@iith.ac.in, rjohniitd@gmail.com (R. John).

http://dx.doi.org/10.1016/j.snb.2016.06.050
0925-4005/© 2016 Elsevier B.V. All rights reserved.

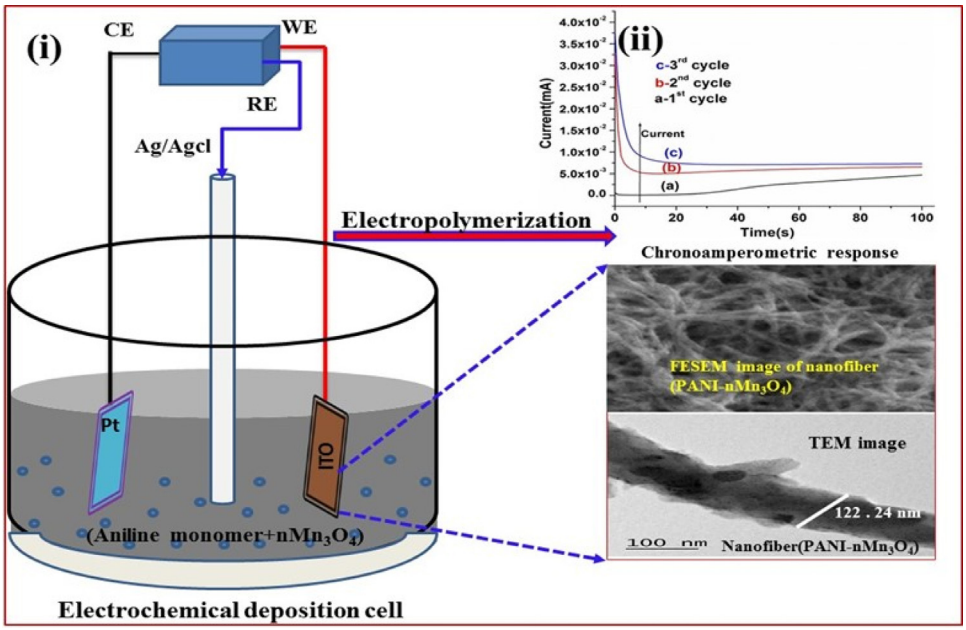


Fig. 1. (i) Schematic representation of In-situ electropolymerization of Mn_3O_4-polyaniline nanocomposite (ii) Chronoamperometric current responses during in-situ electropolymerization of Mn_3O_4 nanoparticles with aniline monomer.

ysis and molecular adsorption [15–17]. Mn_3O_4 is a tetragonal Hausmannite with Mn^{3+} and Mn^{2+} ions occupying octahedral and tetrahedral positions of the spinel structure, respectively. The octahedral symmetry of Mn_3O_4 is tetragonally distorted due to the Jahn–Teller effect on Mn^{3+} ions. The unit cell of Mn_3O_4 contains $Mn_4Mn_8O_{16}$ in which the oxygen atoms are closely packed with Mn^{2+} ion in tetrahedral-site and Mn^{3+} ion in octahedral-site [18,19]. The nMn_3O_4 exhibits ferrimagnetic behavior at Curie temperature (T_c = 40 K) and has excellent electron transport properties [20,21]. Due to excellent electron transfer, stability and electrochemical properties, nMn_3O_4 can perhaps be utilized for biosensing applications [22].

Polyaniline (PANI) is a conducting polymer that is known to be cost-effective, environmentally stable and has interesting tunable conducting properties. The composites of transition metal oxides and conducting polymers have been used for fabrication of supercapacitor electrodes [23,24]. The electrochemical polymerization has been utilized to prepare bioactive nanofiber (NF) of PANI-nMn_3O_4 in presence of aniline, polyvinyl sulphonic acid (PVSA) and hydrochloric acid. PANI-nMn_3O_4 NF is an attractive material that provides a suitable interface for immobilization of proteins due to large specific surface area, highly conductive nature and strong adsorption ability [25–28].

We report results of the studies relating to preparation of spherical nMn_3O_4 via co-precipitation method and electropolymerized with aniline in presence of hydrochloric acid (HCL) and polyvinylsulphonic acid (PVSA) as a binder using chronoamperometric technique. Glutraldehyde (GA) treatment was used to crosslink tyrosinase (Tyrs) with PANI-nMn_3O_4 electrode surface for detection of BPA using amperometric technique. We discuss the merits of this interesting nanohybrid biointerface for BPA detection.

2. Experimental

2.1. Chemicals and reagents

All chemicals used were of analytical grade. Manganese chloride, sodium hydroxide, cetyltrimethylammonium bromide (CTAB), aniline, HCL, PVSA, GA, tyrosinase (Tyrs), BPA, phenol, resorcinol, para-aminophenol, ortho-nitrophenol, and hydroquinone were purchased from Sigma Aldrich, USA. Deionized water used for all experiments was obtained from Millipore. Phosphate buffer saline (PBS) was prepared using sodium monohydrate phosphate (Na_2HPO_4) and sodium dihydrogen phosphate (NaH_2PO_4) reagents, following standard protocols.

2.2. Synthesis of nanostructured manganese oxide

Colloidal solution of Mn_3O_4 was prepared using manganese chloride ($MnCl_2$) as the precursor. 0.5 mol L^{-1} of $MnCl_2$ and 0.2 mol L^{-1} of NaOH were separately dissolved in 250 mL ethanol and distilled water, respectively and then mixed. Spherical nMn_3O_4 was synthesized by co-precipitation method by using cetyltrimethylammoniumbromide (0.4×10^{-3} mol L^{-1}) as a surfactant [29,30]. Thus formed precipitate was washed with deionized water and ethanol seven times and dried at 90 °C for 24 h, and then calcined at 450 °C for 4 h.

2.3. Fabrication of the sensor platform

2 mg of nMn_3O_4 was dispersed in 12 mL of 1 mol L^{-1} HCL by stirring constantly for 6 h and ultrasonicated for 90 min after which 100 μL of 0.1 mol L^{-1} distilled aniline was added. After 3 h of constant stirring in a dark place, 100 μL of 0.5 mol L^{-1} PVSA was added drop-wise while shaking. Subsequently, 10 mL of the solution was used for electropolymerization using chronoamperometric technique. The thin film of PANI-Mn_3O_4 is shown in [Fig. 1(i)]. The solution comprising of distilled aniline, PVSA and nMn_3O_4 dispensed in 1 mol L^{-1} HCL was used to prepare nanocomposite fibers via electropolymerization. During electrochemical deposition, the potential was kept at 1.5 V for three cycles of 100 s. After each cycle, electrode was washed with DI water drop-wise in order to form stable PANI-nMn_3O_4NF/ITO film and the current flowing through the electrode deposition was monitored for 100 s. The high current observed in the initial stage originated due to double layer charging. The stable electrochemical deposition current of PANI-nMn_3O_4 NF [Fig. 1 (ii-curve c)] during third cycle was found to be about 10 times higher compared to the second cycle (curve b) and the cur-

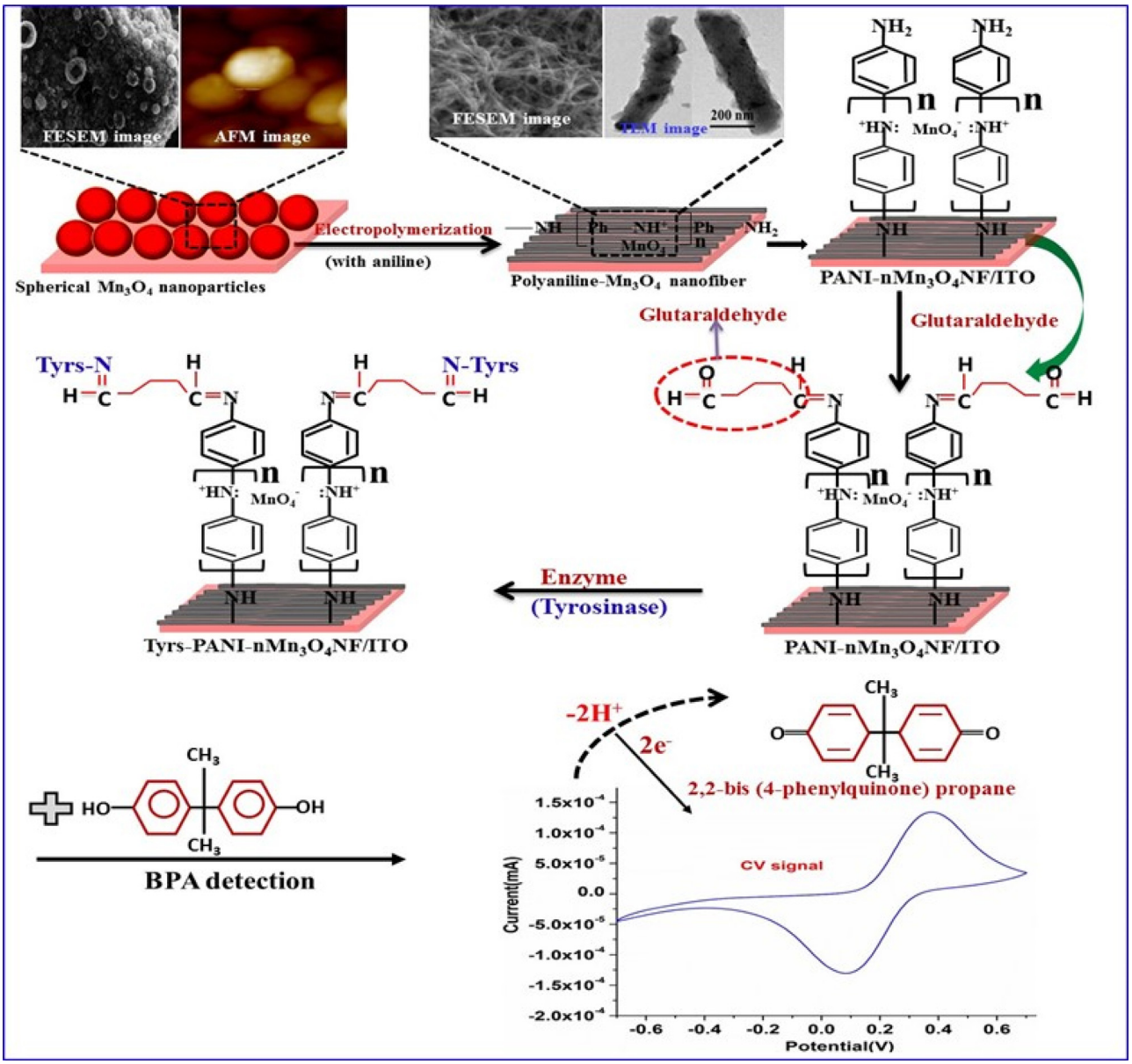


Fig. 2. Schematic representation of fabrication of a biosensor platform for detection of endocrine disrupting chemicals and the mechanism for crosslinking with enzy molecules.

Table 1
Comparison table for various biosensors characteristics with the fabricated Tyrs-PANI-nMn_3O_4NF/ITO bioelectrode.

Electrodes	Techniques	Linear range (μM)	LOD (μM)	Sensitivity	Reference
Molecular Imprinted polymer film	EIS	0–12,000	420	0.00411 Ω mM^{-1} L	Apodaca et al. [37
TyrsAPTES/nTiO_2/Ti	EIS	0.01–1.0	0.01	361.9 kΩ mM^{-1} L	Singh et al. [3]
Pt/Gr-CNTs	CV/DPV	0.06–10	0.042		Zheng et al. [31]
Polypyridyl ruthenium(II)	CV/DPV	5–120	0.29	0.22 μA $μM^{-1}$ L	Li et al. [38]
Tyrs MWNTs-CoPc-SF	CV	0.05–3.0	0.03		Yin et al. [39]
Tyrs/Thionine- carbon	CV	0.15–45	0.15	85.4 ± 1.5 nA $μM^{-1}$ L	Portaccio et al. [40
MIP Au	CV	8–60	13.8	–	Huang et al. [41]
Tyrs@PANI-Mn_3O_4/ITO	CV	0.004–0.8	0.004	0.776 mA $μM^{-1}$ L cm^{-2}	Present Work

rent observed during the second cycle was about 20 times higher as compared to first cycle (curve a). It was found that the PANI-nMn_3O_4 NF could be uniformly deposited during the third cycle (curve c) after which PANI-nMn_3O_4 NF/ITO electrode was dipped in 1% GA for 2 h in a closed vessel for cross linking with enzyme (Tyrs) molecules. Fresh solution of Tyrs enzyme (0.2 unit/mL) was prepared in PBS (50×10^{-3} mol L^{-1}, pH 7.0) and was uniformly spread (10 μL) onto the PANI-nMn_3O_4 NF/ITO electrode surface and kep in a humid chamber for 12 h at room temperature (27°C). The fa ricated Tyrs immobilized PANI-nMn_3O_4NF/ITO bioelectrode w stored at 4 °C when not in use. The proposed mechanism for fabric tion of Tyrs-PANI-nMn_3O_4NF/ITO bioelectrode and immobilizati of Tyrs onto this electrode is shown in Fig. 2.

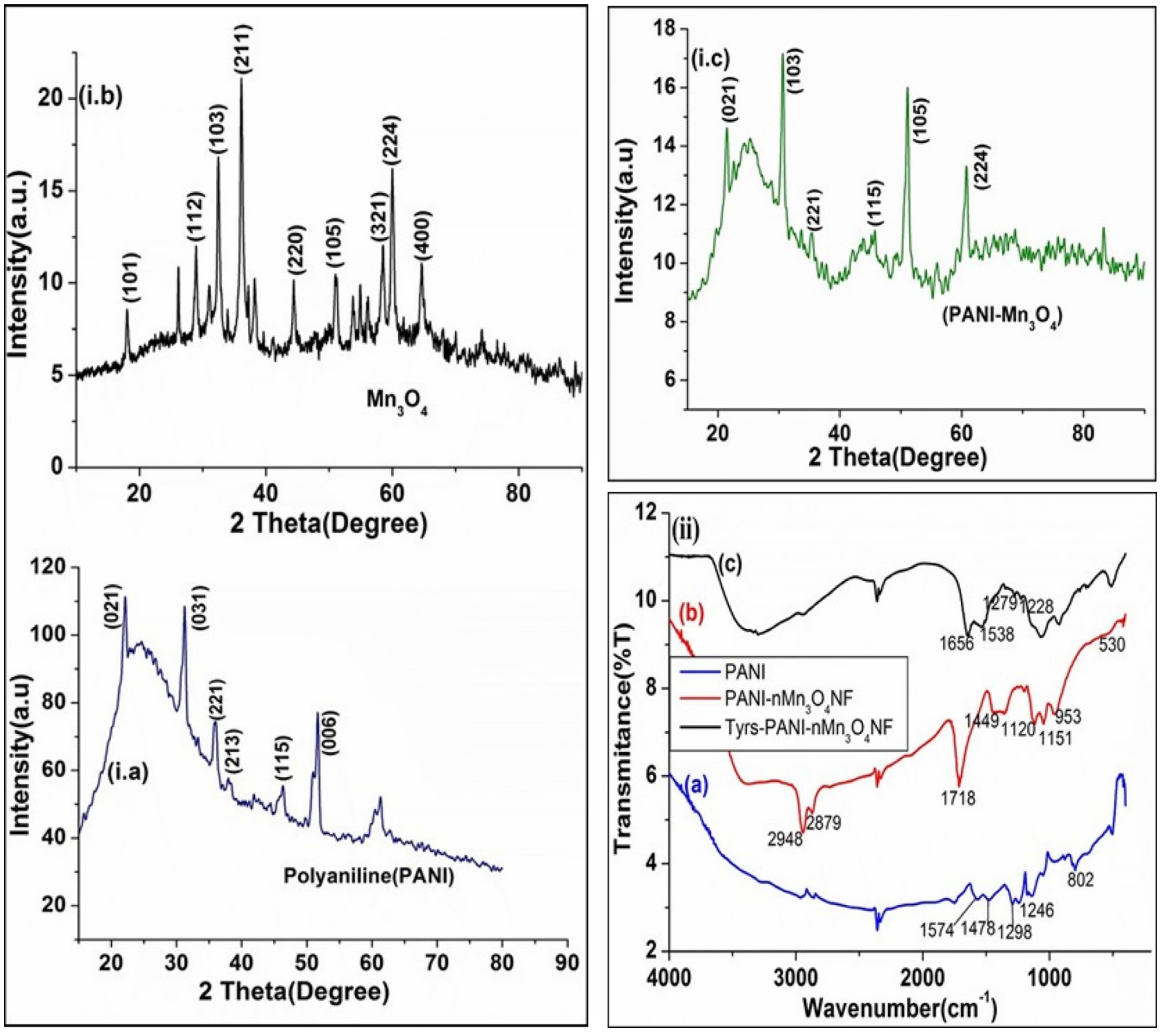


Fig. 3. (i) X-ray diffraction pattern of (i.a) polyaniline, (i.b) spherical Mn_3O_4 nanoparticle, and (i.c) PANI-nMn_3O_4 nanocomposite (ii) FTIR spectra of (a) polyaniline, (b) PANI-nMn_3O_4/ITO electrode and (c) Tyrs-PANI-nMn_3O_4/ITO bioelectrode.

2.4. Real sample preparation

A real sample solution of BPA was prepared using two types of plastic products (polyvinyl chloride and polycarbonate mineral water bottles) available in local market [3,31]. These plastic products were cut into small pieces and washed using double distilled water. Then 15.0 gm. plastic pieces were added into a 100 mL double distilled water and sealed. The solution was then ultrasonicated for 90 min at 60 °C, and kept at 85 °C with a water bath for 48 h. After filtration, the solution was collected in a flask. The extraction process was repeated three times, and the solutions were collected in the same flask and the concentration of the stock solution with BPA was found to be 0.520×10^{-6} mol L^{-1}. For dilution of this stock solution, we used deionized water with desired concentrations.

2.5. Characterization

Spherical nMn_3O_4 and its composite with PANI were characterized using X-ray diffraction (XRD, Rikagu) and high resolution transmission electron microscope (HRTEM, Jeol/JEM 2100). The surface morphology shapes were studied using field emission scanning electron microscope (FESEM, ZEISS) and atomic force microscope (AFM, BRUKER NanoScope®.V-4498BE). The elemental analysis was conducted using energy dispersive X-ray spectroscopy (EDAX). Fourier transform infra-red spectroscopy (FT-IR) from Perkin Elmer, (Spectrum BX II) was used for confirmation of the functional groups in Tyrs enzyme immobilized on electrode surface. X-ray photoelectron spectroscopy (XPS; PHI 5000 Versa Prob II, FEI Inc.) studies have conducted to investigate the functional groups and chemical bonding of the synthesized materials. Electrochemical studies were performed using Autolab Potentiostat/Galvanostat (Metrohm, Netherlands) in a three-electrode system with PANI-nMn_3O_4 deposited on indium tin oxide (ITO) glass substrate as a working electrode, platinum (Pt) as the auxiliary electrode and Ag/AgCl as reference electrode in phosphate buffer saline (PBS) (50×10^{-3} mol L^{-1}, pH 7.4, 0.9% NaCl) containing 5×10^{-3} mol L^{-1} $[Fe(CN)_6]^{3-/4-}$ as mediator.

3. Results and discussion

3.1. Structural properties

Fig. 3.i (a–c) shows the X-ray diffraction (XRD) pattern obtained for PANI, nMn_3O_4, and PANI–nMn_3O_4 nanocomposite. The XRD pattern of PANI film [Fig. 3 (i.a)] shows peaks at $2\theta = 22.07$, 31.16, 35.70, 37.98, 46.22, and 51.65 that correspond to (0 2 1), (0 3 1), (2 2 1), (2 1 3), (1 1 5), and (0 0 6) reflection planes, respectively. These are well-matched with JCPDS file 53-1891. This indicates that PANI film is semi-crystalline [32] and the structure is orthorhombic with cell parameters a = 6.98, b = 8.63, c = 10.44 with respect to α,

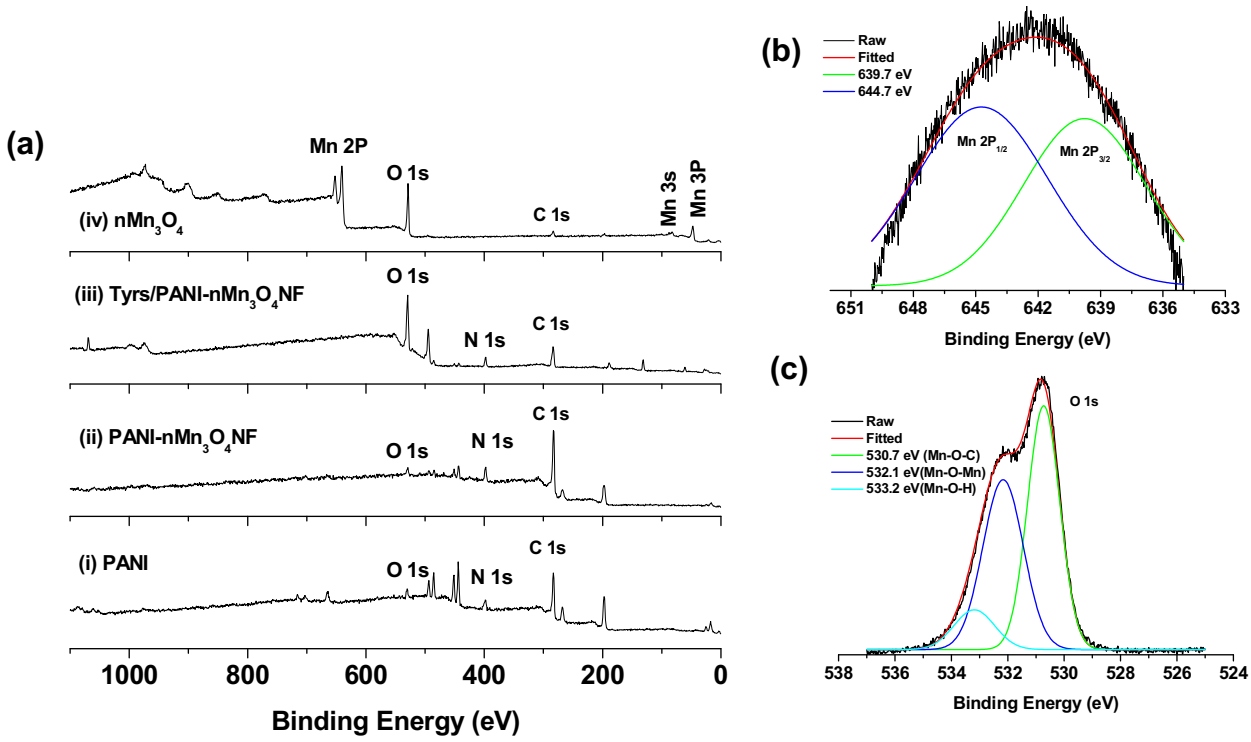


Fig. 4. (a) Wide-scan spectra for various fabricated films in the energy region of 0–1100 eV. (b) The XPS core-level spectra of Mn 2 P and (c) core-level spectra of O 1 s Mn_3O_4 film.

β, γ, respectively. The additional peaks found in the XRD spectra are ascribed to the ITO substrate. The presence of dominant peaks of nMn_3O_4 in the XRD pattern for synthesized spherical nMn_3O_4 [Fig. 3 (i.b)] reveals high degree of crystallinity as well as purity of the sample. The diffraction peaks seen at 2θ = 18.11, 28.84, 32.50, 36.15, 44.44, 51.07, 58.37, 60.02, and 64.60 pertain to (1 0 1), (1 1 2), (1 0 3), (2 1 1), (2 2 0), (1 0 5), (3 2 1), (2 2 4), and (4 0 0) reflection planes, respectively, are well matched to the tetragonal spinel structure of Mn_3O_4. These results are consistent with the values obtained for Mn_3O_4 (JCPDS files, 89-4837, 80-0382 and 24-0734). The average crystallite size of nMn_3O_4 obtained by Debye–Scherrer equation is found to be 25–28 nm for the 2 1 1 plane. The nMn_3O_4 has a tetragonal Hausmanite structure with body centered lattice parameters as a = 5.76 A°, c = 9.44 A° with respect to α, and γ, respectively, which are in agreement with JCPDS 24-0734. The XRD spectra of PANI–nMn_3O_4 nanocomposite [Fig. 3(i.c)] shows diffraction peaks at 2θ = 21.45°, 31.04°, 35.37°, 45.88°, 51°, and 60.60° corresponding to (0 2 1) (1 0 3), (2 2 1) (1 1 5), (1 0 5), and (2 2 4) reflection planes of the tetragonal phase of nMn_3O_4, respectively. The crystallite size for PANI–nMn_3O_4 nanocomposite is found to be 30–35 nm for the (1 0 3) plane. The selected area electron diffraction (SEAD) indicates crystallinity in PANI–nMn_3O_4 nanocomposite with improved charge transfer properties of the electrochemical biosensor [inset, Fig. 4 (iii)]. The results indicate that the nMn_3O_4 interact with the anilinium cation and oligomers, that are formed during the initial stage of the polymerization and act as a template for the self-assembly of the PANI chains in a well-ordered manner.

Fig. 3 (ii) shows the Fourier transform infra-red (FT-IR) spectra of PANI, PANI-nMn_3O_4 NF, and Tyrs-PANI-nMn_3O_4 NF films. The FT-IR spectrum of bare PANI (curve a) shows characteristic vibrational peaks at 1574, 1478, 1298, 1246, and 804 cm^{-1}. The peaks found at 1574 and 1478 cm^{-1} are attributed to the C=C quinoid ring stretching vibrations and benzenoid structure of PANI, respectively. The characteristic peak pertaining to PANI backbone is observed at 804 cm^{-1}. The peaks found at 1298 and 1246 cm^{-1} correspond to the C—N and —C=N stretching vibrations due to emeraldi salt in PANI indicating that aniline is polymerized at the surfa of ITO electrode with free $—NH_2$ groups [25]. The FTIR spectra PANI-nMn_3O_4 NF shown in (curve b) exhibits additional peaks 1718 cm^{-1} and 1449 cm^{-1} due to carbonyl (C=O) stretching of ald hyde and C—C stretching of the aromatic ring, respectively. T peaks observed at 2948 and 2879 cm^{-1} are attributed to the stretc ing of –C—H bond. The FTIR spectra obtained for the nanocompos shows similar characteristic peaks. However, the peaks for ba PANI film are found to be shifted due to the formation of hydrog bonding between Mn_3O_4 and the –NH groups of PANI. In ad tion, the nanocomposite exhibits characteristic peaks at 953 a 530 cm^{-1} in the fingerprint region arising due to the vibrations Mn–O are associated with the coupling between Mn–O stretchi modes of tetrahedral and octahedral sites [33]. After immobiliz tion of Tyrs on the surface of PANI-nMn_3O_4 NF (curve c), t peaks observed at 1228 cm^{-1} and 1279 cm^{-1} correspond to —C= stretching vibrations of the amide. The peaks seen at 1539 cm and 1656 cm^{-1} are attributed to the NH bending in carbonyl ami bond. These results confirm the surface functionalization of PAN nMn_3O_4 NF with Tyrs enzyme.

The X-ray photoelectron spectroscopy (XPS) studies we undertaken to confirm the presence of the functional groups nMn_3O_4, PANI NF, PANI-nMn_3O_4 NF and Tyrs-PANI-nMn_3O_4 films on ITO electrode and the formation of amide betwe enzymes and PANI-nMn_3O_4 NF electrodes. The C 1s, N 1s, and 1 s peaks in the wide-scan spectrum of PANI NF, PANI-nMn_3O_4 and Tyrs-PANI-nMn_3O_4NF films are shown in Fig. 4 (i–iii). The M 2P, Mn 3P, Mn 3s, and O 1 s peaks found in the wide-scan spectra nMn_3O_4 indicate the formation of nMn_3O_4 Fig. 4 (iv). All core-le spectra were deconvoluted into characteristic peaks using a Shirl baseline with a Gaussian profile. The Mn 2 P peak for nMn_3O_4 fi was deconvoluted and split into two characteristic peaks at bindi energies of 639.7 ($Mn2P_{3/2}$) and 644.4 eV ($Mn2P_{1/2}$) due to occu rence of Mn^{4+} (Fig. 4b). The O 1 s peaks for nMn_3O_4 film at 530

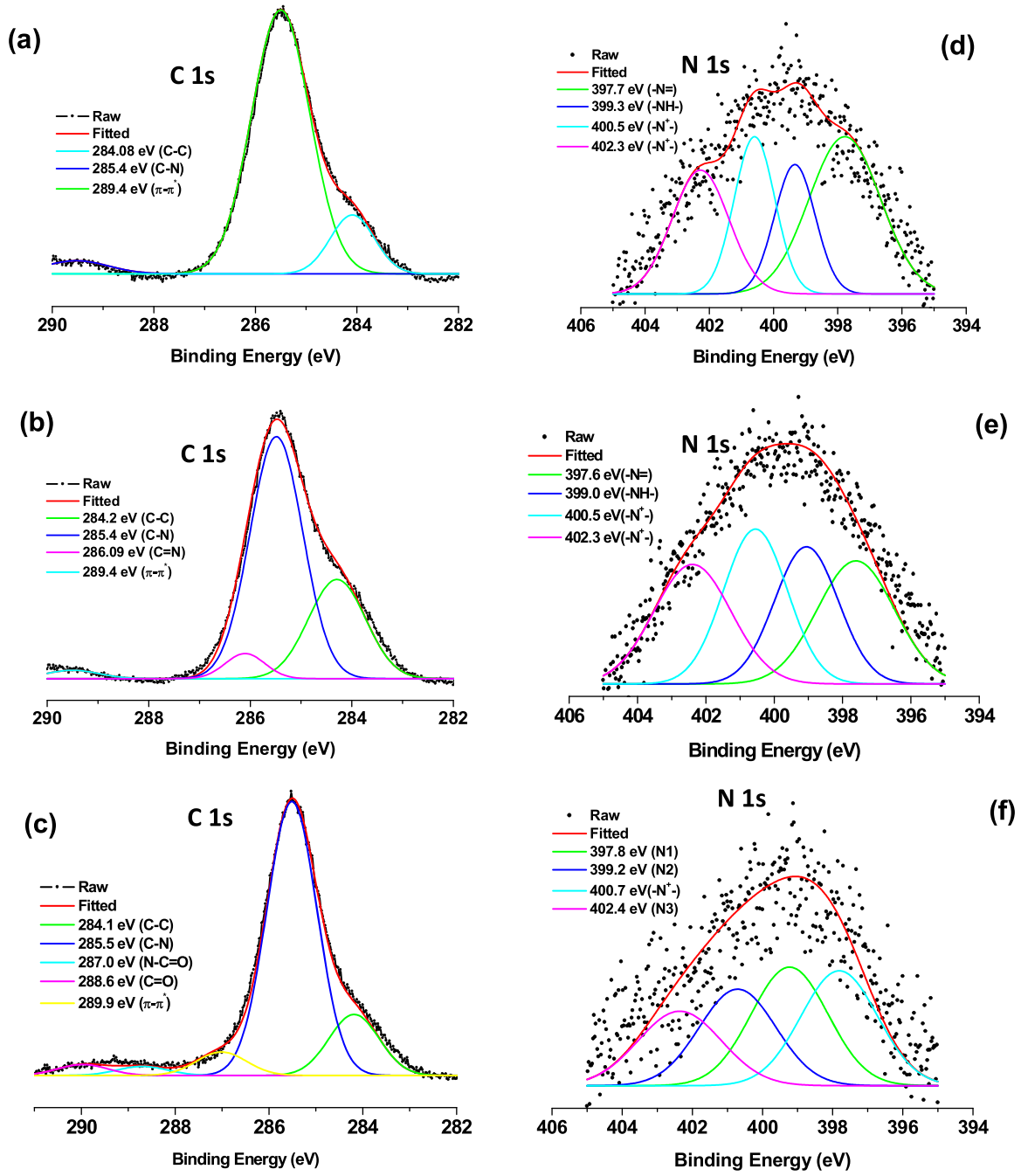


Fig. 5. XPS core-level spectra of C 1 s for the PANI NF (a), PANI-nMn_3O_4 NF (b) and Tyrs/PANI-nMn_3O_4 NF (c) electrodes. Core-level spectra of N 1 s for the PANI NF (a), PANI-nMn_3O_4 NF (b) and Tyrs/PANI-nMn_3O_4 NF (c) electrodes.

532.1 and 533.2 eV correspond to Mn—O—C, Mn—O—Mn and Mn-O—H, respectively and are due to the formation of metal–O—C bond, and metal-O (Fig. 4c).

The XPS C 1 s peaks found at 284.08, 285.4, and 289.4 eV pertain to the PANI NF electrode alone, without nMn_3O_4 and Tyrs enzyme, due to the C—C group in the aromatic ring, C—N bonds, and the p–p* "shake-up" satellite, respectively (Fig. 5a, top graph). On incorporation on nMn_3O_4 into PANI electrode, no significant changes of these C 1 s peaks were observed. However, one additional peak at binding energy of 286.09 eV corresponds to the C=N bond present in the composite formation and the peak due to the C—C groups in PANI is shifted to higher binding energy of 0.2 eV (Fig. 5b). After Tyrs immobilization onto PANI-nMn_3O_4 NF, the additional peaks found at binding energies of 287.0 and 288.6 eV, correspond to N—C=O and C=O bonds due to covalent amide bond formation between Tyrs enzyme and PANI-nMn_3O_4 in presence of glutaraldehyde cross-linker (Fig. 5c). Fig. 3d shows the N 1 s core-level spectra for PANI NF without nMn_3O_4 and Tyrs enzyme. The peaks for N 1 s core level of PANI at the binding energies of 397.7, 399.3, and 400.5 eV are due to presence of —N=, –NH-, and —N^+-, respectively in PANI matrix (Fig. 5d). These peaks with modification of nMn_3O_4 in PANI matrix were not significantly shifted (Fig. 5e). After enzyme immobilization, the peak found at 297.9 eV correspond to the core-level electrons of N 1 s (N1), the peak at 399.2 eV is due to amide bond (CO—NH) formation (N2), and the peak at 402.4 eV is assigned to presence of ≡N species in enzymes (N3) (Fig. 5f). However, the peaks at binding energies of 297.9 eV and 399.2 eV for N 1 s pertaining to enzymes and PANI are perhaps overlapped. These results

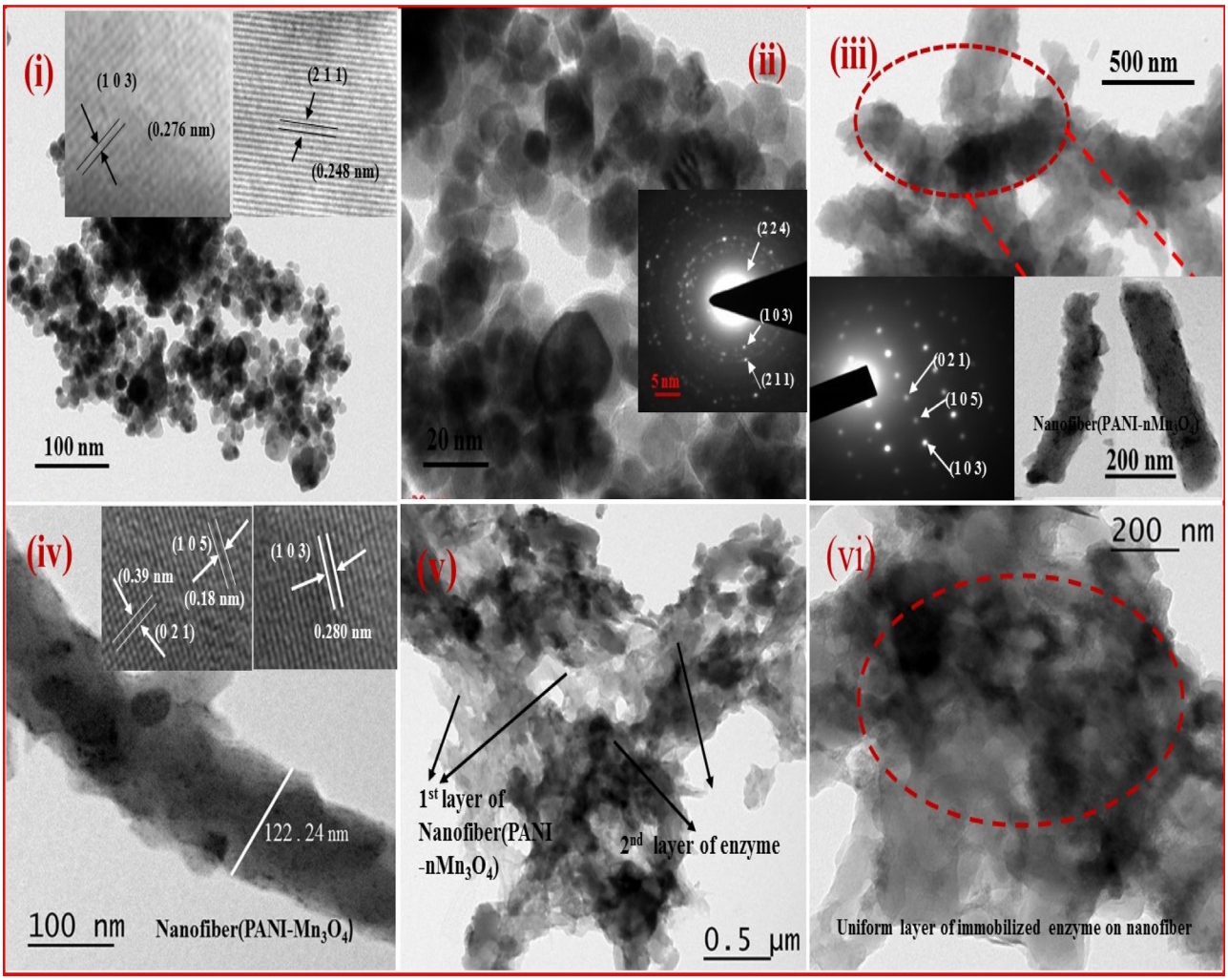


Fig. 6. (i and ii) TEM images of spherical Mn_3O_4 nanoparticles, inset images are HRTEM and SAED pattern, (iii and iv) TEM images of PANI-nMn_3O_4 nanofibers, inset zo image of PANI-nMn_3O_4 nanofiber, inset images are HRTEM and SAED pattern, (v and vi) TEM images of Tyrs-PANI-nMn_3O_4/ITO bioelectrode after Tyrs immobilization.

confirm the formation of composite and covalent immobilization with Tyrs enzyme molecules.

To investigate the size of the synthesized nMn_3O_4 and PANI NF modified with nMn_3O_4, we conducted high resolution-transmission electron microscopy (HR-TEM). It is found that the nanostructure contains uniformly sized fine granules [Fig. 6(i-ii)] of nMn_3O_4 with hexagonal shape (20–25 nm). The clear lattice fringes seen in SAED pattern [inset, Fig. 6(ii)] indicate highly crystalline structure of the nMn_3O_4. In the atomic scale image (i, inset), two different lattice spacings (d) for (2 1 1) and (1 0 3) planes obtained are 0.248 nm and 0.276 nm, respectively. These results are in support of the JCPDS files 24-0734 and 80-0382, respectively indicating that growth of the nanoparticles occurs mostly along the 2 1 1 and 1 0 3 directions. After electropolymerization with aniline, the PANI coated nMn_3O_4 nanocomposite shows NF network [Fig. 6(iii–iv)]. A single PANI coated nMn_3O_4 NF of about 122.24 nm diameter is shown in image (iv). The SAED pattern of PANI-nMn_3O_4 nanocomposite indicates existence of the (1 0 3), (1 0 5) and (0 2 1) planes (inset, iii) that exactly match with the lattice spacing with d values of 0.280 nm, 0.18 nm and 0.39 nm, respectively (inset in Fig. 6(iv)). These results reveal that electropolymerized PANI-nMn_3O_4 NF provides a suitable biointerface for uniform linking of the Tyrs biomolecules. And it can be seen that Tyrs enzyme is uniformly attached with PANI-nMn_3O_4 NF surface due to inter-particle interactions of PANI-nMn_3O_4 NF and Tyrs enzyme molecules via [image (v–vi)].

3.2. Surface morphological studies

The SEM image [Fig. 7(i)] shows that the nMn_3O_4 are clos packed, and porous. The nMn_3O_4 exhibits numerous flower-li aggregations [inset in Fig. 7(i)] and some are elongated in stru ture. To investigate the atomic ratio and weight% of Mn and O, carried out elemental (EDAX) analysis for the synthesized nMn_3 [Fig. 7(ii)]. This study confirms the presence of 35 wt% of O a 65 wt% of Mn in the spherical nMn_3O_4 indicating high concent tion of manganese and oxygen elements. The EDAX mapping nMn_3O_4 after calcination containing mixed elements of Mn a O is shown in Fig. S1(a). The EDAX mapping confirms the pr ence of Mn (image b, Fig. S1) and oxygen elements (image c, S1) in Mn_3O_4 nanoparticles. It appears that most nanoparti have spherical flower-like microsphere morphology, with glob lar 3D structure [Fig. 7 (iii) and (iv)]. After electropolymerization nMn_3O_4 with PANI on ITO, a fibrous film of PANI-coated nMn_3O_4 obtained [Fig. 7(v)]. The electropolymerized PANI-nMn_3O_4 resu in the formation of symmetrical fibers of PANI-coated nMn_3 deposited on the ITO substrate. The porous surface morpholo of nanofibrous PANI-nMn_3O_4 is beneficial for immobilization Tyrs enzyme molecules. Further, the PANI-nMn_3O_4NF/ITO surfa

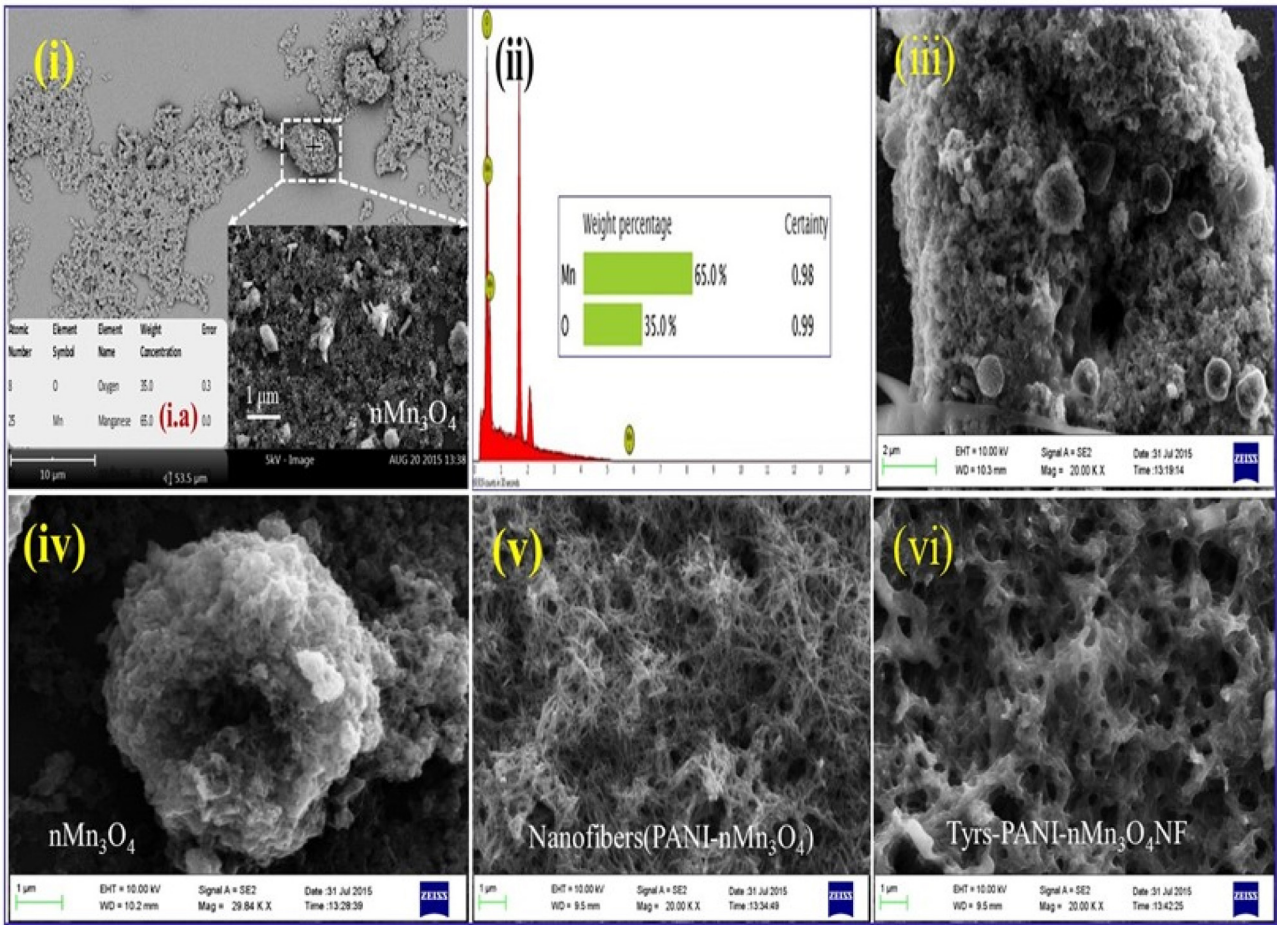


Fig. 7. (i) SEM image of spherical Mn_3O_4 nanoparticles, inset shows magnified image of spherical Mn_3O_4 nanoparticles, (ii) Elemental analysis (EDAX) image of spherical Mn_3O_4 nanoparticles, (iii and iv) FESEM images of spherical Mn_3O_4 nanoparticles, (v) FESEM image of PANI-nMn_3O_4 nanofibers, and (vi) FESEM image of Tyrs-PANI-nMn_3O_4/ITO bioelectrode after Tyrs immobilization.

was functionalized with GA via amino groups of the polyaniline surface for binding of the enzyme molecules.After enzyme immobilization, the change in morphology of Tyrs-PANI-nMn_3O_4NF/ITO surface perhaps occurred [Fig. 7(vi)] due to the covalent interaction of GA and enzyme. The FESEM image of enzyme immobilized on PANI-nMn_3O_4 NF shows a well- arranged and uniform fiber network, that further confirms strong enzyme binding.

The micrograph [Fig. S2 (i)] shows partially uniform spherical nMn_3O_4. The average size of the spherical nMn_3O_4 is calculated as 104 nm with average film roughness of 22.7 nm. The magnified image of nMn_3O_4 and the 3D image are shown in the inset of [Fig. S2 (i.a) and (vi)], respectively. After electropolymerization of PANI-nMn_3O_4 (image ii and iii), the changes in the grain size distribution, structural arrangement and shape of the PANI-nMn_3O_4NF/ITO are observed. The average roughness of PANI-nMn_3O_4NF/ITO film is found to be 90.7 nm. [Fig. S2 (iv)] and its 3D image (v) shows immobilization of the Tyrs enzyme onto the surface of PANI-nMn_3O_4NF/ITO. The Tyrs-PANI-nMn_3O_4NF/ITO electrode surface becomes uneven with increased value of average roughness (331 nm) indicating that Tyrs is adsorbed onto the PANI-nMn_3O_4NF/ITO surface.

3.3. Electrochemical studies

The electrochemical impedance can be represented as the sum of the real (Z′) and imaginary (Z″) components that mainly originate from the resistance and capacitance of an electrochemical cell. Fig. 8(i) shows the EIS spectra of various electrodes obtained as a function of frequency (0.01–105 Hz) at a bias potential of 0.01 V and the equivalent circuit for the EIS measurements [inset in Fig. 8 (i)]. The charge transfer resistance (R_{CT}) between the electrolyte and electrode can be described by (Eq. (1)), [34]

$$Z(\omega) = R_s + \frac{R_{CT} + \sigma\omega^{-1/2}}{(C_d\sigma\omega^{1/2}+1)^2 + \omega^2 C_d^2\left(R_{CT}+\sigma\omega^{-1/2}\right)2} - j\frac{\omega C_d\left(R_{CT}+\sigma\omega^{-1/2}\right)2 + \sigma\omega^{-1/2}\left(\sigma\omega^{1/2}C_d+1\right)}{(C_d\sigma\omega^{1/2}+1)^2 + \omega^2 C_d^2\left(R_{CT}+\sigma\omega^{-1/2}\right)2} \quad (1)$$

where R_s is the solution resistance, C_d is the double layer capacitance, ω is the 2πf, where f is the frequency, and σ is defined by

$$\sigma = \frac{RT}{\sqrt{2}F^2A}\left(\frac{1}{\sqrt{D_o C_o^*}} + \frac{1}{\sqrt{D_R C_R^*}}\right)$$

where A is the area of the electrode, D_o and D_R are respectively the diffusion coefficients of oxidant and reductant, C_o^* and C_R^* are the bulk concentrations of oxidant and reductant, respectively, and other symbols have the standard meanings. The R_{CT} value can be calculated from semicircular region in the Nyquist plot and it is found to be lower (551.4 Ω, curve b) for PANI-nMn_3O_4NF/ITO electrode compared to that of the bare ITO electrode (1.94 kΩ, curve a). This is due to the formation of PANI-nMn_3O_4 NF that provides excellent electrical contact between the PANI-nMn_3O_4NF/ITO elec-

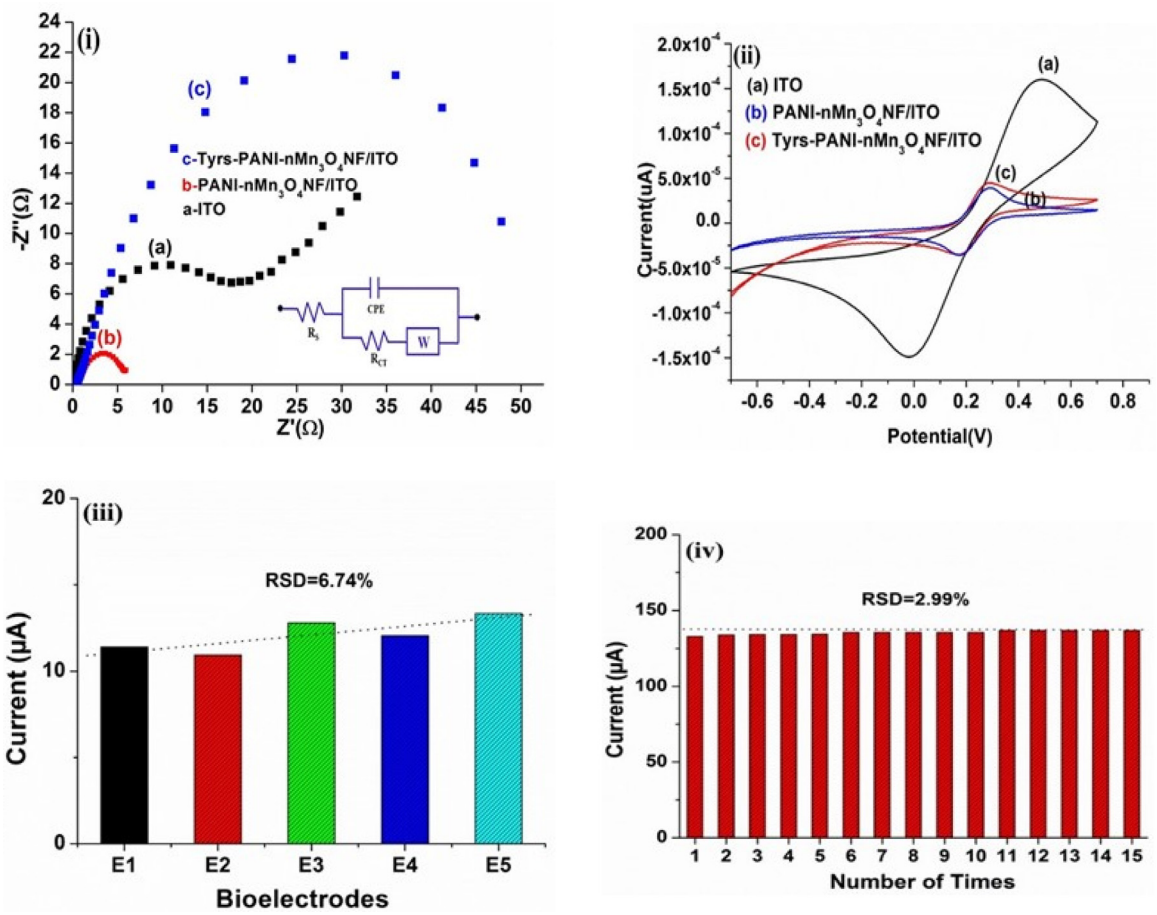


Fig. 8. (i) Electrochemical impedance spectroscopy (EIS) spectra of (a) ITO electrode, (b) PANI-nMn_3O_4/ITO electrode, and (c) Tyrs-PANI-nMn_3O_4/ITO bioelectrode in (50 mM, pH 7.4) solution containing 5 mM $[Fe(CN)_6]^{3-/4-}$. (ii) The cyclic voltammogram of, (a) ITO electrode, (b) PANI-nMn_3O_4/ITO electrode, and (c)Tyrs-PANI-nMn_3O_4/ bioelectrode. (iii) The reproducibility of Tyrs-PANI-nMn_3O_4/ITO bioelectrode, and (iv) Repeatability of Tyrs-PANI-nMn_3O_4/ITO bioelectrode.

trode and electrolyte. The conductive nature of the nanocomposite, facilitates interfacial electron transfer from electrolyte towards the collector. Moreover, it appears that nanofibrous PANI suitably arranges the nMn_3O_4 on its surface and provides a better conformation for enzyme immobilization. Further, immobilization of Tyrs enzyme on PANI-nMn_3O_4NF/ITO surface, increases the R_{CT} value (curve c) due to presence of available functional groups (-NH_2 and −CHO) on the electrode surface. The enhancement of R_{CT} value (5.21 kΩ) for Tyrs-PANI-nMn_3O_4NF/ITO bioelectrode is due to the insulating nature of the Tyrs molecules that covalently bind with $-NH_2$ group of PANI *via* GA. The amount of immobilized enzyme has been optimized at 10.0 μL and the surface coverage of Tyrs-PANI-nMn_3O_4NF/ITO bioelectrode was calculated to be (62.76%), [3].

The electron transfer resistance can be translated into magnitude of current under the equilibrium (Io), heterogeneous electron-transfer rate constant (HET) and the time constant (τ) of the various electrodes have been calculated by the following Eqs. ((2)–(5)) [3].

$$R_{CT} = RT/nFI_0 \quad (2)$$

$$I_0 = nFAHET\,[S] \quad (3)$$

$$HET = RT/n^2F^2AR_{CT}\,[S] \quad (4)$$

$$\tau = R_{CT}C_{dl} \quad (5)$$

where R is gas constant, T is absolute temperature (K), F is Faraday constant, A is the electrode area (cm^2), [S] is the bulk concentration of redox probe (mol cm^{-3}), n is the nu ber of transferred electrons per molecule of the redox pro and C_{dl} is the double layer capacitance. The HET value ITO is found to be 0.014×10^{-6} cm s^{-1}. The HET value of PA nMn_3O_4NF/ITO electrode (0.048×10^{-6} cm s^{-1}) is higher than t of Tyrs-PANI-nMn_3O_4NF/ITO bioelectrode (0.0051×10^{-6} cm s indicating faster electron transfer among the redox couples. T Tyrs enzyme-immobilized electrode provides hindrance to t electron transfer resulting in a sluggish electron transfer. Furth high value of time constant (τ) for Tyrs-PANI-nMn_3O_4NF/ITO b electrode (44.2 cm s^{-1}) shows slower diffusion rate (8.4 cm s^{-1}) $[Fe(CN)_6]^{3-/4-}$ ions at the solution/electrode interface.

The cyclic voltammetry (CV) studies have been conducted investigate the electrochemical properties of the fabricated el trodes in the potential range of −0.7 to 0.7 V at a scan rate of 10 m [Fig. 8(ii)]. After electropolymerization of PANI-nMn_3O_4 nanoco posite on ITO substrate, the oxidation current decreases (0.04 m [curve b] compared to that of the bare ITO electrode (1.6 mA) [cu a] revealing that the increased surface area of PANI-nMn_3O_4NF/I electrode may obstruct electron transfer. Interestingly, after imm bilization of Tyrs enzyme on the surface of PANI-nMn_3O_4NF/IT the electrode shows increased current response (0.05 mA, cu c) compared to that of PANI-nMn_3O_4NF/ITO electrode (curve This may be attributed to the covalently bonded Tyrs molecules the surface of PANI-nMn_3O_4NF/ITO providing a promising enviro ment. The available active sites on Tyrs may be electrochemica activated in presence PANI-nMn_3O_4 NF that perhaps acts as a me ator resulting in accelerated electrons from redox reaction. The

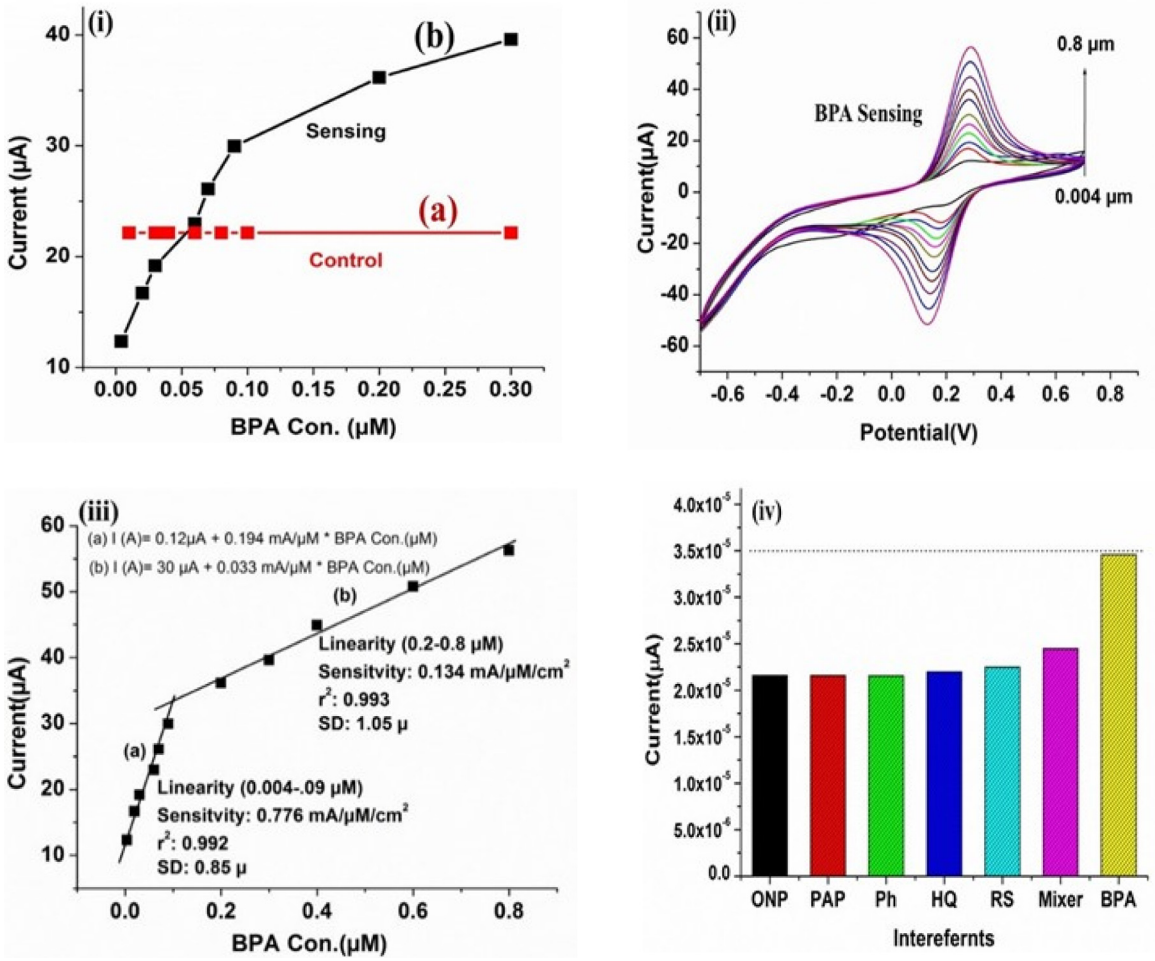


Fig. 9. (i) Control study of Tyrs-PANI-nMn$_3$O$_4$/ITO bioelectrode, (ii) Cyclic voltammogram of Tyrs-PANI-nMn$_3$O$_4$/ITO bioelectrode as a function of BPA concentration (0.004–0.8 μM) in PBS (50 mM, pH 7.4) solution containing 5 mM $[Fe(CN)_6]^{3-/4-}$. (iii) Calibration curve between oxidation current and BPA concentration (μM), and (iv) The selectivity of Tyrs-PANI-nMn$_3$O$_4$/ITO bioelectrode.

studies of Tyrs-PANI-nMn$_3$O$_4$NF/ITO bioelectrode have been conducted as a function of scan rate [Fig. S3]. The anodic (I_A) and cathodic (I_C) peak currents show linear variation with square root of the scan rate [inset in Fig. S3], suggesting that the reaction at the electrode is a quasi-reversible diffusion-controlled process. Both the peak currents are found to increase with increased scan rate (10–100 mV/s). The linear relationship of peak current versus square root of scan rate ($v^{1/2}$) in Tyrs-PANI-nMn$_3$O$_4$NF/ITO bioelectrode can be derived from the Nernst's equation due to presence of electro-active components in the interfacial region. The slope, intercept and correlation coefficient for the bioelectrode obey the following anodic (I_A) and cathodic (I_C) currents given in Eqs. ((6) and (7)):

$$I_A\,(\text{bioelectrode}) = 29.3\,\mu A + 1.60 \times 10^{-5}\left(A^2 mV^{-1} s\right)^{1/2} \times \left[\text{Scanrate}\left(mVs^{-1}\right)\right]^{1/2}; r^2 = 0.999 \quad (6)$$

$$I_C\,(\text{bioelectrode}) = -26.7\,\mu A - 0.76 \times 10^{-5}\left(A^2 mV^{-1} s\right)^{1/2} \times \left[\text{Scanrate}\left(mVs^{-1}\right)\right]^{1/2}; r^2 = 0.999 \quad (7)$$

The peak current is obtained by the Randles-Sevcik method, as described in Eq. (8)

$$I_p = \frac{n^2 F^2 CA\upsilon}{RT} \quad (8)$$

where I_p is the peak current (A), n is the number of electrons transferred in the redox process, F is the Faraday constant (C mol^{-1}), C is the concentration (mM), R is gas constant (8.314 J K^{-1} mol^{-1}), υ is the scan rate (40 mV/s), A is the area of fabricated interface (0.25 cm^2) and T is the absolute temperature (298 K). The diffusion coefficient of redox probe towards the sensing interface is calculated using Randles-Sevcik Eq. (8)

$$I_{p=2.69 \times 10^5 n^{3/2} A D^{1/2} C \upsilon^{1/2}}$$

The diffusion coefficients are found to be 1.41×10^{-6} cm^2/s and 2.21×10^{-6} cm^2/s for PANI-nMn$_3$O$_4$NF/ITO electrode and Tyrs-PANI-nMn$_3$O$_4$NF/ITO bioelectrode, respectively. The higher diffusion after enzyme immobilization may be due to the formation of PANI-nMn$_3$O$_4$ fibrous film that accelerates the transport of electrons due to activation of enzyme active sites.

The reproducibility of Tyrs-PANI-nMn$_3$O$_4$NF/ITO bioelectrode [Fig. 8(iii)] was investigated at 0.01×10^{-6} mol L^{-1} of BPA concentration. No significant change in the oxidation current was observed as was evident by relative standard deviation (RSD=6.74%). The stability of this bioelectrode was tested using repeated measurements under similar conditions. Even after 15 times of repeated

measurements, [Fig. 8(iv)], the Tyrs-PANI-nMn$_3$O$_4$NF/ITO bioelectrode showed identical response as is evident by low relative standard deviation (RSD=2.99%). The storage stability of the Tyrs-PANI-nMn$_3$O$_4$NF/ITO bioelectrode was checked for 8 weeks at an interval of one week. The decrease in the value of current was found to be about 10% up to 4 weeks after which the current value decreases to about 40% within 10 weeks.

3.3.1. Bisphenol A detection

Electrochemical response studies of Tyrs-PANI-nMn$_3$O$_4$NF/ITO biosensor were conducted using CV technique in presence of 50×10^{-3} mol L^{-1} PBS (pH 7.4, 0.9%NaCl) containing 5×10^{-3} mol L^{-1} [Fe(CN)$_6$]$^{3-/4-}$]. The control experiments were conducted on PANI-nMn$_3$O$_4$NF/ITO electrode with and without Tyrs immobilization, using CV technique [Fig. 9(i)] by varying BPA concentrations. A small change observed in oxidation current (curve a) can be attributed to non-specific reaction with proteins on the sensor surface.

During detection of BPA, the bioelectrode was immersed in PBS solution containing various concentrations of BPA ($0.004–0.8 \times 10^{-6}$ mol L^{-1}). Due to the oxidation of BPA into 2, 2-bis (4-phenylquinone) propane in presence of Tyrs enzyme, two electrons are generated [Fig. 9 (ii)] that produce the current. It was observed that magnitude of the current gradually increased with increasing BPA concentration [Fig. 9(ii)]. In addition, this enhancement of electrochemical current may be due to well-arranged and homogenous network of bio-interface of the PANI-nMn$_3$O$_4$ nanofibrous film that provides a good path for electron transfer to current collector via manganese ion [35,36]. The three-dimensional nanofibrous morphology in PANI-nMn$_3$O$_4$NF/ITO electrode resulted in improved electronic and ionic transport due to uniform distribution and conductive nature of PANI-nMn$_3$O$_4$ NF. The detection time of this biosensor was to be 20 s indicating faster electron communication feature of PANI-nMn$_3$O$_4$ NF. The sensor calibration curve [Fig. 9(iii)] showed good linearity in a wide concentration range of $0.004–0.8 \times 10^{-6}$ mol L^{-1}. The current varied linearly with BPA concentration with a correlation coefficient of 0.993. The sensitivity of the fabricated biosensor calculated from the slope of calibration curve was found to be 0.776 mA μM^{-1} Lcm^{-2} and 0.134 mA μM^{-1} L cm^{-2} for a lower concentration range ($0.004–0.09 \times 10^{-6}$ mol L^{-1}) and higher concentration ($0.2–0.8 \times 10^{-6}$ mol L^{-1}), respectively. The high sensitivity of this biosensor was due to high surface-to-volume ratio and conductive nature of PANI-nMn$_3$O$_4$ NF with better electron transportation from electrode surface to the electrolyte. This sensor could be used to detect minute amount of BPA (0.004×10^{-6} mol L^{-1}). The low value of the Michaelis–Menten constant (K$_m$) obtained [0.0075×10^{-6} mol L^{-1}] using Hanes plot reveals that PANI-nMn$_3$O$_4$ NF matrix facilitates increased enzyme activity due to improved conformation of Tyrs. The increased activity of Tyrs with covalent bonding indicates strong affinity between the BPA and the active site of Tyrs resulted in low K$_m$. The observed higher affinity of Tyrs-PANI-nMn$_3$O$_4$NF/ITO based biosensor can be attributed to favorable orientation of Tyrs and higher loading of Tyrs molecules. Table 1 contains characteristics of this sensor along with others reported in literature for BPA detection. The selectivity of Tyrs-PANI-nMn$_3$O$_4$NF/ITO bioelectrode [Fig. 9(iv)] was determined in presence of BPA (0.5×10^{-6} mol L^{-1}) concentration with normal concentration of interferent such as phenol (1.0×10^{-6} mol L^{-1}), ortho-nitrophenol (1.0×10^{-6} mol L^{-1}), para-aminophenol (0.8×10^{-3} mol L^{-1}), resorcinol (1.0×10^{-6} mol L^{-1}), hydroquinone (0.8×10^{-6} mol L^{-1}), and all mixers. The response of the Tyrs-PANI-nMn$_3$O$_4$NF/ITO bioelectrode was not significantly affected in the presence of interferents during BPA detection. The oxidation current value remained nearly same for all interferents with respect to BPA. The prepared biosensor was tested to detect

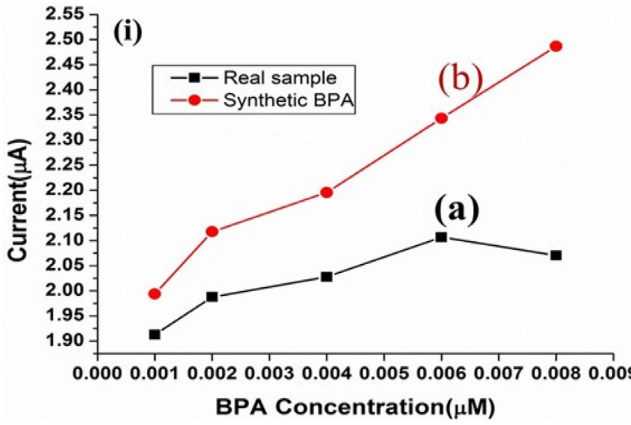


Fig. 10. (i) Cyclic voltammogram comparison study of Tyrs-PANI-nMn$_3$O$_4$/ bioelectrode as a function of synthetic BPA and real sample BPA concentrat (0.001-0.008 μM) in PBS (50 mM, pH 7.4) solution containing 5 mM [Fe (CN)$_6$].$^{3-}$

BPA concentrations in real samples [Fig. 10 (i)]. In comparison to t standard BPA concentrations (curve b), the bioelectrode show little difference at low real BPA concentrations other than high concentration of BPA detection (curve a).

4. Conclusions

A cost-effective, reproducible, selective and highly sensiti PANI-nMn$_3$O$_4$ NF based biosensor platform has been demo strated for BPA detection. We have electropolymerized *in-s* PANI-nMn$_3$O$_4$ NF on an ITO substrate and used that for surfa functionalization with Tyrs enzyme molecules via GA treatme The fibrous surface of PANI-nMn$_3$O$_4$ NF performs a cross li with GA molecules for covalent immobilization of Tyrs enzyr resulting in improved sensing characteristics for monitoring B concentration. This biosensor is sensitive to 0.004×10^{-6} mol L concentration of BPA due to the PANI-nMn$_3$O$_4$ NF biointerfa Mn^{2+} ion and cationic polyaniline that improves the char transfer properties between electrode and electrolyte. The Ty conjugated PANI-nMn$_3$O$_4$ NF provides suitable conduction pa during oxidation of BPA leading to a fast electrochemical respor (20s). This biosensor exhibits higher sensitivity (0.776 mA μM Lcm^{-2}), low detection limit of 0.004×10^{-6} mol L^{-1}, lower K$_m$ val 0.0075×10^{-6} mol L^{-1} with linear regression coefficient at 0.9 and a wide linear range of 0.004-0.8 $\times 10^{-6}$ mol L^{-1}. The Tyrs-PAI nMn$_3$O$_4$NF/ITO-based biosensor provides a suitable platform excellent electrochemical sensing parameters due to the integ tion of PANI-nMn$_3$O$_4$NF and Tyrs via GA. The fabricated biointerfa shows excellent sensitivity, selectivity, and good reproducibil and can be explored for monitoring other clinical substances su as low density lipoprotein, glucose, myoglobin etc.

Appendix A. Supplementary data

Supplementary data associated with this article can be found, the online version, at http://dx.doi.org/10.1016/j.snb.2016.06.05

References

[1] K.K. Reza, M.A. Ali, S. Srivastava, V.V. Agrawal, A.M. Biradar, Tyrosinase conjugated reduced graphene oxide based biointerface for bisphenol A sensor, Biosens. Bioelectron. 74 (2015) 644–651.
[2] L.N. Vandenberg, R. Hauser, M. Marcus, N. Olea, W.V. Welshons, Human exposure to bisphenol A (BPA), Reprod. Toxicol. 24 (2) (2007) 139–177 (Fir This Artic Online.).
[3] N. Singh, K.K. Reza, M.A. Ali, V.V. Agrawal, A.M. Biradar, Self assembled DC sputtered nanostructured rutile TiO2 platform for bisphenol A detection, Biosens. Bioelectron. 68 (2015) 633–641.

[4] J.R. Roy, S. Chakraborty, T.R. Chakraborty, Estrogen-like endocrine disrupting chemicals affecting puberty in humans–a review, Med. Sci. Monit. 15 (2009) RA137–RA145.
[5] M. Regiart, S.V. Pereira, V.G. Spotorno, F.A. Bertolino, J. Raba, Food safety control of zeranol through voltammetric immunosensing on Au–Pt bimetallic nanoparticle surfaces, Analyst 139 (2014) 4702–4709.
[6] C. Nichols, X. Ding, G. Miranda-Carboni, S.A. Krum, Abstract 3192: the environmental estrogen bisphenol A (BPA) regulates mammary gland stem cells, Cancer Res. 74 (2014) 3192.
[7] P. Sohoni, C.R. Tyler, K. Hurd, J. Caunter, M. Hetheridge, T. Williams, C. Woods, M. Evans, R. Toy, M. Gargas, J.P. Sumpter, Reproductive effects of long-term exposure to bisphenol a in the fathead minnow (Pimephales promelas), Environ. Sci. Technol. 35 (2001) 2917–2925.
[8] G. Wang, Z. Chen, T. Bartell, X. Wang, Early life origins of metabolic syndrome: the role of environmental toxicants, Curr. Environ. Health Rep. 1 (2014) 78–89.
[9] D. Melzer, N.J. Osborne, W.E. Henley, R. Cipelli, A. Young, C. Money, P. McCormack, R. Luben, K.-T. Khaw, N.J. Wareham, T.S. Galloway, Urinary bisphenol A concentration and risk of future Coronary artery disease in apparently healthy men and women, Circulation 125 (2012) 1482–1490.
[10] A. Zafra, M. del Olmo, B. Suárez, E. Hontoria, A. Navalón, J.L. Viílchez, Gas chromatographic–mass spectrometric method for the determination of bisphenol A and its chlorinated derivatives in urban wastewater, Water Res. 37 (2003) 735–742.
[11] K. Inoue, Y. Yoshie, S. Kondo, Y. Yoshimura, H. Nakazawa, Determination of phenolic xenoestrogens in water by liquid chromatography with coulometric-array detection, J. Chromatogr. A 946 (2002) 291–294.
[12] K. Ma, T. Ekblad, M.K. Koerkamp, H. Kelderman, M. van Wijlen, A. Duarah, J. Yue, L. Zhang, M.V.-M. Wong, M.H. Lim, Contaminant detection in treated water using Optiqua's MiniLab™ biosensing system: a case study for bisphenol A, Int. J. Environ. Anal. Chem. 95 (2015) 366–378.
[13] Z. Xiao-hong, L. Lan-hua, X. Wei-qi, S. Bao-dong, S. Jian-wu, H. Miao, S. Han-chang, A reusable evanescent wave immunosensor for highly sensitive detection of bisphenol A in water samples, Sci. Rep. 4 (2014).
[14] J.-W. Park, S. Kurosawa, H. Aizawa, Y. Goda, M. Takai, K. Ishihara, Piezoelectric immunosensor for bisphenol A based on signal enhancing step with 2-methacrolyloxyethyl phosphorylcholine polymeric nanoparticle, Analyst 131 (2006) 155–162.
[15] D.K. Kim, P. Muralidharan, H.-W. Lee, R. Ruffo, Y. Yang, C.K. Chan, H. Peng, R.A. Huggins, Y. Cui, Spinel LiMn2O4 nanorods as lithium ion battery cathodes, Nano Lett. 8 (2008) 3948–3952.
[16] E. Hosono, T. Kudo, I. Honma, H. Matsuda, H. Zhou, Synthesis of single crystalline spinel LiMn2O4 nanowires for a lithium ion battery with high power density, Nano Lett. 9 (2009) 1045–1051.
[17] P. Li, C. Nan, Z. Wei, J. Lu, Q. Peng, Y. Li, Mn3O4 nanocrystals: facile synthesis, controlled assembly, and application, Chem. Mater. 22 (2010) 4232–4236.
[18] S. Fritsch, J. Sarrias, A. Rousset, G.U. Kulkarni, Low-temperature oxidation of Mn3O4 hausmannite, Mater. Res. Bull. 33 (1998) 1185–1194.
[19] Z. Weixin, W. Cheng, Z. Xiaoming, X. Yi, Q. Yitai, Low temperature synthesis of nanocrystalline Mn3O4 by a solvothermal method, Solid State Ion. 117 (1999) 331–335.
[20] P.Z. Si, D. Li, C.J. Choi, Y.B. Li, D.Y. Geng, Z.D. Zhang, Large coercivity and small exchange bias in Mn3O4/MnO nanoparticles, Solid State Commun. 142 (2007) 723–726.
[21] A. Vázquez-Olmos, R. Redón, G. Rodríguez-Gattorno, M. Esther Mata-Zamora, F. Morales-Leal, A.L. Fernández-Osorio, J.M. Saniger, One-step synthesis of Mn3O4 nanoparticles: structural and magnetic study, J. Colloid Interface Sci. 291 (2005) 175–180.
[22] K. Kamil Reza, N. Singh, S.K. Yadav, M.K. Singh, A.M. Biradar, Pearl shaped highly sensitive Mn3O4 nanocomposite interface for biosensor applications, Biosens. Bioelectron. 62 (2014) 47–51.
[23] Y. Chen, X.H. Wang, J. Li, J.L. Lu, F.S. Wang, Polyaniline for corrosion prevention of mild steel coupled with copper, Electrochim. Acta 52 (2007) 5392–5399.
[24] Y. Sun, J.A. Rogers, Inorganic semiconductors for flexible electronics, Adv. Mater. 19 (2007) 1897–1916.
[25] C. Dhand, S.K. Arya, S.P. Singh, B.P. Singh, M. Datta, B.D. Malhotra, Preparation of polyaniline/multiwalled carbon nanotube composite by novel electrophoretic route, Carbon 46 (2008) 1727–1735, http://dx.doi.org/10.1016/j.carbon.2008.07.028.
[26] X. Qin, S. Liu, W. Lu, H. Li, G. Chang, Y. Zhang, J. Tian, Y. Luo, A.M. Asiri, A.O. Al-Youbi, X. Sun, Submicrometre-scale polyaniline colloidal spheres: photopolymerization preparation using fluorescent carbon nitride dots as a photocatalyst, Catal. Sci. Technol. 2 (2012) 711–714, http://dx.doi.org/10.1039/C2CY00439A.
[27] G. Chang, Y. Luo, W. Lu, X. Qin, A.M. Asiri, A.O. Al-Youbi, X. Sun, Ag nanoparticles decorated polyaniline nanofibers: synthesis, characterization, and applications toward catalytic reduction of 4-nitrophenol and electrochemical detection of H2O2 and glucose, Catal. Sci. Technol. 2 (2012) 800–806, http://dx.doi.org/10.1039/C2CY00454B.
[28] S. Liu, L. Wang, Y. Luo, J. Tian, H. Li, X. Sun, Polyaniline nanofibres for fluorescent nucleic acid detection, Nanoscale 3 (2011) 967–969, http://dx.doi.org/10.1039/C0NR00873G.
[29] Z.W. Chen, J.K.L. Lai, C.H. Shek, Nucleation site and mechanism leading to growth of bulk-quantity Mn3O4 nanorods, Appl. Phys. Lett. 86 (2005) 181911, http://dx.doi.org/10.1063/1.1923753.
[30] H. Kavas, Z. Durmus, M. Şenel, S. Kazan, A. Baykal, M.S. Toprak, CTAB-Mn3O4 nanocomposites: synthesis, NMR and low temperature EPR studies, Polyhedron 29 (2010) 1375–1380, http://dx.doi.org/10.1016/j.poly.2009.12.034.
[31] Z. Zheng, Y. Du, Z. Wang, Q. Feng, C. Wang, Pt/graphene–CNTs nanocomposite based electrochemical sensors for the determination of endocrine disruptor bisphenol A in thermal printing papers, Analyst 138 (2012) 693–701, http://dx.doi.org/10.1039/C2AN36569C.
[32] A.I. Inamdar, Y.S. Kim, J.S. Sohn, H. Im, H. Kim, D.-Y. Kim, R.S. Kalubarme, C.H. Park, Supercapacitive characteristics of electrodeposited polyaniline thin films grown on indium doped tin oxide substrates, J. Korean Phys. Soc. 59 (2011) 145–149.
[33] D.P. Dubal, D.S. Dhawale, R.R. Salunkhe, S.M. Pawar, C.D. Lokhande, A novel chemical synthesis and characterization of Mn3O4 thin films for supercapacitor application, Appl. Surf. Sci. 256 (2010) 4411–4416, http://dx.doi.org/10.1016/j.apsusc.2009.12.057.
[34] B.-Y. Chang, S.-M. Park, Integrated description of electrode/electrolyte interfaces based on equivalent circuits and its verification using impedance measurements, Anal. Chem. 78 (2006) 1052–1060, http://dx.doi.org/10.1021/ac051641l.
[35] H. Xia, Y.S. Meng, X. Li, G. Yuan, C. Cui, Porous manganese oxide generated from lithiation/delithiation with improved electrochemical oxidation for supercapacitors, J. Mater. Chem. 21 (2011) 15521–15526, http://dx.doi.org/10.1039/C1JM12767E.
[36] H. Jiang, T. Zhao, J. Ma, C. Yan, C. Li, Ultrafine manganese dioxide nanowire network for high-performance supercapacitors, Chem. Commun. 47 (2011) 1264–1266, http://dx.doi.org/10.1039/C0CC04134C.
[37] D.C. Apodaca, R.B. Pernites, R. Ponnapati, F.R. Del Mundo, R.C. Advincula, Electropolymerized molecularly imprinted polymer film: EIS sensing of bisphenol A, Macromolecules 44 (2011) 6669–6682, http://dx.doi.org/10.1021/ma2010525.
[38] Q. Li, H. Li, G.-F. Du, Z.-H. Xu, Electrochemical detection of bisphenol A mediated by [Ru(bpy)3]2+ on an ITO electrode, J. Hazard. Mater. 180 (2010) 703–709, http://dx.doi.org/10.1016/j.jhazmat.2010.04.094.
[39] H. Yin, Y. Zhou, J. Xu, S. Ai, L. Cui, L. Zhu, Amperometric biosensor based on tyrosinase immobilized onto multiwalled carbon nanotubes-cobalt phthalocyanine-silk fibroin film and its application to determine bisphenol A, Anal. Chim. Acta. 659 (2010) 144–150, http://dx.doi.org/10.1016/j.aca.2009.11.051.
[40] M. Portaccio, D. Di Tuoro, F. Arduini, M. Lepore, D.G. Mita, N. Diano, L. Mita, D. Moscone, A thionine-modified carbon paste amperometric biosensor for catechol and bisphenol A determination, Biosens. Bioelectron. 25 (2010) 2003–2008, http://dx.doi.org/10.1016/j.bios.2010.01.025.
[41] J. Huang, X. Zhang, S. Liu, Q. Lin, X. He, X. Xing, W. Lian, Electrochemical sensor for bisphenol A detection based on molecularly imprinted polymers and gold nanoparticles, J. Appl. Electrochem. 41 (2011) 1323–1328, http://dx.doi.org/10.1007/s10800-011-0350-8.

Biographies

Nawab Singh is doing PhD at the Indian Institute of Technology Hyderabad Telangana, India, in the Department of Biomedical Engineering. He received his MSc from Chaudhary Charan Singh University, Meerut, India (2010). Nawab's research interests are in micro/nano fabrication of functional nanomaterials, self and directed assembly, microfluidics based biochips for biomolecules detection, polymer thin-films, biomaterials for biosensing application. He has published 4 papers in peer-reviewed journals.

Md. Azahar Ali received his PhD degree from Biomedical Engineering Department at Indian Institute of Technology Hyderabad, India in collaboration with Biomedical Instrumentation Section at National Physical Laboratory, New Delhi, India. He also received his Master of Technology degree from Department of Electronics Engineering, Tezpur University, Assam in 2009. Currently, he is doing Post-Doctoral Associate at Electrical and Computer Engineering, Iowa State University, USA. He is actively engaged in the area of microfluidic based multiplex biochips for biomolecules detection.

Kali Suresh is doing Project Officer at the Indian Institute of Technology Hyderabad Telangana, India, in the Department of Chemical Engineering. He received his MSc from National Institute of Technology Warangal, Telangana, India (2010). Kali research interests are in Carbon based hierarchical structures. He has published 2 papers in peer-reviewed journals.

Ved Varun Agrawal earned his PhD degree from the Jawaharlal Nehru Center for Advanced Scientific Research in 2008. He now works as a Scientist in the Department of Science & Technology of Biomolecular Electronics, Biomedical Instrumentation Section at National Physical Laboratory (CSIR), New Delhi, India. His current research focuses on utilizing the properties of nanomaterials to improve biosensing characteristics.

Prabhakar Rai is working as INSPIRE Faculty in the Department of Chemical Engineering at Indian Institute of Technology Kanpur, India. He received his Ph.D. degree in Informatic Electronics Materials Engineering in 2012 from Chonbuk National University, South Korea. He was appointed as Research Professor in the Department of Materials Science and Engineering at Korea University, South Korea in 2013. His

research is mainly focused on synthesis of nanoscale metals and metal oxides for energy and chemical sensing applications.

Ashutosh Sharma is a Chair Professor in Chemical Engineering at the Indian Institute of Technology at Kanpur (IITK). Ashutosh received his Ph.D. from the State University of New York at Buffalo (1987), MS from the Pennsylvania State University (1984) and B. Tech. from IITK(1982).Ashutosh's research interests are in soft functional interfaces, micro/nano-mechanics of confined soft matter, self-organized patterning, soft nanofabrication, colloid and interfacial engineering, carbon nanocomposites and carbon MEMS/NEMS in energy, health and environmental applications, and membranes. He is currently Secretary to the Government of India, Department of Science and Technology starting January 2015

B.D. Malhotra received his Ph.D. degree from the University of Delhi, Delhi, India in 1980. He has published more than 270 papers in peer-reviewed journals, filed 10 patents, and edited/co-edited books on biosensors and polymer electronics. After his stint as Chief Scientist and Head of the DST Centre on Biomolecular Electronics at the CSIR-National Physical Laboratory, New Delhi, India, he moved to Delhi Technological University (DTU), India. He has nearly 30 years of research experience in the field of biomolecular electronics and has guided 25 Ph.D. students to date. His current activities include biosensors, nanobiomaterials, conducting polymers, and ordered molecular assemblies including Langmuir–Blodgett films and self-assembled monolayers among others. Dr. Malhotra is a Fellow of the Indian National Science Academy (INSA), the National Academy of Sciences, India (NASI) and an Academician of the Asia- Pacific Academy of Materials (APAM).

Renu John is currently an Associate Professor and Head of the Department of Biomedical Engineering, Indian Institute of Technology Hyderabad. He received his PhD degree from Indian Institute of Technology Delhi in 2006. He carried out his post-doctoral research at Fitzpatrick center for Photonics, Duke University, Durham, NC, USA and Biophotonics Imaging Laboratory, University of Illinois, Urbana-Champaign, USA. His research interests include Nano-Biophotonics, non-invasive NIR bio-imaging, 3-D phase microscopy Optical coherence tomography (OCT), Chemical and optical Biosensors.

2016 The 2nd International Conference on Control, Automation and Robotics

Middle Node Optimization Algorithm for Global Optimal Path Planning

Ananya Chandra, Vibhu Jawa, Ishan Mishra, and M. Sameer Khan
Delhi Technological University
Delhi, India
e-mail: ananyachandra14@gmail.com, vibhujawa@gmail.com, mishra.ishan@outlook.com, sameerkhan7494@gmail.com

***Abstract*—This paper proposes a new algorithm for solving the robot path planning problem which includes finding a path from a source to a destination subject to certain constraints. First, using the overhead view of the surroundings, a free space model is created using MAKLINK graph theory. Then Dijkstra's Algorithm is applied over the MAKLINK graph to obtain a sub-optimal path. This sub-optimal path is further optimized using the proposed Middle Node Optimization (MNO) algorithm. Using computer simulations, MNO algorithm is compared with Basic PSO (Particle Swarm Optimization), RCPSO (Random Coding PSO) and Ant Colony System (ACS) algorithms on the basis of convergence speed and the resultant optimized path lengths.**

Keywords-MAKLINK Graph; Dijkstra's Algorithm; Path Optimization

I. INTRODUCTION

In the problem of navigation of a mobile robot, the fundamental step is to plan an optimal path which involves finding a collision free path from the start point to the end point. The first solution to the path planning problem was the method of free C space which was proposed by Lozano-Perez and Wesley [1]. Since then, a lot of focus has been given to this problem and a number of different methods and strategies have been developed to arrive at an optimal solution.

The main categories in which path planning can be characterized are:

- Classical Approach
- Heuristic Approach

The classical approach is one that requires a large number of computations, especially with the increase in the number of vertices in the polygonal obstacles. An example of the classical approach is the visibility graph method. Also, the computation complexity of this approach is $O(n^2)$ in a two dimensional space, n being the total number of vertices in the polygonal obstacles.

However, one of the major limitations of the approach is the way in which the size of grids is determined, since it affects the accuracy of the environment, memory space and search efficiency.

To further enhance the efficiency of the classical approach, a new approach called the heuristic approach [2] was developed. This approach addresses the complex nature of the NP-complete problem such as rapidly-exploring random tree (RRT) and probabilistic road map.

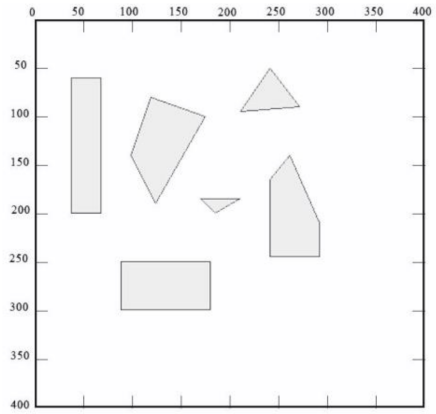


Figure 1. Obstacle Course

While the genetic algorithm has strong optimization ability, the swarm intelligence algorithm is simpler, has fewer parameters and faster convergence, similar to the ant colony optimization which is known to outperform the classical approach for optimization. However, the main drawback of the latter approach is the difficulty in calculating parameters or in converging to the solution quickly.

II. FREE SPACE MODELING

The free space of a mobile robot in an environment is the space in which the robot can move freely.

In this paper, the MAKLINK graph theory [3], [4] is used to create a free space model, then Dijkstra's Algorithm is applied on it to find a sub-optimal collision-free path.

The MAKLINK graph theory used to establish the free space for the robot makes the following assumptions:

1) There exist certain obstacles in the environment. Both the obstacles and the environment have a polygonal shape.
2) The heights of the environment and obstacles can be ignored.
3) In order to avoid the robot's projected path from getting too close to the obstacles, the boundaries of every obstacle can be expanded by an amount that is equal to half of the greater size amongst the length and width of the robot's body, plus the minimum measuring distance of the relevant sensors. In our case, the size of the robot can be ignored as we are

considering the robot to be a point object.

Fig. 1 illustrates a static environment of size 400 metres by 400 metres that includes six polygonal obstacles.

In this experiment, the free space is the area within the environment that isn't covered by obstacles. To establish a constrained free space that can be used for computational purposes, we use the MAKLINK graph theory, the first step of which is to generate free MAKLINK lines.

A free MAKLINK line is denoted as:

1) Either its two end points are two vertices of two different obstacles or one point is a vertex of an obstacle and the other is located on a boundary of the environment.
2) It cannot intersect any of the obstacles.

Free MAKLINK lines can be generated using the following rules:

1) The line joining a vertex of an obstacle to its nearest vertex from another obstacle is a free MAKLINK line.
2) The perpendicular line from each vertex of a peripheral obstacle to its adjacent environment boundary is a free MAKLINK line.

Assume that r denotes the total number of free MAKLINK lines. The middle points of these free MAKLINK lines are called nodes, and are denoted respectively as $v_1, v_2 \ldots v_r$. If each pair of geometrically adjacent nodes are connected together, a network graph known as MAKLINK graph is formed which gives the possible paths for the free motion of the mobile robot.

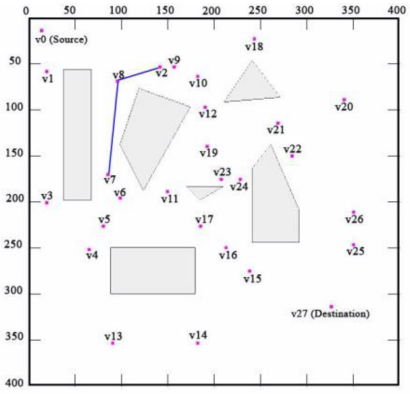


Figure 2. MAKLINK Graph Nodes

For the environment shown in Fig. 1, twenty six nodes (r = 26) are obtained for each free MAKLINK line, that are depicted in Fig. 2. v_7, v_8 and v_9 are connected to display a possible path that the robot can take.

MAKLINK graph is an undirected graph, and is denoted by G(V, E), where V = $\{v_0, v_1, \ldots, v_{r+1}\}$ is the set of all nodes including Source and Destination; E is a set of lines which connects all geometrically adjacent nodes provided they don't intersect any obstacle. Using the undirected graph G(V, E) as the free space model, the global optimal path planning problem can be solved by finding the shortest path between the Source and the Destination.

III. SUB OPTIMAL PATH

Using the MAKLINK graph G (V, E) as the free space model, the global optimal path planning problem can be solved by finding the shortest path between Source and Destination. The sub-optimal path depicted in Fig. 3 is obtained by applying Dijkstra's Algorithm [5] to the MAKLINK graph G(V, E). The set of n nodes constituting the sub-optimal path is S = $\{N_1, N_2 \ldots N_n\}$

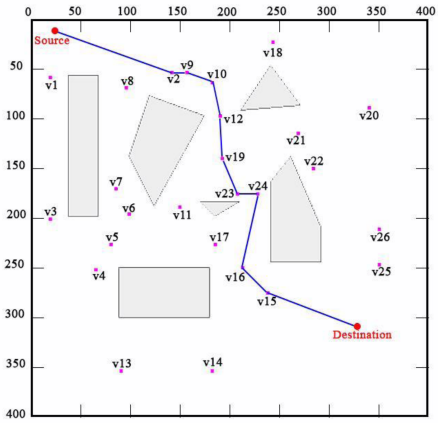


Figure 3. Sub Optimal Path

IV. GLOBAL OPTIMAL PATH

As explained in the above section, a sub-optimal path can be obtained for a mobile object to traverse upon without having to collide with any obstacle. However, the path retrieved is broadly for directional purposes; its length can be further optimized by adjusting the position of the interior nodes.

A. Previous Work

The following techniques have been previously used for optimization of the sub-optimal path obtained by applying Dijkstra's algorithm on MAKLINK graph.

1) Ant Colony System: The Ant Colony System (ACS) algorithm [6] is a subset of a wider range of Ant Colony Optimization methods. In this algorithm, solutions are developed based on probabilistic models of components affecting the overall heuristics data. The set of historical data is updated accordingly.

2) Particle Swarm Optimization: Particle Swarm Optimization (PSO) [7] is a stochastic based optimization algorithm. It regulates the positions of a population similar to how a flock of birds do. The individual candidates in the system adjust to local optimal positions to achieve a global best.

3) Random Coding PSO: Random Coding PSO (RCPSO) [8] is an extension of the above explained PSO algorithm. In this algorithm, random coding and genetic algorithm's

crossover operator are introduced to the concept of particle swarms. Experimentally, the algorithm is comparable to PSO in terms of speed even though it does not converge as fast, but gives a much more optimal path length.

B. Previous Work

In this section the proposed algorithm MNO is explained. Refer to Fig. 12 for the flow chart of the algorithm.

1) Heuristic: In the following sections, the heuristic H will be denoted as H(N_k) to signify the total linear distance from N_{k-1} to N_k to N_{k+1} where N_k is the kth node in the set S. H(N_k) calculates the sum of the Euclidean lengths of L1(N_{k-1}, N_k) which is the line between nodes N_{k-1} and N_k, and L2(N_k, N_{k+1}) which is the line between nodes N_k and N_{k+1}. Refer to Figure 4.

$$|L1| = \sqrt{(N_{k-1}x - N_k x)^2 + (N_{k-1}y - N_k y)^2} \quad (1)$$

$$|L2| = \sqrt{(N_k x - N_{k+1}x)^2 + (N_k y - N_{k+1}y)^2} \quad (2)$$

$$H(N_k) = |L1| + |L2| \quad (3)$$

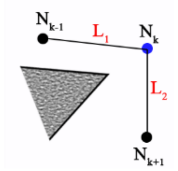


Figure 4. H(Nk) = Length of L1 + Length of L2

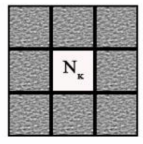


Figure 5. Shaded Area is Delta function of Nk

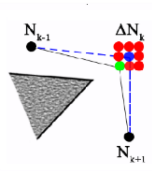


Figure 6. Green Particle is the min heuristic

2) Algorithm: Tolerance Value = 10^{-4}

1. Initialize k $\leftarrow$ 2
2. Consider nodes N_{k-1}, N_k and N_{k+1} from the set of sub-optimal nodes $N_1, N_2, ..., N_n$
3. If L1 (Line between N_{k-1} and N_k) collides with any obstacle: Goto step 7
4. If L2 (Line between N_k and N_{k+1}) collides with any obstacle: Goto step 7
5. Let $\Delta(N_k)$ be the set of 8 particles each at a unit distance in the 8 axial directions of N_k as shown in Fig. 5

(a) If $min(H(\Delta(N_k))) \leq H(N_k)$: N_k = r, where $r \in \Delta(N_k)$, such that H(r) = $min(H(\Delta))$. Refer Fig. 6.

(b) Else (ie N_{k-1}, N_k, and N_{k+1} make a straight line):

i. Remove N_k from the set S.

ii. n $\leftarrow$ n-1

iii. Go to Step 2

6. Go to Step 3
7. (a) Case 1(Only L1 collides with any obstacle at C1) Refer Fig. 7:

i. Insert C1 between N_{k-1} and N_k

ii. $n \leftarrow n+1$

iii. Go to Step 8

(b) Case 2 (Only L2 intersects with obstacle at C2) Refer Fig. 8:

i. Insert C2 between N_k and N_{k+1}

ii. n $\leftarrow$ n+1

iii. Go to Step 9

(c) Case 3 (Both L1 and L2 intersect with obstacles at C1 and C2 respectively) Refer Figures 9 and 10 :

(a) If C1 = C2

i. Go to Step 8

(b) If C1 $\neq$ C2

i. Insert C1 between N_{k-1} and N_k

ii. C2 between N_k and N_{k+1}

iii. n $\leftarrow$ n+2

iv. Go to Step 8

8. k $\leftarrow$ k+1
9. If k $\leq$ n-1 – Go to Step 2
10. If $D_{curr}(N_1, N_n)$ - $D_{prev}(N_1, N_n) \leq Tolerance$: END

Else: Go to Step 1.

Where D_{curr} is the length of the path between Source and Destination in the current iteration through the nodes present in the updated set S $\{N_1, ..., N_m\}$ where m is the updated number of nodes; and similarly D_{prev} is the length obtained from the previous iteration.

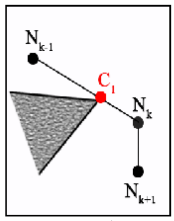


Figure 7. Case 1: When L1 collides

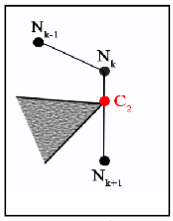


Figure 8. Case 2: When L2 collides

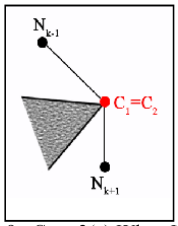


Figure 9. Case 3(a) When L1 and L2 collide at the same point.

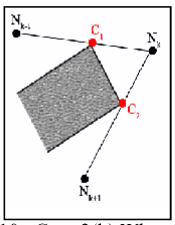


Figure 10. Case 3(b) When L1 and L2 collide at different points

V. Experiment And Results

In this section, the improvements that the MNO algorithm brings over other MAKLINK optimization techniques such as RCPSO, ACS and PSO has been demonstrated. Simulations were run on a personal computer

with specifications of a 2.3 G-Hz i7 processor with 8 GB RAM. The maximum number of iterations allowed for any algorithm during the simulation is 200.

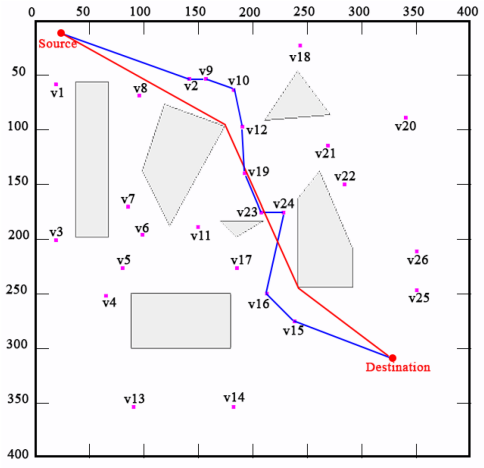


Figure 11. Dijkstra's and Optimized Path

In Fig. 11, the blue line depicts the path obtained using Dijkstra's algorithm on MAKLINK graph as explained in previous sections with a path length of 589.39 metres. The red line depicts the path obtained using MNO algorithm which reduces the path length to 449.93 metres. Table I compares the reduced path lengths obtained using different optimization algorithms.

The second criteria used for comparison is the convergence speed of the algorithms in which the path lengths obtained are plotted against the iteration at which they are obtained. Fig. 13 shows the convergence of our algorithm at near about the 15th iteration; Fig. 14 shows the convergence of Basic PSO algorithm at near about the 13th iteration; Fig. 15 shows the convergence of ACS algorithm at near about the 127th iteration; and Fig. 16 depicts the convergence of RCPSO algorithm at near about the 24th iteration.

TABLE I. EXPERIMENTAL RESULTS OF MAKLINK OPTIMIZATION ALGORITHMS

Algorithm	Path Length(meters)
Dijkstra	589.39
MNO	464.88
RCPSO	469.26
ACS	471.94
Basic PSO	498.51

The experiments show that our algorithm gives a shortest possible distance through a field of obstacles. The convergence is comparable to that of Basic PSO algorithm although not as rapid, but is faster than those achieved from RCPSO and ACS optimization algorithms.

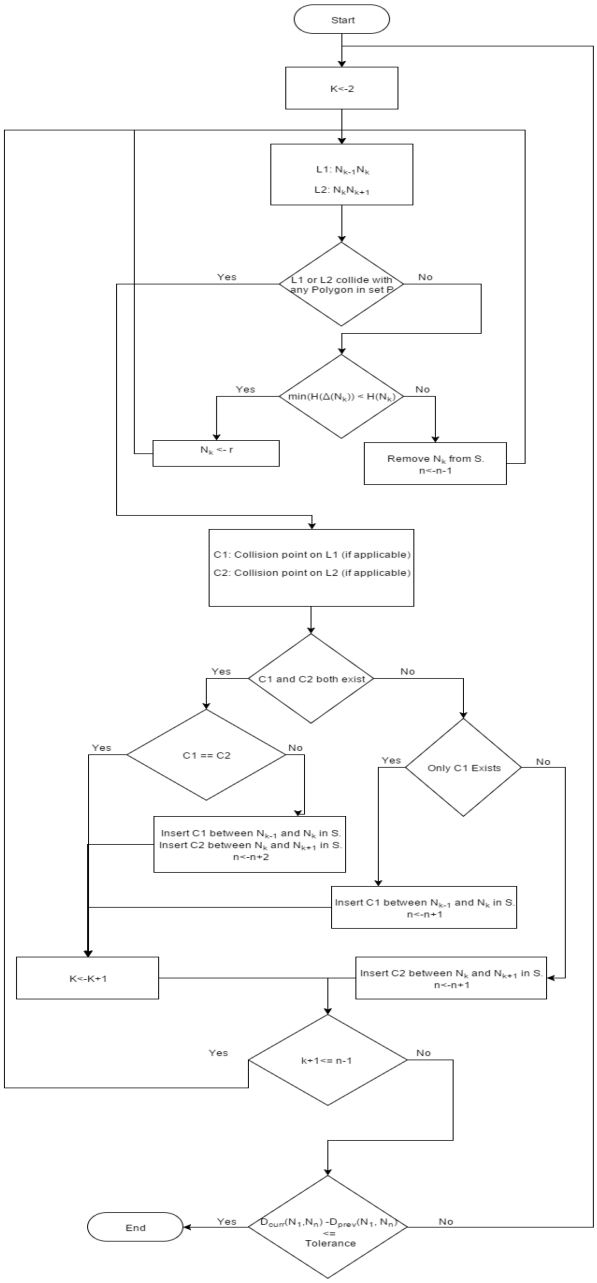


Figure 12. Flowchart of Algorithm

VI. CONCLUSION

The problem of guiding a mobile object through an obstacle field upon an optimized path is duly achieved through the proposed algorithm. The simulations of the environment are developed in the Java language. A combination of MAKLINK theory and Dijkstra's algorithm is applied to achieve a broad directional sub-optimal path through the obstacle course. MNO algorithm is then applied to further optimize the length of the path. The experiment results showcase the effectiveness of the algorithm both in terms of the optimal path length and the speed of

convergence, thus proving it to be a practical substitute for solving the robot path planning problem.

The given algorithm also provides an innate advantage in dynamic environments since the path adjustment can be made at the interior nodes (where a moving obstacle collides) without computing the layout of far away nodes.

The given algorithm does have its limitations though. Being based on optimizing the MAKLINK graph, the algorithm does not work optimally with objects that have curved edges or objects that have no corners at all such as ellipses.

VII. Future Work

The algorithm is yet to be tested in dynamic environments with mobile obstacles that have constant and known velocities. The aim of the problem will be to maintain a shortest path within the dynamic environment keeping in mind the relative position and velocity of the mobile object. The MNO algorithm will be modified accordingly to incorporate the same.

Further research in the field of study will be done to allow the algorithm to work optimally with curved obstacles.

Also, it'll be seen if the algorithm can be based on a probabilistic model to account for randomizations.

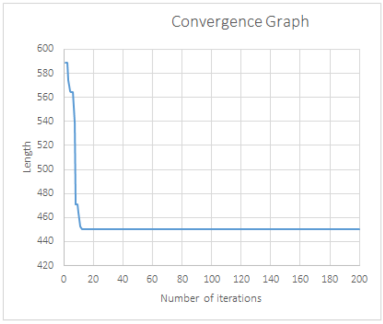


Figure 13. Convergence Graph of MNO

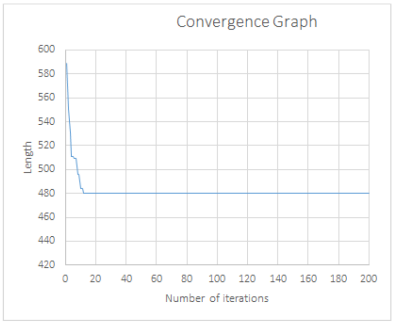


Figure 14. Convergence Graph of Basic PSO

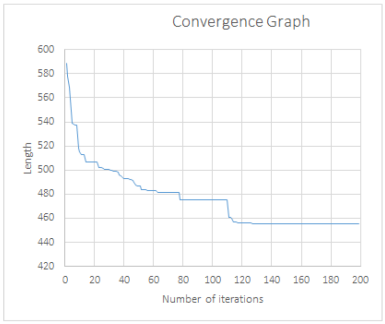


Figure 15. Convergence Graph of ACS

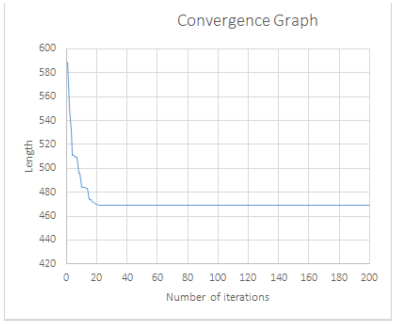


Figure 16. Convergence Graph of RCPSO

References

[1] T. Lozano-Perez' and M. A. Wesley, "An algorithm for planning collision-free paths among polyhedral obstacles," Commun. ACM, vol. 22, no. 10, pp. 560-570, Oct. 1979. [Online]. Available: http://doi.acm.org/10.1145/359156.359164

[2] J. Bruce and M. Veloso, "Real-time randomized path planning for robot navigation," in Intelligent Robots and Systems, 2002. IEEE/RSJ International Conference on, vol. 3. IEEE, 2002, pp. 2383-2388.

[3] M. K. Habib and H. Asama, "Efficient method to generate collision free paths for an autonomous mobile robot based on new free space structuring approach," in Intelligent Robots and Systems' 91.'Intelligence for Mechanical Systems, Proceedings IROS'91. IEEE/RSJ International Workshop on. IEEE, 1991, pp. 563-567.

[4] F. K. Purian, F. Farokhi, and R. S. Nadooshan, "Comparing the perfor-mance of genetic algorithm and ant colony optimization algorithm for mobile robot path planning in the dynamic environments with different complexities," Journal of Academic and Applied Studies, vol. 3, no. 2, pp. 29-44, 2013.

[5] S. Skiena, "Dijkstra's algorithm," Implementing Discrete Mathematics: Combinatorics and Graph Theory with Mathematica, Reading, MA: Addison-Wesley, pp. 225-227, 1990.

[6] T. Guan-Zheng, H. Huan, and A. Sloman, "Ant colony system algorithm for real-time globally optimal path planning of mobile robots," Acta Automatica Sinica, vol. 33, no. 3, pp. 279-285, 2007.

[7] H. I. Kang, B. Lee, and K. Kim, "Path planning algorithm using the particle swarm optimization and the improved dijkstra algorithm," in Computational Intelligence and Industrial Application, 2008. PACIIA'08. Pacific-Asia Workshop on, vol. 2. IEEE, 2008, pp. 1002-1004.

[8] K. Su, Y. Wang, and X. Hu, "Robot path planning based on random coding particle swarm optimization," 2015.

New proposal for MCML based three input logic implementation

Neeta PANDEY [1#], Kirti GUPTA [2^], Bharat CHOUDHARY[1*]

[1]Dept. of Electronics and Communication Engineering, Delhi Technological University, Delhi, India
[2] Dept. of Electronics and Communication Engineering, Bharati Vidyapeeth's College of Engineering, Delhi,India

[#]n66pandey@rediffmail.com, [^]kirtigupta22@gmail.com, [*]bharatchoudhary@dtu.ac.in

Abstract: This paper presents a new proposal for three input logic function implementation in MOS current mode logic (MCML) style. The conventional realization of such logic employs series gating approach leading to three levels of stacked source-coupled transistor pairs. The minimum power supply requirement for proper MCML operation is related to the number of stacked source-coupled transistor pairs, and increases with rising number of inputs. The power consumption of MCML, being product of bias current and power supply, show an upward trend with increasing inputs. The new proposal to reduce of the number of stacked source-coupled transistor levels is put forward. A new circuit element named as quad-tail cell is presented for this purpose which reduces the number of stacked transistor level by two. A three input exclusive-OR (XOR) gate, a vital element in digital system design is chosen to elaborate the approach. Its behavior is analyzed and SPICE simulations using TSMC 180 nm CMOS technology parameters are included to support the theoretical concept. The performance of the proposed circuit is compared with the CMOS Complementary pass transistor logic based XOR gate topology, conventional MCML XOR topology along with two more possible MCML topologies. Additional topologies use triple tail cell concept to lower the number of source coupled transistor pair levels. The first topology employs a cascade of two input XOR gates while the second realization reduces the levels from three to two. The performance of all XOR gate realizations is compared in terms of the minimum power supply requirement, propagation delay, and the power consumption, power delay product, gate and transistor count; and switching current,. It is found that the proposed XOR gate topology outperforms in terms of most of the performance parameters. The sensitivity of different MCML XOR gate realization performance is examined towards process variation. The variation between the best and worst case for the propagation delay is by a factor of 1.63, 1.29, 1.48 and 1.54 respectively for conventional, topologies 1 and 2 and the proposed one. As an extension of the work, a discussion on the realization of three input logic by configuration of a 4:1 multiplexer has also been included.

Keywords: MCML, series gating, Triple-tail cell, Quad-tail cell

1. Introduction

MCML style finds application in communication systems, optical fiber links, digital to analog converter, microprocessors and signal processors [1-3]. As compared to static CMOS logic, MCML has several advantageous features such as improved signal integrity, reduced power

consumption, better power-delay product at high frequencies, stability with technology generations and improved security in cryptography applications [4-9]. A MCML gate consists of three main parts namely a pull down network (PDN), a current source, and a load. The PDN implements the logic function; the current source generates the constant bias current while the load performs the current to voltage conversion.

The logic function is realized using series gating approach which suggests stacking of the source coupled transistors pairs in the PDN. The number of stacked levels has a direct correspondence with number of inputs in the logic function. As the number of inputs becomes larger there is increase in the number of stacked levels (NSL). For proper operation of MCML gate, a minimum power supply is required which is decided by the value of NSL and a higher NSL results in larger minimum power supply. This serve as a main motivation behind using low voltage topology as lesser is the power supply lower will be the power consumption as the later is product of bias current and power supply. Few low voltage techniques are available in the open literature [10-16]. The techniques [10-13] provide single ended output. A NOR based logic realization is proposed in [10, 11] to avoid stacking but it requires multistage realization of logic function. Additional current mirror, voltage and current source are employed in [12, 13] to avoid stacking. The triple-tail cell concept is introduced in [14-16] to reduce NSL by one for the two level MCML gates implementation. This paper introduces a new methodology for the reducing the value of NSL by two and presents a quad-tail cell for this purpose. This method therefore allows three input logic function realization using single level of source coupled pairs and ultimately resulting in significant reduction in minimum power supply. A total of four proposed quad-tail cells are used for three input logic function. The outlined method is generic in nature and can be applied to realize any three input function.

The paper first discusses the basic realization of the three input logic function in MCML style in section 2. A XOR gate is chosen for the purpose. Thereafter, section 3 presents the new quad-tail cell is put forward and its usefulness is illustrated through MCML XOR gate realization. The operation of the proposed XOR gate is explained and analytical formulations for the minimum power supply and voltage swing are put forward. Its performance comparison with the CMOS Complementary pass transistor logic (CPL) based XOR gate, traditional MCML topology and the two additional topologies are included in section 4. A discussion on the general approach for implementing complex logic function in MCML style is also included. Extensive SPICE simulations are carried out to validate the proposed theory. Section 5 concludes the paper.

2. Conventional three input MCML gate realization

The basic architecture of a MCML gate consists of a pull down network (PDN), a current source and a load as shown in Fig. 1a. The PDN implements the logic function, the current source maintains a constant bias current and the load performs the current-to-voltage conversion [4]. The gate works on the principle of current-steering. Depending upon the inputs, the bias current is steered to one of the output branches and produces the output accordingly. The logic function

is realized by using series-gating approach [17]. It is a systematic and a general approach wherein a logic function is implemented as a network of source-coupled transistor pairs having all transistor paths associated with the possible input combinations and then properly connecting each of the upper drain nodes to the output nodes. Based on this, the schematic of a MCML XOR gate with differential inputs A, B and C is shown in Fig. 1. The PDN has three levels of source-coupled transistor pairs (M2-M15), the load transistors (M16, M17) and a constant current source M1 that generates the bias current I_{SS}. The differential inputs A, B and C drive the uppermost (M8-M15), middle (M4-M7) and lowest (M2-M3) levels respectively. Consider for instance that all the inputs are high. Under this condition, the bias current is steered in transistors M2, M4 and M9 such that high and low voltages are obtained at the nodes Q and $\overline{Q}$ through the load transistors.

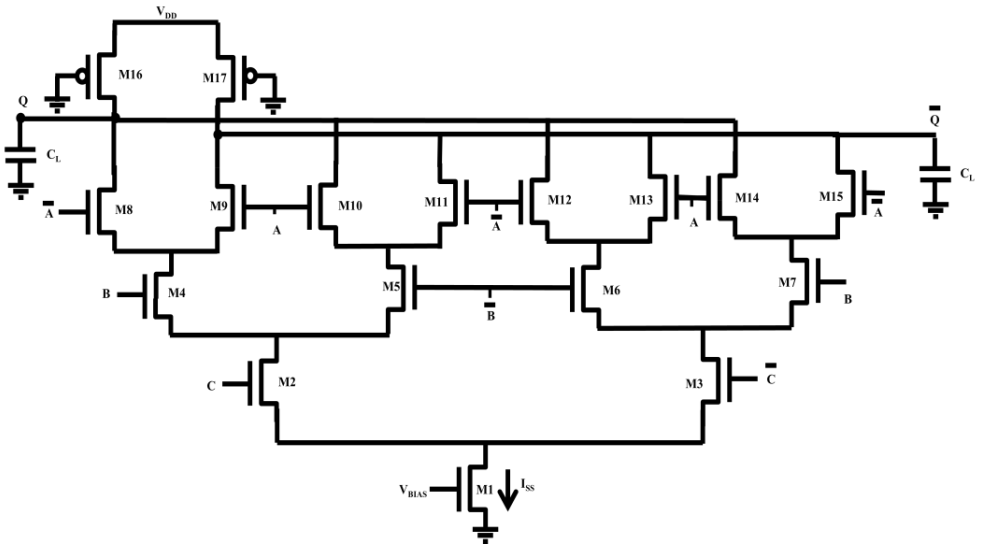


Fig. 1 Conventional three input MCML XOR gate

The minimum supply voltage, $V_{DD_MIN_CON}$ for the gate (Fig. 1) is defined as the lowest voltage at which all the transistors in the three levels and the current source operate in the saturation region [18] and is computed as

$$V_{DD_MIN_CON} = 4V_{BIAS} - 3V_T \quad (1a)$$

where V_T is the threshold voltage of the transistors M1-M15, and V_{BIAS} is the biasing voltage of M1.

The voltage swing of the MCML gate is determined as the difference between the high and the low differential output voltages and is evaluated as

$$V_{SWING_CON} = 2I_{SS} R_{P_CON} \quad (1b)$$

where R_{P_CON} represents the resistance of the PMOS load transistors operating in the linear region [17].

3. The Proposal

A new approach to realize three input MCML gate is presented in this section. The realization employs a novel circuit element named as quad-tail cell to reduce the number of source-coupled transistor levels.

3.1 Quad-tail Cell

A quad-tail cell is an extension of the triple-tail cell concept [14-16] and consists of four source-coupled transistors (M1-M4) as shown in Fig. 2. In the cell, the activation/deactivation of the two outer transistors (M1, M2) is controlled by the two internal transistors (M3, M4). To elaborate this, consider when either one input among Y and Z is high or both these inputs assumes high value. Under these circumstances, the current I_{SS} is steered through transistors M3 or/and M4; and the transistors M1, M2 remain deactivated. Conversely, if both the inputs Y and Z are low, the current I_{SS} will steer to one of the two transistors (M1, M2) depending upon the value of the input X. The requirement for the proper activation/deactivation of the quad-tail cell is similar to triple-tail cell i.e. the aspect ratio of internal transistors M3, M4 should be larger than the others by a factor of N.

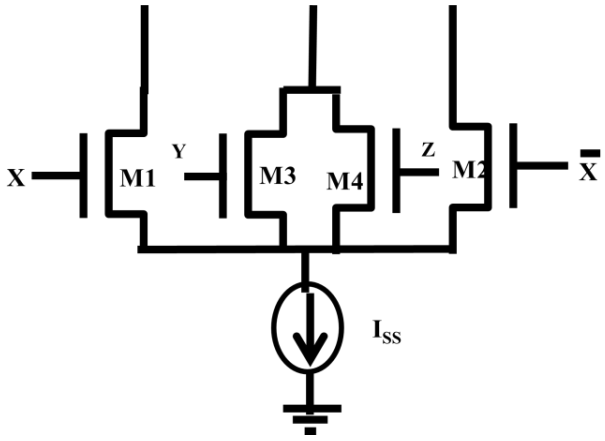


Fig. 2 Proposed Quad-tail cell

3.2 Proposed XOR gate

A three input XOR gate is considered to illustrate the use of quad-tail cell and its complete schematic is shown in Fig. 3. It uses four quad-tail cells (Q1-Q4) each biased by current source of $I_{SS}/4$ value. The inputs connection to the internal transistors of the quad-tail cells is done in a manner so that at any instance of time the outermost transistors in only one quad-tail cell gets

activated. To elaborate this further, consider that all the inputs A, B and C are high. In this condition, the outermost transistors of only Q1 are activated while for the rest (Q2-Q4), the bias current is steered to the internal transistors making deactivation of corresponding outermost transistors.

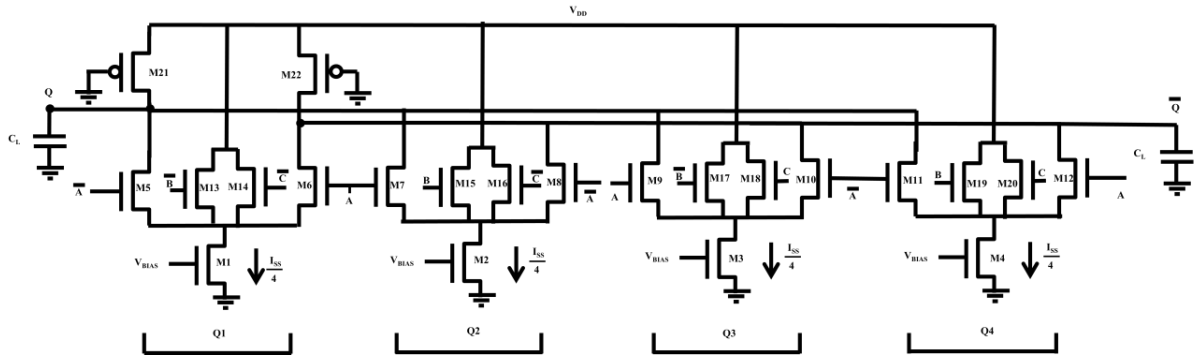


Fig. 3 Proposed Quad-tail cell based three input MCML XOR gate

The minimum supply voltage, $V_{DD_MIN_QC}$ for the proposed three input MCML XOR gate, using the method outlined in [18], is computed as

$$V_{DD_MIN_QC} = 2V_{BIAS} - V_T \quad (2)$$

where V_T is the threshold voltage of transistor M1-M12, and V_{BIAS} is the biasing voltage of M1-M4.

The voltage swing (V_{SWING}) of a MCML gate is defined as the difference of high differential output voltage (V_{OH}) and the low differential output voltage (V_{OL}) [17]. By analyzing the circuit, the differential output voltage ($V_Q - \overline{V_Q}$) for the proposed XOR gate can be calculated as

$$V_Q - \overline{V_Q} = R_P\left[\left(i_{D,6} + i_{D,8} + i_{D,10} + i_{D,12}\right) - \left(i_{D,5} + i_{D,7} + i_{D,9} + i_{D,11}\right)\right] \quad (3)$$

where $i_{D,k}$ is the current through transistor Mk where k = 5-12. The expression requires the determination of the above currents for all the input combinations. To simplify the calculations, the proposed topology is examined by simultaneously considering the input combinations of differential input B and C.

Case 1: Differential input B and C are high

In this condition, the outermost transistors of Q1 (M5-M6) are activated. For high value of differential input A, the transistor M5 is OFF and M6 is ON. Thus, their currents can be written as:

$$i_{D,5} = 0;\ i_{D,6} = \frac{I_{SS}}{4} \quad (4a)$$

At the same time, the quad-tail cells Q2-Q4 are deactivated via the turning ON of their respective inner transistors. But since the complete deactivation of the quad-tail cell cannot be achieved, therefore, small current still flows in the outer transistor of these cells which needs to be considered for calculating the differential output voltage. So, for given factor N, the current flowing in the transistors M7- M12 can be computed as:

$$i_{D,7} = \frac{I_{SS}}{4}\frac{1}{1+N};\ i_{D,8} = 0;\ i_{D,9} = \frac{I_{SS}}{4}\frac{1}{1+N};\ i_{D,10} = 0;\ i_{D,11} = 0;\ i_{D,12} = \frac{I_{SS}}{4}\frac{1}{1+2N} \quad (4b)$$

Substituting these current values in the output voltage expression, we get high differential output voltage (V_{OH}) as

$$V_{OH} = V_Q - \overline{V_Q} = \frac{I_{SS}}{4}\frac{N-1}{N+1}R_P \quad (4c)$$

Similarly, the current through transistors M5-M12, for low value of the differential input A is given as

$$i_{D5}=\frac{I_{SS}}{4};\ i_{D6}=0;\ i_{D7}=0;\ i_{D8}=\frac{I_{SS}}{4}\frac{1}{1+N};\ i_{D9}=0;\ i_{D10}=\frac{I_{SS}}{4}\frac{1}{1+N}\ i_{D11}=\frac{I_{SS}}{4}\frac{1}{1+2N};\ i_{D12}=0 \quad (5a)$$

leading to low differential output voltage (V_{OL}) as

$$V_{OL} = V_Q - \overline{V_Q} = -\frac{I_{SS}}{4}\frac{N-1}{N+1}R_P \quad (5b)$$

Case 2: Differential inputs B and C are low

In this condition, the outer transistors (M11-M12) of Q4 are activated while those of Q1-Q3 (M6-M10) remain deactivated. For high value differential input A, the current through the transistors (M5-M12) can be written as:

$$i_{D5}=0;\ i_{D6}=\frac{I_{SS}}{4}\frac{1}{1+2N};\ i_{D7}=\frac{I_{SS}}{4}\frac{1}{1+N};\ i_{D8}=0;\ i_{D9}=\frac{I_{SS}}{4}\frac{1}{1+N};\ i_{D10}=0;\ i_{D11}=0;\ i_{D12}=\frac{I_{SS}}{4}; \quad (6a)$$

Substituting these current values in the output voltage expression eqn. (3), we get high differential output voltage (V_{OH}) as

$$V_{OH} = V_Q - \overline{V_Q} = \frac{I_{SS}}{4}\frac{N-1}{N+1}R_P \quad (6b)$$

Similarly, for low value of the input A, the current through the transistors (M5-M12) can be written as:

$$i_{D5}=\frac{I_{SS}}{4}\frac{1}{1+2N};\ i_{D6}=0;\ i_{D7}=0;\ i_{D8}=\frac{I_{SS}}{4}\frac{1}{1+N};\ i_{D9}=0;\ i_{D10}=\frac{I_{SS}}{4}\frac{1}{1+N};\ i_{D11}=\frac{I_{SS}}{4};\ i_{D12}=0; \quad (7a)$$

Substituting these current values in the eqn. (3), we get low differential output voltage (V_{OL}) as

$$V_{OL} = V_Q - \overline{V_Q} = -\frac{I_{SS}}{4}\frac{N-1}{N+1}R_P \quad (7b)$$

Case 3: Differential input B is high and input C is low

In this condition, the outer transistors (M9-M10) of Q3 are activated while those of Q1, Q2, Q3 (M5-M8, M11-M12) are deactivated. For high value input A, the current through the transistors (M5-M12) can be written as:

$i_{D5}=0$; $i_{D6}=\frac{I_{SS}}{4}\frac{1}{1+N}$; $i_{D7}=\frac{I_{SS}}{4}\frac{1}{1+2N}$; $i_{D8}=0$; $i_{D9}=\frac{I_{SS}}{4}$; $i_{D10}=0$; $i_{D11}=0$; $i_{D12}=\frac{I_{SS}}{4}\frac{1}{1+N}$; (8b)

Substituting these current values in the output voltage expression, we get low differential output voltage (V_{OL}) as

$$V_{OL} = V_Q - \overline{V_Q} = -\frac{I_{SS}}{4}\frac{N-1}{N+1}R_P \quad (8b)$$

Similarly, for low value of the input A, the current through the transistors (M5-M12) can be written as:

$i_{D5}=\frac{I_{SS}}{4}\frac{1}{1+N}$; $i_{D6}=0$; $i_{D7}=\frac{I_{SS}}{4}\frac{1}{1+2N}$; $i_{D8}=0$; $i_{D9}=0$; $i_{D10}=\frac{I_{SS}}{4}$; $i_{D11}=\frac{I_{SS}}{4}\frac{1}{1+N}$; $i_{D12}=0$; (9b)

Substituting these current values in the eqn. (3), we get high differential output voltage (V_{OH}) as

$$V_{OH} = V_Q - \overline{V_Q} = \frac{I_{SS}}{4}\frac{N-1}{N+1}R_P \quad (9c)$$

Case 4: Differential input B is low and input C is high

In this condition, the outer transistors (M7-M8) of Q2 are activated while those of Q1, Q3, Q4 (M5-M6, M9-M12) are deactivated. For high value input A, the current through the transistors (M5-M12) can be written as:

$i_{D5}=0$; $i_{D6}=\frac{I_{SS}}{4}\frac{1}{1+N}$; $i_{D7}=\frac{I_{SS}}{4}$; $i_{D8}=0$; $i_{D9}=\frac{I_{SS}}{4}\frac{1}{1+2N}$; $i_{D10}=0$; $i_{D11}=0$; $i_{D12}=\frac{I_{SS}}{4}\frac{1}{1+N}$; (10a)

Substituting these current values in the output voltage expression, we get low differential output voltage (V_{OL}) as

$$V_Q - \overline{V_Q} = V_{OL} = -\frac{I_{SS}}{4}\frac{N-1}{N+1}R_P \quad (10b)$$

Similarly, for low value of the input A, the current through the transistors (M5-M12) can be written as:

$i_{D5}=\frac{I_{SS}}{4}\frac{1}{1+N}$; $i_{D6}=0$; $i_{D7}=0$; $i_{D8}=\frac{I_{SS}}{4}$; $i_{D9}=0$; $i_{D10}=\frac{I_{SS}}{4}\frac{1}{1+2N}$; $i_{D11}=\frac{I_{SS}}{4}\frac{1}{1+N}$; $i_{D12}=0$; (11a)

Substituting these current values in the eqn. (3), we get high differential output voltage (V_{OH}) as

$$V_{OH} = V_Q - \overline{V_Q} = \frac{I_{SS}}{4}\frac{N-1}{N+1}R_P \quad (11b)$$

From the above analysis, the voltage swing (V_{SWING_PG}) of the proposed gate can be determined as

$$V_{SWING_PG} = V_{OH} - V_{OL} = \frac{I_{SS}}{2}\frac{N-1}{N+1}R_P \quad (12)$$

This indicates that the voltage swing of the proposed gate is smaller than the conventional MCML gate (eqn. 1b). So in order to achieve the same voltage swing as the conventional MCML gate, the load resistance of the proposed gate (R_P) is increased accordingly.

4. Simulations Results and Discussion

In this section, the functionality of the proposed three input XOR gate is verified through simulations using 180 nm CMOS technology parameters. Its performance is compared with the conventional MCML XOR topology, two more MCML XOR circuits and CMOS complementary pass transistor (CPL) based XOR topology for the sake of fair comparison. Both the MCML topologies use triple tail concept to lower the number of source coupled pair levels. The first topology employs a cascade of two input XOR gates while the second realization reduces the NSL from three to two. All the XOR gates are simulated with their respective minimum power supply and load capacitance of 50 fF. The MCML topologies are so designed that the total current drawn from the power supply is 100 µA and and voltage swing is 400 mV. Further, the total current drawn from the power supply per gate is retained at 100 µA for MCML topologies while maintaining voltage swing of 400 mV. The performance comparison is done on the basis of power, propagation delay, power delay product (PDP), transistor count, gate count and switching current. The simulation of a ring oscillator based on the proposed and the conventional XOR gate is performed for completeness. A discussion on the general approach for implementing complex three input logic function is included in the last.

4.1 Functional Verification of the proposed circuit

The functionality of the proposed quad-tail cell based three input MCML XOR gate is verified through simulations with simulation conditions discussed above. The timing waveforms for differential inputs A, B and C and the corresponding differential output are shown in Fig. 4. It can be observed that differential output voltage is high for all the cases having odd number of high inputs and remains low otherwise. Thus, the proposed MCML XOR gate adheres to desired functionality.

.

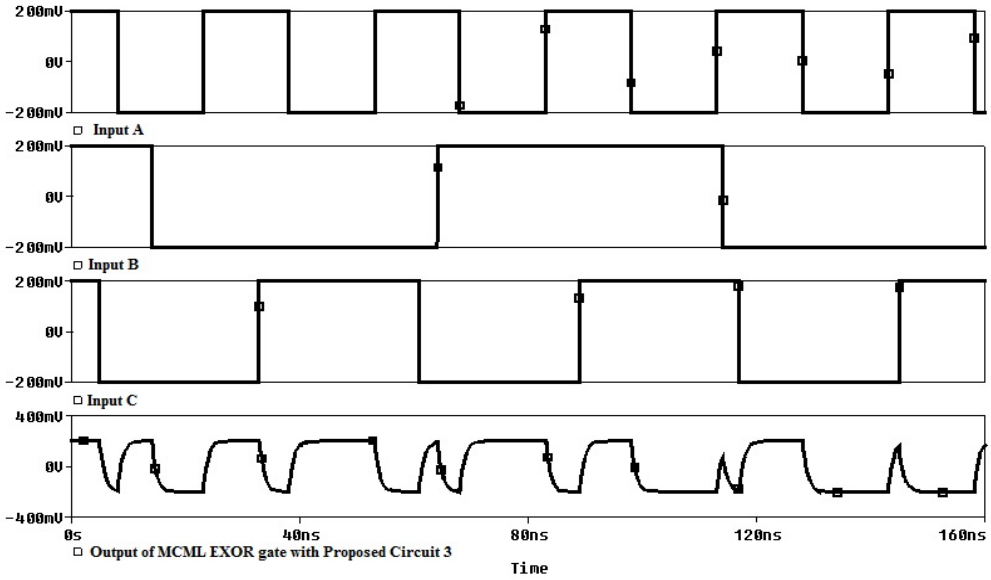
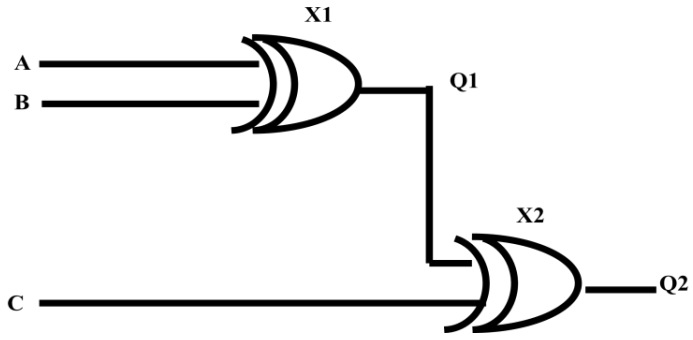


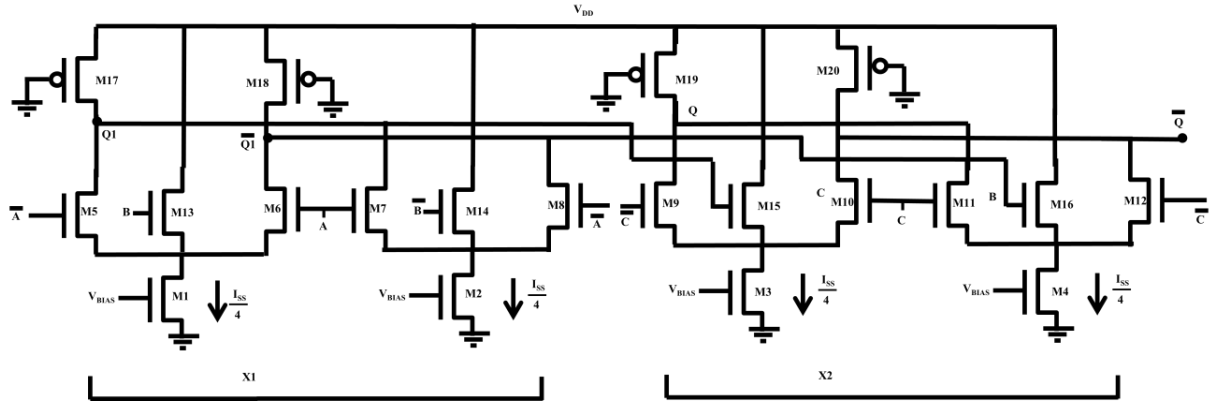
Fig. 4: Simulation waveforms for the proposed three input MCML XOR gate

4.2 Performance Comparison

The performance of the proposed XOR gate is compared with the conventional three input XOR gate (Fig. 1). To give broader perspective, two more possible three input XOR gate circuit realizations are also included. Both the realizations use triple-tail concept to lower the number of source coupled pair levels. The first realization is derived from the fact that the three input XOR gate functionality can be achieved by cascading the two input XOR gates as shown in Fig. 5a. The inputs A, B are connected to XOR gate X1 while its output and the input C are fed to XOR gate X2. The recent implementation of the two input XOR gate [14-16] is chosen for implementation. The complete MOS based schematic of the three input XOR gate is shown in Fig. 5b and is referred to as Topology 1 in the context of the paper.



(a)



(b)

Fig. 5 Topology 1 a) gate level schematic b) complete MOS schematic

The second realization extends the triple-tail cell concept to lower the number of source coupled pair levels from three to two. The resulting topology is shown in Fig. 6 and is referred to as Topology 2 in the paper. It consists of two triple-tail cells biased by separate current sources of $I_{SS}/2$ value. The transistors at the lowest level of the conventional three input XOR gate (Fig. 1) are made the activating/ deactivating transistors of the triple-tail cells. This leads to two levels of stacked source-coupled transistors in the outer branches of the triple-tail cell. The minimum supply voltage, $V_{DD_MIN_TP2}$ for the topology 2 of the three input MCML XOR gate can be obtained by using the method outlined in [18] as

$$V_{DD_MIN_TP2} = 3V_{BIAS} - 2V_T \quad (13)$$

where V_T is the threshold voltage of transistor M1-M14, and V_{BIAS} is the biasing voltage of M1-M2.

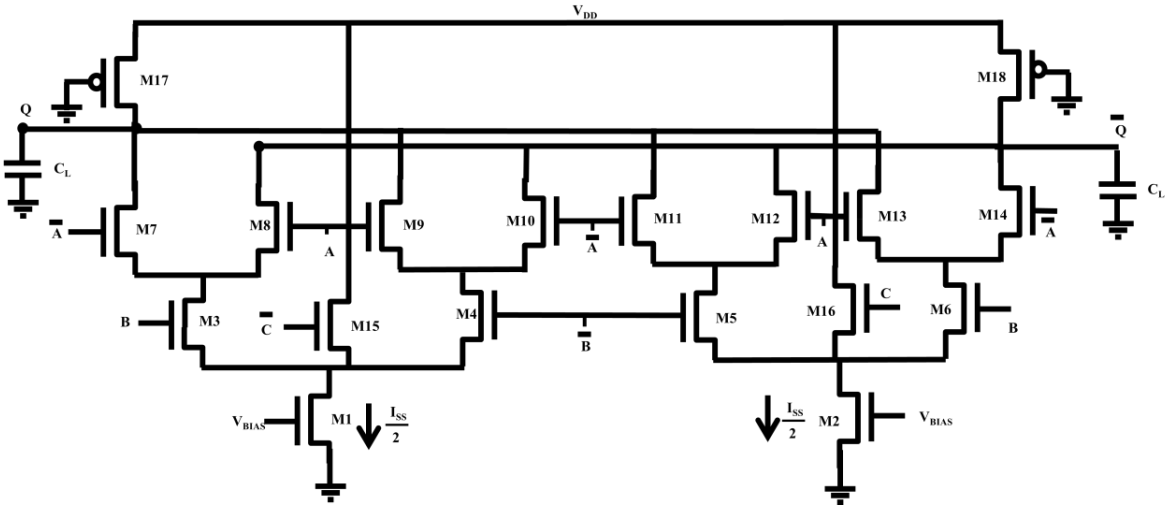


Fig. 6 Complete MOS level schematic of topology 2

Table I: Summary of the results

Parameter \ Circuit	Conventional MCML	Topology 1	Topology 2	Proposed	CMOS CPL
Supply Voltage (V_{DD})	1.7V	1.1V	1.4V	1.1 V	1.0V
Power Consumption (µW)	170	110	140	110	44
Propagation Delay (ps)	1178	1049	732	614	4017
Power Delay Product (fJ)	166.770	115.390	102.480	67.540	176.748
Gate Count	1	2	1	1	1
Transistor Count	17	20	18	22	18
Switching Current (µA)	5	40	25	20	42

The performance of the proposed quad-tail cell based three input MCML XOR gate topology is compared with MCML conventional, topology 1, topology 2 and CMOS CPL based XOR topology with same input conditions. The topologies are powered by their respective minimum power supply. The simulation results are summarized in Table I and the following observations are made:

- The power supply constraint for proposed XOR gate and topology 1 is same whereas conventional topology need largest value and requirement for topology 2 lies in the middle. This is a direct consequence of presence of NSL e.g. topologies (proposed and topology 1) employ single level while conventional and topology 2 use three and two levels respectively.
- Since all the topologies are designed to draw 100 µA current from the power supply, therefore the topologies (proposed and topology 1) consume same power which is lower than the remaining two.
- It is clear from above point that the topologies (proposed and topology 1) consume least power among those listed in Table 1. In terms of the propagation delay, proposed topology show significant improvement which may be attributed to reduced number of stages. This accounts for lowest power delay product values (PDP).
- Though gate count is equal for conventional, topology 2 and proposed topology, but the proposed topology outperforms in terms of propagation delay, power and PDP.
- The transistor count in proposed topology is highest among all.
- The delay in MCML based conventional XOR gate and the topology 1 is comparatively higher than has proposed topology and topology2. It is due to the fact that there are three stacked source-coupled transistors pair levels which contribute large parasitic capacitance at the output node. The delay in topology 1 is due to cascading of two XOR gates. Though the proposed topology and topology 2 employ a single gate but parasitic contribution in later topology is higher than former one. This explains lowest delay of the proposed XOR gate topology among all.
- All the MCML based XOR gate topologies produce less switching current in comparison to CMOS CPL based due to the presence of constant current source. The results thus confirm the preference of MCML based topologies in low noise mixed-signal environments over the CMOS based counterparts [19, 20].

- The CMOS CPL based XOR gate consume the lowest power but show high delay and PDP values in comparison to all MCML based XOR gate topologies. Therefore it is not considered further in the proposal.

To examine the sensitivity of different XOR realization performance towards process variation, the propagation delay and the voltage swing obtained through simulations are comprehended in Table II. The variation between the best and worst case in the propagation delay is by a factor of 1.63, 1.29, 1.48 and 1.54 respectively for conventional, topologies 1 and 2 and the proposed one. Analogously, the corresponding factors for voltage swing are 2.19, 2.28, 2.25 and 2.54 for conventional, topologies 1 and 2 and the proposed one. The voltage swing values should be more than $1.4V_{dssat}$ where V_{dssat} is the saturation drain-source voltage of the differential transistor pair) for functionality to remain intact [21]. It may further be noted that the proposed MCML gates can be maintain constant voltage swing against process variation by modifying their load section by using adaptive bias controller as suggested in [22, 23].

Table II Effect of process variation on propagation delay and voltage swing of three input MCML XOR gate designs

NMOS / PMOS / XOR gate topology	**T T**	**F F**	**S S**	**F S**	**S F**
Propagation Delay (ps)					
Conventional	1178	976	1586	1091	1417
Topology 1	1049	971	1253	1071	1126
Topology 2	732	627	930	723	806
Proposed	614	430	664	659	661
Voltage Swing (mV)					
Conventional	400	444	290	580	264
Topology 1	400	434	286	572	250
Topology 2	400	454	296	576	256
Proposed	400	424	298	550	216

The behavior of proposed XOR gate is also investigated by configuring it as an inverter and cascading five such inverters in a loop to obtain five stage ring oscillator (RO). The timing waveform is shown in Fig. 7. A RO is also constructed with conventional XOR gate with similar connections. It also gives oscillations and timing waveform is similar to that of Fig. 7 which is omitted for the sake of brevity. To verify the functionality of RO constructed with proposed and conventional topologies at all PVT corners, number of simulations have been performed and the results are comprehended in Table III. It can be observed that the oscillations are achieved at all the process corners and the values exhibit the same trend as shown in Table II for individual gate simulation.

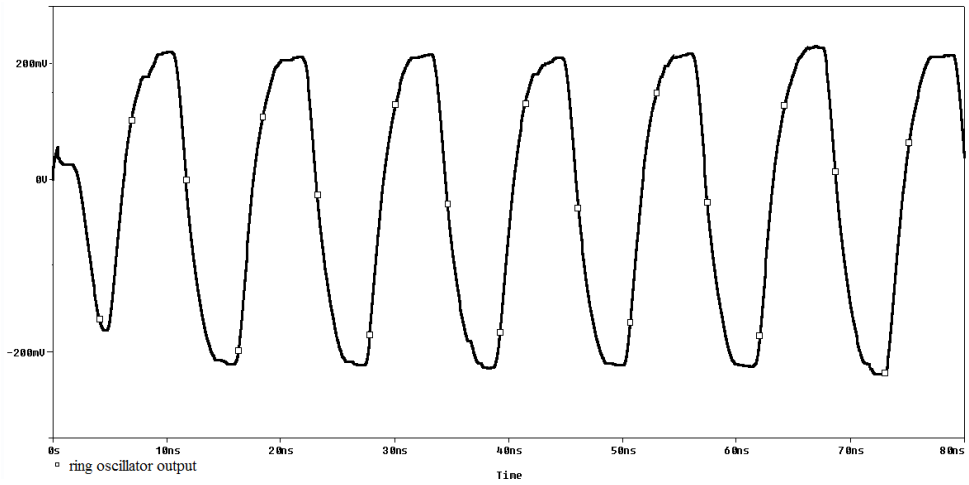


Fig. 7 Ring Oscillator Output by using proposed XOR gate

Table III: Oscillation frequeny at different PVT corners

Topology \ NMOS PMOS T(°C)		TT 70	FF 0	SS 125	FS 70	SF 70	TT 70	TT 70	TT 0	TT 125
Conventional	V_{DD} (V)	1.7	1.87	1.53	1.7	1.7	1.87	1.53	1.7	1.7
	Freq. (MHz)	95	108	65	71	66	100	59	125	77
Proposed	V_{DD} (V)	1.1	1.21	0.99	1.1	1.1	1.21	0.99	1.1	1.1
	Freq. (MHz)	140	181	114	125	139	147	90	163	125

To compare the behavior of the proposed gate with conventional XOR gate under same parasitic contribution case, both gates are redesigned for this and five stage ROs are constructed. The oscillation frequency of 5.1 MHz and 71 MHz are observed for the proposed and the conventional respectively. The corresponding power consumption values are 550 µW and 850 µW for the proposed and the conventional respectively. These observations can be supported with following discussion: The voltage swing, propagation delay and the power are represented as V_{SWING_X}, t_{PD_X} and P_X where x corresponds to CON and PG for conventional and proposed topologies. Using first order approximations, the values of t_{PD_CON} and t_{PD_PG} are computed respectively as:

$$t_{PD_PG} = 0.69\ R_P(C_{PC} + C_{Load}) \quad (14)$$

$$t_{PD_CON} = 0.69\ R_{P_CON}(C_{PC} + C_{Load}) \quad (15)$$

where R_{P_CON} and R_P refer to load resistances of conventional and proposed topologies; and C_{Load} and C_{PC} represent load and parasitic capacitance respectively.

The ratio of t_{PD_PG} and t_{PD_CON} is computes as

$$\frac{t_{PD_PG}}{t_{PD_CON}} = \frac{0.69\,R_P(C_{PC}+C_{Load})}{0.69\,R_{CON}(C_{PC}+C_{Load})} = \frac{R_P}{R_{CON}} \quad (16)$$

Taking N = 2, this ratio is computed as 12 for $V_{SWING_CON} = V_{SWING_PG}$. The RO simulation gives value this ratio as 13.78 giving error of about 15%. Further, as the topologies have been simulated with their respective minimum power supplies ($V_{DD_MIN_PG}$ and $V_{DD_MIN_CON}$), the ratio of power consumption is given by

$$\frac{P_{PG}}{P_{CON}} = \frac{V_{DD_MIN_PG}I_{SS}}{V_{DD_MIN_CON}I_{SS}} = \frac{V_{DD_MIN_PG}}{V_{DD_MIN_CON}} \quad (17)$$

The theoretical and simulated values for this ratio are 0.64 and 0.66 respectively. The power efficient design needs the product of power and delay (PDP) to be calculated and a smaller value is indication of this measure [17]. The ratio of PDP for proposed (PDP_{PG}) and conventional is computed as

$$\frac{PDP_{PG}}{PDP_{CON}} = \frac{V_{DD_MIN_PG}I_{SS}}{V_{DD_MIN_CON}I_{SS}}\frac{0.69\,R_P(C_{PC}+C_{Load})}{0.69\,R_{CON}(C_{PC}+C_{Load})} = \frac{V_{DD_MIN_PG}}{V_{DD_MIN_CON}}\frac{R_P}{R_{CON}} \quad (18)$$

The theoretical and simulated values for this ratio are 7.68 and 9 respectively. Thus the proposed topology is less power efficient if the parasitic contribution of the transistors in the two XOR gate topologies is made equal.

4.3 A generalized Approach

The proposed quad-tail cell can be used to formulate a general design approach for logic function realization. Four number of quad-tail cells can be connected in a configuration given in Fig. 7 to realize a 4:1 multiplexer. The input lines are marked as I0-I3, and select lines are denoted by S0 and S1. The four input lines (I0, I1, I2, I3) forms the input to the outer transistors of the quad-tail cells (Q1, Q2, Q3, Q4) respectively while select lines are tied to inner transistors according to the operation. The availability of the desired input line at the multiplexer output can be achieved by proper activation of the quad-tail cell through select lines S0, S1. For instance, the data on the input line I1 can be made available at the output of the multiplexer for low and high values of S0 and S1 respectively. It is well known that any three input logic function can be implemented using 4:1 MUX so the circuit of Fig. 7 can practically realize $(2^3)^2$ logic functions. The mapping table for I0-I3 and S1-S0 is omitted for the sake of brevity.

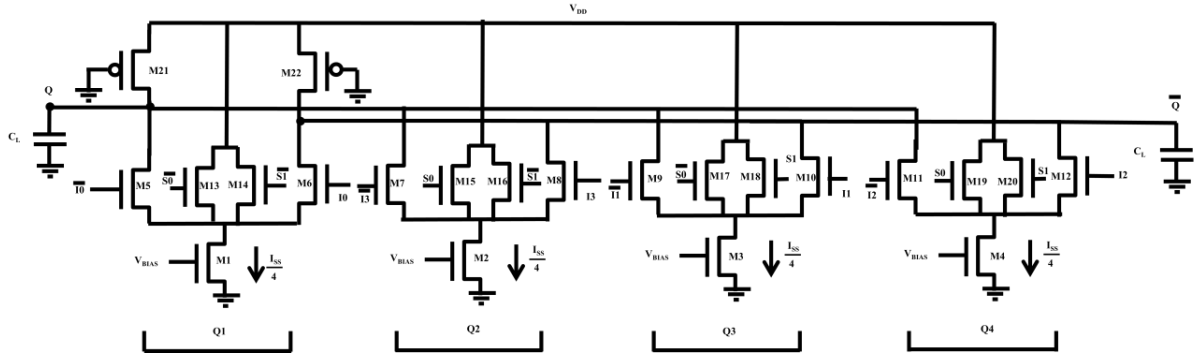


Fig. 7 Multiplexer realization (4:1 MUX) based on the proposed approach

5. Conclusion

A new proposal for three input logic function realization in MCML style is presented. The new proposal reduces the number of stacked source-coupled transistor levels in the logic function realization. A circuit element named as quad-tail cell is presented for this purpose and its use in the implementation of three input exclusive-OR (XOR) gate is elaborated. Its behavior is analyzed and SPICE simulations using TSMC 180 nm CMOS technology parameters are included to support the theoretical concept. The performance of the proposed circuit is compared with the conventional XOR topology along with two more triple-tail cell based topologies. Comparion with CMOS Complementary pass transistor logic based XOR gate is also inclused for the sake of completeness. The performance of all XOR gate realizations is compared and is found that the proposed XOR gate topology outperforms in terms of most of the performance parameters. The sensitivity of different MCML XOR gate realization performance is examined towards process variation which indicates similar values. A discussion on the realization of three input logic by configuration of a 4:1 multiplexer has also been included as an extension of the work.

References

[1] H. Yang, “High-Speed Optical Transceivers: Integrated Circuits Designs And Optical Devices Techniques”, World Scientific Publishing Co. Pvt. Ltd., 2006

[2] Z. V. Chia, S. Y. Simon Ng, and M. Je, “Current Mode Logic Circuits for 10-bit 5GHz High Speed Digital to Analog Converter”, International Journal of Electrical, Computer, Energetic, Electronic and Communication Engineering, Vol:7, No:9, 2013, pp. 1211 – 1214

[3] H. C. Luong, G. Chi and T. Leung, “Low-Voltage CMOS RF Frequency Synthesizers”, Cambridge University Press, 2004

[4] M. Yamashina, H. Yamada, “An MOS Current Mode Logic (MCML) Circuit for Low-Power Sub-GHz Processors”, IEICE Trans. on Electronics, Vol. E75-C ,1992, pp. 1181-1187.

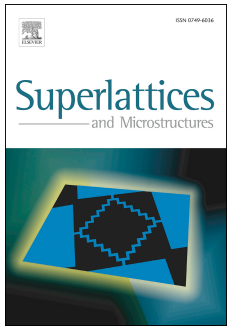
[5] S. Bruma, “Impact of on-chip process variations on MCML performance”, in: Proceedings of IEEE Conference on Systems-on-Chip, 2003, pp. 135–140.

[6] J.M. Musicer, J. Rabaey, “MOS Current Mode Logic for Low Power, Low Noise, CORDIC Computation in Mixed-Signal Environments”, in: Proceedings of the International Symposium of Low Power Electronics and Design, 2000, pp. 102-107.
[7] H. Hassan, M. Anis, M. Elmasry, “MOS Current Mode Circuits: Analysis, Design, and Variability”, IEEE Trans. Very Large Scale Integration (VLSI) Systems. Vol. 13, 2005, pp. 885-898.
[8] M. Anis, M. Allam, and M. Elmasry, “Impact of technology scaling on CMOS logic styles”, IEEE Trans. Circuits Syst. II, vol. 49, 2002, pp. 577–588.
[9] Z. Toprak, Y. Leblebici, “Low-power current mode logic for improved DPA-resistance in Embedded Systems”, in: Proceedings IEEE Int. Symp.on Circuits Syst., May 2005.
[10] Kundan, J., Hasan, S.M.R.: “Enhanced folded source-coupled logic technique for low-voltage mixed-signal integrated circuits”, IEEE Transactions on Circuits and Systems-II, 2005, 47, pp. 810–817.
[11] M. Alioto, L. Pancioni, S. Rocchi, V. Vignoli, “Modeling and Evaluation of Positive-Feedback Source-Coupled Logic”, IEEE Trans. Circuits and Systems-I, Regular Papers, vol. 51, 2004, pp. 2345-2355.
[12] J. Savoj, B. Razavi, “A 10-Gb/s CMOS clock and data recovery circuit with a half-rate linear phase detector”, IEEE J. of Solid-State Circuit, vol. 36, 2001, pp.761–767.
[13] A. Tajalli, M. Atarodi, “Linear phase detection using two-phase latch”, Electronics Letter, vol. 39, issue. 24, pp. 1695-1696.
[14] K. Gupta, N. Pandey, M. Gupta, “MCML D-Latch Using Triple-Tail Cells: Analysis and Design” Active and Passive Electronic Component, Volume. 2013, 2013, Article ID 217674.
[15] K. Gupta, N. Pandey, M. Gupta, “Analysis and design of MOS current mode logic exclusive-OR gate using triple-tail cells,” Microelectronics Journal vol.44, 2013, pp. 561-567.
[16] K. Gupta, N. Pandey, M. Gupta, “Low-Voltage MOS Current Mode Logic Multiplexer”, Radioengineering Journal, vol. 22, 2013, pp. 259-268.
[17] M. Alioto, G. Palumbo, “Model and Design of Bipolar and MOS Current-Mode logic (CML, ECL and SCL Digital Circuits)”, Springer, Neitherlands, (2005).
[18] H. Hassan, M. Anis, M. Elmasry, “Analysis and Design of Low-Power Multi-Threshold MCML”, in: Proceedings of the IEEE International Conference on System-on-Chip, 2004, pp. 25-29.
[19] J. M. Musicer, J. Rabaey, “MOS Current Mode Logic for Low Power, Low Noise, CORDIC Computation in Mixed-Signal Environments,” in: Proceedings of International Symposium of Low Power Electronics and Design, 2000, pp.102-107.
[20] S. Bruma, “Impact of on-chip Process Variations on MCML Performance,” in: Proceedings of IEEE Conference on Systems-on-Chip, 2003, pp. 135–140.
[21] A. Tajalli, and Y. Leblebici, “Extreme low-power Mixed Signal IC Design,” Springer, New York (2010).

[22] M. P. Houlgate, D. J. Olszewski, K. Abdelhalim, and L. M. Eachern, “Adaptable Performance MOS Current Mode Logic for use in a 3GHz Programmable Frequency Divider,” in : Proceedings of IEEE Conference on Circuits and Systems, 2003, pp. 1303-1306.

[23] M. Mizuno, M. Yamashina, K. Furuta, H. Igura, H. Abiko, K. Okabe, A. Ono, and H. Yamada, “A GHz MOS Adaptive Pipeline Technique using MOS Current-Mode Logic,” IEEE Journal of Solid-State Circuits, vol. 31, no. 6, 1996, pp. 784-791.

Accepted Manuscript



Optimization of high-k and gate metal workfunction for improved analog and intermodulation performance of Gate Stack (GS)-GEWE-SiNW MOSFET

Neha Gupta, Rishu Chaujar

PII: S0749-6036(16)30511-0

DOI: 10.1016/j.spmi.2016.07.021

Reference: YSPMI 4425

To appear in: *Superlattices and Microstructures*

Received Date: 24 May 2016

Revised Date: 7 July 2016

Accepted Date: 19 July 2016

Please cite this article as: N. Gupta, R. Chaujar, Optimization of high-k and gate metal workfunction for improved analog and intermodulation performance of Gate Stack (GS)-GEWE-SiNW MOSFET, *Superlattices and Microstructures* (2016), doi: 10.1016/j.spmi.2016.07.021.

This is a PDF file of an unedited manuscript that has been accepted for publication. As a service to our customers we are providing this early version of the manuscript. The manuscript will undergo copyediting, typesetting, and review of the resulting proof before it is published in its final form. Please note that during the production process errors may be discovered which could affect the content, and all legal disclaimers that apply to the journal pertain.

ACCEPTED MANUSCRIPT

Optimization of High-k and Gate Metal Workfunction for Improved Analog and Intermodulation Performance of Gate Stack (GS)-GEWE-SiNW MOSFET

Neha Gupta[1] and Rishu Chaujar[2]

Microelectronics Research Lab, Department of Engineering Physics,
Delhi Technological University, Bawana Road, Delhi-110042, India[1]
E-Mail: nehagupta@dtu.ac.in[1] and rishu.phy@dce.edu[2]

***Abstract*—This work optimizes the gate engineering scheme (both gate stack and gate metal workfunction engineering) of Stacked Gate (SG) Gate Electrode Workfunction Engineered (GEWE)-Silicon Nanowire MOSFET at 300K for improved analog and intermodulation performance. This has been done by evaluating and analyzing the metrics such as Switching Ratio, Subthreshold Swing (SS), Device Efficiency, channel and output resistance, VIP3, IIP3, 1-dB Compression Point, IMD3, HD2 and HD3. Simulation results exhibit that HfO_2 as a gate stack exhibit high linearity at a comparatively low gate bias of 0.56V with higher IIP3 (6.21dBm) and low IMD3 (9.6 dBm). Further, the characteristics/performance is modulated by adjusting the workfunction difference of metal gate. This study demonstrates that SiNW MOSFET modeled with HfO_2 as a gate stack over SiO_2 interfacial layer, and gate metal workfunction difference (ΔW) of 4.4 eV can be considered as a promising potential for low power switching component in ICs and Linear RF amplifiers.**

***Keywords*—Gate Stack, Gate Electrode Workfunction Engineering, Analog, Linearity, Harmonic Distortion, Silicon Nanowire**

I. INTRODUCTION

According to Moore's Law, the transistor size has shrunk to get higher device performance and reduce its cost, but short channel effects (SCEs) such as DIBL, HCEs, Punchthrough, V_{th} roll-off, etc., hinders its performance. To overcome such limitations, various device designs and engineering schemes are reported in literature such as Dual Gate [1], Recessed channel [2], Multi-Gate [3], CNT FET [4], Nanowire FET [5], etc. Among them, Silicon Nanowire (SiNW) emerged as a most promising in electronic devices because its properties such as concentration, dopant type can be changed during synthesis. Also, its mobility is higher than bulk silicon due to stronger quantum confinement. The body thickness (diameter) of the nanowire can readily be reduced to a few nanometers in size scale that is challenging to obtain using bulk silicon [6] and to get further improvement against SCEs the concept of SiNW MOSFET was put forward by Cui et al. [7] in 2003 concluded that silicon nanowires MOSFET as building blocks for future nano-electronics.

Moreover, the most common issue of scaling is oxide thickness. As oxide thickness scales down to 1.5nm or below, the leakage current increases up to $1A/cm^2$ at 1V due to direct tunneling of carriers which, consequently increases the static power and hence affect the circuit operation as reported by [8-9]. High-k films are proved to be the most promising solution. However, these films result in high fringing fields from gate to source/drain regions and thus degrading the device performance. This constraint can be overcome by using gate stack architecture consisting of SiO_2 layer as a passivation between high-k films and bulk by keeping the effective oxide thickness (EOT) constant, high-k dielectrics permit the increase in physical oxide thickness to prevent gate tunneling [10-11] and thus improves the carrier efficiency but at the same time, gate capacitance increases. Therefore, for selection of high-k materials relationship between dielectric constant and band-offset must be considered. The excessive high-k constant is generally undesirable owing to a tradeoff between dielectric constant and band-offset. Hence, selection of metal material becomes necessary. This work is an extension of [12], mainly focusing on effect of high-dielectric constant (such as Si_3N_4, HfO_2, ZrO_2) and gate metal

workfunction in terms of Analog and Intermodulation metrics, since linearity plays an important role in RFIC designing and high-frequency systems because nonlinearity causes harmonic generation, gain compression, desensitization etc. [13-14]. A high linearity with low distortion is preferred in modern communication systems even while working with a weak signal. Thus, previously performed analysis has been extended with an aim to optimize the value of high-dielectric constant and gate metal workfunction difference (ΔW) which can be used as a reference tool for designing circuits for different analog and RF applications where linearity is a major concern.

II. Device Structure and its Description

Fig.1 (a-b) shows the 3D and 2D cross-sectional view of gate stack (GS) GEWE SiNW MOSFET. The channel length of the device is 30nm and radius of SiNW is 5nm. The length of region 1 (L_1) and region 2 (L_2) are 15nm each which is towards the 45nm node CMOS technology as stated in ITRS Roadmap[15]. The Source/Drain region is heavily doped with an n-type impurity of 1×10^{19} $cm^{-3}$of 5nm long, while the SiNW is doped with a p-type impurity of 1×10^{16} $cm^{-3}$and effective oxide thickness is 1.5nm. The gate metal work function at the source end (Φ_{m1}) is 4.8 eV (Au) and metal gate work function at the drain end (Φ_{m2}) is 4.4 eV (Ti) as shown in Fig. 1. In this analysis, all the junctions are assumed as abrupt, and the doping profiles are uniform. All simulations have been performed using ATLAS and DEVEDIT 3D device simulator [16].

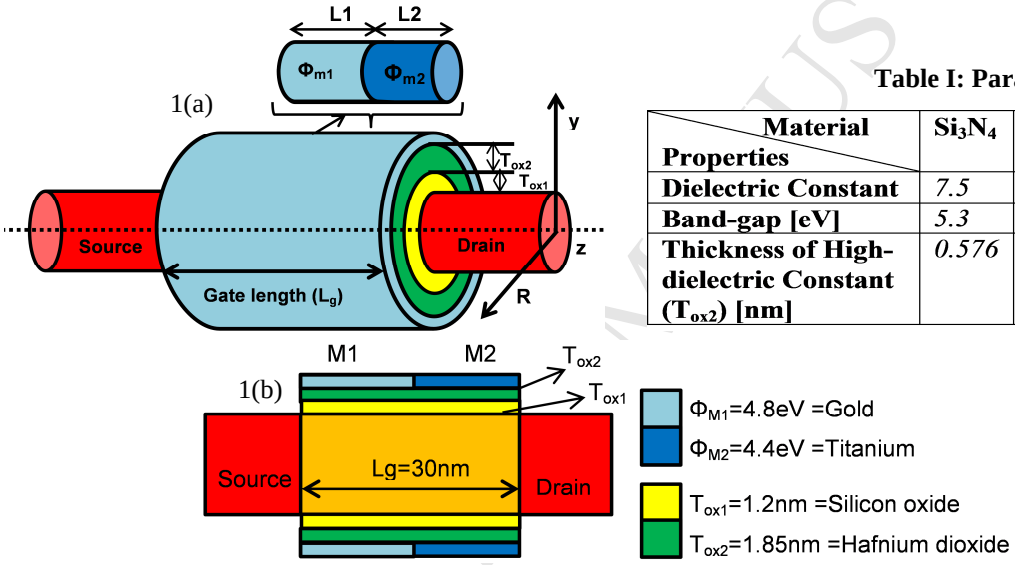


Table I: Parameters

Material / Properties	Si_3N_4	HfO_2	ZrO_2
Dielectric Constant	*7.5*	*24*	*30*
Band-gap [eV]	*5.3*	*5.8*	*5-7*
Thickness of High-dielectric Constant (T_{ox2}) [nm]	*0.576*	*1.85*	*2.3*

Fig.1 (a-b): Schematic Representation and its 2D cross-sectional view of GS-GEWE-SiNW MOSFET, Table I show the default parameters of high-k.

III. Simulation Methodology

All the simulations have been executed using physical models accounting for the electric field-dependent and concentration-dependent carrier mobilities, Shockley–Read–Hall (SRH) recombination/generation with doping dependent carrier lifetime, inversion layer Lombardi CVT mobility model, wherein concentration-dependent mobility, high field saturation model are all included [15]. To incorporate all non-local effects, we have adopted the quantum mechanical models which are more accurate than drift-diffusion method. To characterize the device performance accurately, it is very important to define the carrier transport with proper models. The quantum confinement effect in the deep scaled device may not be negligible [17]. Since the inversion charge layer thickness in the conducting silicon nanowire channel is comparable to the nanowire dimension, thus the effect of quantum confinement in the sub-nm device may not be negligible. The Bohm Quantum Potential (BQP) model [18] can also be used with Energy balance and hydrodynamic models, where the semi-classical potential is modified by the quantum potential in a similar way as for the continuity equations. The model introduces a position dependent quantum potential, Q, which is added to the Potential Energy of a given carrier type. This quantum potential is derived using the Bohm interpretation of quantum mechanics [19] and is described below:

Time-independent Schrodinger equation can be written as:

$$\left(\frac{-\hbar}{2m^*}\nabla^2 - V\phi\right)\psi_j = E_j\psi_j \quad \text{..... (1)}$$

According to Bohm's interpretation of quantum mechanics, the wave function in a polar representation can be written as:

$$\psi = R.\exp\left(\frac{iS}{\hbar}\right) \quad \text{..... (2)}$$

where R is probability density per unit volume, S has dimensions of action (energy×time)
By substituting equation 2 in 1, the Schrodinger equation can be written as:

$$\frac{\hbar^2}{2}\nabla\left\{M^{-1}\nabla\left[R.\exp\left(\frac{iS}{\hbar}\right)\right]\right\} + V.\mathrm{Re}\,xp\left(\frac{iS}{\hbar}\right) = E.R.\exp\left(\frac{iS}{\hbar}\right) \quad \text{..... (3)}$$

Where M^{-1} is the inverse of effective mass tensor and $M^{-1}\nabla S$ is the local velocity of particle associated to wave function. Real part of Eq. 3 is interpreted as continuity equation of probability density while imaginary part states that the total energy, E is conserved and equal to the sum of potential (V) and kinetic energy ($0.5\, M^{-1}\nabla S$). Therefore, Quantum potential is defined as:

$$V = \frac{-\hbar^2}{2}\frac{\nabla\left(M^{-1}\nabla R\right)}{R} \quad \text{..... (4)}$$

Potential V is obtained by the single particle Schrodinger equation and use "*mean field approximation*" and consider an effective quantum Bohm Potential defined as the weighted average potential for all carriers constrained in confining potential. Effective Quantum Potential is written as:

$$Q_{eff} = \frac{-\hbar^2}{2}\gamma\nabla\frac{[M^{-1}\nabla\left(n^{\alpha}\right)]}{n^{\alpha}} \quad \text{..... (5)}$$

where α and γ are two adjustable parameters, M^{-1} is the inverse effective mass tensor, n is the electron (or hole) density and h is a Planck's constant.

Bohr Quantum Potential (BQP) Model with alpha=0.5 and gamma=1.2 was used to take quantum mechanical effects into consideration. Additionally, numerical methods such as BICGST (bi-conjugate gradient stabilized) have been considered to obtain the solutions with improved convergence in 3D device structure [16]. Default simulator coefficients for all parameters have been employed. In order to fairly analyze the device performances, all the three devices are optimized to have the same threshold voltage, i.e., 0.32V by changing channel doping. The calibration of model parameters used in simulation has been performed according to the experimental results [20] and closed proximity of simulated results with the experimental results as shown in Fig. 2 validates the choice of parameters invoked during simulation. A proposed summary of the process flow, outlining the fabrication process of GEWE-SiNW MOSFET is shown in Table II.

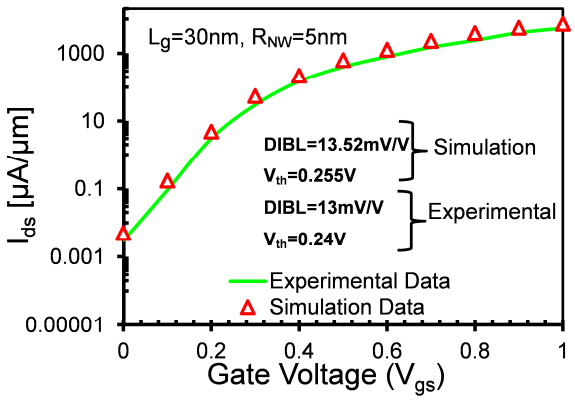


Fig.2: Calibration of simulated models with experimental results with L=30nm, R=5nm and V_d=1.0V.

Table II: Process Flow of GEWE-SiNW MOSFET

P-type SiNWs synthesized by LPCVD with silane as the silicon precursor and gold as the catalyst [21]

↓

SiNWs were oxidized in CVD reactor at 800° C in O_2 atmosphere to obtain uniform SiO_2 shell of t_{ox}=1.5-5nm, wrapping SiNW [22]

↓

Gate, Source and Drain regions with desired lengths are defined by E. beam lithography [23]

↓

S/D regions doped with Arsenic through implantation at a dose of 5×10^{19} cm^{-2}

↓

Deposit Gate Metal 1 by Precise Tilt angle evaporation and Gate Metal 2 by Normal Evaporation [24]

↓

Metal Electrodes deposited using thermal evaporation in ultra-high-vacuum and anneal

↓

GEWE-SiNW is formed and Continue Processing

IV. Results and Discussion

A. Analog Figure of Merits (FOMs)

In this subsection, the effect of dielectric constant and gate metal workfunction engineering are examined in terms of switching ratio, subthreshold slope (SS), device efficiency, channel resistance and output resistance as analog FOMs.

1. Switching Ratio and Device Efficiency

As is evident from Fig. 3(a), on-current is higher in the case of HfO_2 due to lowering of tunneling current owing to higher band-gap and band-offset in comparison to Si_3N_4 and ZrO_2. Consequently, a switching ratio which is an important criterion for any analog application also enhances in HfO_2 due to reduced off-current as indicated by Fig. 3(a). Further, as high-k dielectric increases, the threshold voltage (V_{th}) increases due to a reduction in off-current but subthreshold swing (SS) decreases as shown in Fig, 3(b).

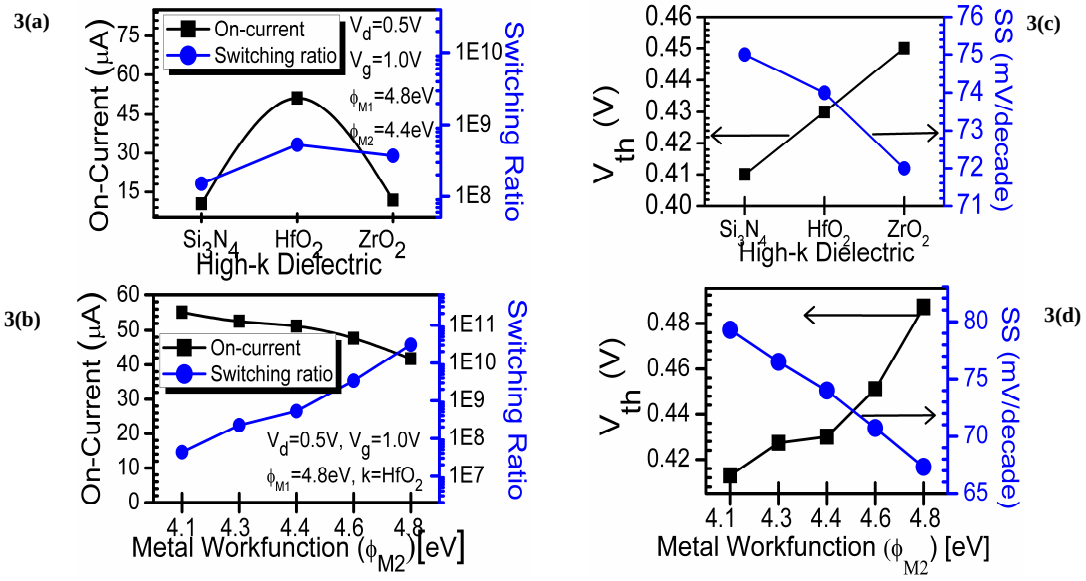


Fig. 3: (a-d) On-Current, switching ratio and Threshold Voltage, Subthreshold Swing for different high-dielectrics and metal gate workfunction (Φ_{M2}) at V_d=0.5V and V_g=1.0V.

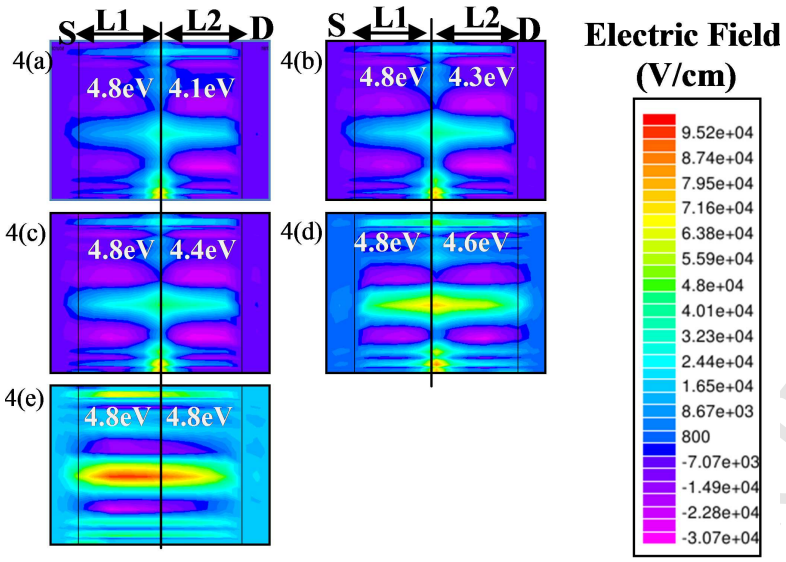


Fig. 4: (a-e) Electric Field Distribution for different metal gate workfunction (Φ_{M2}) at $V_{d;}$=0.5V and V_g=1.0V.

Moreover, the effect of workfunction difference is also examined by considering HfO_2 as a gate-stack and varying the workfunction at the drain end (Φ_{M2}) by keeping source side metal workfunction constant (Φ_{M1}). As gate metal workfunction at the drain end (Φ_{M2}) decreases or workfunction difference increases (ΔW), on-current rises significantly as shown in Fig. 3(b) due to redistribution of the electric field in the channel region owing to step potential due to workfunction difference which enhances carrier transport efficiency and thus current driving capability as is manifest from contour plots shown in the Fig. 4(a-e) and this effect is more apparent if workfunction difference increases as stated in [25], thus, also signifying the suppression of short channel effects. On the contrary, switching ratio reduces with increase in workfunction difference as exhibited in Fig. 3(c). This reduction is due to workfunction engineering scheme in which there is a high electric field in the channel that results into tunneling of carriers and causes higher off-current and thus degrades switching ratio. Hence, the trade-off between on-current and off-current is required to optimize the switching ratio depending upon the applications. Moreover, V_{th} rises with an increase in workfunction at the drain end. As workfunction difference decreases, the efficacy of GEWE scheme reduces and thus reduces the on-current as shown in Fig. 3(c) thereby enhancing threshold voltage as reported in Fig. 3(d). As revealed by Fig. 3(c) that sub-threshold current (off-current) decreases as workfunction difference increases due to which subthreshold swing reduces as demonstrated in Fig. 3(d).

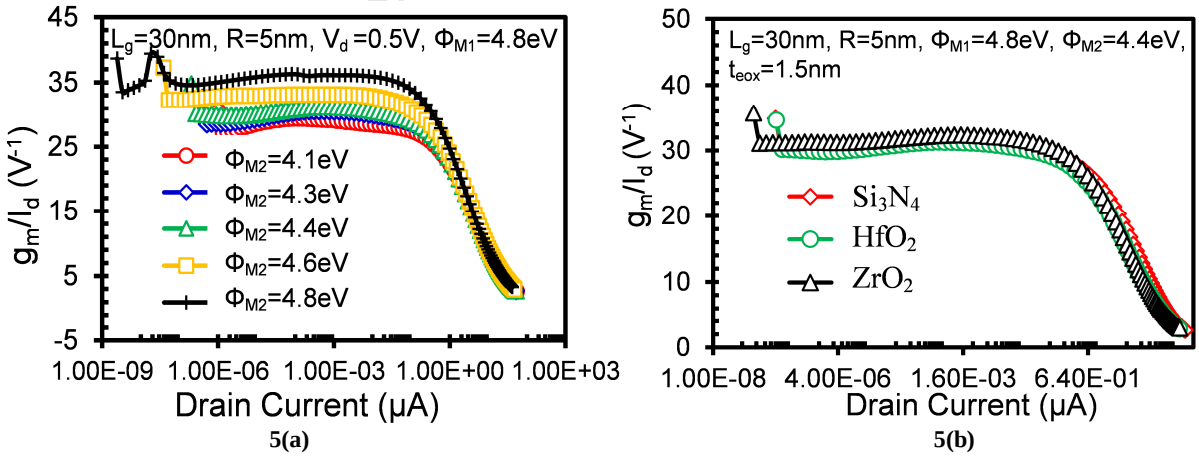


Fig. 5: Device Efficiency as a function of drain current for different high-dielectrics and metal gate workfunction (Φ_{M2}) at V_d=0.5V and V_g=1.0V.

Also, device efficiency [D.E] (g_m/I_d) is an important parameter in the design of analog circuits, which offers the measure of efficiency to convert power into speed. Fig.5 (a) shows the device efficiency as a function of drain current for different high-k materials. It is clearly shown that the variation of D.E occurs mainly at the weak-

inversion region of operation and in the saturation region, device efficiency reduces due to a reduction in transconductance and increment in on-current. The decrease in D.E. with HfO_2 is due to large deviation in drain current as compared to transconductance. Further, with the tuning of workfunction difference of metal gates, D.E. of HfO_2 gate stack increases as revealed by Fig. 5(b) owing to enhanced transconductance with an increase in workfunction difference.

2. Output Resistance and Channel Resistance

The output resistance (R_{out}) of a MOSFET is the inverse of the output conductance. The most important characteristics of R_{out} in the circuit design are maximum R_{out} which decides the maximum available power gain for the device. Fig. 6(a-d) shows that in the linear region (V_d=0-0.2V), R_{out} decreases, and it is desirable when the circuit is to act as an ideal voltage source, and as drain bias reaches to saturation region (V_d=0.4-0.8V) R_{out} rises due to increasing drain current. This effect is more pronounced for HfO_2 in comparison to other high-k dielectrics.

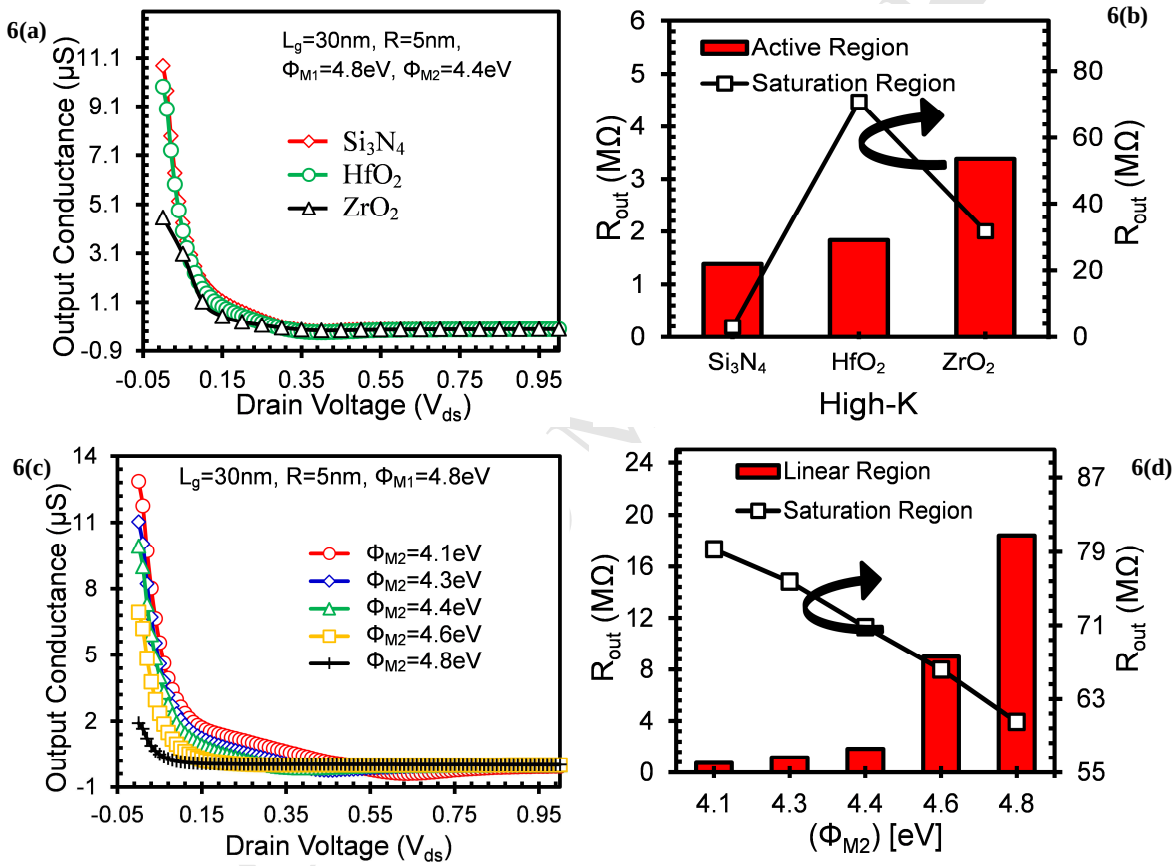
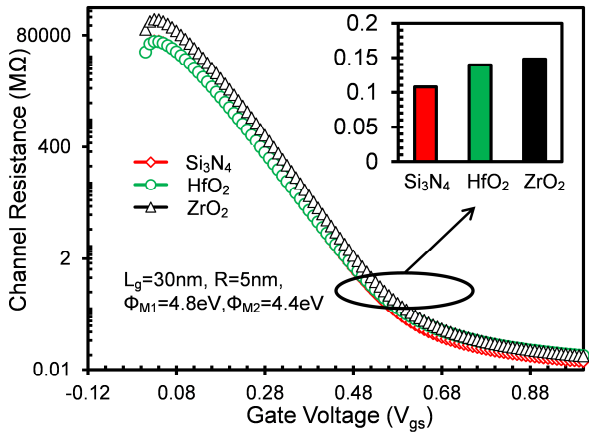
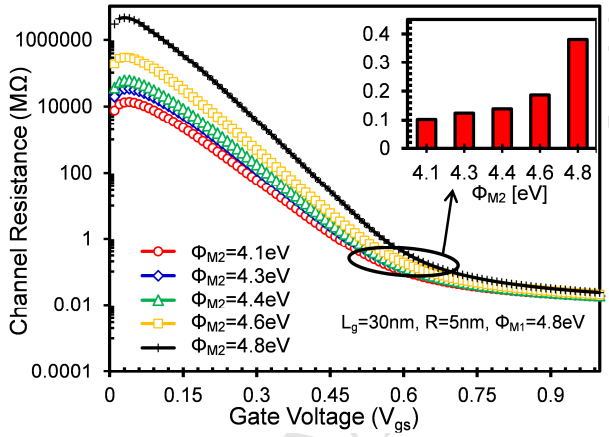


Fig. 6(a-d): Output conductance as a function of drain voltage for different high-dielectrics and metal gate workfunction (Φ_{M2}) at V_g=1.0V

As ΔW increases, output resistance (=1/g_D) reduces in the linear region, and as drain bias increases to saturation, its value increases as evident from Fig. 6(c). Thus, higher ΔW (approx. 0.7eV) of GS-GEWE-SiNW is beneficial for analog applications. Likewise, channel resistance (R_{ch}) of a MOSFET reveals the resistance of carriers in the channel region. As is clearly shown in Fig. 7(a) that with the incorporation of HfO_2 as a high-k layer onto the interfacial layer, R_{ch} decreases and as V_{gs} increases, electrostatic gate control enhances and thus reduces channel resistance. This region is called linear, ohmic or triode region. On the other hand, as workfunction at the drain end increases, carrier concentration decreases in the channel as is evident in contours of Fig. 8(a-e), due to which R_{ch} increases as shown in Fig. 7(b) which implies enhancement in the current driving capability of GS-GEWE-SiNW as ΔW increases. Thus, we have to choose optimum values of both high-k and workfunction difference for improved analog performance.



7(a)



7(b)

Fig. 7(a-b): Channel Resistance as a function of gate voltage for different high-dielectrics at V_d=0.5V.

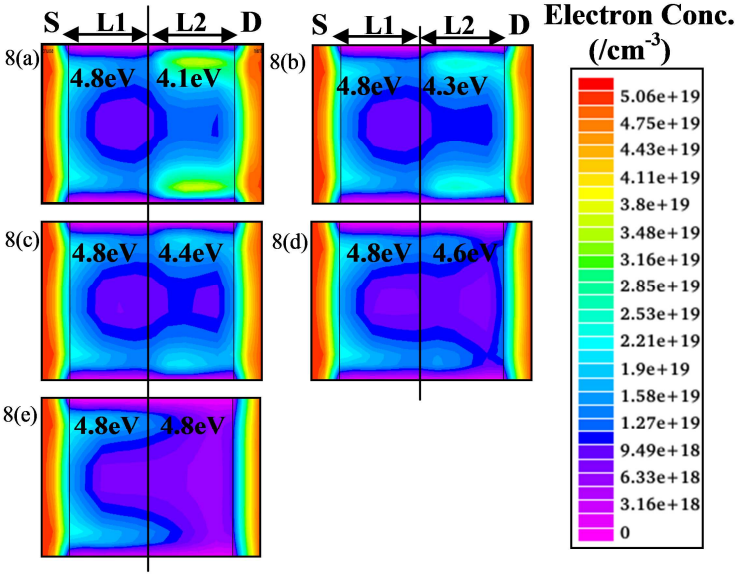


Fig. 8: (a-e) Electron Concentration Distribution for different metal gate workfunction (Φ_{M2}) at V_d=0.5V and V_g=1.0V.

B. Linearity and Harmonic Distortion Analysis

In this sub-section, linearity and distortion performance of GS-GEWE-SiNW MOSFET is investigated with an aim to find optimum high-k and gate workfunction difference for highly linear performance with low harmonic distortion. Non-linearity of MOS amplifiers is mainly from transconductance higher order harmonics (g_{m3}) that may interfere with the fundamental frequency and causes non-linearity. The metrics used in this work to evaluate the device linearity performance and intermodulation distortion are higher order transconductance

coefficients, *VIP3*, third-order input intercept point (IIP3), 1-dB intercept point and distortion such as second and third order harmonic distortion (HD2, HD3), third-order intermodulation distortion (IMD3) [26-27] which are defined as follows:

$$VIP3 = \sqrt{\frac{24 \times g_{m1}}{g_{m3}}} \quad \text{..... (6)}$$

$$IIP3 = \frac{2}{3}\frac{g_{m1}}{g_{m3} \times Rs} \quad \text{.... (7)}$$

$$1-dB\ Compression\ Point = 0.22 \times \sqrt{\frac{g_{m1}}{g_{m3}}} \quad \text{.... (8)}$$

where $g_{m1} = \frac{\partial I_d}{\partial V_{gs}}$, $g_{m3} = \frac{\partial^3 I_d}{\partial V^3{}_{gs}}$ and $R_S = 50\Omega$

g_{m3} is a high-order derivative of I_d-V_{gs} characteristics and their amplitudes should be minimized for lower distortion. The value of V_{GS} at which the higher order of transconductance parameters (g_{m3}) becomes zero is known as zero crossover point (ZCP) which decides the optimum DC bias point for device operation. Higher gain can be realized by setting DC bias point close to V_{th}. Fig. 9(a-b) shows the variation of g_{m3} as a function of gate overdrive voltage (V_{gs}-V_{th}) and the results indicate that incorporation of GS over GEWE-SiNW MOSFET lowers the amplitude of g_{m3} in comparison to GEWE-SiNW due to lowering of tunneling current which improves gate controllability and hence, transconductance and its harmonic distortion.

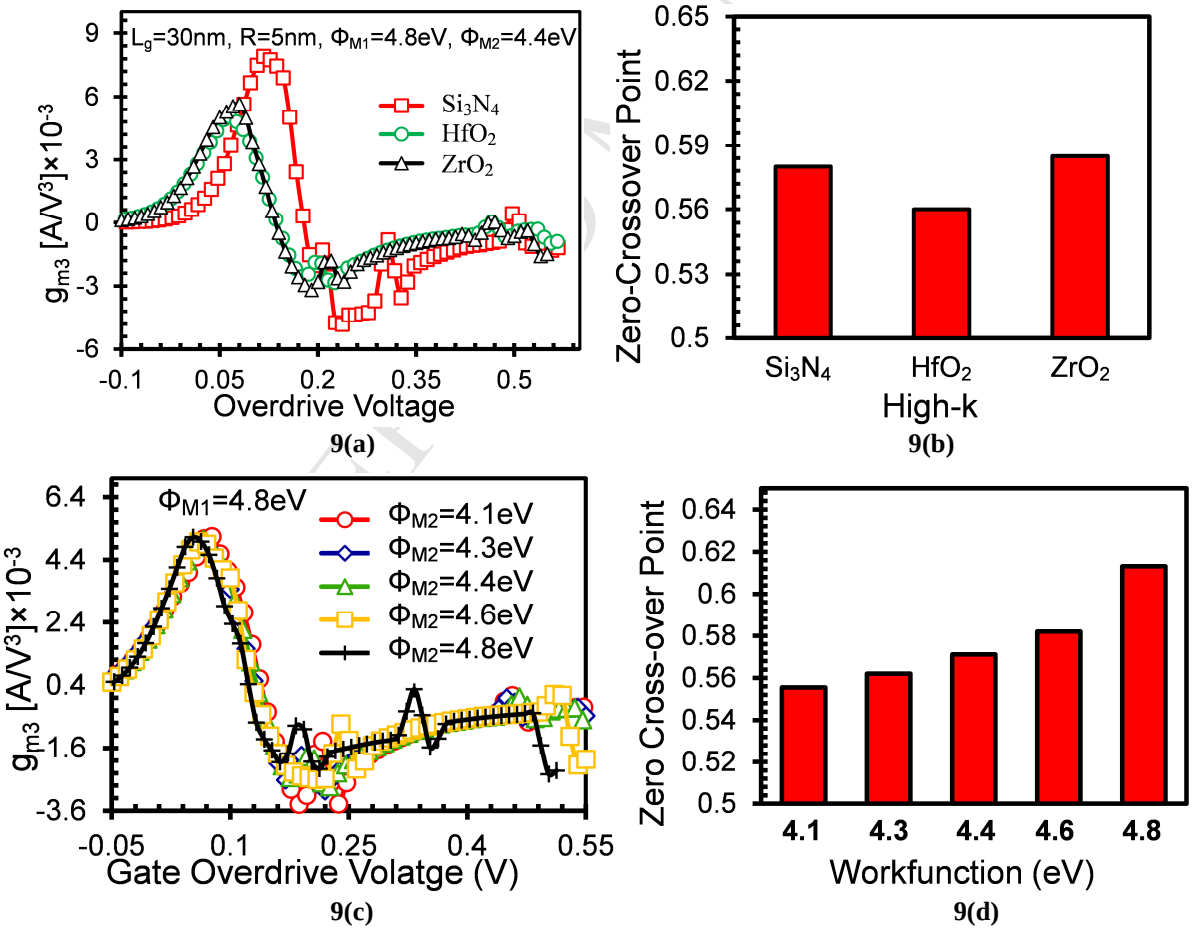


Fig. 9(a-d): Higher order transconductance coefficients g_{m2} and g_{m3}, (c) Zero-Crossover Point for different high-dielectric materials at V_d=0.5V.

Also, the DC bias points shifts towards lower V_{gs} by changing the dielectric constant as shown in Fig. 9(b). Among all dielectrics, HfO_2 shows better improvement in terms of lower distortion (g_{m3}) and lower bias point in comparison to other high-k. With the increase in metal gate workfunction at the drain end (or reduces ΔW), there is not as much change in amplitude of g_{m3} as is evident from Fig. 9(c) due to change in on-current as reflected by Fig. 3(c) but the DC bias point shifts towards lower V_{gs} if ΔW increases as shown in Fig. 9(d).

1. VIP3/IIP3 and 1-dB Compression Point

In all linearity FOMs, generally two peaks are appearing: one at a lower gate bias and maxima at higher gate bias for GS-GEWE-SiNW MOSFET. However, for analog circuit applications, it is desired that device should operate in moderate inversion region and not in the saturation region where power dissipation is more. So, in this analysis, a maximum appearing at a lower value of V_{gs} is considered for comparison. VIP3 represents extrapolated input voltage at which first and third order harmonics of drain current are equal and expressed as in Eq. 1. The peak of VIP3 reveals the cancellation of third-order nonlinearity coefficient by device internal feedback around second-order nonlinearity. Fig 10(a) shows that peak value of VIP3 increases significantly in the case of gate-stack architecture at lower V_{gs}-V_{th} due to lowering of g_{m3} as given by eq.1 and enhancement in transconductance (g_{m1}) owing to high on-current and improvement in carrier mobility. The peak value of VIP3 increases by 34% in HfO_2 in comparison to Si_3N_4 and is observed at lower bias voltage as shown in Fig. 10(a). Moreover, there are two important FOMs which govern amplifier's efficiency and linearity i.e. third-order intercept point (IIP3) and 1-dB compression point (1dB CP). In general for MOS based amplifiers, higher the output at the intercept, the better the linearity. Third-order intercept is a theoretical point at which the third-order distortion signal amplitudes equal the input signals, and it is useful in determining the linearity condition of an amplifier. IIP3 increases to a peak value (i.e. g_{m3}=0) and IIP3 peak enhances with the incorporation of gate stack scheme, and its magnitude is higher in the case of HfO_2 due to high band offset which reduces the off-current, improves transconductance and thus enhances IIP3 as shown in Fig, 10(c).

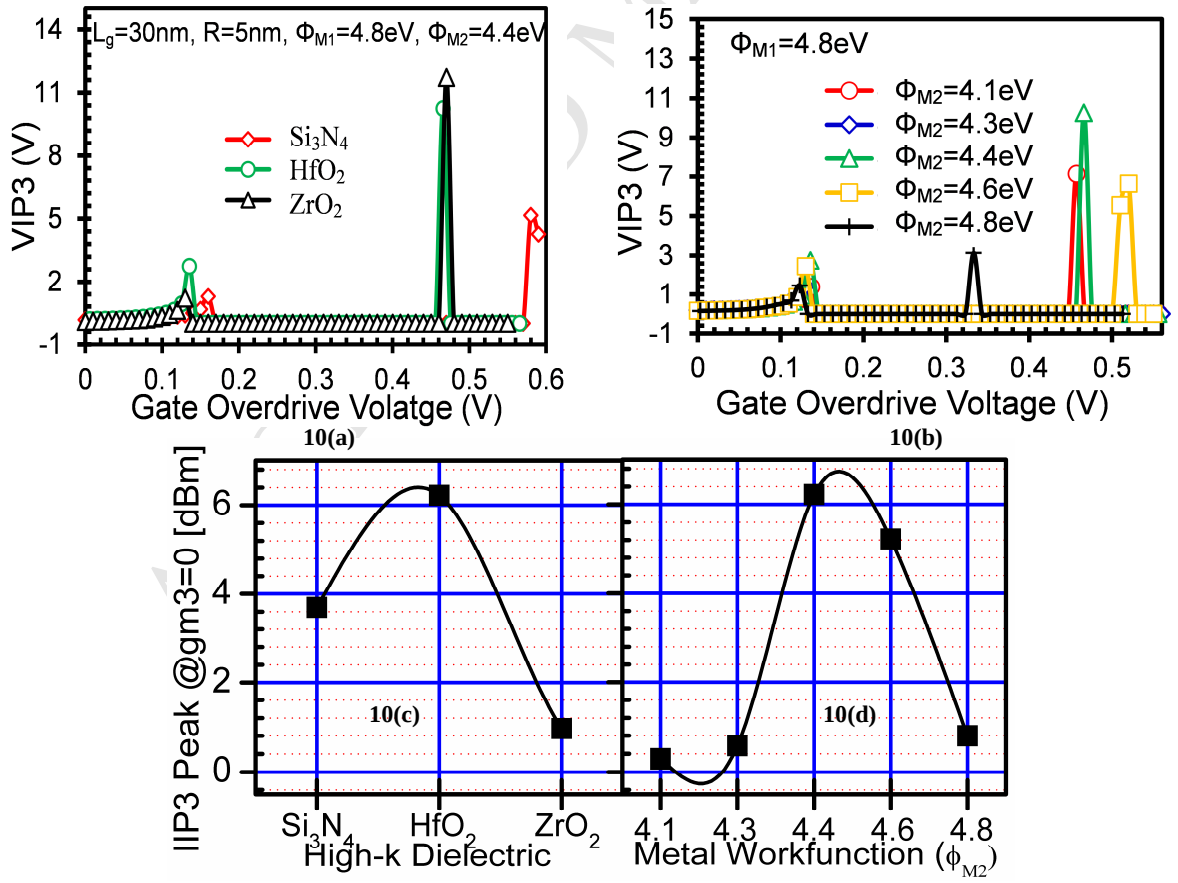


Fig. 10 (a-d): VIP3 as a function of gate overdrive voltage and Peak value of IIP3 for different high-k and gate metal workfunction at the drain end (Φ_{M2}) at V_d=0.5V and V_g=1.0V

The 1-dB compression point is the parameter that describes a circuit's tolerance to desensitization. It is essential to identify at what point compression occurs so that input levels can be limited to prevent distortion. It is usually the input power that causes the gain to decrease 1 dB from the normal linear gain specification. This parameter signifies the maximum input power that the amplifier circuit can handle by providing a fixed amount of gain, and if the input power surpasses the compression point, the gain starts falling. Hence, it is desirable that a 1-dB compression point should be as high as possible for the high linear amplifier. The effect of high-dielectrics on 1-dB compression point is presented in Fig. 11(a). The result shows 1-dB compression point in case of HfO_2 enhances by 1.4 and 2.3 times in comparison to Si_3N_4 and ZrO_2 respectively owing to reduced signal distortions and transconductance as stated in Eq. 4. Moreover, by modulating ΔW, linearity improves appreciably in terms of high VIP3, IIP3 and 1-dB CP peak in comparison to other cases due to a reduction in higher order harmonics and improvement in on-current as evident from Fig.10 (b), 10(c) and 11(b).

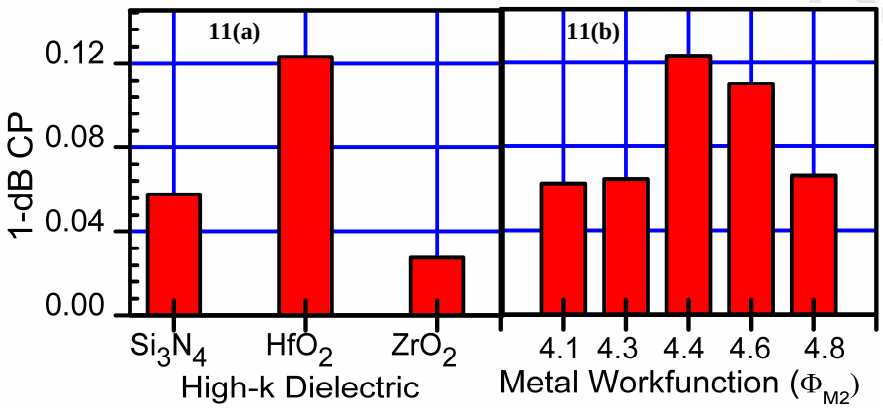


Fig. 11 (a-b): 1-dB Compression Point for different high-dielectrics and metal gate workfunction (Φ_{M2}) at V_d=0.5V and V_g=1.0V

2. Harmonic Distortions

Harmonic distortion (HD) is an essential reliability issue in analog and RF circuit applications that arises owing to the non-linear performance of devices. Nonlinearity may induce intermodulation (IM), which generate signals with frequencies different from the input ones. These unwanted signals may fall into the band of interest, interfering or even corrupting the desired components [28]. Therefore, improved linearity performance of GEWE-SiNW MOSFET with HfO_2 as a gate stack is observed in the previous sub-section. In the following sub-section, Harmonic Distortion FOMs such as 2nd order HD (HD2), 3rd Order HD (HD3) and 3rd Order Intermodulation Distortion (IMD3) for the device are analyzed considering the effect of the gate stack and workfunction engineering. The distortion has been calculated through the integral function method (IFM) since this approach permits the distortion extraction from DC measurements without the need of an AC characterization, contrary to Fourier-based methods [29-30]. The approximate analytical expressions for HD2, HD3 and IMD3 are given as:

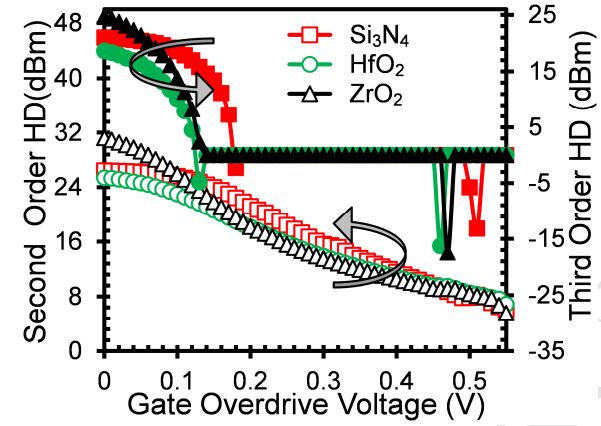
$$HD2 = 0.5V_a \frac{\left(\frac{dg_{m1}}{dV_{GT}}\right)}{2g_{m1}} \quad \text{.... (9)}$$

$$HD3 = 0.25V_a^2 \frac{\left(\frac{d^2 g_{m1}}{dV^2{}_{GT}}\right)}{6g_{m1}} \quad \text{.... (10)}$$

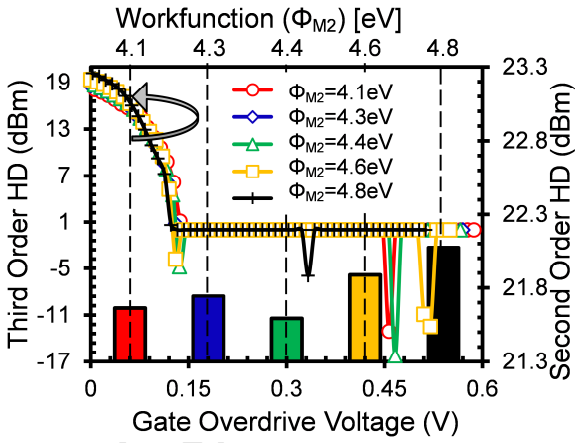
$$IMD3 = \left(\frac{9}{2} \times (VIP3)^3 \times g_{m3}\right)^2 \times R_S \quad \text{.... (11)}$$

Where V_a is the amplitude of AC signal and considered to be very small, of about 50mV for the IFM analysis. Fig.12 (a) shows HD2 and HD3 as a function of gate overdrive voltage for GEWE-SiNW incorporating different high-k as a gate stack. It is observed that HD2 and HD3 are significantly reduced in HfO_2 at lower V_{GT} in comparison to other high-k materials. This reduction is due to higher transconductance owing to high on-current

and is in accordance with Eq. 4 and 5. IMD3 denotes the intermodulation harmonic power at which the first and third order intermodulation harmonic powers are equal. IMD3 plays a major role in determining intermodulation distortion in CMOS RF amplifiers, since these applications make use of both phase and amplitude modulation. Therefore, reduction of IMD3 in the RF front-end transceiver parts is of great importance for maximizing overall system performance and minimizing distortions.



12(a)



12(b)

Fig. 12(a-b): 2nd order Harmonic Distortion and 3rd Order Harmonic Distortion as a function of V_{GT} for different high-k and metal gate workfunction (Φ_{M2}) at V_g=1.0V, V_d=0.5V.

Fig 13(a) exhibits that IMD3 reduces with the incorporation of gate-stack design on GEWE-SiNW MOSFET, and this decrement is due to a reduction in higher order harmonics (g_{m3}) which originates from the non-linear transistor's I_d-V_{gs} characteristic according to Eq. 6. Moreover, distortions in GS (HfO_2+SiO_2)-GEWE-SiNW is further reduced by tuning gate metal workfunction as indicated by Fig. 12(b) and 13(b). As ΔW increases, gate controllability improves due to enhancement in carrier velocity which enhances g_{m1} and so from Eq. 4-6 again, it is reflected that HD2, HD3 and IMD3 reduces. Thus, by appropriate selection of high-k material and gate metal workfunction, GS-GEWE-SiNW achieves high linearity with minimum distortion for RF amplifier.

ACCEPTED MANUSCRIPT

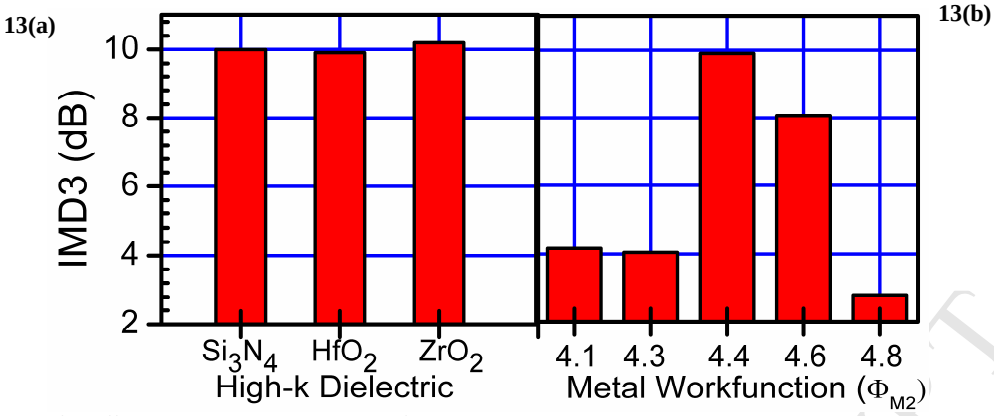


Fig. 13(a-b): IMD3 for different high-k and metal gate workfunction (Φ_{M2}) at V_g=1.0V, V_d=0.5V

V. CONCLUSION

In this work, improved analog and intermodulation performance of GS-GEWE-SiNW MOSFET is demonstrated by considering the effect of both high-k materials and metal gate workfunction difference. It is observed that high-k material (HfO_2) as a gate stack over SiO_2 interfacial layer in GEWE-SiNW significantly influence the analog performance of the device by enhancing the current driving capability and lowering of leakage current owing to large band-gap of HfO_2. Moreover, reduction in the electric field at the drain end and high carrier concentration in the channel region is achieved by tuning of gate workfunction difference which results in improved analog metrics such as switching ratio, channel resistance, device efficiency for low power analog applications. The enhancement in on-current and lowering of g_{m3} results into 2.14 and 2.28 times improvement in VIP3 in comparison to Si_3N_4 and ZrO_2 respectively and the input power rises to 0.128 dB in HfO_2 with ΔW=0.4eV, which the device can handle without compression. It is also examined that the DC bias point is shifted towards lower input voltage which indicates lowering of dynamic power consumption for circuit applications.

ACKNOWLEDGMENT

The authors would like to thank the Microelectronics Research Lab, Department of Engineering Physics, Delhi Technological University (formerly DCE) and one of the authors (Neha Gupta) is grateful to the University Grant Commission (UGC) for providing the necessary financial assistance to carry out this research work.

REFERENCES

[1] R.M. Barsan, “Analysis and Modeling of Dual- Gate MOSFETs”, IEEE Transactions on Electron Devices, Vol. 28, pp. 523-534, 1981.

[2] A. Kumar, N. Gupta and R. Chaujar, “Power gain assessment of ITO-based Transparent Gate Recessed Channel (TGRC) MOSFET for RF/wireless applications”, Superlattices and Microstructures, Vol. 91, pp. 290-301, 2015.

[3] C. P. Auth and J. D. Plummer, “Scaling Theory for Cylindrical, Fully-Depleted, Surrounding-Gate MOSFET’s”, IEEE Electron Device Letters, vol. 18, pp. 74-76, 1997

[4] E. Gnani, A. Marchi, S. Reggiani, M. Rudan and G. Baccarani, “Quantum-mechanical analysis of the electrostatics in silicon-nanowire and carbon nanotube FETs”, Solid-State Electronics, Vol.50, pp. 709-715, 2006.

[5] W. Xu, H. Wong, K. Kakushima and H. Iwai, “Quasi-analytical model of ballistic cylindrical surrounding gate nanowire MOSFET”, Microelectronic engineering, Vol. 138, pp. 111- 117, 2015.

[6] X. Chen and C. M. Tan, “Modeling and analysis of gate-all-around silicon nanowire FET”, Microelectronics Reliability, vol. 54, no. 6-7, pp. 1103-1108, July 2014.

[7] Y. Cui, Z. Zhong, D. Wang, W.U. Wang, C.M. Lieber, “High performance silicon nanowire field effect transistors”, Nano Lett., Vol. 3, pp. 149–152, 2003.

[8] S.H. Lo, D. A. Buchanan, Y. Taur, and W. Wang, “Quantum-Mechanical Modeling of Electron Tunneling Current from the Inversion Layer of Ultra-Thin-Oxide nMOSFET’s,” IEEE Electron Device Letters, vol. 18, no. 5, pp. 209-211, 1997

[9] G. Ribes, J. Mitard, M. Denais, S. Bruyere, F. Monsieur, C. Parthasarathy, E. Vincent, and G. Ghibaudo, “Review on High-k Dielectrics Reliability Issues”, IEEE Transactions on Device and Materials Reliability, Vol. 5 (1), 2005

[10] B.H. Lee, J. Oh, H.H. Tseng, R. Jammy and H. Huff, “Gate stack technology for nanoscale devices”, Materials today, Vol. 9, pp. 32-40, 2006.

ACCEPTED MANUSCRIPT

[11] R. Chau, S. Datta, Member, M. Doczy, B. Doyle, J. Kavalieros, and M. Metz "High-k/Metal–Gate Stack and Its MOSFET Characteristics" IEEE ELECTRON DEVICE LETTERS, Vol. 25, pp. 408-410, 2004.

[12] N. Gupta, A.Kumar and R. Chaujar, "Effect of Dielectric Engineering on Analog and Linearity performance of Gate Electrode Workfunction Engineered (GEWE) Silicon Nanowire MOSFET", Proceedings of the 15th IEEE International Conference on Nanotechnology, pp. 928-931, 2015.

[13] C. Yu, J.S. Yuan, H. Yang, MOSFET linearity performance degradation subject to drain and gate voltage stress, IEEE Trans. Device Mater. Rel. 4 (4) (2004) 681–689.

[14] A. Razavieh, D. B. Janes, and J. Appenzeller, "Transconductance Linearity Analysis of 1-D, Nanowire FETs in the Quantum Capacitance Limit", IEEE Transactions on Electron Devices, Vol. 60, pp. 2071-2076, 2013

[15] C. Hu, "Modern Semiconductor Device for Integrated Circuit", Prentice Hall, pp. 261–274, 2009.

[16] ATLAS User's Manual. SILVACO Int. Santa Clara, CA (2014)

[17] A. Chaudhry and J. N. Roy, "Mosfet Models, Quantum Mechanical Effects and Modeling Approaches: A Review", Journal of Semiconductor Technology and Science, Vol.10: 20-27, 2010.

[18] V. S. Patnaik, A. Gheedia and M.J. Kumar, "3D Simulation of Nanowire FETs using Quantum Models", 2008, http://web.iitd.ac.in/~mamidala/HTMLobj 1227/jul_aug_sep08

[19] G. Iannaccone, G. Curatola and G. Fiori, "Effective Bohm Quantum Potential for device simulators based on drift-diffusion and energy transport", Simulation of Semiconductor Processes and Devices (SISPAD), 275-278, 2004

[20] S. D. Suk et al, "High performance 5 nm radius twin silicon nanowire MOSFET (TSNWFET): fabrication on bulk Si wafer, characteristics, and reliability", IEEE IEDM Tech Digest, pp. 717-720, 2005.

[21] O. Shirak, O. Shtempluck, V. Kotchtakov, G. Bahir and Y. E. Yaish "High performance horizontal gate-all-around silicon nanowire field-effect transistors", Nanotechnology, Vol. 23, pp. 395202 (8pp), 2012.

[22] D. Moon, S-J. Choi, J. P. Duarte and Y-K. Choi, "Investigation of Silicon Nanowire Gate-All-Around Junctionless Transistors Built on a Bulk Substrate", IEEE Trans. Electron Devices, Vol. 60, pp. 1355-1360, 2013.

[23] J-H. Lee, B-S. Kim, S-H. Choi, Y. Jang, S. W. Hwangc and D. Whang, "A facile route to Si nanowire gate-all-around field effect transistors with a steep subthreshold slope", Nanoscale, Vol. 5, pp. 8968–8972, 2013.

[24] W. Long, H. Ou, J. M. Kuo, and K. K. Chin, "Dual-material gate (DMG) field effect transistor," IEEE Trans. Electron Devices, vol. 46, no. 5, pp. 865–870, May 1999.

[25] W. Long and K. K. Chin, "Dual material gate field effect transistor (DMGFET)," in IEDM Tech. Dig., 1997, pp. 549–552.

[26] R. Chaujar, R. Kaur, M. Saxena, M. Gupta, and R. S. Gupta, "Intermodulation distortion and linearity performance assessment of 50-nm gate length L-DUMGAC MOSFET for RFIC design," Superlattices Microstruct., vol. 44, no. 2, pp. 143–152, August 2008.

[27] Ó. Breandán and T. J. Brazil, "An Accurate Nonlinear MOSFET Model for Intermodulation Distortion Analysis," IEEE Microwave and wireless Components Letters, vol. 14, pp. 352–354, 2004.

[28] A. Dutta, K. Koley, and C. K. Sarkar, "Analysis of Harmonic distortion in asymmetric underlap DG-MOSFET with high-k spacer," Microelectron. Reliab., vol. 54, pp. 1125–1132, 2014.

[29] A. Cerdeira, M. A. Alemán, M. Estrada, and D. Flandre, "Integral function method for determination of nonlinear harmonic distortion," Solid. State. Electron., vol. 48, pp. 2225–2234, 2004.

[30] R. T. Doria, A. Cerdeira, J. P. Raskin, D. Flandre, and M. A. Pavanello, "Harmonic distortion analysis of double gate graded-channel MOSFETs operating in saturation," Microelectronics J., vol. 39, pp. 1663–1670, 2008.

ACCEPTED MANUSCRIPT

ACCEPTED MANUSCRIPT

HIGHLIGHTS

1. Optimizes the Gate Engineering Scheme for enhanced Analog and Intermodulation Performance

2. HfO_2 as a gate stack exhibit high linearity at comparatively low gate bias of 0.56V with higher IIP3 (6.21dBm) and low IMD3 (9.6 dBm).

3. It is also observed that the DC bias point shifted towards lower input voltage which indicates lowering of dynamic power consumption for circuit applications.

4. Characteristics/performance of GS-GEWE-SiNW is further improved by modulating the workfunction difference of metal gate (ΔW).

5. SiNW MOSFET modeled with HfO_2 as a gate stack and ΔW of 4.4 eV can be considered as a promising potential for low power switching component in ICs and Linear RF amplifiers.

ACCEPTED MANUSCRIPT

AIP | Journal of Applied Physics

Potential application of mono/bi-layer molybdenum disulfide (MoS2) sheet as an efficient transparent conducting electrode in silicon heterojunction solar cells

Rimjhim Chaudhary, Kamlesh Patel, Ravindra K. Sinha, Sanjeev Kumar, and Pawan K. Tyagi

Citation: Journal of Applied Physics **120**, 013104 (2016); doi: 10.1063/1.4955071
View online: http://dx.doi.org/10.1063/1.4955071
View Table of Contents: http://scitation.aip.org/content/aip/journal/jap/120/1?ver=pdfcov
Published by the AIP Publishing

Articles you may be interested in

Enhanced monolayer MoS2/InP heterostructure solar cells by graphene quantum dots
Appl. Phys. Lett. **108**, 163901 (2016); 10.1063/1.4946856

Gate tunable monolayer MoS2/InP heterostructure solar cells
Appl. Phys. Lett. **107**, 153904 (2015); 10.1063/1.4933294

Multilayer graphene as a transparent conducting electrode in silicon heterojunction solar cells
AIP Advances **5**, 077165 (2015); 10.1063/1.4927545

Transport mechanisms and effective Schottky barrier height of ZnO/a-Si:H and ZnO/μc-Si:H heterojunction solar cells
J. Appl. Phys. **114**, 184505 (2013); 10.1063/1.4831661

Infrared light management in high-efficiency silicon heterojunction and rear-passivated solar cells
J. Appl. Phys. **113**, 013107 (2013); 10.1063/1.4772975



Reuse of AIP Publishing content is subject to the terms at: https://publishing.aip.org/authors/rights-and-permissions. Download to IP: 14.139.251.107 On: Thu, 14 Jul 2016 04:23:19

JOURNAL OF APPLIED PHYSICS **120**, 013104 (2016)

Potential application of mono/bi-layer molybdenum disulfide (MoS_2) sheet as an efficient transparent conducting electrode in silicon heterojunction solar cells

Rimjhim Chaudhary,[1] Kamlesh Patel,[1,2] Ravindra K. Sinha,[1,3] Sanjeev Kumar,[4] and Pawan K. Tyagi[1,a)]
[1]*Department of Applied Physics, Delhi Technological University, Delhi–110042, India*
[2]*Department of Electronic Science, University of Delhi South Campus, Delhi–110021, India*
[3]*Central Scientific Instruments Organisation, Chandigarh–160030, India*
[4]*Department of Physics, Rajiv Gandhi University, Itanagar, Arunachal Pradesh–791112, India*

(Received 10 February 2016; accepted 18 June 2016; published online 7 July 2016)

In this paper, we have simulated the structure of n-type MoS_2/silicon heterojunction solar cell and studied its function under different conditions. The optimization of parameters of the cell's layer has been carried out by using AFORS-HET software. In the present study, MoS_2 has been considered as 3-D in nature instead of the reported 2-D nature. In order to ensure the formation of Schottky junction, electric contact has been made along the c-axis to collect the minority charge carriers. After optimizing the various parameters of n-type single layer MoS_2, power efficiency of 12.44% has been achieved at the room temperature, which has further decreased to 9.042% as the layer number has increased up to 40. Furthermore, after optimizing the parameters of silicon wafer maximum efficiency of 16.4% has been achieved. Temperature dependence of the cell performance has also been studied and the maximum efficiency has been achieved at 300 K. In the present study, we have demonstrated that n-type ultrathin layer of MoS_2 can be used as an excellent transparent conducting electrode. *Published by AIP Publishing.* [http://dx.doi.org/10.1063/1.4955071]

I. INTRODUCTION

The advent of two-dimensional (2-D) graphene, single atomic thick layer of graphite, has stimulated the research interest in other 2-D materials. Transition-metal dichalcogenides (TMDs) are among them. Recently, TMDs have demonstrated a promising material from the perspective of both fundamentals as well as applications.[1] They exhibit unique optoelectronic properties, which can be largely tuned by varying the thickness of the sheet. Recently, layered TMDs have been reported as a novel class of materials, in which minimum d-electron inter layer interactions result in the novel physical characteristics such as valley polarization, bandgap in the visible to near-IR regions and mobility as high as 50 cm^2/V s compared to 20 cm^2/V s as reported in graphene.[2,3]

In recent reports, high mobility as well as low sheet resistance has been confirmed in multilayer graphene and it has been demonstrated as an emerging transparent conducting electrode (TCE) material.[4] However, its main deficiencies for practical applications are low photo responsivity and poor external quantum efficiency (QE), which originate from the zero bandgap and low light absorption coefficient.[5] These disadvantages of graphene can be overcome by using 2-D layered semiconductors, as they posses finite band gap as well as carrier mobility as high as 50 cm^2/V s. Among such semiconductors, molybdenum disulfide (MoS_2) has been reported to posses mobility as high as 200 cm^2/V s in monolayer and ~517 cm^2/V s in few layers[6] with high on/off ratio of 10^8.[7,8] Electronic band gap of 1.2 eV (indirect) in bulk and 1.9 eV (direct) in single layer MoS_2 has also been reported.[1] Besides, it is cheap and has high flexibility with more than 85% optical transparency in visible region for double layer.[9] Recently, it was reported that work function of MoS_2 depends upon layer numbers.[10,11] Its unique layered design structure has an inherent advantage of forming smooth surface, thus enabling the design of highly efficient Schottky-barrier solar cells. Theoretically, Carvalho and Neto have reported that it is possible to dope MoS_2 with electrons or holes by chemical substitution at the S site or adsorption on the top of the layer.[12] In further advances, Laskar *et al.*, have reported that Niobium can make MoS_2 p-type with high hole density of 4×10^{20} cm^{-3} and Hall mobility of 8.5 cm^2 V^{-1} s^{-1} as determined in few layer films of MoS_2.[13] Du *et al.*, have reported that molecular doping with polyethyleneimne (PEI) made the MoS_2 film strong n-type and sheet resistance was lowered to 7.65 ± 1.81 Ω/sq.[14] These properties discussed above ensure that MoS_2 can be utilized as a new TCE material in MoS_2/silicon heterojunction solar cells. However, till date application of MoS_2 in solar cells did not draw much interest. There are a few recent reports on the application of MoS_2 in organic solar cells as well as heterojunction solar cell, where it acts as an excellent hole extraction layer. The power conversion efficiency of organic solar cells was reported to be typically 7%–8%.[1,9,15,16] It has been demonstrated that semiconductor MoS_2 with metallic contact formed Schottky barrier.[17] Shanmugan *et al.*, have demonstrated that photo-conversion efficiency of 1.8% was achieved in ITO/MoS_2/Au for ~220 nm thick MoS_2 layer.[6] In further advances, WS_2/MoS_2

a)Electronic addresses: pawan.phy@dce.edu and pawankumartyagi@gmail.com

Reuse of AIP Publishing content is subject to the terms at: https://publishing.aip.org/authors/rights-and-permissions. Download to IP: 14.139.251.107 On: Thu, 14 Jul 2016 04:23:19

and MoS_2/graphene monolayer based solar cells were reported to be the thinnest solar cell device with power efficiency of only 1.5% and 1.0%, respectively.[18,19] In recent reports, it has been reported that if high quality monolayer of MoS_2 forms a heterojunction with p-cSi then an efficiency of up to 5.23% (Ref. 17) and 4.25% (Ref. 20) can be achieved.

For developing an effective heterojunction cell, optimization of both MoS_2 layer as well as silicon is required. Hence, in this report, we have simulated the n-MoS_2/p-silicon structure under air mass 1.5 (AM1.5) illuminations withpower density of 100 mW/cm^2 using AFORS-HET (Automat FOR Simulation of HETero-structures) software version 2.4.1.[21,22] This software uses 1-D semiconductor equations related to Shockley–Reed–Hall statistics solver and Lambert–Beer law based optical model to obtain the optimized parameters. The n-type MoS_2 film, presumed to be 3-D in nature, has been taken as cathode and the parameters of both MoS_2 and crystalline silicon (c-Si) layers have been optimized in order to achieve highest efficiency of MoS_2/silicon heterojunction cell. The aim of the present simulation is to study the independent effects of the variation of layer's parameter on the performance of the given cell/structure and to discuss the observations made behind the cell responses.

II. SIMULATION STRUCTURE

Mobility higher than other semiconductors has motivated us to use MoS_2 as a transparent conducting electrode in the heterojunction solar cell. To explain the carrier transport in MoS_2, drift and diffusion model was developed, in which the differential transport equation for electrons and holes was considered to be 2-D in nature with carrier densities given in cm^{-2} and current densities in A/cm.[23] At multilayer or single layer MoS_2/silicon interface, 2-D equations were coupled with 3-D equations to represent the transport and boundary conditions at the interface. In the proposed device structure, ITO is taken as a transparent conducting oxide (ITO) and configured as ITO/n- MoS_2/p-cSi/Ag as shown in Figure 1. In the proposed structure, the transport of minority charge carriers was taken along the c-axis. Diffusion-drift solver and Metal-Schottky junction were used in AFORS-HET software to describe the model of MoS_2/Si heterojunction solar cell. Furthermore, SiO_2 layer was introduced to ensure the transport through MoS_2 layer only by insulating the carrier transport through TCO from p-cSi wafer. Since Fermi energy of 2 D system is given by the relation $E_F = \frac{\hbar^2 n}{2 m_e^* e^2}$, where $m_e = 0.35\ m_0$, m_0 is the electron mass and n is the sheet carrier density in cm^{-2}. Thus, the relation for Fermi wavelength ($\lambda_F = \frac{h}{\sqrt{2 m_e^* E_F}}$) can be modified to $\lambda_F = \frac{2\times 10^7 \sqrt{\pi}}{\sqrt{n}}$. Suh *et al.* have reported that by doping with Nb, sheet carrier density of 1.8×10^{14} cm^{-2}, corresponding to a bulk concentration 3.0×10^{19} cm^{-3}, was achieved.[24] So, if n approaches to $\sim 2 \times 10^{14}$ cm^{-2}, then λ_F would be $\approx$2.11 nm. It can be assumed, if doping in MoS_2 layer further improved then even bilayer MoS_2 cannot satisfy the condition $\langle t \rangle \leq \lambda_F$, where $\langle t \rangle$ is the average thickness for a 2-D electron system. Furthermore, n-type doping in MoS_2 can be achieved either by chemical or molecular doping. At the doping site, effective thickness of the layer changes.[25] It may happen because, depending on the atomic size, dopants tend to locally increase the lattice constant and further reduce the coupling between the layers as reported in graphene.[26] In addition, some defects are introduced because of the doping that increases the interlayer spacing.[27] Hence, it is justified here to consider MoS_2 as quasi 3-D in nature.

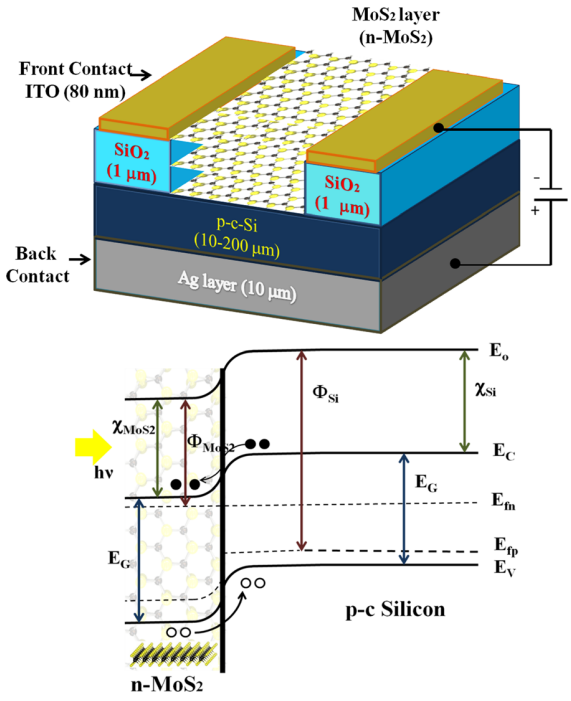


FIG. 1. MoS_2/silicon heterojunction solar cell. (a) Schematic diagram of configuration used in simulation. (b) Schematic band diagram of a forward biased junction, where Φ_{MoS_2},Φ_{Si}, and χ_{Si} are the MoS_2 work function, silicon work function, and the silicon electron affinity, respectively.

The details about the front and back contacts of the simulated cell have been given in Table I, and the values as well as the range of the parameters of MoS_2 and silicon have been tabulated in Table II.[9,11,28–34] Simulated parameters selected the optimization of MoS_2 layer were donor concentration (N_D), bandgap (E_g), effective conduction and valance band densities (N_C/N_V), electron affinity (χ), relative permittivity (ε_r), and electron mobility (μ_n). The initial simulation was started considering single atomic thick layer of MoS_2. Thickness of layer was taken as $\sim$0.65 nm.[17] Other parameters were varied accordingly and then the variation of open circuit voltage (V_{OC}), short circuit current (J_{SC}), fill factor (FF), and quantum efficiency (η) were plotted with the respective parameters. The simulation with optimized cell

TABLE I. Details of the parameters of the cell contacts used in simulation.

Contact parameters	Front contact	Back contact
Width (m)	8×10^{-8}	1×10^{-4}
File	ITO.nk	Ag.nk
Metal work function	Yes (flatband)	Yes (flatband)
Absorption loss	ITO.abs	0
External reflection constant	aSicSi_ITO.ref	0
Surface condition	Plane	Plane
Internal reflection constant	0	0

Reuse of AIP Publishing content is subject to the terms at: https://publishing.aip.org/authors/rights-and-permissions. Download to IP: 14.139.251.107 On: Thu, 14 Jul 2016 04:23:19

TABLE II. Simulation parameters and their ranges taken for the simulation of the proposed cell structure.

Input parameters	n-MoS_2	p-cSi
Relative permittivity, ε_r	2–15	11.9
Electron mobility, μ_n (m^2/V s)	5×10^{-6}–2×10^{-2}	0.1350
Hole mobility, μ_p (m^2/V s)	8.5×10^{-4}	4.5×10^{-2}
Electron affinity(χ)	3.8 – 4.8	3.2 – 4.4
Band gap, E_g (eV)	1.9 – 2.1	1.12
Acceptor concentration N_A (m^{-3})	0	3×10^{18}–2×10^{23}
Donor concentration N_D (m^{-3})	1×10^{12}–1×10^{24}	0
Effective conduction band density, N_c (m^{-3})	3×10^{20}–3×10^{32}	3×10^{25} – 3×10^{31}
Effective valance band density, N_v (m^{-3})	3×10^{20}–3×10^{32}	3×10^{25} – 3×10^{31}
Thermal velocity of electrons (ms^{-1})	1×10^5	1×10^5
Thermal velocity of holes (ms^{-1})	1×10^5	1×10^5
Layer density (kg m^{-1})	0.2328	0.2328
Thickness (m)	6.65×10^{-10}–2.66×10^{-8}	1×10^{-5}–3×10^{-4}
Mid bandgap density of states ($m^{-3}eV^{-1}$)	…	Single acceptor
Switch-over energy (eV)	…	0.56
Auger recombination coefficient for electron (m^6 s^{-1})	0	0
Auger recombination coefficient for hole (m^6 s^{-1})	0	0
Direct band-to-band recombination coefficient (m^3 s^{-1})	0	0

parameters was extended to multilayer MoS_2 sheet to view the effect of thickness on the cell results. Subsequently, after optimizing MoS_2 layer thickness, the optimization of p-cSi layer was done for achieving the highest efficiency. Parameters considered for optimizing p-cSi layer were acceptor concentration (N_A), effective conduction and valance band densities (N_C/N_V), and the electron affinity (χ) and thickness. The values of relative permittivity (ε_r), electron mobility (μ_n), and bandgap (E_g) were kept fixed as found in previous literatures.[32–34] Finally, the highest efficiency in MoS_2/cSi heterojunction cell was achieved after optimizing the parameters of both n-MoS_2 and p-cSi layers.

III. RESULTS AND DISCUSSION

A. Simulation and optimization of n-MoS_2 layer

In MoS_2/Si heterojunction solar cells, formation of Schottky junction is a prerequisite. In the proposed structure, a built in voltage (V_{BI}) was developed at the MoS_2/Si interface which was generated due to recombination of majority charge carriers, i.e., electrons and holes in n-MoS_2 and p-cSi layers, respectively. This voltage (V_{BI}) facilitated the separation of the minority charge carriers, i.e., electrons in p-cSi wafer moved towards the MoS_2 layer and caused the energy levels to bend downward at the interface. The built in voltage (V_{BI}) is the difference of the barrier height (Φ_{BI}) and the energy gap in silicon. The barrier height (Φ_{BI}) is defined as per the following equations:

$$\Phi_{BI} = \Phi_{MoS_2} - \Phi_{Si} = \chi_{MoS_2} + kT\ln\left(\frac{N_C}{N_D}\right) - \chi_{Si} - kT\ln\left(\frac{N_A}{N_V}\right), \quad (1)$$

where Φ_{MoS_2}, χ_{MoS_2}, Φ_{Si}, and χ_{Si} are the work function and affinity of MoS_2, and work function and affinity of the silicon, respectively. N_D and N_C are the donor ion doping concentration and effective conduction band density of MoS_2, whereas N_A and N_V are acceptor ion doping concentration and the effective valence band density of the p-cSi.

As the device was illuminated, the generated electron and hole (e-h) pairs were separated due to the built in voltage (V_{BI}) at the interface. These newly generated free minority charge carriers in both the regions moved towards the opposite polarities, i.e., electrons to p-cSi region and holes to n-MoS_2 region, as shown in Figure 1(b). As the carrier density became higher in the respective regions, these separated photo-generated carriers developed an open circuit voltage when cell is open circuited,[17,35] whereas when it is short-circuited, the excess carriers were collected at the electrodes, creating a short circuited current that flows in the external circuit.

In this work, first optimization of donor concentration (N_D) of MoS_2 layer was carried out while keeping other parameters to some relevant values that were reported in literature as mentioned in panels 2(a)–2(d).[9,29,31] As it has been reported, efficient electron injection was possible even if work function of the MoS_2 electrodes was reduced. As the doping with $NaBH_4$ was increased, Φ_{MoS_2} was reported to decrease from 4.36 eV to 3.45 eV and this lifted-up the Fermi level towards conduction band,[9] thus reducing the barrier height. The barrier to forward current flow was reported as small as 0.3 eV in some Si Schottky diodes.[36] Hence, as N_D was increased, the conductivity of the MoS_2 layer was reported to increase and the short-circuited current density was enhanced a little from 25.34 mA/cm^2 to 25.42 mA/cm^2. Results are shown in Figures 2(a)–2(d). The carrier accumulation became higher in n-MoS_2 with increasing value of N_D. As a consequence, photo-generated electrons easily moved to p-cSi layer from the MoS_2 layer. This process effectively increased V_{OC} to 616.4 mV. In turn, the efficiency (η) and fill factor (FF) improved. However, J_{SC} started exponentially decreasing as N_D was increased above 10^{14} cm^{-3}. Increase in FF was also observed. This might have happened due to lowering of the

Reuse of AIP Publishing content is subject to the terms at: https://publishing.aip.org/authors/rights-and-permissions. Download to IP: 14.139.251.107 On: Thu, 14 Jul 2016 04:23:19

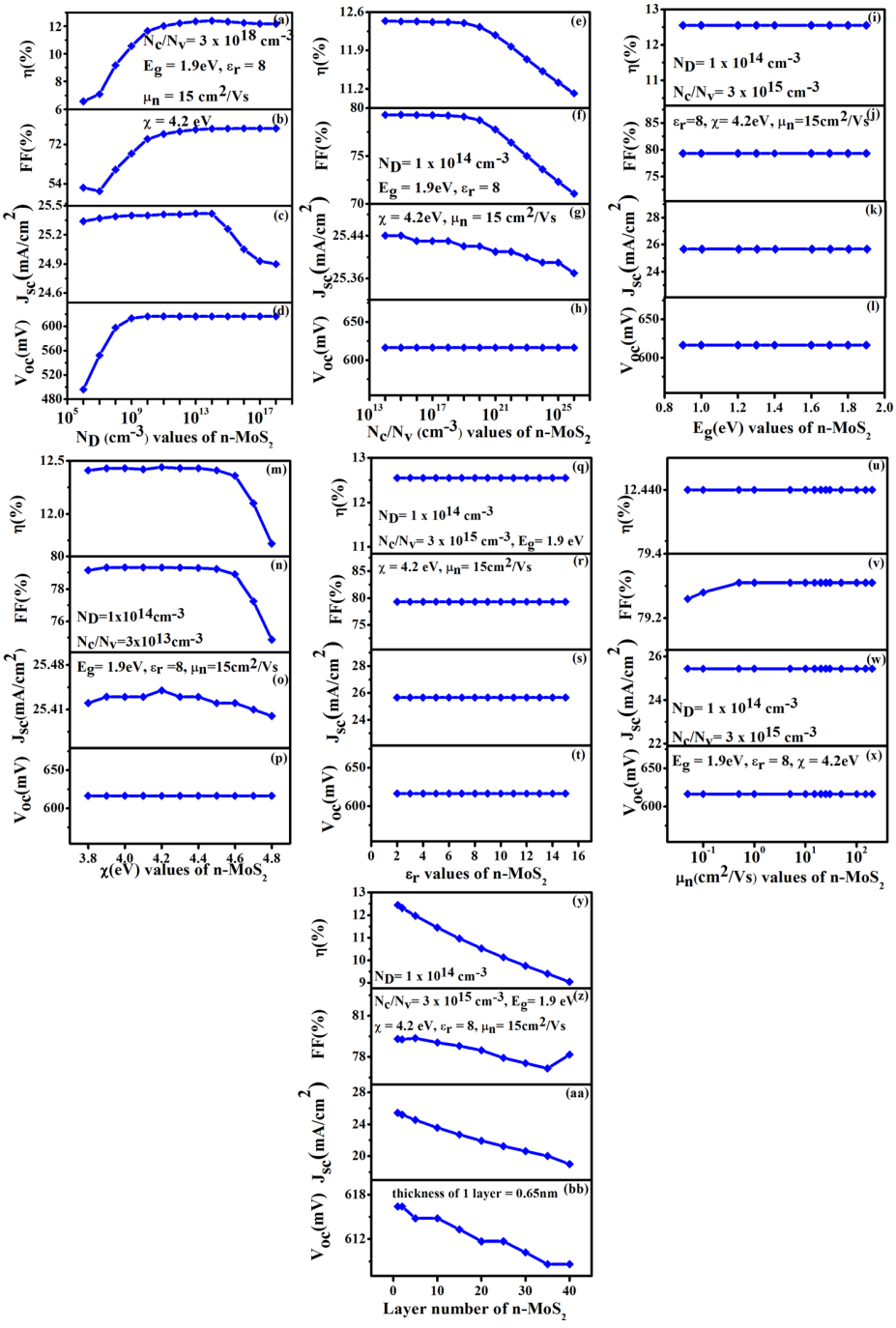


FIG. 2. The optimization of the parameters of n-MoS_2 layer with: (a)–(d) the donor concentration N_D (cm^{-3}); (e)–(h) the effective density of states N_C/N_V (cm^{-3}); (i)–(l) the bandgap energy E_g (eV); (m)–(p) the electron affinity χ (eV); (q)–(t) the relative permittivity ε_r; (u)–(x) the electron mobility μ_n (cm^2/V s); and (y)–(bb) layer number. The parameters of p-cSi were the acceptor ion concentration $N_A = 1 \times 10^{16}\,cm^{-3}$; the effective density of states $N_C/N_V = 3 \times 10^{19}\,cm^{-3}$; the electron affinity $\chi = 4.0$ eV; and thickness 100 μm.

sheet resistance of MoS_2, which is inversely proportional to the carrier density in MoS_2.[14] Of course, in photovoltaic, it is highly desirable to maximize the electron mobility of TCE instead of carrier concentration. The mobility is given by relation $\mu = \frac{e\tau}{m^*}$ and depends on both the effective mass of electron and the relaxation time. For 2-D materials, electron mobility and relaxation time are mostly dominated by charged impurity scattering, phonon scattering only contributes at higher temperature.[37] So, as the carrier concentration increases mobility first increases and then decreases. This may also affect the J_{SC} at high doping concentration. The maximum value of η was found to be 12.4% at $N_D \sim 10^{14}\,cm^{-3}$, and then small decrement was observed. Work function of MoS_2 (Φ_{MoS_2}) has been reported to reduce as doping concentration increases.[9] This reduction resulted in a drop in the value of J_{SC} due to reduction in the tunneling probability of carriers and increase in electron-hole recombination in p-cSi wafer.

After optimizing N_D to $10^{14}\,cm^{-3}$, we observed that as N_C/N_V was increased, J_{SC} started decreasing. This might have happened due to an increase in the recombination rate in both the layers,[32] which led to trimming of the minority carrier density, as a result sheet resistance of the cell increases.[9] It was observed that V_{OC} remains constant as shown in Figure 2(h), whereas FF was found to be constant at the lower values of N_C/N_V and reduced linearly after $3 \times 10^{17}\,cm^{-3}$. This reduction in both J_{SC} and FF resulted in a significant decrement in efficiency from 12.44% to 11.12%

Reuse of AIP Publishing content is subject to the terms at: https://publishing.aip.org/authors/rights-and-permissions. Download to IP: 14.139.251.107 On: Thu, 14 Jul 2016 04:23:19

to at $3 \times 10^{25}\,cm^{-3}$. The maximum η of 12.44% was obtained at $N_C/N_V \sim 3 \times 10^{15}\,cm^{-3}$.

We found that other parameters of MoS_2, namely, the bandgap energy (E_g), the relative permittivity (ε_r) and the electron mobility (μ_n) did not seem to contribute to the efficiency in their simulation ranges and the cell parameters were found to be constant. We have taken feasible values reported in the previous literatures[29,31] and simulated the cell. We found that η of 12.44% was constant as shown in Figures 2(i)–2(l), 2(q)–2(t), and 2(u)–2(x).

Recently, it was demonstrated that Fermi level in 2-D material can be manipulated by the doping or decoration by nanoparticles.[38–41] This can manipulate the work function as well as carrier concentration. In simulation, Fermi level and work function manipulation was taken into account as described by Equation (1). As χ was increased, efficiency remained constant up to 4.6 eV and then dramatically reduced as shown in Figure 2(m). V_{OC} remained unaffected with change in χ value. This can be attributed to the fact that the change in electron affinity does not affect work function. Thus, V_{BI} remained constant resulting in constant V_{OC}. With increasing χ, the conduction band lowered down making faster carrier transport across the interface and eventually no free carriers were available. As a result, J_{SC} and FF decreased causing overall η to decrease. We observed that as χ_{MoS_2} increased, Fermi level started pinning to conduction band.

After optimizing the parameters of single layer MoS_2, we have extended the simulation of the cell up to 40 layers of MoS_2. As layer numbers can control the transmittance of the MoS_2, with increase in the layer numbers, optical transmittance reduces.[42,43] This was later observed from Figure 4, that for higher layer numbers all the three parameters, internal quantum efficiency (IQE), external quantum efficiency (EQE), and spectral response (SR) were observed to decrease compared to single layer. The spectral response was lower in the region of 400–900 nm for 40 layers of MoS_2 than single layer, thus, giving the evidence of lower absorption of photons causing reduction of optical transmittance with the layer numbers. In addition, the electron-hole pair generation rate was observed to decrease as layer number increases, thus, almost linearly decreasing the efficiency from 12.44% to 9.042%. Similarly, J_{SC}, V_{OC}, and FF were also found to decrease. Hence, we can conclude that the number of layers of MoS_2 is playing an active role in the photo-carrier generation. This happened due to the reduction of optical transparency and subsequent carrier generation rate.

B. Optimization and simulation of p-cSi wafer

After optimization of the MoS_2 parameters, further simulation was carried out to optimize the parameters of p-cSi layer. As acceptor concentration (N_A) increases from $10^{12}\,cm^{-3}$, Φ_{Si} decreases (Equation (1)). Reduced Φ_{Si} led to linear increase in V_{OC}. Further reduction in the depletion region also improved V_{BI}, which facilitated the fast separation of photo-generated carriers. Thus, J_{SC} should improve. However, J_{SC} was found to be decreasing as N_A was increased. This can be attributed to an increase in recombination rate which might have been caused by scattering with ionized impurities and carrier-carrier scattering in a p-cSi layer.[32] Beyond $N_A = 10^{15}\,cm^{-3}$, electron-hole pairs generation rate was observed to increase and result in improved J_{SC} as shown in Figure 3(g). The collective response of V_{OC}, J_{SC} and FF, enhanced the efficiency to 16.4% at $N_A = 2 \times 10^{17}\,cm^{-3}$. From the band diagram of MoS_2/Si interface, we can observe that as acceptor concentration increases, Fermi level was found to be approaching towards conduction band, thus making transfer of electrons from valence band to conduction band easier. This resulted in the increase in efficiency. In this work, we have not discussed heavier N_A values (e.g., $1 \times 10^{18}\,cm^{-3}$). Recently, Zhong *et al.*, by using AFORS-HET, have also reported that as N_A increases, Fermi level starts pinning in the conduction band.[32] As a result, Fermi energy value increases beyond lowest level of conduction band thereby defying the Fermi–Dirac statistics that needs further consideration, which has not been incorporated into the software yet.

After optimizing N_A to $2 \times 10^{17}\,cm^{-3}$, simulation was performed to optimize N_C/N_V in the range of 3×10^{19} to $3 \times 10^{25}\,cm^{-3}$. Results are shown in Figures 3(e)–3(h). As N_C/N_V was increased, efficiency was observed to linearly deteriorate and the highest value of $\eta \sim 16.4\%$ was obtained at $3 \times 10^{19}\,cm^{-3}$. The observed carrier recombination rate at the interface and inside the wafer caused a little current flow in the cell, thus decreasing J_{SC}.[4] The trapping of free charge carrier inside p-cSi layer, further resulted in drop of V_{OC} and FF values of the cell. The efficiency dropped to zero at N_C/N_V value of $3 \times 10^{25}\,cm^{-3}$.

The electron affinity (χ) is responsible for the carrier transport at interface on both sides of the silicon wafer. The value of V_{OC} did not change with the increase in the electron affinity of p-cSi wafer from 3.2 eV to 4.5 eV, as shown in Figure 3(l). Again, this can be understood by Equation (1), work function (Φ) does not change with χ and remains constant. This made V_{OC} constant. However, the values of η and FF increased linearly in the range from 3.2 eV to 3.6 eV, and then became constant at $\chi = 3.6$ eV as shown in Figures 3(i)–3(k). This can be attributed to the change in χ, which resulted in the change of position of the bottom edge of the conduction band, as can be seen from Figure 1. So, χ increased minima of conduction band moved downward. This might have facilitated electron-hole pair generation and caused J_{SC} and FF to increase, while increasing the overall efficiency.

To study the effect of wafer thickness of p-cSi, we have started the simulation with 10 μm thick p-cSi wafer and then increased the thickness up to 300 μm. Spectral response of the cell for both thin and thick p-cSi wafers was studied. It was found that as thickness of wafer increased, more photon of longer wavelength of the illumination get absorbed, which in turn resulted in more electron-hole pair generation. Besides, for thin layer of wafer, the back contact will be closer to the depletion region and results in the capture of electrons at the back contact.[44] Thus, as thickness increased, both J_{SC} and V_{OC} improved. For thick wafer, V_{OC} almost saturated. We observed that first FF decreased up to 250 μm and then increased. Increment of about 6% was observed when thickness was increased from 250 μm to 300 μm. Finally, after optimization the parameters of both single

Reuse of AIP Publishing content is subject to the terms at: https://publishing.aip.org/authors/rights-and-permissions. Download to IP: 14.139.251.107 On: Thu, 14 Jul 2016 04:23:19

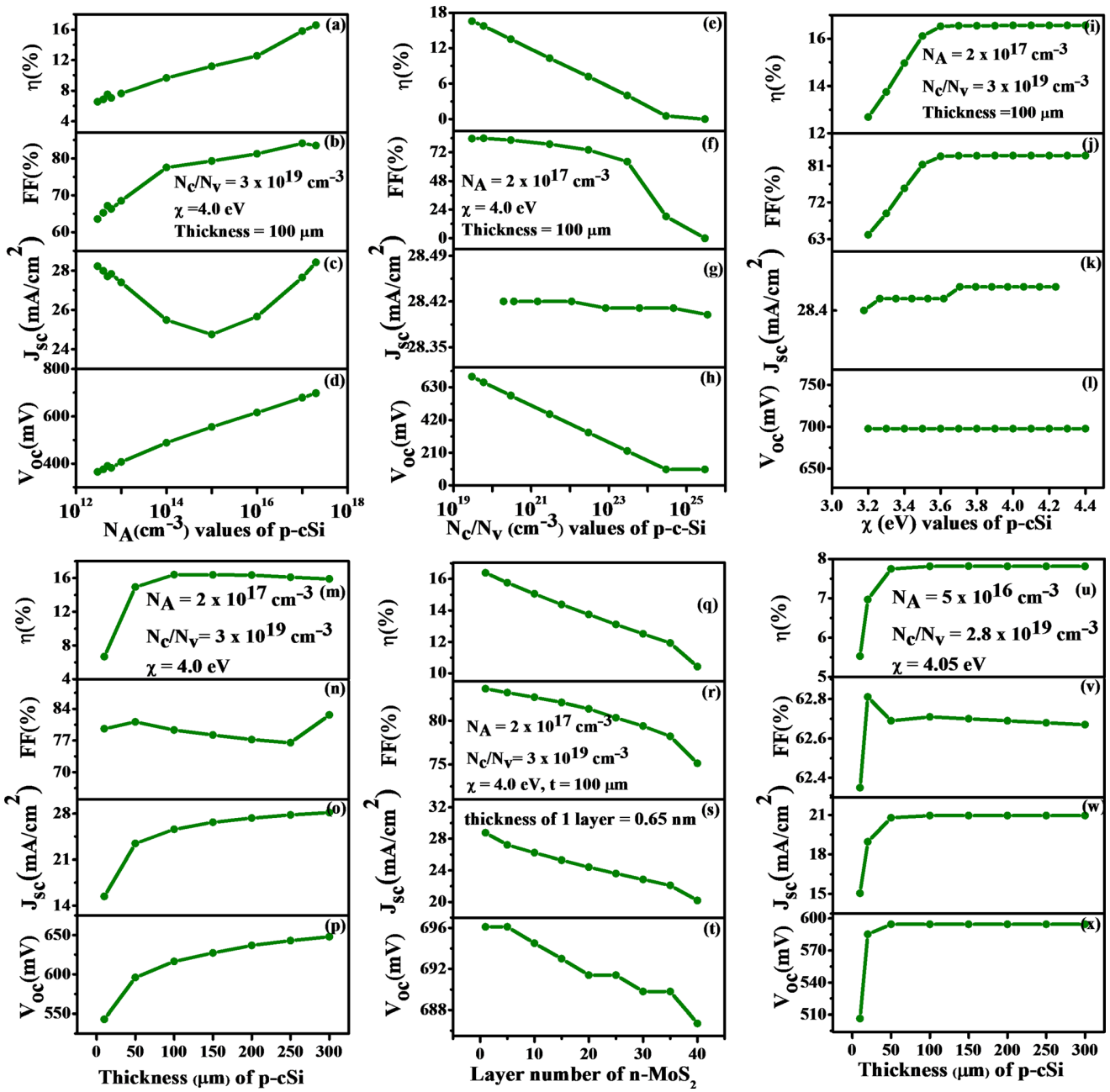


FIG. 3. The optimization of the parameters of p-cSi wafer: (a)–(d) the acceptor concentration N_A (cm^{-3}); (e)–(h) the effective density of states Nc/Nv (cm^{-3}); (i)–(l) the electron affinity χ (eV); (m)–(p) thickness (μm); and (q)–(t) layer number of MoS_2. The optimized parameters of n-MoS_2 were kept as $N_D = 1 \times 10^{14}\,cm^{-3}$; $N_C/N_V = 3 \times 10^{15}\,cm^{-3}$; $E_g = 1.9$ eV; $\chi = 4.2$ eV; $\varepsilon_r = 8$; and $\mu_n = 15\,cm^2/V$ s. (u)–(x) Optimization of thickness of comercially available silicon wafer. The parameters of MoS_2 were $N_D = 1 \times 10^{9}\,cm^{-3}$; $N_C/N_V = 3 \times 10^{18}\,cm^{-3}$. The parameters of silicon were taken as reported by Tsai *et al.*[17]

layer MoS_2 and Si, highest efficiency of 16.4% was achieved.

After optimizing the p-cSi parameters, the cell structure was further simulated with layer number of MoS_2 as shown in Figures 3(q)–3(t). V_{OC}, J_{SC}, FF, and η were found to decrease with layer numbers. As stated earlier, it can be attributed to the fact that efficiency of the solar cells depends on the optical transmittance and generation rate of the carriers in multilayer MoS_2. As it can be seen in Figure 4, the value of internal quantum efficiency (IQE), external quantum efficiency (EQE), and spectral response (SR) decreased with layer numbers. The spectral response was lower in the region of 400–900 nm for 40 layers of MoS_2 than single layer. This provides the evidence of reduction of optical transmittance with the layer number.[42,43] Furthermore, the generation rate of carriers was observed to decrease as layer number increased. For fully optimized n-MoS_2/p-cSi cell, the efficiency reduced to about 10% for 40 MoS_2 layers.

In order to validate the simulated results, comparison has been made with experimentally reported results. Recently, Tsai *et al.*[17] and Pradhan *et al.*, have fabricated the heterojunction solar cell by using single layer MoS_2 as a transparent electrode.[20] They have used the commercial available silicon with doping concentration in the range of 3.2×10^{16} to

Reuse of AIP Publishing content is subject to the terms at: https://publishing.aip.org/authors/rights-and-permissions. Download to IP: 14.139.251.107 On: Thu, 14 Jul 2016 04:23:19

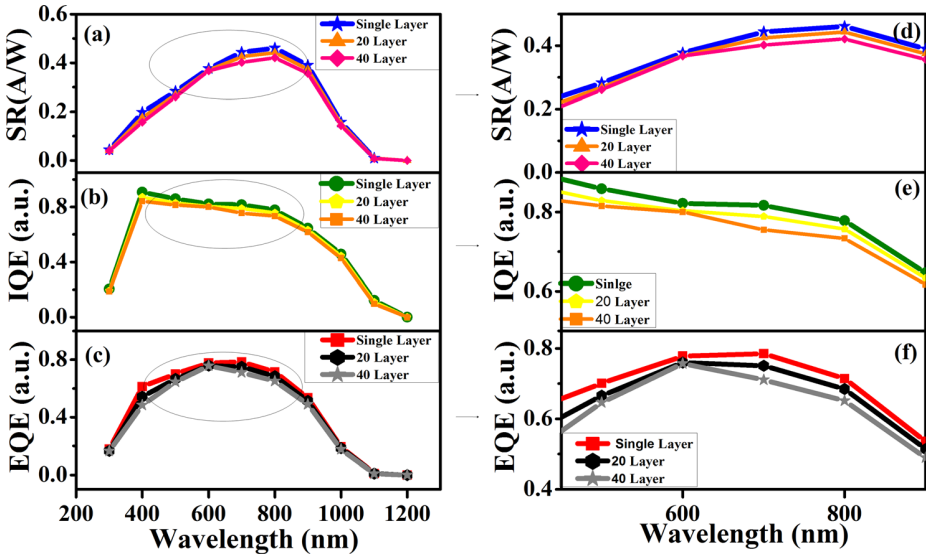


FIG. 4. (a) Spectral response (SR), (b) internal quantum efficiency (IQE), and (c) external quantum efficiency (EQE) of single layer, 20 layers and 40 layers of MoS_2 in the wavelength range of 300–1200 nm and (d) Spectral response (SR), (e) Internal quantum efficiency (IQE), and (f) External quantum efficiency (EQE) of single layer, 20 layers and 40 layers of MoS_2 in the wavelength range of 450–900 nm.

$2.7 \times 10^{17}\,cm^{-3}$, band gap (1.1 eV), work function (4.45 eV), and thickness 250 μm. Hence, we have simulated a similar solar cell by taking the doping concentration and thickness of both silicon as well as MoS_2 film as reported by them. The values of other parameters as conduction/valence band density, band gap, electron affinity, electron and hole mobility, recombination rates and defects were used which were reported in commercially available silicon wafers. Results are shown in Figures 3(u)–3(x). In simulated results, efficiency of 7.812% was achieved for 250 μm thick silicon wafer. This value matches with the reported values ~5.23% by Tsai *et al.*[17] and ~4.25% by Pradhan *et al.*[20] The small difference in the simulated and experimental results was observed because we have taken tentative values of different parameters. As can be seen from the result of variation of acceptor ion concentration of silicon on the efficiency, change in the acceptor ion concentration from $1 \times 10^{16}\,cm^{-3}$ to $2 \times 10^{17}\,cm^{-3}$ changed the efficiency from 12.44% to 16.4%. Also, experimental limitations such as uneven distribution of the dopant in the solar cell's layer causing non-uniform distribution of acceptor or donor ion concentration, local recombination of newly created e-h pairs, heat generation, improper formation of Schottky junction, etc., may cause the efficiency of the solar cell to decrease. Thus, it can be stated that the simulated results are in accordance with the experimental results.

Later, the simulation was further carried out by varying both the back contact and front contact. We have simulated the cell by changing the front contact from ITO to aluminum ($n = 1.0972$, $k = 6.7943$) and the back contact from silver to chromium/silicon ($n = 3.0504$, $k = 4.2504$) as used by Tsai *et al.*, and lower work function material like Titanium ($n = 1.906$, $k = 3.0606$).[17] No change in the simulated results was observed by doing so.

C. Quantum efficiency, spectral response and temperature dependence

For the quantum efficiency (QE) of the simulated structure, the illumination conditions were set at the monochromatic intensity (photon flux) of $1 \times 10^{16}\,cm^{-2}\,s^{-1}$ with 10 nm spectral width in the range of 300 nm – 1200 nm. The wavelength dependent characteristics, external QE (EQE) and internal QE (IQE) of the best optimized cell, are shown in Figures 4(b) and 4(c). The EQE and IQE of optimized cell were found to be 0.18 and 0.2 at 300 nm, respectively, and found to be increasing for longer wavelengths of illumination. The IQE reached at its maximum value of 0.9 at 400 nm, while maximum value of EQE ~ 0.78 was obtained at 700 nm. IQE was always found to be higher than EQE and both became zero after 1100 nm. The spectral response reveals that most of the photons have been absorbed in the range of 600 nm–900 nm. The spectral response was further found to enhance a little with the increase in the doping concentration of the layers, which can be contributed to significant increase in J_{SC}. From Figure 4, it was observed that the value of internal quantum efficiency (IQE), external quantum efficiency (EQE), and spectral response (SR) was found to be decreasing with increasing layer numbers of MoS_2, which explains the decrement in cell efficiency as the number of layers was increased from single to 40 layers. The EQE of a heterojunction solar cell includes the effect of optical losses such as transmission and reflection, which occurred in MoS_2 layer. Whereas IQE refers to the efficiency, with which photons, which are not reflected or transmitted out of the cell, can generate collectable carriers. As shown in Figure 4, EQE and IQE are almost same. This might happen due to less optical losses occurred in single layer MoS_2. It was reported that optical transparency of MoS_2 layer decreased from 90% to 40% as the layer number increases from 1 to 6. Furthermore, despite having the weakest light absorption, single layer MoS_2 was reported to have the highest photoresponse because its effective tunneling barrier at the metal/MoS_2 junction is the lowest, allowing for more efficient collection of photoexcited charge carriers via tunneling.[9] As evidenced from Figure 4, efficiency was higher when single layer was used as electrode. This is due to the highest photoresponse which is observed in single layer because of a direct bandgap rather than an indirect one, making the photoexcitation process much more efficient.[45] In case of MoS_2,

Reuse of AIP Publishing content is subject to the terms at: https://publishing.aip.org/authors/rights-and-permissions. Download to IP: 14.139.251.107 On: Thu, 14 Jul 2016 04:23:19

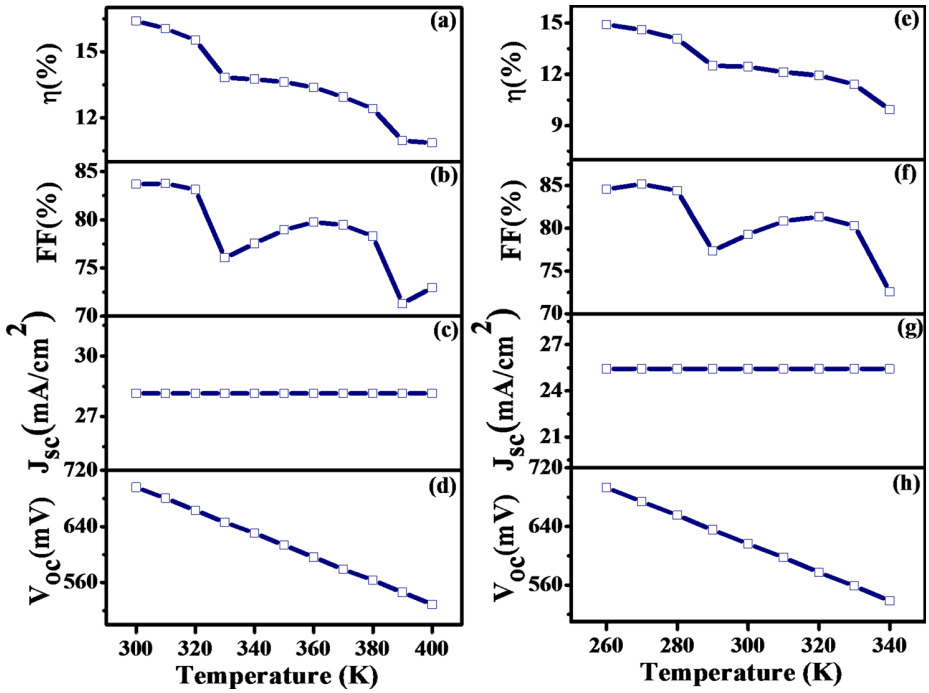


FIG. 5. Dependence on temperature variation of cell parameter (a)–(d) for $N_A = 2 \times 10^{17}\,cm^{-3}$ and (e)–(h) for $N_A = 1 \times 10^{16}\,cm^{-3}$ in silicon.

photoresponse might be dominated due to more photon absorption and subsequent higher carrier generation.

Finally, temperature dependence of cell responses for optimized cell was studied. The simulation of best-optimized cell provided the result only in the temperature range of 300 K–400 K. The band gap of the semiconductors depends upon the temperature. It tends to increase with the decrease in temperature.[46] Thus, at lower temperature levels the electrons are not able to cross the depletion region to conduct electricity. For understanding the lower temperature response on the solar cell, the simulation was done by taking the acceptor ion concentration (N_A) of silicon as $1 \times 10^{16}\,cm^{-3}$. At this value of N_A, the simulation of the cell provided the result only in the temperature range of 260 K to 340 K. At higher temperature, the Fermi level started pinning the conduction band. The simulation result for the cell at both $N_A = 2 \times 10^{17}\,cm^{-3}$ and $N_A = 1 \times 10^{16}\,cm^{-3}$ is plotted in Figures 5(a)–5(d), and 5(e) and 5(f), respectively. As can be observed from the temperature plots, the trend of variation of cell parameters for both carrier concentrations is similar. The best optimized cell with efficiency of 16.4% was obtained at 300 K for $N_A = 2 \times 10^{17}\,cm^{-3}$ (Table III). As seen from Figure 5, V_{OC} decreased linearly with rise in temperature. Increase in temperature reduces the band bending, thus reducing the photo excited carrier density in the cell. At higher temperature, the thermal vibrations increase. This resulted in the increase in the recombination of electron-hole pairs between conduction band and the valence band.[44] Therefore, the charge carrier transport becomes low at the interface and no further charge accumulation occurs in the layers, which kept J_{SC} constant.[4] Further, as discussed earlier with the increase in temperature, the band gap of the semiconductor decreases,[46] thus enabling the electrons to cross the depletion region and conduct electricity. While, on the other hand, the recombination rate increases with the temperature,[44] thus inhibiting the conduction of charge carriers. The combined effect of the two resulted in different rates of carrier transport at different temperature values leading to random variation in the series resistance, which controlled the variation of FF.

TABLE III. Summary of the parameters of best optimized n-MoS_2/Si cell.

Cell parameters	MoS_2 layer optimized cell	MoS_2 layer and c-Si wafer optimized cell	Cell values of commercially available MoS_2 and Si
V_{oc} (V)	0.6164	0.6961	0.594.5
J_{sc} (A/m^2)	2.54×10^{-6}	2.87×10^{-6}	2.09×10^{-6}
FF (%)	79.3	83.64	62.68
Efficiency	12.44% (@Single layer MoS_2 at $N_D = 1 \times 10^{20}\,m^{-3}$ at $N_C/N_V = 3 \times 10^{21}\,m^{-3}$, $E_g = 1.9$ eV, $\chi = 4.2$ eV, $\varepsilon_r = 8$, $\mu_n = 1.5 \times 10^{-4}$ m^2/Vs and@100 μm p-cSi at $N_A = 1 \times 10^{22}\,m^{-3}$, $N_C/N_V = 3 \times 10^{25}\,m^{-3}$ and $\chi = 4$ eV)	16.4% (@Single layer MoS_2 at $N_D = 1 \times 10^{20}\,m^{-3}$ at $N_C/N_V = 3 \times 10^{21}\,m^{-3}$, $E_g = 1.9$ eV, $\chi = 4.2$ eV, $\varepsilon_r = 8$, $\mu_n = 1.5 \times 10^{-3}$ m^2/Vs and @100 μm p-cSi at $2 \times 10^{23}\,m^{-3}$, N_C/N_V at $3 \times 10^{25}\,m^{-3}$ and χ at 4 eV)	7.812% (@Single layer MoS_2 at $N_D = 1 \times 10^{15}\,m^{-3}$, $N_C/N_V = \times 10^{24}$ m^3 and $E_g = 1.9$ eV, $\chi = 4.2$ eV, $\varepsilon_r = 8$, $\mu_n = 1.5 \times 10^{-3}$ cm^2/Vs @250 μm p-cSi at $5 \times 10^{22}\,m^{-3}$, N_C/N_V at $2.8 \times 10^{25}\,m^{-3}$ and χ at 4.05 eV)

Reuse of AIP Publishing content is subject to the terms at: https://publishing.aip.org/authors/rights-and-permissions. Download to IP: 14.139.251.107 On: Thu, 14 Jul 2016 04:23:19

IV. CONCLUSIONS

We have simulated the TCO/n-MoS_2/p-cSi/Ag structure. Independent effects of seven parameters of MoS_2 layer were analyzed individually and the parameters, which primarily influence the cell performance of MoS_2/Si cell, are N_D, N_C/N_V, χ, and number of layers of MoS_2. After optimizing the parameters of both multilayers (up to 40 layers) of MoS_2 and p-cSi wafer, the highest value cell efficiency of 10.42% was obtained on 100 μm p-cSi at 300 K. Highest efficiency of 16.4% was achieved for single layer MoS_2 on 100 μm thick p-cSi layer. It has been demonstrated that the n-type multilayer MoS_2 can act as an efficient transparent conducting electrode.

A. Method

The proposed device structure for the simulation was configured as TCO(ITO)/n- MoS_2/p-cSi/Ag as shown in Figure 1. An additional layer of SiO_2 was added to ensure the transport through MoS_2 layer only, by insulating the carrier transport through TCO from p-cSi wafer. The simulation was carried out using the AFORS-HET software version 2.4.1, under air mass 1.5 (AM1.5) illuminations with power density of 100 mW/cm^2. The front and back contacts were configured according to the values given in Table I. The optimization of MoS_2 layer was carried out first and the parameters selected for optimization were donor concentration (N_D), bandgap (E_g), effective conduction and valance band densities (N_C/N_V), electron affinity (χ), relative permittivity (ε_r), and electron mobility (μ_n). The values as well as the range of the parameters of MoS_2 have been tabulated in Table II.[9,12] The simulation was carried out by varying different parameters in their given range. The initial simulation was initiated by considering single layer of MoS_2 and was extended to multilayer MoS_2. The variation of open circuit voltage (V_{OC}), short circuit current (J_{SC}), fill factor (FF), and quantum efficiency (η) has been plotted with respective parameters. After optimizing the MoS_2 layer, the optimization of p-cSi layer was done for achieving the highest efficiency. The parameters considered for optimizing the p-cSi layer were acceptor concentration (N_A), effective conduction and valance band densities (N_C/N_V), the electron affinity (χ), and thickness. Finally, after getting a fully optimized cell, the simulation was carried out with variation in temperature. Furthermore, the cell was simulated considering the parameters of commercially available silicon to compare the result with experimentally available data.

ACKNOWLEDGMENTS

We thank the financial support from DST-SERB, fast track Program (SR/FTP/PS-055/2012). The authors gratefully acknowledged Helmholtz-Zentrum Berlin for providing AFORS-HET simulation software.

[1]X. Yang, W. Fu, W. Liu, J. Hong, Y. Cai, C. Jin, M. Xu, H. Wang, D. Yang, and H. Chen, J. Mater. Chem A **2**, 7727 (2014).
[2]A. Ayari, E. Cobas, O. Ogundadegbe, and M. S. Fuhrer, J. Appl. Phys. **101**, 014507 (2007).
[3]A. D. Yoffe, Adv. Phys. **51**, 799 (2002).
[4]K. Patel and P. K. Tyagi, AIP Adv. **5**, 077165 (2015).
[5]X. Zhong, W. Zhou, Y. Peng, Y. Zhou, F. Zhou, Y. Yin, and T. Dongsheng, RSC Adv. **5**, 45239 (2015).
[6]M. Shanmugam, C. A. Durcan, and B. Yu, Nanoscale **4**, 7399 (2012).
[7]B. Radisavljevic, A. Radenovic, J. Brivio, V. Giacometti, and A. Kis, Nat. Nano. **6**, 147 (2011).
[8]B. Radisavljevic and A. Kis, Nat. Mater. **12**, 815 (2013).
[9]J. M. Yun, Y. J. Noh, J. S. Yeo, Y. J. Go, S. I. Na, H. G. Jeong, J. Kim, S. Lee, S. S. Kim, H. Y. Koo, T. W. Kim, and D. Y. Kim, J. Mater. Chem. C **1**, 3777 (2013).
[10]O. Ochedowski, K. Marinov, N. Scheuschner, A. Poloczek, B. K. Bussmann, J. Maultzsch, and M. Schleberger, Nanotechnol. **5**, 291 (2014).
[11]S. Choi, Z. Shaolin, and W. Yang, J. Korean Phys. Soc. **64**, 1550 (2014).
[12]A. Carvalho and A. H. C. Neto, Phys. Rev. B **89**, 081406 (2014).
[13]M. Laskar, D. N. Nath, L. Ma, E. Lee, C. H. Lee, T. Kent, Z. Yang, R. Mishra, M. A. Roland, J. C. Idrobo, S. T. Pantelides, S. J. Pennycook, R. Myers, Y. Wu, and S. Rajan, Appl. Phys. Lett. **104**, 092104 (2014).
[14]Y. Du, H. Liu, A. T. Neal, M. Si, and P. D. Ye, IEEE Electron Device Lett. **34**, 1328 (2013).
[15]X. Gu, W. Cui, H. Li, Z. Wu, Z. Zeng, S. T. Lee, H. Zhang, and S. Sun, Adv. Energy Mater. **3**, 1262 (2013).
[16]X. Yang, W. Liu, M. Xiong, Y. Zhang, T. Liang, J. Yang, M. Xu, J. Ye, and H. Chen, J. Mater. Chem. **2**, 14798 (2014).
[17]M. L. Tsai, S. H. Su, J. K. Chang, D. S. Tsai, C. H. Chen, C. I. Wu, L. J. Li, L. J. Chen, and J. R. He, ACS Nano. **8**, 8317 (2014).
[18]L. Y. Gan, Q. Zhang, Y. Cheng, and U. Schwingenschlögl, J. Phys. Chem. Lett. **5**, 1445 (2014).
[19]M. Bernardi, M. Palummo, and J. C. Grossman, Nano Lett. **13**, 3664 (2013).
[20]S. K. Pradhan, B. Xiao, and A. K. Pradhan, Sol. Energy Mater. Sol. Cells **114**, 117 (2015).
[21]R. Stangl, A. Froitzheim, M. Kriegel, T. Brammer, S. Kirste, L. Elstner, H. Stiebig, M. Schmidt, and W. Fuhs, in *Proceedings of the 19th European Photovoltaic Solar Energy Conference, Paris, France*, 7–11 June 2004, pp. 1497–1500.
[22]R. Stangl, M. Kriegel, and M. Schmidt, in *Proceedings of WCPEC-4, 4th World Conference on Photovoltaic Energy Conversion, Hawaii, USA*, 7–12 May 2006, pp. 1350.
[23]D. Jiménez, Appl. Phys. Lett. **101**, 243501 (2012).
[24]J. Suh, T. E. Parl, D. Y. Lin, D. Fu, J. Park, H. J. Jung, Y. Chen, C. Ko, C. Jang, Y. Sun, R. Sinclair, J. Chang, S. Tonngay, and J. Wu, Nano. Lett. **14**, 6976 (2014).
[25]Z. Huang, X. Peng, H. Yang, C. He, L. Xue, G. Hao, C. Zhang, W. Liu, X. Qi, and J. Zhong, RSC. Adv. **3**, 12939 (2013).
[26]X. Meng, S. Tongay, J. Kang, Z. Chen, F. Wu, S. Li, J. Xia, J. Li, and J. Wu, Carbon **57**, 507 (2013).
[27]Z. Lin, B. R. Carvalho, E. Kahn, R. Lv, R. Rao, H. Terrones, M. A. Pimenta, and M. Terrones, 2D Matter. **3**, 022002 (2016).
[28]Y. L. Huang, Y. Chen, W. Zhang, S. Y. Queck, C. H. Chen, L. J. Li, W. T. Hsu, W. H. Chang, Y. J. Zheng, W. Chen, and A. T. S. Wee, Nat. Commun. **6**, 6298 (2015).
[29]A. Dashora, U. Ahuja, and K. Venugopala, Comput. Mater. Sci. **69**, 216 (2013).
[30]A. T. Neal, H. Liu, J. J. Gu, and P. D. Ye, in *Proceedings of Device Research Conference published in IEEE Explore, University Park, TX USA*, 18–20 June 2012, pp. 65–66.
[31]C. P. Lu, G. Li, J. Mao, L. M. Wang, and E. Y. Andrei, Nano Lett. **14**, 4628 (2014).
[32]S. Zhong, X. Hua, and W. Shen, J. IEEE Trans. Electron Devices **60**, 2104 (2013).
[33]U. Gangopadhyay, S. Roy, S. Garain, S. Jana, and S. Das, IOSR J. Eng. **2**, 41 (2012).
[34]K. Yamamoto, JSAP Int. **7**, 12 (2003).
[35]M. Fontana, T. Deppe, A. K. Boyd, M. Rinzan, A. Y. Liu, M. Paranjape, and P. Barbara, Sci. Rep. **3**, 1634 (2013).
[36]R. Singh and B. J. Baliga, *Cryogenic Operation of Silicon Power Device* (Springer, 1998), pp. 25–35.
[37]N. Ma and D. Jena, Phys. Rev. X **4**, 011043 (2014).
[38]J. Shakya, A. S. Patel, F. Singh, and T. Mohanty, App. Phys. Lett. **108**, 013103 (2016).
[39]B. G. Rao, H. S. S. R. Matte, and C. N. R. Rao, J. Cluster Sci. **23**, 929 (2012).
[40]J. Kim, S. Byun, A. J. Smith, J. Yu, and J. Huang, J. Phys. Chem. Lett. **4**, 1227 (2013).

Reuse of AIP Publishing content is subject to the terms at: https://publishing.aip.org/authors/rights-and-permissions. Download to IP: 14.139.251.107 On: Thu, 14 Jul 2016 04:23:19

[41]M. J. S. Matos, M. S. C. Mazzoni, and H. Chacham, Nanotechnol. **25**, 165705 (2014).
[42]A. Castellanos-Gomez, J. Quereda, H. P. V. D. Meulen, N. Nicolás Agraït, and G. Gabino Rubio-Bollinger, Nanotechnol. **27**, 115705 (2016).
[43]J. Park, N. Choudhary, J. Smith, G. Lee, M. Kim, and W. Choi, Appl. Phys. Lett. **106**, 012104 (2015).
[44]M. Rashid, K. S. Rahman, M. I. Hossain, N. Tabet, F. H. Alharbi, and N. Amin, Chalcogenide Lett. **11**, 397 (2014).
[45]Y. Son, Q. H. Wang, J. A. Paulson, C. Shih, A. G. Rajan, K. Tvrdy, S. Kim, B. Alfeeli, R. D. Braatz, and M. S. Strano, ACS Nano. **9**, 2843 (2015).
[46]W. Zhao, R. M. Riberio, M. Toh, A. Carvalho, C. Kloc, A. H. C. Neto, and G. Eda, Nano Lett. **13**, 5627 (2013).

Reuse of AIP Publishing content is subject to the terms at: https://publishing.aip.org/authors/rights-and-permissions. Download to IP: 14.139.251.107 On: Thu, 14 Jul 2016 04:23:19

Int'l Journal of Advances in Chemical Engg., & Biological Sciences (IJACEBS) Vol. 3, Issue 1 (2016) ISSN 2349-1507 EISSN 2349-1515

Preclinical evaluation of Di-sodium Alpha ketoglutarate against Isoniazid-Rifampicin Induced Hepatotoxicity

Lalita Mehra, Priyanka Chhabra, Amit Kumar, Aseem Bhatnagar, Yasha Hasija, and Gaurav Mittal

***Abstract*— The combination of Isoniazid (INH) and Rifampicin (RIF) is extensively used for the treatment of tuberculosis, but drug induced hepatotoxicity remains the major clinical challenge during treatment. The hepatoprotective role of AKG (Di-sodium Alpha ketoglutarate) is assessed on experimental animal study model. Male Sprague Dawley rats were divided into three groups of 6 animals each. Group I, (Vehicle control): given distilled water only, Group II (INH-RIF): Isoniazid and Rifampicin (50 mg/kg, orally) for 4 weeks, Group III, Treatment group: was given INH-RIF as in group II followed by AKG treatment at a dose of 2gm/kg, orally for 4 weeks. At the end of the experiment animals were sacrificed, blood samples were collected and biochemical and antioxidant assay were performed. Serum biochemical analysis showed elevated ALT, AST levels following INH and RIF exposure which significantly improved with AKG treatment. Antioxidants parameters were correlative to biochemical and histopathological findings. So from the present study it is concluded that AKG protects against INH and RIF induced hepatic injury.**

***Keywords*— Di-sodium Alpha ketoglutarate, Isoniazid, Rifampicin, Hepatotoxicity.**

I. INTRODUCTION

Tuberculosis (TB) is not only the most prevalent among infectious diseases, but also a leading cause of mortality in the developing world [1]. With the introduction of anti-tubercular drugs; Isoniazid (INH) and Rifampicin (RIF) the incidence of tuberculosis has steadily come down, but the associated side effects notably, drug induced hepatotoxicity remains a major treatment challenge more of so with the emergence of drug resistant tuberculosis [2].

INH and RIF are extensively metabolized in the liver by Phase 1 and 2 enzymes (n-acetyl transferase2 and cytochrome P450 2E1). For INH metabolism, Phase 1 mediated acetylation results in metabolites formation which are largely non-toxic, while Phase 2 mediated hydrolysis leads to formation of reactive electrophilic metabolite such as isoniazid hydrazine, which are highly toxic to hepatocytes. Also RIF by acting on Nuclear pregame X- receptor (PxR) activates cytochrome P 450 (Cyt P450 3A4) resulting in increased hydrolysis of INH into INH-Hydrazine [3]. Thus RIF and its metabolites though directly toxic themselves, does also potentiates the INH induced hepatotoxicity by the formation of excessive electrophilic molecules and reactive oxygen species (ROS).

There is a growing body of literature appreciating the role of exogenous Alpha ketoglutatre (AKG) in detoxification of reactive oxygen species (ROS). This keto-acid neutralizes ROS in non-enzymatic/NADPH independent fashion with concomitant formation of succinate and CO2. The present study evaluates the role of AKG in protecting anti-TB drug induced hepatotoxicity owing to its (ROS) scavenging properties.

II. MATERIAL AND METHOD

A. Experimental Animals

18 male Sprague Dawley rats weighing (200 to 250 g) were obtained from the Experimental animal facility of Institute of Nuclear Medicine and Allied Sciences (INMAS), Delhi. The study protocol was approved by the Institutional Animal Ethics Committee (IAEC) of the institute (INM/IAEC/2009/06/009).

Male Albino rats were divided into three groups of 6 animals each. Group I (Vehicle control): Normal Saline, Group II (Drug Group, INH-RIF): Isoniazid and Rifampicin (50 mg/kg, orally) for 4 weeks, INH and RIF were prepared in sterile water and the pH of RIF solution was adjusted to 3.0 with 0.1 mol/L HCl [4]. Group III (Treatment Group, INH-RIF + AKG,), INH-RIF as in group II treated simultaneously with AKG at a dose of 2gm/kg, orally for 4 weeks [5][6]. The animals were sacrificed after 24 h of the exposure and intervention using diethyl ether by cervical dislocation. Blood and liver tissue samples were collected. Serum was separated by centrifugation at 3000 rpm for 10 min for LFT (Liver Profile Test). Liver tissue was placed in formaldehyde solution for routine histopathological examination by light microscopy. The other part of liver was placed in liquid nitrogen and stored in -80º C for evaluating antioxidant status.

B. Measurement of Liver Function test and antioxidant activities

Hepatocellular integrity (ALT, AST) with hepatic functioning (bilirubin) were determined using commercially available kits. The homogenate of frozen liver tissue (stored at -80ºC) was used for evaluating antioxidant activities. Lipid peroxidation, GSH and MPO was determined by the method of Mihara[7], Ellman[8] and Hillegass [9] respectively.

C. Statistical analysis

The data is expressed as mean ±SD. The data was analyzed using SPSS software. Statistical significance was determined

Manuscript received May. 15, 2016. This work was supported by University Grant Commission (UGC), Delhi, India and Institute of Nuclear Medicine and Allied Sciences (INMAS), Defense Research & Development Organisation (DRDO), Delhi, India

Lalita Mehra, Priyanka Chhabra, Amit Kumar, Aseem Bhatnagar, Gaurav Mittal, INMAS, DRDO, Delhi, India.

Correspondence Author: Dr. Gaurav Mittal

Yasha Hasija, Delhi Technological University, Delhi, India

using one way analysis of variance (ANOVA). $p < 0.05$ is taken as statistical significance value.

III. RESULTS

Effect on Body weight: There was no mortality in any of the groups. The body weight and relative liver weights of the experimental animals calculated at the end of the study had no statistically significant difference when compared to the control animals (Table I).

TABLE I: BODY WEIGHT AND LIVER WEIGHTS OF ANIMALS (N=6)

Treatment	Body weight (g)	Relative liver weight (g)
Control	155 ± 7	4.46 ± 0.53
INH-RIF	153 ± 5*	4.38 ± 0.30
INH-RIF+AKG	154 ± 4*	4.52 ± 0.46

*No significant difference among groups

Effect of AKG on INH + RIF induced hepatotoxicity: As shown in (Table II), the levels of hepatic markers ALT and AST were significantly higher in the INH-RIF group as compared to the control group. AKG treatment significantly reversed the elevations in these parameters. Also the significant increase in serum bilirubin levels in INH-RIF group animals were significantly reversed with AKG.

Effect of AKG on lipid peroxidation: The levels of liver MDA, a parameter for lipid peroxidation showed significant increment in INH-RIF group compared to control group animals. Whereas, AKG treatment following the INH-RIF challenge reversed the alterations (Table III).

Effect of AKG on GSH concentration: In the INH-RIF group there is a significant decrement of hepatic GSH as compared to normal control group. The treatment of AKG achieved a considerably increase in GSH levels as compared to INH-RIF alone group (Table III).

Effect of AKG on MPO levels: Tissue MPO activity was measured as an indirect evident of neutrophil infiltration. INH-RIF caused significant increase in the liver MPO activity, which was significantly higher than the control group, while AKG treatment revered the levels (Table III).

TABLE II: LIVER PROFILE TEST (N=6)

Treatment	Control	INH+RIF	INH-RIF+AKG
ALT (IU/L)	40.57 ± 6.78	128 ± 11.97**	54 ± 7.76#
AST(IU/L)	140 ± 7.53	468 ± 36.9**	191 ± 24.2 #
Bilirubin (mg/dL)	0.502 ±0.13	2.65±0.43*	0.98±0.76#

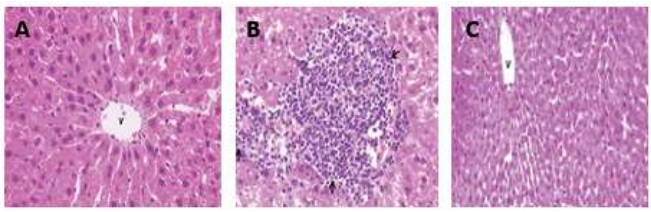
**p<0.01, highly significant, *p<0.05, significant (when compare to control), # values comparable to control

TABLE I: EFFECT OF AKG ON INH+RIF -INDUCED OXIDATIVE STRESS

Parameter	Control	INH-RIF	INH-RIF+AKG
MDA (nmol/g tissue)	44.0 ± 6.4	81.04 ± 6.3**	58.2 ± 0.55#
GSH (nmol/g tissue)	2.51 ± 0.3	0.89 ± 0.1**	1.54 ± 0.2#
MPO (U/g protein)	12.4 ± 2.1	23.2 ±2.5*	15.2 ± 3.4#

**p<0.01, highly significant, *p<0.05, significant (when compare to control), # values comparable to control

FIGURE I: HISTOPATHOLOGY



Photomicrographs of rat liver (H and E, x100, x50) from: (A) control group showing normal hepatic architecture; (B) INH-RIF group showing intense cellular degeneration, cellular inflammation of hepatocytes; (C) AKG treatment group showing normal hepatic architecture; V, represents hepatic portal vein

IV. DISCUSSION

The present study was conducted to evaluate the curative effect of AKG against INH-RIF induced hepatotoxicity in rat. This study gives some scientific evidences on the effect of AKG on enzymatic, antioxidant status and histological observations from oxidative damage induced by INH and RIF treatment in rats.

Oxidative stress mediated liver injury is the main mechanism of antituberculosis drugs induced hepatotoxicity [10]. Unifying the various proposed hypothesis of INH-RIF induced hepatotoxicity reveals that it's not the potential drugs but metabolites generated from phase 1 and 2 enzymes (NAT2, Cytochrome P4502E1), action via nuclear pregame receptor (PxR) causing dysregulation of transporters (ATP binding cassettes Subfamily B, member1) results in the formation of reactive oxygen species (ROS) [11]. Serum hepatobiliary enzymes such as AST, ALT are present in high concentrations in the liver cells under normal conditions and the elevations of these enzymes indicate hepatocytes membrane damage [12]. The present study revealed that serum AST, ALT and Bilirubin were significantly increased in rats intoxicated with INH-RIF in comparison with control group. The treatment of AKG significantly ameliorated the toxic effects. Recent microbial studies on AKG had shed newer light to its antioxidant properties, are in agreement with our result [13]. Oxidative stress is a prominent feature in the pathophysiology of liver disease [14]. Oxidative stress occurs when reactive oxygen species (ROS) are not adequately neutralized by cellular antioxidant defense mechanisms [15]. The present study reveals that treatment with AKG has a critical role in abrogating the oxidative stress-mediated toxicity of INH-RIF.

INH-RIF induced significant lipid peroxidation in rat liver, which was quantified by measuring malondialdehyde (MDA). INH-RIF treated rats showed significantly raised MDA levels, which was in agreement with previous INH-RIF induced hepatotoxic models. AKG significantly suppressed the INH-RIF induced lipid peroxidation as evident from our results. Besides replenishing the intracellular GSH pool, another important function of AKG consists of formation of carnitine, which leads to physiological normalization of fat metabolism offering protection against lipid peroxidation. Our results are supported from a previous investigation on the effects of α-KG on MDA levels, where it was observed AKG prevented lipid peroxidation in rat livers when they were exposed to alcohol [16], ammonium acetate [17] or sodium valproate [18].

The molecular mechanism for AKG to offer protection

against oxidative damages is likely due to its ability to participate in non-enzymatic NADPH independent oxidative decarboxylation of free radicals [19]. Ammonia is known to inhibit antioxidant enzymes, AKG by acting as a scavenger of amino groups transforms the ammonia to nontoxic amino acids like glutamate or glutamine. AKG is also known be involved in GSH synthesis and being a strong ammonia and phosphate binding factor may indirectly stabilize redox state in organism [20]. Thus, the present study shows that AKG offers protection against oxidative damage caused by INH-RIF.

REFERENCES

[1] Garner P, Holmes A, Ziganshina L, "Tuberculosis. *Clin Evid*," pp. 1081–1093, 2004.

[2] Sharma SK, "Antituberculosis drugs and hepatotoxicity," *Infect Genet Evol*, vol.4, pp. 167–170, 2004. http://dx.doi.org/10.1016/j.meegid.2003.01.001

[3] Sodhi CP, Rana SV, Mehta SK, Vaiphei K, Attari S, Mehta S, "Study of oxidative-stress in isoniazid-rifampicin induced hepatic injury in young rats," *Drug Chem Toxicol*, vol.20, pp.255-269, 1997. http://dx.doi.org/10.3109/01480549709003881

[4] Bahri AK, Chiang CS, "Timbrell JA. Acetylhydrazine hepatotoxicity," *Toxicol Appl Pharmacol*, vol. 60, pp. 561-569, 1981. http://dx.doi.org/10.1016/0041-008X(81)90343-4

[5] Mittal G, Singh T, Kumar N, Bhatnagar A, Tripathi RP, Tulsawani R, Vijayaraghavan R, Bhattacharya R, "Radiolabeling and dose fixation study of oral alpha-ketoglutarate as a cyanide antidote in healthy human volunteers," *Clinical Toxicology*, vol. 48(6), pp. 509-515,2010. http://dx.doi.org/10.3109/15563650.2010.496371

[6] Bhattacharya R, Tulsawani RK, "In vitro and in vivo evaluation of various carbonyl compounds against cyanide toxicity with particular reference to alpha-ketoglutaric acid", *Drug Chem Toxicol*; vol. 31, pp.149–161,2008. http://dx.doi.org/10.1080/01480540701688865

[7] Mihara M, Uchiyama M, "Determination of malonaldehyde precursor in tissues by thiobarbituric acid test," *Analytical Biochemistry*, vol. 86(1), pp. 271-278, 1978 http://dx.doi.org/10.1016/0003-2697(78)90342-1

[8] EllmanGL, "Tissue sulfhydryl groups," *Arch Biochem Biophys*, vol. 82(1), pp. 70-77, 1959. http://dx.doi.org/10.1016/0003-9861(59)90090-6

[9] Hillegass LM, Griswold DE, Brickson B, Albridghtson Winslow C, "Assessment of myeloperoxidase activity in whole rat kidney," *J. Pharmacol. Methods*, vol. 24, pp. 285–295, 1990. http://dx.doi.org/10.1016/0160-5402(90)90013-B

[10] Tasduq SA, Peerzada K, Koul S, Bhat R, Johri RK, "Biochemical manifestations of anti-tuberculosis drugs induced hepatotoxicity and the effect of silymarin", *Hepatol Res*, vol 31, pp.132-135, 2005. http://dx.doi.org/10.1016/j.hepres.2005.01.005

[11] Amina I, Shehu, Guangming Li, Wen Xie, Xiaochao Ma, "The Pregnane X Receptor in Tuberculosis," *TherapeuticsExpert Opin Drug Metab Toxicol*, vol. 12(1): pp. 21–30, Jan2016. http://dx.doi.org/10.1517/17425255.2016.1121381

[12] R.B. Drotman, GT Lawhorn, "Serum enzymes as indicators of chemically induced liver damage," *Drug ChemToxicol*, vol. 1(2), pp.163-171, 1978. http://dx.doi.org/10.3109/01480547809034433

[13] M. Randall, Chin, F. Xudong, Y. Melody, Pai et al, "The metabolite α-ketoglutarate extends lifespan by inhibiting ATP synthase and TOR," *Nature*, 2014.

[14] C.S. Lieber, "Role of oxidative stress and antioxidant therapy in alcoholic and nonalcoholic liver diseases," *Adv Pharmacol*, vol. 38, pp. 601–28, 1997. http://dx.doi.org/10.1016/S1054-3589(08)61001-7

[15] E.C. Opara, "Oxidative stress," Dis Mon, vol. 52, pp. 183–98, 2006. http://dx.doi.org/10.1016/j.disamonth.2006.05.003

[16] M. Vidya, P. Subramanian,"Effect of α-ketoglutarate on antioxidants and lipid peroxidation products in rats treated with sodium valproate,"*J.Appl. Biomed*, vol. 4, pp. 141-46, 2006.

[17] S. Velvizhi, T. Nagalashmi, M.M. Essa, K.B. Dakshayani, P. Subramanian, " Effect of α-ketoglutarate on lipid peroxidation and antioxidant status during chronic ethanol administration in wistar rats," *Polish Journal of Pharmacology*, vol. 54, pp. 231-236, 2002.

[18] S. Velvizhi, B. Kadiyala, K.B. Dakshayani, "Effects of α-ketoglutarate on antioxidants and lipid peroxidation products in rats treated with ammonium acetate," *Nutrition*, vol. 18, pp. 747-750, 2002. http://dx.doi.org/10.1016/S0899-9007(02)00825-0

[19] Lasch , T. Petras , O. Ullrich O, J. Backmann, D. Naumann, T.Grune, "Hydrogen peroxide-induced structural alterations of RNAse," *A. J. Biol. Chem*, vol. 276, pp. 9492–9502, 2001. http://dx.doi.org/10.1074/jbc.M008528200

[20] T. Niemiec, J. Sikorskai,A. Harrison et al, "Alpha-ketoglutarate stabilizes redox homeostasis and improves arterial elasticity in aged mice," *Journal of physiology and pharmacology*, vol. 62(1), pp. 37-43, 2011.

Question Answering over Knowledge Base using Factual Memory Networks

Sarthak Jain
Department of Computer Engineering
Delhi Technological University
DL, India
successar@gmail.com

Abstract

In the task of question answering, Memory Networks have recently shown to be quite effective towards complex reasoning as well as scalability, in spite of limited range of topics covered in training data. In this paper, we introduce Factual Memory Network, which learns to answer questions by extracting and reasoning over relevant facts from a Knowledge Base. Our system generate distributed representation of questions and KB in same word vector space, extract a subset of initial candidate facts, then try to find a path to answer entity using multi-hop reasoning and refinement. Additionally, we also improve the run-time efficiency of our model using various computational heuristics.

1 Introduction

Open-domain question answering (Open QA) is a longstanding problem that has been studied for decades. Early systems took an information retrieval approach, where question answering is reduced to returning passages of text containing an answer as a substring. Recent advances in constructing large-scale knowledge bases (KBs) have enabled new systems that return an exact answer from a KB.

A key challenge in Open QA is to be robust to the high variability found in natural language and the many ways of expressing knowledge in large-scale KBs. Another challenge is to link the natural language of questions with structured semantics of KBs. In this paper, we present a novel architecture based on memory networks (Bordes et al., 2015) that can be trained end-to-end using (question, answer) pairs as training set, instead of strong supervision in the form of (question, associated facts in KB) pairs.

The major contributions of this paper are two-fold: first, we introduce factual memory networks, which are used to answer questions in natural language (e.g *"Where was Bill Gates born?"*) using facts stored in the form of (subject, predicate, object) triplets in a KB (e.g *('Bill Gates', 'place of birth', 'Seattle')*). We evaluate our system against current baselines on various benchmark datasets. Since KBs can be extremely large, making it computationally inefficient to search over all entities and paths, our second goal of this paper is to increase the efficiency of our model in terms of various performance measures and provide better coverage of relevant facts, by intelligently selecting which nodes to expand.

2 Related Work

The state-of-the-art methods for QA over a knowledge base can be classified into three classes: semantic parsing, information retrieval and embedding based.

Semantic parsing (Cai and Yates, 2013; Berant et al., 2013; Kwiatkowski et al., 2013; Berant and Liang, 2014; Fader et al., 2014) based approaches aim to learn semantic parsers which parse natural language questions into logical forms and then query knowledge base to lookup answers. Even though these approaches are difficult to train at scale because of the complexity of their inference, they tend to provide a deep interpretation of the question.

Information retrieval based systems retrieve a set of candidate answers and then conduct further analysis to rank them. Their main difference lies in select-

Proceedings of NAACL-HLT 2016, pages 109–115,
San Diego, California, June 12-17, 2016. ©2016 Association for Computational Linguistics

ing correct answers from the candidate set. Yao and Van Durme (2014) used rules to extract question features from dependency parse of questions, and used relations and properties in the retrieved topic graph as knowledge base features.

Embedding based approaches (Bordes et al., 2014b; Bordes et al., 2014a) learn low-dimensional vectors for words and knowledge base constitutes, and use the sum of these vectors to represent questions and candidate answers. However, simple vector addition ignores word order information and higher order n-grams. For example, the question representations of *"who killed A?"* and *"who A killed?"* are same in the vector addition model. (Bordes et al., 2015) used strong supervision signal in form of supporting facts for a question during training to improve their performance.

3 Preprocessing KB and Questions

3.1 Processing FREEBASE

Freebase : Freebase (Bollacker et al., 2008) is a huge and freely available database of factual information, organized as triplets (subject Entity, Relationship, object Entity). All Freebase entities and relationships are typed and the lexicon for types and relationships is closed. Each entity has an internal id and a set of alternative names (called aliases, e.g. JFK for John Kennedy) that can refer to that entity in text.

The overall structure of Freebase is a hypergraph, in which more than two entities can be linked together in a n-ary fact. The underlying triple storage involves dummy entities to represent such facts, effectively making actual entities involved linked through paths of length 2, instead of 1. For example, a statement like *"A starred as character B in movie C"* is represented in Freebase as (A, 'starring', dummy entity), (dummy entity, 'movie', C), (dummy entity, 'character', B), where dummy entity has same internal id in all three facts.

To obtain direct links between entities in such cases, we modify these facts by removing the dummy entities and using the second relationship as the relationship for the new condensed facts. In our example, we condense aforementioned facts into two : (A, 'character', B) and (A, 'movie', C). Also, we label these condensed facts as siblings of each other. Therefore, (A, 'character', B) is **sibling** of (A, 'movie', C) and vice versa. Moving forward, we use the term 'fact' to refer to a triplet in Freebase, containing actual entities only (no dummy entities).

After above preprocessing, we represent each entity and relationship in KB as a vector $\in \mathbb{R}^d$. Each such entity/relationship vector is computed as the average of its word vectors, where each word vector $\in \mathbb{R}^d$. In case of entities, we also include word vectors of all its aliases when calculating the average. Such a scheme has the additional advantage that we can benefit from pre-trained unsupervised word vectors (e.g. from Word2Vec), which in general capture some distributional syntactic and semantic information.

3.2 Processing Question

Let a question be given as sequence of words $(x_1, x_2, \ldots, x_{|q|})$. Each word x_i mapped to its word vector. We experimented with two different ways to compose the question embedding q out of these word-vectors:

Bag-of-words (BOW): It is sum of individual word vectors i.e. $q = \sum_{i=1}^{|q|} x_i$.

Position Encoding (PE): This heuristic take in account order of words in the question. The embedding is of form $q = \sum_{i=1}^{|q|} l_i \odot x_i$ where $\odot$ is an element-wise multiplication. For each i, l_i is a column vector $\in \mathbb{R}^d$ with the structure $l_{ij} = \min(\frac{i \times d}{j \times |q|}, \frac{j \times |q|}{i \times d})$, where d is the dimension of the embedding and j runs from 1 to d. This type of function ensures that initial part of summed vector is weighed higher for initial word vectors and vice versa. Thus, a statement like 'Who is parent of Darth Vader?' will map to a different embedding than statement like 'Who is Darth Vader parent of?'.

4 Model Description

4.1 Fact Extraction

To begin, we generate an initial list of facts (called candidate fact list) which is fed as input to our network. To generate this list, we match all possible n-grams of words of the question to aliases of Freebase entities and discard all n-grams (and their matched entities) that are a subsequence of another n-gram. All facts having one of the remaining entities as subject are added to candidate fact list.

4.2 Factual Memory Network

A L-Hop Factual Memory Network consists of L Computation Layers $C_1 \dots C_L$ connected one after another in a linear chain, and an Output Function. The initial Computation Layer C_1 takes as input the candidate fact list (from previous step) and the initial question embedding (from Section 3.2). The Output Function takes as input the output of final Computation Layer C_L and generates a list of answers (in form of Freebase entities). Layer C_i takes as input the output of layer C_{i-1}.

4.2.1 Computation Layer

A Computation layer accesses two inputs : 1) a fact list (our 'memory') $F = \{f_1 \dots f_{|F|}\}$, where each fact f is of form (s, R, o), s and o being the entity vectors and R the relationship vector, 2) a question embedding $q \in \mathbb{R}^d$. For each fact $f \in F$, we calculate an unnormalised score $g(f)$ and a normalized score $h(f)$.

We visualize a fact $f = (s, R, o)$ as a question-answer pair with (s, R) forming the question and o the answer. Therefore, $g(f)$ calculates similarity between the given question embedding and a hypothetical question of form $q' = (s, R)$.

$$g(f) = q^T(s + R) \tag{1}$$

For example, given a question q = *"Where was Bill Gates born?"* and a fact f = ('Bill Gates', 'place of birth', 'Seattle'), $g(f)$ will compute similarity between the question q and a hypothetical question q' of form *"Bill Gates place of birth?"*.

In case a fact f has some siblings $b_1, b_2, \dots, b_k$ (Section 3.1), we re-calculate its $g(f)$ as follows:

$$g(f) = \text{average}(g(f), g(b_1), g(b_2), \dots, g(b_k)) \tag{2}$$

where $g(f)$ on RHS is calculated using Eq.(1). For each sibling b_i, we calculate $g(b_i)$ using Eq.(1), but with b_i's subject replaced by its object in the formula.

Continuing with example in Section 3.1, if f = (A,'character',B) and b_1 = (A,'movie',C) is sibling of f, then this kind of processing is helpful in answering questions like *"What character does A play in movie C?"*, where fact f alone would not be enough to answer the question. Thus, above processing corresponds to a hypothetical question of form *"A character C movie ?"* for the fact f.

The normalized score $h(f)$ for a fact f is calculated using softmax function over all facts to determine their relative importance.

$$h(f) = \frac{exp(g(f))}{\sum_{f' \in F} exp(g(f'))} \tag{3}$$

Next we modify the fact list and the question embedding on basis of above calculated scores.

Step 1. Fact Pruning: We choose a threshold value ϵ and remove facts from fact list with $h(f) < \epsilon$. We found in our experiments that setting $\epsilon = \frac{\max_{f' \in F} h(f)}{2}$ gives best results. Performing pruning seems to remove non-relevant facts from subsequent computation, significantly improving our response time and allowing us to explore larger search space around the subgraphs of our question entities.

Step 2. The question embedding is modified as follows:

$$q' = q + \sum_{f \in F} h(f)(s + R) \tag{4}$$

Each such modification allows us to incorporate knowledge gathered (in form of hypothetical questions (s, R), weighted by their relevance h) at a particular layer about the question and pass it on to subsequent layer.

Step 3. Fact Addition: For each object entity o belonging to a fact f, we find all the facts (o, R', o') connected to it in KB and assign a score $h(f)q'^T(o + R')$ to each of them. If the new fact's score is $> \epsilon$, it is added to the fact list, effectively increasing path-length of our search space by 1.

The modified fact list along with the new question embedding(q') form the outputs of this layer, which are fed as input to next Computation Layer or the Output function.

4.2.2 Output Function

Output Function takes as input the output of final Computation Layer C_L (i.e. its output fact list and q') and calculate scores $h(f)$. The answer set is formed by the object entity of highest scoring fact as well as object entities of all those facts that have same s **and** R **as the highest scoring fact**.

This simple heuristic can increase utility of our model when there are multiple correct answers for a question. For example, a question like *'Who is*

Anakin Skywalker father of?' has more than one answer entities i.e. [*'Leia Organa'*, *'Luke Skywalker'*], and they are all linked by same s ('Anakin Skywalker') and R ('children') in Freebase. Of course, this follows the assumption that all such facts survive till this stage and atleast one of them is highest scoring fact.

4.3 Training Objectives

Let the QA training set $\mathcal{D}$ be set of question-answer pairs (q, A), where q is the question with list of correct answers A, e.g. (q = *'Who is Anakin Skywalker father of?'*, A = [*'Leia Organa'*, *'Luke Skywalker'*]). To train our parameters, we minimize the following loss function:

$$L_{QA} = \sum_{(q,A)} \sum_{n=1}^{L} \frac{n}{L} \| |F_n| \sum_{a \in A} a - |A| \sum_{f \in F_n} h(f).o \|^2 \quad (5)$$

Here n refers to n-th Computation Layer in our network (with F_n as its input fact list) and L is total number of Computation layers/hops in the network. This loss function defines the degree to which the object entities in fact list of a given layer are near to given answer list, weighted by $h(f)$, by taking pairwise difference between entities in answer list and objects in fact list. It was observed that minimizing this function gives higher weights to facts in which object entities are similar to answer entities as well as allow our network to generate shorter paths to reach answers from the question.

Paraphrasing Loss: Following previous work such as (Fader et al., 2013; Bordes et al., 2015), we also use the question paraphrases dataset **WikiAnswers**[1] to generalize for words and question patterns which are unseen in the training set of question-answer pairs. We minimize hinge loss so that a question and its paraphrases should map to similar representations. For the paraphrase dataset $\mathcal{P}$ of set of tuples (p, p') where p and p' are paraphrases of each other, the loss is defined as:

$$L_{PP} = \sum_{(p,p')} max\{0, 0.1 - p^T p' + p^T p''\} \quad (6)$$

where p'' is random example in $\mathcal{P}$ that is not a paraphrase of p and 0.1 is the margin hyper-parameter.

[1] http://knowitall.cs.washington.edu/paralex/

Backpropagation is used to calculate gradients while Adagrad was used to perform optimisation using max-norm regularisation. At each time step, a sample is drawn from either $\mathcal{P}$ with probability 0.25 or $\mathcal{D}$ with probability 0.75. If sample from $\mathcal{P}$ is chosen, gradient of L_{PP} is calculated. Otherwise, gradient of L_{QA} is calculated. The only parameters optimised in our model are the word vectors.

5 Experimental Setup

5.1 Baselines

We evaluate our model on following datasets:

WebQuestions[2]: This dataset, introduced in (Berant et al., 2013), contains 5,810 question-answer pairs where answer can be a list of entities, similar to (q, A) pairs described before. It was created by crawling questions through the Google Suggest API, and then obtaining answers using Amazon Mechanical Turk. WebQuestions is built on Freebase since all answers are defined as Freebase entities.

On **WebQuestions**, we evaluate against following baselines : (Berant et al., 2013; Berant and Liang, 2014; Yih et al., 2015) (semantic parsing based methods), (Fader et al., 2013) (uses a pattern matching scheme), (Bordes et al., 2014b; Bordes et al., 2014a; Bordes et al., 2015) (Embedding based approaches). Results of the baselines have been extracted from respective papers, except for (Berant et al., 2013; Berant and Liang, 2014) where we use the code provided by the author to replicate the results[2].

We compare our system in terms of F1 score as computed by the official evaluation script [2] (Berant et al., 2013), which is the average, over all test questions, of the F1-score of the sets of predicted answers.

SimpleQuestions[3]: The SimpleQuestions dataset, introduced in (Bordes et al., 2015), consists of a total of 108,442 questions written in natural language by human English-speaking annotators each paired with a corresponding Freebase fact. Our model only use the answer entity during the training, instead of whole fact. For example, {q = *'Which forest is Fires Creek in?'*, *Fact = '(fires creek, contained by, nantahala national forest)'*} could be data point in SimpleQuestions but we only use {q = *'Which forest is*

[2] www-nlp.stanford.edu/software/sempre/

[3] fb.ai/babi

Fires Creek in?', A = ['nantahala national forest']} for training.

On **SimpleQuestions**, we evaluate against previous result (Bordes et al., 2015) in terms of path-level accuracy, in which a prediction is correct if the subject and the relationship of highest scoring fact were correctly retrieved by the system.

5.2 Experimental Setup

The current dump of Freebase data was downloaded[4] and processed as described before. Our data contained 1.9B triplets. We used following splits of each evaluation dataset for training, validation and testing, same as (Bordes et al., 2015).
WebQuestions (WQ) : [3000, 778, 2032]
SimpleQuestions (SQ) : [75910, 10845, 21687]
We also train on automatic questions generated from the KB, which are essential to learn embeddings for the entities not appearing in either WebQuestions or SimpleQuestions. We generated one training question per fact following the same process as that used in (Bordes et al., 2014a).

The embedding dimension d was chosen 64 and max-norm cutoff was chosen as 4 using validation dataset. We pre-train our word vectors using method described by (Wang et al., 2014) to initialize our embeddings.

We experimented with variations of our model on both test sets. Specifically, we analyze the effect of question encoding **(PE vs BOW)**, number of Hops and inclusion of pruning/fact-additions **(P/FA)** in our model. In subsequent section, the word 'significant' implies that the results were statistically significant ($p < 0.05$) with paired T-test

6 Results

The results of our experiments are presented in Table 1. It shows that our best model outperforms considered baselines by about 3% in case of WebQuestions and even comparable to previous results in case of SimpleQuestions. Note that the best performing system for SimpleQuestions used strong supervision (question with supporting fact) while our model used only answer entities associated with a question for training.

[4]https://developers.google.com/freebase/data

Setup	WQ F1	SQ Acc
Random Guess	1.9	4.9
(Berant et al., 2013)	31.3	n/a
(Bordes et al., 2014a)	39.2	n/a
(Berant and Liang, 2014)	39.9	n/a
(Yih et al., 2015)	52.5	n/a
(Bordes et al., 2015)	42.2	**63.9**
PE + 3-Hop	**55.6**	59.7
BOW + 3-Hop	48.5	54.6
PE + 2-Hop	53.8	57.3
PE + 1-Hop	47.9	55.2
without P/FA	44.3	53.8

Table 1: Results on Evaluation datasets. Acc = Accuracy

We also give the performance for the variations of our model. Position Encoding improves our performance by 7% on WQ and by 5% on SQ, validating our choice of heuristic. Also, most answers in both datasets can be found within path length of two from candidate fact list, thus a 3-Hop network shows only 2% improvement over 2-Hop network.

	WQ	SQ
Top-2	70.1	68.7
Top-3	76.4	74.5
Top-5	80.3	77.6
Top-10	88.9	85.2

Table 2: Top-K results of our best model on each test set

Top-K Performance: In Table 2, we present the top-k results on both datasets. A large majority of questions can be answered from the top two or three candidates. By providing these alternative results (in addition to the top-ranked candidate) to the user, many questions can be answered correctly.

6.1 Efficiency and Error Analysis

Efficiency: All experiments for this paper were done on an Intel Core i5 CPU @ 2.60GHz, 8GB RAM with average HDD Access time of 12.3 ms. We calculated the Average Response time / Query (ART/Q), defined as average time taken by the system from input of query till the generation of answer list, including both computational and search-and-access time for KB. ART/Q for 1, 2 and 3 Hop Networks was 200, 350 and 505 ms respectively. Also the training time (including time to search for

hyper-parameters) for each of these networks was 740, 1360 and 2480 min respectively.

The major bottleneck in ART/Query for our network was the search-and-access of large amount of KB Data, therefore we implemented efficient search procedures using Prefix Trees for String Matching and pipelined different stages of the model using multi-threading (i.e. Fact Extraction, Computation and Back-Propagation were performed on individual threads) to improve our response and training time.

Effect of Pruning/Fact-Additions : From Table 1, we can see that pruning and fact-additions have significantly improved scores on all datasets. We analyzed 200 random data points from set of examples that were correctly answered only when P/FA was used (for each test set). In 97.5% of these samples, we observed that pruning allowed our model to remove spurious facts generated during initial fact extraction, making soft-max calculation in Eq. (3) more robust.

We also observed that the set of correctly answered questions using model without P/FA was proper subset of one with P/FA on each evaluation dataset, signifying that if relevant facts were scored higher in previous Computation layers, their scores are not reduced as more facts are added in subsequent layers. Removing pruning alone didn't improve our performance by more than 0.4% on any dataset while exponentially increasing the response time, signifying that pruning itself didn't remove relevant/correct fact in majority of examples.

On the computational end, we tried to determine the effect of pruning on our model response time (excluding search and access time). Including pruning improved our ART/Q by approximately 44% during test phase and by 21% during training phase for our 3 Hop network.

Manual Error Analysis : We sampled 100 examples from each test set to identify major sources of errors made by our model. Following classes of errors were determined :

Complex Questions (55%) : These types of questions involved temporal or superlative qualifier like 'first', 'after', 'largest', etc. This problem occurred in both test sets. We may be able to solve this problem using small set of rules for comparison on final answer set or better semantic representations for numerical values and qualifiers.

Question Ambiguity (20%) : This error class contains those questions that may have ambiguity in their interpretation. For example, a question like 'Where is shakira from?' generated answer as 'place_of_birth' (Baranquilla) while ground truth is 'nationality' (Colombia). This occurred mostly in WebQuestions dataset.

Ground truth Inconsistency (10%) : This type of error occurred when ground truth differed from correct entity present in Freebase KB (even though both are correct in many cases). For example, the question 'Where did eleanor roosevelt died?' have ground truth as 'New York City' whereas KB delivers the entity 'Manhattan', even though both are entities in Freebase. It occurred only in WebQuestions dataset.

Miscellaneous (15%) : This error class contains bad entity/relationship extraction (for example, mapping Anakin Skywalker to Darth Vader), bad question/answer pairs (e.g. q = "what time does american horror story air?" A = [Tom Selleck]), Typos in Question, etc.

7 Conclusion

This paper presents a Factual Memory Network model that aims to perform question-answering using facts from Knowledge bases like Freebase. The system uses a multi-hop neural network that can perform reasoning over facts generated from named entities in a given question as well as traverse the knowledge graph to include more information.

In future, we hope to extend our system so that it can work better with n-ary relations present in Freebase to deal with qualifiers, improve entity disambiguation mechanism in our model as well as include a mechanism to involve user interaction with system to improve our rates. Another goal is to add support for KBs with noisy data generated through automated relation extraction from unstructured data (for example OLLIE, etc) as well as for unstructured sources of knowledge (like Wikipedia) in our model, to extend and improve its utility.

References

Hannah Bast and Elmar Haussmann. 2015. More accurate question answering on freebase. In *Proceedings*

of the 24th ACM International on Conference on Information and Knowledge Management, pages 1431–1440.

Jonathan Berant and Percy Liang. 2014. Semantic parsing via paraphrasing. In *Proceedings of the 52nd Annual Meeting of the Association for Computational Linguistics*, pages 1415–1425.

Jonathan Berant, Andrew Chou, Roy Frostig, and Percy Liang. 2013. Semantic parsing on freebase from question-answer pairs. In *Proceedings of the 2013 Conference on Empirical Methods in Natural Language Processing*, pages 1533–1544.

Kurt Bollacker, Colin Evans, Praveen Paritosh, Tim Sturge, and Jamie Taylor. 2008. Freebase: a collaboratively created graph database for structuring human knowledge. In *Proceedings of the 2008 ACM SIGMOD international conference on Management of data*, pages 1247–1250.

Antoine Bordes, Sumit Chopra, and Jason Weston. 2014a. Question answering with subgraph embeddings. In *Proceedings of the 2014 Conference on Empirical Methods in Natural Language Processing*, pages 615–620.

Antoine Bordes, Jason Weston, and Nicolas Usunier. 2014b. Open question answering with weakly supervised embedding models. In *Machine Learning and Knowledge Discovery in Databases*, pages 165–180. Springer.

Antoine Bordes, Nicolas Usunier, Sumit Chopra, and Jason Weston. 2015. Large-scale simple question answering with memory networks. *arXiv preprint arXiv:1506.02075*.

Qingqing Cai and Alexander Yates. 2013. Semantic parsing freebase: Towards open-domain semantic parsing. In *Second Joint Conference on Lexical and Computational Semantics (*SEM), Volume 1: Proceedings of the Main Conference and the Shared Task: Semantic Textual Similarity*, pages 328–338.

Li Dong, Furu Wei, Ming Zhou, and Ke Xu. 2015. Question answering over freebase with multi-column convolutional neural networks. In *Proceedings of the 53rd Annual Meeting of the Association for Computational Linguistics*, pages 260–269.

Anthony Fader, Stephen Soderland, and Oren Etzioni. 2011. Identifying relations for open information extraction. In *Proceedings of the Conference on Empirical Methods in Natural Language Processing*, pages 1535–1545.

Anthony Fader, Luke Zettlemoyer, and Oren Etzioni. 2013. Paraphrase-driven learning for open question answering. In *Proceedings of the 51st Annual Meeting of the Association for Computational Linguistics*, pages 1608–1618.

Anthony Fader, Luke Zettlemoyer, and Oren Etzioni. 2014. Open question answering over curated and extracted knowledge bases. In *Proceedings of the 20th ACM SIGKDD international conference on Knowledge discovery and data mining*, pages 1156–1165.

Tom Kwiatkowski, Eunsol Choi, Yoav Artzi, and Luke Zettlemoyer. 2013. Scaling semantic parsers with on-the-fly ontology matching. In *Proceedings of the 2013 Conference on Empirical Methods in Natural Language Processing*, pages 1545–1556.

Thomas Lin, Oren Etzioni, et al. 2012. Entity linking at web scale. In *Proceedings of the Joint Workshop on Automatic Knowledge Base Construction and Web-scale Knowledge Extraction*, pages 84–88.

Siva Reddy, Mirella Lapata, and Mark Steedman. 2014. Large-scale semantic parsing without question-answer pairs. *Transactions of the Association for Computational Linguistics*, 2:377–392.

Richard Socher, Danqi Chen, Christopher D Manning, and Andrew Ng. 2013. Reasoning with neural tensor networks for knowledge base completion. In *Advances in Neural Information Processing Systems*, pages 926–934.

Sainbayar Sukhbaatar, Jason Weston, Rob Fergus, et al. 2015. End-to-end memory networks. In *Advances in Neural Information Processing Systems*, pages 2431–2439.

Zhen Wang, Jianwen Zhang, Jianlin Feng, and Zheng Chen. 2014. Knowledge graph and text jointly embedding. In *Proceedings of the Conference on Empirical Methods in Natural Language Processing*.

Jason Weston, Sumit Chopra, and Antoine Bordes. 2014. Memory networks. *arXiv preprint arXiv:1410.3916*.

Min-Chul Yang, Nan Duan, Ming Zhou, and Hae-Chang Rim. 2014. Joint relational embeddings for knowledge-based question answering. In *Proceedings of the 2014 Conference on Empirical Methods in Natural Language Processing*, pages 645–650.

Wen-tau Yih, Ming-Wei Chang, Xiaodong He, and Jianfeng Gao. 2015. Semantic parsing via staged query graph generation: Question answering with knowledge base. In *Association for Computational Linguistics (ACL)*.

Volume 4, Issue 1 (2016) 43-47 ISSN 2347 - 3258
International Journal of Advance Research and Innovation

Ranking of Software Effort Estimation Selection Criteria Based On Fuzzy Set Theory

Aparna Jindal*, Rakesh Garg, Ashu Bansal
Department of Production and Industrial Engineering, Delhi Technological University, New Delhi, India

Article Info
Article history:
Received 25 January 2016
Received in revised form
20 February 2016
Accepted 28 February 2016
Available online 15 Marchr 2016

Keywords
Selection Criteria; Fuzzy-Set Theory.

Abstract
The selection and evaluation of Software effort estimation models has always been a challenging task for the software developers and the project managers. A lot of research has been done by various researchers on this by considering it as multi-criteria decision making problem. So, a better understanding of various selection criteria and their importance in this regard is required. In this paper, first the identification of the various software effort estimation model selection criteria is done, then by applying fuzzy set theory the local and global weights of these selection criteria are calculated and finally the selection criteria are ranked according to their global weights showing the importance of each criterion.

1. Introduction

Over the past decades, software has become a crucial component in all aspects of life. The development of the software with a better quality and less effort is the prime motive of the software developers. Several research surveys have focused on software project effort and schedule estimation. Manpower, Effort (usually in person- months), and Project Duration (in calendar time) are the three main elements considered while estimating the effort of any software development. Effort estimation obtains essential data in the form of how estimates are made, what factors motivate the choice of estimation methods and the current level of estimation accuracy. For both developers and customers the accurate software effort estimation are to be critical which can be used for generating request for proposals, contract negotiation, scheduling, monitoring and control.

To get accurate estimates, effort estimation may be used an input to project plans, iteration plans, budgets, investment analyses and pricing processes and bidding rounds. Effort estimation methods can be divided into model based and expert-based methods. Model-based methods use some algorithm to summarize old data and make predictions about new projects where as Expert-based methods use human expertise (possibly augmented with process guidelines, checklists, and data) to generate predictions. The precision of size estimation directly impacts the accuracy of effort estimation.

The rest of the paper is structured as: A literature review about the effort estimation model is provide in section 2, in section 3 a brief introduction about Adopted methodology, A ranking procedure is given in section 4, and section 5 contains the conclusion of the paper.

1. Literature Review

Tim Menzies et al. [1] proposed a methodology based on heuristic rejection rules named coseekmo to rank various software effort estimation models by considering mean relative error (MRE), mean magnitude of relative error (MMRE) and prediction (PRE) as selection criteria.

Basha and Dhavachelvan [2] proposed mean relative error (MRE), mean magnitude of relative error (MMRE), prediction (PRE), root mean square (RMS), relative root mean square (RRMS) for the ranking of software effort estimation models. In the contemporary work, Kaur et al. [3] used some attributes as mean magnitude of relative error (MMRE), mean square error (MSE), root mean square error (RMSE) and RMSSE as the selection criteria.

Kaur Sehra et al. [4] proposed a model based on Fuzzy Analytic Hierarchy Process by accounting reliability (REL), mean magnitude of relative error (MMRE), Prediction (PRE) as selection criteria. Noel Garcia-Diaza et al. [5] developed a methodology based on fuzzy logic for the comparison of two fuzzy logic models for software development effort estimation. Prediction (PRE), mean error relative (MER), (mean magnitude of error relative) MMER were used as selection criteria in this research.

A hybrid model was developed by Predicate.C. Eberendu [6] for the comparison of various software effort estimation models by considering Technical complexity factor (TCF), Environmental complexity factor (ECF), Unadjusted use case points (UCP), Productivity factors (PF) as the selection criteria. Moløkken-Østvold [7] provide mean relative error (MRE), balance relative error bias (BREbias) and balance relative error (BRE) as the selection criteria for the evaluation of software effort estimation models. Leung and Fan [8] published Software Cost Estimation using different criteria as mean relative error (MRE), mean absolute relative error (MARE), balance relative error (BREbias).

3. Adopted Methodology

In the present research, fuzzy set theory is adopted to rank the various software effort estimation selection models selection criteria according to their global weights.

3.1 Fuzzy Sets

Fuzzy set theory, involving the fuzziness of data, was introduced by Zadeh [8] to solve problems, in which descriptions of activities and observations were imprecise,

Corresponding Author,
E-mail address: jindalaparna5@gmail.com
M: 91-8818013022

All rights reserved: http://www.ijari.org

vague, and uncertain. A fuzzy set is a class of objects, with a continuum of membership grades, in which the membership grade ranges between 0 and 1. A fuzzy subset A of a universal set X is defined by a membership function $f_A(x)$ which maps each element x in X to a real number (0, 1). The grade 1 of membership for an element means that the element is in that set. The grade of membership is 0, meaning that the element is not in that set. Ambiguous cases are assigned values between 0 and 1. The theory also allows mathematical operations such as addition, subtraction, multiplication, and division, to be applied to the fuzzy sets [9, 10].

3.2 Triangular Fuzzy Numbers

In this study, triangular fuzzy numbers due to their easy calculation are used as membership functions, corresponding to the elements in a set. A fuzzy number is a triangular fuzzy number if its membership function can be denoted as follows [9].

$$f_{(A)}(x)=\begin{cases}\dfrac{x-c}{a-c}, c\le x\le a\\ \dfrac{b-x}{b-a}, a\le x\le a\\ 0, otherwise\end{cases}$$ where a, b, and c

are real numbers and $c \le a \le b$.

In this study, addition and multiplication from the Zadeh extension principle are used to calculate the membership functions. Let we have two triangular fuzzy numbers A_1 and A_2 represented by triplets as

A1= (c1, a1, b1) and A2 = (c2, a2, b2), the addition and multiplication operations these can be expressed as follows:

Addition: if $\oplus$ denotes addition.

$A1 \oplus A2 : (c1,a1,b1) \oplus (c2,a2,b2)=(c1+c2,a1+a2,b1+b2)$ (2)

Multiplication: if $\otimes$ denotes multiplication.

$A1 \otimes A2 : (c1,a1,b1) \otimes (c2,a2,b2)=(c1\times c2,a1\times a2,b1\times b2), c1\ge 0, c2\ge 0$ (3)

3.3. Linguistic Terms in Triangular Fuzzy Numbers

In this study, we are using linguistic terms for the weight of various criteria. A linguistic term can be defined as a variable whose values are in words rather than numbers. The weights can be evaluated by linguistic terms such as Extremely More Important, Very More Important, More Important, Important, Less Important, Less Important, Very Less Important, Extremely Less Important. These linguistic terms can be expressed in a triangular fuzzy numbers, as shown in Table I.

3.4 A Fuzzy Algorithm for Selection Criteria Ranking Problem

A systematic approach for the ranking of various selection criteria related to software effort estimation model based on fuzzy set theory is described in this section. A lot of operators as mean, median max etc. can be used to aggregate the expert's opinion but in this study average is applied for this purpose. For software effort estimation selection criteria ranking problem, Let us assume that there are a group of *n* experts (*E*1, *E*2, ..., *En*), who evaluate the weights of *k* criteria *(C*1,*C*2, . . .,*Ck)* and Let *Wte (t* =1, 2*, ...,k; k* ; *e*=1,2, . . .,*n)* be the weight given to *Ct* by expert *Ee*

$$Wt = 1/n \otimes (Wt1 \oplus Wt2 \oplus \cdots \oplus Wtn) = \frac{1}{n}\sum_{e=1}^{n} W_{te} \quad (1)$$

Where *Wt* is the average weight of criterion

Table 1: Linguistic terms for the weight of each criterion

Linguistic term	Membership function	Linguistic te	Membership Function
Extremely More important (EMI)	**(1,1,1)**	**Less Important (LI)**	**(0.2,0.3,0.4)**
Very More Important (VMI)	**(0.8,0.9,1)**	**Very Less Important (VLI)**	**(0,0.1,0.2)**
More Important (MI)	**(0.6,0.7,0.8)**	**Extremely Less Important (ELI)**	**(0,0,0)**
Important (I)	**(0.4,0.5,0.6)**		

3.5 Conversion of Fuzzy Numbers to Crisp Scores

In this research, maximizing and minimizing methods are used to convert the triangular fuzzy numbers into crisp score.

For maximizing

$$f_{m(y)}=\begin{cases}\dfrac{y-y_{\min}}{y_{\max}-y_{\min}}, y_{\min}\le y\le y_{\max}\\ 0, otherwise\end{cases}$$

For minimizing

$$f_A(x)\, f_G(x)=\begin{cases}\dfrac{x-x_{\max}}{x_{\min}-x_{\max}}, x_{\min}\le x\le x_{\max}\\ 0, otherwise\end{cases}$$

where xmin=inf S, xmax=sup S, S=$\cup$mi =1 Fi , Fi ={x| fFi (x)>0}, i =1,2, . . .,m.

4. Ranking Procedure

4.1 Effort Estimation Model Selection Criteria

In the open literature, a lot of selection criteria were used by the various researchers for the selection of software effort estimation model. After the extensive study of past researches, total twenty four criteria were identified as shown in figure 1.

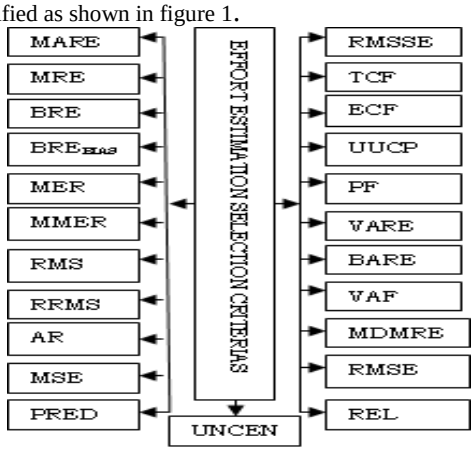


Fig. 1: Software Effort Estimation Model Selection Criteria

4.2 Expert Identification and Selection

In existing literature review, there was no sufficient data available which can lead to find out the importance of each

selection criteria. So, we rely on different expert's opinion to overcome the problem of collecting relevant data. In this research, a team of five experts (E1, E2, E3, E4, E5) from software development companies, academia as well as laboratories was constituted who provide the weights of each selection criteria in linguistic terms as defined in table 1. These experts have a wide experience in the field of software development.

Table 2: Aggregated Triangular Fuzzy Numbers

S No	Criteria	Local Weight	Global Weight	S No.	Criteria	Local Weight	Global Weight
1.	MARE	0.84	0.05740842	2.	MMER	0.7	0.04784035
3.	VAF	0.62	0.042372881	4.	RMSE	0.86	0.058775287
5.	REL	0.88	0.060142154	6.	RMSSE	0.42	0.02870421
7.	MMRE	0.76	0.051940951	8.	TCF	0.46	0.031437944
9.	PRE	0.78	0.053307818	10.	ECF	0.34	0.023236741
11.	UNC	0.3	0.020503007	12.	UUCP	0.38	0.025970476
13.	MSE	0.66	0.045106616	14.	PF	0.1	0.006834336
15.	AR	0.58	0.039639147	16.	VARE	0.26	0.017769273
17.	BRE	0.72	0.049207217	18.	BRE bia	0.74	0.050574084
19.	RME	0.54	0.036905413	20.	MRE	0.94	0.064242756
21.	RRME	0.82	0.056041553	22.	MMRE	0.632	0.043193002
23.	MER	0.5	0.034171679	24.	MDMRE	0.8	0.054674686

4.3 Data Collection

The weight in linguistic terms was assigned to each selection criteria by all five experts. The weight so obtained is represented in table 2 and given in appendix-1 with their membership function.

4.4 Selection Criteria Weight Calculation

The aggregate triangular fuzzy numbers for each selection criteria are obtained by using equation1 and are given in table 3.

$$W1 = \frac{1}{5}[(1,1,1) \oplus (0.8, 0.9,1) \oplus (0.8, 0.9,1) \oplus (0.4, 0.5, 0.6) \oplus (0.8, 0.9,1)]$$

$$= \frac{1}{5}(3.8, 4.2, 4.6) = (0.76, 0.84, 0.92)$$

After analyzing all criteria weight as in table 2, the crisp score (local and global weight) for each selection criteria is obtained and given in table 3.

4.5 Final Ranking

The software effort estimation model selection criteria are ranked according to global weights as shown in figure 2.

Table 3: Crisp Scores (Local and Global Weights) of Selection Criteria

S. No.	Criteria	Aggregate Weight	S. No.	Criteria	Aggregate Weight
1.	MARE	0.76,0.84,0.92	2.	MMER	0.6,0.7,0.8
3.	VAF	0.52,0.62,0.72	4.	RMSE	0.8,0.86,0.92
5.	REL	0.84, 0.88, 0.92	6.	RMSSE	0.32,0.42,0.52
7.	MMRE	0.72, 0.76,0.8	8.	TCF	0.36,0.46,0.56
9.	PRE	0.68,0.78,0.88	10.	ECF	0.24,0.34,0.44
11.	UNC	0.2,0.3,0.4	12.	UUCP	0.28,0.38,0.48
13.	MSE	0.56,0.66,0.76	14.	PF	0,0.1,0.2
15.	AR	0.48,0.58,0.68	16.	VARE	0.16,0.26,0.36
17.	BRE	0.64,0.72,0.8	18.	BRE bias	0.64,0.74,0.84
19.	RME	0.44,0.54,0.64	20.	MRE	0.92,0.94,0.96
21.	RRME	0.72,0.82,0.92	22.	MMRE	0.88,0.92,0.96
23.	MER	0.4,0.5,0.6	24.	MDMRE	0.72,0.8,0.88



Fig.2: Ranking of Software Effort Estimation Model Selection Criteria

The figure depicts that mean relative error (MRE) is ranked at number-1 due to its largest global weight followed by reliability (REL) at number-2 and relative mean square error (RMSE) at number-3. It also depicts that product factor (PF) is ranked at last or number-24 due to the smallest value of its global weight.

5. Conclusions

In this research, fuzzy set theory is applied to rank the various software effort estimation model selection criteria identified. The ranking of selection criteria relates to the importance of each selection criteria. Simply, it can be stated that ranking represents that which selection criteria is more important than another one. The better understanding of the importance of selection criteria can lead to the more precise and accurate selection and evaluation of software effort estimation model.

References

[1] Menzies, T., Chen, Z., Hihn, J., & Lum, K. (2006). Selecting best practices for effort estimation. Software Engineering, IEEE Transactions on, 32(11), 883-895.

[2] Basha, S., & Ponnurangam, D. (2010). Analysis of empirical software effort estimation models. arxiv preprint arxiv:1004.1239.

[3] Kaur, J., Singh, S., Kahlon, K. S., & Bassi, P. (2010). Neural network-a novel technique for software effort estimation. International Journal of Computer Theory and Engineering, 2(1), 1793-8201

[4] Sehra, S. K., Brar, D., Singh, Y., & Kaur, D. (2013). Multi criteria decision making approach for selecting effort estimation model. arXiv preprint arXiv:1310.5220.

[5] Garcia-Diaz, N., Lopez-Martin, C., & Chavoya, A. (2013). A comparative study of two fuzzy logic models for software development effort estimation. Procedia Technology, 7, 305-314.

[6] Eberendu, A. C. Software Project Cost Estimation: Issues, Problems and Possible Solutions. International Journal of Engineering Science Invention, 3, 38-43.

[7] Moløkken-Østvold, K., Jørgensen, M., Tanilkan, S. S., Gallis, H., Lien, A. C., & Hove, S. E. (2004, September). A survey on software estimation in the norwegian industry. In Software Metrics, 2004. Proceedings. 10th International Symposium on (pp. 208-219). IEEE.

[8] Leung, H., & Fan, Z. (2002). Software cost estimation. Handbook of Software Engineering, Hong Kong Polytechnic University.

[9] Kaufmann, A., & Gupta, M. M. (1988). Fuzzy mathematical models in engineering and management science. Elsevier Science Inc.

[10] 10. Dubois, D., & Prade, H. (1979). Fuzzy real algebra: some results. Fuzzy sets and systems, 2(4), 327-348.

APPENDIX- 1

Table 2: Linguistic Value With Their Corresponding Membership Function For Selection Criteria

Selection Criteria	E1	E2	E3	E4	E5
MARE	EMI(1,1,1)	VMI(0.8,0.9,1)	VMI(0.8,0.9,1)	Imp(0.4,0.5,0.6)	VMI(0.8,0.9,1)
VAF	MI(0.6,0.7,0.8)	LI(0.2,0.3,0.4	MI(0.6,0.7,0.8)	M.I(0.6,0.7,0.8)	MI(0.6,0.7,0.8)
REL	EMI(1,1,1)	EMI(1,1,1)	EMI(1,1,1)	M.I(0.6,0.7,0.8)	MI(0.6,0.7,0.8
MMRE	E.M.I(1,1,1)	EMI(1,1,1)	EMI(1,1,1)	L.I(0.2,0.3,0.4	Imp(0.4,0.5,0.6)
PRE	MI(0.6,0.7,0.8)	MI(0.6,0.7,0.8)	VMI(0.8,0.9,1)	M.I(0.6,0.7,0.8)	VMI(0.8,0.9,1)
UNC	LI(0.2,0.3,0.4)	LI(0.2,0.3,0.4)	LI(0.2,0.3,0.4)	LI(0.2,0.3,0.4)	LI(0.2,0.3,0.4)
MSE	Imp(0.4,0.5,0.6)	VMI(0.8,0.9,1)	VMI(0.8,0.9,1)	Imp(0.4,0.5,0.6)	Imp(0.4,0.5,0.6)
AR	MI(0.6,0.7,0.8)	Imp(0.4,0.5,0.6)	Imp(0.4,0.5,0.6)	MI(0.6,0.7,0.8)	Imp(0.4,0.5,0.6)
BRE	MI(0.6,0.7,0.8)	MI(0.6,0.7,0.8)	Imp(0.4,0.5,0.6)	EMI(1,1,1)	Imp(0.4,0.5,0.6)
RME	Imp(0.4,0.5,0.6)	Imp(0.4,0.5,0.6)	Imp(0.4,0.5,0.6)	MI(0.6,0.7,0.8)	Imp(0.4,0.5,0.6)
RRME	VMI(0.8,0.9,1)	Imp(0.4,0.5,0.6)	VMI(0.8,0.9,1)	VMI(0.8,0.9,1)	VMI(0.8,0.9,1)
MER	Imp(0.4,0.5,0.6)	Imp(0.4,0.5,0.6)	Imp(0.4,0.5,0.6)	Imp(0.4,0.5,0.6)	Imp(0.4,0.5,0.6)
MMER	MI(0.6,0.7,0.8)	Imp(0.4,0.5,0.6)	VMI(0.8,0.9,1)	VMI(0.8,0.9,1)	Imp(0.4,0.5,0.6)
RMSE	EMI(1,1,1)	EMI(1,1,1)	VMI(0.8,0.9,1)	MI(0.6,0.7,0.8)	MI(0.6,0.7,0.8)
RMSSE	Imp(0.4,0.5,0.6)	LI(0.2,0.3,0.4)	Imp(0.4,0.5,0.6)	Imp(0.4,0.5,0.6)	LI(0.2,0.3,0.4)
TCF	Imp(0.4,0.5,0.6)	Imp(0.4,0.5,0.6)	LI(0.2,0.3,0.4)	Imp(0.4,0.5,0.6)	Imp(0.4,0.5,0.6)
ECF	LI(0.2,0.3,0.4)	LI(0.2,0.3,0.4)	LI(0.2,0.3,0.4)	Imp(0.4,0.5,0.6)	LI(0.2,0.3,0.4)
UUCP	Imp(0.4,0.5,0.6)	LI(0.2,0.3,0.4)	LI(0.2,0.3,0.4)	LI(0.2,0.3,0.4)	Imp(0.4,0.5,0.6)
PF	VLI(0,0.1,0.2)	VLI(0,0.1,0.2)	VLI(0,0.1,0.2)	VLI(0,0.1,0.2)	VLI(0,0.1,0.2)
VARE	LI(0.2,0.3,0.4)	LI(0.2,0.3,0.4)	VLI(0,0.1,0.2)	LI(0.2,0.3,0.4)	LI(0.2,0.3,0.4)
BRE bias	MI(0.6,0.7,0.8)	Imp(0.4,0.5,0.6)	VMI(0.8,0.9,1)	MI(0.6,0.7,0.8)	VMI(0.8,0.9,1)
MRE	EMI(1,1,1)	EMI(1,1,1)	EMI(1,1,1)	EMI(1,1,1)	MI(0.6,0.7,0.8)
MMRE	EMI(1,1,1)	EMI(1,1,1)	EMI(1,1,1)	VMI(0.8,0.9,1)	MI(0.6,0.7,0.8)
MDMRE	EMI(1,1,1)	MI(0.6,0.7,0.8)	MI(0.6,0.7,0.8)	VMI(0.8,0.9,1)	MI(0.6,0.7,0.8)

This article has been accepted for inclusion in a future issue of this journal. Content is final as presented, with the exception of pagination.

Sequential Optimization for PV Panel Parameter Estimation

Pallavi Bharadwaj, *Student Member, IEEE*, Kunal Narayan Chaudhury, *Senior Member, IEEE*, and Vinod John, *Senior Member, IEEE*

***Abstract*—The output of a solar photovoltaic (PV) system can be predicted using a parameterized model. The parameters can be obtained from the datasheet of the panel or from the measured current–voltage (I-V) characteristics. Measurement-based parameter estimation is shown to provide better results, as compared with the datasheet-based method. This effect magnifies for older panels due to the deterioration of panel characteristics with time, leading to a deviation from the datasheet specifications. Least-squares minimization is applied on the measured data using the Levenberg–Marquardt algorithm (LMA), trust region reflective Newton, and steepest descent optimization, which are compared on the basis of accuracy and speed. Low computational complexity and high parameter accuracy is ensured by introducing a novel sequential parameter estimation, in which two of the parameters are analytically evaluated, and a separate sequential evaluation of the shunt resistance parameter is performed. The predicted maximum power from the proposed method matches the experimental measurements with high accuracy.**

***Index Terms*—Gradient methods, least-squares minimization, maximum power point (MPP), parameter estimation, photovoltaic (PV) cells.**

I. Introduction

SOLAR energy utilization can be greatly enhanced by the use of improved models of photovoltaic (PV) resources with accurate parameters [1], [2]. Consequently, various modeling attempts have been carried out over the last few decades. Based on the terminal electrical characteristics of a PV module and the physical principle behind its working, a solar cell is modeled as a current source in parallel with a p-n junction diode [3]. The inherent losses in the cell are modeled using series and shunt resistances. This model is called the single-diode model [4]–[12] with five modeling parameters: light-induced current I_L, diode dark saturation current I_s, diode quality factor m, series resistance R_s, and shunt resistance R_{sh}. Another diode, when added in parallel to the first diode, models the effect of recombination in the junction space charge region and is called the double-diode model [13]–[16]. Introduction of the second diode adds two additional parameters, namely the diode quality factor m_2 and the dark saturation current I_{s_2}. In this study, the single-diode model of the solar cell will be discussed, which offers a good tradeoff between accuracy and computational simplicity [17].

PV model parameters can be estimated using two main approaches: datasheet-based and measurement-based. In the former approach, parameters of the single-diode model are determined based on the standard test condition specifications. In a majority of these methods, I_L and I_s are determined analytically, and R_s, R_{sh}, and m are determined via numerical solution of nonlinear equations, using, for example, the Gauss–Seidel method [18]. Convergence issues related to the solution of nonlinear equations can be avoided by the use of explicit methods [6], [19]–[22]. Simplification of nonlinear equations is achieved by using the Lambert W function for modifying the exponential expression [21]. The reliability of explicit equations is shown in [22] for amorphous solar cells, wherein the single-diode model is modified to account for the effect of recombination current. The parameter values obtained from the explicit methods can be used as an initial solution, followed by further calculation for higher accuracy [21]. For computational ease, some methods ignore shunt resistance [7], [8], [14], [17], [23]–[25] and series resistance R_s [7], [14], [24], while some methods fix the diode quality factor [15], [26], [27]. This leads to an error in the prediction of the maximum power point (MPP) [11]. Additionally, the datasheet-based methods cannot be used for modeling old PV panels as the parameters degrade with time [4], [28].

The second major approach of modeling a PV array is based on actual measurements [9], [15]–[17], [25], [27]. Here, an error function is defined as the difference between the actual measured output and the predicted output of the parameterized PV model equation. Minimization of the error function is achieved using optimization techniques. For this, a number of approaches such as genetic algorithm [16], particle swarm optimization [29], Levenberg–Marquardt algorithm (LMA) [15], and gradient-based algorithms [27] are utilized. Some of these methods use datasheet specifications for estimating initial values of the parameters and then minimize the cost function using the measured data [15], [27].

A. Contributions of the Work

1) In this study, three optimization methods, namely, the LMA, trust region reflective Newton (TRRN), and steepest descent, are compared on the basis of empirical convergence speed and model-fit accuracy. The former two algorithms are a part of the optimization toolbox of MATLAB, and the third method is coded directly.

Manuscript received February 11, 2016; accepted May 17, 2016. This work was supported by CPRI, Ministry of Power, Government of India, under project "Power conversion, control, and protection technologies for microgrid."

The authors are with the Department of Electrical Engineering, Indian Institute of Science, Bangaluru 560012, India (e-mail: bharadwaj@ee.iisc.ernet.in; kunal@ee.iisc.ernet.in; vjohn@ee.iisc.ernet.in).

Color versions of one or more of the figures in this paper are available online at http://ieeexplore.ieee.org.

Digital Object Identifier 10.1109/JPHOTOV.2016.2574128

2156-3381 © 2016 IEEE. Personal use is permitted, but republication/redistribution requires IEEE permission.
See http://www.ieee.org/publications_standards/publications/rights/index.html for more information.

This article has been accepted for inclusion in a future issue of this journal. Content is final as presented, with the exception of pagination.

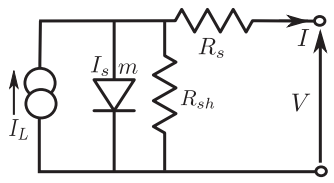


Fig. 1. Single-diode model of a solar cell.

Out of these three methods, LMA is shown to perform consistently better in terms of accuracy and speed.

2) It is shown that the convergence of the five parameter model is affected by the diode nonlinearity, and therefore, an analytical approach is better suited to evaluate I_L and I_s parameters, as already suggested in [14] and [18]. This is further modified to accommodate the measured PV data, which leads to lower errors.
3) The other three parameters are extracted from the measured data by applying least-squares minimization using LMA. However, the five- and three-parameter optimization approaches lead to a poor convergence of $R_{\rm sh}$, and therefore, it is evaluated sequentially, after the four parameters are established, again using LMA. This is shown to result in faster convergence of $R_{\rm sh}$.
4) The proposed method works well, even in the absence of a datasheet and, therefore, can be applied for old and degraded panels.
5) The proposed method is shown to perform better than the datasheet-based method and predicts the maximum power output of the PV panels with more than 97% accuracy for new panels and 95% accuracy for old panels.

This paper is organized as follows. Theoretical background of a single-diode solar cell model is discussed in Section II. Section III discusses the five parameter estimation approach. In Section IV, analytical estimation of I_L and I_s are discussed. The proposed sequential parameter estimation algorithm is presented in Section V. Results and their validation are produced in Section VI. The conclusions are summarized in Section VII.

II. Photovoltaic Panel Modeling

The single-diode model of a solar cell is shown in Fig. 1. The current–voltage (I-V) equation for a PV panel [18], with $n_{\rm s}$ cells in series, is given by

$$I = I_L - I_s\left(\exp\left(\frac{V+IR_s}{mn_sV_t}\right)-1\right)-\frac{V+IR_s}{R_{\rm sh}}. \quad (1)$$

This equation forms the basis for modeling a PV panel. Here, V and I refer to the terminal voltage and current. The thermal voltage is defined as $V_t = kT/q$, where k is Boltzman's constant, T is the temperature in K, and q is the charge of an electron. Parameter estimation refers to the evaluation of the parameters of (1), namely, the light-induced current I_L, diode dark saturation current I_s, diode quality factor m, series resistance R_s, and shunt resistance $R_{\rm sh}$. For a PV array, the above-mentioned parameters represent the equivalent values as per the series and parallel connection of panels [18].

TABLE I
Details of The Dataset Under Case Study

Dataset	Date	Time	Sky	Panel	Data points
A	21/3/15	16:00	Clear	300 W new	17
B	20/8/15	12:00	Cloudy	300 W new	13
C	21/5/13	16:00	Clear	210 W old	37

III. Parameter Estimation

The first step in measurement-based parameter estimation is the characterization of PV panels. Characterization refers to the measurement of terminal characteristics of a PV panel for different irradiation and temperature conditions. To obtain the complete characteristics, load resistance, as seen by the PV panels, is varied from open-circuit to short-circuit condition. This is done for different times of the day, over several months, as discussed below.

A. Data Collection

Details of the measurement setup are provided in this section. PV array terminal voltage and current were measured using Fluke 115 true RMS multimeter and LEM LA 100-P current sensor, respectively. Irradiation measurement was done using polycrystalline solar-cell-based reference cell meter. Fluke 61 infrared thermometer was used for temperature measurement. A variable load was connected across the PV panel terminals. This variable load could be controlled mechanically, when a rheostat was used, or electronically, with an electronic converter, to obtain the complete I–V characteristics.

The PV parameters are estimated for two types of panels. The first is a 300-W newly installed polycrystalline silicon panel, whose datasheet specifications are known. The second is for a 210-W 20-year-old panel array, whose datasheet specifications are not known. The location of panel placement has a latitude of 13° and a longitude of 77.6°. The panels have a fixed inclination angle of 13° to South. Panels suffered from no shadows or partial shading at the time of measurements. Climate, day, and time information for different datasets is provided in Table I. For 300-W newly installed panels, the terminal characteristics were obtained for the months of March and August. The 210-W 20-year-old array consists of six 35-W polycrystalline silicon panels, connected in parallel. The array's output characteristics were noted for the months of May, June, and July in summer and November and December in winter. As a case study, this paper discusses three distinct datasets for old and new panels, the details of which are provided in Table I. On these different datasets, least-squares minimization is applied to obtain the panel parameters.

B. Five Parameter Optimization

As a result of characterization, a large amount of data is collected in the form of I–V data points. All the sets of data points are modeled to fit PV panel's I–V equation (1) by the least-squares minimization. Each set corresponds to the current

This article has been accepted for inclusion in a future issue of this journal. Content is final as presented, with the exception of pagination.

versus voltage characteristic of the panel at a given irradiation G and panel temperature T. Data points, namely terminal voltage and current, are represented by $\{(V_i, I_i)\}_{i=1}^{n}$, where V_i and I_i represent measurements and the index $i \in [1, n]$, where n is the number of data points collected. Using the dataset, a cost function Π is constructed, which measures the quality of fit. Least-squares minimization is applied to this cost function (2), which is a nonlinear equation in five variables, as mentioned in Section II. The cost is a function of β, which is a vector of the parameters to be estimated. This cost function Π can be minimized using various optimization methods. Three of these methods are discussed in Section III-D. Considerations related to the initial conditions required for the estimation of parameters are discussed as follows:

$$\Pi(\beta) = \sum_{i=1}^{n} \left(I_i - I_L + I_s \left(\exp\left(\frac{V_i + I_i R_s}{m n_s V_t} \right) - 1 \right) + \frac{V_i + I_i R_s}{R_{\text{sh}}} \right)^2 \quad (2)$$

$$\beta = [I_L, I_s, m, R_s, R_{\text{sh}}]'. \quad (3)$$

C. Initial Conditions

For 300-W new PV panel, the initial value for the light-induced current I_L is kept the same as the short-circuit current I_{sc} for the given dataset [15]. Diode dark saturation current is taken to be $I_s = 10^{-12}$ A initially [30]. Diode quality factor m is given an initial value between 1 and 2 [15], [16], [26]. Initial values of series resistance and shunt resistance are taken as per the datasheet [31] to be $R_s = 0.5\ \Omega$ and $R_{\text{sh}} = 340\ \Omega$, respectively. For 210-W old panel array, I_L and I_s are initialized in the same manner as the new panels. However, the diode quality factor m is given an initial value close to 2.5, as this case deals with very old panels, in which the recombination effect rises in the junction, increasing m value [32]–[34]. Series resistance is generally lesser than 1 Ω, and shunt resistance is in the 1-kΩ range. To start with, R_{sh} is fixed to 1000 Ω. The initial value for R_s is set to 0.65 Ω, as it is seen to lead toward minimum cost function value in minimum number of iterations.

D. Optimization Method Comparison

Steepest descent with exact line search [35], TRRN [36], and LMA [37], [38] were used for optimization. A comparison of these three optimization methods is given in Table II for a particular characteristic of the new 300-W PV panel, corresponding to Dataset A from Table I. Based on the results of the presented dataset and other datasets considered, a detailed summary is given below.

1) The steepest descent algorithm, with the step size selected using exact line search, has slowest convergence, due to the ill-conditioned Hessian matrix. This is reflected by the highest objective function value of $\Pi = 0.05$ and maximum number of iterations, as shown in Table II.
2) LMA and TRRN have high convergence rates as seen by the number of iterations in Table II. The objective function value of LMA is seen to be the lowest for different datasets of both new and old panels. The result shown in Table II shows equal objective function value of $\Pi = 0.03$ for both LMA and TRRN, but for other datasets, LMA was seen to give lower Π values.
3) Light-induced current parameter I_L is seen to converge to its analytically predicted value, using short-circuit current, in invariably all the datasets, as shown to be 3.3 A for the present dataset A in Table II.
4) Due to diode nonlinearity, the gradient with respect to the diode dark saturation current I_s is seen to be orders of magnitude higher than the other parameters. This polarizes the gradient and, therefore, biases the optimization.
5) Gradient with respect to the shunt resistance parameter R_{sh} is seen to be orders of magnitude smaller with respect to the other parameters, as can be observed from Table II. This is expected due to the high value of R_{sh}, which appears as a square term in the denominator of the gradient expression. This leads to slow convergence with respect to R_{sh} parameter.

TABLE II
PARAMETERS OBTAINED BY THE FIVE-PARAMETER OPTIMIZATION FOR DATASET A USING THREE OPTIMIZATION ALGORITHMS

Parameters	Steepest descent	LMA	TRRN
I_L (A)	3.33	3.29	3.28
I_s (μA)	1.55	0.06	0.09
m	1.42	1.22	1.25
R_s (Ω)	0.11	0.26	0.25
R_{sh} (Ω)	340.0	340.0	417.7
Π	0.05	0.03	0.03
Gradient			
$\partial\Pi/\partial I_L$	1.2×10^{-1}	-2.8×10^{-4}	3.0×10^{-4}
$\partial\Pi/\partial I_s$	-1.1×10^{4}	9.3×10^{3}	3.3×10^{1}
$\partial\Pi/\partial m$	2.4×10^{-1}	-0.9×10^{-2}	-2.9×10^{-3}
$\partial\Pi/\partial R_s$	2.5×10^{-1}	6.4×10^{-4}	3.0×10^{-4}
$\partial\Pi/\partial R_{\text{sh}}$	-5.9×10^{-4}	3.3×10^{-6}	-9.3×10^{-8}
Iterations	800	126	128
Π versus R_{sh}	monotonically dec	minima @ 341 Ω	minima @ 429 Ω

Following this comparison, LMA will be the method of optimization for further analysis in the paper, and the results obtained by LMA will only be presented.

From the third observation, the light-induced current can be evaluated analytically. The diode dark saturation current is also evaluated analytically to prevent the influence of large gradient magnitude, which is introduced by the diode nonlinearity.

IV. THREE PARAMETER ESTIMATION WITH I_L AND I_s EVALUATED ANALYTICALLY

An approach discussed in the existing literature is to evaluate both light-induced current I_L and diode dark saturation current I_s, based on the ambient conditions at the time of measurement [14], [18], [26]. In this study, I_L is evaluated using (4) from [26]

$$I_L = I_{\text{sc}} \left(1 + \frac{R_s}{R_{\text{sh}}} \right). \quad (4)$$

I_s is evaluated using two methods, namely 1) method A, wherein I_s is estimated based on datasheet parameters [26] and 2) method

This article has been accepted for inclusion in a future issue of this journal. Content is final as presented, with the exception of pagination.

TABLE III
COMPARISON OF METHOD A AND METHOD B, OF ANALYTICALLY EVALUATING I_L AND I_s, WITH OTHER THREE PARAMETERS OBTAINED USING LMA, FOR DATASETS A AND B

	Dataset A	
	Method A	Method B
Parameter	$I_L = 3.29$ A $I_s = 0.47\ \mu$ A	$I_L = 3.29$ A $I_s = 0.39\ \mu$ A
m	1.32	1.30
R_s (Ω)	0.16	0.17
$R_{\rm sh}$ (Ω)	588.2	555.8
Π	0.0322	0.0318
Gradient		
$\partial\Pi/\partial m$	-3.8×10^{-2}	-3.8×10^{-2}
$\partial\Pi/\partial R_s$	-4.0×10^{-3}	4.0×10^{-3}
$\partial\Pi/\partial R_{\rm sh}$	-8.0×10^{-8}	8.8×10^{-8}
Stopping condition	$\frac{\Delta\Pi}{\Pi} < $ tol	$\frac{\Delta\Pi}{\Pi} < $ tol
	Dataset B	
	Method A	Method B
Parameter	$I_L = 7.10$ A $I_s = 0.80\ \mu$A	$I_L = 7.10$ A $I_s = 0.82\ \mu$A
m	1.32	1.31
R_s (Ω)	0.34	0.34
$R_{\rm sh}$ (Ω)	135.9	139.7
Π	0.0834	0.0816
Gradient		
$\partial\Pi/\partial m$	2.0×10^{-1}	-1.8×10^{-6}
$\partial\Pi/\partial R_s$	-3.4×10^{-3}	-3.2×10^{-6}
$\partial\Pi/\partial R_{\rm sh}$	3.3×10^{-8}	-0.1×10^{-8}
Stopping condition	$\frac{\Delta\Pi}{\Pi} < $ tol	$\frac{\Delta\Pi}{\Pi} < $ tol

B, where a new approach of evaluating I_s based on experimental data is introduced. In method A, I_s is computed from the measured temperature and datasheet parameters [26] as

$$I_s = \frac{I_{\text{sc},n} + K_I \Delta T}{\exp\left(\dfrac{V_{\text{oc},n} + K_V \Delta T}{m n_s V_T}\right) - 1}. \tag{5}$$

However, when the datasheet is not available, method A cannot be used, as the nominal values of the short-circuit current $I_{\text{sc},n}$, the open-circuit voltage $V_{\text{oc},n}$, and their temperature coefficients K_I and K_V are not available. In that case, experimental values of $I_{\rm sc}$ and $V_{\rm oc}$ can be taken and I_s can be computed from the proposed method B, wherein experimental values are used as shown in (6). The value of the diode quality factor, m, in method A is taken in a range from [1, 1.5] [26]. This factor for the proposed method B is based on the initial conditions discussed in Section III-C

$$I_s = \frac{I_{\text{sc,exp}}}{\exp\left(\dfrac{V_{\text{oc, exp}}}{m n_s V_T}\right) - 1}. \tag{6}$$

Table III gives a comparison of method A versus the proposed method B of analytically evaluating I_s, using experimentally obtained terminal characteristics. This proposed approach works even in the absence of datasheet. Therefore, parameters can be evaluated for dataset C, only by using the proposed method B, and hence, there cannot be a comparison of the two methods for dataset C. Datasets A and B show that the experimental method of evaluating I_s gives lower error, as shown by the objective function Π in Table III, as compared to method A. Therefore, method B is adopted. For obtaining the remaining three parameters, a refinement using sequential parameter estimation is proposed in Section V.

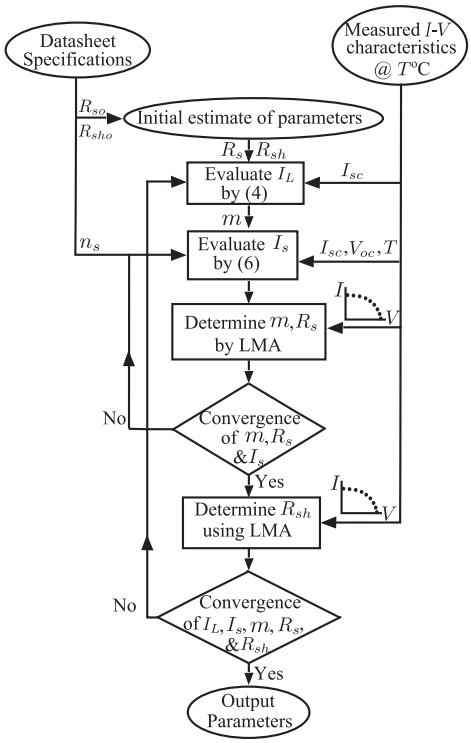


Fig. 2. Flowchart of the proposed sequential parameter estimation.

V. SEQUENTIAL PARAMETER ESTIMATION APPROACH

The five-parameter and three-parameter estimation approaches discussed above suffer from poor convergence with respect to $R_{\rm sh}$ parameter. This problem can be handled by separate evaluation of $R_{\rm sh}$, once all other parameters are established. The resulting algorithm is named as the sequential parameter estimation approach. In this method, I_L and I_s are analytically evaluated using method B, introduced in Section IV. Then, m and R_s are evaluated by applying LMA on measured data. Once all four parameters are obtained, $R_{\rm sh}$ is evaluated by single-parameter LMA optimization. This sequence is repeated till all parameters converge. The stepwise procedure is presented in the form of a flowchart in Fig. 2. As can be observed, datasheet information is required only to know the number of series-connected solar cells in a panel, which can also be observed by visual inspection of the panel. Datasheet may also be used, if available, to estimate the initial values of series and shunt resistances. Otherwise, initial parameter values can be fixed based on the existing literature or equivalent datasheets. The approach in Fig. 2 is iterative based on the convergence of the parameters. However, it is observed in the present case that the parameters converge to the third digit accuracy in the first iteration itself for all three datasets. This proposed approach is seen to solve the two problems identified

This article has been accepted for inclusion in a future issue of this journal. Content is final as presented, with the exception of pagination.

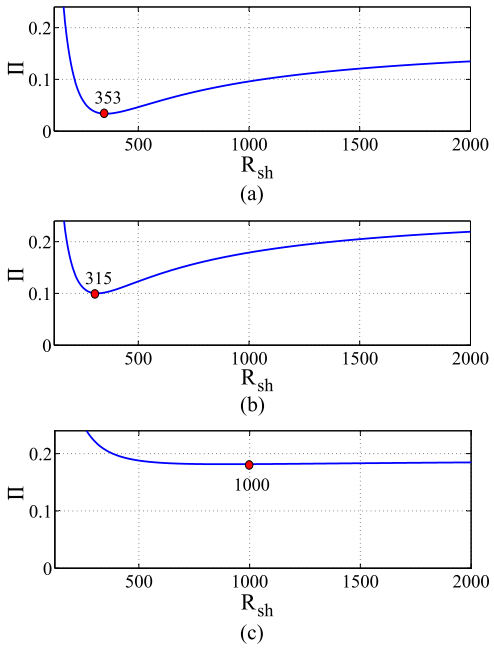


Fig. 3. Objective function Π versus $R_{\rm sh}$ for (a) dataset A, (b) dataset B, and (c) dataset C with minima for the respective curves marked.

with the PV panel parameter estimation namely: high gradient with respect to the diode dark saturation current and nonconvergence toward the shunt resistance. Thus, the advantages of the proposed approach are the lower computational complexity, owing to analytical evaluation of two parameters, and high parameter accuracy, as all parameters including $R_{\rm sh}$ converge. The convergence of $R_{\rm sh}$ is quantified in the objective function Π versus $R_{\rm sh}$ waveforms for the three considered datasets, as shown in Fig. 3. The parameters obtained using this proposed sequential parameter estimation approach are given in Table IV.

TABLE IV
PARAMETERS OBTAINED BY THE SEQUENTIAL PARAMETER ESTIMATION USING LMA FOR DIFFERENT DATASETS

Dataset A	
Parameter	$I_L = 3.29$ A $I_s = 0.39\ \mu$A
m	1.30
R_s (Ω)	0.14
Π	0.03
Gradient	
$\partial\Pi/\partial m$	-3.6×10^{-2}
$\partial\Pi/\partial R_s$	0.4×10^{-3}
$R_{\rm sh}$ (Ω)	353.4
Stopping condition	$\frac{\Delta\Pi}{\Pi} < $ tol
Π versus $R_{\rm sh}$	minima @ 353 Ω
Dataset B	
Parameter	$I_L = 7.10$ A $I_s = 0.82\ \mu$A
m	1.31
R_s (Ω)	0.36
Π	0.10
Gradient	
$\partial\Pi/\partial m$	-3.6×10^{-6}
$\partial\Pi/\partial R_s$	-4.0×10^{-6}
$R_{\rm sh}$ (Ω)	314.5
Stopping condition	$\frac{\Delta\Pi}{\Pi} < $ tol
Π versus $R_{\rm sh}$	minima @ 315 Ω
Dataset C	
Parameter	$I_L = 2.61$ A $I_s = 1.22$ mA
m	2.47
R_s (Ω)	0.71
Π	0.18
Gradient	
$\partial\Pi/\partial m$	2.6×10^{-6}
$\partial\Pi/\partial R_s$	4.6×10^{-6}
$R_{\rm sh}$ (Ω)	1000.0
Stopping condition	current step size $<$ tol
Π vs. $R_{\rm sh}$	minima @ 1000 Ω

VI. RESULTS AND VALIDATION

A. Discussion of Obtained Parameters

As the light intensity increased from dataset A to B, light-induced current is seen to scale linearly. Temperature of the 300-W PV panel for dataset A was noted to be 41 °C, and for dataset B, it was 47 °C. The ratio of the dark saturation currents for the two cases is seen to be 2.1, which is in close agreement with 2.4 as evaluated from the method described in [11], for given temperatures. Due to the increase in the light intensity, $R_{\rm sh}$ is seen to decrease, in agreement with the results predicted in [11], [39], and [40]. With the increase in temperature, R_s is seen to increase from dataset A to dataset B, as expected from [23]. When old panel and new panel parameters are compared, it can be observed that the diode quality is deteriorated in old panels as depicted by almost doubling of the diode quality factor and an increase in the diode dark saturation current from microampere to milliampere range. The power output for the old panels is seen to be around one-tenth of its rating, for a 4:00 P.M. measurement, depicted by dataset C, as compared with one-third output by the new panels for 4:00 P.M. reading, shown as dataset A. This is due to the deterioration with time of the 20-year-old panels.

B. Comparison With the Datasheet Method

To validate the proposed method, experimental results are compared with the PV panel terminal characteristics as estimated from the proposed method and compared with the results, as predicted from the datasheet-based method [18]. The results for two such datasets are shown in Fig. 4(a) and (b) for the 300-W newly installed PV panel. Fig. 4(a) depicts a clear sky measurement corresponding to dataset A. For this case, both the datasheet method and the proposed method give good results. However, for the cloudy sky case of dataset B, depicted in Fig. 4(b), the datasheet-based method has significant error in the output, when compared with the actual measurements. It can be observed that the proposed measurement-based method is more reliable than the datasheet-based approach, when the percentage

This article has been accepted for inclusion in a future issue of this journal. Content is final as presented, with the exception of pagination.

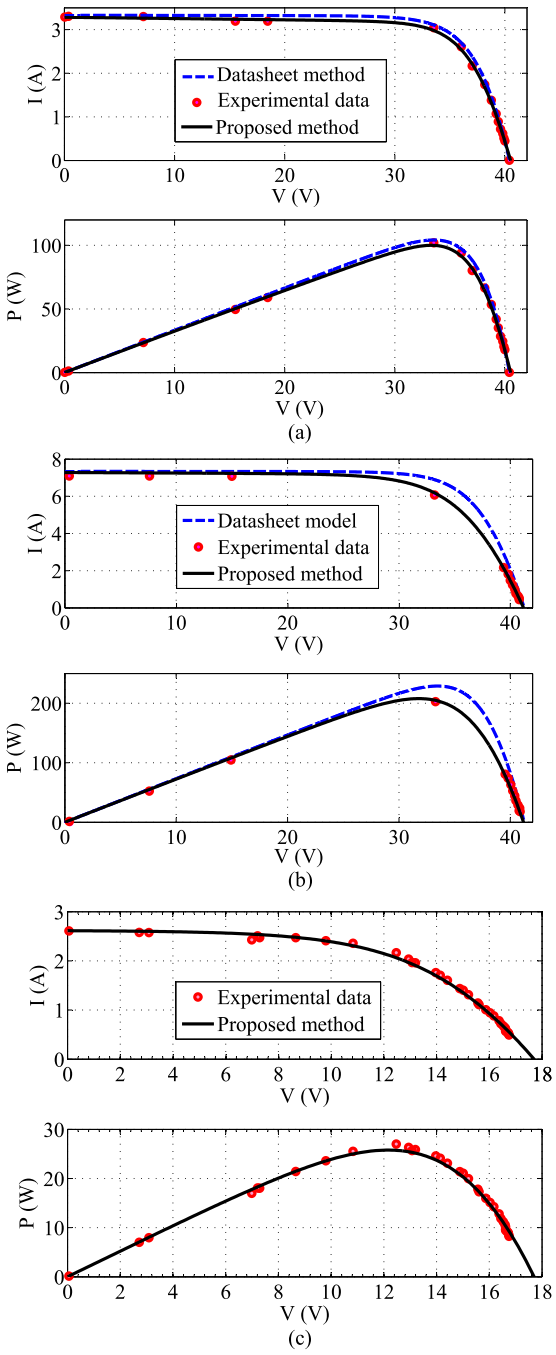


Fig. 4. Dataset and curve-fit for (a) dataset A, $G = 385$ W/m^2, $T = 41\,^\circ$C, (b) dataset B, $G = 830$ W/m^2, $T = 47\,^\circ$C, and (c) dataset C, $G = 300$ W/m^2, $T = 38\,^\circ$C. Circular points represent the actual experimental I–V and P–V characteristics of the PV panel array, the solid line shows the curve obtained from the estimated parameters of the proposed method, and the dashed line shows the I–V and P–V curves obtained from the datasheet method [18].

of the diffused light is higher, and performs equally well with the datasheet-based method when the direct irradiation is dominant. Fig. 4(c) shows the I–V and P–V characteristics obtained using the proposed method and the experimental dataset C, representing old panels. Since there is no datasheet for these panels, to validate the results, the MPP predicted from the model is compared with the experimental results, as shown in Section VI-C.

TABLE V
DEVIATION OF THE DATASHEET METHOD AND THE PROPOSED METHOD FROM EXPERIMENTAL MPP FOR DIFFERENT DATASETS

Dataset A					
MPP	Exp	Datasheet	Error	Sequential optimization	Error
V (V)	33.5	33.4	−0.3%	32.8	−2.1%
I (A)	3.0	3.1	3.3%	3.0	0.1%
P (W)	102.0	104.1	2.1%	100.0	−2.0%
Dataset B					
MPP	Exp	Datasheet	Error	Sequential optimization	Error
V (V)	33.0	34.0	3.0%	32.0	−3.0%
I (A)	6.1	6.7	9.8%	6.5	6.6%
P (W)	202.0	228.0	12.9%	208.0	3.0%
Dataset C					
MPP	Exp	Datasheet	Error	Sequential optimization	Error
V (V)	12.47 V	–	–	12.21 V	2.08%
I (A)	2.17 A	–	–	2.12 A	2.07%
P (W)	27.0 W	–	–	25.9 W	4.15%

C. Theoretical Estimation of Maximum Power Point

The relationship between MPP voltage V_{mpp} and MPP current I_{mpp}, as a function of irradiation and temperature, is derived in [18]. This along with the derived PV model parameters can be used to estimate the MPP. A comparison of the datasheet method and the proposed sequential parameter estimation method, with the experimental MPP values, is presented in Table V for the new 300-W PV panel by datasets A and B. It must be noted that for the clear sky case, the proposed method performs as good as the datasheet method. However, for cloudy sky conditions, error for the proposed method is 3%, as compared with 12.9% for the datasheet-based model. As shown in Table V, MPP estimated from the proposed method for dataset C matches well with the experimental MPP, with an error of less than 5%, even for old panels.

The parameters obtained from the sequential optimization approach can be applied to a general array configuration and for varying environmental conditions of irradiation and temperature, as discussed in Appendix A. It is also seen that the use of the proposed approach provides better accuracy at predicting the MPP when compared with the datasheet-based approach, when applied to cloudy conditions.

VII. CONCLUSION

PV array parameter extraction was achieved using sequential optimization method along with the LMA. It was demonstrated that fast convergence and high parameter accuracy can be ensured by analytical evaluation of the light-induced current I_L and diode dark saturation current I_s, and separate sequential evaluation of the shunt resistance R_{sh}, respectively. A modification to the analytical evaluation of I_s was suggested, which made the proposed method compatible to situations where the datasheet is not available or if the panels are old and degraded. The sequential optimization approach is seen to perform at par with the datasheet-based method for clear

This article has been accepted for inclusion in a future issue of this journal. Content is final as presented, with the exception of pagination.

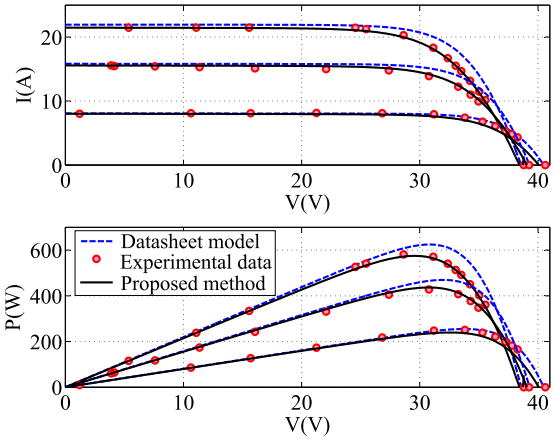


Fig. 5. Dataset and predicted output for (i) 2:00 P.M., April 25, 2016, $G = 830$ W/m^2, $T = 62\,^\circ$C, (ii) 3:00 P.M., April 25, 2016, $G = 600$ W/m^2, $T = 53\,^\circ$C, and (iii) 4:00 P.M., April 25, 2016, $G = 300$ W/m^2, $T = 36\,^\circ$C. Circular points represent the actual experimental I–V and P–V characteristics of the PV panel array, solid line shows the curve obtained from the estimated parameters of the proposed method, and dashed line shows the I–V and P–V curves obtained from datasheet method [18].

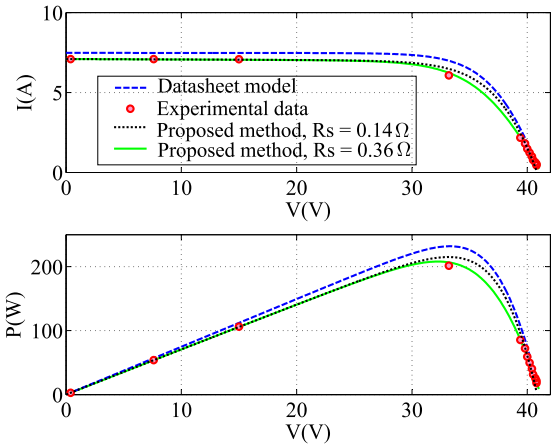


Fig. 6. Dataset and predicted output for dataset B, $G = 830$ W/m^2, and $T = 47\,^\circ$C. Circular points represent the actual experimental I–V and P–V characteristics of the PV panel array, the solid line shows the curve obtained from the estimated parameters of the proposed method ($R_s = 0.36\,\Omega$), the dotted line shows the use of scaled clear sky parameters ($R_s = 0.14\,\Omega$), and the dashed line shows the I–V and P–V curves obtained from the datasheet method [18].

sky conditions and better than the datasheet-based method for cloudy sky conditions, with an improvement in MPP prediction accuracy of 10%. This method being measurement-based also applies to old panels, for which degradation with time cannot be predicted with datasheet specifications. The novel parameter estimation algorithm predicts the parameters of new as well as old panels with an overall MPP prediction accuracy of more than 95%.

Appendix A
Scaling of Parameters With Ambient Conditions

To predict the output of the PV system for any varying ambient conditions, the system parameters need to be expressed as the function of irradiation and temperature. I_L as a function of G and T can be written as (7) [11] and can be computed once its value at a given light G_o and temperature T_o is known. I_s as a function of T is given in (5) from [26]

$$I_L = I_{L,G_o} \times \left(\frac{G}{G_o}\right) \times (1 + K_I(T - T_o)). \tag{7}$$

The diode quality factor, series resistance, and shunt resistance are considered constant [26]. Output prediction can further be improved when variation of these three parameters with ambient conditions is considered. To show the validity of the proposed method in predicting the output of the system for any given ambient conditions, three new 300-W PV panels are connected in parallel, and their output, irradiation, and temperature are noted for three different times of a day. For these ambient conditions, the output predicted by the datasheet model [18] and the proposed method are compared with the experimental output. The results shown in Fig. 5 indicate a good match between the measured data and that obtained using the parameters from Table IV.

Appendix B
Use of Clear Sky Parameters for Cloudy Ambient Conditions

The clear sky parameters from Table IV scaled using (5) and (7) are used to evaluate the output characteristics of the panel under cloudy conditions. It is observed from Fig. 6 that using the clear sky parameters ($R_s = 0.14\,\Omega$) leads to 94% MPP prediction accuracy as compared with 97% when the cloudy sky parameters ($R_s = 0.36\,\Omega$) are used. However, it can be seen that the MPP prediction accuracy with clear sky parameters is better than the 87% MPP prediction accuracy obtained with datasheet model parameters.

References

[1] E. DallAnese, S. V. Dhople, B. B. Johnson, and G. B. Giannakis, "Optimal dispatch of residential photovoltaic inverters under forecasting uncertainties," *IEEE J. Photovoltaics*, vol. 5, no. 1, pp. 350–359, Jan. 2015.

[2] J. W. Zapata, M. A. Perez, S. Kouro, A. Lensu, and A. Suuronen, "Design of a cleaning program for a PV plant based on analysis of energy losses," *IEEE J. Photovoltaics*, vol. 5, no. 6, pp. 1748–1756, Nov. 2015.

[3] M. Sitbon, J. Leppaho, T. Suntio, and A. Kuperman, "Dynamics of photovoltaic-generator-interfacing voltage-controlled buck power stage," *IEEE J. Photovoltaics*, vol. 5, no. 2, pp. 633–640, Mar. 2015.

[4] J. D. Bastidas-Rodrguez, E. Franco, G. Petrone, C. A. Ramos-Paja, and G. Spagnuolo, "Model-based degradation analysis of photovoltaic modules through series resistance estimation," *IEEE Trans. Ind. Electron.*, vol. 62, no. 11, pp. 7256–7265, Nov. 2015.

[5] E. A. Silva, F. Bradaschia, M. C. Cavalcanti, and A. J. Nascimento, "Parameter estimation method to improve the accuracy of photovoltaic electrical model," *IEEE J. Photovoltaics*, vol. 6, no. 1, pp. 278–285, Jan. 2016.

[6] S. Shongwe and M. Hanif, "Comparative analysis of different single-diode PV modeling methods," *IEEE J. Photovoltaics*, vol. 5, no. 3, pp. 938–946, May 2015.

[7] W. Xiao, F. F. Edwin, G. Spagnuolo, and J. Jatskevich, "Efficient approaches for modeling and simulating photovoltaic power systems," *IEEE J. Photovoltaics*, vol. 3, no. 1, pp. 500–508, Jan. 2013.

[8] O. Breitenstein, "An alternative one-diode model for illuminated solar cells," *IEEE J. Photovoltaics*, vol. 4, no. 3, pp. 899–905, May 2014.

[9] F. Caracciolo, E. Dallago, D. G. Finarelli, A. Liberale, and P. Merhej, "Single-variable optimization method for evaluating solar cell and solar

This article has been accepted for inclusion in a future issue of this journal. Content is final as presented, with the exception of pagination.

module parameters," *IEEE J. Photovoltaics*, vol. 2, no. 2, pp. 173–180, Apr. 2012.
[10] V. Lo Brano, A. Orioli, and G. Ciulla, "On the experimental validation of an improved five-parameter model for silicon photovoltaic modules," *Sol. Energy Mater. Sol. Cells*, vol. 105, pp. 27–39, Oct. 2012.
[11] W. De Soto, S. Klein, and W. Beckman, "Improvement and validation of a model for photovoltaic array performance," *Sol. Energy*, vol. 80, no. 1, pp. 78–88, Jan. 2006.
[12] H. Tian, F. Mancilla-David, K. Ellis, E. Muljadi, and P. Jenkins, "A cell-to-module-to-array detailed model for photovoltaic panels," *Sol. Energy*, vol. 86, no. 9, pp. 2695–2706, Sep. 2012.
[13] M. Pavlov *et al.*, "Experimental and numerical study of the influence of string mismatch on the yield of pv modules augmented by static planar reflectors," *IEEE J. Photovoltaics*, vol. 5, no. 6, pp. 1686–1691, Nov. 2015.
[14] B. C. Babu and S. Gurjar, "A novel simplified two-diode model of photovoltaic (PV) module," *IEEE J. Photovoltaics*, vol. 4, no. 4, pp. 1156–1161, Jul. 2014.
[15] F. Attivissimo, A. Di Nisio, M. Savino, and M. Spadavecchia, "Uncertainty analysis in photovoltaic cell parameter estimation," *IEEE Trans. Instrum. Meas.*, vol. 61, no. 5, pp. 1334–1342, May 2012.
[16] L. Zhang and Y. F. Bai, "Genetic algorithm-trained radial basis function neural networks for modelling photovoltaic panels," *Eng. Appl. Artif. Intell.*, vol. 18, no. 7, pp. 833–844, Oct. 2005.
[17] L. Cristaldi, M. Faifer, M. Rossi, and F. Ponci, "A simple photovoltaic panel model: Characterization procedure and evaluation of the role of environmental measurements," *IEEE Trans. Instrum. Meas.*, vol. 61, no. 10, pp. 2632–2641, Oct. 2012.
[18] A. Chatterjee, A. Keyhani, and D. Kapoor, "Identification of photovoltaic source models," *IEEE Trans. Energy Convers.*, vol. 26, no. 3, pp. 883–889, Sep. 2011.
[19] A. Ortiz-Conde, D. Lugo-Munoz, and F. J. Garcia-Sanchez, "An explicit multiexponential model as an alternative to traditional solar cell models with series and shunt resistances," *IEEE J. Photovoltaics*, vol. 2, no. 3, pp. 261–268, Jul. 2012.
[20] P. H. Huang, W. Xiao, J. C. H. Peng, and J. L. Kirtley, "Comprehensive parameterization of solar cell: Improved accuracy with simulation efficiency," *IEEE Trans. Ind. Electron.*, vol. 63, no. 3, pp. 1549–1560, Mar. 2016.
[21] C. A. R.-P. J. Accarino, G. Petrone and G. Spagnuolo, "Symbolic algebra for the calculation of the series and parallel resistances in pv module model," in *Proc. Int. Conf. Clean Elect. Power*, Jun. 2013, pp. 62–66.
[22] G. Petrone and G. Spagnuolo, "Parameters identification of the single-diode model for amorphous photovoltaic panels," in *Proc. Int. Conf. Clean Elect. Power*, Jun. 2015, pp. 105–109.
[23] W. Xiao, W. Dunford, and A. Capel, "A novel modeling method for photovoltaic cells," in *Proc. Power Electron. Spec. Conf.*, Jun. 2004, vol. 3, pp. 1950–1956.
[24] Y. Mahmoud, W. Xiao, and H. Zeineldin, "A simple approach to modeling and simulation of photovoltaic modules," *IEEE Trans. Sustain. Energy*, vol. 3, no. 1, pp. 185–186, Jan. 2012.
[25] J. M. Blanes, F. J. Toledo, S. Montero, and A. Garrigós, "In-site real-time photovoltaic I-V curves and maximum power point estimator," *IEEE Trans. Power Electron.*, vol. 28, no. 3, pp. 1234–1240, Mar. 2013.
[26] M. Villalva, J. Gazoli, and E. Filho, "Comprehensive approach to modeling and simulation of photovoltaic arrays," *IEEE Trans. Power Electron.*, vol. 24, no. 5, pp. 1198–1208, May 2009.
[27] F. Adamo, F. Attivissimo, A. Di Nisio, A. Lanzolla, and M. Spadavecchia, "Parameters estimation for a model of photovoltaic panels," in *Proc. XIX IMEKO World Congr. Fundam. Appl. Metrol.*, Sep. 2009, pp. 6–11.
[28] E. L. Meyer and E. E. van Dyk, "Assessing the reliability and degradation of photovoltaic module performance parameters," *IEEE Trans. Rel.*, vol. 53, no. 1, pp. 83–92, Mar. 2004.
[29] V. Khanna, B. Das, D. Bisht, and P. Singh, "A three diode model for industrial solar cells and estimation of solar cell parameters using PSO algorithm," *Renew. Energy*, vol. 78, pp. 105–113, Feb. 2015.
[30] C. Andres, "The recombination parameter J0," *Energy Procedia*, vol. 55, pp. 53–62, Mar. 2014.
[31] *Photovoltaic Module, ES 275-295 P72*, EMMVEE Photovoltaics, Bengaluru, India, 2012.
[32] S. Steingrube *et al.*, "Explanation of commonly observed shunt currents in c-Si solar cells by means of recombination statistics beyond the Shockley-Read-Hall approximation," *J. Appl. Phys.*, vol. 110, no. 1, Jul. 2011, Art. no. 014515.
[33] K. Nishioka, N. Sakitani, Y. Uraoka, and T. Fuyuki, "Analysis of multicrystalline silicon solar cells by modified 3-diode equivalent circuit model taking leakage current through periphery into consideration," *Sol. Energy Mater. Sol. Cells*, vol. 91, no. 13, pp. 1222–1227, Aug. 2007.
[34] R. Chavali, J. Wilcox, B. Ray, J. Gray, and M. Alam, "Correlated nonideal effects of dark and light I-V characteristics in a-Si/c-Si heterojunction solar cells," *IEEE J. Photovoltaics*, vol. 4, no. 3, pp. 763–771, May 2014.
[35] D. G. Luenberger and Y. Ye, *Linear and Nonlinear Programming*, vol. 116. New York, NY, USA: Springer, 2008.
[36] MathWorks, (2016). Optimization Toolbox: lsqnonlin (R2016a). Retrieved Jan., 2016 from http://in.mathworks.com/help/optim/ug/lsqnonlin.html
[37] E. K. Chong and S. H. Zak, *An Introduction to Optimization*, vol. 76. New York, NY, USA: Wiley, 2013.
[38] A. D. Belegundu and T. R. Chandrupatla, *Optimization Concepts and Applications in Engineering*. Cambridge, U.K.: Cambridge Univ. Press, 2011.
[39] K. Ruhle, M. K. Juhl, M. D. Abbott, and M. Kasemann, "Evaluating crystalline silicon solar cells at low light intensities using intensity-dependent analysis of I-V parameters," *IEEE J. Photovoltaics*, vol. 5, no. 3, pp. 926–931, May 2015.
[40] K. J. Sauer, T. Roessler, and C. W. Hansen, "Modeling the irradiance and temperature dependence of photovoltaic modules in PVsyst," *IEEE J. Photovoltaics*, vol. 5, no. 1, pp. 152–158, Jan. 2015.



Pallavi Bharadwaj (S'16) received the B.E. degree in electrical engineering from the Delhi College of Engineering, New Delhi, India, in 2012 and the M.E. degree in electrical engineering from the Indian Institute of Science, Bangaluru, India, in 2014, where she is currently working toward the Ph.D. degree with the Department of Electrical Engineering.

Her current research interests include photovoltaic power conversion, power electronics for renewable energy systems, grid connected power converters, and energy storage issues.



Kunal Narayan Chaudhury (SM'14) received the B.E. in electrical engineering from Jadhavpur University in 2003, the M.E. degree in electrical engineering from the Indian Institute of Science in 2005, and the Ph.D. degree in computer, communication, and information sciences from the Ecole Polytechnique Federale de Lausanne (EPFL), Lausanne, Switzerland, in 2011.

He is currently an Assistant Professor in electrical engineering with the Indian Institute of Science, Bangaluru, India. His research interests include fast algorithms for image and video processing, convex optimization models and fast solvers, sensor network localization, multiview registration, and Fourier and wavelet analysis.

Dr. Chaudhury is a Senior Member of the IEEE Signal Processing Society and a Member of the Society for Industrial and Applied Mathematics. He is on the Editorial Board of the *SPIE Journal of Electronic Imaging*.



Vinod John (SM'07) received the B.Tech. degree in electrical engineering from the Indian Institute of Technology, Madras, Chennai, India in 1992; the M.S.E.E. degree from the University of Minnesota, Minneapolis, MN, USA in 1994; and the Ph.D. degree from the University of Wisconsin-Madison, Madison, WI, USA in 1999.

He has worked in research and development positions with GE Global Research, Niskayuna, NY, USA, and Northern Power Systems Inc., Barre, VT, USA. He is currently an Associate Professor with the Department of Electrical Engineering, Indian Institute of Science, Bangaluru, India. His primary research interests include power electronics and distributed generation, power quality, high-power converters, and motor drives.

Accepted Manuscript



Spectroscopic investigation on thermally stable Dy^{3+} doped zinc phosphate glass for white light emitting diodes

Kaushal Jha, M. Jayasimhadri

PII: S0925-8388(16)32056-4

DOI: 10.1016/j.jallcom.2016.07.024

Reference: JALCOM 38192

To appear in: *Journal of Alloys and Compounds*

Received Date: 21 April 2016

Revised Date: 16 June 2016

Accepted Date: 3 July 2016

Please cite this article as: K. Jha, M. Jayasimhadri, Spectroscopic investigation on thermally stable Dy^{3+} doped zinc phosphate glass for white light emitting diodes, *Journal of Alloys and Compounds* (2016), doi: 10.1016/j.jallcom.2016.07.024.

This is a PDF file of an unedited manuscript that has been accepted for publication. As a service to our customers we are providing this early version of the manuscript. The manuscript will undergo copyediting, typesetting, and review of the resulting proof before it is published in its final form. Please note that during the production process errors may be discovered which could affect the content, and all legal disclaimers that apply to the journal pertain.

ACCEPTED MANUSCRIPT

Spectroscopic investigation on thermally stable Dy^{3+} doped zinc phosphate glass for white light emitting diodes

Kaushal Jha, M. Jayasimhadri*

Luminescent Materials Research Lab, Department of Applied Physics, Delhi Technological University, Delhi 110 042, India

Abstract:

Optically transparent dysprosium ions doped lead zinc phosphate glasses have been prepared via melt quenching technique to study the luminescent properties and their applications for white light emitting diodes (w-LEDs). X-ray diffraction (XRD) spectrum confirmed the amorphous nature of the as-prepared glass. The glass transition temperature (T_g) and thermal stability (ΔT) were determined by using Differential Scanning Calorimetry (DSC). The vibrational features were characterized by Raman and FT-IR, which indicate the presence of poly-phosphate structure dominated by Q^2 and Q^1 structural units. The intense emission bands observed at 482 nm (blue) and 574 nm (yellow), where the yellow to blue intensity ratio for all excitation wavelengths (NUV to blue range) were found to lie in the vicinity of unity, yielding to intense white light emission. The evaluated CIE chromaticity coordinates (0.309, 0.341) for the optimized glass (GP10) at 350 nm excitation fall in the pure white region, which is in proximity with commercial w-LED (Blue LED +YAG:Ce^{3+}) and NTSC system for white light emission. The correlated color temperature (CCT) of the optimized glass is 6547 K, which represents cool white light emission. The decay profiles have been measured for the excited $^4F_{9/2}$ level and analyzed.

****Corresponding author:*** *Tel.:* +91-9013553360

E-mail: jayaphysics@yahoo.com (M. Jayasimhadri)

ACCEPTED MANUSCRIPT

1. Introduction

In recent years, solid-state lighting (SSL) has evolved as the vital and viable alternative in lighting technology, as it is environment-friendly, reliable and contributes to the reduction in energy consumption. In SSL, w-LEDs are receiving great importance as they have longer life-span, highly efficient and consume less power as compared with their counterparts such as incandescent bulbs and fluorescent tubes. At present, w-LEDs are fabricated by using blue/ near-ultraviolet (NUV)/UV LED chips as optical excitation sources with single or multiple phosphor wavelength converter models [1, 2]. In recent years, research in the field of phosphors for the development of w-LEDs has been passionately examined [3-5]. The phosphor in the form of powder suspended in the encapsulant/sealant (epoxy resin), which is a polymer material. The output emission of w-LEDs primarily depends on the thickness of the phosphor-containing epoxy and the concentration of the phosphor suspended. The luminous efficiency and color-rendering characteristics of the LEDs are dependent on the polymer sealant. However, the polymer sealant will be damaged at high temperatures, high-power and/or high-energy excitation light sources. Therefore, inorganic glasses are the right choice for potential phosphor candidate for futuristic applications, as they are highly durable and possess excellent emission property. Also, they have added advantages such as homogenous light emission, simpler manufacturing technique, lower production cost, excellent thermal and mechanical stabilities [6].

Phosphate glasses have a wide range of applications [7, 8]. However, the hygroscopic nature and poor chemical durability limit their practical applications. The addition of metal oxides in phosphate network improves the chemical durability and spontaneous emission probabilities of the glass [9, 10]. Lead oxide is a heavy metal oxide and its incorporation in the

phosphate glasses improves the chemical stability due to the formation of P-O-Pb bonds and makes it moisture resistant. Along with this, the addition of lead oxide makes these glasses more moisture resistant, since PbO plays the dual role, one as a modifier in PbO_6 structural units and the other as a glass former in PbO_4 structural units. Also, the chemical stability of lead phosphate glasses has been further improved through the creation of non-bridging oxygen atoms by incorporating a third metal oxide to the glass host [11, 12]. In recent years, ZnO-based materials have drawn the significant interest of researchers due to non-toxic, non-hygroscopic nature, low cost, direct wide band gap, intrinsic emitting property and large exciton binding energy [13]. P_2O_5-ZnO-PbO glasses show significant improvement in the chemical and physical durability while maintaining low glass transformation and softening points [14]. Rare earth ions doped glasses have a wide range of applications in the field of photonic devices such as solid state lasers, optical fibers, waveguides, w-LEDs, display devices, temperature sensors, etc. [15-21]. Among various rare earth ions, Dy^{3+} ions doped glasses are considered to be a potential candidate for white light application as they exhibit emission in the blue and yellow region.

In the present study, P_2O_5-PbO-ZnO glasses with different Dy^{3+} ion concentrations were prepared. The optimized glass has been used to examine the thermal and structural properties by using different characterization tools like XRD, DSC, FT-IR and Raman spectroscopy. The photoluminescence properties of the prepared glasses were revealed with an aim to develop it for w-LEDs application by exciting with NUV/blue LEDs.

2. Experimental procedure

Dy^{3+} ions doped zinc-lead phosphate glasses were prepared with molar composition 40 P_2O_5 - 40 PbO - 20 ZnO - x Dy_2O_3 (where x = 0.1, 0.5, 1.0, 1.5 and 2.0 mol% represented as

GP01, GP05, GP10, GP15 and GP20, respectively) via melt quenching technique. The desired quantity of $NH_4H_2PO_4$ (99%), PbO (99%), ZnO (99%) and Dy_2O_3 (99.99%) chemicals were weighed and thoroughly mixed in mortar-pestle for an hour using acetone as a wetting medium. The thoroughly mixed chemicals were placed in an alumina crucible and then placed in microcontroller based programmable muffle furnace. The mixture was kept for 1 hour at 500 °C to favor the complete decomposition of $NH_4H_2PO_4$ and was melted at 1000 °C for 1 hour to obtain a homogenized transparent melt. The melt was then poured onto a preheated brass plate held at 300 °C to obtain colorless and transparent glass samples and were annealed at the same temperature for 3 hours to remove thermal and mechanical stresses.

The XRD spectrum for the optimized glass GP10 was recorded with high-resolution X-ray diffractometer (Bruker; Model D8 advance) having nickel-filtered cu Kα radiation (λ=1.5406 Å) in the 2θ range from 20 to 60°. Thermal analysis of glass sample GP10 was carried out by Mettler Toledo, Differential Scanning Calorimetry (DSC) equipment (Model: Star-e system) under N_2 atmosphere at a heating rate of 10 °C /min from ambient temperature to 1100 °C. The Raman spectrum was recorded with Renishaw 1000 B micro-Raman spectrometer consisting of argon ion laser with an excitation wavelength of 488 nm and 17 mW of power with a spot size of 1 µm. The FT-IR was performed by Perkin Elmer's Frontier FT-IR Spectrometer, for which the pellet was prepared by mixing the glass GP10 in powdered form with KBr and then compressed mechanically at 1.5 ton. The optical absorption studies were recorded by using Shimadzu-Solidspec 3700 UV-VIS-NIR spectro-photometer.

The photoluminescence properties of the glasses were measured using Shimadzu RF-5301PC spectrofluorophotometer fitted with Xenon flash lamp. The decay analysis was

performed using an Edinburgh FLSP900, where a xenon lamp was used as an excitation source. All these characterizations were performed at room temperature (30 °C ± 3 °C).

3. Results and Discussion

3.1. Thermal and structural properties:

The XRD spectrum of the powdered glass GP10 has been represented in Fig. 1. The XRD spectrum does not indicate any crystalline features and clearly reveal the amorphous nature of the glass. The DSC curve recorded for the glass GP10 is depicted in Fig. 2. The glass transition temperature (T_g), onset crystallization temperature (T_x), peak crystallization temperature (T_p) and melting temperature (T_m) were analyzed from the DSC curve. The sharp exotherm at 560 °C depicts the peak crystallization temperature (T_p) and the other important temperatures T_g , T_x and T_m were at 390 °C, 510 °C and 920 °C, respectively. The thermal stability of the glass was determined using relation

$$\Delta T = T_x - T_g \qquad (1)$$

The higher the value of ΔT, better is the thermal stability of the glass system and the nucleation phenomenon takes place between the temperature range T_g and T_x. The value of ΔT was found to be 120 °C, which indicates that the glass is thermally stable and also better than the MgO–Al_2O_3–SiO_2–TiO_2 glass system [22], fluorophosphates glasses [23] and 50 Li_2O-50 P_2O_5:x Fe_2O_3 glass system [24]. Another, parameter for determination of thermal stability is Hurby's parameter, which is estimated by [25]:

$$K_H = \frac{T_x - T_g}{T_m - T_x} \qquad (2)$$

Where, K_H is Hruby parameter of glass stability, and higher value of this parameter indicate higher thermal stability. For thermally stable glass system, the value of K_H should be equal to or more than 0.1 [26]. The value of K_H for present glass was found to be 0.33, which confirms high thermal stability. Based on the above results, it can be stated that this glass has high thermal stability, which is one of the main prerequisites for the glass to use in w-LEDs.

3.2. Vibrational spectroscopy

The Raman and FT-IR spectrum of glass GP10 are represented in Figs. 3 and 4, respectively. The Raman spectrum represents two dominant bands around 1130 and 720 cm^{-1}. In addition to this, two shoulders are located around 990 and 1050 cm^{-1}. The peak present at 1130 cm^{-1} is ascribed to the symmetric stretching vibrations, $\upsilon_s(PO_2)^-$ of non bridging oxygen (NBO) atoms bonded to the phosphorous atoms in the Q^2 structural units, while the peak present at 720 cm^{-1} has been ascribed to the symmetric stretching vibrations of P-O-P linkages, υ_s(P-O-P). The shoulders located at 990 and 1050 cm^{-1} is designated to symmetric, $\upsilon_s(PO_3)^{2-}$ and anti-symmetric, $\upsilon_{as}(PO_3)^{2-}$ stretching vibrations of phosphorous atoms in the Q^1 chain terminating structural units [27-29]. The 1130 cm^{-1} peak represents the maximum vibrational energy of the glass and could be its phonon energy.

The FT-IR spectrum of the optimized glass (GP10) was recorded in the range 400-4000 cm^{-1}. The FT-IR spectrum has shoulders located in the range 400-550 cm^{-1} and near 739, 910, 1090, 1630, 2923 and 3460 cm^{-1}. The band in the range 400-550 cm^{-1} may be attributed to the Pb-O stretching vibrations of the PbO_4 structural units along the deformation modes of the P-O glass network [30], Zn-O tetrahedral bonds and due to the harmonic of the P–O–P bending vibrations [31]. The shoulder at 739 cm^{-1} may be ascribed to the symmetric stretching, $\upsilon_s(PO_2)$

of P-O-P linkage of Q^1 tetrahedra with non-bridging oxygens (NBOs) while the shoulder located at 910 cm^{-1} was ascribed to the asymmetric stretching, $\upsilon_{as}(PO_2)$ of P-O-P linkages of Q^2 tetrahedra [14, 32]. The shoulder ascribed at 1090 cm^{-1} is characteristic of the asymmetric stretching vibration of $P–O^-$ mode, $\upsilon_{as}(P–O^-)$, in Q^2 units. It may also be recognized that the shoulder present at 1090 cm^{-1} corresponds stretching band of P–O–Pb and/or P–O–Zn, P–O–Pb(Zn) linkages [33]. The band at 1260 cm^{-1} has been ascribed to the P=O bond stretching mode in phosphate tetrahedral. However, this peak was diminished, which indicates deploymerisation of the phosphate network [14]. The band at 1630 cm^{-1} has been ascribed to the bending vibrations of O-H bonds incorporated due to the air mixture during preparation of the KBr pellets for FTIR measurement [34]. The bands present at 2923 and 3460 cm^{-1} are due to the asymmetric stretching and symmetric stretching of the water molecule, respectively [35].

The phosphate glasses have different structures based on the ratio of oxygen to phosphorous (O/P) atoms. Depending on the O/P atomic ratio they can be either in ultra-phosphate, meta-phosphate or poly-phosphate structure. The O/P atomic ratio for ultra-phosphate structures lies in the range of 2.5 to 3 and the network consist of Q^2 and Q^3 structural units. For meta-phosphate structure, the O/P ratio is 3 and the network consist of long chains and/or ring of Q^2 structural units. The O/P atomic ratio is greater than 3 for polyphosphate structure and consists of shorter chains of Q^2 terminated by Q^1 structural units [36]. For the present glass, the O/P atomic ratio was found to be 3.25 indicating the poly-phosphate structure. The Raman and FTIR results indicated the presence of Q^2 and Q^1 structural units suggesting the poly-phosphate structure. The conclusion made from the calculated O/P atomic ratio matches well with the experimental results obtained from the Raman and FTIR spectra. The poly-phosphate structure is more stable than the meta-phosphate structure as it contains lesser number

of Q^2 structural units [37]. Therefore, the synthesized glass (GP10) containing polyphosphate structure may be more suitable for w-LEDs application.

3.3 Absorption spectra and Optical Band gap

The absorption spectrum of the glass GP10 in the region 300-1500 nm has been depicted in the inset of Fig. 5. The absorption spectrum for the glass revealed several transitions originating from the ground state $^6H_{15/2}$ to different excited states of Dy^{3+} ions such as $^6F_{11/2}$+$^6H_{9/2}$, $^6F_{9/2}$+$^6H_{7/2}$, $^6F_{7/2}$, $^6F_{5/2}$, $^6F_{3/2}$, $^4F_{9/2}$, $^4I_{15/2}$, $^4F_{7/2}$+$^4I_{13/2}$, $^6P_{7/2}$, $^4M_{17/2}$+$^6P_{3/2}$ [38]. The activator absorption bands in the UV region are less intense, which might be due to the strong absorption of the host glass in that region. The transition $^6F_{11/2}$ and $^6H_{9/2}$ corresponding to the hypersensitive transition obeying the selection rule $|\Delta S|=0$, $|\Delta L|\leq 2$, $|\Delta J|\leq 2$ and were found to be more intense as compared with other transitions [39].

The optical band gap for the glasses was estimated from the absorption spectra near the optical absorption edge by Davis and Mott through following relation [40]:

$$\alpha h\upsilon = B\left(h\upsilon - E_{opt}\right)^n \qquad (3)$$

Where, α is the absorption coefficient, h is the Planck's constant, υ is the frequency of radiation, B is constant related to band tailing parameter, E_{opt} is the optical band gap energy. The value of n depends on transition type and are assigned 1/2, 2, 1/3 and 3 for direct allowed, indirect allowed, direct forbidden and indirect forbidden transitions, respectively. The value of absorption coefficient was calculated using the following relation [41]:

$$\alpha(\upsilon) = \frac{1}{d}\, ln(\frac{I_0}{I_t}) \qquad (4)$$

Where, $\alpha(\upsilon)$ is the absorption coefficient, d is the thickness of glass sample and I_0 and I_t are the intensities of the incident and transmitted radiation, respectively. The factor $ln(I_0/I_t)$ represents the absorbance. The optical band gap energies for direct and indirect allowed transitions were calculated through Tauc's plot by extrapolating the linear region of the plot $(\alpha h\upsilon)^{1/2}$ versus $h\upsilon$ and $(\alpha h\upsilon)^2$ versus $h\upsilon$, respectively. The optical band gap E_{opt} value is the intercept on the energy axis and the slope calculated from the extrapolated linear region gives the value of B (band tailing parameter). The optical band gap values for direct and indirect allowed transitions along with band tailing parameters are tabulated in Table 1 and the band gap values for indirect allowed transitions can be observed from Fig. 5.

In most of the amorphous materials, the fundamental absorption edge follows the Urbach rule, which characterizes the extent of exponential tail. The absorption edges of an amorphous material may be due to the inter-band transitions involving tails of the localized states where the density of states fall exponentially [42]. The Urbach empirical formula is given by:

$$\alpha(\upsilon) = C\ exp(^{h\upsilon}/_{\Delta E}) \qquad (5)$$

where C is constant, ΔE is the Urbach energy indicating the width of the band tails of the localized state. The value of Urbach energy is determined by plotting a graph between $ln(\alpha(\upsilon))$ and $h\upsilon$ and then calculating the inverse of the slope obtained. The values of ΔE are presented in Table 1 and it can be observed that there is very minute variation in the values for different glasses. The lower values of ΔE, indicates lower defect concentration in the materials [43].

3.4. Luminescence properties

The photoluminescence excitation (PLE) for the glass GP10 was obtained by monitoring at emission wavelength of 574 nm as depicted in Fig. 6. The excitation spectrum reveals eight

different peaks centered at 324, 337, 350, 364, 387, 425, 452 and 473 nm corresponding to the ($^6H_{15/2} \rightarrow {}^4M_{17/2}$, $^6P_{3/2}$), ($^6H_{15/2} \rightarrow {}^4I_{9/2}$), ($^6H_{15/2} \rightarrow {}^6P_{7/2}$), ($^6H_{15/2} \rightarrow {}^4I_{11/2}$, $^6P_{5/2}$), ($^6H_{15/2} \rightarrow {}^4I_{13/2}$, $^4F_{7/2}$), ($^6H_{15/2} \rightarrow {}^4G_{11/2}$), ($^6H_{15/2} \rightarrow {}^4I_{15/2}$) and ($^6H_{15/2} \rightarrow {}^4F_{9/2}$) f-f electronic transitions of Dy^{3+} ions, respectively [30,44]. The prepared glass may be a potential candidate for w-LEDs when excited in UV/blue region. The peaks observed at 350 nm has the maximum intensity and the emission spectra were recorded for four intense excitation bands centered at 350, 364, 387 and 452 nm. In addition to these excitation bands, emission spectrum was also measured by monitoring excitation at 400 nm, as this wavelength matches with the emission of commercial GaN LED and may be combined with Dy^{3+} doped glass for generation of w-LEDs [45].

The emission spectra for glasses exhibit two intense emission peaks at 482 (blue) and 574 nm (yellow) under 350 nm excitation, which corresponds to $^4F_{9/2} \rightarrow {}^6H_{15/2}$ and $^4F_{9/2} \rightarrow {}^6H_{13/2}$ electronic transitions of Dy^{3+} ions, respectively as shown in Fig. 7. The $^4F_{9/2} \rightarrow {}^6H_{15/2}$ transition corresponds to magnetic dipole transition while the $^4F_{9/2} \rightarrow {}^6H_{13/2}$ transition belongs to forced electric dipole (hypersensitive) transition obeying the selection rule ($\Delta S=0$, $\Delta L=2$, $\Delta J=2$). The intensity of $^4F_{9/2} \rightarrow {}^6H_{15/2}$ transition is stronger than that of $^4F_{9/2} \rightarrow {}^6H_{13/2}$ transition and can be explained according to the mentioned reason: The $^4F_{9/2} \rightarrow {}^6H_{13/2}$ transition is hypersensitive and strongly depends on the host lattice while the $^4F_{9/2} \rightarrow {}^6H_{15/2}$ transition hardly varies with the crystal field strength of host lattice. When Dy^{3+} ions are located at high-symmetry sites with an inversion center, $^4F_{9/2} \rightarrow {}^6H_{15/2}$ transition is prominent and when Dy^{3+} ions are located at low-symmetry sites without inversion centers then $^4F_{9/2} \rightarrow {}^6H_{13/2}$ transition is dominant [46]. The $^4F_{9/2} \rightarrow {}^6H_{15/2}$ transition being prominent confirms the location of the active ions in the high symmetry environment with an inversion center. The shape of the emission band and position did not vary significantly with increasing Dy^{3+} ions concentration as 4f electrons remain shielded by the external electric fields of outer $5s^2 5p^6$ electrons

[47]. Fig. 8 and the inset of Fig. 8 clearly represent the relative emission intensity variation for glass GP10 under 350, 364, 387, 400 and 452 nm excitations. The maximum emission intensity was obtained at 350 nm excitation and the inset of Fig. 8 clearly indicates that the glass (GP10) can be efficiently excited by wide range of wavelengths (n-UV to blue) for white light generation.

The simplified energy level diagram of Dy^{3+} doped zinc-lead phosphate glass has been depicted in Fig. 9. The $^4F_{9/2}$ electronic state gets highly and rapidly populated by non- radiative relaxation of the higher lying states. The radiative transition takes place from $^4F_{9/2}$ giving rise to intense blue and yellow emission. These intense emission bands arise as the energy difference between the states lying above $^4F_{9/2}$ (21000 cm^{-1}) is minutely small, and there is large separation (~6000 cm^{-1}) between $^4F_{9/2}$ and the next lower state $^6F_{1/2}$. In addition to this, high phonon energy of the lead-zinc phosphate is another important parameter for this intense visible emission [48].

The intensity of the blue ($^4F_{9/2}\rightarrow{}^6H_{15/2}$) and yellow ($^4F_{9/2}\rightarrow{}^6H_{13/2}$) emission bands enhanced with increasing Dy^{3+} ions concentration up to 1 mol % and decreased with further increase in Dy^{3+} ions concentration. The decrease in the intensity arises due to concentration quenching phenomenon. This effect arises due to resonant energy transfer (RET) between Dy^{3+}-Dy^{3+} ions and various cross relaxation channels as shown in Fig. 9. The resonant energy transfer takes place between $^4F_{9/2}\rightarrow{}^6H_{15/2}$ energy levels of Dy^{3+} ions. The cross relaxation channels CRC1 and CRC2 are denoted as $^4F_{9/2}+{}^6H_{15/2}\rightarrow{}^6H_{5/2}+({}^6H_{7/2},{}^6F_{9/2})$ and $^4F_{9/2}+{}^6H_{15/2}\rightarrow{}^6F_{3/2}+({}^6H_{9/2},\ {}^6F_{11/2})$ [49].

The luminescence intensity ratio of yellow to blue (Y/B) is vital for white light emission and was calculated for four different excitations at 350, 387, 400 and 452 nm for different concentration of Dy^{3+} ions and is given in Table 2. The Y/B intensity ratio varied minutely in the proximity of unity (0.86 to 0.98) by varying the concentration and excitation wavelengths, which represents the

excellent stability of the color coordinates against both parameters. The intensity ratio was almost constant, which indicates that the local environment around Dy^{3+} ions is invariant with concentration [50].

3.5. Colorimetry calculations

Various colorimetric properties of Dy^{3+} doped zinc-lead phosphate glasses for different concentrations, and excitation wavelengths are represented in Table. 2. The finest CIE coordinates calculated based on the emission spectra of different glasses under few different excitations 350, 387, 400, 452 nm are shown in Fig. 10. The excellent white light chromaticity coordinates (0.309, 0.341) observed for glass GP10 at 350 nm excitation and are very close to the standard equal energy white light point (0.333, 0.333). The optimized glass GP10 exhibits better white light luminescence coordinates when compared with Dy^{3+} doped different glass hosts LBO [44] (0.342, 0.372), ZBP [45] (0.340, 0.390), NbFS [51] (0.330, 0.370) and extremely close to the chromaticity coordinates of commercial pc-LED [52] (0.32, 0.32) and NTSC white light (0.310, 0.316).

The correlated color temperature (CCT) of a white light source has been defined as the temperature of a Planckian black-body radiator whose color is closest to the color of the white light source and usually measure the quality of light source [53]. The value of CCT has been calculated by an analytical equation proposed by McCamy [54] given by:

$$CCT = - 449\, n^3 + 3525\, n^2 - 6823.3\, n + 5520.33 \qquad (6)$$

where $n = (x - x_e) / (y - y_e)$ and $x_e = 0.332$, $y_e = 0.186$ is the epicenter. The CCT observed for different excitations with varying Dy^{3+} ions concentration has been presented in Table 2. The values of CCT for all synthesized glasses were found to be in the range 5174 to 8366 K, which

falls in the cool white light region. The value of CCT for the glass GP10 at 350, 387, 400 and 452 nm excitations were found to be 6547, 5173, 6138 and 7674 K, respectively. The higher value of CCT indicates better visual acuity and high brightness perception [55]. The CCT values lie in the cool white light region signifying the possibility of these glasses for the application in w-LEDs for outdoor illumination.

The color purity or color saturation of a light source has been defined the distance on the chromaticity diagram between the (*x*, *y*) color-coordinate point of the test source and the coordinates of the equal-energy point divided by the distance between the equal-energy point and the dominant wavelength point. The color purity has been calculated from the equation:

$$\text{Color purity} = \frac{\sqrt{(x-x_{ee})^2+(y-y_{ee})^2}}{\sqrt{(x_d-x_{ee})^2+(y_d-y_{ee})^2}} \qquad (7)$$

where *(x, y)*, (x_{ee}, y_{ee}) and (x_d, y_d) represent the chromaticity coordinates of the light source under test, equal-energy reference illuminant, and dominant-wavelength point, respectively [53]. The color purity was calculated corresponding to the finest chromaticity coordinates obtained at 350, 387, 400, 452 nm excitations and were found to be 7.66×10^{-2}, 6.28×10^{-2}, 5.91×10^{-2} and 9.45×10^{-2}, respectively, and the dominant wavelengths points are given in Fig. 10. The value of the color purity should be as low as possible for white light emission [51]. The above mentioned results indicate that these glasses could be considered as a potential candidate for fabrication w-LEDs based on n-UV/blue LED chip as the excitation source.

3.6. Lifetime Decay analysis:

The lifetime decay profiles measured at 350 nm excitation for the prepared glasses are represented in Fig.11. The decay profiles were evaluated by monitoring the emission at 482 nm

to measure the lifetime of $^4F_{9/2}$ excited level. The decay curves were fitted to different exponential equations, and the best fit was observed for the bi-exponential equation for all the concentrations. The bi-exponential fit indicates that the interaction between rare earth ions becomes prominent, and the energy transfer process takes place from an excited Dy^{3+} ion (donor) to an unexcited Dy^{3+} ion (acceptor) [56]. The intensity of the luminescence spectra is given by [57]:

$$I = I_0 + A_1 exp\left(-\frac{t}{\tau_1}\right) + A_2\, exp\left(-\frac{t}{\tau_2}\right) \quad (8)$$

where, I and I_0 represent the luminescence intensities at time t and 0, τ_1 and τ_2 represents the two components of the lifetime, corresponding to the fast and slow lifetimes for exponential components, respectively; A_1 and A_2 are fitting constant, and t is the time. The calculated values of the average decay time (τ_{avg}) for the glasses GP01, GP05, GP10, GP15, and GP20 were found to be 365.77, 278.04, 228.87, 206.84 and 145.25 μs respectively, and the values are represented in Fig. 11. The value of average decay time has been determined by the following formula [57]:

$$\tau_{avg} = \frac{A_1\tau_1^2 + A_2\tau_2^2}{A_1\tau_1 + A_2\tau_2} \quad (9)$$

It can be observed that the average lifetime decreases with increasing doping concentration, which indicates the existence of energy transfer process between donor and acceptor.

4. Conclusions:

Transparent and colorless Dy^{3+} ions doped P_2O_5-PbO-ZnO glasses were prepared by melt quenching technique. The amorphous nature of the glass was confirmed by XRD spectrum. The thermal studies indicate that the as-prepared glass was thermally stable. The vibrational spectroscopic properties measured by Raman and FT-IR spectroscopy indicate the presence of poly-phosphate network dominated by Q^2 and Q^1 structural units. The FTIR studies also

indicated deploymerisation of phosphate network and presence of P–O–Pb and/or P–O–Zn linkages. The optical band gaps, band tailing parameters, and Urbach energies were calculated from the absorption spectra. The photoluminescent studies revealed that the glass exhibit intense white light by the combination of blue and yellow emission bands under n-UV excitation and the yellow to blue emission intensity ratio also lies in the proximity of unity. The CIE chromaticity coordinates (0.309, 0.341) lies in the pure white region and are very close to the commercial pc-LED and NTSC white light. The value of CCT also indicated that the emission lies in the cool white light region. The fluorescence lifetime decay analysis exhibits bi-exponential curve, indicating the energy transfer process between Dy^{3+}-Dy^{3+} ions and the value of lifetime decreased with increasing Dy^{3+} ions concentration. The above result indicates that the synthesized glass is a potential candidate for fabrication of cool w-LED using NUV/blue based chips.

Acknowledgements

Kaushal Jha is grateful to the University Grants Commission (UGC) for providing financial support in the form of Junior Research Fellowship (JRF). The author (M. Jayasimhadri) is grateful to DST-SERB, Govt. of India for the sanction of a research project (No. SB/FTP/PS-082/2014, dt. 02/03/2015).

References

[1] R.J. Xie, N. Hirosaki, M. Mitomo, K. Takahashi, K. Sakuma, Appl. Phys. Lett. 88 (2006) 101104-3.

[2] J.S. Kim, P.E. Jeon, J.C. Choi, H.L. Park, S.I. Mho, G.C. Kim, Appl. Phys. Lett. 84 (2004) 2931–2933.

ACCEPTED MANUSCRIPT

[3] G. Blasse, A. Bril , J. Chem. Phys. 47 (1967) 5139–5145.

[4] N. Hirosaki, R.J. Xie, K. Kimoto, T. Sekiguchi, Y. Yamamoto, T. Suehiro, M. Mitomo, Appl. Phys. Lett. 86 (2005) 211905-3.

[5] H. Daicho, T. Iwasaki, K. Enomoto, Y. Sasaki, Y. Maeno, Y. Shinomiya, S. Aoyagi, E. Nishibori, M. Sakata, H. Sawa, S. Matsuishi, H. Hosono, Nat. Comm. 3 (2012) 1132.

[6] H.Masai, Y.Yamada, Y. Suzuki, K. Teramura, Y. Kanemitsu, T. Yoko, Sci. Rep. 3 (2013) 3541.

[7] M.J. Weber, J. Non-Cryst. Solids 123 (1990) 208-222.

[8] B.C. Sales, L.A. Boatner, Science 226 (1984) 45.

[9] M. Sobczyk, P. Starynowicz, R. Lisiecki, W. Ryba-Romanowski, Opt. Mater. 30 (2008) 1571–1575.

[10] B.C. Jamalaiah, J.S. Kumar, A.M. Babu, L.R. Moorthy, K. Jang, H.S. Lee, M. Jayasimhadri, J.H. Jeong, H. Choi, J. Lumin. 129 (2009) 1023-1028.

[11] B.C. Sales, L.A. Boatner, J. Am. Ceram. Soc. 70 (1987) 615-621.

[12] J. Schwarz, K. Vosejpková, J. Therm. Anal. Calorim. 104 (2011) 1051-1054.

[13] K. Annapurna, M. Das, P. Kundu, R.N. Dwivedi, S. Buddhudu, J. Mol. Struct. 741 (2005) 53-60.

[14] H.S. Liu, T.S. Chin, S.W. Yung, Mater. Chem. Phys. 50 (1997) 1-10.

[15] J.H. Campbell, T.I. Suratwala, J. Non-Cryst. Solids 263 (2000) 318-341.

[16] S.D. Jackson, Appl. Phys. Lett. 83 (2003) 1316-1318.

[17] D. Umamaheswari, B.C. Jamalaiah, T. Sasikala, T. Chengaiah, II-Gon Kim, L. Rama Moorthy, J. Lumin. 132 (2012) 1166–1170.

ACCEPTED MANUSCRIPT

[18] S.F. León-Luisa, U.R. Rodríguez-Mendoza, E. Lalla, V. Lavín, Sensor. Actuat. B-Chem. 158 (2011) 208–213.

[19] M.C. Marco de Lucas, C. Garapon, E. Lebrasseur, J. Mugnier, B. Jacquier, O. Perrot, B. Boulard, C. Jacoboni, E. Josse, J.L. Adam, G. Fonteneau, J. Lucas, J.E. Broquin, R. Rimet, J. Lumin. 72 (1997) 321–323.

[20] Y. Zhao, D. Shi, J. Rare. Earth 31 (2013) 857–863.

[21] M. Jayasimhadri, L.R. Moorthy, R.V.S.S.N. Ravikumar, Opt. Mater. 29 (2007) 1321-1326.

[22] A. Goel, E.R. Shaaban, F.C.L. Melo, M.J. Ribeiro, J.M.F. Ferreira, J. Non-Cryst. Solids 353 (2007) 2383-2391.

[23] M. Liao, H. Sun, L. Wen, Y. Fang, L. Hu, Mater. Chem. Phys. 98 (2006) 154-158.

[24] E. B. Arauâ JO, J. A. Eiras, E. F. De Almeida, J. A. C. De Paiva, A. S. B. Sombra, J. Mater. Sci. Lett. 17 (1998) 497-499.

[25] A. Hrubý, J. Phys B 22 (1972) 1187-1193.

[26] D.D. Thornburg, Mater. Res. Bull. 9 (1974) 1481-1486.

[27] G. L. Saout, P. Simon, F. Fayon, A. Blin, Y. Vaills, J. Raman Spectrosc. 40 (2009) 522-526.

[28] G.L. Saout, P. Simon, F. Fayon, A. Blin, Y. Vaills, J. Raman Spectrosc. 33 (2002) 740–746.

[29] S.P. Valappil, D. Ready, E.A.A. Neel, D.M. Pickup, W. Chrzanowski, L.A. O'Dell, R.J. Newport, M.E. Smith, M. Wilson, J.C. Knowles, Adv. Funct. Mater.18 (2008) 732–741.

[30] W.A. Pisarski, L. Żur, T. Goryczka, M. Sołtys, J. Pisarska, J. Alloys Comp. 587 (2014) 90–98.

[31] A.H. Khafagy, M.A. Ewaida, A.A. Higazy, M.M.S. Ghoneim, I.Z. Hager, R. El-Bahnasawy, J. Mater. Sci. 27 (1992) 1435-1439.

ACCEPTED MANUSCRIPT

[32] R. Lakshmikantha, R. Rajaramakrishna, R.V. Anavekar, N.H. Ayachit, Mater. Chem. Phys. 133 (2012) 249-252.

[33] Y. Saddeek, Physica B- Condens Mat 406 (2011) 562-566.

[34] A.M. Efimov, V.G. Pogareva, J. Non-Cryst. Solids 275 (2000) 189–198.

[35] E. Mansour, G.E. Damrawi, Physica B- Condens. Mat. 405 (2010) 2137–2143.

[36] E.A.A. Neel, D.M. Pickup, S.P. Valappil, R.J. Newport, J.C. Knowles, J. Mater. Chem. 19 (2009) 690-701.

[37] R.K. Brow, J. Non-Cryst. Solids 263 (2000) 1-28.

[38] W. T. Carnall, P. R. Fields, K. Rajnak, J. Chem. Phys. 49 (1968) 4424.

[39] A. Thulasiramudu, S. Buddhudu, Spectrochim. Acta. A 67 (2007) 802-807.

[40] E.A. Davis, N.F. Mott, Phil. Mag. 22 (1970) 903-922.

[41] A. Agarwal, V. P. Seth, S. Sanghi, P. Gahlot, D. R. Goyal, Rad. Eff. Def. Solids 158 (2003) 793-801.

[42] M. Altaf, M. A. Chaudhry, M. Zahid, J. Res. Sci. 14 (2000) 253-259.

[43] B.H. Venkataraman, K.B.R. Varma, Opt. Mater. 28 (2006) 1423-1431.

[44] X.Y. Sun, S. Wu, X. Liu, P. Gao, S.M. Huang, J. Non-Cryst. Solids 368 (2013) 51–54.

[45] M. Jayasimhadri, K. Jang, H.S. Lee, B. Chen, S.S. Yi, J.H Jeong, J. Appl. Phys. 106 (2009) 013105-3.

[46] G.S.R. Raju, H.C. Jung, J.Y. Park, C.M. Kanamadia, B.K. Moon, J.H. Jeong, S.M. Son, J.H. Kim, J. Alloys Comp. 481 (2009) 730–734.

[47] A.K. Vishwakarma, K. Jha, M. Jayasimhadri, A.S. Rao, K. Jang, B. Sivaiah, D. Haranath, J. Alloys Comp. 622 (2015) 97-101.

[48] J. Pisarska, L. Żur, W.A. Pisarski, Phys. Status Solidi A 209 (2012) 1134–1140.

[49] K. Linganna, Ch. Srinivasa Rao, C.K. Jayasankar, J. Quant. Spectrosc. Radiat. Transfer 118 (2013) 40-48.

[50] A.A. Reddy, M.C. Sekhar, K. Pradeesh, S.S. Babu, G.V. Prakash, J. Mater. Sci. 46 (2011) 2018–2023.

[51] K.V. Krishnaiah, K.U. Kumar, C.K. Jayasankar, Mater. Express 3 (2013) 61-70.

[52] T.W. Kuo, W.R. Liu, T.M. Chen, Opt. Express 18 (2010) 8187-8192.

[53] E.F. Schubert, *Light Emitting Diodes* 2nd ed., Cambridge University Press, New York, 2006, pp 292-310.

[54] C.S McCamy, Color Res. Appl. 17 (1992) 142-144.

[55] S.M. Berman, M. Navvab, M.J Martin, J. Sheedy, W. Tithof, Lighting Res. Technol. 38 (2006) 41-52.

[56] K. Linganna, V.B. Sreedhar, C.K. Jayasankar, Mater. Res. Bull. 67 (2015) 196-200.

[57] K. Li, X. Liu, Y. Zhang, X. Li, H. Lian, J. Lin, Inorg. Chem. 54 (2015) 323-333.

ACCEPTED MANUSCRIPT

ACCEPTED MANUSCRIPT

Tables:

Table 1: Optical band gap (E_{opt}), band tailing parameter (B) for indirect and direct allowed transitions and Urbach energy of the glasses.

Table 2: Colorimetric properties of Dy^{3+} doped zinc lead phosphate glasses for different concentrations and excitation wavelengths.

ACCEPTED MANUSCRIPT

Figure Captions:

Fig.1: XRD spectrum for glass GP10 at room temperature.

Fig.2: DSC Curve for glass GP10.

Fig.3: Raman Spectrum for glass GP10 at room temperature.

Fig.4: FTIR Spectrum for glass GP10 at room temperature.

Fig.5: Indirect band gap plot for different glasses at room temperature (Inset: Represent the absorption spectrum for glass GP10)

Fig.6: PLE (photoluminescence excitation) spectrum for glass GP10 at room temperature by monitoring emission at 574 nm.

Fig.7: Concentration dependent emission spectra (λ_{ex}=350 nm) for zinc lead phosphate glasses at room temperature

Fig.8: Emission spectra for glass GP10 under 350, 387, 400 and 452 nm excitations at room temperature (Inset: Represents the relative emission for different excitations in bar graph form).

Fig.9: Energy level diagram for Dy^{3+} doped glass.

Fig.10: CIE chromaticity coordinates and dominant wavelength points for different glasses under 350, 387, 400 and 452 nm excitations.

Fig.11: Decay profiles for different glasses at room temperature.

ACCEPTED MANUSCRIPT

ACCEPTED MANUSCRIPT

Table 1:

Glass samples	n=1/2 (Indirect allowed)		n=2 (Direct allowed)		Urbach energy (eV)
	E_{opt} (eV)	B ($cm^{-1/2}$ eV)	E_{opt} (eV)	B (cm^{-2} eV)	
GP01	4.20	36.66	4.36	271.79	0.22
GP05	4.23	34.36	4.33	241.10	0.20
GP10	4.17	34.23	4.29	236.10	0.23
GP15	4.18	37.50	4.38	253.14	0.22
GP20	4.22	36.28	4.37	252.77	0.21

ACCEPTED MANUSCRIPT

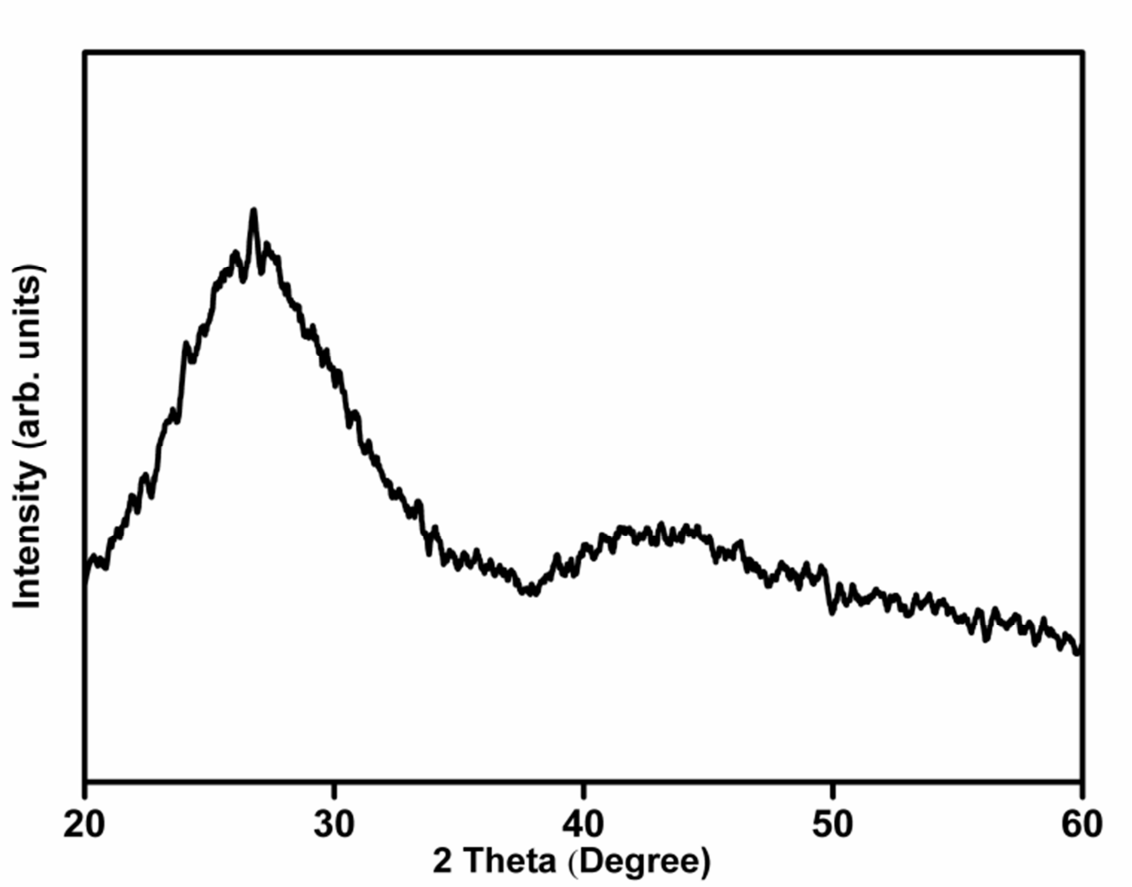
ACCEPTED MANUSCRIPT

Table 2:

Excitation Wavelength	*Parameters*	**Glass samples**				
		GP01	***GP05***	***GP10***	***GP15***	***GP20***
350 nm	***(x, y)***	(0.309, 0.360)	(0.308, 0.347)	(0.309, 0.341)	(0.309, 0.350)	(0.310, 0.351)
	Y/B ratio	0.90	0.93	0.92	0.97	0.98
	CCT (K)	6476	6627	6547	6629	6461
387 nm	***(x, y)***	(0.310, 0.360)	(0.321, 0.370)	(0.342, 0.387)	(0.322, 0.362)	(0.317, 0.364)
	Y/B ratio	0.91	0.97	0.92	0.97	0.98
	CCT (K)	6444	5944	5174	5897	6106
400 nm	***(x, y)***	(0.298, 0.350)	(0.313, 0.367)	(0.316, 0.362)	(0.321, 0.370)	(0.319, 0.369)
	Y/B ratio	0.88	0.93	0.92	0.96	0.97
	CCT(K)	7049	6283	6139	5907	5990
452 nm	***(x, y)***	(0.307, 0.345)	(0.283, 0.325)	(0.304, 0.356)	(0.300, 0.290)	(0.312, 0.368)
	Y/B ratio	0.86	0.89	0.88	0.94	0.97
	CCT (K)	6642	8366	7675	6705	6337

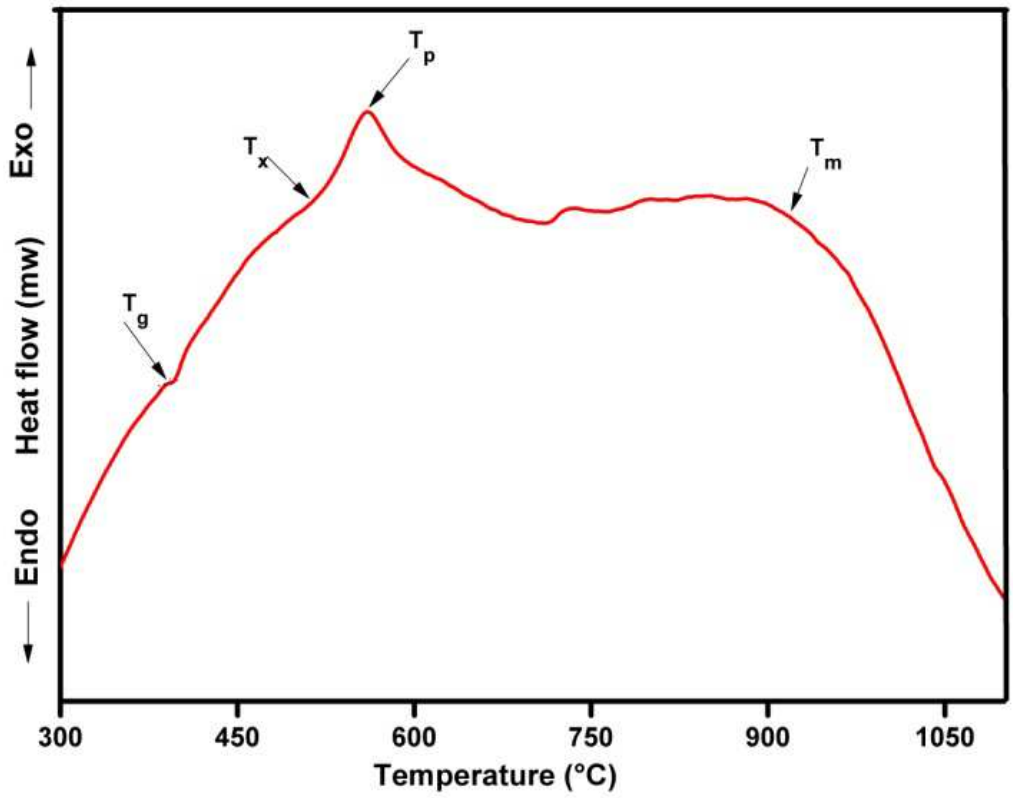
ACCEPTED MANUSCRIPT

Fig. 1.



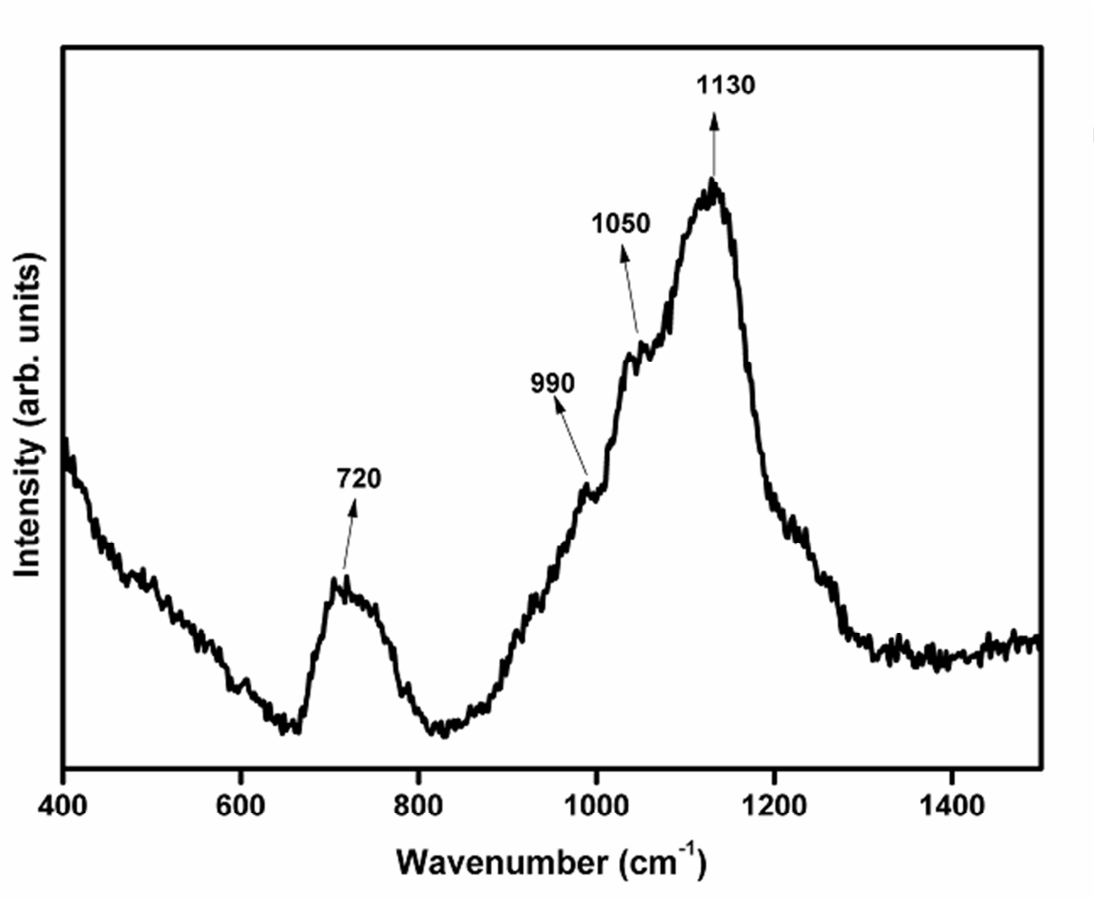
ACCEPTED

Fig. 2.



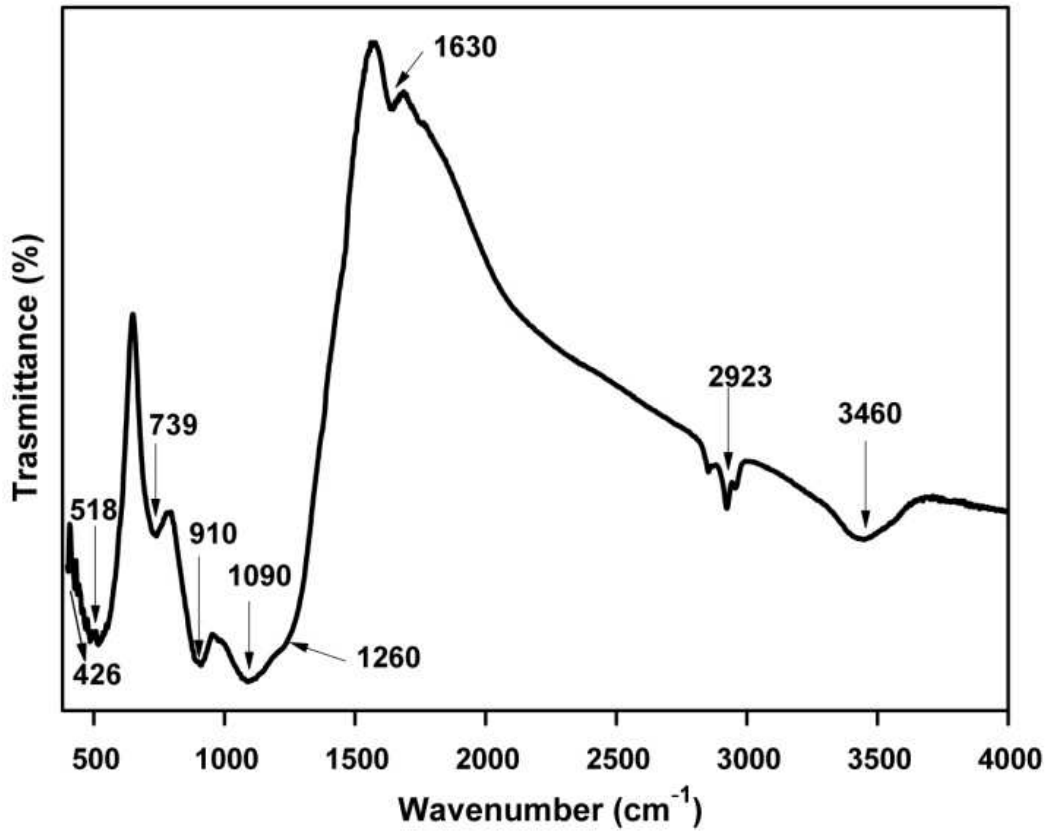
ACCEPTED MANUSCRIPT

Fig. 3.



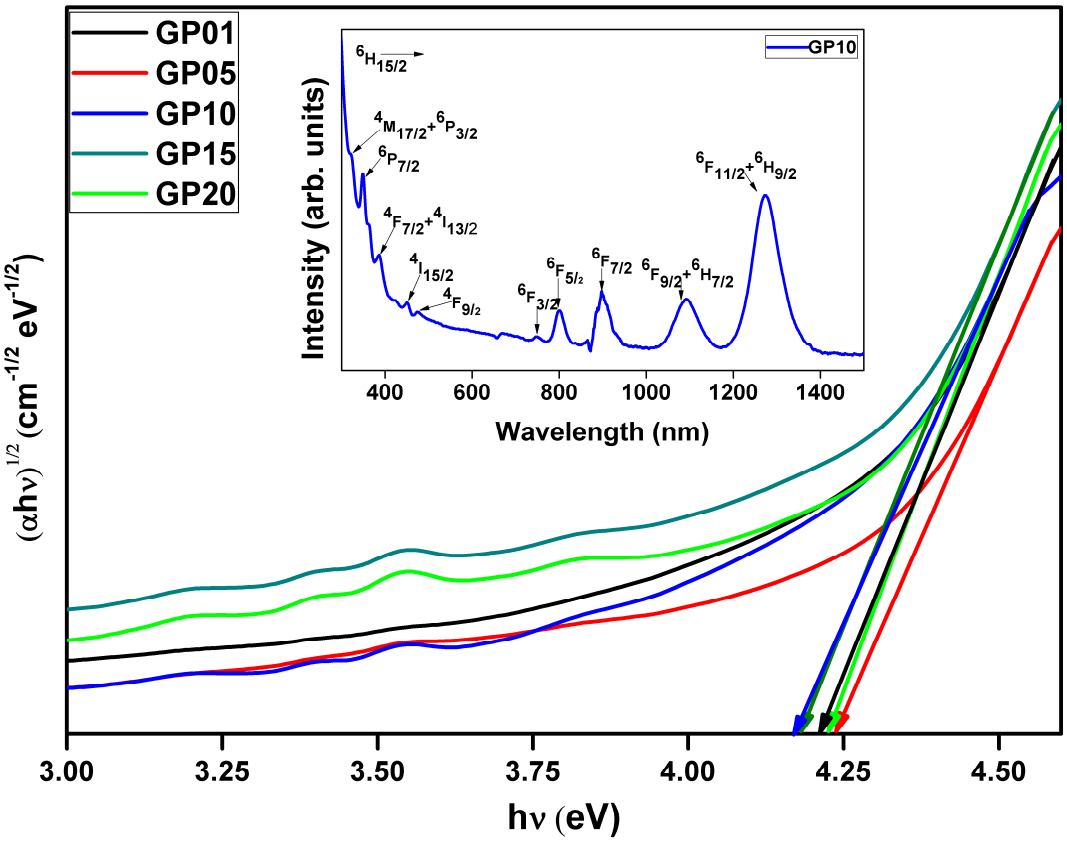
ACCEPTED

Fig. 4.



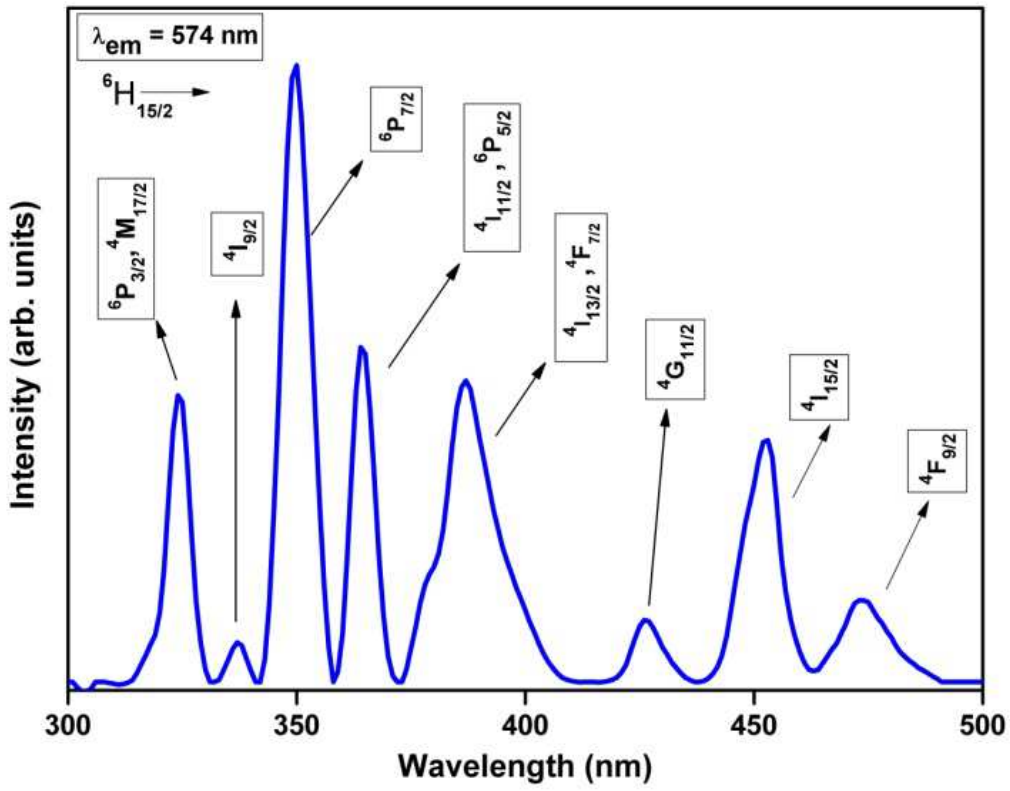
ACCEPTED MANUSCRIPT

Fig. 5.



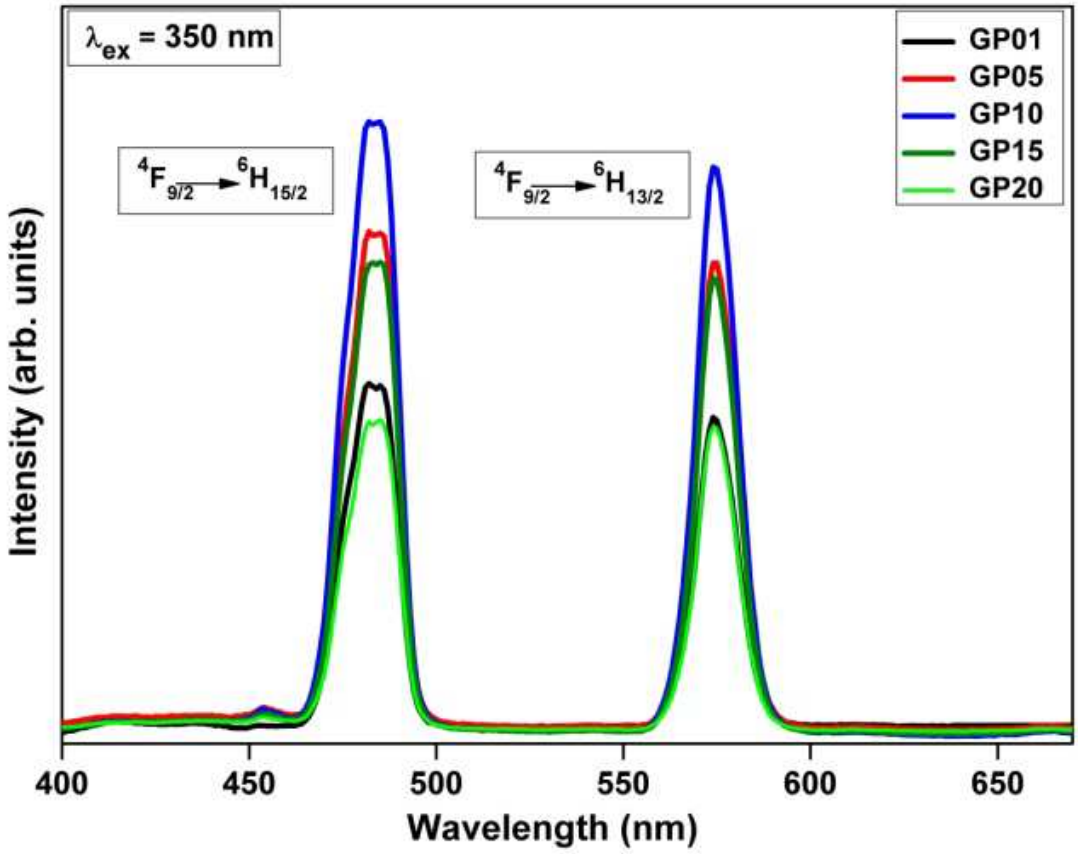
ACCEPTED MANUSCRIPT

Fig. 6.



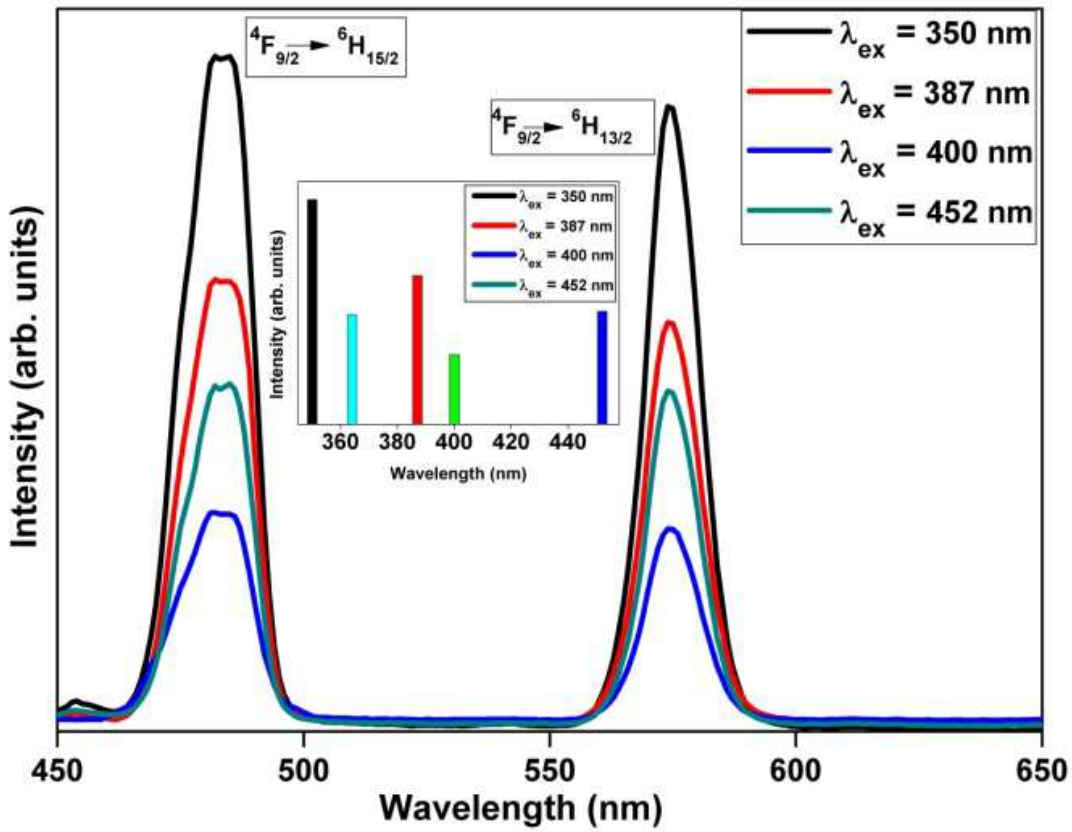
ACCEPTED MANUSCRIPT

Fig. 7.



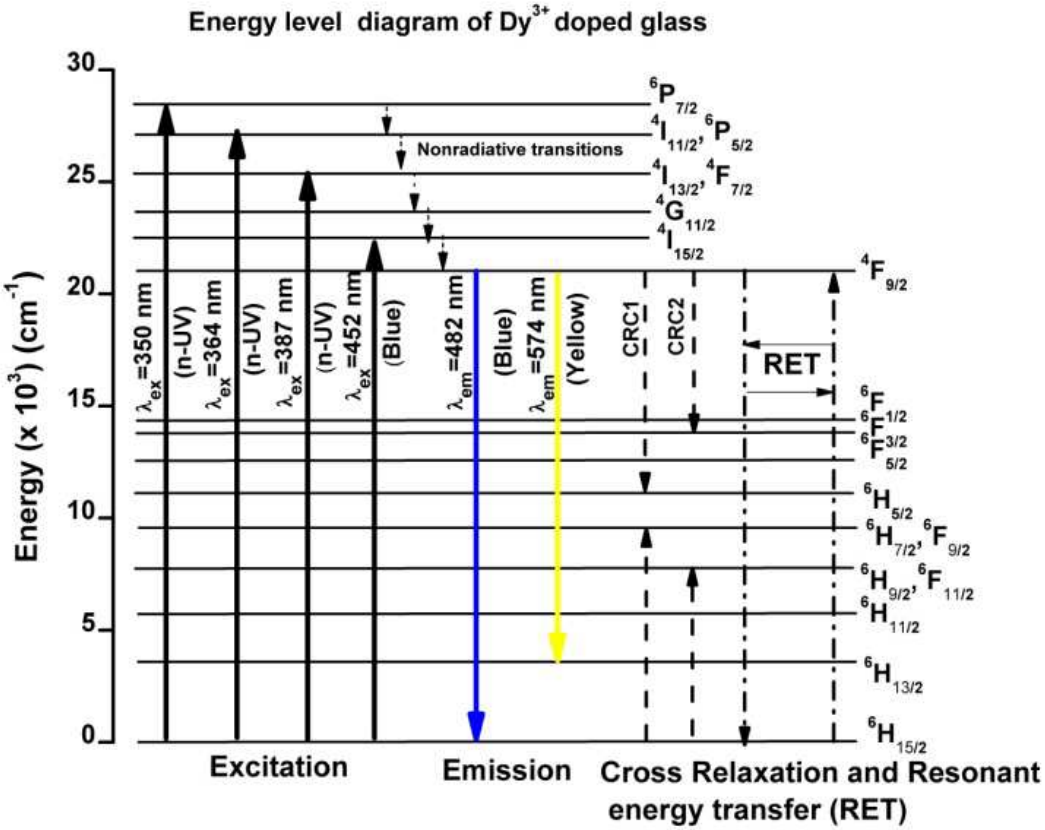
ACCEPTED

Fig. 8.



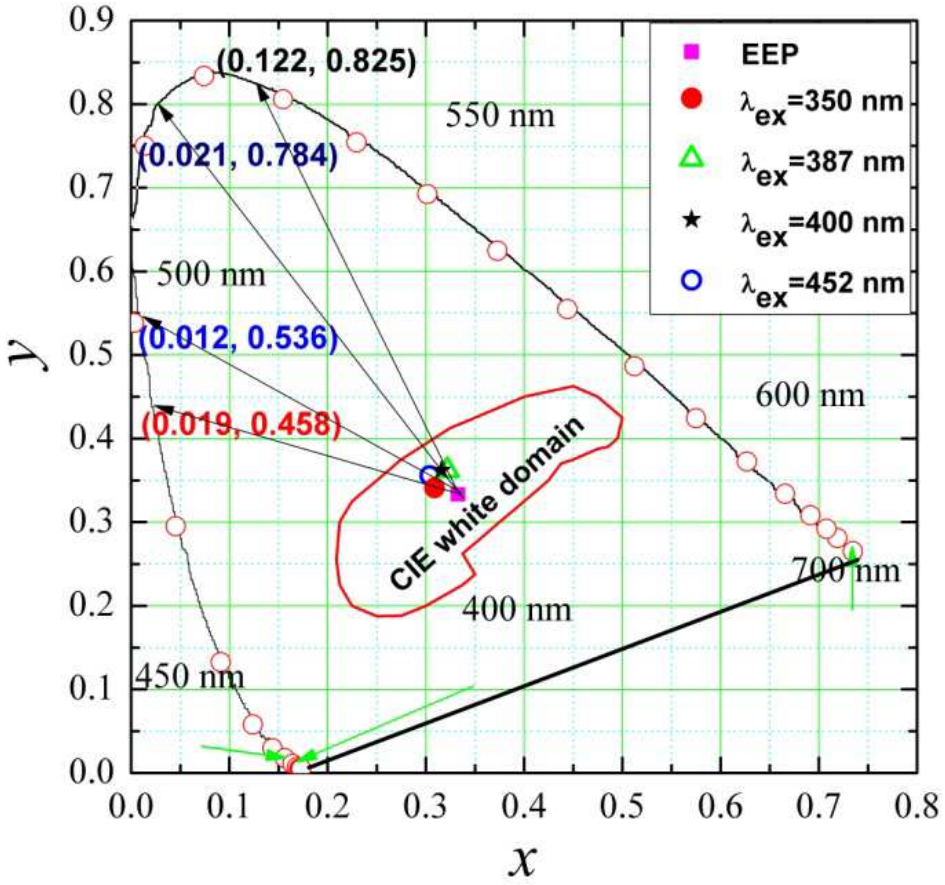
ACCEPTED

Fig. 9.



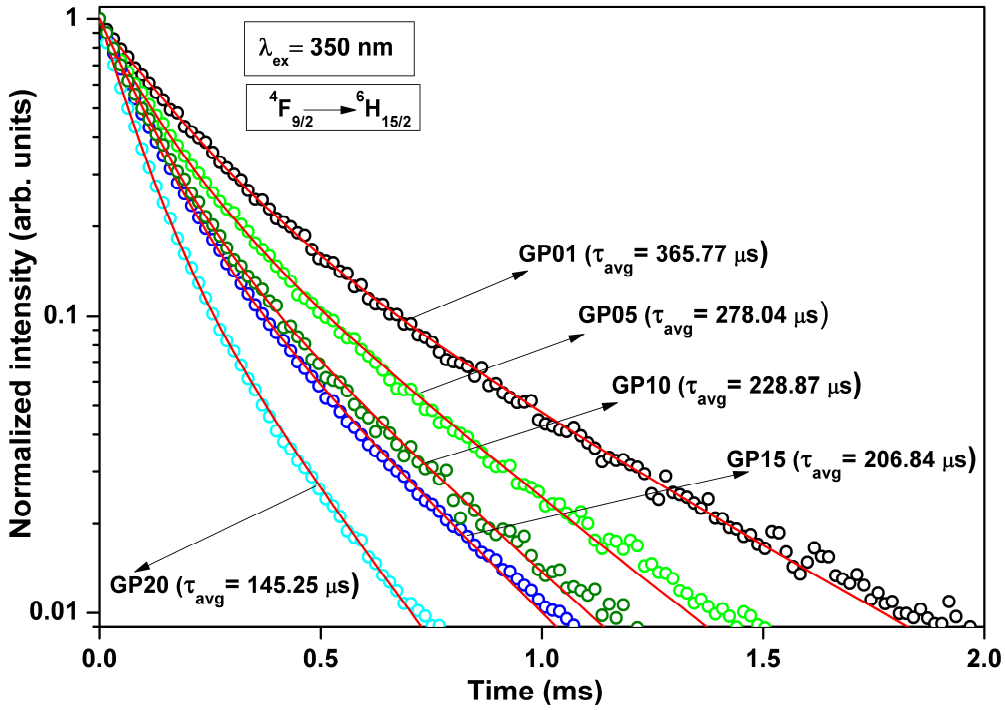
ACCEPTED MANUSCRIPT

Fig. 10.



ACCEPTED MANUSCRIPT

Fig. 11.



ACCEPTED MANUSCRIPT

ACCEPTED MANUSCRIPT

Highlights of the work

- Thermally stable Dy^{3+}:P_2O_5-PbO-ZnO glass prepared by melt quenching technique
- Optimized CIE chromaticity coordinates (0.309, 0.341) indicate pure white emission
- CCT values indicates cool white light emission for zinc phosphate glasses.
- Decay measurements indicate energy transfer between Dy^{3+} ions.
- Suggest that this glass may be useful for manufacturing organic resin free w-LEDs

ACCEPTED MANUSCRIPT

IJARCCE

ISSN (Online) 2278-1021
ISSN (Print) 2319 5940

International Journal of Advanced Research in Computer and Communication Engineering
Vol. 5, Issue 6, June 2016

SVM-KNN and Pixel Gradient based Segmentation Technique for Brain MRI Tumor Images Classification

Sahil Dalal[1], Rajesh Birok[2], Sanchit Kumar[3]

Department of ECE, Delhi Technological University, Delhi, India[1, 3]

Associate Professor, Department of ECE, Delhi Technological University, Delhi, India[2]

Abstract: The research paper proposes a novel and robust segmentation technique for the classification of Brain MRI Tumor Images. It is a completely automatic technique for the segmentation of tumor in a tumor pretentious brain MRI image with its classification from a normal image. In this technique, method is able to detect brain tumor utilizing the pixel intensities differences among the tumor and its neighbouring tissues. Here, it also uses the associated tumor's pixels labelling which can efficiently segments the brain tumor from the image. After that, SVM-kNN is exploited for the classification of brain MRI image from the normal one. For the feature vector's computation, GLCM technique is utilized. From the results, it can be observed that with only less number of feature vectors, in terms of speed and computational power used, the method is much better. As accuracy of nearly 98% is computed using the proposed method which is very good in comparison to the other methods used.

Keywords: GLCM, MRI, Solidity and Thresholding, SVM-kNN.

I. INTRODUCTION

In the world, Brain tumor [2] [12] is a foremost cause of death. It is caused by an evolution of some anomalous tissues inside the brain. Tumor is of two kinds: one is malignant tumor and the other is benign tumor. If the Malignant tumor is not detected at an early stage it can cause to death as it is cancerous in nature and has the ability to grow inside the brain. Hence, it is more precarious than the benign tumor. For such diagnosis, Magnetic Resonance Imaging (MRI) is used. MRI technique is utilized to detect the tumor in the brain by the Radiologists. They can observe a brain MRI image to accomplish whether it is a normal or cancerous image. In this field, there may be numerous images which need to be scrutinized. Therefore, it leads to decrease in the accuracy and increase in time consumption for the diagnosis. Hence, automatic classification method exploiting the computer technology is desirable so that an increase the accuracy can be achieved with minimum time consumption. The proposed method in this research paper has the following steps: (a) Image pre-processing, (b) segmentation, (c) feature extraction, and (d) classification. Image pre-processing is done to eliminate unwanted noise elements from the image so that it becomes apt for further processing. It is required for the perfect segmentation of tumor from the image. Segmentation is stated as the way in which only the preferred amount of part of the image is retained and the unwanted parts (i.e. noise) is eliminated. Here, it is done to extract the area of tumor in the image so that the classification may become easier and accurate. In the feature extraction stage, processing of some calculated parameters is made from the segmented images which are used as input to the classifiers for the classification. At this step, further reduction in the information of the image to a minimum level is occurred. For efficient classification, features which are extracted should be significant and beneficial. Now, at the classification step, classifiers are utilized to differentiate a normal image from a diseased image which are having tumor exploiting some of the classification algorithms. There can be so many such algorithms which have been already utilized for the classification purposes. These are as follows: Support Vector Machine (SVM) [1] [3], k-Nearest Neighbours (kNN) [4], Artificial Neural Network (ANN) [5], Probabilistic Neural Network (PNN) [6] etc. Each and every classifier has some benefits as well as shortcomings. k-NN [4] has the limitation of its high computational cost. It is also difficult in the kNN for choosing a proper value of 'K' parameter. Even though k-NN is very efficient in classifying something but its performance is degraded by its limitations. PNN [6] also has a problem of its very slow speed. ANN [5] also performs better than the above mentioned classifiers with the high dimension of feature vectors, but it also has a problem of high computational cost. As feature vector is small in our method, SVM-kNN will perform the best amongst all of the other classifiers.

The Research Paper is systematized as follows. Section II describes about the proposed method with block diagram. Section III tells about the experimental work used in the proposed method. The tumor classification and experimental results are shown in section IV followed by conclusion in section V.

II. PROPOSED METHOD

The block diagram shown in the Fig.1 represents the classification of brain MRI image of a normal person and a person having brain tumor. This proposed method

Copyright to IJARCCE

IJARCCE
ISSN (Online) 2278-1021
ISSN (Print) 2319 5940
International Journal of Advanced Research in Computer and Communication Engineering
Vol. 5, Issue 6, June 2016

contains the following sections: Pre-processing (RGB to grayscale conversion, resizing and filtering), segmentation, feature extraction, training and testing.

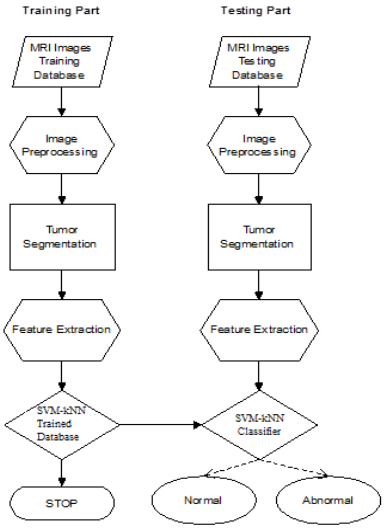
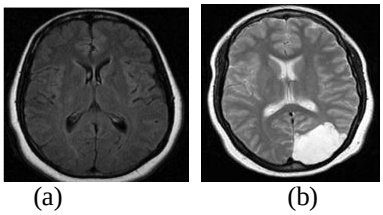


Fig.1. Block Diagram

Firstly, system is trained using the training dataset of brain MRI images for the training of classifier. After that dataset which needs to be tested is provided to the trained classifier which classifies it into two categories i.e. normal and abnormal (having brain tumor in this case) based on the training.

A. MRI Image

The Magnetic Resonance Imaging (MRI) is exploited for medical diagnosis of various diseases. It is considered as one of the best tools used in hospitals and clinics [7]. Advantages of having MRI images are: (a) It can provide very high contrast among the tissues, (b) It also checks on the body to exposure from ionizing radiations. MRI images of normal and abnormal brains, respectively, are shown in the Fig.2. It is clearly observable from the figure that the tissues which are affected by the tumor are having higher intensity as compared to the normal tissues.



(a) (b)

Fig.2. Brain MRI (a) Normal and (b) Abnormal

The images taken at the time of MRI are in the form of RGB images. Hence, before providing it to the model, images are being, firstly, converted to the gray scale image. It is also resized to a size of 500x500.

B. Pre-processing of image

At this stage, median filter is utilized for filtering the image and this is known as pre-processing of the image. Pre-processing is required because the image gets distorted due to the addition of noise at the time of acquisition and hence, the contrast of the image is also becomes low. This results in lowering of efficiency in the further steps of the analysis. Therefore, Filtering is desirable so that the noise can be removed and image contrast level can also be enhanced. In the Fig.3, Filtered image is shown.

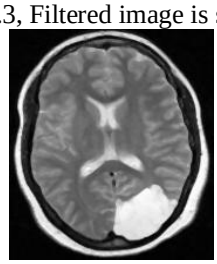
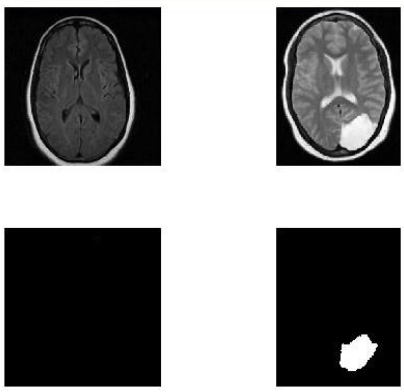


Fig.3. Filtered image

There are various filtering techniques present but here, median filtering is used because using median filter is advantageous in a way that it can eliminate the noise and preserve the edges which is helpful in improving the contrast of the image. Increase in tumor segmentation accuracy can also be done by this step.

C. Segmentation

Tumor detection is an essential task in the field of biomedical imaging. It is so because brain tumor is a severe disease and can cause death if it is not properly diagnosed. When any MRI image of the brain is taken, it is generally observed that the place where the tumor is present have higher intensity level compared to the neighbouring tissues intensity level. In this research, intensity values and solidity of the tumor is exploited to identify the tumor from its neighbouring tissues using the segmentation technique. Thresholding is the first step of segmentation. In this, the intensity values greater than the predefined threshold value is selected and using this, the values which are lower than the threshold values are ignored. The threshold values for the research are chosen by hit and trial method and 164 is the value taken during this research for the threshold. Even after thresholding, image still comprises unwanted regions along with the tumor region. For the removal of these unwanted regions, solidity and area [8] of the segmented regions are computed. For this, 0.2 value is selected for the solidity and only those regions which are having solidity values greater than 0.2 are to be considered as tumor intensity values. The second criteria of identification is the area where the maximum area of the region is considered as the tumor based region.



(a) (b)

Fig.4. (a) Normal Brain MRI with its segmented image and
(b) Abnormal Brain MRI with its segmented image

IJARCCE
ISSN (Online) 2278-1021
ISSN (Print) 2319 5940
International Journal of Advanced Research in Computer and Communication Engineering
Vol. 5, Issue 6, June 2016

After utilizing these properties, the brain MRI image is segmented to identify the tumor as the foreground image and neighboring tissues as background image. Fig.4 shows the segmentation results. In this, the two images are shown such that (a) represents the segmented image containing the tumor and (b) represents the segmentation of a normal MRI image. The segmented results are also represented as there counterpart images.

D. Feature extraction

After the segmentation, features extraction is a very vital role in the image processing or computer vision for pattern recognition and classification. A raw segmented image is not the ideal one to be given to the classifier directly for the classification purpose because it contains some unwanted data which only increases the computational time and cost of the analysis. Hence, some of the significant and important data points are extracted from the segmented image using the feature extraction process. These features extraction process contains many types of features such as intensity based features [12], texture based features [13] and shape based features [14]. Numerous features are computed from a segmented image which forms a feature vector. Now this feature vector is given as input to the classifier for efficient classification of normal and abnormal MRI image. In this research, we are using Grey Level co-occurrence matrix (GLCM) [9] technique for computing 5 texture features which constitutes a feature vector of 5x1 dimension for each image. Features calculated using GLCM are given as follows:

CORRELATION: Correlation is computed into what is known as the correlation coefficient, which ranges between -1 and +1.

$$Correlation = \sum_{j,i=0}^{N-1} G_{ji} \frac{(j-\mu)(i-\mu)}{\sigma^2} \quad (1)$$

CONTRAST: Contrast is defined as the separation between the darkest and brightest area.

$$Contrast = \sum_{j,i=0}^{N-1} G_{ji}(j-i)^2 \quad (2)$$

ENTROPY: Entropy is a measure of the uncertainty in a random variable.

$$Entropy = \sum_{j,i=0}^{N-1} -\ln(G_{ji})G_{ji} \quad (3)$$

HOMOGENEITY: Homogeneity is defined as the quality or state of being homogeneous.

$$Homogeneity = \sum_{j,i=0}^{N-1} \frac{G_{ji}}{1+(j-i)^2} \quad (4)$$

ENERGY: It provides the sum of squared elements in the GLCM .Also known as the uniformity or the angular second moment.

$$Energy = \sum_{j,i=0}^{N-1} G_{ji}^2 \quad (5)$$

Where G_{ji} is the Grey Level Co-occurrence matrix (GLCM).

E. Classification using SVM-kNN

Classification a process of classifying the data into their respective classes and this can be done in two parts: training and testing. During training, classifier is trained using the known data. And, after that unknown data is taken and given to that trained classifier for classification for testing. The efficiency of classification mainly depends upon the training. During this research work, SVM-kNN is utilized for the classification purpose. Support vector machine (SVM) [1] is an algorithm of classification which is based on the supervised learning model. And, SVM-kNN is a hybrid model of the two separate classifiers namely Support Vector Machine and k-Nearest Neighbour classifiers. According to the nearest neighbour approach, SVM utilizes only single representative point for each class as the support vector and hence, can be considered as a 1NN classifier [10]. However, in the hybrid of SVM and kNN, more than one support vector points are chosen from the sample points. Say these are k in number and hence, the class is decided for the tested samples.

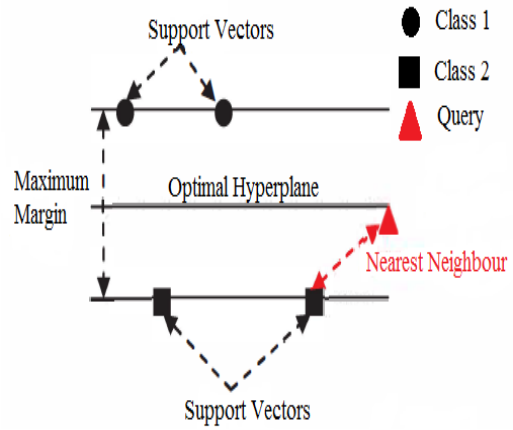


FIG.5. SVM-KNN CLASSIFICATION

It can be observed in the Fig.5 that SVM-kNN algorithm considers more than one support vectors as the representative points for any class. This is a much better classifier than the SVM because in SVM only sample point that is present nearest to the hyperplane represents the support vector. While in SVM-kNN, all the support vectors are considered as as representative points for the classes so that maximum of information of a class can be exploited in the classification process. During this analysis modeling, nearest neighbour (that is, support vector) is calculated as the query point utilizing the k-nearest neighbour algorithm. Performance of a classification algorithm can be measured by a specific table layout which is called the Confusion Matrix [10].

III. EXPERIMENTAL DISCUSSION

The proposed method, shown in the Fig.1, includes following stages: image pre-processing, segmentation, feature extraction and classification. At the image pre-processing stage, MRI images are first converted to grayscale from RGB and resized to a size of 500x500. Then median filter is utilized to remove noise from the image and to make segmentation accurate.

IJARCCE

ISSN (Online) 2278-1021
ISSN (Print) 2319 5940

International Journal of Advanced Research in Computer and Communication Engineering
Vol. 5, Issue 6, June 2016

TABLE I
FEATURES EXTRACTED

GLCM FEATURES	NORMAL IMAGE	ABNORMAL IMAGE
Correlation	0.7867	0.9543
Contrast	1.7382 e-04	2.2134 e-04
Entropy	-2.4343 e06	-1.2361 e07
Homogeneity	0.9999	0.9999
Energy	0.99983	0.9922

During the segmentation stage, Tumor region is extracted from an abnormal brain MRI image leaving behind all other unwanted parts of the image. These stages make the classification process easier and faster as the unwanted portion is already removed. In the feature extraction stage, as the unwanted portion is already removed from the image, hence only 5 features are computed for the classification. As the number of features in the feature vector is small, the proposed method is fast and also takes less computational power in comparison to the other methods. During the classification process, training and testing is to be done. In training section, known data (i.e. 5 features*40 images) is given to the classifier for its training. After the completion of training, nor during the testing, 50 unknown images are given to this trained classifier for the classification. The classification is performed using SVM-kNN.

IV. RESULTS & DISCUSSION

In the proposed method, brain MRI images of 90 patients are utilized. From these 90 images, 40 images have been exploited to train the classifier and other 50 images are used for testing. Firstly, features are computed for the 40 training images which are given to the classifier (based on SVM-kNN). After the training, 50 unknown images have been selected and given to this trained classifier for classification into normal and abnormal (Tumor). In table II, confusion matrix is shown for the classification results of SVM-kNN. Accuracy is calculated based on the confusion matrix shown in Table II and it can be seen that accuracy is come out as 98%.

TABLE II
Confusion Matrix

	PREDICTED CLASS			
		Abnormal	Normal	Accuracy
ACTUAL CLASS	Abnormal	24/25	1/25	96%
	Normal	0/25	25/25	100%

TABLE III
Comparison of proposed method with other methods used.

REFRENCES	METHOD	ACCURACY
PROPOSED METHOD	Segmentation + SVM-kNN	98%
Sanchit Kumar, Sahil Dalal [1]	Segmentation + SVM	96%
Hari Babu Nandpuru et al [10]	Skull Masking + SVM	84%
Ketan Machhale et al [11]	Skull Masking + SVM-kNN	98%

Table III shows the comparison of the proposed method on the basis of the proposed technique and accuracy with the other methods. And our method i.e. SVM-kNN with segmentation gives much better results compared to the other methods with only fewer number of features used.

V. CONCLUSION

This research paper comprises of segmentation technique for the extraction of tumor region from the abnormal image. With that, its classification is also performed from the normal image using SVM-kNN. Results obtained from the proposed method shows very efficient results with an accuracy of classifying the brain MRI tumor images as 98%. This mehod is also advantageous in a way that it is fast in speed and exploits only small amount of computational power in comparison to the other methods.

REFERENCES

1. Sanchit Kumar, Sahil Dalal, "A New and Robust Segmentation Technique Based on Pixel Gradient and Nearest Neighbors for Efficient Classification of MRI Images", International Journal of Advanced Researches in Electronics & Communication Engineering, vol. 5, issue 6, pp. 1708-1712, 2016.
2. http://www.bic.mni.mcgil1.calbrainweb/.
3. M. F. B. Othman, N. B. Abdullah, N. F. B. Kamal, "MRI brain classification using Support vector machine", IEEE, Centre for Artificial Intelligence & Robotics (CAIRO), University Teknology Malaysia, 2011.
4. Dr. R J. Ramteke and Khachane Monali Y, "Automatic Medical Image Classification and Abnormality Detection Using K Nearest Neighbor", International Journal of Advanced Computer Research, Volume-2 Number-4 Issue-6 December-20l2.
5. E. A. El-Dihshan, T. Hosney, A B. M. Salem, "Hybrid intelligence techniques for MRI Brain images classification", ELSEVIER, Digital Signal Processing, Volume 20, pp,433-441, 2010.
6. Lashkari Amir Ehsan "A Neural Network-Based Method for Brain Abnormality Detection in MR Images Using Zernike Moments and Geometric Moments", UCA-IO.
7. Chinnu A, "MRI Brain Tumor Classification Using SVM and Histogram Based Image Segmentation", International Journal of Computer Science and Information Technologies, Vol. 6 (2) , 2015, 1505-1508.
8. K. Somasundaram. T. Kalaiselvi. "Automatic brain extraction methods for TI magnetic resonance images using region labeling and morphological operations", ELSEVIER, Computers in Biology and Medicine 41 (2011) 716-725.
9. Shweta Jain, "Brain Cancer Classification Using GLCM Based Feature Extraction in Artificial Neural Network", IJCSET, ISSN: 2229-3345, VoL 4 No. 07 JuI2013.
10. Evangelia I. Zacharaki, Sumei Wang, Sanjeev Chawla, Dong Soo Yoo, Ronald Wolf, Elias R. Melhem, and Christos Davatzikos, "Classification of brain tumor type and grade using MRI texture and shape in a machine learning scheme", PMC 2010 December 1.
11. Hari Babu Nandpuru, Dr. S. S. Salankar, Vibha Bora, "Mri Brain Cancer Classification Using Support Vector Machine", 2014 IEEE Students' Conference on Electrical, Electronics and Computer Science.
12. Ketan Machhale, Hari Babu Nandpuru, Vivek Kapur, Laxmi Kosta, "MRI Brain Cancer Classification Using Hybrid Classifier (SVM-KNN)", 2015 International Conference on Industrial Instrumentation and Control (ICIC) College of Engineering Pune, India. May 28-30,2015.
13. V.P.GladisPushparathi, S.Palani, "Linear Discriminant analysis for brain tumor classification using Feature Selection",Int. J. Communication and Engineering, vol 5, issue 4 , pp 1179-1185.
14. Dr.S.Palani, V.P. Gladis Pushpa Rathi, "Detection and characterization of brain tumor using segmentation based on HSOMWaveletpacketfeaturespacesandANN",Ieeeexplore.ieee.org/ xpl/freeabstract.jsp/number=5942097(2010).

International Journal of Engineering Studies.
ISSN 0975-6469 Volume 8, Number 1 (2016), pp. 11-19
© Research India Publications
http://www.ripublication.com

Thermoexergetic analysis of Steam Power Plant

Rajat Pardal[1], B. B. Arora[2] and Subhashish Maji[3]

[1]Directorate of Training & Technical Education, Delhi (India)*
[2]Deptt. of Mech. Engg., Delhi College of Engineering, Delhi (India)
[3]School of Engineering & Technology, IGNOU, Delhi (India)
[*]Corresponding Author E-mail: rp0160@yahoo.com

Abstract

The present paper investigates the effectiveness of the power plant to offset the increasing demand of power. Energy and Exergy analysis has been carried out to determine the efficiency of each componet and the overall efficiency of the plant, Further evaluation of energy and exergy loss and destruction has been analysed. This has been done in order to identify the component where useful energy loss can be recoverd by making the necessary arrangements to the system components so that it improves the efficiency of the component and the plant thereoff. Boiler and turbine are the sources of maximum exergy loss which needs to be redesigned.

Introduction

The use of various energy by humans in a range of activities has dominated the scene for several centuries. However, in last two centuries, the per capita consumption of energy has assumed great importance. Demand of energy is increasing day by day. To meet this demand there are two ways one is to generate more energy and the second one is to tap the otherwise waste energy. First one requires huge amount of money whereas the second one can be easily achieved by changing the strategy to generate universal energy namely Electrical energy. Most of the power/energy is generated by burning fossil fuel namely coal. To reduce the rate of consumption of fossil fuel for same amount of energy in a coal fired power plant is one of the important aspects, with rapid growth of civilization and increasing consumption of energy.

Researchers such as Evans, 1962; Tribus et al., 1960; Tribus and Evans, 1963,El-Sayed and Aplenc, 1970; El-Sayed and Evans, 1970, Darwish, Al-Najem and Al-Ahmad, 1993; El-Nashar,1993 Al-Sulaiman and Ismail, 1995; Hamed et al., 1999; have been striving for generating more power using all resources but the thermal

plants based upon coal, gas and liquid fossil fuels are still in vogue rather in predominant use.Needless to say that energy in form of electricity, has become one of the most important aspect of human life. Most of the activities of time rely upon electrical emergy and its breakdown simply perturbs all of them. It would not be an exaggeration to say basic need for human beings next to food, clothing and shelters is electrical energy.

Generation of electrical power/energy seems to be simple however it a formidabale task. Its generation necessitates high investment and a sound technical know- how. Besides, it poses several hazards. Effiecient advanced, and a proven technical know-how is essential for economical generation of electrical power/energy.

The generation process of electrical power/energy being complex energy system can be analyzed in terms of its economics and efficiency as a function of resource consumption. Thermoexergetics, and its applications to energy systems, can help us to formulate improved and effcient designs.

Energy analysis is based on first law of thermodynamic where irreversibility of the systems is not distinguished which means degradation of energy quality is not considered. So the first law of thermodynamics does not differentiate between the quality and quantity of energy. Therfore the justification of real useful energy loss cannot be predicted by the first law of thermodynamics, though it is the starting point of any thermodunamic analysis.

So in order to achieve higher efficiency an analysis which could take into accout the irreversibilities of the system is necessary. Exergy analysis based on second law of thermodynamics is appropriate ome to take care of the possible irreversibilities in the system or system components.

Exergy (an energetic property) analysis locates and quantifies irreversibilities(losses) in a process and hence tells us about the quality of energy. Exergy based thermoeconomic methods are also referred to as “exergoeconomics” (Tsatsaronis and Winhold, 1985).

Destruction in exergy is proportional to entropy generation, which accounts for inefficiencies. The exergy analysis identifies the area where and how much the loss or destruction occurrs. It also analyses the components where there is a possibility to improve the efficiency of the power plant.

In the present work Energy and Exergy analysis has been carried out to determine the efficiency of each componet and the overall efficiency of the 122 MW Steam Power plant.

Methodology

Major components of steam power plant were listed. Terminal points were selected in order to measure the thermodynamic parameters such as temperature, pressure, mass flow rate etc. Readings were recorded at each entryand exit of components of the system.

At full load condition parameter reading were recorded.

Enthalpy and entropy values at these terminal points were computed from the steam tables. Energy and exergy analysis was computed for each components of the system.

The Exergy destruction at each terminal point was computed and the loss was determined with location and magnitude. The energy and exergy efficiency was also computed and in order to identify the loss occurring in power plant components.

Energy and Exergy equations of steam power plant

Figure 1 shows the schematic diagram of steam power plant and Figure 2, describes the Temperature Entropy diagram for the plant.

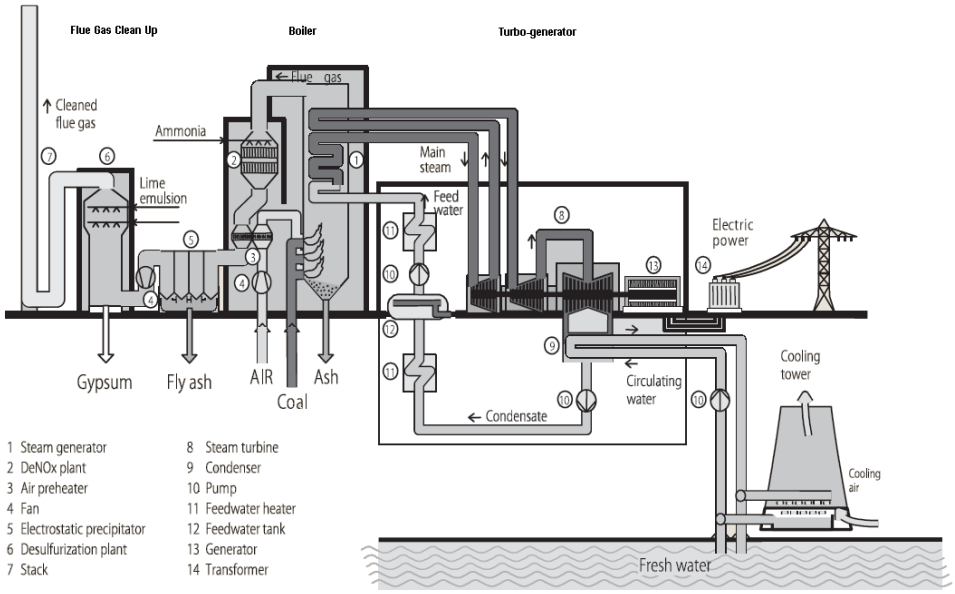


Figure 1: Steam power plant

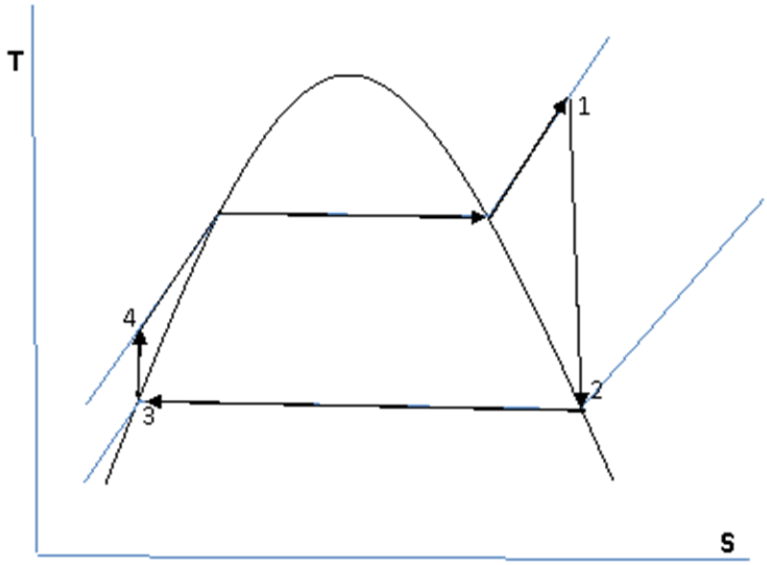


Figure 2: T-S diagram of steam cycle

Operating conditions of the power plant

Feed water inlet temperature to boiler= 494.15 K
Steam Flow rate (100%: 311.5 ton/h) (75%: 225 ton/h) (50% 198 ton/h)
Steam temperature 811K
Steam pressure 166.4 bar
Power output 122 MW max

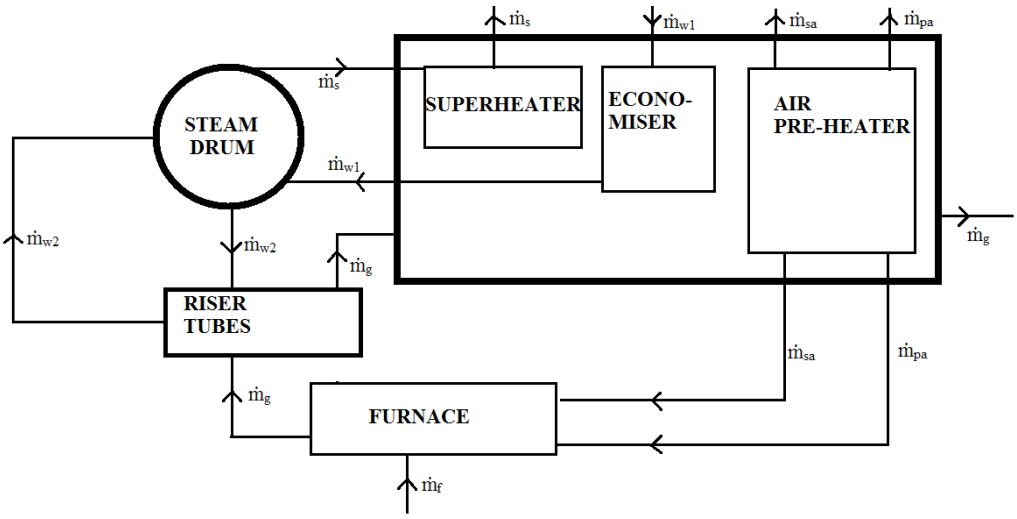


Figure 3: Boiler and its components

(a) Furnace:

Energy analysis:-

$E_i = \dot{m}_f h_f + \dot{m}_{pa} h_{pa} + \dot{m}_{sa} h_{sa}$

$E_o = \dot{m}_g h_g$

$E_{loss} = E_i - E_o$

$\eta_I = E_o/E_i$

Exergy analysis:-

$X_i = \varepsilon_f + \varepsilon_{pa} + \varepsilon_{sa}$

$X_o = \varepsilon_g$

$I = X_i - X_o$

$\eta_{II} = X_o/X_i$

Where-

$\mathcal{E}_{pa} = \dot{m}_{pa} (h_{pa} - T_o s_{pa})$

$\mathcal{E}_{sa} = \dot{m}_{sa} (h_{sa} - T_o s_{sa})$

$\mathcal{E}_{g} = \dot{m}_{g} (h_{g} - T_o s_{g})$

Exergy of fuel is given by the equation proposed by Shieh and Fan for calculating the Exergy of fuel

$\mathcal{E}_f$ =34183.16(C) +21.95 (N) +11659.9 (H) +18242.90 (S) +13265.9 (O) KW

(b). Heat Recovery System-

Energy analysis:-

$E_i = \dot{m}_g (\Delta h_{i-o})_g$

$E_o = \dot{m}_{sup} (\Delta h_{i-o})_{sup} + \dot{m}_w (\Delta h_{i-o})_w + \dot{m}_{pa} (\Delta h_{i-o})_{pa} + \dot{m}_{sa} (\Delta h_{i-o})_{sa}$

$E_o = \dot{m}_{sup} (h_o - h_i)_{sup} + \dot{m}_w (h_o - h_i)_w + \dot{m}_{pa} (h_o - h_i)_{pa} + \dot{m}_{sa} (h_o - h_i)_{sa}$

$E_{loss} = E_i - E_o$

$\eta_I = E_o/E_i$

Exergy Analysis:-

$X_i = \varepsilon_{gi} - \varepsilon_{go} = \dot{m}_g (h_g - T_o s_g)_i - \dot{m}_g (h_g - T_o s_g)_o$

$X_o = (\varepsilon_{sup\,(o)} - \varepsilon_{sup\,(i)}) + (\varepsilon_{w\,(o)} - \varepsilon_{w\,(i)}) + (\varepsilon_{pa\,(o)} - \varepsilon_{pa\,(i)}) + (\varepsilon_{sa\,(o)} - \varepsilon_{sa\,(i)})$

$X_o = [\dot{m}_{sup} (h_{sup} - T_o s_{sup})_o - \dot{m}_{sup} (h_{sup} - T_o s_{sup})_i] + [\dot{m}_w (h_w - T_o s_w)_o - \dot{m}_w (h_w - T_o s_w)_i] + [\dot{m}_{pa} (h_{pa} - T_o s_{pa})_o - \dot{m}_{pa} (h_{pa} - T_o s_{pa})_i] + [\dot{m}_{sa} (h_{sa} - T_o s_{sa})_o - \dot{m}_{sa} (h_{sa} - T_o s_{sa})_i]$

$I = X_i - X_o$

$\eta_{II} = X_o/X_i$

Analysis of Turbine:

(a) Energy analysis:

For adiabatic turbine-

$E_i = \dot{m}_s h_1$

$E_o = \dot{m}_s h_2$

Energy balance

$E_i = E_o + W$

$\eta_I = 1 - E_o / E_i$

(b) Exergy analysis:

$X_i = \dot{m}_s (h_1 - T_o s_1)$

$X_0 = \dot{m}_s (h_2 - T_o s_2)$

Exergy balance

$X_i - I - W_o = X_0$

$\eta_{II} = 1 - I / (X_i - X_0)$

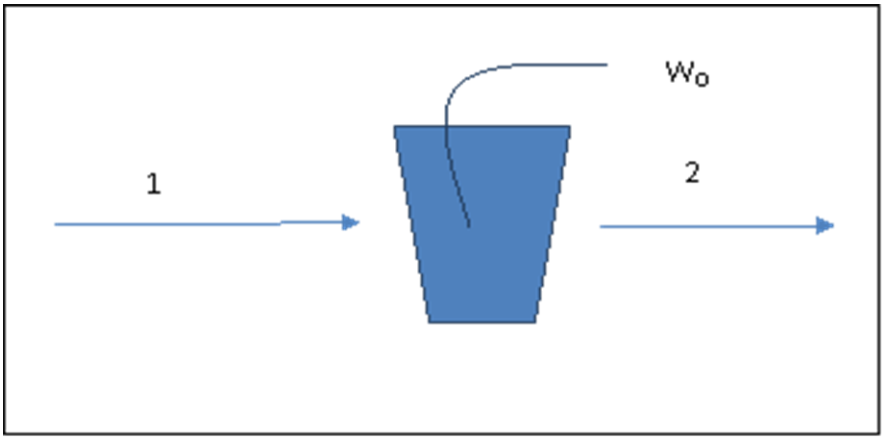


Figure 4: Steam Turbine TURBINE

Table 1: Exergy destruction rate and the exergy efficiency plant

COMPONENTS	EXERGY DESTRUCTION	EXERGY EFFICIENCY
1.PUMP	$I_P = X_3 + W_P - X_4$	$\eta = \frac{X4 - X3}{W_P}$
2. CONDENSOR	$I_{con} = (X_2 - X_3) - (X_{3'} - X_{2'})$	$\eta = 1 - \frac{Icon}{(X_2 - X_3)}$
3. TURBINE	$I_t = X_i - X_o - W_t$	$\eta = \frac{W_t}{(X_i - X_o)}$

Results and discussion

The energy losses at various components of power plant were analysed and the results computed for energy as well as exergy analysis were as under

Table 2: Comparision of Energy and Exergy analysis

	I Law (Energy Efficiency(%))	II Law (Energy Efficiency(%))
Boiler	76	42
Turbine	87	65
Condenser	18	13
Condenser Pump	90	84
Low Pressure Heater	91	86
Deaerator	68	66
Boiler feed Pump	98	96
Economizer	85	72
Air Pre Heater	75	71

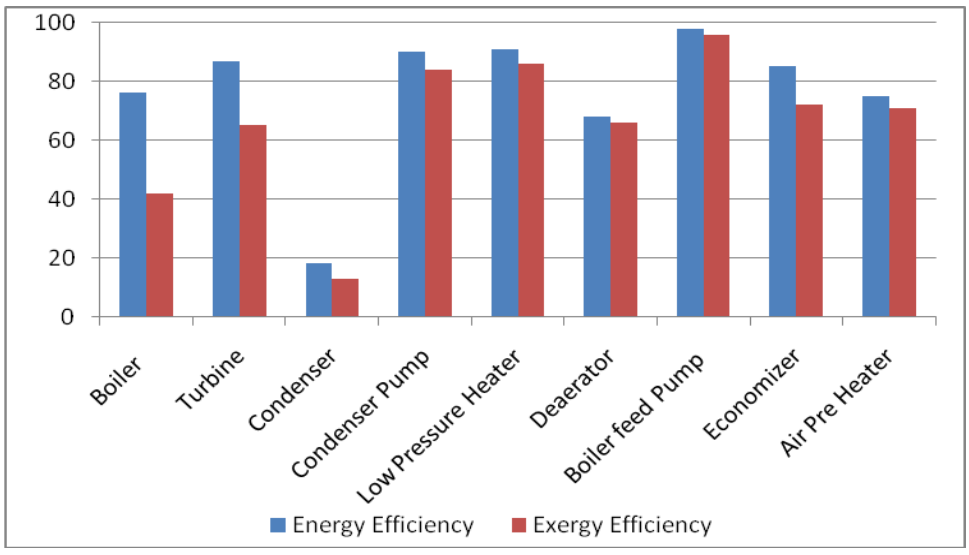


Figure 5: Comparision of Energy and Exergy analysis

The Exergy analysis of major components were carried out, where from the above graph we can identify the useful energy loss that is taking place in the plant are determined through various components as listed above. Boiler and turbine show major losses are in boiler and turbine both in energy and exergy estimatation.
So there is need to redesign the Boiler as well as turbine is in order to reduce the heat loss and better heat transfer in boiler and turbine.

Conclusion

The following conclusions have been drawn from the drawn from the site study at thermal power plant,

- The exergy analysis of the power plant components identifies that useful energy is less in almost all the components of the power plant as computed from the energy analysis. This
- Boiler and turbine of a power plant are the major sources of useful energy loss.
- Only negligible amounts of useful waste energy can be recovered through implementing some heat recovery system.
- In order to achieve significant improvement of energy efficiency the boiler and turbine systems need to be redesigned.

Nomenclature-

$\dot{m}$	mass flow rate (kg/sec)
h	specific enthalpy (kJ/kg)
T_o	surrounding temperature (Kelvin)
s	specific entropy (kJ/kg K)
I	exergy destruction (kJ/sec)
X	exergy rate (kJ/sec)
W	power (KW)
e	specific exergy (KJ/Kg)
x	mole fraction of constituents

Suffix-

f	fuel
pa	primary air
sa	secondary air
g	hot gas stream
i	input
o	output
sup	superheated steam
t	Turbine
p	pump
con	condenser
cc	combustion chamber

com compressor
t turbine
ph physical
ch chemical

Greek symbols-

η_I first law efficiency
η_{II} second law efficiency
$\mathcal{E}$ exergy associated with individual's component (kJ/sec)
X exergy rate (kJ/sec)

References:

[1] Abdel-Jawad, M.,Al-Tabtabaei, M.(1999). *Impact on Current Power Generation and Water Desalination Activities on Kuwait Marine Enviornment*. Proceedings of the IDA word congress on desalination and water reuse. San Deiego.USA

[2] Ahrendts, J. (1980). *Reference States.*Energy 5, Vol. 8, pp. 667-677.

[3] Aljundi, I.H." Energy and exergy analysis of a steam power plant in Jordan" Applied Thermal Engineering, Volume 29, Issues 2-3, February 2009, Pages 324-328.

[4] American Society of Mechanical Engineers (ASME) (1967). *1967 ASME Steam Tables.*

[5] The American Society of Mechanical Engineers. New York, USA.

[6] Badr, O., Probert, S. D., O'Callaghan, P. (1990).*Rankyne Cycles for Steam Power-Plants.*Applied Energy 36, pp. 191-231.

[7] Barner, H. E., Scheuerman, R. V. (1978). *Handbook of Thermochemical Data for Compounds and Acqueous Species.* John Wiley and Sons Inc.

[8] Brown Boveri Co. (BBC) (1979). *Thermal Kit, Simplified Instructions for the Thermal Calculation of the Antikokan Units*. HTGD 12246 E.

[9] Bejan,A., Tsatsaronis,G.,Moran, M.(1997). *Thermal Design And Optimization*.John Wiley and Sons Inc., New York.

[10] Benelmir,R(1989). *Second Law Analysis of a Co-generation Cycle*. Ph.D thesis, Georgia Institute of Technology.

[11] Boehm,R.. F. (1987). *Design Analysis of Thermal Systems*. Ed John Wiley and Sons, New York.

[12] Cengel, Y.A., Boles, M.A.," Thermodynamics: An Engineering Approach", fifth ed. McGraw-Hill, New York. 2006.

[13] Cooke,D.H. (1985) *On Prediction of off design Multistage Turbine Pressures by Stodola's Ellipse. Journal of Engineering for Gas Turbines and Power*. Transactions of ASME. Vol.107,pp.596-606.

[14] Corripio,A. B.,Chrien, K. S., Evans, L,B. (1982). *Estimate Costs of Heat Exchangers and Storage Tanks Via Correlations*. Chemical Engineering, January 1982, pp125-127.

[15] El-Sayed,Y. M., Aplenc,A. J.(1970). *Application of the Thermoeconomic Approach in the Analysis and Optimization of Vapor-Compression Desalting System*. Transactions of the ASME. Journal of Engineering and Power,Vol. 92 no. 1, pp 17-26.

[16] El-Sayed,Y. M., Tribus, M. (1983). *Strategic Use of Thermoeconomics for Systems Improvement*. Acs Symposium series, no. 235, pp. 215-238. Washington D.C., U.S.A..

[17] Frangopoulus,C.A. (1988). *Optimal Design of a Gas Turbine Plant by a Thermoeconomic Approach*. ASME COGEN-TURBO, pp. 563-571. ASME, New York, USA.

[18] Gaggioli, R. A., El- Sayed, Y.M.(1987). *A Critical Review of Second Law Costing Methods. Proceedings of IV International Symposium on Secon Law Analysis of thermal Systems*.(ASME Book I00236). ASME, pp. 59-73. New York, USA.

[19] Kotas, T. (1985). *The Exergy Method of Thermal Plant Analysis*. Butteerworth eds., London UK.

[20] Lozano, M.A., Valero,A. (1993). *Theory of Exergetic Cost*. Energy, Vol. 18, no.3, pp. 939-960. Elsevier Science Ltd., UK.

[21] Sarang, J and Amit, k.,Exergy Analysis of Boiler In cogeneration Thermal Power Plant, 2013, Volume-02, Issue-10, pp-385-392.

[22] Sciubba, E.; Wall, G. "A brief Commented History of Exergy From the Beginnings to 2004" Int. J. of Thermodynamics ISSN 1301-9724 Vol. 10 (No. 1), pp. 1-26, March 2007.

AIP | Journal of Applied Physics

Tunable unidirectional scattering of ellipsoidal single nanoparticle

Reena, Yogita Kalra, Ajeet Kumar, and R. K. Sinha

Citation: Journal of Applied Physics **119**, 243102 (2016); doi: 10.1063/1.4954675
View online: http://dx.doi.org/10.1063/1.4954675
View Table of Contents: http://scitation.aip.org/content/aip/journal/jap/119/24?ver=pdfcov
Published by the AIP Publishing

Articles you may be interested in

Influence of Au nanoparticles on the photoluminescent and electrical properties of Bi3.6Eu0.4Ti3O12 ferroelectric thin films
J. Appl. Phys. **116**, 034101 (2014); 10.1063/1.4887810

Influence of Cr2O3 nanoparticles on the physical properties of polyvinyl alcohol
J. Appl. Phys. **112**, 093525 (2012); 10.1063/1.4764864

Spectrally tunable magnetic nanoparticles designed for distribution/recollection applications
J. Appl. Phys. **107**, 09B327 (2010); 10.1063/1.3355900

Ag nanoparticle dispersed Pb Ti O 3 percolative composite thin film with high permittivity
Appl. Phys. Lett. **93**, 222901 (2008); 10.1063/1.3037207

Single metal nanoparticle absorption spectroscopy and optical characterization
Appl. Phys. Lett. **88**, 063109 (2006); 10.1063/1.2172143



Reuse of AIP Publishing content is subject to the terms at: https://publishing.aip.org/authors/rights-and-permissions. Download to IP: 14.139.251.107 On: Tue, 12 Jul 2016 05:16:16

JOURNAL OF APPLIED PHYSICS **119**, 243102 (2016)

Tunable unidirectional scattering of ellipsoidal single nanoparticle

Reena,[1] Yogita Kalra,[1] Ajeet Kumar,[1] and R. K. Sinha[1,2,a)]
[1]*TIFAC-center of Relevance and Excellence in Fiber Optics and Optical Communication, Department of Applied Physics, Delhi Technological University (Formerly Delhi College of Engineering, University of Delhi), Bawana Road, Delhi 110042, India*
[2]*CSIR-Central Scientific Instruments Organisation, Sector 30 C, Chandigarh 160 030, India*

(Received 24 February 2016; accepted 5 June 2016; published online 24 June 2016)

We report unidirectional scattering by tri-axial single ellipsoidal dielectric nanoparticle, which is applicable in the design and development of tunable, low-loss and ultra-compact nanoantennas. Based on the orientation and rotation of the ellipsoidal nanoparticle, three types of modes, one longitudinal mode and two transverse modes, have been excited. Electric and magnetic dipoles have been optically induced in the nanoparticle. Generalized Kerker's conditions have been applied at the interference of optically induced electric and magnetic dipoles. Azimuthally symmetric forward scattering with complete suppression of backward scattering using first Generalized Kerker's condition has been achieved at three different wavelengths for the allowed longitudinal mode and transverse modes in the optical region using single ellipsoidal nanoparticle. Due to 3-fold symmetry, forward scattering can be tuned at different wavelengths, using single ellipsoidal nanoparticle just by changing the direction of the incident electric field. *Published by AIP Publishing.*
[http://dx.doi.org/10.1063/1.4954675]

I. INTRODUCTION

Scattering properties of light by various types of nanoparticles have been studied to manipulate and confine electromagnetic waves on the nanometer scale due to their numerous applications such as sensing, nanoantennas, photovoltaics, and medicine.[1–6] Metallic nanoparticles have been used due to their unique property of generation of surface plasmon polaritons at the metal surfaces that has attracted many applications in nanophotonics and metamaterials.[7–9] But metal's losses and absorption affect the quality of the metallic nanostructure.[6,10] Moreover, it is not possible to achieve magnetic resonance in the visible spectrum region using metallic split ring resonators. Therefore, large permittivity dielectrics are being used as the counterpart of metals due to negligible absorption.[11–14] However, absorption is requisite in applications such as photovoltaics[15] and sensing[16] but in case of nanoantennas, absorption should be as low as possible. So, dielectrics with high permittivity are the prevalent choice in application of nanoantennas. First of all, Kuznetsov *et al*. demonstrated experimentally magnetic resonance in the visible spectrum region using high-dielectric nanoparticles.[14] Due to the light-matter interaction, electric and magnetic dipoles are produced in the dielectric nanoparticles of large permittivity at resonant frequencies.[17] Wavelengths at which magnitude of electric and magnetic moments is equal, and generalized Kerker's (GKs) conditions have been applied. When the first generalized Kerker's condition is satisfied, forward scattering takes place by suppressing the backward scattering to zero and when the second generalized Kerker's condition is satisfied, most of the light is scattered in the backward direction.[18] Unidirectional forward scattering (Huygen's source) and backward scattering (Huygen's reflector) are used to design all-dielectric optical nanoantennas.[11,12]

Complete forward scattering and high directivity has been achieved in many symmetrical structures like sphere[5] and cube.[18] Fu *et al*. have calculated forward to backward scattering ratio for spheroidal Si nanoparticles.[19] In spheroidal nanoparticle, two axes are equal and only one axis has different dimensions. But ellipsoidal nanoparticle has all the axes unequal. Ellipsoidal nanoparticle has the advantage that it has three-fold symmetry which leads to three types of modes, two transverse modes (TM) and one longitudinal mode (LM). Our work is based on the ellipsoidal germanium (Ge) nanoparticle. Polarizability of the nanoparticle changes by changing the direction of incident electric field along three unequal axes of the ellipsoid. Hence, the forward scattering can be tuned at different wavelengths by changing the direction of incident electric field, which is not possible in the case of symmetric structures like sphere and cube. Kalkbrenner *et al*. experimentally demonstrated the rotation of the single gold ellipsoidal nanoparticle attached to the tip of glass fiber.[20] Eventually, it is also feasible to rotate dielectric nanoparticle using this technique, so that it is useful in various nanophotonic applications such as optical imaging, energy harvesting, and sensing.

II. DESIGN

Triaxial ellipsoidal dielectric nonmagnetic nanoparticle has been considered with lengths of semi-principal axes as "*a*," "*b*," and "*c*," where length along "*a*" has been taken as semi-major axis. Ellipsoidal particles are classified into three categories based on the relative length of the three principal axes, namely, oblate spheroids ($a = b > c$), prolate spheroids ($a = b < c$), and scalene ellipsoids ($a > b > c$). In this paper, scalene ellipsoid has been considered which leads to three

a)E-mail: dr_rk_sinha@yahoo.com

Reuse of AIP Publishing content is subject to the terms at: https://publishing.aip.org/authors/rights-and-permissions. Download to IP: 14.139.251.107 On: Tue, 12 Jul 2016 05:16:16

distinct modes, one longitudinal mode and two transverse modes. The effective radius of the equivolume sphere for the ellipsoidal nanoparticle is given by $r_{\text{eff}} = (a * b * c)^{1/3}$. Material of the nanoparticle has been taken to be Ge.[21] Ge is a dielectric with high permittivity, $\varepsilon_r = 20$, required for the design of low loss high dielectric nanoantennas. Dimensions of ellipsoid have been taken as $a = 125$ nm, $b = 100$ nm, and $c = 50$ nm. The dimensions of the nanoparticle are chosen in such a way that wavelength of forward scattering falls in the optical region. Incident radiation has been taken to be linearly polarized in the y-direction and propagates in the x-direction. Orientation of the nanoparticle has been shown in Figure 1(a) and rotation of the nanoparticle when major axis is parallel to the x-axis has been shown in Figure 1(b).

III. DIPOLE ANALYSIS

Due to the light-matter interaction, electric and magnetic dipoles are generated at the particular wavelengths λ_{ED} and λ_{MD}. The electric dipole moment "p" and magnetic dipole moment "m" can be expressed as[22]

$$p = \varepsilon_0(1-\varepsilon_r)\oint_V E(r')dV', \tag{1a}$$

$$m = \frac{i\omega(1-\varepsilon_r)}{2c}\oint_V [r \times E(r')]dV', \tag{1b}$$

where i denotes the imaginary part of the complex variable, ω is the angular frequency, ε_0 is the vacuum permittivity, r is the observation point, r' is the source point, c is the speed of light in vacuum, ε_r is the relative permittivity of the nanoparticle, $\times$ denotes the vector product of position vector "r," and electric field vector "$E(r')$". Calculations have been done in the vectorial field with the finite element method (FEM) based "Comsol Multiphysics" software package.

Further, scattering cross section of the nanoparticle for both electric and magnetic dipoles has been calculated as

$$\sigma^p_{sca} = \frac{\langle P_{sca,ED}\rangle}{I_0}, \tag{2a}$$

$$\sigma^m_{sca} = \frac{\langle P_{sca,MD}\rangle}{I_0}, \tag{2b}$$

where I_0 is the incident power density, $\langle P_{sca,ED}\rangle$ and $\langle P_{sca,MD}\rangle$ are the power scattered by electric and magnetic dipole, respectively, which can be expressed as

$$\langle P_{sca,ED}\rangle = \frac{c^2 k_0^4 z_0}{12\pi}|p|^2, \tag{3a}$$

$$\langle P_{sca,MD}\rangle = \frac{c^2 k_0^4 z_0}{12\pi}|m|^2, \tag{3b}$$

where c is the speed of light in vacuum, k_0 and z_0 are the free space wavenumber and free space impedance, respectively. Electric dipole moment "p" and magnetic dipole moment "m" have been calculated using Equations (1a) and (1b), respectively.

Further, the effect of orientation and rotation of the ellipsoidal nanoparticle on electric and magnetic dipole moments has been analyzed. Three distinct modes, one longitudinal mode (LM) and two transverse modes (TM), are excited at distinct combinations of incident angle and rotation angle. LM mode is excited when major axis is parallel to the incident electric field (E) or at $\theta = 90°$. Two TM modes are excited when major axis is perpendicular to the incident electric field or at $\theta = 0°$. One TM mode is excited when $\phi = 0°$ or b-axis is parallel to the incident electric field and another transverse mode is excited when $\phi = 90°$ or c-axis is parallel to the incident electric field.

Scattering cross section has been calculated with Matlab using Equations (2a) and (2b). The variation of scattering cross-section of the ellipsoidal nanoparticle with wavelength for the incident electric field parallel to a-axis has been obtained as shown in Figure 2(a). Peaks in the scattering cross section, one at the wavelength 500 nm corresponds to electric dipole resonance and another at 650 nm, correspond to the magnetic dipole resonance as shown in Figure 2(a). Electric field distribution in the nanoparticle at the wavelengths $\lambda_{\text{ED}} = 500$ nm and $\lambda_{\text{MD}} = 650$ nm has been shown in Figures 2(b) and 2(c), respectively. So, at $\theta = 90°$, LM has been excited at the wavelengths λ_{ED} and λ_{MD}. Figure 2(a) indicates that electric dipole and magnetic dipole interfere at the wavelengths 607 nm and 680 nm. At these wavelengths, electric and magnetic responses are equal.

Further, angle of orientation has been changed from $\theta = 90°$ to $\theta = 0°$, major axis is now parallel to the direction of propagation and two minor axes have been taken to be parallel to the incident electric field one by one. Then two transverse modes are excited, one is called b-TM when $\phi = 0°$ and another is called c-TM when $\phi = 90°$.

First, b-axis has been taken to be parallel to the incident electric field, so b-TM mode has been excited. Scattering cross section has been calculated and has been plotted versus wavelength as shown in Figure 3(a). Peaks in the scattering spectra denote the electric and magnetic dipole resonances.

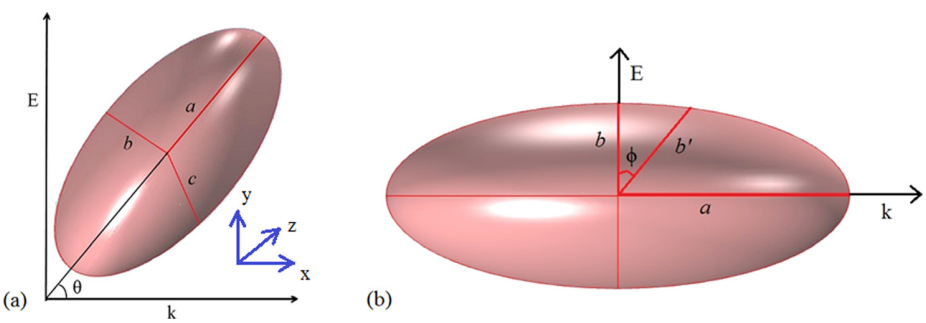


FIG. 1. (a) Orientation of the major-axis of the ellipsoidal nanoparticle in the laboratory frame around the x-axis or the direction of propagation k with angle θ. (b) Rotation of the nanoparticle around the major-axis with angle ϕ.

Reuse of AIP Publishing content is subject to the terms at: https://publishing.aip.org/authors/rights-and-permissions. Download to IP: 14.139.251.107 On: Tue, 12 Jul 2016 05:16:16

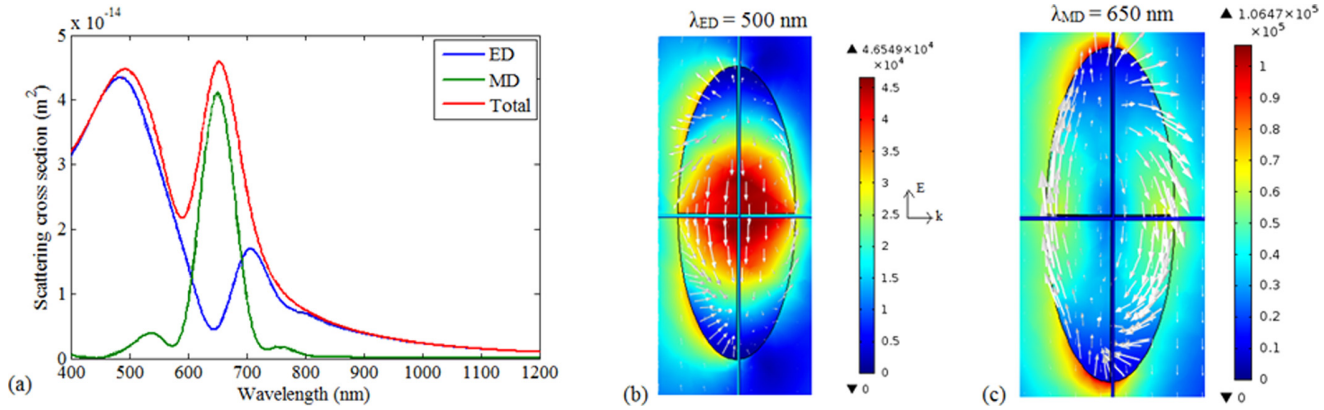


FIG. 2. (a) Scattering cross-section of the ellipsoidal nanoparticle when E || to *a*-axis of the ellipsoid. (b) and (c) Electric field inside the nanoparticle forming electric dipole and magnetic dipole. White arrows indicate electric lines of force.

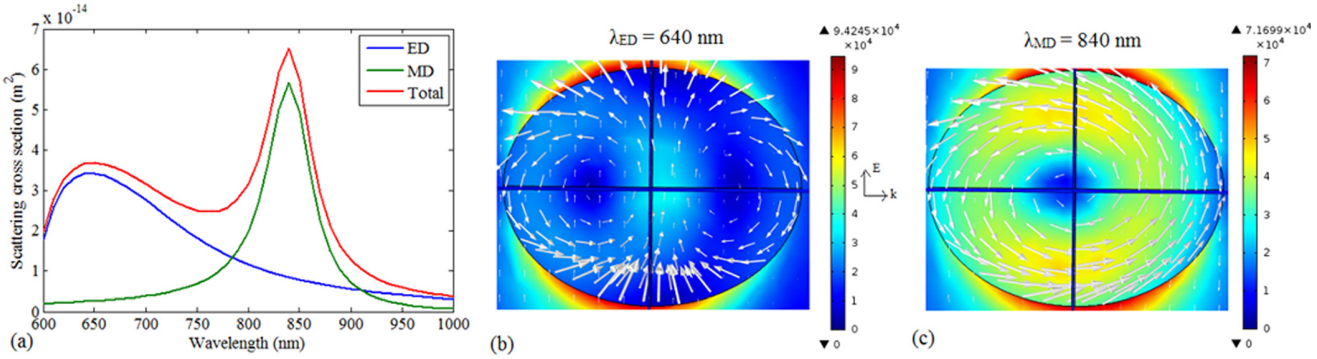


FIG. 3. (a) Variation of scattering cross-section with wavelength when E || *b*-axis of the ellipsoid. (b) and (c) Electric field distribution patterns at the wavelengths where electric dipoles are created.

Electric dipole and magnetic dipole are created at the wavelengths $\lambda_{ED} = 640$ nm and $\lambda_{MD} = 840$ nm, respectively, as shown in Figure 3(a). The electric field distribution at $\lambda_{ED} = 640$ nm and $\lambda_{MD} = 840$ nm has been shown in Figures 3(b) and 3(c), respectively.

Now, *c*-axis has been taken to be parallel to the incident electric field, leading to the excitation of *c*-TM mode. The position of the electric dipole and magnetic dipole has been shifted to the wavelengths $\lambda_{ED} = 560$ nm and $\lambda_{MD} = 660$ nm as shown in Figure 4(a). An electric field distribution at the wavelengths λ_{ED} and λ_{MD} has been shown in Figures 4(b) and 4(c), respectively.

Hence, electric and magnetic dipoles can be tuned at different wavelengths by changing the direction of the incident electric field.

IV. UNIDIRECTIONAL SCATTERING USING GENERALIZED KERKER'S (GK) CONDITIONS

Far field scattering pattern of pure electric and magnetic dipoles is symmetrically distributed in forward and backward directions, when there is no interference between the dipoles.[22] In the case of interference of electric dipole and magnetic dipole, unidirectional scattering takes place. Positions of

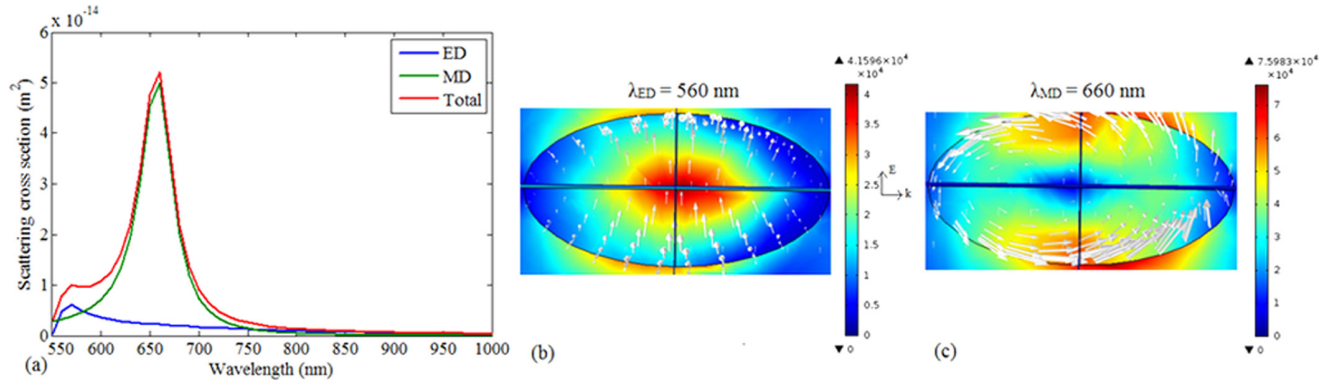


FIG. 4. (a) Plot of scattering cross section with wavelength when E || *c*-axis of the ellipsoidal nanoparticle. (b) and (c) Electric field distribution and direction of electric field shown by white lines.

Reuse of AIP Publishing content is subject to the terms at: https://publishing.aip.org/authors/rights-and-permissions. Download to IP: 14.139.251.107 On: Tue, 12 Jul 2016 05:16:16

electric dipoles, magnetic dipoles, and their interference have been shown in Figures 2–4 for longitudinal as well as transverse modes.

Further, to discriminate whether there is forward scattering or backward scattering, electric polarizability and magnetic polarizability have been calculated and generalized Kerker's conditions have been applied. Electric polarizability α_e and magnetic polarizability α_m can be expressed as

$$\alpha_e = \frac{p_y}{\varepsilon_0 |E_0|}, \tag{4a}$$

$$\alpha_m = \frac{m_x}{|H_0|}, \tag{4b}$$

where E_0 and H_0 are the electric and magnetic fields of the incident plane wave fallen on the nanoparticle, p_y and m_x are the electric dipole moment along y-axis and magnetic dipole moment along x-axis, respectively.[23]

According to the first GK condition, unidirectional forward scattering takes place, when

$$\frac{\alpha_e}{\varepsilon_s} = \mu_s \alpha_m, \tag{5}$$

which results in backward scattering zero or

$$\frac{d\sigma_{sca}}{d\Omega}(180^\circ) = 0, \tag{6}$$

where ε_s and μ_s are the relative permittivity and permeability of the surrounding medium. In our case, surrounding medium is air, so $\varepsilon_s = \mu_s = 1$.

Further, according to the second GK condition, backward scattering takes place when

$$\mathrm{Re}\left(\frac{\alpha_e}{\varepsilon_s}\right) = -\mathrm{Re}(\mu_s \alpha_m), \tag{7a}$$

$$\mathrm{Im}\left(\frac{\alpha_e}{\varepsilon_s}\right) = \mathrm{Im}(\mu_s \alpha_m). \tag{7b}$$

Forward scattering is not zero in this case and has a value equal to

$$\frac{d\sigma_{sca}}{d\Omega}(0^\circ) = \frac{16 k_0^{10}}{9} |\alpha_e / \varepsilon_s|^4. \tag{8}$$

In this case, as medium is taken to be air, so $\varepsilon_s = \mu_s = 1$, so that real part of the electric polarizability is equal to negative of the real part of the magnetic polarizability as shown in Equation (7a). Also, imaginary parts of the electric and magnetic polarizabilities are equal as shown in Equation (7b). In case of backward scattering there is a very small lobe in the forward direction. Thus, forward scattering is not completely suppressed in this case, value of scattered intensity in the forward direction is given by Equation (8).

Now, real and imaginary parts of the electric and magnetic polarizabilities of the nanoparticle have been calculated using Equations (4a) and (4b) and variations have been plotted with respect to the wavelength for all the three distinct modes to analyze the GK conditions of forward scattering and backward scattering as shown in Figures 5(a)–7(a).

Real and imaginary parts of electric and magnetic polarizabilities have been plotted in Figure 5(a) for the longitudinal mode when incident electric field is parallel to the a-axis or semi-major axis. First generalized Kerker's condition is satisfied at the wavelength 680 nm leading to forward scattering at 680 nm. Far field scattering pattern is shown in Figure 5(b). At this wavelength, no backward scattering has been obtained, further verified this fact. At the wavelength of 607 nm, second GK condition is satisfied, thus backward scattering takes place with a small lobe in the forward direction. Far field scattering pattern at this wavelength is shown in Figure 5(c).

Further, electric and magnetic polarizabilities have been calculated for the transverse mode when incident electric field is along the b-axis of the nanoparticle. Here, real and imaginary parts of electric and magnetic polarizabilities are equal at 912 nm as shown in Figure 6(a). Hence, first GK condition is satisfied at this wavelength. Far-field scattering pattern at this wavelength indicates forward scattering shown in Figure 6(b). Second GK condition is satisfied at the wavelength 784 nm. So, there is backward scattering at this wavelength which is also shown by far field scattering pattern in Figure 6(c).

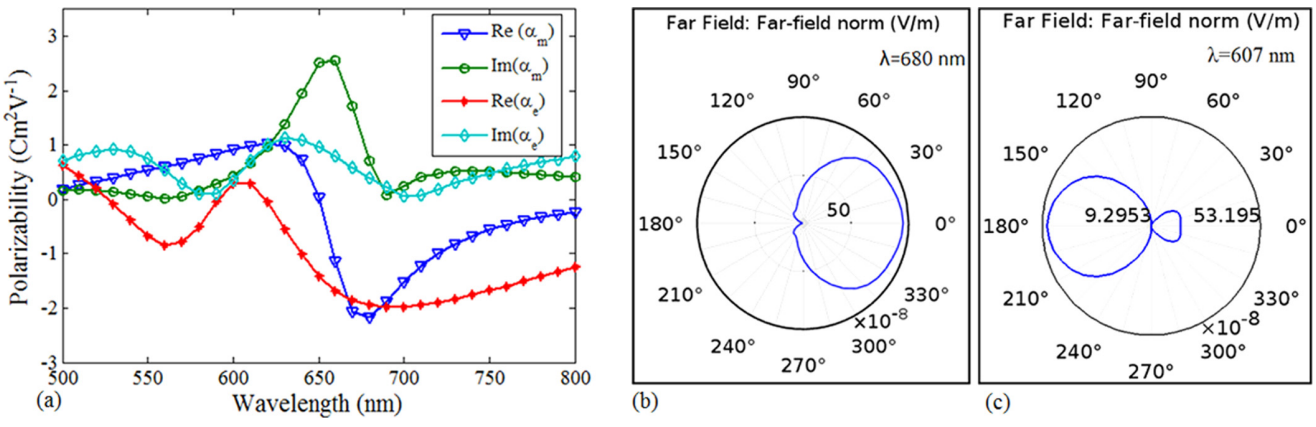


FIG. 5. (a) Plot of real and imaginary parts of electric and magnetic polarizabilities of the nanoparticle with wavelength when E || a-axis. (b)-(c) Far field scattering patterns show forward scattering at wavelength 680 nm and backward scattering at 607 nm.

Reuse of AIP Publishing content is subject to the terms at: https://publishing.aip.org/authors/rights-and-permissions. Download to IP: 14.139.251.107 On: Tue, 12 Jul 2016 05:16:16

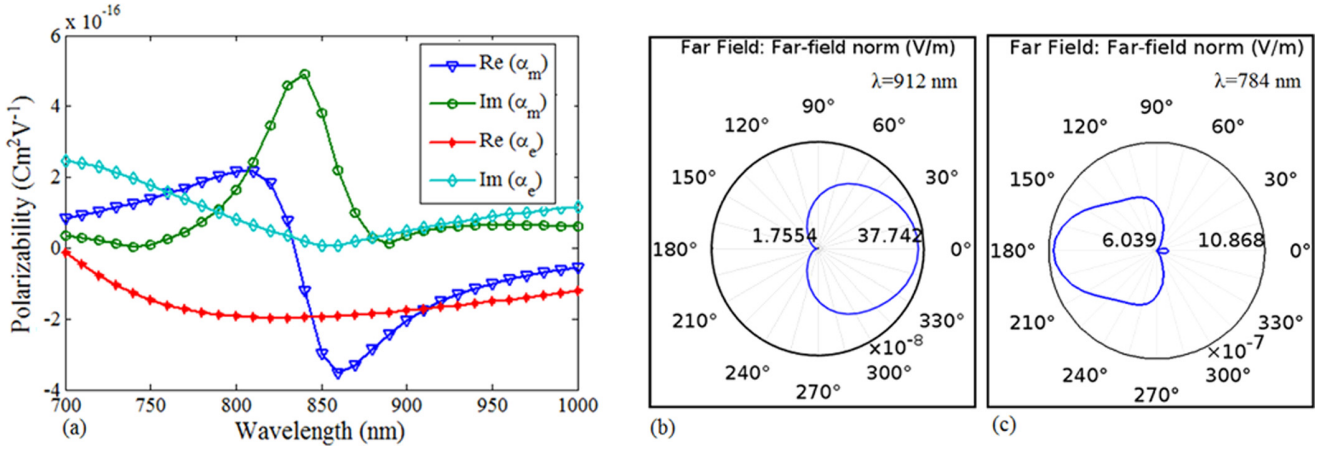


FIG. 6. (a) Variation of electric and magnetic polarizabilities of the nanoparticle with wavelength when E || *b*-axis. (b) and (c) Far field scattering patterns show forward scattering at wavelength 912 nm and backward scattering at 784 nm.

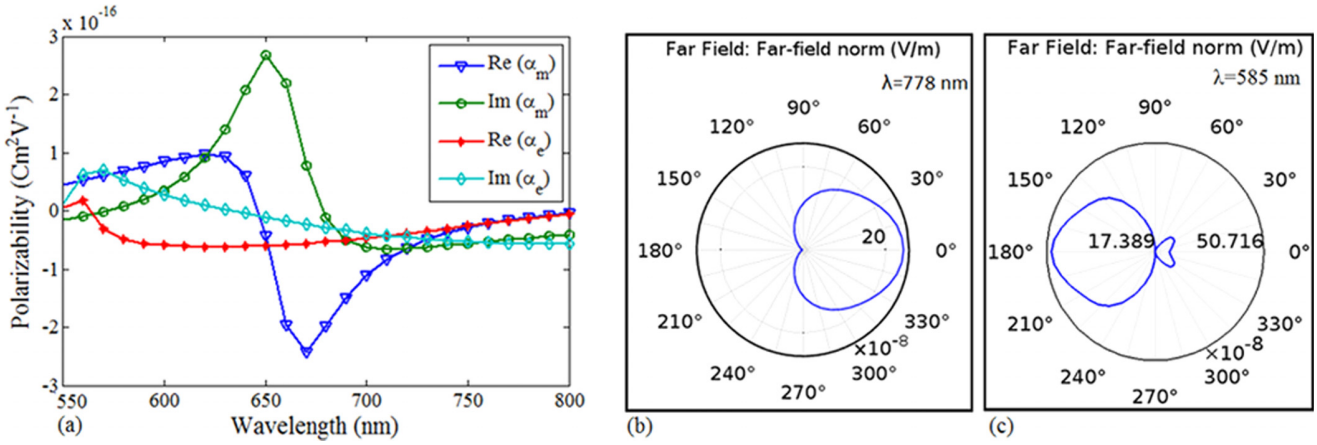


FIG. 7. (a) Wavelength dependence of real and imaginary parts of electric and magnetic polarizabilities of the nanoparticle when E || *c*-axis. (b) and (c) Far field scattering patterns show forward scattering at wavelength 778 nm and backward scattering at 585 nm.

Finally, polarizabilities have been calculated and plotted versus wavelength for the second transverse mode in which incident electric field has been taken along *c*-axis, i.e., smallest axis of the nanoparticle. In this case, first generalized condition is satisfied at the wavelength $\lambda = 778$ nm. Hence, at this wavelength scattering takes place in forward direction which is also verified by far field scattering pattern in Figure 7(b) and backward scattering takes place at the wavelength 585 nm, where far field scattering patterns have been calculated using finite element method. Thereby, ellipsoidal nanoparticles are the suitable candidates for tunable unidirectional applications.

V. CONCLUSION

In this paper, tunable and azimuthally symmetric unidirectional scattering of ellipsoidal dielectric nanoparticle has been analyzed. Electric and magnetic dipoles have been optically induced in the ellipsoidal nanoparticle at the resonance wavelengths, where peaks of the scattering spectra denote the positions of resonance. Due to three fold symmetry, ellipsoidal nanoparticle exhibits three types of resonant modes, one longitudinal mode and two transverse modes. Due to the three types of longitudinal and transverse modes, complete forward unidirectional scattering takes place in the visible and near infrared region at three wavelengths 680 nm, 912 nm, and 778 nm just by changing the direction of incident electric field, satisfying the generalized Kerker's condition. Thus, ellipsoidal nanoparticles can be used to achieve tunable unidirectional scattering. The electric and magnetic resonances have been experimentally demonstrated in the ordered array of nanodisks by Staude *et al.*[24] Tunable unidirectional properties exhibited by these nanoparticles can lead to a large number of applications for the development of low loss and ultra-compact optical nanoantennas, nanolasers, spectroscopy, high resolution near field microscopy, optical imaging and sensing.

ACKNOWLEDGMENTS

The authors gratefully (i) acknowledge the initiatives and the support from TIFAC-Center of Relevance and Excellence in Fiber Optics and Optical Communication at Delhi College of Engineering, now DTU, and Delhi under

Reuse of AIP Publishing content is subject to the terms at: https://publishing.aip.org/authors/rights-and-permissions. Download to IP: 14.139.251.107 On: Tue, 12 Jul 2016 05:16:16

Mission REACH Program of Technology vision-2020, Government of India and (ii) the support through DST-RMES (Indo-Russian) joint research project on "All Dielectric, Plasmonic and Hybrid Photonic Nanostructures."

[1]L. Novotony and B. Hecht, *Principles of Nano-Optics* (Cambridge University Press, 2012).
[2]C. M. Soukoulis and M. Wegener, "Past achievement and future challenges in the development of three-dimensional photonic metamaterials," Nat. Photonics **5**, 523–530 (2011).
[3]W. Xiong, D. Sikdar, M. Walsh, K. J. Si, Y. Tang, Y. Chen, R. Mazid, M. Weyland, I. D. Rukhlenko, J. Etheridge, M. Premaratne, X. Li, and W. Cheng, "Single-crystal caged gold nanorods with tunable broadband plasmon resonances," Chem. Commun. **49**, 9630–9632 (2013).
[4]D. Sikdar, I. D. Rukhlenko, W. Cheng, and M. Premaratne, "Optimized gold nanoshell ensembles for biomedical applications," Nanoscale Res. Lett. **8**, 142–146 (2013).
[5]L. Novotony and N. Van Hulst, "Antennas for light," Nat. Photonics **5**, 83–90 (2011).
[6]S. Lal, S. Link, and N. J. Halas, "Nano-optics from sensing to waveguiding," Nat. Photonics **1**, 641–648 (2007).
[7]M. Alsawafta, M. Wahbeh, and V.-V. Truong, "Plasmonic modes and optical properties of gold and silver ellipsoidal nanoparticles by the discrete dipole approximation," J. Nanomater. **2012**, 457968 (2012).
[8]K. Kishor, M. N. Baitha, R. K. Sinha, and B. Lahiri, "Tunable negative refractive index metamaterial from V-shaped SRR structure: Fabrication and characterization," J. Opt. Soc. Am. B **31**, 1410–1414 (2014).
[9]V. Dillu and R. K. Sinha, "Enhanced Fano resonance in silver ellipsoidal plasmonic crystal cavity," J. Appl. Phys. **114**, 234305 (2013).
[10]U. Kreibig and M. Vollmer, *Optical Properties of Metal Clusters* (Springer-Verlag, Berlin, 1995).
[11]A. E. Krasnok, A. E. Miroshnichenko, P. A. Belov, and Y. S. Kivshar, "Huygens optical elements and Yagi-Uda nanoantennas based on dielectric nanoantennas," JETP Lett. **94**, 593–598 (2011).
[12]A. E. Krasnok, I. S. Maksymov, A. I. Denisyuk, P. A. Belov, A. E. Miroshnichenko, C. R. Simovski, and Y. S. Kivshar, "Optical nanoantennas," Phy. Usp. **56**(6), 539–564 (2013).
[13]A. E. Krasnok, A. E. Miroshnichenko, P. A. Belov, and Y. S. Kivshar, "All-dielectric optical nanoantennas," Opt. Express **20**, 20599 (2012).
[14]A. I. Kuznetsov, A. E. Miroshnichenko, Y. H. Fu, J. Zhang, and B. Luk'yanchuk, "Magnetic light," Sci. Rep. **2**, 492 (2012).
[15]P. Mathew, S. H. Lim, D. Derkacs, C. McPheeters, and E. T. Yu, "Metal and dielectric nanoparticle scattering for improved optical absorption in photovoltaic devices," Appl. Phys. Lett. **93**, 113108 (2008).
[16]D. M. Schaadt, B. Feng, and E. T. Yu, "Enhanced semiconductor optical absorption via surface plasmon excitation in metal nanoparticles," Appl. Phys. Lett. **86**, 063106 (2005).
[17]C. F. Bohren and D. R. Huffman, *Absorption and Scattering of Light by Small Particles* (Wiley, New York, 1983).
[18]D. Sikdar, W. Cheng, and M. Premaratne, "Optically resonant magneto-electric cubic nanoantennas for ultra-directional light scattering," J. Appl. Phys. **117**, 083101 (2015).
[19]Y. H. Fu, A. I. Kuznetsov, A. E. Miroshnichenko, Y. F. Yu, and B. Luk'yanchuk, "Directional visible light scattering by silicon nanoparticles," Nat. Commun. **4**, 1527 (2013).
[20]T. Kalkbrenner, U. Håkanson, and V. Sandoghdar, "Tomographic plasmon spectroscopy of a single gold nanoparticle," Nano Lett. **4**(12), 2309–2314 (2004).
[21]H. H. Li, "Refractive index of silicon and germanium and its wavelength and temperature derivatives," J. Phys. Chem. Ref. Data **9**, 561 (1980).
[22]C. H. Papas, *Theory of Electromagnetic Wave Propagation* (Courier Dover Publications, 2013).
[23]R. Gomez-Medina, B. Garcia-Camara, I. Suarez-Lacalle, F. Gonzalez, F. Moreno, M. Nieto-Vesperinas, and J. J. Saenz, "Electric and magnetic dipolar response of germanium nanospheres: Interference effects, scattering anisotropy and optical forces," J. Nanophotonics **5**, 053512 (2011).
[24]I. Staude, A. E. Miroshnichenko, M. Decker, N. T. Fofang, S. Liu, E. Gonzales, J. Dominguez, T. S. Luk, D. N. Neshev, I. Brener, and Y. Kivshar, "Tailoring directional scattering through magnetic and electric resonances in subwavelength silicon nanodisks," ACS Nano **7**(9), 7824–7832 (2013).

Reuse of AIP Publishing content is subject to the terms at: https://publishing.aip.org/authors/rights-and-permissions. Download to IP: 14.139.251.107 On: Tue, 12 Jul 2016 05:16:16

This article has been accepted for publication in a future issue of this journal, but has not been fully edited. Content may change prior to final publication. Citation information: DOI 10.1109/TIE.2016.2582460, IEEE Transactions on Industrial Electronics

ZVS-ZCS High Voltage Gain Integrated Boost Converter For DC Microgrid

Shelas Sathyan, *Student Member*, *IEEE*, H. M. Suryawanshi, *Senior Member*, *IEEE*, Bhim Singh, *Fellow*, *IEEE*, Chandan Chakraborty, *Fellow*, *IEEE*, Vishal Verma, and M. S. Ballal, *Senior Member*, *IEEE*

***Abstract*—A non-isolated soft switched integrated boost converter having high voltage gain is proposed for the module integrated PV systems, fuel cells and other low voltage energy sources. Here a bidirectional boost converter is integrated with a resonant voltage quadrupler cell to obtain higher voltage gain. The auxiliary switch of the converter, which is connected to the output port acts as an active clamp circuit. Hence ZVS (zero voltage switching) turn on of the MOSFET switches are achieved. Coupled inductor's leakage energy is recycled to the output port through this auxiliary switch. In the proposed converter, all the diodes of the quadrupler cell are turned off with ZCS (zero current switching). This considerably reduces the high frequency turn off losses and reverse recovery losses of the diodes. ZCS turn off of the diodes also remove the diode voltage ringing caused due to the interaction of the parasitic capacitance of the diodes and the leakage inductance of the coupled inductor. Hence to protect the diodes from the voltage spikes, snubbers are not required. The voltage stress on all the MOSFETs and diodes are lower. This helps to choose switches of low voltage rating (low $R_{DS}(ON)$) and thus improve the efficiency. Design and mathematical analysis of the proposed converter are made. A 250W prototype of the converter is built to verify the performance.**

***Index Terms*—DC-DC Converter, Zero voltage switching, Zero current switching, High voltage gain.**

I. Introduction

EFFICIENT utilization of the different renewable energy sources is one of the main challenge of power and energy sector. In order to interconnect the renewable sources to the grid, power electronics interface are necessary [1]. Solar PV systems are the most sought after renewable energy source due to the universal availability of the solar irradiation and the flexibility to install the PV panel at the consumer end. In order to improve the efficiency of the PV system by overcoming the losses due to the partial shading and module mismatches, modular PV systems are preferred for low power applications [2], [3]. Here a highly efficient, high voltage gain dc-dc converter is required to step up the low voltage output of the PV to that of the dc bus voltage. High voltage gain dc-dc converters are also required for various applications like UPS systems, fuel cells systems, battery bank, high intensity discharge (HID) lamps and server power supply etc. [4], [5].

In a conventional boost converter obtaining a high voltage gain is limited by the poor efficiency operation caused due to the conduction losses and diodes's reverese recovery losses [6]. Isolated converters can be used to achieve high voltage gain. However, for low power applications, nonisolated converters are preferred due to their higher efficiency, good power density and lower cost [7], [8]. Changes in electric codes also favours the use of nonisolated converters for low power solar PV systems. Among the various nonisolated high gain dc-dc converters, coupled inductor based converters are attractive due to the freedom of increasing the voltage conversion gain by simply changing the turn's ratio. Voltage spike on the switches due to the coupled inductor's leakage energy is the main concern of these converters. Lossless passive clamp [4], [9] or active clamp [10], [11] technique is used to limit this voltage spike on the switches. In [9], a boost converter is integrated with a flyback converter (Integrated boost converter) to obtain high voltage gain. Here the boost converter is acting as a passive clamp circuit which recycle the leakage energy. However, these converters suffer from high voltage stress on the output diode and thus necessary to use snubber circuit or high voltage rated diodes.

In isolated high voltage gain converters, different voltage multipliers like conventional full wave doubler, Greinacher multiplier and voltage tripler are used to reduce the turn's ratio of the transformer [12]. In [13], by connecting two Greinacher multipliers a voltage quadrupler circuit is proposed for high voltage step up applications. Natural voltage balancing of the output capacitor and lower device stress are the advantage of this voltage multiplier. In nonisolated coupled inductor converters, to reduce the voltage stress on the output diode and also to improve the voltage gain, voltage multipliers which are used in the isolated converters are introduced at the secondary side of the coupled inductor [3], [5], [14]–[21]. These converters achieve higher voltage gain without extreme

Manuscript received December 8, 2015; revised April 1, 2016; accepted May 9, 2016. This work was supported by the Department of Science and Technology (DST), Government of India, and RCUK under the project "RESCUES" .

Shelas Sathyan, H. M. Suryawanshi and M. S. Ballal are with the Department of Electrical Engineering, Visvesvaraya National Institute of Technology, Nagpur, 440010, India (e-mail: shelassathyan@yahoo.co.in; hms_1963@rediffmail.com).

Bhim Singh is with the Department of Electrical Engineering, Indian Institute of Technology Delhi, New Delhi, 110016, India (e-mail: bsingh@ee.iitd.ac.in).

Chandan Chakraborty is with the Department of Electrical Engineering, Indian Institute of Technology Kharagpur, Kharagpur, 721 302, India (e-mail: chakraborty@ieee.org).

Vishal Verma is with the Department of Electrical Engineering, Delhi Technological University, New Delhi, 110042, India (e-mail: vishalverma@dce.ac.in).

0278-0046 (c) 2016 IEEE. Personal use is permitted, but republication/redistribution requires IEEE permission. See http://www.ieee.org/publications_standards/publications/rights/index.html for more information.

This article has been accepted for publication in a future issue of this journal, but has not been fully edited. Content may change prior to final publication. Citation information: DOI 10.1109/TIE.2016.2582460, IEEE Transactions on Industrial Electronics

duty ratio operation. Moreover in these converters, the leakage inductance of the coupled inductor limits the reverse recovery losses of the diodes. In [5], integrated boost converter with ZVS is proposed for high voltage gain applications. Here, ZVS of the main switch depends only on the stored energy of the leakage inductance. Therefore to achieve ZVS, large leakage inductance (often an extra inductor) is required. In light load conditions where the large leakage inductance failed to provide ZVS, frequency modulation technique is proposed in [5]. All the above mentioned voltage multipliers consist of diodes and capacitors. Here resonant interaction of the leakage inductance and the stray capacitance of the diodes cause unwanted voltage spike or ringing on the diodes [3]. Moreover, in these converters all these diodes are hard switched which reduce the efficiency.

In this work, a nonisolated, soft switched integrated boost converter is proposed for dc microgrid. A resonant voltage quadrupler cell is integrated at the secondary terminals of the coupled inductor to obtain high voltage gain. The energy of the coupled inductor is transferred to the voltage multiplier cell during all the switching state of the MOSFET switch. Hence instead of a large magnetic core, a small sized core can be utilized to construct the coupled inductor. Thus overall power density of the converter is improved. Coupled inductor's leakage energy is recycled to the output port by utilizing the boost integration technique [5], [9]. The auxiliary switch which is connected to the output, functions as an active clamp circuit to provide ZVS turn on of the MOSFETs. By utilizing the bidirectional magnetizing current, ZVS turn on of main MOSFET is maintained for light loads without any external or large leakage inductance. In the proposed converter, capacitors of the voltage multiplier cell and the the secondary leakage inductance form a quasi resonant circuit [22], [23]. Hence all the diodes of the converter turn off with ZCS. The ZCS turn off reduces the high frequency turn off losses and reverse recovery losses of the diodes. In addition to this, ZCS turn off eliminates high voltage spike or ringing on the diodes caused due to the resonance between the stray capacitance of the diodes and the secondary leakage inductance. Proposed converter provide high voltage step up without large turns ratio and extreme duty ratio operation. Moreover, all the MOSFETs and diodes are subjected low voltage stress. Hence low voltage rated MOSFETs can be used to reduce the conduction losses. Aforementioned advantages makes the proposed converter a good candidate to integrate low voltage renewable energy resources to the DC microgrid.

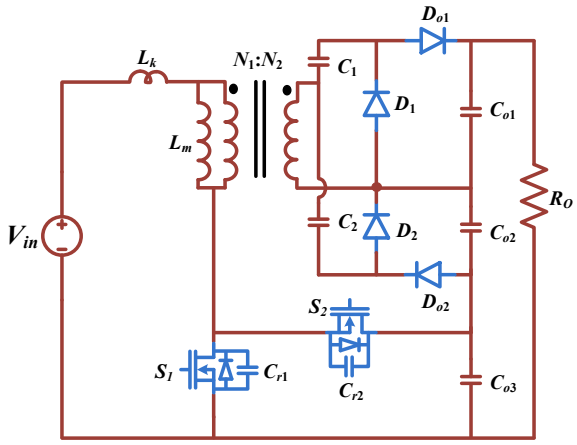


Fig. 1. Proposed ZVS- ZCS integrated boost Converter.

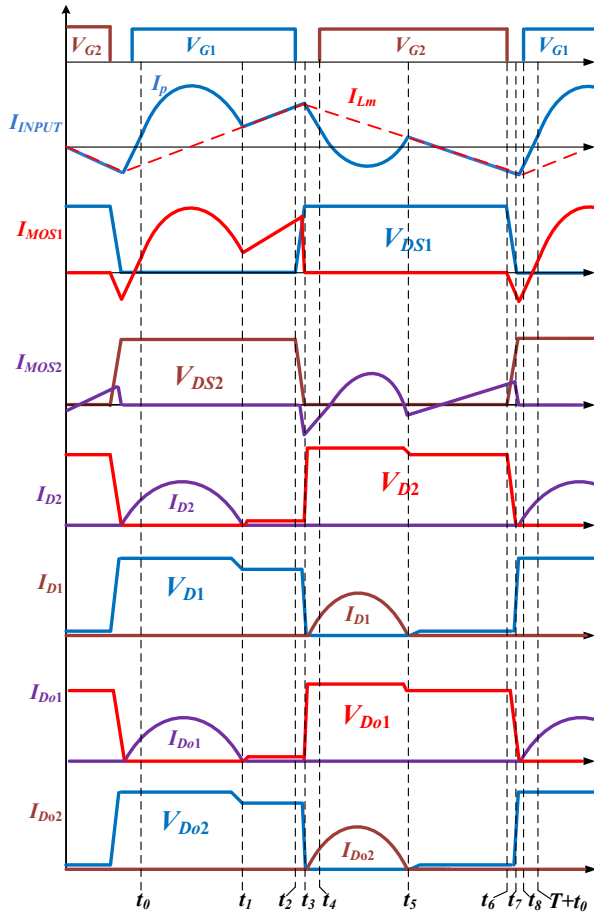


Fig. 2. Key waveforms of the converter.

II. Proposed Converter and Operation

Proposed converter is shown in Fig. 1. Here, L_m and L_k represent the equivalent magnetizing and leakage inductance of the coupled inductor referred to the primary side. The diodes D_1, D_2, D_{o1} and D_{o2} along with capacitors C_1, C_2, C_{o1} and C_{o2} form the resonant voltage quadrupler circuit. Compared to the conventional voltage quadrupler [13], the capacitors C_1 and C_2 of the proposed converter are designed to form a resonant circuit with the leakage inductance. The resonance between the leakage inductance and capacitors C_1 and C_2 shapes the diode current to a quasi-sinusoidal nature and realize ZCS turn off of all the diodes. The capacitors C_{o1} and C_{o2} are the output capacitors of the quarupler cell and designed based on the allowable output voltage ripples. The MOSFET switch S_2 and output capacitor C_{o3} form the clamp circuit. By connecting the clamp circuit to the output port, coupled inductor's leakage energy is effectively recycled to

0278-0046 (c) 2016 IEEE. Personal use is permitted, but republication/redistribution requires IEEE permission. See http://www.ieee.org/publications_standards/publications/rights/index.html for more information.

This article has been accepted for publication in a future issue of this journal, but has not been fully edited. Content may change prior to final publication. Citation information: DOI 10.1109/TIE.2016.2582460, IEEE Transactions on Industrial Electronics

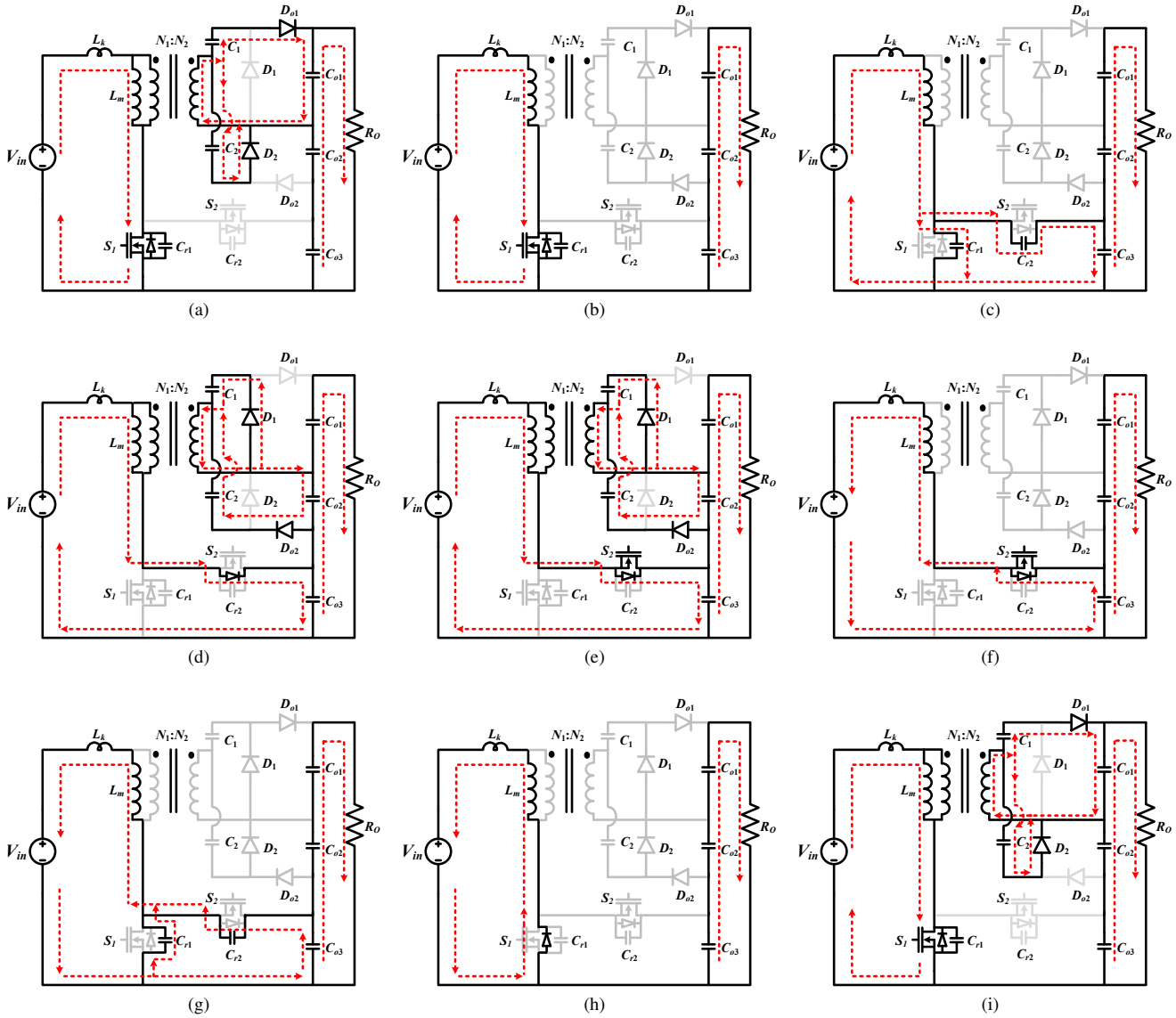


Fig. 3. Different modes of operation of the converter. (a) Mode 1 (t_o - t_1). (b) Mode 2 (t_1 - t_2). (c) Mode 3 (t_2 - t_3). (d) Mode 4 (t_3 - t_4). (e) Mode 5 (t_4 - t_5). (f) Mode 6 (t_5 - t_6). (g) Mode 7 (t_6 - t_7). (h) Mode 8 (t_7 - t_8). (i) Mode 9 (t_8 - $T + t_0$).

the output and thus improves the voltage gain. Capacitors C_{r1} and C_{r2} represent the parasitic capacitance of the MOSFETs. Operating waveforms of the converter at steady state is given in Fig. 2. In steady state operation, there are nine operating modes. These modes of operations are shown in Fig. 3.

Mode 1 (t_o - t_1): In this mode, switch S_1, diodes D_2 and D_{o1} are in conduction. Magnetizing current increases linearly. Reflected energy on the secondary winding charges the capacitor C_2 through diode D_2. At the same time, energy on the secondary winding and capacitor C_1 charges the output capacitor C_{o1} through diode D_{o1}. Since the leakage inductance and the capacitor C_1 and C_2 are in resonance, the currents $i_{D_2(t)}$ and $i_{Do1}(t)$ are quasi sinusoidal in nature. The load is supplied by output capacitors C_{o1}, C_{o2} and C_{o3}. In this mode, magnetizing inductor current and diode currents are given as

$$i_{Lm}(t) = i_{Lm}(t_0) + \frac{L_m}{L_m + L_k} V_{in}(t - t_0) \tag{1}$$

$$i_{D_2}(t) = i_{D_2}(t_o) + \frac{NV_{Lm} - V_{C2}(t)}{Z_0} \sin(\omega_0(t - t_0)) \tag{2}$$

$$i_{D_{o1}}(t) = i_{D_{o1}}(t_o) + \frac{NV_{Lm} + V_{C_1(t)} - V_{Co1}(t)}{Z_1} \sin(\omega_1(t - t_0)) \tag{3}$$

Where $Z_0 = \sqrt{\frac{N^2 L_K}{C_2}}$, $Z_1 = \sqrt{\frac{N^2 L_K}{C_1}}$, $\omega_0 = \frac{1}{\sqrt{N^2 L_K C_2}}$, $\omega_1 = \frac{1}{\sqrt{N^2 L_K C_1}}$ and turn's ratio $N = \frac{N_2}{N_1}$.

Mode 2 (t_1 - t_2): At time t_1, magnetizing current i_{Lm} equals to primary current i_p and increases linearly. Resonating diode currents i_{D2} and i_{Do1} become zero. Thus diodes D_2 and

0278-0046 (c) 2016 IEEE. Personal use is permitted, but republication/redistribution requires IEEE permission. See http://www.ieee.org/publications_standards/publications/rights/index.html for more information.

This article has been accepted for publication in a future issue of this journal, but has not been fully edited. Content may change prior to final publication. Citation information: DOI 10.1109/TIE.2016.2582460, IEEE Transactions on Industrial Electronics

D_{o1} turns off with ZCS. In this mode, magnetizing current is expressed as,

$$i_{Lm}(t) = i_P(t) = i_{Lm}(t_1) + \frac{L_m}{L_m + L_k} V_{in}(t - t_1) \quad (4)$$

Mode 3 (t_2 - t_3): In this period, main switch S_1 is turned off at t_2. Magnetizing current $i_{Lm}(t_2)$ starts to charge the capacitance C_{r1} of main MOSFET switch (S_1) to $V_{C_{O3}}$ and discharge the capacitance C_{r2} of auxiliary switch S_2 to zero.

Mode 4 (t_3 - t_4): This mode starts at t_3, where diodes D_2 and D_{o1} get reverse biased. Capacitor (C_{r2}) of auxiliary switch S_2 is discharged to zero. Now body diode of switch S_2 starts to conduct and charges capacitor C_{O3}. Thus voltage across switch S_1 is clamped to V_{CO3}. This alleviate the voltage spike on the main switch. Diodes D_1 and D_{o2} get forward biased. Leakage inductance and the capacitors C_1 and C_2 forms resonant circuits. The energy of the secondary winding charges capacitor C_1 through diode D_1. During this period, secondary winding and capacitor C_2 discharge its energy to capacitor C_{o2} through diode D_{o2}. Magnetizing current i_{Lm}, primary current i_p, resonating diode currents i_{D1} and i_{DO2} are given as,

$$i_{Lm}(t) = i_{Lm}(t_3) + \frac{(V_{C2} - V_{CO2})}{NL_m}(t - t_3) \quad (5)$$

$$i_p(t) = i_p(t_3) + \frac{V_{in} - V_{CO3} - \frac{(V_{C2} - V_{CO2})}{N}}{Z_2} \sin(\omega_2(t - t_3)) \quad (6)$$

$$i_{D1}(t) = \frac{N(V_{in} - V_{CO_3}) - V_{C1}(t)}{Z_3} \sin(\omega_3(t - t_3)) \quad (7)$$

$$i_{DO2}(t) = \frac{N(V_{in} - V_{CO3} + V_{CO2} - V_{C2}(t))}{Z_4} \sin(\omega_4(t - t_3)) \quad (8)$$

Where $Z_2 = \sqrt{\frac{L_K}{C_{O3}}}$, $Z_3 = \sqrt{\frac{N^2 L_K}{C_1}}$, $Z_4 = \sqrt{\frac{N^2 L_K}{C_2}}$, $\omega_2 = \frac{1}{\sqrt{L_K C_{O3}}}$, $\omega_3 = \frac{1}{\sqrt{N^2 L_K C_1}}$ and $\omega_4 = \frac{1}{\sqrt{N^2 L_K C_2}}$.

Mode 5 (t_4 - t_5): At t_4, while the body diode of switch S_2 is in conduction, gate signal is applied to auxiliary switch S_2. Hence switch S_2 turns on with ZVS. To achieve ZVS for S_2, gate pulse to the switch should be applied before the direction of the primary current $i_p(t_4)$ changes.

Mode 6 (t_5 - t_6): At t_5, resonating currents i_{D1} and i_{DO2} become zero. The diodes D_1 and D_{O2} turns off with ZCS. Magnetizing current becomes equal to the primary current and decrease linearly. Magnetizing current i_{Lm} is given as,

$$i_{Lm}(t) = i_p(t) = i_{Lm}(t_5) + \frac{L_m}{L_m + L_k}(V_{in} - V_{CO3})(t - t_5) \quad (9)$$

Mode 7 (t_6 - t_7): Switch S_2 is turned off at t_6. Now the primary current (i_p) charges the parasitic capacitance (C_{r2}) of S_2 to V_{CO3} and discharges the parasitic capacitance C_{r1} of the main switch S_1 to zero.

Mode 8 (t_7 - t_8): At t_7, parasitic capacitance (C_{r1}) discharges completely. Hence the body diode of switch S_1 conducts the primary current. In this period, gate signal to switch S_1 is applied. Hence ZVS turn on of switch S_1 is obtained. The diodes D_1 and D_{O2} get reverse biased.

Mode 9 (t_8 - $T + t_0$): This mode starts at t_8, where the main switch S_1 turn on with ZVS. Magnetizing current starts to increase linearly due to the application of V_{in}. Diodes D_{O1} and D_2 forward biased and start to conduct. After this period operating modes repeat.

III. Analysis and Design of converter at steady state

Following assumptions are made to simplify the analysis. (1) Leakage inductance of the coupled inductor is neglected ($L_k << L_m$), (2) Average capacitor voltages $V_{C_1}, V_{C_2}, V_{C_{O1}}$, $V_{C_{O2}}$ and V_{CO3} are constant (voltage ripple is neglected), (3) Relatively small time intervals ($t_1 - t_4$) and ($t_5 - T + t_0$) are not considered for the analysis.

A. Voltage Gain of Converter

In *Mode* 1, switch S_1 is conducting and switch S_2 is in OFF state. Average voltage across the magnetizing inductance L_m, capacitors C_2 and C_{O1} are given as,

$$V_{L_m}^{ON} = V_{in} \quad (10)$$

$$V_{C_2} = NV_{L_m}^{ON} \quad (11)$$

$$V_{CO_1} = NV_{L_m}^{ON} + V_{C_1} \quad (12)$$

In *Mode* 5, switch S_2 is conducting and switch S_1 is in OFF state. Following equation can be written in this period as,

$$V_{L_m}^{OFF} = V_{in} - V_{CO_3} \quad (13)$$

$$V_{C_1} = -NV_{L_m}^{OFF} \quad (14)$$

$$V_{CO_2} = V_{C_2} - NV_{L_m}^{OFF} \quad (15)$$

From the volt-second balance of the magnetizing inductance, one gets as,

$$V_{CO_3} = \frac{V_{in}}{1 - D} \quad (16)$$

From (10) to (16), one gets,

$$V_{CO_1} = V_{CO_2} = \frac{NV_{in}}{1 - D} \quad (17)$$

Summation of the average voltage across capacitors C_{O1},C_{O2} and C_{O3} gives the output voltage of the converter. Therefore,

$$V_O = V_{CO_1} + V_{CO_2} + V_{CO_3} \quad (18)$$

Hence from (16)-(18), the ideal voltage gain of the proposed converter is obtained as,

$$M = \frac{V_O}{V_{in}} = \frac{1 + 2N}{1 - D} \quad (19)$$

0278-0046 (c) 2016 IEEE. Personal use is permitted, but republication/redistribution requires IEEE permission. See http://www.ieee.org/publications_standards/publications/rights/index.html for more information.

This article has been accepted for publication in a future issue of this journal, but has not been fully edited. Content may change prior to final publication. Citation information: DOI 10.1109/TIE.2016.2582460, IEEE Transactions on Industrial Electronics

B. Voltage Stress on Semiconductor Switches

Voltage stress on the MOSFET switches S_1 and S_2 are given

$$V_{DS_1} = V_{DS_2} = \frac{V_O}{1+2N} \tag{20}$$

From (19)-(20), it is evident that as the turn's ratio of the coupled inductor increases, voltage gain of the converter increases and voltage stress on the MOSFETs switches decreases. Voltage stress of the diodes are obtained as

$$V_{D1} = V_{D2} = V_{DO_1} = V_{DO_2} = \frac{NV_O}{1+2N} \tag{21}$$

C. Soft switching condition and component selection

1) ZVS condition: Proposed converter make use of bidirectional nature of the magnetizing current to achieve ZVS turn on of main MOSFET. In Mode 7, to obtain ZVS turn on of main switch S_1, following conditions need to be satisfied. (1) Stored energy of the magnetizing inductance should be high enough to discharge the parasitic capacitance of switch S_1 and charge parasitic capacitance of switch S_2. (2) Should provide sufficient dead time to charge and discharge the parasitic capacitance of MOSFETs. For this, magnetizing inductance current should reach the negative valley point as shown in Fig. 2. Therefore,

$$i_{Lm}(t)_{valley} = I_{Lm} - \frac{1}{2}\Delta i_{Lm} \tag{22}$$

This is obtained as

$$\Big(\frac{1+2N}{1-D}\Big)I_o - \frac{V_{in}DT}{2L_m} < 0 \tag{23}$$

Hence, the maximum value of magntizing inductance required to achieve ZVS is obtained as

$$L_{m_{max}} < \frac{V_{in}D_{max}(1-D_{max})}{2(1+2N)I_o f_s} \tag{24}$$

where f_s is the switching frequency and D_{max} is the maximum duty ratio of the converter. ZVS of switch S_1 is load depended. At any load condition, to maintain ZVS of S_1, following condition should satisfied.

$$\frac{1}{2}L_m i^2_{Lm_{(valley)}} \geq \frac{1}{2}C_{reff}V^2_{CO3} \tag{25}$$

From (19), (23) and (25), condition for achieving ZVS of S_1 at desired output load is obtained as

$$\sqrt{I_o} \geq \frac{C_{reff}V^2_{CO3}}{L_m[M - \frac{R_o D}{2ML_m f_s}]^2} \tag{26}$$

Where $C_{reff} = C_{r1} + C_{r2}$. The delay time between the gate signals are given by

$$\Delta T \geq \frac{\Pi}{2}\sqrt{L_m C_{reff}} \tag{27}$$

From (24) and (26), $L_m = 11\mu$H is selected to maintain ZVS turn on of S_1 up to 10% of full load. ZVS of switch S_2 is obtained naturally by stored energy of the magnetizing and leakage inductance if proper dead time is provided between the gate signals.

2) Design of coupled inductor: Size of the coupled inductor core is selected based on the magnetic core area product (A_p) and is given by [24].

$$A_p = A_c A_w = \frac{2L_m i^2_{Lm(peak)}}{K_u J B_{max}} 10^8 cm^4 \tag{28}$$

Where, A_c is the cross sectional area of the core, A_w is the window area of the core, L_m is the magnetizing inductance, $i_{Lm_{(peak)}}$ is the peak magnetizing current, K_u is the window utilization factor = 0.3, J is the current density = $4A/mm^2$ and $B_{max} = 0.2T$ for ferrite core. Peak value of the magnetizing inductance current is given as

$$i_{Lm_{(peak)}} = \frac{1+2N}{1-D}\frac{P_o}{V_O} + \frac{V_{in}D}{2L_m f_s} \tag{29}$$

Hence magnetic core area product A_p is obtained as

$$A_p = \frac{2 \times 11 \times 10^{-6} \times 19.35^2}{0.3 \times 4 \times 10^6 \times 0.2} 10^8 = 3.4cm^4 \tag{30}$$

EPCOS made EE-42 core (was readily available in the laboratory) of cross sectional area $A_c = 2.29cm^2$ is selected for coupled inductor. Number of turns of primary winding is obtained as

$$N_1 = \frac{L_m i_{Lm(peak)}}{A_c B_{max}} 10^4 \approx 5 \tag{31}$$

Number of secondary winding is obtained from the turns ratio and found to be 11. Required length of air gap is given by [6]

$$l_g = \frac{\mu_o L_m i^2_{Lm(peak)} 10^4}{B_{max} A_c} \approx 0.6mm \tag{32}$$

To reduce the skin effect, litz wires are used to wound the coupled inductor. To have good thermal protection for the coupled indictor, Kapton made polyimide masking tape is used. Measured magnetizing inductance is 10.38μH.

3) ZCS condition for diodes: To have ZCS turn off of diodes D_{O1} and D_2, one half of the resonant period formed between the secondary leakage inductance of the coupled inductor and capacitors C_1 and C_2 should be lower than the minimum turn on time of switch S_1. Therefore,

$$C_1, C_2 < \frac{D^2_{min}T^2_s}{\pi^2 L_{ks}} \tag{33}$$

similarly, condition for ZCS turn off of diodes D_1 and D_{O2} is given as,

$$C_1, C_2 < \frac{(1-D_{max})^2 T^2_s}{\pi^2 L_{ks}} \tag{34}$$

Hence to have ZCS condition for all the diodes, capacitance value of C_1 and C_2 are obtained as,

$$C_1, C_2 < \Big(\frac{D^2_{min}T^2_s}{\pi^2 L_{ks}}, \frac{(1-D_{max})^2 T^2_s}{\pi^2 L_{ks}}\Big) \tag{35}$$

4) Selection of Output Capacitance: The output voltage ripple is the main criteria for selecting the output capacitance. Output capacitance required for the desired value of the voltage ripple (ΔV_O) is obtained as,

$$C_O \geq \frac{I_O D}{\Delta V_O f_s} \tag{36}$$

$$C_O = \frac{C_{O1}C_{O2}C_{O3}}{C_{O1}C_{O2} + C_{O2}C_{O3} + C_{O1}C_{O3}} \tag{37}$$

0278-0046 (c) 2016 IEEE. Personal use is permitted, but republication/redistribution requires IEEE permission. See http://www.ieee.org/publications_standards/publications/rights/index.html for more information.

This article has been accepted for publication in a future issue of this journal, but has not been fully edited. Content may change prior to final publication. Citation information: DOI 10.1109/TIE.2016.2582460, IEEE Transactions on Industrial Electronics

D. Performance Comparison of Proposed Converter

Performance of the proposed converter is compared with other high voltage gain converters presented in [3], [5], [25], [26] and shown in Table I. Schematic of these converters are given in Fig. 4. For different duty cycle and turns ratio, comparison of the voltage conversion gain of the proposed converter is shown in Fig. 5. It is clear that, the proposed converter has higher voltage gain compared to that of [3], [5], [25] and [26]. In a high voltage step up DC-DC converters, voltage stress on various semiconductor switches are one of the main concern. However as evident from Fig. 6 and Fig. 7, voltage stress on the MOSFETs and all the diodes are lower in the proposed converter. This helps us to choose MOSFETs of low $R_{DS(ON)}$ and thus improves the efficiency by reducing the conduction loss. Moreover in the proposed converter, voltage stress on the semiconductor devices depends on the turns ratio of the coupled inductor and independent of the input voltage variations as given by (20)-(21). Hence the turns ratio of the coupled inductor can be selected properly to reduce the voltage stress. In [3], [5], [25] and [26], reverse recovery losses of the diodes are reduced by the secondary leakage inductance of the coupled inductor. However compared to these converters, in the proposed converter, reverse recovery losses are very small due to the ZCS turn off of all the diodes. In [3], the resonance between the leakage inductance and the parasitic capacitance of the diodes causes large voltage spike on the diodes. However, in the proposed converter, the ZCS turn off of all the diodes helps to eliminate this voltage spike. Hence snubber circuits are not required to protect the output diodes from the voltage stress.

Converter in [26] is a hard switched passive clamp converter. However, MOSFET turn on losses are lower in [26] compared to the conventional coupled inductor converters. In soft switched converter of [3], [5] and [25], ZVS of the main MOSFET switch depends purely on the stored energy of the leakage inductance. Hence to achieve ZVS of the main MOSFET switch for a moderate light loads (50%-25% of the full load), large leakage inductance or an external inductor is required. To obtain ZVS of main MOSFET at 25% of the full load, a leakage inductance of 10μH is required for the converter presented in [5]. This is realized by connecting an external inductor in series with the coupled inductor in [5]. This reduces the voltage gain of the converter due to the increased duty cycle losses. In order to compensate the duty cycle loss, converter in [5] need to operate at higher duty cycle which results into high RMS current and thus increased conduction losses. Moreover utilizing a large external inductor to maintain ZVS at lighter loads (below 20% of full load) is found to be less effective. To overcome these issues, at light loads (below 20% of full load), a complex light load frequency modulated control is introduced in [5]. However, in proposed converter, by utilizing the fixed frequency (PWM) - quasi resonant operation [23], ZVS of the main MOSFET switch is obtained by the negative valley current of the magnetizing inductance. This bidirectional magnetizing inductance current helps to achieve ZVS of the main MOSFET without using any external inductance or large leakage inductance. Hence the duty cycle loss due to the large leakage inductance can be reduced in the proposed converter. By properly selecting the value of magnetizing inductance, proposed converter can maintain ZVS turn on of main switch for below 20% of the full load.

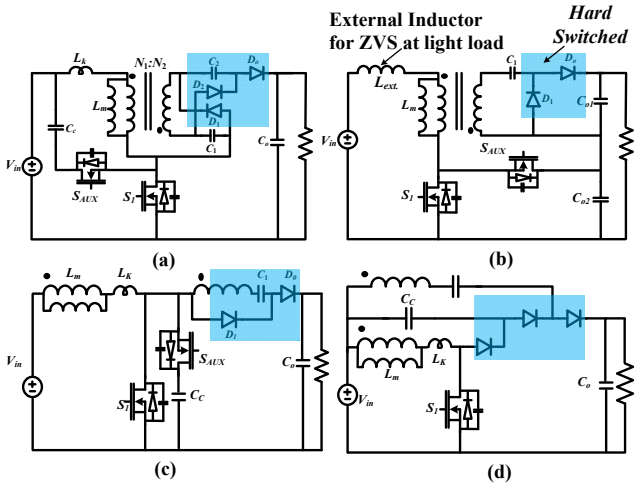


Fig. 4. Schematic of converter topologies: (a) converter presented in [3]. (b) converter presented in [5]. (c) converter presented in [25]. (d) converter presented in [26]. (The shaded portion represents the hard switched diodes).

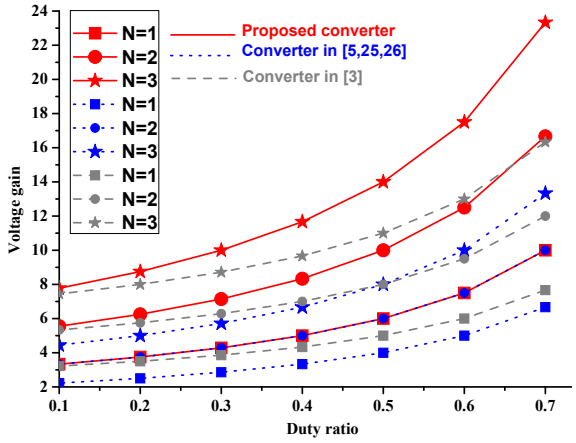


Fig. 5. Comparison of voltage gain of the converter.

Power density of a DC/DC converter is mainly depends on the size of magnetic components. To improve the power density of a converter, size of the magnetic components need to be reduced. In conventional high voltage gain coupled inductor converters [10-11], coupled inductor transfer its energy to output during only one switching state (either on or off state). Hence to obtain high voltage gain, coupled inductor need to store high amount of energy which leads to the selection of large magnetic core. In the proposed converter, energy of the coupled inductor is transferred to the voltage multiplier cell during all switching state of the MOSFET switch. Hence a small sized core can be utilized to construct the coupled inductor. Compared to the converters of [3], [5], [25] and [26],

0278-0046 (c) 2016 IEEE. Personal use is permitted, but republication/redistribution requires IEEE permission. See http://www.ieee.org/publications_standards/publications/rights/index.html for more information.

This article has been accepted for publication in a future issue of this journal, but has not been fully edited. Content may change prior to final publication. Citation information: DOI 10.1109/TIE.2016.2582460, IEEE Transactions on Industrial Electronics

TABLE I
COMPARISON BETWEEN THE CONVERTERS PRESENTED IN [5], [3], [25], [26] AND PROPOSED CONVERTER

Parameter	Converter in [5]	Converter in [3]	Converter in [25]	Converter in [26]	Proposed converter
MOSFETs	2	2	2	1	2
Diodes	2	3	2	3	4
Voltage gain	$\frac{1+N}{1-D}$	$\frac{1+2N-ND}{1-D}$	$\frac{1+N}{1-D}$	$\frac{1+N}{1-D}$	$\frac{1+2N}{1-D}$
Voltage stress on MOSFET	$\frac{V_o}{1+N}$	$\frac{V_o}{1+2N-ND}$	$\frac{V_o}{1+N}$	$\frac{V_o}{1+N}$	$\frac{V_o}{1+2N}$
Voltage stress on output diode	$\frac{NV_o}{1+N}$	$\frac{(1+N)V_o}{1+2N-ND}$	V_O	$\frac{NV_o}{1+N}$	$\frac{NV_o}{1+2N}$
Soft switching of MOSFETs	ZVS	ZVS	ZVS	Hard switch with low turn on losses	ZVS
Soft switching of Diodes	Hard switching	Hard switching	Hard switching	Hard switching	ZCS
Reverse recovery losses	Small	Small	small	small	Very small

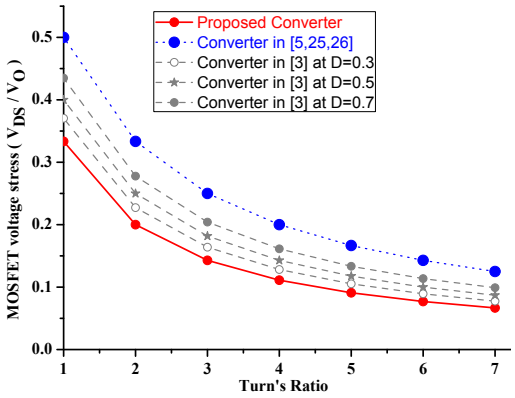


Fig. 6. Voltage stress comparison of MOSFETs .

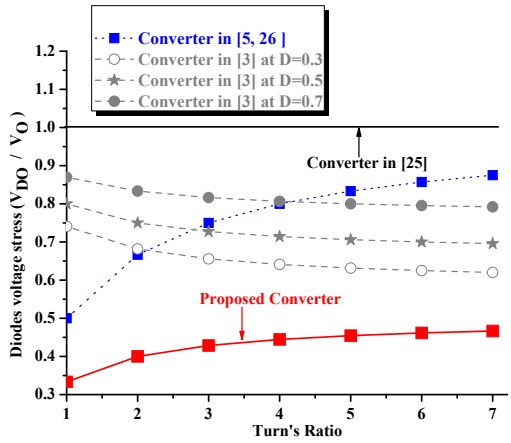


Fig. 7. Comparison of voltage stress on diodes.

proposed converter require lower sized magnetic core. This is justified as follows. Size of the magnetic core is selected based on the magnetic core area product (A_p) [24]. From (28),

$$A_p \propto L_m i^2_{Lm(peak)} \tag{38}$$

From (24) and (26), magnetizing inductance of proposed

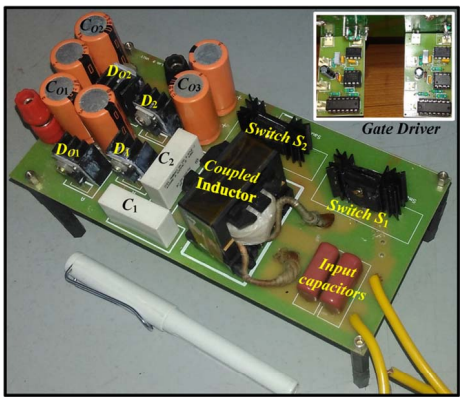


Fig. 8. Photograph of the experimental prototype (insight: gate driver mounted directly on switches)

converter is obtained as 11μH. Magnetizing inductance of the converter in [5] is obtained as follows,

$$L_{m[5]} = \frac{R_O D_{[5]}(1-D_{[5]})^2}{2(1+N)^2 f_s} \tag{39}$$

To have a fair comparison, value of magnetizing inductance of the converter in [5] is obtained for same specifications of the proposed converter (given in Table II) for 40V input voltage and obtained as 35.39μH. Peak value of the magnetizing current of proposed converter and the converter in [5] is obtained as

$$i_{Lm(peak-[prop.])} = \left[\frac{1+2N}{1-D_{[prop.]}}\right]\frac{P_O}{V_O} + \frac{V_{in}D_{[prop.]}}{2L_{m[prop.]}f_s} \tag{40}$$

$$i_{Lm(peak-[5])} = \left[\frac{1+N}{1-D_{[5]}}\right]\frac{P_O}{V_O} + \frac{V_{in}D_{[5]}}{2L_{m[5]}f_s} \tag{41}$$

By substituting (39) to (41) in (38), Ratio of magnetic core area product of proposed converter and the converter in [5] is obtained as

$$Ratio\ of\ Area Product = \frac{L_{m[prop.]}i^2_{Lm(peak-[prop.])}}{L_{m[5]}i^2_{Lm(peak-[5])}} = 0.76 \tag{42}$$

0278-0046 (c) 2016 IEEE. Personal use is permitted, but republication/redistribution requires IEEE permission. See http://www.ieee.org/publications_standards/publications/rights/index.html for more information.

This article has been accepted for publication in a future issue of this journal, but has not been fully edited. Content may change prior to final publication. Citation information: DOI 10.1109/TIE.2016.2582460, IEEE Transactions on Industrial Electronics

TABLE II
SPECIFICATIONS OF HARDWARE PROTOTYPE

Components	Specifications
Power	250W
Input voltage	40V-60V
Output voltage	380V
MOSFETs	IRFP4227pbf
Diodes	BYC10D600
Switching frequency	60KHz
Turn's ratio	1:2.2
Capacitors C_1 and C_2	0.47μF, film capacitors
Output capacitors C_{O1}, C_{O2} and C_{O3}	94μF ($2 \times 47\mu$F), electrolytic
Magnetizing Inductance	10.38μH, EE 42 core
Leakage inductance L_{kp}, L_{ks}	0.212μH, 1.02μH

Ratio is found to be 0.76. This shows that proposed converter require a magnetic core of lower size (24% lower than that of [5]. Similarly, magnetic core size of the proposed converter is found to be 31%, 24% and 12% lower than that of the converters presented in [10-11], [25-26] and [3] respectively. As given in Table I, component count of the proposed converter is slightly higher than [3], [5], [25] and [26]. However, compared to these converters, proposed converter have higher voltage gain, lower voltage stress on all semiconductor switches, ZCS turn off of all diodes which reduces the diodes turn off losses and reverse recovery losses, ZVS turn on of MOSFETs up to light loads without any external inductance or large leakage inductance, and lower sized magnetic core which improve the magnetic utilization etc. These features justify the component count of the converter.

IV. EXPERIMENTAL RESULTS

A 250W prototype of the proposed converter is build to verify the design and theoretical analysis. In Table II, specifications of the hardware are given. Photograph of the prototype is shown in Fig. 8. Unipolar driver MIC4451 and the opto-coupler 6N137 are used to build the isolated gate driver circuit. As shown in Fig. 8, this gate driver is mounted directly on the MOSFETs to reduce the noise. The control of the converter is achieved through the TMS320F28335 floating point DSP from Texas Instruments. Coupled inductor's magnetizing and leakage inductance is measured by the Fluke PM6304 R-C-L meter. Methods given in [27] is adopted for this measurements. Proposed converter is designed for an output voltage of 380V for input voltage range of 40V-60V.

Experimental results of the proposed converter at full load (250W) is shown in Fig. 9 for an input voltage of 48V. In Fig. 9 (a), gate signal (V_{G1}) of the switch S_1, primary current of the coupled inductor (I_p) and currents through the MOSFET switches I_{S_1} and I_{S_2} are shown. Fig. 9 (b) shows the soft switching (ZVS turn on) of the MOSFET switches S_1 and S_2 with zoomed ZVS region. The MOSFETs voltage spike due to the leakage inductance are actively clamped below 140V by recycling the leakage energy to the output port. Steady state voltage stress (V_{DS1}, V_{DS2}) on switches S_1 and S_2 are below 80V. This low voltage stress on the switches enable to use MOSFETs of low $R_{ds(ON)}$. ZCS turn off of the diodes D_{O1} and D_1 are shown in Fig. 9 (c) with zoomed portion of the ZCS region. In Fig. 9 (d), ZCS of the diodes D_2 and D_{O2} are shown. Voltage stress on all the diodes are below 160V. Due to the ZCS turn off, reverse recovery losses of all the diodes are minimum. Moreover, large voltage spike on the diodes due to the parasitic resonance of the leakage inductance and the stray capacitance of the diodes are eliminated.

In Fig. 10 (a), ZVS turn on of switches S_1 and S_2 are shown at full load for an input voltage of 40V. In Fig. 10 (b), output voltage of the converter is shown with voltage stress on the switch S_1 and primary current I_p for the designed lowest input voltage ($V_{in} = 40$V) at D=0.48. Above results clearly show that without increasing the turn's ratio and duty cycle, proposed converter is capable of achieving a high voltage gain with lower voltage stress. In Fig. 10 (c), ZVS turn on of switch S_1 is shown with primary current I_p for an input voltage of 60V ($V_{in} = 60$V), which is the designed maximum input voltage for the converter. In Fig. 10 (d), ZVS turn on of switch S_1 is given at 15% of the full load for an input voltage of 40V. This shows that, compared to the converter presented in [3], [5] and [25], proposed converter can maintain ZVS for light loads without any large leakage or external inductance.

Proposed converter is a PWM converter and the output voltage is regulated by duty ratio control. Applications like regulated power supply, output voltage is regulated by voltage mode or current mode control. To analysis the performance of the converter during load variations, voltage mode control is implemented and the results are provided for step change in load in Fig. 11. In Fig. 11 (a), output voltage response for step change in load from full load to 50% of the full load is given. Here converter maintain the desired output voltage and thus regulate for load variation. In Fig. 11 (b), output voltage variation for step change in load from full load to 10% of the load is shown. To have better understanding of the transient behaviour of the output voltage, oscilloscope is set in ac mode here. In Fig. 11 (c), output voltage variation for step load change form no load to full load is provided (oscilloscope is set in ac mode). The converter is able to regulate the output voltage during all these load variations. The voltage transient behaviour of the converter can further improved by current mode controller where an outer voltage loop and faster inner current loop provide better dynamic performance.

For different output power levels and input voltages, efficiency of the proposed converter is measured and shown in Fig. 12. Measured maximum efficiency of the proposed converter is 96.46% at 125W for a 60V input. Theoretical efficiency of the proposed converter is compared with the converters presented in [3] and [5] for an input voltage of 60V. Efficiency of the converter presented in [5] is closely matching to the proposed converter in lower power ranges. However, converter of [5] has lower efficiency as moves from light load to full load. Efficiency of the converter in [3] is closely matching to the proposed converter for a power range of 175W to full load. However, at light load, the efficiency of the proposed converter is better than that of [3]. From efficiency comparison, it can be seen that, proposed converters

0278-0046 (c) 2016 IEEE. Personal use is permitted, but republication/redistribution requires IEEE permission. See http://www.ieee.org/publications_standards/publications/rights/index.html for more information.

This article has been accepted for publication in a future issue of this journal, but has not been fully edited. Content may change prior to final publication. Citation information: DOI 10.1109/TIE.2016.2582460, IEEE Transactions on Industrial Electronics

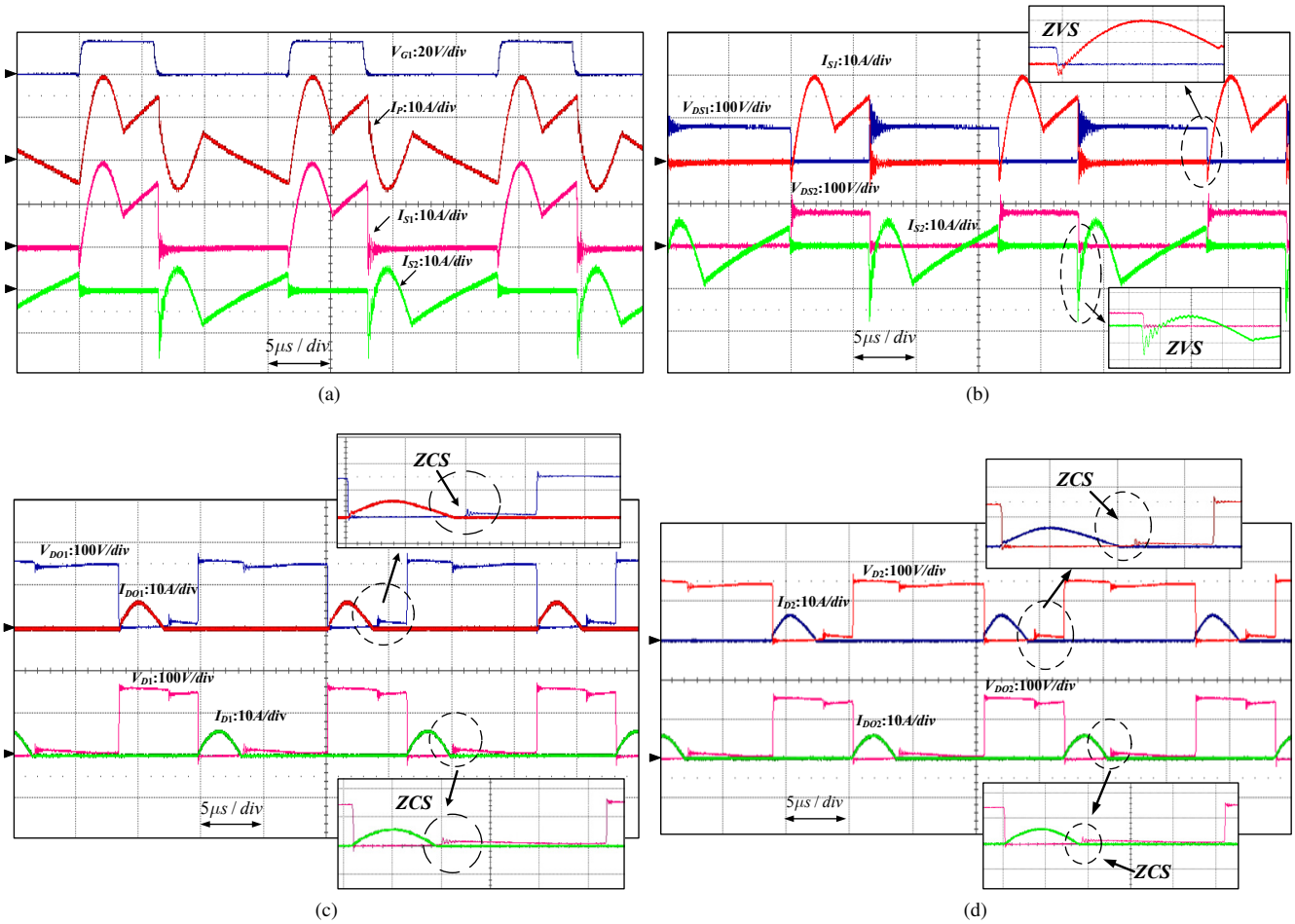


Fig. 9. Experimental results at full load, $V_{in} = 48V$: (a) Gate pulse of the switch S_1 (V_{G1}), primary current (I_p), Current through the switch S_1 (I_{S1}), Current through the switch S_2 (I_{S2}). (b) ZVS of the switch S_1 and S_2 with zoomed ZVS region. (c) ZCS of the diodes D_{O1} and D_1 with zoomed ZCS region. (d) ZCS of the diodes D_2 and D_{O2} with zoomed ZCS region.

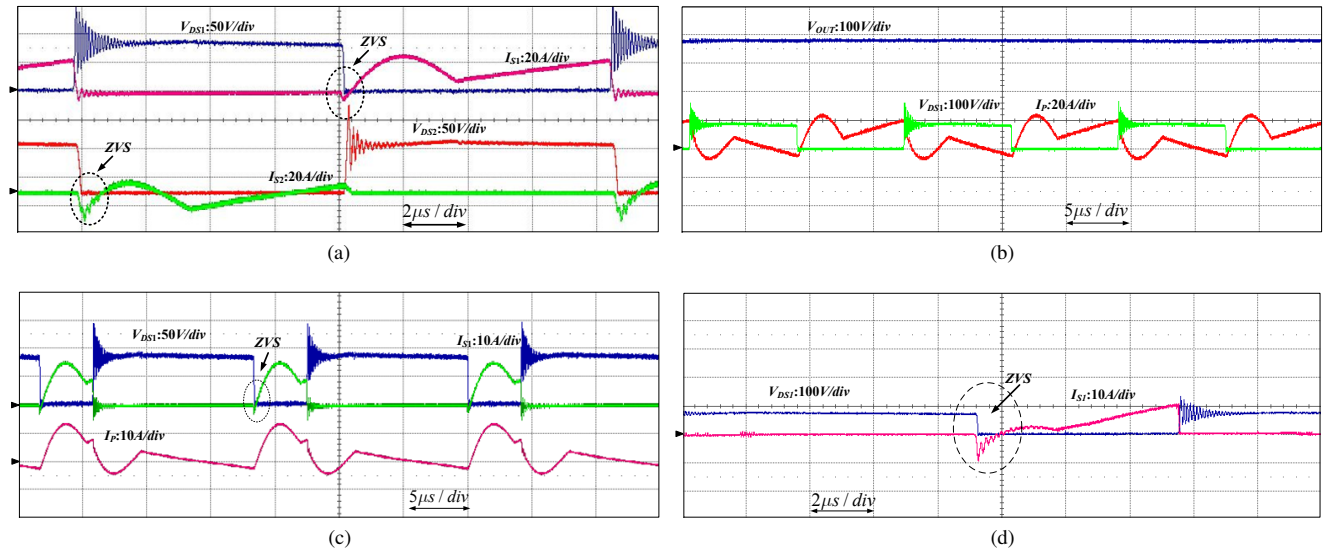


Fig. 10. Experimental results at full load: (a) Voltage across the switches S_1 and S_2 with switch currents showing ZVS turn on at $V_{in} = 40V$. (b) Output voltage of the converter, voltage stress (V_{DS1}) of the switch S_1 and primary current I_p at $V_{in} = 40V$. (c) voltage across the switch S_1 (V_{DS1}), switch current I_{S1} and primary current I_p at $V_{in} = 60V$. (d) ZVS turn on of switch S_1 at 15% of full load for $V_{in} = 40V$.

0278-0046 (c) 2016 IEEE. Personal use is permitted, but republication/redistribution requires IEEE permission. See http://www.ieee.org/publications_standards/publications/rights/index.html for more information.

This article has been accepted for publication in a future issue of this journal, but has not been fully edited. Content may change prior to final publication. Citation information: DOI 10.1109/TIE.2016.2582460, IEEE Transactions on Industrial Electronics

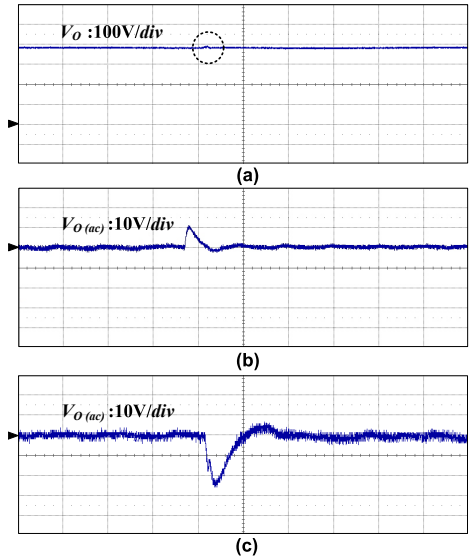


Fig. 11. Response of the output voltage for step load changes: (a) Output voltage for step change in load from full load to 50% of load (Oscilloscope in DC mode). (b) Output voltage response for step change in load from full load to 10% of load (Oscilloscope in AC mode). (c) Output voltage response for step change in load from no load to full load (Oscilloscope in AC mode). Time scale: 20ms/div.

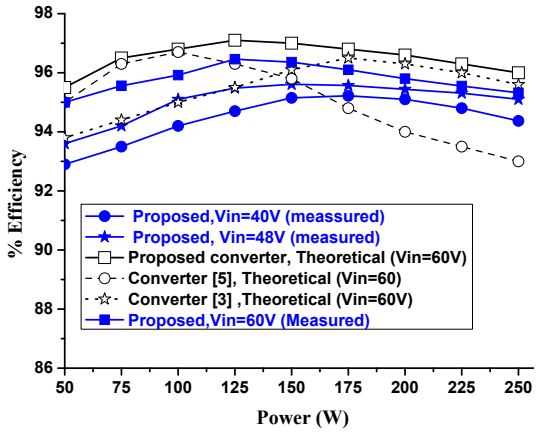


Fig. 12. Theoretical and measured efficiency of the proposed converter.

have good efficiency over the wide load range compared to the converter presented in [3] and [5].

V. Conclusion

In this paper, a soft switched integrated boost converter with resonant voltage quadrupler cell has been proposed to integrate different low voltage energy sources to the DC microgrid. By incorporating the coupled inductor and the resonant quadrupler cell, proposed converter can easily obtain high voltage step up gain with lower turn's ratio and duty cycle. All the MOSFETs and diodes of the proposed converter is subjected to very low voltage stress. Hence MOSFETs of low ON state resistance can be utilized in the proposed converter to improve the efficiency. Fixed frequency, quasi resonant operation of the proposed converter provide ZCS turn off of all the diodes. This reduces the reverse recovery and the switching losses of the diodes. Diode voltage spikes caused due to the unwanted resonance between the stray capacitance of the diodes and the secondary leakage inductance of the coupled inductor are reduced due to the ZCS turn off. Hence no snubber protection circuit is required for the diode. Bidirectional boost integration circuit provides ZVS turn on of MOSFETs and also clamps the voltage stress across the MOSFETs. In proposed converter, no large leakage inductance or external inductance is required to achieve ZVS for a wide range of loads. This improves the voltage gain by reducing the duty cycle loss caused due to the leakage inductance effect. Coupled inductor of proposed converter transfers its energy during all the switching state. Hence smaller magnetic components can be used to improve the power density of the converter. A prototype of 250W is tested in the laboratory and the results are verified. Maximum efficiency of 96.46% is obtained for the proposed converter.

References

[1] J. M. Carrasco, L. G. Franquelo, J. T. Bialasiewicz, E. Galván, R. C. P. Guisado, M. Á. M. Prats, J. I. León, and N. Moreno-Alfonso, "Power-electronic systems for the grid integration of renewable energy sources: A survey," *IEEE Trans. Ind. Electron.*, vol. 53, no. 4, pp. 1002–1016, Jun. 2006.

[2] K. Sun, L. Zhang, Y. Xing, and J. M. Guerrero, "A distributed control strategy based on dc bus signaling for modular photovoltaic generation systems with battery energy storage," *IEEE Trans. Power Electron.*, vol. 26, no. 10, pp. 3032–3045, Oct. 2011.

[3] S. Sathyan, H. M. Suryawanshi, M. S. Ballal, and A. B. Shitole, "Soft-switching dc-dc converter for distributed energy sources with high step-up voltage capability," *IEEE Trans. Ind. Electron.*, vol. 62, no. 11, pp. 7039–7050, Nov. 2015.

[4] Q. Zhao and F. C. Lee, "High-efficiency, high step-up dc-dc converters," *IEEE Trans. Power Electron.*, vol. 18, no. 1, pp. 65–73, Jan. 2003.

[5] H.-W. Seong, H.-S. Kim, K.-B. Park, G.-W. Moon, and M.-J. Youn, "High step-up dc-dc converters using zero-voltage switching boost integration technique and light-load frequency modulation control," *IEEE Trans. Power Electron.*, vol. 27, no. 3, pp. 1383–1400, Mar. 2012.

[6] R. W. Erickson and D. Maksimovic, *Fundamentals of power electronics*, 2nd ed. New York, NY, USA: Springer-Verlag, 2001.

[7] S. A. Arshadi, B. Poorali, E. Adib, and H. Farzanehfard, "High step-up dc-ac inverter suitable for ac module applications," *IEEE Trans. Ind. Electron.*, vol. 63, no. 2, pp. 832–839, Feb. 2016.

[8] D. Meneses, F. Blaabjerg, O. Garcia, and J. A. Cobos, "Review and comparison of step-up transformerless topologies for photovoltaic ac-module application," *IEEE Trans. Power Electron.*, vol. 28, no. 6, pp. 2649–2663, Jun. 2013.

[9] K. Tseng and T.-J. Liang, "Novel high-efficiency step-up converter," *IEE Proc., Electr. Power Appl.*, vol. 151, no. 2, pp. 182–190, Mar. 2004.

[10] S. Dwari and L. Parsa, "An efficient high-step-up interleaved dc–dc converter with a common active clamp," *IEEE Trans. Power Electron.*, vol. 26, no. 1, pp. 66–78, Jan. 2011.

[11] T.-F. Wu, Y.-S. Lai, J.-C. Hung, and Y.-M. Chen, "Boost converter with coupled inductors and buck–boost type of active clamp," *IEEE Trans. Ind. Electron.*, vol. 55, no. 1, pp. 154–162, Jan. 2008.

[12] A. Ioinovici, *Power Electronics and Energy Conversion Systems, Vol. 1: Fundamentals and Hard-Switching Converters*. Chichester, U.K.: John Wiley & Sons Ltd, 2013.

[13] Y. Zhao, X. Xiang, W. Li, X. He, and C. Xia, "Advanced symmetrical voltage quadrupler rectifiers for high step-up and high output-voltage converters," *IEEE Trans. Power Electron.*, vol. 28, no. 4, pp. 1622–1631, Apr. 2013.

[14] Y.-P. Hsieh, J.-F. Chen, T.-J. Liang, and L.-S. Yang, "A novel high step-up dc–dc converter for a microgrid system," *IEEE Trans. Power Electron.*, vol. 26, no. 4, pp. 1127–1136, Apr. 2011.

[15] S. Sathyan, H. M. Suryawanshi, and A. B. Shitole, "Soft switched coupled inductor based high step up converter for distributed energy resources," in *Industrial Electronics Society, IECON 2014 - 40th Annual Conference of the IEEE*, Oct. 2014, pp. 1799–1805.

0278-0046 (c) 2016 IEEE. Personal use is permitted, but republication/redistribution requires IEEE permission. See http://www.ieee.org/publications_standards/publications/rights/index.html for more information.

This article has been accepted for publication in a future issue of this journal, but has not been fully edited. Content may change prior to final publication. Citation information: DOI 10.1109/TIE.2016.2582460, IEEE Transactions on Industrial Electronics

[16] A. Ajami, H. Ardi, and A. Farakhor, "A novel high step-up dc/dc converter based on integrating coupled inductor and switched-capacitor techniques for renewable energy applications," *IEEE Trans. Power Electron.*, vol. 30, no. 8, pp. 4255–4263, Aug. 2015.
[17] J. V. Mapurunga Caracas, G. de Carvalho Farias, L. F. Moreira Teixeira, and L. A. de Souza Ribeiro, "Implementation of a high-efficiency, high-lifetime, and low-cost converter for an autonomous photovoltaic water pumping system," *IEEE Trans. Ind. Appl.*, vol. 50, no. 1, pp. 631–641, Jan. 2014.
[18] Y. J. A. Alcazar, D. de Souza Oliveira, F. L. Tofoli, and R. P. Torrico-Bascope, "Dc–dc nonisolated boost converter based on the three-state switching cell and voltage multiplier cells," *IEEE Trans. Ind. Electron.*, vol. 60, no. 10, pp. 4438–4449, Oct. 2013.
[19] B. Axelrod, Y. Beck, and Y. Berkovich, "High step-up dc–dc converter based on the switched-coupled-inductor boost converter and diode-capacitor multiplier: steady state and dynamics," *IET Power Electron.*, vol. 8, no. 8, pp. 1420–1428, Aug. 2015.
[20] K.-C. Tseng and C.-C. Huang, "High step-up high-efficiency interleaved converter with voltage multiplier module for renewable energy system," *IEEE Trans. Ind. Electron.*, vol. 61, no. 3, pp. 1311–1319, Mar. 2014.
[21] A. A. A. Freitas, F. L. Tofoli, S. Júnior, E. Mineiro, S. Daher, and F. L. M. Antunes, "High-voltage gain dc–dc boost converter with coupled inductors for photovoltaic systems," *IET Power Electron.*, vol. 8, no. 10, pp. 1885–1892, Oct. 2015.
[22] K. B. Park, G. W. Moon, and M. J. Youn, "High step-up boost converter integrated with a transformer-assisted auxiliary circuit employing quasi-resonant operation," *IEEE Trans. Power Electron.*, vol. 27, no. 4, pp. 1974–1984, Apr. 2012.
[23] J.-K. Park, W.-Y. Choi, and B.-H. Kwon, "A step-up dc–dc converter with a resonant voltage doubler," *IEEE Trans. Ind. Electron.*, vol. 54, no. 6, pp. 3267–3275, Dec. 2007.
[24] M. K. Kazimierczuk, *High-frequency magnetic components*, 2nd ed. Chichester, U.K.: John Wiley & Sons, 2014.
[25] Y. Zhao, W. Li, and X. He, "Single-phase improved active clamp coupled-inductor-based converter with extended voltage doubler cell," *IEEE Trans. Power Electron.*, vol. 27, no. 6, pp. 2869–2878, Jun. 2012.
[26] M. Das and V. Agarwal, "Design and analysis of a high-efficiency dc-dc converter with soft switching capability for renewable energy applications requiring high voltage gain," *IEEE Trans. Ind. Electron.*, vol. 63, no. 5, pp. 2936–2944, May. 2016.
[27] C. Basso, *How to deal with leakage elements in flyback converters*, ON Semiconductor, Appl. Notes, AN1679/D, Sep. 2005.



Shelas Sathyan (S'16) received B. Tech degree in electrical & electronics engineering from Government College of Engineering Kannur, Kerala, India in 2009 and M. Tech degree in Power electronics and Drives from Visvesvaraya National Institute of Technology Nagpur, India in 2012. Currently he is working towards PhD degree in electrical engineering at Visvesvaraya National Institute of Technology Nagpur, India. His research interest includes DC-DC converters for renewable energy sources, soft switching and power factor correction.



H. M. Suryawanshi (M'06-SM'12) received the B. E. degree in Electrical Engineering from Walchand College of Engineering, Sangli, India, in 1988 and M. E. degree in Electrical Engineering from Indian Institute of Science, Bangalore, in 1994. He has been awarded PhD degree by Nagpur University, Nagpur (India) in 1999. He is currently a Professor in the department of Electrical Engineering , Visvesvaraya National Institute of Technology,Nagpur, (India). He is an Associate Editor of IEEE TRANSACTIONS ON INDUSTRIAL ELECTRONICS. His research interests include the field of Power Electronics, emphasising developmental work in the area of resonant converters, power factor correction, active power filters, FACTs Devices, Multilevel converters, High Frequency Electronic Ballast and electric drives.



Bhim Singh (SM'99-F'10) received his B.E. (Electrical) from the University of Roorkee, India, in 1977 and his M.Tech. (Power Apparatus & Systems) and Ph.D. from the Indian Institute of Technology Delhi, India, in 1979 and 1983, respectively. In 1983, he joined the Department of Electrical Engineering, University of Roorkee (Now IIT Roorkee), as a Lecturer. He became a Reader there in 1988. In December 1990, he joined the Department of Electrical Engineering, IIT Delhi, India, as an Assistant Professor, where he has become an Associate Professor in 1994 and a Professor in 1997. He has been ABB Chair Professor from September 2007 to September 2012. Since October 2012, he is a CEA Chair Professor. Presently he is also Head of the Department of Electrical Engineering at IIT Delhi. His areas of research interest include power electronics, electrical machines and drives, renewable energy, active filters, FACTS, HVDC, and power quality.



Chandan Chakraborty (S'92-M'97-SM'01-F'15) received the B.E. and M.E. degrees in electrical engineering from Jadavpur University, Kolkata, India, in 1987 and 1989, respectively, and Ph.D. degrees from the Indian Institute of Technology Kharagpur, Kharagpur, India, and Mie University, Tsu, Japan, in 1997 and 2000, respectively. He is currently a Professor with the Department of Electrical Engineering, Indian Institute of Technology Kharagpur. His research interests include power converters, motor drives, electric vehicles, and renewable energy. He is one of the Associate Editors of the IEEE TRANSACTIONS ON INDUSTRIAL ELECTRONICS and *IEEE Industrial Electronics Magazine* and an Editor of the IEEE TRANSACTIONS ON SUSTAINABLE ENERGY. He is the Founding Editorin- Chief of IE Technology News (ITeN), a Web-only publication for the IES.



Vishal Verma received the B.E. (Electrical) degree from the G. B. Pant University of Agriculture and Technology, Pantnagar, India, in 1989 and the M.Tech. degree and Ph.D from the Indian Institute of Technology (IIT), New Delhi. His field of interest includes power electronics, drives, active filters, and power quality issues. In 1991, he joined as an Assistant Professor in the Department of Electrical Engineering, G. B. Pant University of Agriculture and Technology, and in 2004, he joined Delhi College of Engineering, Delhi. Currently he is a Professor in the department of Electrical Engineering, Delhi Technological university, New Delhi.



Makarand Sudhakar Ballal (M'15-SM'16) received his B.E. in Electrical Engineering from Government College of Engineering, Aurangabad, India in 1993, M. Tech degree in Integrated Power System from Visvesvaraya National Institute of Technology Nagpur, India in 1997 and Ph.D. in Electrical Engineering from R.T.M Nagpur University, Nagpur, India in 2007. From 1997 to 2012, he was with Maharashtra State Electricity Transmission Company Limited, Maharashtra, India. He is currently an associate professor in the Department of Electrical Engineering, Visvesvaraya National Institute of Technology, Nagpur, India. His current research interests includes condition monitoring of electrical machines, power quality, power electronics and drives.

0278-0046 (c) 2016 IEEE. Personal use is permitted, but republication/redistribution requires IEEE permission. See http://www.ieee.org/publications_standards/publications/rights/index.html for more information.